molecules

Metal-Based Drugs

Past, Present and Future

Edited by
Adriana Corina Hangan and Roxana Liana Lucaciu

MDPI

Metal-Based Drugs: Past, Present and Future

Metal-Based Drugs: Past, Present and Future

Editors

Adriana Corina Hangan
Roxana Liana Lucaciu

MDPI ● Basel ● Beijing ● Wuhan ● Barcelona ● Belgrade ● Manchester ● Tokyo ● Cluj ● Tianjin

MDPI

Editors

Adriana Corina Hangan
Inorganic Chemistry
University of Medicine and
Pharmacy, Iuliu-Hațieganu
Cluj-Napoca
Romania

Roxana Liana Lucaciu
Pharmaceutical Biochemistry
and Clinical Laboratory
University of Medicine and
Pharmacy, Iuliu-Hațieganu
Cluj-Napoca
Romania

For citation purposes, cite each article independently as indicated on the article page online and as indicated below:

LastName, A.A.; LastName, B.B.; LastName, C.C. Article Title. *Journal Name* **Year**, *Volume Number*, Page Range.

Contents

About the Editors

Adriana Corina Hangan

Adriana Corina Hangan, PhD, is a Professor of Inorganic Chemistry at the Department of Inorganic Chemistry, Faculty of Pharmacy, University of Medicine and Pharmacy, "Iuliu-Hațieganu", Cluj-Napoca. Her research interests focus on (bio)inorganic chemistry, biological inorganic chemistry, and coordination chemistry. She published several scientific papers, reviews, and book chapters, and she also won several research projects and received various research prizes. She is a member of some academic societies, an editor at *Frontiers in Chemistry* Journal, and an international reviewer for MDPI, Springer, Elsevier, Hindawi, and Wiley Journals.

Roxana Liana Lucaciu

Roxana Liana Lucaciu, PhD, is a Professor of Biochemistry and Clinical laboratory at the Department of Pharmaceutical Biochemistry and Clinical Laboratory, Faculty of Pharmacy, University of Medicine and Pharmacy "Iuliu Hațieganu", Cluj-Napoca. Her research interests focus on anticancer research, drug discovery, metal complexes, natural products, medicinal chemistry, and (clinical) biochemistry. She published several scientific papers, reviews, and book chapters, and she also won several research projects and received various research prizes. She is a member of some academic societies and an international reviewer for MDPI, Springer, Elsevier, Hindawi, and Wiley Journals.

Preface to "Metal-Based Drugs: Past, Present and Future"

The drug discovery process is a challenging, multi-step path towards the identification of potential new medicines. New drugs are needed to prevent a disease, fight a pathology, or diagnose a medical condition when there are currently no suitable medical products. The pharmaceutical potential of metals and their derivatives has been recognized for millennia in very different cultures, and with the advent of modern medicine, several metal-based drugs have been approved for clinical treatment as effective therapeutic tools. Coordination compounds of transition metals such as Pt, Cu, Ru, and Au have proven their effectiveness as diagnostic and/or antiproliferative agents. Nanomedicine is a promising anticancer niche area for developing novel diagnostic and therapeutic strategies. The green synthesis of NPs is a new strategy used for various biomedical applications. This is a cost-effective, eco-friendly, and biocompatible approach for the synthesis of NPs with varied biological properties. Green synthesis uses plants and microbes and allows large-scale production of NPs without extra impurities. Such NPs show enhanced catalytic activity and limit the use of expensive and toxic chemically synthesized NPs. Recently, numerous metal oxide NPs, such as CuO, TiO, and ZnO, have been synthesized through a green approach. Moreover, ZnO NPs have become popular in biomedical molecular recognition and optics applications due to their inexpensive, easy, and safe synthetic protocols. Microbial drug resistance has also become a serious medical problem, causing morbidity and mortality, which has attracted the attention of different researchers working on the discovery of antimicrobial drugs. The broad-spectrum silver-containing antimicrobial agents are well represented by N-heterocyclic carbene silver complexes. Due to their stability, this class of complexes can release the active Ag^+ cations for prolonged periods of time. Furthermore, AgNPs can be good metal-based antibacterial drugs. AgNPs can perform synergistically with classic antibiotics, decreasing the concentrations needed of both agents in the inhibition of bacterial growth, which may be of interest for fighting infections and lowering toxicity against the bacterial hosts. The reprint entitled "Metal-Based Drugs: Past, Present, and Future" covers some recent research and review articles in the field of metal-based drugs used in medicine. By purpose and content, this reprint is addressed to the vast number of life science researchers and health care workers. Our initiative to publish the Special Issue entitled "Metal-Based Drugs: Past, Present, and Future" in *Molecules* Journal was honored by 13 groups totaling 74 scientists from Asia, Europe, North America, and Africa. The number of involved researchers and the geographic distribution of their academic institutions indicate the great interest of the worldwide scientific community in discovering new metal-based drugs that can treat different diseases.

<div align="right">

Adriana Corina Hangan and Roxana Liana Lucaciu
Editors

</div>

Review

Metallo-Drugs in Cancer Therapy: Past, Present and Future

Roxana Liana Lucaciu [1] , Adriana Corina Hangan [2,*] , Bogdan Sevastre [3] and Luminița Simona Oprean [2]

1   Department of Pharmaceutical Biochemistry and Clinical Laboratory, Faculty of Pharmacy, "Iuliu-Hațieganu" University of Medicine and Pharmacy, 400012 Cluj-Napoca, Romania
2   Department of Inorganic Chemistry, Faculty of Pharmacy, "Iuliu-Hațieganu" University of Medicine and Pharmacy, 400012 Cluj-Napoca, Romania
3   Clinic Department, Faculty of Veterinary Madicine, University of Agricultural Science and Veterinary Medicine, 400372 Cluj-Napoca, Romania
*   Correspondence: acomsa6@yahoo.com

Abstract: Cancer treatments which include conventional chemotherapy have not proven very successful in curing human malignancies. The failures of these treatment modalities include inherent resistance, systemic toxicity and severe side effects. Out of 50% patients administrated to chemotherapy, only 5% survive. For these reasons, the identification of new drug designs and therapeutic strategies that could target cancer cells while leaving normal cells unaffected still continues to be a challenge. Despite advances that have led to the development of new therapies, treatment options are still limited for many types of cancers. This review provides an overview of platinum, copper and ruthenium metal based anticancer drugs in clinical trials and in vitro/in vivo studies. Presumably, copper and ruthenium complexes have greater potential than Pt(II) complexes, showing reduced toxicity, a new mechanism of action, a different spectrum of activity and the possibility of non-cross-resistance. We focus the discussion towards past, present and future aspects.

Keywords: cancer; metal complexes; platinum; copper; ruthenium

1. Introduction

Cancer is a frequently lethal ilness caused by an abnormal cell growth with the ability to invade and spread throughout the organism; thus, it has the greatest incidence and mortality rate worldwide [1]. In the year 2020, the US was anticipated to witness 606,520 deaths and 1.8 million new cases [2]. About 4.5 million premature cancer-caused deaths were reported worldwide in 2016 [3]. Based on current data, the International Agency for Research on Cancer (IARC) forecasts that around 13 million cancer-related deaths will occur by 2030 [4].

There are hundreds different types of cancer affecting various organs, tissues, and cells (i.e., breast, bone, blood, colon, liver, lung, etc.) in the form of carcinomas, lymphomas, sarcomas, or leukemia, each one requiring specific treatment [5]. The most common clinical approaches for cancer treatment are chemotherapy, radiation therapy, surgery, hormone therapy, and targeted therapy with anticancer drugs [6].

The need for new and better pharmacological therapies for the treatment of cancer still exists. While there are succesful specific treatment frameworks against some types of cancer, such as anti-hormonal therapy in breast cancer [7], or monoclonal antibodies targeting aberrant receptors, the intrinsic heterogeneity found in cancer forces the use of highly toxic chemotherapeutic regimes [8].

The development of effective antitumor drugs with high selectivity and low toxicity is currently a major challenge for the scientific community. Indeed, the wide range of adverse effects resulting from cancer therapy have an impact on therapeutic adherence and general quality of life for patients and their families [9].

Cisplatin efficacy in the treatment of various cancers places coordinative chemistry among viable antitumor design alternatives. Although highly efficacious, treatment with

cisplatin is still limited by side effects, inherited resistance, or acquired resistance, which has only partially been eliminated by the introduction of new Pt(II) drugs [10].

Other metal complexes containing ions such as copper, gold and zinc chelating agents have received great interest as anticancer agents [11–13]. Recently, the chemistry of ruthenium compounds has been intensively analyzed due to the interest in providing an alternative to cisplatin, because of their promising cytotoxic and potential anticancer properties [14–16].

Recently, there has been growing demand for metal-based compounds in the treatment of cancer. This may be due to the level of in vitro cytotoxic effects exhibited by recently synthesized metal-based compounds and to the fact that ligand substitution and the modification of existing chemical structures have led to the synthesis of a wide range of metal-based compounds, some of which have demonstrated an enhanced cytotoxic and pharmacokinetic profile [17].

The objective of this review is to provide an overview of previous studies on platinum, copper and ruthenium metalo-drugs in cancer therapy, focusing on past, present and future aspects.

2. Chemical and Biochemical Properties of Metallo-Drugs

The therapeutic potential of metal complexes in cancer therapy has attracted a lot of interest, mainly because metals exhibit unique characteristics, such as redox activity, variable coordination modes and reactivity towards the organic substrate. These properties have become an attractive probe in the design of metal complexes that selectively bind to the biomolecular target with a resultant alteration in the cellular mechanism of proliferation.

Several metal-based compounds have been synthesized with promising anticancer properties, some of which are already in use in clinical practice for diagnosis and treatment, while some are undergoing clinical trials [17].

2.1. Platinum Compounds

Platinum drugs attracted attention in cancer treatment once the antineoplastic activity of cisplatin was discovered in the 1960s. Cisplatin was the first metal-based anticancer drug introduced into clinical use. Since then, more platinum derivatives have been synthesised and tested against cancer cells; however, only a few have reached clinical trials. Nowadays, cisplatin and its derivatives are among the most frequently applied antitumor drugs in treating lung, colon, ovary, testicles, bladder, cervix and many more cancers. Cisplatin, carboplatin and oxaliplatin are used as worldwide anticancer drugs, while heptaplatin, nedaplatin and lobaplatin are used as regional anticancer drugs. Their chemical structures are shown in Figure 1 [18,19].
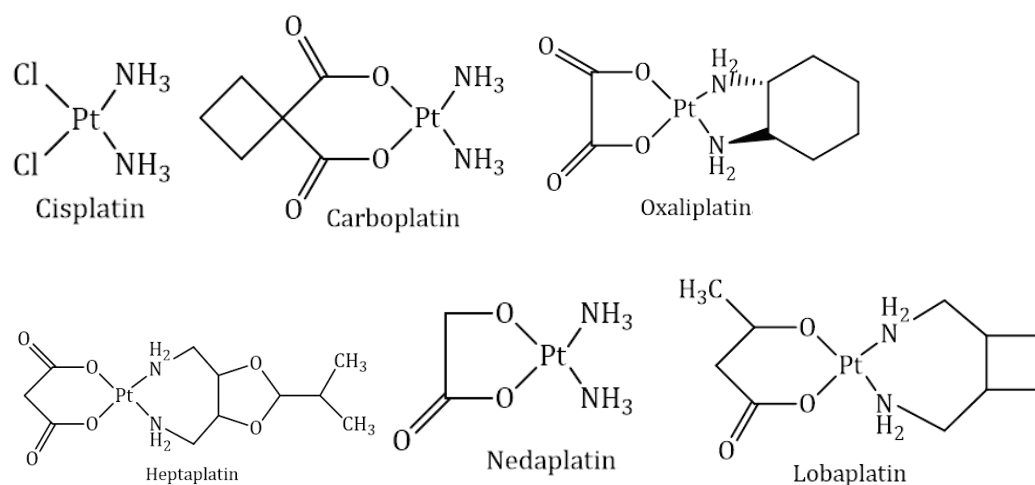
Figure 1. Chemical structures of cisplatin and its derivatives.

The platinum compounds currently used in therapy have common structural characteristics, namely, they are neutral compounds, with planar-square geometry and cis isomerism; they contain two ligands, ammonia molecules or other structures containing -NH$_2$ groups (they do not leave the coordination sphere once the compound enters the tumor cell non-leaving groups) and they contain two anionic ligands that leave the coordination sphere (leaving groups) as a result of the intracellular activation process.

Nevertheless, cisplatin-based therapy has several disadvantages: it is highly toxic and cancer cells can acquire resistance relatively fast. Among the most negative side effects are neurotoxicity, nephrotoxicity and ototoxicity. To overcome these pharmacological limitations, new cisplatin derivatives are considered [19].

Cisplatin (1978):

Structurally, cisplatin has an arrangement whereby platinum ion is bounded to two chloride ions and two amine groups aligned in a square (Figure 1). Amine groups act as the carrier ligands, while chlorides act as the leaving groups. The arrangement of chloride ion is next to each other in cisplatin, which is biologically essential. Interestingly, transplatin, the trans isomer of cisplatin, does not exhibit anticancer activity [18].

The generalized mechanism of action for cisplatin and its derivatives involves four key steps: (1) cellular uptake, (2) aquation/activation, (3) DNA binding and (4) the cellular processing of DNA lesions, leading to apoptosis [20]. The two pathways by which this molecule is most likely to be taken up are passive diffusion through the plasma membrane and active transport, mediated by membrane proteins [21]. Cisplatin becomes activated intracellularly via hydrolysis reactions, where one of the two chloride leaving groups is replaced by a water molecule. Activated aqua platinum species react with nucleophilic sites in DNA, preferentially the nitrogen on position 7 of guanine (G), and form either monofunctional (via one leaving group) or bifunctional adducts (via two leaving groups). Although both inter- and intrastrand cross-links are possible, 1,2-interstrand d(GpG) cross-links (60–65% of all adducts) and d(ApG) cross-links (20–25% of all adducts) are the major products [22]. After the formation of DNA-platinum adducts in the nucleus, the consequent DNA damage is critical to cisplatin cytotoxicity, with several molecular mechanisms. For example, DNA damage initiates the release of cytochrome-c under the regulation of Bcl-2 family proteins, which activates procaspase-9, and then, forms an active apoptosome complex; DNA damage induces the activation of p53 protein, which could regulate cell death by counteracting the anti-apoptotic function of B-cell lymphoma-extra-large (Bcl-xL), the degradation of flice-like inhibitory protein, etc. In addition to DNA damage, it was reported cisplatin could induce reactive oxygen species to trigger cell death [19,23,24].

Cisplatin is accepted worldwide and is generally is used in the treatment of many types of cancer: ovarian, testicular, cervical, bladder, head, neck and lung (particularly the small cell type) [18].

Unfurtunatelly, cisplatin treatment produces several toxicities such as nephrotoxicity, hepatotoxicity, cardiotoxicity, myelosuppression, ototoxicity, gastrotoxicity, allergic reactions and some reproductive toxicities [18,25].

The fact that cisplatin occurs in the process of cell multiplication explains its more pronounced activity against tumor cells, with an accelerated rate of division, compared to that against healthy cells. This fact also explains the toxic effects that this compound has on the hematoforming marrow [18,26].

Mechanism of cisplatin resistance:

Cispaltin resistance happens once there is an insufficient amount of platinum ions to reach the target DNA or an insufficient number of Pt-DNA adducts generated to induce cell death [27].

For small molecular cisplatin, copper transporter-1 (CTR1), as the major plasma-membrane transporter, plays a substantial role in cisplatin influx. It was reported that the loss of CTR1 led to a 2- to 3-fold increase in drug resistance. In addition, efflux proteins such as ATP7A and ATP7B induce a decrease in intracellular cisplatin. Intracellular

cisplatin exposure would trigger the rapid trafficking of ATP7A/B in the trans-Golgi towards cell periphery; during this process, ATP7A/B sequester cisplatin and consequently mediate the efflux of cisplatin [28]. Furthermore, once it has formed the Pt(GS)2 complex with glutathione (GSH), the cisplatin can also be eliminated by a multidrug resistance protein. There is still some cisplatin left inside the cancer cells, which could interact with intracellular thiol, amino, hydroxyl, etc. For example, the thiol-containing molecules, including glutathione/glutathione-S-transferase and metallothioneins, could inactivate and detoxify cytoplasmic cisplatin, leading to cisplatin resistance [29]. Even after Pt-DNA adducts are formed, cellular survival may still occur via several pathways, including DNA repair, the removal of these adducts and tolerance mechanisms, and eventually induce platinum resistance. Nucleotide-excision repair, mismatch repair, base-excision repair and double-strand-break repair are four major DNA repair pathways to remove cisplatin-induced DNA damage. Among them, as the main DNA repair pathway, nucleotide-excision repair involves the recognition and incision of DNA damage, followed by DNA synthesis to replace the excised fragments. Additionally, the core incision reaction requires the protein factors, including ERCC1-XPF, XPA, RPA, XPC-HR23B, TFIIH, XPG, etc. Additionally, mismatch repair is another important pathway to correct single base mispairs or looped intermediates through the identification and excision of the mismatch, and subsequent re-synthesis of the excised strand [22,24].

Carboplatin (1986):

Structurally, carboplatin it is diammine(1,1-cyclobutane dicarboxylato)platinum(II) (Figure 1). Carboplatin was developed in order to reduce the dose-limiting toxicity of cisplatin. It is obtained by replacing two chloride ions of cisplatin with a cyclobutane dicarboxylate ligand. It shows good aqueous solubility and high stability, resulting minimal side effects [18].

The mechanism of action of carboplatin is very similar to that of cisplatin; however, it has lower reactivity due to the bidentate ligand that replaces the chloride anions and that leaves the coordination sphere with a lower speed [24]. As a result of reduced reactivity, the nephrotoxicity, neurotoxicity and ototoxicity after carboplatin treatment are much less pronounced. Additionally, nausea and vomiting are less severe side effects and can be controlled easily. Due to its reduced toxicity profile, carboplatin is suitable for more aggressive high-dose chemotherapy. The myelosuppressive effect is considered to be one of the major drawbacks associated with carboplatin, with thrombocytopenia being more severe than neutropenia and anemia [18].

Carboplatin is accepted worldwide and generally is used in the treatment of ovarian cancer and of small cells lung cancer. It almost replaced cisplatin in combination regimens with paclitaxel for treatment of ovarian cancer [18,30]. The single intermittent bolus or short infusion shedule are more practical than the protracted infusion of cisplatin. Additionally, although carboplatin is more expensive than cispatin, the complete cost of the treatment is cheaper [31].

As in the case of cisplatin, tumor resistance to carboplatin poses a major clinical problem. The mechanisms underlying carboplatin resistance are generally similar to the mechanisms of cisplatin resistance. Unfortunately, cross-resistance ocurs to both platinum drugs [24].

Oxaliplatin (1996)

Oxaliplatin is a platinum complex with a 1,2-diaminocyclohexane ligand and oxalate as a leaving group (Figure 1) and was developed to overcome resistance against cisplatin and carboplatin. Oxaliplatin was initially launched in France in 1996 and was formally available in the countries of Europe in 1999 and in the US in 2002 [32]. It is licensed to be used as a combination therapy with other chemotherapeutic agents in the management of colon cancer and non-small-cell lung cancer [17,33]. In combination with 5-fluorouracil and folinate, oxaliplatin is used as an efficient treatment of adjuvant and metastatic colorectal cancer and is intrinsically insensitive to cisplatin. The bidentate oxalate significantly

reduces the reactivity of oxaliplatin and thereby limits the toxic side effects to peripheral sensory neuropathy [34]. The diaminocyclohexane ligand is more lipophilic, increasing the passive uptake of oxaliplatin compared to cisplatin and carboplatin. Higher lipophilicity may also be a reason why oxaliplatin also employs some different routes of cellular entry to cisplatin and carboplatin. The organic cation transporters OCT1 and OCT2 have been implicated in mediating oxaliplatin uptake, as their overexpression significantly increases the cellular accumulation of oxaliplatin, but not cisplatin or carboplatin. Colorectal cancer cells overexpress organic cation transporters, which may explain the efficacy of oxaliplatin in this particular type of cancer [35]. The clinical relevance of these transporters remains, however, unclear. Regarding copper transporter-1 (CTR1), evidence that the transporter is involved in oxaliplatin uptake is not very strong, as in the case of cisplatin; nevertheless, the acquisition of oxaliplatin resistance was reported to be accompanied by CTR1 downregulation. Additionally, reduced expression of the $\beta 1$-subunit of Na^+, K^+-ATPase was found in some oxaliplatin-resistant cells. Copper efflux transporters appear to play an important role in oxaliplatin sensitivity, too. Low levels of ATP7B in colorectal cancer patients were associated with a favorable outcome [36]. Similar to cisplatin, oxaliplatin mainly forms crosslinks on the adjacent guanine bases or between guanine and adenine, but to a lower extent. However, oxaliplatin-DNA adducts are more efficient in the inhibition of DNA synthesis. Due to the bulkier diaminocyclohexane ligand, oxaliplatin induces different conformational distortion on DNA. The bulkiness and lipophilicity of diaminocyclohexane are considered responsible for the differential processing of oxaliplatin-DNA adducts. The latter are not recognized by mismatch repair proteins. Interestingly, it does not lead to decreased cytotoxicity but makes oxaliplatin antitumor-activity mismatch repair proteins independent. Additionally, an increase in replicative bypass, i.e., DNA synthesis bypassing platinum-DNA adducts, was reported not to correlate with cytotoxicity of oxaliplatin. All these factors result in different activity spectra of oxaliplatin compared to cisplatin or carboplatin [24].

The diaminocyclohexane ligand plays a major role in cytotoxicity and protects oxaliplatin against cross-resistance with cisplatin [32]. Major side effects of oxaliplatin include nausea, numbness, low blood cell counts, allergic reactions and diarrhea [37]. It has a better safety profile than cisplatin, and is used for patients who cannot tolerate cisplatin [32].

Nedaplatin (1995)

Structurally, nedaplatin is a diammine-glycolatoplatinum compound (Figure 1) and is significantly more soluble in water compared to cisplatin. Like cisplatin, nedaplatin also has two amines: the carrier ligands and a glycolate containing a five-membered ring which is bonded to the platinum ion. It interacts with the nucleophilic groups of DNA, causing cell apoptosis [18].

It was approved only in Japan to treat head, neck, testicular, lung, esophageal, ovarian and cervical cancers [31,38].

A randomised clinical trial compared nedaplatin to cisplatin, both in combination with vindesine. Nedaplatin showed no advantage over cisplatin in objective response and overall survival, but was less toxic. More thrombocytopenia was observed, but there was less leucopenia, nephrotoxicity and gastrointestinal toxicity [31]. The drug is said to have a better safety profile than cisplatin and similar efficacy [17,18,39]. Compared to carboplatin, it is more toxic. Unfortunately, nedaplatin is cross-resistant with cisplatin [31].

Heptaplatin (1999)

Structurally, heptaplatin consists of malonate as a chelating leaving group and of 2-(1-methylethyl)-1,3-dioxolane-4, 5-dimethanamine as a chelating group (Figure 1). It was demonstrated to be stable in solution. Heptaplatin is currently applied in the Republic of Korea for the treatment of gastric cancer. Its antitumoral mechanism of action is assumed to be similar to that of cisplatin [18]. Heptaplatin was demonstrated to have fewer and milder side effects than cisplatin and to retain cytotoxic activity in cisplatin-resistant cell lines. A Phase III study showed that heptaplatin's combination with 5-fluorouracil is comparable to

cisplatin/5-fluorouracil regimen with less severe hematological side effects [34]. Studies regarding the use of heptaplatin as monotherapy or in combination with other antitumor agents continue [18,24,40].

Lobaplatin (2010)

Structurally, lobaplatin is represented as 1,2-diammino-l-methyl-cyclobutane-platinum(II)-lactate (Figure 1). Lobaplatin is approved in China for the therapy of metastatic breast cancer, chronic myelogenous leukemia and small cell lung cancer [34].

The antitumor activities of this compound span through the human lung, and ovarian and gastric cancer xenografts [32]. A phase I clinical trial of dose escalation of lobaplatin in combination with fixed-dose docetaxel in the treatment of human solid tumor was established. In this study, the maximum tolerable dose of lobaplatin when combined with docetaxel for the treatment of solid tumor, known to have progressed after chemotherapy, was established. Positive results from the phase I trial prompted the researchers to recommend the same dosage for the phase II clinical trial [18,41].

It has non-cross-resistance to cisplatin, particularly human sensitive cancer cells [17,21]. Concerning toxicity, its presence reduced nephrotoxicity, neurotoxicity and ototoxicity, but the hematotoxic effects are significant. Its dose-limiting toxicity is thrombocytopenia [34].

2.2. Copper Compounds

The development of cisplatin as one of the most powerful anticancer drugs has opened new fields in the design of less toxic and more effective chemotherapy drugs based on the use of essential metals. It has been proposed that endogenous metals might be less toxic to normal cells than platinum, silver, or gold. In this regard, copper-based complexes present an attractive chemotherapy drug option [42,43].

The physiological concentration of copper in the body is ensured by several mechanisms involving ceruloplasmin and albumin in the liver, as well as copper transport proteins. However, an excess of copper can be toxic to normal cells due to the generation of reactive oxygen species (ROS) or reactive nitrogen species (RNS) [44,45].

Unlike normal cells, tumor cells have reduced vascularity, and therefore, a low oxygen level, which explains the invasion, metastasis and activation of an anaerobic process known as the Warburg effect [46] As a result, tumor hypoxia can be exploited to develop new prodrugs that become active in the reducing environment of cancer cells [47]. In this sense, copper ions become very attractive because they can exist in two different oxidation states in cells. The presence of hypoxia in cancer cells causes the reduction of Cu(II) ions to Cu(I), and thus, allows copper compounds to act as targets at the tumor level. The Cu(I) ion, once formed, catalyzes the production of ROS and RNS, which will ultimately induce pro-apoptotic oxidative stress [48].

In the last two decades, copper coordination compounds have consolidated their position in the design of metallo-drugs, as evidenced by the increase in the number of compounds that have demonstrated their efficacy following in vitro or in vivo testing. Initially, it was assumed that most Cu(II) coordination compounds have a similar mechanism of action to Pt(II) compounds, considering DNA as the main biological target. The newly synthetized complexes were structurally and physico-chemically characterized; then, they were tested via in vitro screening on human cancer cell lines and/or interaction studies with the DNA molecule. Particular attention has been paid to Cu(II) complexes including N,N-diimine ligands (and other extended aromatic planar systems contained in thiosemicarbazone or Schiff base assemblies) due to their binding/intercalating action in the DNA structure. Although damage to the DNA molecule is the primary mechanism by which these copper complexes (and many other conventional chemotherapeutic agents) act, the antiproliferative process does not always guarantee selective cytotoxicity to cancer cells. That is why the studies were directed towards the discovery of compounds with other mechanisms of action, at the level of cellular components [49].

The main mechanisms underlying the antitumor action of Cu(II) complexes are:

- Intercalation—the insertion of a copper complex between two pairs of adjacent bases through van der Waals bonds;
- Interaction with the nucleotides in the chains at the "small cavity" level ("minor groove") of the DNA molecule;

The oxidative mechanism—the production of ROS or RNS species in the immediate neighborhood of the DNA molecule. Electron spin resonance demonstrated mainly the formation of hydroxyl radicals in the process of reducing the Cu(II) ion to Cu(I) in the presence of reducing agents (e.g., H_2O_2). These radicals, along with other ROS, are produced by a Fenton or Haber-Weiss type reaction as follows:

$$LCu\,(II) + H_2O_2 \rightarrow LCu\,(I) + \bullet OOH + H^+$$

$$LCu\,(I) + H_2O_2 \rightarrow LCu\,(II) + \bullet OH + OH$$

where L, represents an organic ligand.

- In the hydrolytic mechanism, the interactions of Cu(II) ions with the phosphate anion from the nucleotides cause the breaking of the phosphodiester bonds and the destruction of nucleic acid molecules;
- The inhibition of topoisomerase I or II, with a role in DNA replication and transcription;
- Proteasome inhibition (proteasomes represent multiprotein complexes located both in the nucleus and in the cytoplasm, which selectively degrades and recycles intracellular proteins) [50–52].

2.3. Ruthenium Compounds

The chemical element ruthenium, [44]Ru, has properties that recommend it as a complex generator in coordinative compounds, with biomedical implications:

- The ability to form labile complexes that can participate in a slow exchange of ligands with molecules in biological environments. Ru(II) and Ru(III) complexes have ligand-exchange kinetics similar to those of Pt(II) complexes. It was demonstrated that the Ru(II) ion has a greater preference for ligands containing S donor atoms, such as glutathione and methionine, and a lower preference for O or N donor ligands [53].
- The ability to have several oxidation states: Ru(II), Ru(III) and Ru(IV); their oxidation or reduction processes are possible under physiological conditions. Ruthenium is unique in the fact that its oxidation states, II, III and IV, are all accessible under physiological conditions. In these oxidation states, the metal ion which generates the complex is hexacoordinated, and the complex geometry is octahedral. Due to this orientation of the ligands, the formation of "intrastand cross-linking" bonds with residues of nitrogenous bases belonging to the same DNA chain encountered in the case of platinum complexes is very low. The bonds that are formed between these Ru complexes and DNA molecules are of the "interstand cross-linking" type, with residues of nitrogenous bases from two different chains. However, this is not the main mechanism of antitumor action. The altered metabolism of cancer cells causes, at their level, hypoxia, a high level of glutathione and a lower pH, which provides the premise for an environment with reducing properties. To increase the selectivity of ruthenium complexes against cancer cells and to reduce, as much as possible, the toxic effects on normal cells, the redox potential of ruthenium can be modified once it enters the body. For example, these agents can be administered as relatively inert Ru(III) complexes (prodrugs), which are then activated by reduction inside the malignant cell [53,54].
- The ability to replace Fe(III) ions transported in the body by various plasma proteins (for example, transferrin).

Due to the structural similarities between Fe(III) and Ru(III) ions, the latter can replace the Fe(III) ion in its site in serum transferrin and albumin (proteins that solubilize and transport iron in plasma). The transport of ruthenium complexes in the blood is an aspect that has attracted the attention of the scientific community since the first studies. The similar

chemical behavior of Ru(III) to that of Fe(III) explains the interest in ruthenium compounds for serum proteins, especially for transferrin. This explains the fact that physiological iron transport mechanisms (the so-called "transferrin pathway") could be exploited by ruthenium species as a smart way to enter cells, according to the "Trojan horse" strategy. Because rapidly dividing cells (including cancer cells) have a greater requirement for iron, there is an increase in the number of transferrin receptors on the cell surface, resulting in more iron-loaded transferrin in the blood circulation. Thus, in vivo studies have shown that there is a 2- to 12-fold increase in the concentration of ruthenium in cancer cells compared to healthy cells. Since ruthenium complexes preferentially target tumor cells, its systemic toxicity is expected to be minimized. Furthermore, it has been shown that ruthenium is transported into cells via both transferrin-dependent pathways and other plasma protein-independent mechanisms [53,55].

In the last 30 years, a large number of ruthenium complexes with octahedral geometry characteristic of Ru(III) and Ru(II) ions, have been synthesized and tested for potential antitumor activity. The initial studies started from the premise that ruthenium will form coordinating compounds that will manifest their antitumor action through direct interaction with the DNA molecule, analogously with platinum compounds. It was later shown that there are significant differences between the two types of antitumor agents in terms of their mechanism of action [17,53].

First, ruthenium complexes seem to accumulate preferentially in neoplastic cells, not in normal ones, using transferrin as a transporter to enter into the tumor cell. The Ru(III) complex remains relatively inactive until it reaches the interior of the target cell where it binds to the transferrin receptor. Here, the reduction of the Ru(III) ion to a Ru(II) ion and an exchange of ligands with molecules from the biological environment take place. The low oxygen content and the more acidic pH in tumor cells favors reduction to the more reactive Ru(II) ion. This process was named "activation by reduction" and results in selective antitumor activity on hypoxic tumors resistant to chemotherapy and radiotherapy. On the other hand, some Ru(III) complexes have shown greater efficiency against metastases than against primary tumors. This antimetastatic effect is explained by inhibition of the detachment of tumor cells, and therefore, the prevention of the formation of a new growth substrate. Given these properties, ruthenium complexes show different patterns of antitumor activity and toxicity to platinum complexes [56,57].

3. New Metallo-Drugs in Clinical Trials

The literature abounds with data on new metal complexes with antitumor activity, but few of them have reached preclinical and clinical trials, and very few have passed them. In this review, we stopped only on platinum, copper and ruthenium complexes, presenting only those that have reached clinical trials in different phases, or that have materialized into metallo-drugs [58].

3.1. New Platinum Compounds

While cisplatin is used widely in the clinic to treat many tumour types, clinical utility is limited by two major factors: (i) drug resistance, either intrinsic or acquired, and (ii) the principal dose-limiting side effects of nephrotoxicity and neurotoxicity. Unfortunately, although the initial tumour response to cisplatin in many tumours may be high, most patients will nevertheless relapse and die of their disease.

3.1.1. BBR 3464

BBR 3464 is a charged (+4), triplatinum complex whose structure derives from that of trans-diammindichloroplatinum(II), in which the bridges between the Pt(II) ions are represented by 1,6-diaminohexane (Figure 2).
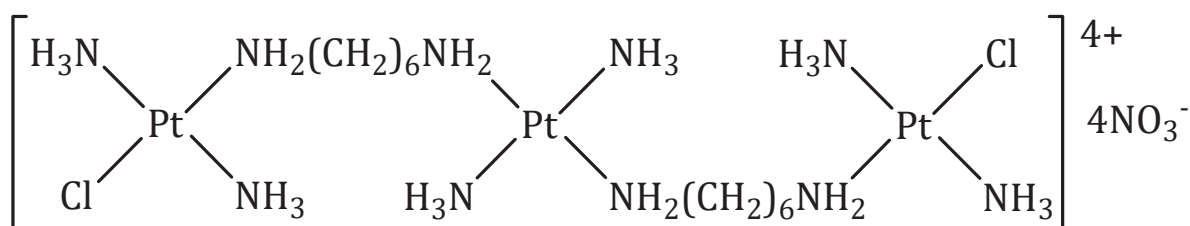
$$\left[\begin{array}{c} H_3N \diagdown \underset{\diagup}{Pt} \diagup NH_2(CH_2)_6NH_2 \diagdown \underset{\diagup}{Pt} \diagup NH_3 \quad H_3N \diagdown \underset{\diagup}{Pt} \diagdown Cl \\ Cl \quad\quad NH_3 \quad H_3N \quad NH_2(CH_2)_6NH_2 \quad NH_3 \end{array} \right]^{4+} \quad 4NO_3^-$$

Figure 2. Chemical structure of BBR 3464.

BBR 3464 has notable preclinical characteristics. It is approximately fourty to eighty fold more potent than cisplatin on a molar-dose basis and is active in vivo in cisplatin-sensitive and -resistant tumors, as well as in insensitive xenografts. Additionally, BBR 3464 was shown to be more active than cisplatin in *p53* mutant tumors. The characteristic DNA-interaction of BBR 3464 results in the inhibition of DNA replication and RNA transcription, with triggering of the apoptotic cascade leading to cell death. Unlike cisplatin, BBR 3464 leads to prolonged tumor-growth inhibition after the discontinuation of treatment, suggesting that the two drugs could differ significantly in their ability to perturb the cell cycle. As a distinctive feature, BBR 3464 achieves a high proportion of interstrand and intrastrand DNA adducts in contrast to the effects of cisplatin, which predominantly produces the latter type of DNA damage. While cisplatin-damaged DNA is recognized by HMG proteins, the conformational changes resulting from BBR 3464 interaction with DNA are not. This observation might explain the resistance to cisplatin, and the lack of resistance to BBR 3464 in tumors expressing mutations of the *p53* oncosuppressor gene [59].

In vitro and in vivo studies have shown that BBR 3464 manifests its cytotoxic properties at concentrations 10 times lower than cisplatin and is effective on cell lines resistant to it [60].

Preclinical toxicology in mice, rats and dogs treated on a single or five-timed-daily refracted schedule showed that target organs for BBR 3464 toxicity was bone marrow, resulting in leukopenia, while renal tubulopathy was only minimal or slight. A slight pulmonary interstitial reaction, with fibroblast proliferation and inflammatory infiltration, was observed in mice and dogs. This unusual effect was more extensive after intravenous bolus, given as a single or weekly dose, than after slow infusion or a bolus given every two weeks. The schedule dependency of the lung toxicity prompted the clinical evaluation of a five-times-daily refracted schedule in addition to a single dose schedule.

Phase I clinical studies established the value of the maximum tolerated dose as $0.12 \text{ mg} \cdot \text{m}^{-2} \cdot \text{day}^{-1}$ at a daily administration rate, for 5 days. The toxicity of this compound is its main disadvantage. In the case of increasing the dose to $0.17 \text{ mg} \cdot \text{m}^{-2} \cdot \text{day}^{-1}$, severe myelosuppression and gastrointestinal toxicity were recorded. On the other hand, no nephrotoxic effects were reported [59].

Phase II studies performed on patients with non-small cell lung carcinomas and ovarian tumors in advanced stages highlight the increased efficiency of BBR 3464 compared to therapeutic combinations of platinum compounds with taxanes, but also a lack of activity of the compound against gastric tumors and cancer small cell lung [61–63]. In the case of a phase II study regarding the effectiveness of this compound in the treatment of pancreatic cancer, although the completion deadline has been exceeded, the results have not yet been made public [64].

3.1.2. Satraplatin

Satraplatin (codenamed JM216), structurally, is [bis-(acetato)-ammine dichloro-(cyclohexyl-amine) platinum(IV) (Figure 3a) and was the first orally active platinum agent to be reported.
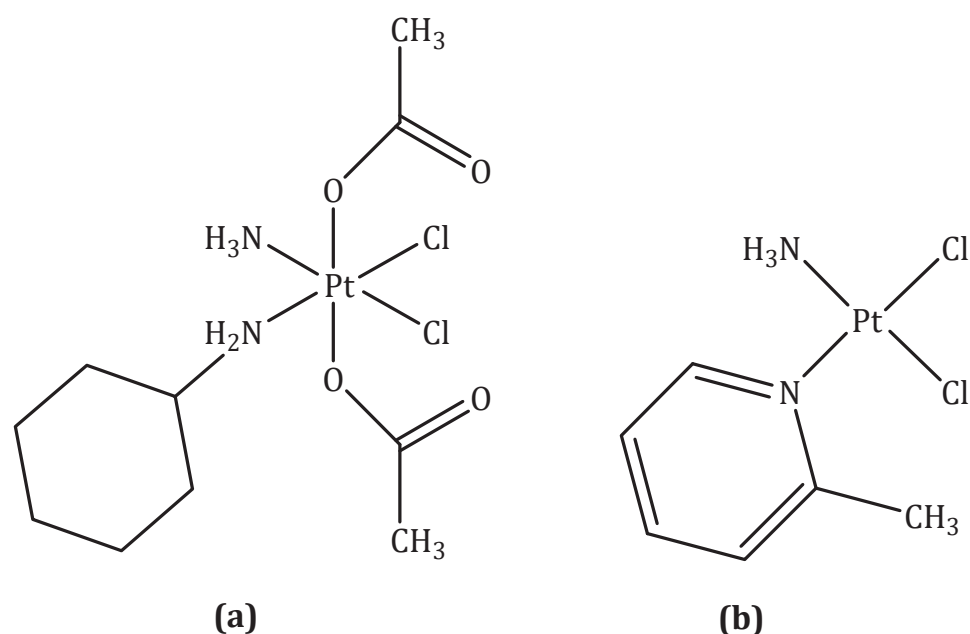
Figure 3. Chemical structure of: (**a**) Satraplatin; (**b**) Picoplatin.

Satraplatin was rationally designed such that the lipophilicity and stability were suitable for oral administration. The half-life of reduction of satraplatin by 5 mM ascorbate takes 50 min, which is an adequate time for absorption by the gastrointestinal mucosa in the platinum(IV) form once ingested [21]. Upon entry into the bloodstream, satraplatin undergoes reduction to give six distinct platinum(II) species. Ammine dichloro-(cyclohexyl-amine)platinum(II), derived from the loss of two acetate ligands, is the major metabolite and also exhibits the most potent anticancer activity [65].

Like cisplatin, satraplatin acts through the formation DNA cross-links, DNA distortion, and subsequent inhibition of DNA transcription and replication. The ability of satraplatin to overcome cisplatin resistance is thought to arise from the asymmetric nature of the DNA lesions, which unlike cisplatin adducts, can evade recognition by DNA repair proteins [21].

In preclinical studies, satraplatin exhibited a better toxicity profile than cisplatin, and showed activity in cisplatin-resistant human tumor cell lines [66].

In vivo studies in mice bearing murine ADJ/PC6 plasmacytoma, which we note was the same model used to identify carboplatin as a viable alternative to cisplatin, showed satraplatin to exhibit markedly superior antitumor efficacy relative to cisplatin and carboplatin. Also, in four ovarian carcinoma xenograft models of varying cisplatin and carboplatin resistance, satraplatin displayed activity similar to that of cisplatin and carboplatin, which were administered intravenously. In rodents, the dose-limiting toxicity of satraplatin was myelosuppression.

We emphasize that less hepatotoxicity and fewer gastrointestinal effects were observed as compared to treatment with cisplatin or carboplatin [21].

In the first Phase I study, satraplatin was administered at doses ranging from 60–170 mg·m^{-2} as a single oral dose. The pharmacokinetics data suggested that gastrointestinal absorption was being saturated, preventing the maximum tolerated dose from being reached. To improve absorption into the bloodstream, patients were treated on a five-times daily schedule with lower doses (30–140 mg·m^{-2}) [67]. The dose-limiting toxicities were thrombocytopenia and neutropenia and in about 10% of the patients treated, nausea, vomiting, and diarrhea were also observed. Based on the Phase I studies, doses of 100–120 and 45–50 mg·m^{-2} were recommended for repeated daily dosing for 5 and 14 days, respectively, in Phase II/III trials [21].

Several Phase II/III trials have been carried out to determine the efficacy of satraplatin. A Phase II study on metastatic NSCLC patients, in which satraplatin was administered as

single daily 120 mg·m^{-2} doses for 5 days on 3 week cycles, failed to provide any objective responses. Nevertheless, 46% of the patients were noted to express some palliation. A more advanced Phase II study on patients with small-cell lung cancer and squamous cell head and neck cancer, with escalated doses of satraplatin, produced a response rate of 38%, similar to that observed with cisplatin. Furthermore, this study found no signs of severe neurotoxicity or nephrotoxicity. Other Phase II studies in patients with relapsed ovarian cancer and advanced/recurrent squamous cancer of the cervix produced clinically beneficial or partial rates of response in several patients. The former study noted that the most common form of toxicity were neutropenia and thrombocytopenia [67]. Satraplatin has also been heavily studied as a potential second-line chemotherapeutic for patients with metastatic castration-resistant prostate cancer. Treatment with 120 mg·m^{-2} satraplatin daily for 5 days, used in patients with castration-resistent prostate cancer who had undergone front-line hormone therapy, resulted in 62% of patients expressing stable disease or partial response [68,69]. Currently, a phase I clinical trial is underway regarding the efficacy of satraplatin in the treatment of prostate cancer without metastases [64].

3.1.3. Picoplatin

Picoplatin (codenamed AMD473 or ZD0473), structurally, is diammine dichloro-(2-methylpiridine) platinum(II) (Figure 3b). It was primarily designed to overcome one of the known mechanisms of platinum resistance-detoxification by intracellular thiols—through the introduction of a bulky methylpyridine ring to provide steric hindrance to direct interaction with platinum [58,70].

Preclinical evaluation of picoplatin confirmed that this drug was also able to overcome platinum complex resistance in cell lines with high levels of glutathione (GSH) [71]. In studies with human ovarian cell lines, it has been shown that increasing levels of reduced GSH are associated with increasing platinum resistance. In addition, lower levels of glutathione S-transferase (GST) activity have been shown to be associated with enhanced clinical response to platinum-based chemotherapy in head and neck cancer [72]. Additionally, picoplatin was able to overcome resistance because of decreased cellular uptake of the drug in some cell lines or enhanced DNA repair/increased tolerance of platinum adducts in others. Picoplatin forms interstrand cross-links, but does so at a rate intermediate to that of cisplatin and carboplatin, because of its reduced reactivity relative to cisplatin. Using a Taq polymerase stop assay to identify the site of DNA adducts, a novel pattern of DNA binding was identified in pBR322 DNA after incubation with 10 and 100 mM picoplatin for 2 h [71]. This finding may also, in part, account for the observed capability of picoplatin to circumvent adduct tolerance and DNA-repair mechanisms associated with resistance to cisplatin.

Preclinical pharmacology studies in mice have demonstrated that the maximum tolerated dose is 45 mg·kg^{-1}, given as a single intraperitoneal administration, with the dose-limiting toxicity being myelosuppression. Owing to the limited aqueous solubility of picoplatin, preclinical toxicology studies were conducted by intraperitoneal injection following a pharmacokinetic demonstration of the equivalent bioavailability of intraperitoneal and intravenous administration. No renal toxicity was observed. Antitumour activity was noted in several tumour models including human ovarian carcinoma xenografts with acquired resistance to cisplatin and carboplatin. Picoplatin showed an improved antitumour effect compared with cisplatin and satraplatin against the CH1cisR xenograft (34 days growth delay vs 10.4 and 3.5 days, respectively). The antitumour activity was similar when picoplatin was given daily at 60 mg·kg^{-1} for 5 days every week for 4 weeks or by weekly administration (300 mg·kg^{-1} every 7 days for 4 weeks) [73].

Results from preclinical studies have highlighted the effectiveness of picoplatin against some types of ovarian cancer, mesothelioma, small cell lung cancer and non-small cell lung carcinomas resistant to cisplatin and oxaliplatin. It is interesting to mention that this compound manages to avoid all three major methods of resistance to cisplatin (deficient absorption, inactivation by thiol compounds and DNA repair mechanisms) [70].

On the basis of the preclinical antitumour activity seen with picoplatin, especially in models with acquired platinum resistance, and its lack of nonhematological toxicity, the drug was taken into clinical development.

A Phase I trial was carry out at the Royal Marsden Hospital under the auspices of the Cancer Research UK Phase I/II Committee. The initial schedule chosen was a short intravenous infusion given once every 3 weeks. A pharmacokinetically guided dose-escalation scheme was used, for several reasons. Firstly, there is no evidence of metabolism of picoplatin in vivo, and thus, the free platinum AUC (area under the concentration vs. time curve) should reflect the biologically important species in both man and mouse. Secondly, previous experience with cisplatin and carboplatin has demonstrated the close relation between the AUC at maximum tolerated dose in mice and humans. It was hoped that this approach would reduce the number of dose escalations required to reach the maximum tolerated dose [74].

Following phase I studies, the maximum tolerated dose value was established as 150 mg·m^{-2} and the picoplatin administration regimen as doses of 120 mg·m^{-2}, intravenously, once every 3 weeks, with the possibility of increasing the dose for patients who had not previously undergone antitumor treatment. The limiting toxic effects were neutropenia and thrombocytopenia, whereas alopecia, neurotoxicity and nephrotoxicity were not reported. Other adverse effects included nausea and vomiting, anorexia and metallic taste [58].

Phase II clinical trials in patients suffering from various types of lung tumors resulted in a response rate of 15.4% in small cell lung cancer resistant to other platinum compounds [75]. Other phase II studies have highlighted the fact that picoplatin is also active on ovarian tumors sensitive and resistant to other platinum compounds, bringing a benefit in terms of survival rate and the limitation of disease progression [76]. Similar results have been reported in the case of patients with mesothelioma and metastatic breast cancer; for approximately 50% of patients, a stop was found in the progression of the disease [77,78]. In the case of some phase II studies regarding the effectiveness of picoplatin in the treatment of colorectal and prostate cancer refractory to hormone therapy, although the completion deadline has been exceeded, the results have not yet been made public [64].

Only one phase III study was undertaken targeting small cell lung cancer. The study showed that patients who did not respond to treatment up to that point or who had experienced rapid disease progression benefited from an extension of life after treatment with picoplatin [32].

3.1.4. Ormaplatin

Ormaplatin (also known as tetraplatin, codenamed NSC 363812), structurally, is tetrachloro (1,2-diaminocyclohexane) platinum(IV) (Figure 4a).

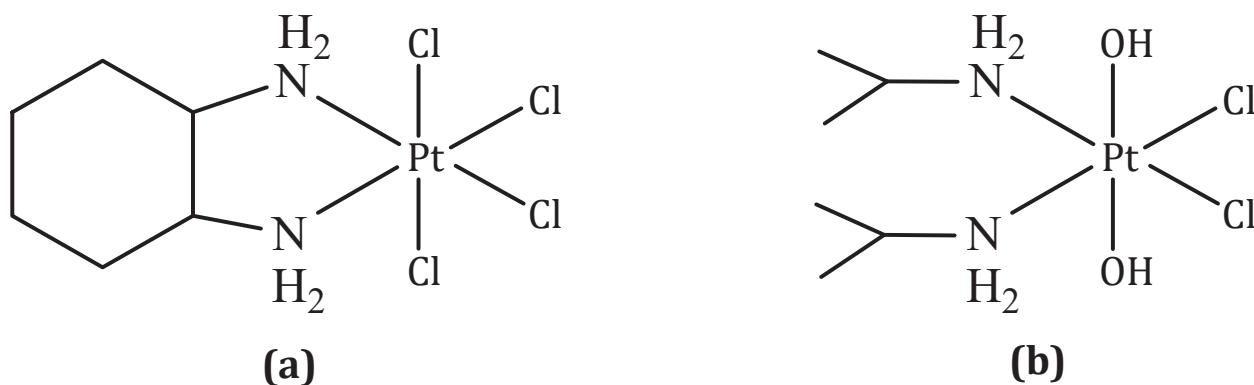**Figure 4.** Chemical structure of: (**a**) Ormaplatin; (**b**) Iproplatin.

Ormaplatin is rapidly reduced to the corresponding dichloro (1,2-diaminocyclohexane) platinum(II) form in tissue culture medium (t$_{1/2}$ = 5–15 min) and undiluted rat plasma

($t_{1/2}$ = 3 s) [21]. The active platinum(II) species is similar to oxaliplatin. Ormaplatin displayed in vitro and in vivo activity against some cisplatin-resistant cancers and was taken forward to clinical trials [79]. Various doses, dose patterns, and modes of administration (intravenous and intraperitoneal) were investigated in six Phase I clinical trials; however, no Phase II clinical trials have been planned [80,81]. Ormaplatin was found to induce severe neurotoxicity at the maximum tolerated dose, and in some cases, a safe maximum tolerated dose could not be determined. Toxicity is thought to arise from fast reduction to the active platinum(II) form as a consequence of the axial chloride ligands [21].

3.1.5. Iproplatin

Iproplatin (also known as JM9 or CHIP), structurally, is dichloro-dihydroxy-bis (iso-propylamine) platinum(IV) (Figure 4b). Iproplatin is structurally similar to ormaplatin in the sense that it contains two equatorial chloride groups which are cis to each other [21].

Carbon-14 labelling studies showed that the mechanism of action of iproplatin involves the reduction of the platinum(IV) center to platinum(II) followed by covalent bond formation with DNA. Iproplatin is less prone to reduction and deactivation by biological reducing agents than ormaplatin, presumably because of the presence of hydroxide axial ligands, allowing less hindered distribution throughout the body. Another advantage of iproplatin is its very high water solubility (44.1 mM), which allows simpler formulation and administration [82].

Iproplatin is one of the most clinically studied platinum agents to have not been approved for marketing, with 38 clinical trials ranging from Phase I to III having been concluded. Phase I studies revealed that the dose-limiting toxic effect was myelosuppression, which, in one study involving children, was partly correlated with the amount of prior therapy chemo- and radiotherapy received. The same study recommended intravenous doses of 324 mg·m^{-2} over 2 h every 3–4 weeks for Phase II trials in children. Other studies proposed doses of 45–65 mg·m^{-2} and 95 mg·m^{-2} for patients treated on a five-times-daily schedule every three weeks and a four-times-weekly schedule with two-week break periods, respectively [83]. Phase II trials were carried out in patients with a variety of different cancer types, and Phase III trials were conducted in ovarian cancer patients and those with metastatic epidermoid carcinoma of the head and neck [84,85]. The ultimate conclusion of these studies was that iproplatin did not exhibit overall effectiveness that surpassed that of cisplatin or carboplatin and no further trials were undertaken [21].

3.2. New Copper Compounds

The differential response of normal and tumor cells exposed to Cu(II) ions is the starting point for obtaining new compounds with antineoplastic properties. Many of the copper complexes are active against tumor cell lines resistant to cisplatin and analogous compounds, and exhibit lower toxicity than established platinum derivatives as antitumor agents.

Preclinical and clinical studies provide encouraging evidence to support the therapeutic potential of copper complexes despite their high toxicity. Due to the promising results obtained from in vitro and in vivo testing, some of these complexes have reached the clinical testing phase. In this context, Cu(I) and Cu(II) complexes present encouraging perspectives [86].

3.2.1. Elesclomol

Elesclomol (codenamed STA-4783), structurally, is N-malonil-bis(N-metil-N-tiobenzoyl hidrazide). The structural formulas of elesclomol and its Cu(II) complex are shown in Figure 5.
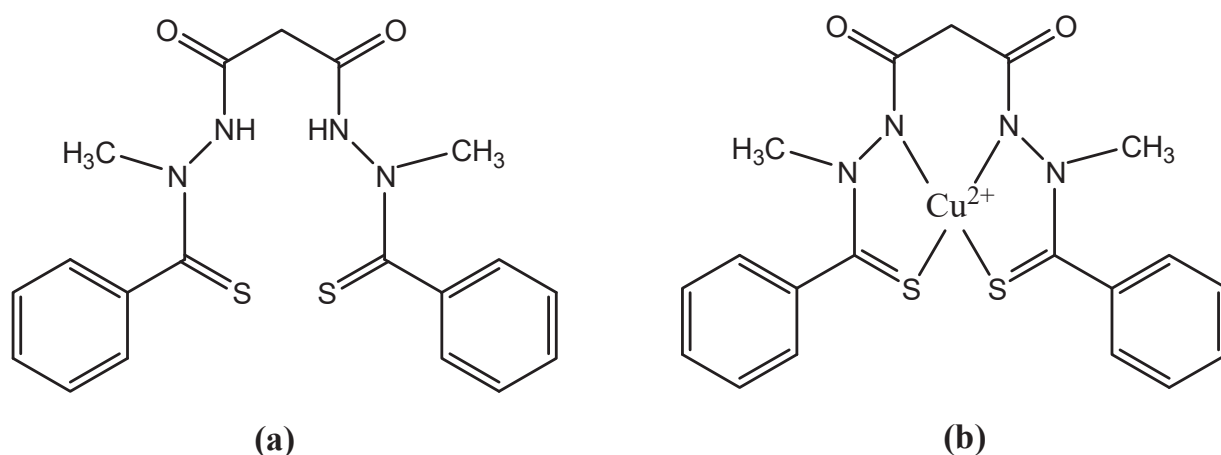
(a)   **(b)**

Figure 5. Chemical structure of: (**a**) Elesclomol; (**b**) Complex Cu(II)-Elesclomol.

Elesclomol is an injectable, small molecule. It has been developed as a sodium salt formulation for single-agent use or for combination use with other anti-cancer drugs. The free acid form of elesclomol is the active ingredient in both elesclomol and sodium elesclomol. While in the bloodstream, elesclomol binds to copper (II) ions present in the serum. Cancer cells efficiently take up this complex, unlike free elesclomol. Once inside the cell, the copper in the complex undergoes a redox reaction whereby Cu(II) is reduced to Cu(I). This reaction, which is mediated by elesclomol, creates ROS and oxidative stress in the cell. The anti-cancer activity of elesclomol is attributed to its ability to directly increase this oxidative stress [87]. Cancer cells already have an elevated level of oxidative stress relative to most normal cells. It was hypothesized that the further increase in ROS induced by elesclomol would exceed a critical threshold in cancer cells, enhancing the sensitivity to traditional cytotoxic chemotherapeutic agents and triggering tumor cell death while sparing most normal cells [88].

Elesclomol exerts its activity by disrupting the metabolism of mitochondria in cancer cells. This activity requires the presence of oxygen that results in energy metabolism being driven primarily through oxidative phosphorylation in mitochondria. Under hypoxic conditions, energy metabolism occurs through glycolysis in cytoplasm, rather than in mitochondria. Under hypoxic conditions, often associated with elevated lactate dehydrogenase (LDH) levels, elesclomol's activity is diminished. These observations are consistent with findings in a phase 3 metastatic melanoma study, where elesclomol activity was found only in subjects with normal baseline LDH levels [87–89].

Elesclomol and Cu(II)-elesclomol are both highly active in vitro and typically inhibit tumor cell growth at low (nanomolar) concentrations. In preclinical models, elesclomol has demonstrated synergistic anti-tumor activity with both paclitaxel and docetaxel, as well as single-agent activity [88]. Elesclomol showed antitumor activity against a broad range of cancer cell types and substantially enhanced the efficacy of chemotherapeutic agents such as paclitaxel in human tumor xenograft models [90].

In a phase I clinical trial, in combination with paclitaxel in patients with refractory solid tumors, elesclomol was well tolerated, with a toxicity profile similar to that observed with single agent paclitaxel [91].

In a double-blinded, randomized, controlled phase II clinical trial in 81 patients with stage IV metastatic melanoma, elesclomol, in combination with paclitaxel doubled median progression-free survival compared with paclitaxel alone. Cutaneous melanoma is a highly malignant tumor derived from melanocytes, the pigment-producing cells in the epidermis of the skin. If diagnosed and surgically removed while localized in the outermost skin layer, melanoma is potentially curable. However, for patients with deeper lesions or metastatic disease, the prognosis is poor, with an expected median survival of only 6 to 9 months for patients with stage IV metastatic melanoma [92]. Interestingly, under hypoxic conditions,

often associated with elevated LDH levels, the activity of elesclomol is diminished. Thus, the combination of elesclomol with paclitaxel proved effective only in patients with normal LDH levels, and no changes were observed in those with elevated LDH levels. Despite intensive efforts to improve disease prognosis, little progress has been made [87,90].

In another phase I study, elesclomol, given in combination with paclitaxel in women with refractory ovarian cancer, obtained a favorable opinion at this stage, with the combination being well tolerated. Currently, elesclomol combined with paclitaxel is in a phase II study in patients with ovarian, fallopian tube or peritoneal cancer that is recurrent or resistant to cisplatin treatment. Only patients with normal LDH levels were selected for the study [88]. Researchers have also planned to start a phase I study for the combined administration of elesclomol+docetaxel+prednisone in patients with metastatic prostate cancer [93].

3.2.2. Casiopeinas: Casiopeina III and Casiopeina II-gly

Structurally, Casiopeinas are mixed Cu complexes with the general formula [Cu(N-N)(X-Y)H_2O]NO_3, where N-N is a diimine ligand (phenanthroline or dipyridyl) and X-Y is a bidentate ligand (acetylacetone, salicylaldehyde, peptide, benzimidazole). The representatives selected for preclinical and clinical testing are Casiopeina III (CasIII) and Casiopeina II-gly (CasII-gly). Their structural formulas are presented in Figure 6.

Figure 6. Chemical structure of Casiopeinas: (**a**) Casiopeina III; (**b**) Casiopeina II-gly.

These are chelated complexes of Cu(II) with 4,7-dimethyl-1,10-phenanthroline and glycocol (CasII-gly) or with 4,7-dimethyl-1,10-phenanthroline and acetylacetone (CasIII) [55].

Casiopeinas are a group of copper-based chemical compounds with cytotoxic, genotoxic, antiproliferative and antineoplastic activity, as demonstrated in vitro and in vivo [42]. Casiopeinas were developed based on the rationale that copper compounds, unlike other metallic-based therapies, are more readily metabolized; this property decreases the incidence of side effects found in several other chemotherapies [94].

The main cytotoxic effect that representatives of this class have demonstrated is the activation of pro-apoptotic processes in malignant cells. There are at least two ways in which these compounds act on tumor cells: intercalation into the DNA structure followed by preventing its proper replication, and biochemical mechanisms leading to programmed cell death (apoptosis). Casiopeinas increase the level of ROS produced near DNA, most likely through a redox mechanism involving the Cu(II) ion. These species, once produced, will react with the DNA molecule causing damage to its structure most often by launching a radical attack at the level of the deoxyribose residue. Additionally, by increasing the level of ROS in the mitochondria, dysfunctions occur through the oxidation of thiol residues at

the level of mitochondrial proteins and, finally, cell apoptosis occurs. Other mechanisms of action attributed to this class of Cu(II) chelate complexes, discovered later, involve DNA fragmentation and cell death through caspase-dependent pathways, or inhibition of energy metabolism and mitochondrial toxicity. In addition, CasII-gly exhibits an anti-tumor effect by inhibiting the cell cycle, regulating the transformation processes in fibroblasts or reducing the phenomenon of uncontrolled migration of tumor cells [94,95].

CasIII was entered into a phase I clinical trial, to test for acute myeloid leukemia and colon cancer. CasII-gly, because it blocks the migration and proliferation of HeLa cells, was entered into clinical trials to treat cervical cancer [96].

CasII-gly is currently in phase I clinical trials looking at its toxicity in humans. Tests have shown that it inhibits energy metabolism and induces a high cardiotoxic effect, a fact that will probably cause the clinical trials to be stopped [42,55].

The advantage observed in the case of clinical trials performed on Casiopeinas consists in an increase in the immunity of the patients; this is accompanied by a mechanism of high protection of the liver through the repair of damaged cells, compared to other cytotoxic drugs. A CasII-gly-based therapy may prevent the problematic side effects of chemotherapy, which often compromise patients' health [54].

3.3. New Ruthenium Compounds

The success of cisplatin stimulated the scientific world in the development of other metal complexes with antitumor activity that are superior to platinum complexes, have lower toxicity or are active on other types of tumors. In this context, ruthenium complexes seem to be promising. Two such compounds have been entered into clinical trials. Despite their structural and chemical similarities, the two Ru(III) complexes show distinct antitumor behaviors. In preclinical studies, NAMI-A has demonstrated an inhibitory effect against the formation of cancer metastases in a variety of animal tumor models, but does not show direct cytotoxic effects on primary tumors, while KP1019 exhibits antitumor activity against a wide range of primary tumors humans through a cytotoxic mechanism of apoptosis induction [57,97–99].

3.3.1. NAMI-A

Structurally, NAMI-A is [ImH][trans-RuCl$_4$(DMSO)(Im)] (Im=imidazol, DMSO= dimetil-sulfoxid) (Figure 7).
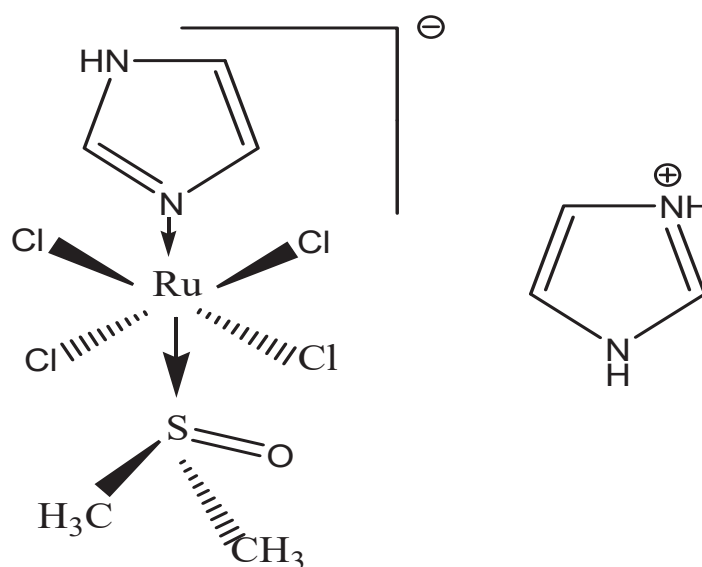

Figure 7. Chemical structure of NAMI-A.

The proposed mechanisms of action of NAMI-A in metastasis control include the following: limiting actin dependent adhesion in vitro [100]; limiting in vitro tumor cell motility via cytoskeleton remodeling (the activation of collagen receptor integrin β1 on the cell surface results in RhoA activation and, subsequently, in rearrangement of the cytoskeleton in vitro [101,102]; and exerting anti-invasive effects in vitro and in vivo by promoting capsule formation (NAMI-A increases the extracellular matrix around tumor cells and tumor vasculature by triggering fibrotic reactions, regulates TGFβ1 expression, binds to collagen and stimulates collagen production [103–105] and anti-angiogenic effect (e.g., NAMI-A inhibits the angiogenic effect induced by vascular endothelial growth factor in vitro) [106].

NAMI-A transiently blocks cell cycle progression in vitro at G2M phase [107,108]. The mechanism might be activation of Chk1, resulting in the inhibition of CDC25 and, subsequently, in inactive phosphorylated CDC2, thereby preventing mitotic entry [101].

In vitro, NAMI-A inhibits the mitogen-activated protein kinase/extracellular signal-regulated kinase (MAPK/ERK) signaling pathway and c-myc transcription [109,110]; DNA binding—although the intrastrand adduct formation of NAMI-A is significantly less than that of cisplatin, Ru-G and Ru-AG intrastrand adducts—was observed in vitro [111]. The AG:CG adduct ratio was four times higher for NAMI-A compared to cisplatin. NAMI-A sporadically forms interstrand crosslinks, whereas the formation of DNA protein crosslinks is comparable to cisplatin [101].

Due to its fast ligand exchange kinetics, it was found that NAMI-A is not significantly internalized by cells, but rather, binds to extracellular collagen matrix and to cell surface integrins, leading to increased adhesion and reduced cancer cell spread. If these results are consistent with the ability of NAMI-A to inhibit the growth of new metastases, its activity against already-developed metastases is probably due to its antiangiogenic properties [112].

Contrary to cisplatin, the cytotoxic effect of NAMI-A is not remarkable (on average, 1053 times less than cisplatin) [113]; its cytotoxicity has been found to be correlated with DNA binding (which is also the case for cisplatin) [101,111].

In preclinical studies, administration of NAMI-A in more frequent smaller dosages showed more prominent antimetastatic effects. Notably, the action of NAMI-A seems to be independent of the type of primary tumor or the stage of growth of metastases. NAMI-A is capable not only of preventing the formation of metastases, but also of inhibiting their growth once established [56]. Preclinical animal studies using NAMI-A have shown selective activity against lung metastases from a variety of primary tumors in murine models. NAMI-A reduced the weight of lung metastases more than their number. Since larger concentrations of NAMI-A in the lungs than in other tissues was ruled out, this finding was assumed to be related to the selective interference of NAMI-A with the growth of metastases already established in the lungs [114].

Toxicologic studies in dogs and mice have revealed an acceptable toxicity profile. The calculated half-life was approximately 18 h. Toxicity was observed at concentrations greater than 50 mg/kg/day, and in mice that survived treatment, was reversed within 3 weeks of the end of the treatment [115].

NAMI-A was the first ruthenium compound which entered into clinical trials. A phase I study was performed with NAMI-A as a single agent, given as an infusion over 3 h daily for 5 consecutive days every 3 weeks in patients with different types of solid tumors (including colorectal cancer, non-small cell lung cancer, melanoma, ovarian cancer, pancreatic cancer and mesothelioma). In total, 24 patients were treated at 12 different dose levels (2.4–500 mg/m^2/day). All 24 patients underwent refractory to conventional treatment. The advised dose for further testing was 300 mg/m^2/day. Adverse events included only mild hematologic toxicity, quite disabling nausea, vomiting, and diarrhea; furthermore, patientsexperienced stomatitis, fatigue, common toxicity criteria grade 1 and 2 creatinine increase, fever and sensitivity reactions to NAMI-A. Finally, phlebitis at the infusion site was observed when NAMI-A was administered intravenously without a port-a-cath. There was also painful blister formation on hands, fingers and toes, although

no part of the formal common toxicity criteria was considered dose-limiting. Twenty out of twenty-four patients were evaluable for response evaluation. One patient (4%) with non-small cell lung cancer experienced stable disease for 21 weeks, and nineteen patients (79%) showed disease progression. The transport of NAMI-A was achieved via binding to plasma proteins. It was found that NAMI-A accumulates in white blood cells, but accumulation was not directly proportional to daily dose or total drug exposure. Studies of this phase have shown stabilization of the disease in patients with advanced lung cancer. This result, together with the excellent activity shown by NAMI-A against lung metastases in mice, led to the recommendation of NAMI-A for a phase II study in the treatment of non-small cell lung cancer. As the combination of cisplatin and gemcitabine is widely used for the first-line treatment of non-small cell lung cancer, researhers decided to test a similar combination with NAMI-A [56,107,112].

A phase I/II study in which NAMI-A was given in combination with gemcitabine to 32 patients with advanced non-small cell lung cancer was performed. Phase I of the study was directed towards establishing the optimal dose of the combination of NAMI-A and gemcitabine (given at the typical dose of 1000 mg m^{-2}). The maximum tolerated dose of NAMI-A was found to be 300 mg· m^{-2} in the 28-day cycle (3 h infusion on days 1, 8, and 15, and gemcitabine given on days 2, 9, and 16) and 450 mg·m^{-2} in the 21-day cycle (NAMI-A administered on days 1 and 8, and gemcitabine on days 2 and 9). A further dose escalation of NAMI-A to 600 mg m^{-2} was found to induce dose-limiting toxicity. Besides neutropenia, the main non-hematological adverse events involved elevated liver enzymes, transient creatinine elevation, nausea, vomiting, constipation, diarrhea, fatigue and renal toxicity. Blister formation on fingers was observed only at 600 mg· m^{-2}.

The 21-day regimen was used for the phase II part of the study, in which 15 patients were treated with the maximum tolerated dose of NAMI-A established in phase I with the aim of assessing the antitumor activity according to the response of evaluation criteria for solid tumors [116]. Out of the 27 patients evaluable for response, partial remission was observed in one case (at 300 mg·m^{-2} in the 21-day schedule) and stable disease for at least 6–8 weeks in 10 patients. These results were not sufficient to warrant further expansion of the phase II cohort with additional 12 patients. Overall, the efficacy of the treatment was lower than expected for gemcitabine alone and it was declared to be "insufficiently effective for further use" [107,112].

3.3.2. KP1019 and KP1339

Structurally, KP1019 is [InH][trans-RuCl$_4$(In)$_2$] (In = indazol) and KP1339 it is KP1019 sodium salt (Figure 8).

The mode of action of KP1019 is very distinct from that of NAMI-A. These differences probably arise from the observed kinetic differences in the aquation processes and ruthenium activation. A key point is represented by the large difference in ruthenium uptake in the two cases, leading to significantly higher ruthenium concentrations in the cytosol for KP1019. Accordingly, the in vivo activity of KP1019 on primary tumor growth is believed to be predominantly due to cytotoxic effects on tumor cells arising from direct interference with cell signaling and metabolic pathways; in other words, KP1019 behaves as a classical cytotoxic drug. Furthermore, one of the recent interpretation of the molecular mechanism of KP1339 tends to rule out direct DNA damage as the main determinant of its cytotoxic action. In contrast, the postulated mode of action involves strong interactions with cytosol proteins, leading to ROS overproduction, oxidative stress and endoplasmic reticulum stress through targeting the chaperone protein GRP78. Eventually, this cellular damage triggers apoptosis through a mitochondrial pathway [117,118].
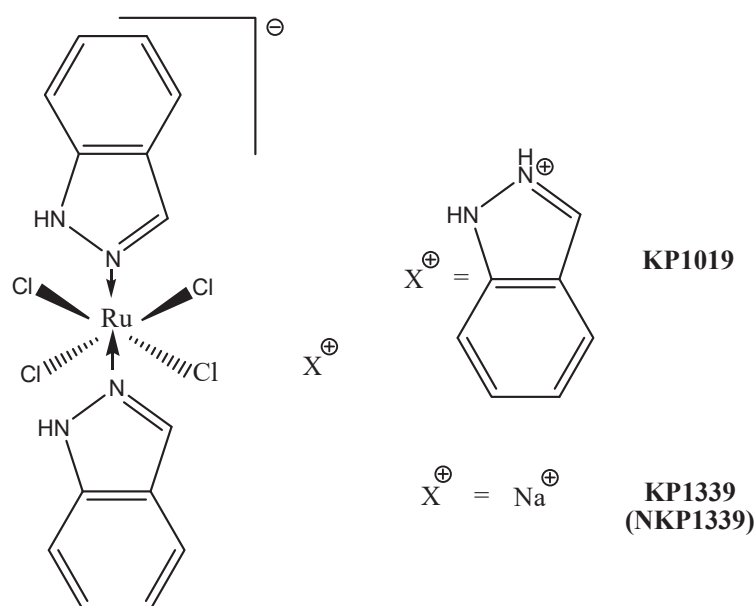
Figure 8. Chemical structure of KP1019 and of it's sodium salt, KP1339.

Based on a quite complex investigative strategy relying on transcriptomics and a genetic screening approach in a budding-yeast model, various genetic targets and a plethora of cellular pathways targeted by KP1019 were identified. Then, the actions produced by KP1019 in yeast were compared with those produced by the same ruthenium drug in Hela cells, and reasonable extrapolations were made. On the grounds of the obtained results, a comprehensive model depicting the mode of action of KP1019 and the targeted cellular pathways was proposed. According to this model, KP1019 induces ROS generation, causes DNA damage (and thus cell cycle arrest), activates mitogen-activated protein kinase signaling, alters intracellular metal ion and lipid homeostasis and also affects the chromatin assembly. Cells activate transcriptional responses to alleviate cellular damage [119]

Moreover, it was found that the toxicity potential of KP1019 is enhanced in the presence of various metal ions but suppressed by the supplementation of Fe^{2+} ions, and reduced glutathione, *N*-acetylcysteine, and ethanolamine. Thus, this model postulates for KP1019 a realistic multifactorial mechanism mediated by a variety of yet-unknown molecular targets [99].

KP1019 is moderately cytotoxic in vitro. Therefore, when tested against a panel of chemosensitive cell lines and their chemoresistant sublines, IC50 values in the range of 50 to 180 μM were measured. When compared with its sodium salt, KP1339, in a few cancer cell lines, KP1019 tended to be moderately more cytotoxic. Nevertheless, the significant correlation between the cytotoxicity profiles suggests that the two complexes have similar modes of action. For both compounds, no correlation between total ruthenium uptake and cytotoxicity was found [120]. Both KP1019 and KP1339 were found to be moderately cytotoxic (30–95 μM), but more cytotoxic than cisplatin, in SW480 and HT29 colorectal carcinoma cells, upon 24 h exposure; moreover, they induced apoptosis, predominantly via the intrinsic mitochondrial pathway. Upon 72 h exposure, cisplatin is much more efective than the two ruthenium compounds [121]. Studies concerning the antimetastatic ability of KP1019 in vitro gave controversial results. The complex revealed some anti-invasive activity in monolayer cultures of breast cancer cell lines, causing the significant reduction of cell migration and invasion [122].

KP1019 was tested in vitro against more than 50 primary tumors explanted from humans; in this highly predictive model, the complex proved a positive response rate higher than 70% [99].

KP1019 has antitumor activity in colon cancer in rats. Treatment with KP1019 resulted in a 95% reduction in tumor volume, with no mortality and no significant weight loss.

In addition, its efficacy was superior to 5-fluorouracil, the standard agent used against colorectal cancer [123].

The time-dependent tissue distribution of KP1339 (given i.v.) in non-tumor-bearing BALB/c nude mice was recently determined [124]. The highest (and comparable) ruthenium concentrations were found in the liver, lungs, kidneys and thymus, followed by the spleen and colon (~50% less). Consistent with the trend of total ruthenium in blood plasma, the peak levels in the mentioned tissues were found one to six hours after administration and decreased slowly with time, with the exception of the spleen, where the highest amount was found 24 h post-injection. Based on this promising activity, the two ruthenim compounds were selected for further clinical evaluation [99].

A preliminary phase I dose-escalation study was performed with KP1019 (total doses from 25 to 600 mg) on only eight patients with advanced solid tumors [125]. KP1019, given i.v. twice a week over 3 weeks, was well tolerated in the investigated dose range, and only mild toxicity was observed [126]. Disease stabilization for 8 to 10 weeks, unrelated to the dose, was observed for five out of six evaluable patients. The maximum tolerated dose of KP1019 could not be determined due to insuffcient solubility (too large a volume of infusion solution required for further dose escalation). Therefore, a full-scale phase I study was later performed on 34 patients with the more soluble sodium derivative KP1339. The investigation comprised nine dose levels (20–780 mg/m^2/day), and KP1339 was given by i.v. infusion on days 1, 8, and 15 in a 28-day cycle [123]. Only minor adverse effects were observed. Grade 2–3 nausea, together with increased creatinine levels, was found to be dose-limiting toxicity at the highest dose. Stable disease up to 88 weeks was found for seven patients with different types of tumors, including two cases of non-small cell lung cancer, and one patient with a neuroendocrine tumor had a partial response. Then, the phase I clinical investigation was repeated on 46 patients, with the same dose levels and treatment schedule [127]. The maximum dose tolerated was established to be 625 mg/m^2. Addtionally, the tolerability and safety profile were similar to those prior established; no significant hematological toxicity or neurotoxicity were found, with the main adverse events being clinically manageable grade $\leq$2 nausea, fatigue, and vomiting. KP1339 showed moderate antitumor activity, with a 26% disease control rate targeting three of five patients with carcinoid neuroendocrine tumors and a partial response in one patient with colon cancer [99].

In conclusion, NAMI-A and KP1019/KP1339 are suited for pharmacological investigations, although their stability is not high, and they undergo facile chemical transformations. Their behavior is typical of classical prodrugs, and similar to that of cisplatin and related platinum drugs. In addition, these compounds manifest an acceptable solubility in biological fluids, and their toxicity is limited and tolerable.

The fact that both compounds have been investigated in clinical trials producing scarce evidence of systemic toxicity increases their chances of clinical use. Even though their anticancer effects seem to be rather limited when they are used as standalone agents, there is still the chance to explore a larger number of cancer models, and also use these compounds in combination therapies [99].

4. Future Perspectives

Although platinum drugs have brought major advances in oncology, their clinical success is often hindered by the adverse side effects and development of resistance. Additional obstacles include low bioavailability and low water solubility. The strategies for the development of new platinum compounds, which take advantage of the affinity of the Pt(II) ion towards DNA while substantially modifying the mode of action, are multiple and complex. They include:

- The design of Pt(II) compounds target tumor cells by including in the coordination sphere some structures that promote a specific interaction with receptors on the surface of the tumor cell (receptors for glucose, estrogens, etc.). An example is C6-glucose-

Pt(II) type conjugates, which could be efficiently transferred intracellularly by glucose transporters, promoting, in this way, preferential accumulation in tumor cells [21,128];

- Compounds that do not bind covalently to DNA, but contain a ligand capable of intercalating between pairs of adjacent nitrogenous bases (ligands with extended aromatic structures: 1,10-phenanthroline, bipyridine, quinoxaline derivatives, etc.) [21,61];

- Compounds of Pt(IV) which, following the intracellular reduction process, release, on the one hand, active species of Pt(II), and on the other hand, ligands with biological activity (dual-threat prodrugs)—for example, complexes with ethacrynic acid (inhibitor of glutathione-S-transferase, the enzyme that catalyzes the binding of platinum compounds to glutathione and their inactivation) and with valproic acid (inhibitor of histone deacetylase, which causes cell differentiation and apoptosis) [21,24,128];

Recently, Pt(IV)-based anticancer prodrugs have been studied extensively, with the aim of reducing the side effects and drug resistance associated with the original Pt(II) anticancer drugs such as oxaliplatin [22–28]. The administration of Pt(IV) prodrugs, however, still faces significant challenges. For example, small-molecule Pt(IV) prodrugs may not be stable enough in the circulation system and are also limited by an insufficient circulatory half-life, which reduces Pt accumulation in tumor tissues, and thus, restricts the drug efficacy [29,30]. Additionally, conventional Pt(IV) prodrugs do not have the property of controllable activation, leading to adverse effects in off-target tissues [129–131].

- Non-toxic compounds that are activated at the target by enzymes that are found in much higher concentrations around tumor tissues—for example, complexes of platinum with cephalosporins, activated by β-lactamases, and complexes with β-glucuronyl, activated by β-glucuronidase [132];

- Compounds for photodynamic therapy (non-toxic, stable in the presence of thiol compounds); they are activated following light irradiation at a certain wavelength, generating active species of Pt(II) and ROS [24,128].

Photoactivatable Pt(IV) antitumor agents represent a promising area for new drug development. Small-molecule photoactivatable Pt(IV) prodrugs have been developed; their activation wavelengths still fall within the visible spectrum and are subject to limited penetration depths. Furthermore, although platinum drugs such as oxaliplatin have been reported to induce immunogenic cell death (ICD), most of these studies were carried out in vitro. The prolonged circulation of oxaliplatin may significantly enhance the associated immune response induced in vivo. Taken together, a comprehensive study to obtain an NIR-activatable and clinical drug-based Pt(IV) complex that exhibits enhanced circulation and elicits an elevated immune response in vivo is warranted. The development of photoactivatable prodrugs of platinum-based antitumor agents is aimed at increasing the selectivity, and hence, lowering toxicity of this important class of antitumor drugs. These drugs could find use in treating localized tumors accessible to laser-based fiber-optic devices. Pt(IV) complexes appeared attractive because these octahedral complexes are usually substitution-inert and require reduction to the Pt(II) species to become cytotoxic. Based on the knowledge of Pt(IV) photochemistry, Pt(IV) analogs of cisplatin, [Pt(en)Cl$_2$] and transplatin were designed, synthesized and investigated for their ability to be photoreduced to cytotoxic Pt(II) species. Two classes of photoactivatable Pt complexes have been looked at thus far: diiodo-Pt(IV) and diazido-Pt(IV) diammine complexes. The first generation, diiodo-Pt(IV) complexes, represented by [Pt(en)(I)$_2$(OAc)$_2$], react to visible light by binding irreversibly to DNA and forming adducts with 5′-GMP in the same manner as [Pt(en)Cl$_2$]. Furthermore, the photolysis products are cytotoxic to human cancer cells in vitro. However, these complexes are too reactive towards biological thiols (i.e., glutathione), which rapidly reduced them to cytotoxic Pt(II) species, thus making them unsuitable as drugs. The second generation, diazido-Pt(IV) complexes, represented by cis, trans, cis-[Pt(N$_3$)$_2$(OH)$_2$(NH$_3$)$_2$] and cis, trans-[Pt(en)(N$_3$)$_2$(OH)$_2$], are also photosensitive, binding irreversibly to DNA and forming similar products with DNA and 5′-GMP in the presence of light as the respective Pt(II) complexes. Recently the Pt(IV) prodrug trans, trans, trans-[Pt(pyridine)2(N3)2(OH)2]

(Pt1) and its coumarin derivative trans, trans, trans-[Pt(pyridine)2(N3)2(OH)(coumarin-3-carboxylate)] (Pt2) were discovered as agents for photoactivated chemotherapy. These complexes are inert in the dark but release Pt(II) species and radicals upon visible light irradiation, resulting in photocytotoxicity toward cancer cells [129–131].

Some authors suggest that all these approaches basically have the same mechanism of action, namely that of cisplatin, and therefore their success is debatable. More recently, a different mechanism of action has been demonstrated for nanocrystals or nanoclusters based on platinum ions, and hence, these structures seem promising for the success of targeted and selective therapies or in combating the resistance phenomena associated with chemotherapeutics based on platinum ions [22].

Although there have been many studies performed on Cu(II) ion complexes with anti-tumor activity, a relatively small number of compounds entered the phase of in vitro and in vivo studies, mainly due to their low solubility and bioavailability. Solving the solubility problems of the complexes that end up being tested, from the point of view of biological activity, can be tried by different methods: obtaining inclusion complexes between the cyclodextrin and the metal complex, or the synthesis and characterization of nanoparticles as delivery systems for Cu (II) complexes [133]. Moreover, the corroboration of empirical screening methods with new knowledge from genome and proteome research could allow the progress, from the simple synthesis of cytotoxic agents, with unknown mechanisms of action, to the rational design of active principles based on metal complexes [42,95,96].

Possible cytotoxicity mechanisms, such as DNA damage, DNA intercalation, telomerase inhibition and apoptosis induction, have been investigated on Cu(II) and Cu(I) complexes with 2-thioxoimidazolones as ligands. ROS formation in MCF-7 cells and three-dimensional (3D) spheroids was proven using the Pt-nanoelectrode. Drug accumulation and ROS formation at 40–60 μm spheroid depths were found to be the key factors for drug efficacy in the 3D tumor model, governed by the Cu(II)/Cu(I) redox potential [134].

Ruthenium compounds have been extensively studied over the past two decades from both chemical and biological perspectives.

The unique characteristics of Ru(II) or Ru(III) ions make their compounds attractive antitumor agents through: their selectivity for accumulation in tumor cells through interaction with transferrin receptors; activation via reduction, from inactive Ru(III) to active Ru(II); favorable ligand exchange kinetics; antimetastatic effects through inhibiting tumor cell detachment and migration; and different binding modes to the DNA molecule compared to platinum complexes (due to different geometries). These distinct behaviors have led researchers to recommend ruthenium complexes as potential antitumor agents, useful in malignancies resistant to treatment with platinum derivatives, as they have a different mechanism of action and low toxicity. Optimizing the physico-chemical parameters of the complexes by improving their stability and their ability to directly target cancer cells, ruthenium complexes may constitute an alternative to consider for antitumor therapy [57,97,107].

Transport and target delivery systems with metallo drugs as antitumor agents:

However, although effective, these drugs have a number of shortcomings: limited spectrum of activity, high toxicity, significant side effects, resistance of some types of tumors, low solubility in water, low bioavailability and short retention time in the blood circulation. Research on obtaining new antitumor metallo-drugs aims to solve these problems, as well as to adapt the new structures to modern therapies, personalized therapies and targeted molecular therapies. The design of new inorganic antitumor compounds aims to optimize their chemical design and pharmacological properties. Ideally, the new chemotherapeutic agent should be active in low doses, have minor adverse effects, have good bioavailability, high affinity for tumor cells, be able to be targeted to tumor cells without affecting healthy cells. In the same context, the development of efficient systems of transport and delivery to the target of chemotherapeutic drugs represents a major challenge for the scientific community [135,136].

Currently, studies are focused on the design of delivery systems that allow the transport of a large number of platinum ions, protect the chemotherapeutic agent from premature degradation and inactivation processes, and allow its transport to the target while preventing interaction with healthy tissues. The indisputable advantages of using effective systems for transport and delivery to the target, macroscopic or nano-sized, are the possibility of drastically reducing the doses of chemotherapy administered and increasing the concentration of the bioactive agent accumulated in tumor cells and tissues [137,138].

N-(2-hydroxypropyl)methacrylamide is one of the most commonly used polymers for conjugation with antineoplastic agents. In the case of AP5280, the chloride anions in cisplatin are replaced by a bidentate malonate anion in the terminal position in the N-(2-hydroxypropyl)methacrylamide structure [139]. Based on the results of preclinical studies, which show a 20-fold reduced toxicity compared to ciplatin and a clearly superior tissue accumulation, the compound was advanced to clinical trials [140]. The less promising results led to the abandonment of clinical trials in phase I, the developer company turning its attention to its analogue, AP5346 or ProLindac, in which the compound DACHPt, (1,2-diaminocyclohexane)Pt(II), is conjugated to the N-(2-hydroxypropyl)methacrylamide polymer via an amidomalonate group. The polymeric conjugate, stable at physiological pH, releases DACHPt at lower pH values from the hypoxic extracellular space of the neoplastic tissue [141]. The results of preclinical studies and of phase I clinical studies indicate an efficiency comparable to that of oxaliplatin on various tumor cell lines and in the treatment of solid tumors, good tolerance and reduced hematotoxicity. Phase I/II clinical studies that included patients with ovarian cancer in advanced stages, confirmed that the efficiency of the conjugate is similar to that of standard oxaliplatin. Administration of ProLindac was not associated with the onset of acute neurotoxicity, the main adverse effect that limits dose escalation in oxaliplatin treatment. In the case of a clinical trial in which ProLindac is used together with Paclitaxel in the combined therapy of advanced ovarian cancer, although the completion deadline has been exceeded, the results have not yet been made public [142].

BP-C1 is a cisplatin derivative in which the chemotherapeutic agent is fixed by some polycarboxylic acid residues at the level of an amphiphilic polymer derived from lignin. The product has passed the stage of preclinical and phase I and II clinical studies on stage IV metastatic breast cancer and on inoperable metastatic pancreatic cancer. The results of monotherapy in breast cancer indicate an efficiency comparable to cisplatin and superior to carboplatin, as well as a lower toxicity compared to cisplatin. The treatment was associated with a low incidence of adverse effects and, as a result, with a significant improvement in the patients quality of life [143].

Another type of polymeric nanoparticle, derivative of cisplatin, is NC-6004 or nanoplatin. Hydrophobic micellar particles functionalized with PEG are currently in phase I, II or III clinical trials, being evaluated in the treatment of different types of neoplasia: pancreatic cancer (phase III clinical trials), head and neck cancer (phase I clinical trials), and other solid tumors (phase II clinical studies) [144]. The first results indicated a good tolerance to the treatment and a reduced incidence of adverse effects, with greatly reduced nephrotoxic effects compared to cisplatin. Nanoplatin is also included in other ongoing clinical trials evaluating combined therapy with 5-fluorouracil and cetuximab (phase II clinical trials), with pembrolizumab (phase II clinical trials) and with gemcitabine (phase II clinical trials phase I and II clinics) [145,146].

The results of clinical studies demonstrate the important role that these transport and target delivery systems play especially in reducing the incidence and severity of adverse effects associated with therapy with platinum ion compounds. Although the reduction of toxicity brings enormous benefits in terms of the patients' quality of life, the efficiency, which is often comparable to that of cisplatin, justifies the continuation of studies in order to identify new strategies that significantly improve clinical results.

In the near future, advanced techniques of metalloproteomics, genomics and molecular biology will be able to fully elucidate the mechanism of action of metal complexes. Thus,

the physico-chemical and structural properties of the coordinating compounds will be able to be anticipated in order to obtain effective antitumor agents [19].

5. Conclusions

The discovery of platinum drugs have a great impact on the clinical cancer chemotherapy in that they have been used to treat different malignancies including colorectal, non-small cell lung and genitourinary cancers. Unfortunately, the treatment efficacy of cisplatin was hindered by drug resistance and severe side effects. Recently researchers have been engaged in the discovery of the non platinum complexes, and mononuclear and multinuclear metallic complexes. The understanding of the mechanisms of action of an increasing number of metal complexes impressively demonstrates the broad variety of cell death pathways activated by metal complexes. Metal complexes that can activate alternative pathways of cell death highlight possible opportunities for the treatment of tumors resistant to the currently available drugs. Copper and ruthenium complexes probably have greater potential over platinum complexes, showing reduced toxicity, a new mechanism of action, selectivity for tumor cells and the posibility of non-cross-resistance. The current article briefly reviews the achievements concerning the anticancer activity of platinum, copper and ruthenium metal complexes, focusing the discussion on past, present and future aspects.

References

1. Hernández-Romero, D.; Rosete-Luna, S.; López-Monteon, A.; Chávez-Piña, A.; Pérez-Hernández, N.; Marroquín-Flores, J.; Cruz-Navarro, A.; Pesado-Gómez, G.; Morales-Morales, D.; Colorado-Peralta, R. First-row transition metal compounds containing benzimidazole ligands: An overview of the anticancer and antitumor activity. *Coord. Chem. Rev.* **2021**, *439*, 213930. [CrossRef]
2. Clinton, S.K.; Giovannucci, E.L.; Hursting, S.D. The world cancer research fund/American institute for cancer research third expert report on diet, nutrition, physical activity, and cancer: Impact and future directions. *J. Nutr.* **2019**, *150*, 663–671. [CrossRef] [PubMed]
3. Karimi, B.; Shokrinezhad, B. Air pollution and the number of daily deaths due to respiratory causes in Tehran. *Atmos. Environ.* **2021**, *246*, 118161. [CrossRef]
4. Yu, P.; Guo, S.; Xu, R.; Ye, T.; Li, S.; Sim, M.R.; Abramson, M.J.; Guo, Y. Cohort studies of long-term exposure to outdoor particulate matter and risks of cancer: A systematic review and meta-analysis. *Innovation* **2021**, *2*, 100143. [CrossRef] [PubMed]
5. Martínez-Jiménez, F.; Muiños, F.; Sentís, I.; Deu-Pons, J.; Reyes-Salazar, I.; Arnedo-Pac, C.; Mularoni, L.; Pinch, O.; Bonet, J.; Kranas, H.; et al. A compendium of murational cancer driver genes. *Nat. Rev. Cancer* **2020**, *20*, 555–572. [CrossRef]
6. Shumi, G.; Desalegn, T.; Demissie, T.B.; Ramachanfran, V.P.; Eswaramoorthy, R. Metal complexes in target-spcific anticancer therapy: Recent trends and challenges. *J. Chem.* **2022**, *2*, 9261683.
7. de Anda-Jauregui, G.; Mejia-Pedroza, R.A.; Espinal-Enriquez, J.; Hernandez-Lemus, E. Crosstalk events in the estrogen signaling pathway may affect tamoxifen efficacy in breast cancer molecular subtypes. *Comput. Biol. Chem.* **2015**, *59*, 42–54. [CrossRef]
8. Zitvogel, L.; Rusakiewicz, S.; Routy, B.; Ayyoub, M.; Kroemer, G. Immunological off-target effects of imatinib. *Nat. Rev. Clin. Oncol.* **2016**, *13*, 431–446. [CrossRef]
9. Greer, J.A.; Amoyal, N.; Nisotel, L.; Fishbein, J.N.; MacDonald, J.; Stagl, J.; Lennes, I.; Temel, J.S.; Safren, S.A.; Pirl, W.F. A systematic review of adherence to oral antineoplastic therapies. *Oncologist* **2016**, *21*, 354–376. [CrossRef]
10. Hangan, A.; Turza, A.; Lucaciu, R.L.; Sevastre, B.; Pall, E.; Oprean, L.S.; Borodi, G. New Cu^{+2} complexes with N-sulfonamide ligands: Potential antitumor, antibacterial and antioxidant agents. *Molecules* **2022**, *27*, 3338. [CrossRef]
11. Tesauro, D. Metal complexes in diagnosis and therapy. *Int. J. Mol. Sci.* **2022**, *23*, 4377. [CrossRef] [PubMed]
12. Anthony, E.A.; Bolitho, E.M.; Bridgewater, R.J.; Carter, O.W.L.; Donnelly, J.M.; Imberti, C.; Lant, E.C.; Lermyte, F.; Needham, R.J.; Palau, M.; et al. Metallodrugs are unique: Opportumities and challenges of discovery and development. *Chem. Sci.* **2020**, *11*, 12888–12917. [CrossRef] [PubMed]
13. Guk, D.A.; Krasnovskaya, O.O.; Beloglazkina, E.K. Coordination compounds of biogenic metals as cytotoxic agents in cancer therapy. *Russ. Chem. Rev.* **2021**, *90*, 1566–1623. [CrossRef]

14. Sun, Q.; Li, Y.; Shi, H.; Wang, Y.; Zhang, Q. Ruthenium complexes as promising candidates against lung cancer. *Molecules* **2021**, *26*, 4389. [CrossRef] [PubMed]

15. Golbaghi, G.; Castonguay, A. Rationally designed ruthenium complexes for brest cancer therapy. *Molecules* **2020**, *25*, 265. [CrossRef] [PubMed]

16. Sang, Y.L.; Kim, C.Y.; Nam, T.G. Ruthenium complexes as anticancer agents: A brief history and perspectives. *Drug Des. Dev. Ther.* **2020**, *14*, 5375.

17. Ndagi, U.; Mhlongo, N.; Soliman, M.E. Metal complexes on cancer therapy—An update from drug design perspective. *Drug Des. Dev. Ther.* **2017**, *11*, 599–616. [CrossRef]

18. Srivastava, S.K. Transitional metal based anticancer drug: A review on current cancer chemotherapy drug. *JETIR* **2018**, *5*, 943–959.

19. Paprocka, R.; Wiese-Szadkowska, M.; Janciauskiene, S.; Kosmalski, T.; Kulik, M.; Helmin-Basa, A. Latest developments in metal complexes as anticancer agents. *Coord. Chem. Rev.* **2022**, *452*, 214307. [CrossRef]

20. Johnstone, T.C.; Suntharalingam, K.; Lippard, S.J. Third row transition metals for the treatment of cancer. *Trans. Math. Phys. Eng. Sci.* **2015**, *373*, 20140185. [CrossRef]

21. Johnstone, T.C.; Suntharalingam, K.; Lippard, S.J. The next generation of platinum drugs: Targeted Pt(II) agents, nanoparticle delivery and Pt(IV) prodrugs. *Chem. Rev.* **2016**, *116*, 3436–3486. [CrossRef] [PubMed]

22. Hu, X.; Li, F.; Noor, N.; Ling, D. Platinum drugs: From Pt(II) compounds, Pt(IV) prodrugs, to Pt nanocrystals/nanoclusters. *Sci. Bull.* **2017**, *62*, 589–596. [CrossRef]

23. Dasari, S.; Tchounwou, P.B. Cisplatin in cancer therapy: Molecular mechanisms of action. *Eur. J. Pharmacol.* **2014**, *740*, 364–378. [CrossRef] [PubMed]

24. Dilruba, S.; Kalayda, G.V. Platinum-based drugs: Past, present and future. *Cancer. Chemother. Pharmacol.* **2016**, *77*, 1103–1124. [CrossRef]

25. Oh, G.S.; Kim, H.J.; Shen, A.H.; Lee, S.B.; Khadka, D.; Pandit, A.; So, H.S. Cisplatin induces kidney dysfunction and perspective on improving treatment strategies. *Electrolye Blood Press.* **2014**, *12*, 55–65. [CrossRef]

26. Bergamo, A.; Dyson, P.J.; Sava, G. The mechanism of tumour cell death by metal-based anticancer drugs is not only a matter of DNA interactions. *Coord. Chem. Rev.* **2018**, *360*, 17–33. [CrossRef]

27. Kelland, L. The resurgence of platinum-based cancer chemotherapy. *Nat. Rev. Cancer* **2007**, *7*, 573–584. [CrossRef]

28. Tadini-Buoninsegni, F.; Bartolommei, G.; Moncelli, M.R.; Inesi, G.; Galliani, A.; Sinsi, M.; Losacco, M.; Natile, G.; Arnesano, F. Translocation of platinum anticancer drugs by human copper ATPases ATP7A and ATP7B. *Angew. Chem. Int. Ed. Engl.* **2014**, *53*, 1297–1301. [CrossRef]

29. Gansukh, T.; Donizy, P.; Halon, A.; Lage, H.; Surowiak, P. In vitro analysis of the relationships between metallothionein expression and Cisplatin sensitivity of non-small cellular lung cancer cells. *Anticancer Res.* **2013**, *33*, 5255–5260.

30. Ozols, R.F.; Bundy, B.N.; Greer, B.E.; Fowler, J.M.; Clarke-Pearson, D.; Burger, R.A.; Mannel, R.S.; DeGeest, K.; Hartenbach, E.M.; Baergen, R. Phase III trial of carboplatin and paclitaxel compared with cisplatin and paclitaxel in patients with optimally resected stage III ovarian cancer: A Gynecologic Oncology Group study. *J. Clin. Oncol.* **2003**, *21*, 3194–3200. [CrossRef]

31. Desoize, B. Metals and metal compounds in cancer treatment. *Anticancer Res.* **2004**, *24*, 1529–1544. [PubMed]

32. Monneret, C. Platinum anticancer drugs. From serendipity to rational design. *Ann. Pharm. Fr.* **2011**, *69*, 286–295. [CrossRef] [PubMed]

33. Raez, L.E.; Kobina, S.; Santos, E.S. Oxaliplatin in first-line therapy for advanced non-small-cell lung cancer. *Clin. Lung Cancer* **2010**, *11*, 18–24. [CrossRef] [PubMed]

34. Wheate, N.J.; Walker, S.; Craig, G.E.; Oun, R. The status of platinum anticancer drugs in the clinic and in clinical trials. *Dalton Trans.* **2010**, *39*, 8113–8127. [CrossRef] [PubMed]

35. Zhang, S.; Lovejoy, K.S.; Shima, J.E.; Lagpacan, L.L.; Shu, Y.; Lapuk, A.; Chen, Y.; Komori, T.; Gray, J.W.; Chen, X.; et al. Organic cation transporters are determinants of oxaliplatin cytotoxicity. *Cancer Res.* **2006**, *66*, 8847–8857. [CrossRef]

36. Martinez-Balibrea, E.; Martínez-Cardús, A.; Ginés, A.; Ruiz de Porras, V.; Moutinho, C.; Layos, L.; Manzano, J.L.; Bugés, C.; Bystrup, S.; Esteller, M.; et al. Tumor-related molecular mechanisms of oxaliplatin resistance. *Mol. Cancer Ther.* **2015**, *14*, 1767–1776. [CrossRef]

37. Oun, R.; Moussa, Y.E.; Wheate, N.J. The side effects of platinum-based chemotherapy drugs: A review for chemists. *Dalton Trans.* **2018**, *47*, 6645–6653. [CrossRef]

38. Kuwahara, A.; Yamamori, M.; Nishiguchi, K.; Okuno, T.; Chayahara, N.; Miki, I.; Tamura, T.; Inokuma, T.; Takemoto, Y.; Nakamura, T.; et al. Replacement of cisplatin with nedaplatin in a definitive 5-fluorouracil cisplatin-based chemoradiotherapy in Japanese patients with esophageal squamous cell carcinoma. *Int. J. Med. Sci.* **2009**, *6*, 305–311. [CrossRef]

39. Uehara, T.; Yamate, J.; Torii, M.; Maruyama, T. Comparative nephrotoxicity of cisplatin and nedaplatin: Mechanisms and histopathological characteristics. *J. Toxicol. Pathol.* **2011**, *24*, 87–94. [CrossRef]

40. Ali, I.; Wani, W.A.; Saleem, K.; Haque, A. Platinum compounds: A hope for future cancer chemotherapy. *Anticancer Agents Med. Chem.* **2013**, *13*, 296–306. [CrossRef]

41. Peng, Y.; Liu, Y.E.; Ren, X.C.; Chen, X.J.; Su, H.L.; Zong, J.; Feng, Z.L.; Wang, D.Y.; Lin, Q.; Gao, X.S. A phase I clinical trial of dose escalation of lobaplatin in combination with fixed—Dose docetaxel for the treatment of human solid tumours that had progressed following chemotherapy. *Oncol. Lett.* **2015**, *9*, 67–74. [CrossRef] [PubMed]

42. Silva-Platas, C.; Guerrero-Beltrán, C.E.; Carrancá, M.; Castillo, E.C.; Bernal-Ramírez, J.; Oropeza-Almazán, Y.; González, L.N.; Rojo, R.; Martínez, L.E.; Valiente-Banuet, J.; et al. Antineoplastic copper coordinated complexes (Casiopeinas) uncouple oxidative phosphorylation and induce mitochondrial permeability transition in cardiac mitochondria and cardiomyocytes. *J. Bioenerg. Biomembr.* **2016**, *48*, 43–54. [CrossRef] [PubMed]

43. Cetean, S.; Ciuleanu, T.; Leucuța, D.C.; Căinap, C.; Constantin, A.M.; Cazacu, I.; Căinap, S.; Gherman, A.; Oprean, L.; Hangan, A.; et al. Hypersensitivity reactions to platinum derivatives: Findings of new predictive markers. *J. BUON* **2015**, *20*, 1617–1623. [PubMed]

44. Tabti, R.; Tounsi, N.; Gaiddon, C.; Bentouhami, E.; Désaubry, L. Progress in Copper Complexes as Anticancer Agents. *Med. Chem.* **2017**, *7*, 875–879. [CrossRef]

45. Hangan, A.C.; Stan, R.L.; Sevastre, B.; Gheorghe-Cetean, S.; Oprean, L. DNA cleavage study and SOD-mimetic activity of a new Cu (II) complex. *Farmacia* **2017**, *65*, 368–373.

46. Schwartz, L.; Supuran, C.T.; Alfarouk, K.O. The Warburg Effect and the Hallmarks of Cancer. *Anticancer Agents Med. Chem.* **2017**, *17*, 164–170. [CrossRef]

47. Sevastre, B.; Sarpataki, O.; Olah, N.K.; Stan, R.L.; Taulescu, M.; Marcus, I.; Cătoi, C. Anti-tumor effect of *Euonymus Europaeus* on Ehrlich tumor cells in vivo. *Farmacia* **2014**, *62*, 907–917.

48. Hangan, A.; Vicaș, L.; Stan, R.L.; Pall, E.; Oprean, L.; Ionescu, C.; Andrei, S.; Sevastre-Berghian, A.; Marian, E.; Sevastre, B. Synthesis, characterization and biological activity of two new Copper (II) complexes with N-sulfonamide ligand. *Rev. Chim.* **2019**, *70*, 4060–4067. [CrossRef]

49. Hangan, A.; Borodi, G.; Filip, X.; Tripon, C.; Morari, C.; Oprean, L.; Filip, C. Structure of N-(5-ethyl-[1,3,4]-thiadiazole-2-yl) toluenesulfonamide by combined X-ray powder diffraction, ^{13}C solid-state NMR and molecular modelling. *Acta Crystallogr. B.* **2010**, *66*, 615–621. [CrossRef]

50. Kadiiska, M.B.; Mason, R.P. In vivo copper-mediated free radical production: An ESR spin-trapping study. *Spectrochim. Acta A Mol. Biomol. Spectrosc.* **2002**, *58*, 1227–1239. [CrossRef]

51. Hangan, A.; Borras, J.; Liu-Gonzalez, M.; Oprean, L. Synthesis, Crystal Structures and Properties of [Cu(L1)$_2$(py)$_2$(H$_2$O)](H$_2$O) [HL1=N-(5-ethyl-[1,3,4]–thiadiazole-2-yl)-toluenesulfonamidate] and [Cu(L2)$_2$(py)$_2$(H$_2$O)] [HL2=N-(5-ethyl-[1,3,4]–thiadiazole-2-yl)-benzenesulfonamidate]. *ZAAC* **2007**, *633*, 1837–1841. [CrossRef]

52. Hangan, A.C.; Turza, A.; Stan, R.L.; Stefan, R.; Oprean, L.S. Synthesis, crystal structure, properties and nuclease activity of a new Cu(II) complex [Cu(L)$_2$(py)$_2$(H$_2$O)]. (HL=N-(5-(4-methylphenyl)-[1,3,4]–thiadiazole–2-yl)-toluenesulfonamide). *Russ. J. Coord. Chem.* **2015**, *41*, 395–404. [CrossRef]

53. Liang, J.X.; Zhong, H.J.; Yang, G.; Vellaisamy, K.; Ma, D.L.; Leung, C.H. Recent development of transition metal complexes with in vivo antitumor activity. *J. Inorg. Biochem.* **2017**, *177*, 276–286. [CrossRef] [PubMed]

54. Campero-Peredo, C.; Bravo-Gómez, M.E.; Hernández-Ojeda, S.L.; Olguin-Reyes, S.R.; Espinosa-Aguirre, J.J.; Ruiz-Azuara, L. Effect of [Cu(4,7-dimethyl-1,10-phenanthroline)(acetylacetonato)](NO$_3$), Casiopeína III-Ea, on the activity of cytochrome P450. *Toxicol. Vitro* **2016**, *33*, 16–22. [CrossRef] [PubMed]

55. Serment-Guerrero, J.; Bravo-Gomez, M.E.; Lara-Rivera, E.; Ruiz-Azuara, L. Genotoxic assessment of the copper chelated compounds Casiopeinas: Clues about their mechanisms of action. *J. Inorg. Biochem.* **2017**, *166*, 68–75. [CrossRef]

56. Antonarakis, E.S.; Emadi, A. Ruthenium-based chemotherapeutics: Are they ready for prime time? *Cancer Chemother. Pharmacol.* **2010**, *66*, 1–9. [CrossRef]

57. Alessio, E.; Messori, L. The deceptively similar Ruthenium(III) drug candidates KP1019 and NAMI-A have different actions. What did we learn in the past 30 years? *Met. Ions Life. Sci.* **2018**, *18*, 303–324. [CrossRef]

58. Beale, P.; Judson, I.; O'Donnell, A.; Trigo, J.; Rees, C.; Raynaud, F.; Turner, A.; Simmos, L.; Etterley, L. A Phase I clinical and pharmacological study of cis-diamminedichloro(2-methylpyridine) platinum II (AMD473). *Br. J. Cancer* **2003**, *88*, 1128–1134. [CrossRef]

59. Sessa, C.; Capri, G.; Gianni, L.; Peccatori, F.; Grasselli, G.; Bauer, J.; Zucchetti, M.; Viganò, L.; Gatti, A.; Minoia, C.; et al. Clinical and pharmacological phase I study with accelerated titration design of a daily times five schedule of BBR3464, a novel cationic triplatinum complex. *Ann. Oncol.* **2000**, *11*, 977–983. [CrossRef]

60. Pratesi, G.; Perego, P.; Polizzi, D.; Righetti, S.C.; Supino, R.; Caserini, C.; Manzotti, C.; Giuliani, F.C.; Pezzoni, G.; Tognella, S.; et al. A novel charged trinuclear platinum complex effective against cisplatin-resistant tumours hypersensitivity of p53-mutant human tumour xenografts. *Br. J. Cancer* **1999**, *80*, 1912–1919. [CrossRef]

61. Lazarevic, T.; Rilak, A.; Bugarcic, Z.D. Platinum, palladium, gold and ruthenium complexes as anticancer agents: Current clinicaluses, cytotoxicity studies and future perspectives. *Eur. J. Med. Chem.* **2017**, *142*, 8–31. [CrossRef] [PubMed]

62. Calvert, A.H.; Thomas, H.; Colombo, N.; Gore, M.; Earl, H.; Sena, L.; Camboni, G.; Liati, P.; Sessa, C. Phase II clinical study of BBR 3464, a novel, bifunctional platinum analogue, in patients with advanced ovarian cancer. *Eur. J. Cancer* **2001**, *37*, S260. [CrossRef]

63. Hensing, T.A.; Hanna, N.H.; Gillenwater, H.H.; Camboni, G.M.; Allievi, C.; Socinski, M.A. Phase II study of BBR 3464 as treatment in patients with sensitive or refractory small cell lung cancer. *Anticancer Drugs* **2006**, *17*, 697–704. [CrossRef] [PubMed]

64. U.S. National Institutes of Health. Clinical Trials Database, clinicaltrials.gov. Available online: https://clinicaltrials.gov/ (accessed on 14 May 2022).

65. Raynaud, F.I.; Mistry, P.; Donaghue, A.; Poon, G.K.; Kelland, L.R.; Barnard, C.F.; Murrer, B.A.; Harrap, K.R. Biotransformation of the platinum drug JM216 following oral administration to cancer patients. *Cancer Chemother. Pharmacol.* **1996**, *38*, 155–162. [CrossRef] [PubMed]

66. Fink, D.; Nebel, S.; Aebi, S.; Zheng, H.; Cenni, B.; Nehmé, A.; Christen, R.D.; Howell, S.B. The role of DNA mismatch repair in platinum drug resistance. *Cancer Res.* **1996**, *56*, 4881–4886.

67. Choy, H.; Park, C.; Yao, M. Current status and future prospects for satraplatin, an oral platinum analogue. *Clin. Cancer. Res.* **2008**, *14*, 1633–1638. [CrossRef]

68. Sternberg, C.N.; Petrylak, D.; Witjes, F.; Ferrero, J.; Eymard, J.; Falcon, S.; Chatta, K.; Vaughn, D.; Berry, W.; Sartor, O. Satraplatin (S) demonstrates significant clinical benefits for the treatment of patients with HRPC: Results of a randomized phase III trial. *J. Clin. Oncol.* **2007**, *25* (Suppl. S18), 5019. [CrossRef]

69. Latif, T.; Wood, L.; Connell, C.; Smith, D.C.; Vaughn, D.; Lebwohl, D.; Peereboom, D. Phase II study of oral bis (aceto) ammine dichloro (cyclohexamine) platinum (IV) (JM-216, BMS-182751) given daily x 5 in hormone refractory prostate cancer (HRPC). *Investig. New Drugs* **2005**, *23*, 79–84. [CrossRef]

70. Kelland, L. Broadening the clinical use of platinum drug–based chemotherapy with new analogues. *Expert Opin. Investig. Drugs* **2007**, *16*, 1009–1021. [CrossRef]

71. Holford, J.; Raynaud, F.; Murrer, B.A.; Grimaldi, K.; Hartley, J.; Abrams, M.; Kelland, L.R. Chemical, biochemical and pharma cological activity of the novel sterically hindered platinum co-ordination complex, cis-[amminedichloro(2-methylpyridine)] plati num (II) (AMD473). *Anti-Cancer Drug Des.* **1998**, *13*, 1–18.

72. Nishimura, T.; Newkirk, K.; Sessions, R.; Andrews, P.A.; Trock, B.J.; Rasmussen, A.A.; Montgomery, E.A.; Bischoff, E.K.; Cullen, K.J. Immunohistochemical staining for glutathione S-transferase predicts response to platinumbased chemotherapy in head and neck cancer. *Clin. Cancer Res.* **1996**, *2*, 1859–1865. [PubMed]

73. Raynaud, F.I.; Boxall, F.E.; Goddard, P.M. Cis-ammine dichloro(2-methylpyridine) platinum (II) (AMD473), a novel sterically hindered platinum complex: In vivo activity, toxicology and pharmacokinetics in mice. *Clin. Cancer Res.* **1997**, *3*, 2063–2074. [PubMed]

74. Van Hennik, M.B.; van der Vijgh, W.J.; Klein, I. Comparative pharmacokinetics of cisplatin and three analogues in mice and humans. *Cancer Res.* **1987**, *47*, 6297–6301. [PubMed]

75. Treat, J.; Schiller, J.; Quoix, E.; Mauer, A.; Edelman, M.; Modiano, M.; Bonomi, P.; Ramlau, R.; Lemarie, E. ZD0473 ment in lung cancer: An overview of the clinical trial results. *Eur. J. Cancer* **2002**, *38* (Suppl. S8), S13–S18. [CrossRef]

76. Gore, M.E.; Atkinson, R.J.; Thomas, H.; Cure, H.; Rischin, D.; Beale, P.; Bougnoux, P.; Dirix, L.; Smit, W.M. A phase II trial of ZD0473 in platinum-pretreated ovarian cancer. *Eur. J. Cancer* **2002**, *38*, 2416–2420. [CrossRef]

77. Giaccone, G.; O'Brien, M.E.R.; Byrne, M.J.; Bard, M.; Kaukel, E.; Smit, B. Phase II trial of ZD0473 as second-line therapy in mesothelioma. *Eur. J. Cancer* **2002**, *38*, S19–S24. [CrossRef]

78. Gelmon, K.A.; Vandenberg, T.A.; Panasci, L.; Norris, B.; Crump, M.; Douglas, L.; Walsh, W.; Matthews, S.J.; Seymour, L.K. A phase II study of ZD0473 given as a short infusion every 3 weeks to patients with advanced or metastatic breast cancer: A National Cancer Institute of Canada Clinical Trials Group trial, IND 129. *Ann. Oncol.* **2003**, *14*, 543–548. [CrossRef]

79. Rahman, A.; Roh, J.K.; Wolpert-DeFilippes, M.K.; Goldin, A.; Venditti, J.M.; Woolley, P.V. Therapeutic and pharmacological studies of tetrachloro (d,l-trans) 1,2-diaminocyclohexane platinum (IV) (Tetraplatin), a new platinum analogue. *Cancer Res.* **1988**, *48*, 1745–1752.

80. Schilder, R.J.; LaCreta, F.P.; Perez, R.P.; Johnson, S.W.; Brennan, J.M.; Rogatko, A.; Nash, S.; McAleer, C.; Hamilton, T.C.; Roby, D. Phase I and pharmacokinetic study of ormaplatin (tetraplatin, NSC 363812) administered on a day 1 and day 8 schedulede. *Cancer Res.* **1994**, *54*, 709–717.

81. Tutsch, K.D.; Arzoomanian, R.Z.; Alberti, D.; Tombes, M.B.; Feierabend, C.; Robins, H.I.; Spriggs, D.R.; Wilding, G. Phase I clinical and pharmacokinetic study of an one-hour infusion of ormaplatin (tetraplatin, NSC 363812). *Investig. New Drugs* **1999**, *17*, 63–72. [CrossRef]

82. Pendyala, L.; Arakali, A.V.; Sansone, P.; Cowens, J.W.; Creaven, P.J. DNA binding of iproplatin and its divalent metabolite cis-dichloro-bis-isopropylamine platinum (II). *Cancer Chemoth. Pharmacol.* **1990**, *27*, 248–250. [CrossRef] [PubMed]

83. Paolozzi, F.P.; Gaver, R.; Poiesz, B.J.; Louie, A.; DiFino, S.; Comis, R.L.; Newman, N.; Ginsberg, S. Phase I –preliminary phase II trial of iproplatin, a cisplatin analogue. *Investig. New Drugs* **1988**, *6*, 199–206. [CrossRef] [PubMed]

84. Sessa, C.; Vermorken, J.; Renard, J.; Kaye, S.; Smith, D.; ten Bokkel Huinink, W.; Cavalli, F.; Pinedo, H. Phase II study of iproplatin in advanced ovarian carcinoma. *J. Clin. Oncol.* **1988**, *6*, 98–105. [CrossRef] [PubMed]

85. de Wit, R.; Tesselaar, M.; Kok, T.C.; Seynaeve, C.; Rodenburg, C.J.; Verweij, J.; Helle, P.A.; Stoter, G. Randomosed phase II trial of carboplatin and iproplatin in advanced urothelial cancer. *Eur. J. Cancer* **1991**, *27*, 1383–1385. [CrossRef]

86. Mjos, K.D.; Orvig, C. Metallodrugs in medicinal inorganic chemistry. *Chem. Rev.* **2014**, *114*, 4540–4563. [CrossRef]

87. Hasinoff, B.B.; Wu, X.; Yadav, A.A.; Patel, D.; Zhang, H.; Wang, D.S.; Chen, Z.S.; Yalowich, J.C. Cellular mechanisms of the cytotoxicity of the anticancer drug elesclomol and its complex with Cu(II). *Biochem. Pharmacol.* **2015**, *93*, 266–276. [CrossRef]

88. Monk, B.J.; Kauderer, J.T.; Moxley, K.M.; Bonebrake, A.J.; Dewdney, S.B.; Secord, A.A.; Ueland, F.R.; Johnston, C.M.; Aghajanian, C. A phase II evaluation of elesclomol sodium and weekly paclitaxel in the treatment of recurrent or persistent platinum resistant ovarian, fallopian tube or primary peritoneal cancer: An NRG oncology/gynecologic oncology group study. *Gynecol. Oncol.* **2016**, *151*, 422–427. [CrossRef]

89. O'Day, S.J.; Eggermont, A.M.; Chiarion-Sileni, V.; Kefford, R.; Grob, J.J.; Mortier, L.; Robert, C.; Schachter, J.; Testori, A.; Mackiewicz, J.; et al. Final results of phase III SYMMETRY study: Randomized, double-blind trial of elesclomol plus paclitaxel versus paclitaxel alone as treatment for chemotherapy-naive patients with advanced melanoma. *J. Clin. Oncol.* **2013**, *31*, 1211–1218. [CrossRef]

90. Kirshner, J.R.; He, S.; Balasubramanyam, V.; Kepros, J.; Yang, C.Y.; Zhang, M.; Du, Z.; Barsoum, J.; Bertin, J. Elesclomol induces cancer cell apoptosis through oxidative stress. *Mol. Cancer Ther.* **2008**, *7*, 2319–2327. [CrossRef]

91. Berkenblit, A.; Eder, J.P., Jr.; Ryan, D.P.; Seiden, M.V.; Tatsuta, N.; Sherman, M.L.; Dahl, T.A.; Dezube, B.J.; Supko, J.G. Phase I clinical trial of STA-4783 in combination with paclitaxel in patients with refractory solid tumors. *Clin. Cancer Res.* **2007**, *13 Pt 1*, 584–590. [CrossRef]

92. Korn, E.L.; Liu, P.Y.; Lee, S.J.; Chapman, J.A.W.; Niedzwiecki, D.; Suman, V.J.; Moon, J.; Sondak, V.K.; Atkins, M.B.; Eisenhauer, E.A.; et al. Meta-analysis of phase II cooperative group trials in metastatic stage IV melanoma to determine progression-free and overall survival benchmarks for future phase II trials. *J. Clin. Oncol.* **2008**, *26*, 527–534. [CrossRef] [PubMed]

93. Rae, C.; Mairs, R.J. Evaluation of the radiosensitizing potency of chemotherapeutic agents in prostate cancer cells. *Int. J. Radiat. Biol.* **2017**, *93*, 194–203. [CrossRef] [PubMed]

94. de Anda-Jáuregui, G.; Espinal-Enríquez, J.; Hur, J.; Alcalá-Corona, S.A.; Ruiz-Azuara, L.; Hernández-Lemus, E. Identification of Casiopeina II-gly secondary targets through a systems pharmacology approach. *Comput. Biol. Chem.* **2019**, *78*, 127–132. [CrossRef]

95. Vértiz, G.; García-Ortuño, L.E.; Bernal, J.P.; Bravo-Gómez, M.E.; Lounejeva, E.; Huerta, A.; Ruiz-Azuara, L. Pharmacokinetics and hematotoxicity of a novel copper-based anticancer agent: Casiopeina III-Ea, after a single intravenous dose in rats. *Fundam. Clin. Pharmacol.* **2014**, *28*, 78–87. [CrossRef] [PubMed]

96. Chavez-Gonzalez, A.; Centeno-Llanos, S.; Moreno-Lorenzana, D.; Sandoval-Esquivel, M.A.; Aviles-Vazquez, S.; Bravo-Gomez, M.E.; Ruiz-Azuara, L.; Ayala-Sanchez, M.; Torres-Martinez, H.; Mayani, H. Casiopeina III-Ea, a copper-containing small molecule, inhibits the in vitro growth of primitive hematopoietic cells from chronic myeloid leukemia. *Leuk. Res.* **2017**, *52*, 8–19. [CrossRef]

97. Allardyce, C.S.; Dyson, P.J. Ruthenium in medicine: Current clinical uses and future prospects. *Platin. Met. Rev.* **2001**, *45*, 62–69.

98. Mehvash, Z.; Farukh, A.; Sartaj, T. Current and future potential of metallo drugs: Revisiting DNA-binding of metal containing molecules and their diverse mechanism of action. *Inorg. Chim. Acta* **2016**, *444*, 1–22.

99. Alessio, E.; Messori, L. NAMI-A and KP1019/1339, two iconic ruthenium anticancer drug candidates face-to-face: A case story in medicinal inorganic chemistry. *Molecules* **2019**, *24*, 1995. [CrossRef]

100. Sava, G.; Frausin, F.; Cocchietto, M.; Vita, F.; Podda, E.; Spessotto, P.; Furlani, A.; Scarcia, V.; Zabucchi, G. Actin-dependent tumour cell adhesion after short-term exposure to the antimetastasis ruthenium complex NAMI-A. *Eur. J. Cancer* **2004**, *40*, 1383–1396. [CrossRef]

101. Bergamo, A.; Gaiddon, C.; Schellens, J.H.; Beijnen, J.H.; Sava, G. Approaching tumour therapy beyond platinum drugs: Status of the art and perspectives of ruthenium drug candidates. *J. Inorg. Biochem.* **2012**, *106*, 90–99. [CrossRef]

102. Bergamo, A.; Sava, G. Ruthenium complexes can target determinants of tumour malignancy. *Dalton Trans* **2007**, *13*, 1267–1272. [CrossRef] [PubMed]

103. Gava, B.; Zorzet, S.; Spessotto, P.; Cocchietto, M.; Sava, G. Inhibition of B16 melanoma metastases with the ruthenium complex imidazolium trans-imidazoledimethylsulfoxide-tetrachlororuthenate and down-regulation of tumor cell invasion. *J. Pharmacol. Exp. Ther.* **2006**, *317*, 284–291. [CrossRef] [PubMed]

104. Sava, G.; Zorzet, S.; Turrin, C.; Vita, F.; Soranzo, M.; Zabucchi, G.; Cocchietto, M.; Bergamo, A.; DiGiovine, S.; Pezzoni, G.; et al. Dual action of NAMI-A in inhibition of solid tumor metastasis: Selective targeting of metastatic cells and binding to collagen. *Clin. Cancer Res.* **2003**, *9*, 1898–1905. [PubMed]

105. Casarsa, C.; Mischis, M.T.; Sava, G. TGF beta1 regulation and collagen-release-independent connective tissue remodelling by the ruthenium complex. NAMI-A in solid tumours. *J. Inorg. Biochem.* **2004**, *98*, 1648–1654. [CrossRef]

106. Vacca, A.; Bruno, M.; Boccarelli, A.; Coluccia, M.; Ribatti, D.; Bergamo, A.; Garbisa, S.; Sartor, L.; Sava, G. Inhibition of endothelial cell functions and of angiogenesis by the metastasis inhibitor NAMI-A. *Br. J. Cancer* **2002**, *86*, 993–998. [CrossRef]

107. Leijen, S.; Burgers, S.A.; Baas, P.; Pluim, D.; Tibben, M.; van Werkhoven, E.; Alessio, E.; Sava, G.; Beijnen, J.H.; Schellens, J.H. Phase I/II study with ruthenium compound NAMI-A and gemcitabine in patients with non-small cell lung cancer after first line therapy. *Investig. New Drugs* **2015**, *33*, 201–214. [CrossRef]

108. Zorzet, S.; Bergamo, A.; Cocchietto, M.; Sorc, A.; Gava, B.; Alessio, E.; Iengo, E.; Sava, G. Lack of In vitro cytotoxicity, associated to increased G(2)-M cell fraction and inhibition of matrigel invasion, may predict In vivo-selective antimetastasis activity of ruthenium complexes. *J. Pharmacol. Exp. Ther.* **2000**, *295*, 927–933.

109. Debidda, M.; Sanna, B.; Cossu, A.; Posadino, A.M.; Tadolini, B.; Ventura, C.; Pintus, G. NAMI-A inhibits the PMA-induced ODC gene expression in ECV304 cells: Involvement of PKC/Raf/Mek/ERK signalling pathway. *Int. J. Oncol.* **2003**, *23*, 477–482. [CrossRef]

110. Sanna, B.; Debidda, M.; Pintus, G.; Tadolini, B.; Posadino, A.M.; Bennardini, F.; Sava, G.; Ventura, C. The anti-metastatic agentimidazolium trans-imidazole-dimethyl-sulfoxide-tetrachloro ruthenate induces endothelial cell apoptosis by inhibiting the mitogen activated protein kinase/extracellular signal-regulated kinase signaling pathway. *Arch. Biochem. Biophys.* **2002**, *403*, 209–218. [CrossRef]

111. Pluim, D.; van Waardenburg, R.C.; Beijnen, J.H.; Schellens, J.H. Cytotoxicity of the organic ruthenium anticancer drug Nami-A is correlated with DNA binding in four different human tumor cell lines. *Cancer Chemother. Pharmacol.* **2004**, *54*, 71–78. [CrossRef]

112. Alessio, E. Thirty years of the drug candidate NAMI-A and the myths in the field of ruthenium anticancer compounds: A personal perspective. *Eur. J. Inorg. Chem.* **2017**, *2017*, 1549–1560. [CrossRef]

113. Brabec, V.; Novakova, O. DNA binding mode of ruthenium complexes and relationship to tumor cell toxicity. *Drug Resist. Updat.* **2006**, *9*, 111–122. [CrossRef] [PubMed]

114. Sava, G.; Clerici, K.; Capozzi, I.; Cocchietto, M.; Gagliardi, R.; Alessio, E.; Mestroni, G.; Perbellini, A. Reduction of lung metastasis by ImH[trans-RuCl4(DM-SO)Im]: Mechanism of the selective action investigated on mouse tumors. *Anticancer Drugs* **1999**, *10*, 129–138. [CrossRef] [PubMed]

115. Cocchietto, M.; Sava, G. Blood concentration and toxicity of the antimetastasis agent NAMI-A following repeated intravenous treatment in mice. *Pharmacol. Toxicol.* **2000**, *87*, 193–197. [CrossRef]

116. Therasse, P.; Arbuck, S.G.; Eisenhauer, E.A.; Wanders, J.; Kaplan, R.S.; Rubinstein, L.; Verweij, J.; Van, G.M.; van Oosterom, A.T.; Christian, M.C.; et al. New guidelines to evaluate the response to treatment in solid tumors. European Organization for Research and Treatment of Cancer, National Cancer Institute of the United States, National Cancer Institute of Canada. *J. Natl. Cancer Inst.* **2000**, *92*, 205–216. [CrossRef]

117. Meier-Menches, S.M.; Gerner, C.; Berger, W.; Hartinger, C.G.; Keppler, B.K. Structure activity relationships for ruthenium and osmium anticancer agents towards clinical development. *Chem. Soc. Rev.* **2018**, *47*, 909–928. [CrossRef]

118. Flocke, L.S.; Trondl, R.; Jakupec, M.A.; Keppler, B.K. Molecular mode of action of NKP-1339 a clinically investigated ruthenium-based drug—Involves ER- and ROS-related e_ects in colon carcinoma cell lines. *Investig. New Drugs* **2016**, *34*, 261–268. [CrossRef]

119. Golla, U.; Swagatika, S.; Chauhan, S.; Tomar, R.S. A systematic assessment of chemical, genetic, and epigenetic factors influencing the activity of anticancer drug KP1019 (FFC14A). *Oncotarget* **2017**, *8*, 98426–98454. [CrossRef]

120. Heffeter, P.; Böck, K.; Atil, B.; Hoda, M.A.R.; Körner, W.; Bartel, C.; Jungwirth, U.; Keppler, B.K.; Micksche, M.; Berger, W.; et al. Intracellular protein binding patterns of the anticancer ruthenium drugs KP1019 and KP1339. *J. Biol. Inorg. Chem.* **2010**, *15*, 737–748. [CrossRef]

121. Kapitza, S.; Pongratz, M.; Jakupec, M.A.; He_eter, P.; Berger, W.; Lackinger, L.; Keppler, B.K.; Marian, B. Heterocyclic complexes of ruthenium(III) induce apoptosis in colorectal carcinoma cells. *J. Cancer Res. Clin. Oncol.* **2005**, *131*, 101–110. [CrossRef]

122. Bergamo, A.; Masi, A.; Jakupec, M.A.; Keppler, B.K.; Sava, G. Inhibitory Effects of the ruthenium complex KP1019 in models of mammary cancer cell migration and invasion. *Met. Based Drugs* **2009**, *2009*, 681270. [CrossRef]

123. Trondl, R.; Heffeter, P.; Kowol, C.R.; Jakupec, M.A.; Berger, W.; Keppler, B.K. NKP-1339, the first ruthenium-based anticancer drug on the edge to clinical application. *Chem. Sci.* **2014**, *5*, 2925–2932.

124. Bytzek, A.K.; Koellensperger, G.; Keppler, B.K.; Hartinger, C.G. Biodistribution of the novel anticancer drug sodium trans-[tetrachloridobis(1H-indazole)ruthenate(III)] KP-1339/IT139 in nude BALB/c mice and implications on its mode of action. *J. Inorg. Biochem.* **2016**, *160*, 250–255. [CrossRef] [PubMed]

125. Hartinger, C.G.; Jakupec, M.A.; Zorbas-Seifried, S.; Groessl, M.; Egger, A.; Berger, W.; Zorbas, H.; Dyson, P.J.; Keppler, B.K. KP1019, a new redox-active anticancer agent—Preclinical development and results of a clinical phase I study in tumor patients. *Chem. Biodivers.* **2008**, *5*, 2140–2155. [CrossRef] [PubMed]

126. Henke, M.M.; Richly, H.; Drescher, A.; Grubert, M.; Alex, D.; Thyssen, D.; Jaehde, U.; Scheulen, M.E.; Hilger, R.A. Pharmacokinetic study of sodium trans[tetrachlorobis(1H-indazole)-ruthenate (III)]/-indazole hydrochloride (1:1.1) (FFC14A) in patients with solid tumors. *Int. J. Clin. Pharmacol. Ther.* **2009**, *47*, 58–60. [CrossRef]

127. Fuereder, T.; Berger, W. Metal drugs become targeted. *ESMO Open* **2017**, *2*, e000239. [CrossRef]

128. Kenny, R.G.; Marmion, C.J. Toward multi-targeted platinum and ruthenium drugs—A new paradigm in cancer drug treatment regimens? *Chem. Rev.* **2019**, *119*, 1058–1137. [CrossRef]

129. Bednarski, P.J.; Mackay, F.S.; Sadler, P.J. Photoactivatable platinum complexes. *Anticancer Agents Med. Chem.* **2007**, *7*, 75–93. [CrossRef]

130. Wang, N.; Deng, Z.; Zhu, Q.; Zhao, J.; Xie, K.; Shi, P.; Wang, Z.; Chen, X.; Wang, F.; Shi, J.; et al. An erythrocyte-delivered photoactivatable oxaliplatin nanoprodrug for enhanced antitumor efficacy and immune response. *Chem. Sci.* **2021**, *12*, 14353–14362. [CrossRef]

131. Bolitho, M.E.; Sanchez-Cano, C.; Shi, H.; Quinn, P.D.; Harkiolaki, M.; Imberti, C.; Sadler, P.J. Single-cell chemistry of photoactivatable platinum anticancer complexes. *J. Am. Chem. Soc.* **2021**, *143*, 20224–20240. [CrossRef]

132. van Zutphen, S.; Reedijk, J. Targeting platinum anti-tumour drugs: Overview of strategies employed to reduce systemic toxicity Coord. *Chem. Rev.* **2005**, *249*, 2845–2853. [CrossRef]

133. Marian, E.; Duțeanu, N.; Vicaș, L.; Rusu, G.; Jurca, T.; Mureșan, M.; Micle, O.; Hangan, A.C.; Stan, R.L.; Ionescu, C.; et al. Synthesis, characterization of inclusion compounds of amygdalin with β-cyclodextrin and sod-like activity and cytotoxicity on hela tumor cells. *Arab. J. Chem.* **2020**, *13*, 6828–6837. [CrossRef]

134. Krasnovskaya, O.O.; Guk, D.A.; Naumov, A.E.; Nikitina, V.N.; Semkina, A.S.; Vlasova, K.Y.; Pokrovsky, V.; Ryabaya, O.O.; Karshieva, S.S.; Skvortsov, D.A.; et al. Novel Copper-Cytotoxic Agents Based on 2-Thioxoimidazolones. *J. Med. Chem.* **2020**, *63*, 13031–13063. [CrossRef] [PubMed]

135. Simpson, P.V.; Desai, N.M.; Casari, I.; Massi, M.; Falasca, M. Metal-based antitumor compounds: Beyond cisplatin. *Future Med. Chem.* **2019**, *11*, 119–135. [CrossRef] [PubMed]

136. Gomes, B.S.; Simoes, B.; Mendes, P.M. The increasing dynamic, functional complexity of bio-inetrface materials. *Nat. Rev. Chem.* **2018**, *2*, 0120. [CrossRef]

137. Zhao, R.; Xiang, J.; Wang, B.; Chen, L.; Tan, S. Recent advances in the development of noble metal NPs for cancer therapy. *Bioinorg. Chem. Appl.* **2022**, 2444516.

138. Zumaya, A.L.V.; Mincheva, R.; Raquez, J.M.; Hassouna, F. Nanoclusters-based drug delivery and theranostic systems: Towards cancer therapy. *Polymers* **2022**, *14*, 1188. [CrossRef]

139. Gianasi, E.; Buckley, R.G.; Latigo, J.; Wasil, M.; Duncan, R. HPMA copolymers platinates containing dicarboxylato ligands. Preparation, characterisation and in vitro and in vivo evaluation. *J. Drug Target.* **2002**, *10*, 549–556. [CrossRef]

140. Rademaker-Lakhai, J.M.; Terret, C.; Howell, S.B.; Baud, C.M.; de Boer, R.F.; Pluim, D.; Beijnen, J.H.; Schellens, J.H.; Droz, J.P. A Phase I and Pharmacological Study of the Platinum Polymer AP5280 Given as an Intravenous Infusion Once Every 3 Weeks in Patients with Solid Tumors. *Clin. Cancer Res.* **2004**, *10*, 3386–3395. [CrossRef]

141. Sood, P.; Thurmond, K.B.; Jacob, J.E.; Waller, L.K.; Silva, G.O.; Stewart, D.R.; Nowotnik, D.P. Synthesis and characterization of AP5346, a novel polymer-linked diaminocyclohexyl platinum chemotherapeutic agent. *Bioconjug. Chem.* **2006**, *17*, 1270–1279. [CrossRef]

142. Nowotnik, D.P.; Cvitkovic, E. ProLindac™ (AP5346): A review of the development of an HPMA DACH platinum polymer therapeutic. *Adv. Drug Deliv. Rev.* **2009**, *61*, 1214–1219. [CrossRef] [PubMed]

143. Larsen, S.; Butthongkomvong, K.; Manikhas, A.; Trishkina, E.; Poddubuskaya, E.; Matrosova, M.; Srimuninnimit, V.; Lindkaer-Jensen, S. BP-C1 in the treatment of patients with stage IV breast cancer: A randomized, double-blind, placebo-controlled multicenter study and an additional open-label treatment phase. *Breast Cancer* **2014**, *6*, 179–189. [CrossRef] [PubMed]

144. Browning, R.J.; Reardon, P.J.T.; Parhizkar, M.; Pedley, R.B.; Edirisinghe, M.; Knowles, J.C.; Stride, E. Drug delivery strategies for platinum-based chemotherapy. *ACS Nano.* **2017**, *11*, 8560–8578. [CrossRef] [PubMed]

145. Doi, T.; Hamaguchi, T.; Shitara, K.; Iwasa, S.; Shimada, Y.; Harada, M.; Naito, K.; Hayashi, N.; Masada, A.; Ohtsu, A. C-6004 Phase I study in combination with gemcitabine for advanced solid tumors and population PK/PD analysis. *Cancer Chemoter. Pharmacol.* **2017**, *79*, 569–578. [CrossRef] [PubMed]

146. Subbiah, V.; Grilley-Olson, J.E.; Combest, A.J.; Sharma, N.; Tran, R.H.; Bobe, I.; Osada, A.; Takahashi, K.; Balkissoon, J.; Camp, A.; et al. Phase Ib/II Trial of NC-6004 (Nanoparticle Cisplatin) plus Gemcitabine in patients with advanced solid tumors. *Clin. Cancer Res.* **2018**, *24*, 43–51. [CrossRef]

Review

Recent Trends in the Development of Novel Metal-Based Antineoplastic Drugs

Lozan Todorov * and **Irena Kostova**

Department of Chemistry, Faculty of Pharmacy, Medical University-Sofia, 1504 Sofia, Bulgaria
* Correspondence: ltodorov@pharmfac.mu-sofia.bg

Abstract: Since the accidental discovery of the anticancer properties of cisplatin more than half a century ago, significant efforts by the broad scientific community have been and are currently being invested into the search for metal complexes with antitumor activity. Coordination compounds of transition metals such as platinum (Pt), ruthenium (Ru) and gold (Au) have proven their effectiveness as diagnostic and/or antiproliferative agents. In recent years, experimental work on the potential applications of elements including lanthanum (La) and the post-transition metal gallium (Ga) in the field of oncology has been gaining traction. The authors of the present review article aim to help the reader "catch up" with some of the latest developments in the vast subject of coordination compounds in oncology. Herewith is offered a review of the published scientific literature on anticancer coordination compounds of Pt, Ru, Au, Ga and La that has been released over the past three years with the hope readers find the following article informative and helpful.

Keywords: platinum; ruthenium; gallium; gold; lanthanum; coordination complexes; oncology; cancer research

1. Introduction

Oncological diseases are the second leading cause of death worldwide with 9.6 million deaths in 2018 as per the World Health Organization fact sheet. Cancer treatment involves surgery, chemotherapy and radiotherapy [1]. Novel photodynamic therapy is a method that involves administration of a photosensitizing compound, followed by irradiation with an absorbance maximum wavelength and subsequent, localized formation of reactive oxygen species (ROS), such as singlet oxygen [2]. The aim is to produce significant, toxicological effects in the area of the tumor tissue, causing apoptosis, necrosis and finally—cell death [3]. Transition metals play an essential role in the chemistry of life. Serving as cofactors in enzymatic active sites, they enable the great multitude of selective catalytic conversions necessary for maintaining biological processes [4]. In living organisms, transition metals can be found in trace amounts. Excessive intake of such elements can cause a variety of toxicological effects, including carcinogenesis [5]. Yet exactly that toxicological potential presents the fundament of transition-metal-based anticancer therapies [6]. Intracellular release of toxic metal ions such as Pt(II)/(IV), Au(I)/(III), Ru(II)/(III), La(III), Ga(III) and many others has been a staple of metal-based anticancer treatments ever since the discovery of cisplatin's antiproliferative properties more than half a century ago [7]. The authors of the present review aim to inform the reader about developments over the past three years in the research of Pt, Ru, Au and La transition metal complexes with potential antitumor properties. Gallium as a post-transition metal is also discussed since the biological activity of its ion is well-established [8] and the search for novel gallium complexes with anticancer action is gaining traction once again [9,10].

2. Novel Metal Complexes in Cancer Therapy

2.1. Platinum Coordination Compounds

Platinum-based drugs are widely used in anticancer chemotherapy. The first coordination complex discovered with clinically viable antitumor action was *cis*-diamminedichloroplatinum(II) ubiquitously known as cisplatin. Its biological activity was serendipitously discovered in the 1960s by Rosenberg and coworkers [11]. Together with carboplatin, oxaliplatin, nedaplatin and lobaplatin it is a choice drug for treatment of a variety of malignancies such as testicular, colorectal, ovarian and breast cancer [12]. Cisplatin is characterized by low specificity and its clinical use is therefore associated with systemic toxicities [12]. Carboplatin is considered a second-generation platinum-based drug with a higher degree of biosafety [13] that allows for treatment with higher dosages. The main mechanism of action of Pt(II) involves DNA binding, forming intra-strand and inter-strand crosslinks, changing DNA structure, resulting in cell cycle arrest and apoptosis in actively proliferating tumor cells [14]. Platinum drug resistance is a significant issue in chemotherapy. In order to be overcome, a third-generation complex, oxaliplatin, was introduced in 1996 [15]. The mechanisms of action of these drugs, their toxicities and modes of development of drug resistance are well-known and described in detail in the scientific literature [16,17], and a number of exhaustive reviews on the subject have been published [6,18,19]. An alternative area of research when it comes to platinum-based anticancer drugs involves Pt(IV) coordination compounds. Compared to Pt(II) they have higher coordination numbers (6 vs. 4), improved stability and reduced side effects. The ability to coordinate axial ligands allows for greater structural modification. Additionally, within the intracellular medium they are reduced to their active Pt(II) counterparts, with the axial ligands leaving. For these reasons, Pt(IV) complexes are viewed as potential platinum prodrugs [20,21]. A very attractive and informative review on the subject of Pt(IV) in cancer research [21] presents exciting results both in terms of safety and drug resistance. Notably, coordinating biologically active ligands could produce "multi-action" and "cancer-seeking" Pt(IV) prodrugs with enhanced efficacy and multiple mechanisms of action [21]. Promising results have been observed in vitro when treating cancer cell lines; however, there is a long way to go until safety and efficacy in humans would be properly assessed. Below are introduced the most recent Pt(II) and Pt(IV) complexes discussed in the scientific literature over the past three years.

Zhu and coworkers tested a variety of mitochondria-targeted platinum complexes for anticancer activity against lung cancer [22]. They modified pyriplatin with a triphenylphosphonium moiety (Figure 1) with the aim to selectively target and penetrate the inner mitochondrial membrane.
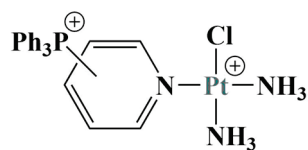
Figure 1. Modified pyriplatin, described in [22].

Three complexes were synthesized with a triphenylphosphonium substitute, attached at the ortho-, meta- and para-positions of the pyridine ring. They were tested for antiproliferative activity against lung cancer A549, cervical cancer HeLa, hepatocellular carcinoma SMMC cells and normal liver HL-7702, with the aid of the 3-(4,5-dimethylthiazol-2-yl)-2,5-diphenyltetrazolium bromide (MTT, 48 h) assay. The ortho-substituted complex manifested the highest anticancer cytotoxicity (IC_{50} = 8.7 μM against A549), even compared to the positive standards cisplatin and pyriplatin. Its IC_{50} against healthy HL-7702 cells was about six times higher (IC_{50} = 64.5), speaking to the improved selectivity of the compound. Tumor growth in mice, implanted with A549, was significantly suppressed. Pt was discovered to accumulate primarily in liver and kidneys. More Pt was accumulated in the lungs and tumor tissue, compared to cisplatin. After 24 h of cultivation the ortho-substituted complex was found to produce mitochondrial DNA (mtDNA) lesions, reduce oxygen consumption

and decrease dramatically (by 87%) the mitochondrial membrane potential in A549 cells. Cellular uptake was observed to increase with lipophilicity.

Eskandari et al. [23] synthesized a triangular polynuclear complex, containing three Pt(II) centers and tested it against cancer stem cell (CSC)-enriched human mammary epithelial cells HMLER-shEcad and CSC-depleted HMLER lines (MTT assay, 72 h). Mono- and dinuclear analogs were also tested. Notably, the more Pt(II) centers in the complex, the greater the antiproliferative activity. The trinuclear complex had the lowest IC_{50} (2.24 μM against HMLER and 1.26 against HMLER-shEcad). Its activity was greater than the positive controls cisplatin, carboplatin and salinomycin. The IC_{50} against non-malignant breast MCF10A cells was about two times greater than against HMLER-shEcad, showing good selectivity. It manifested significant non-covalent DNA-intercalative and groove-binding activity.

He et al. [24] synthesized a folate-containing Pt(II) complex (Figure 2) with the idea to specifically target folate receptors that tend to be overexpressed on the surfaces of breast cancer cells.
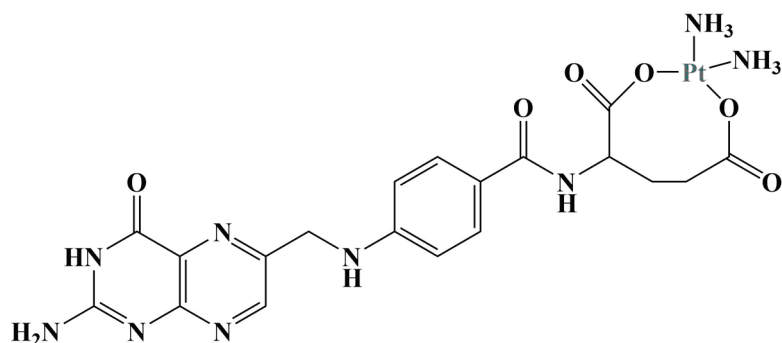
Figure 2. The folate-Pt(II) complex described in [24].

After 72 h's exposure, the complex significantly suppressed MCF-7 cell viability (IC_{50} = 87) compared to the negative control. The complex increased Bak1/Bclx ratios after 24 h of incubation, compared to cisplatin, a possible sign of pro-apoptotic activity. Caspase-3 activity was also increased.

Adams and coworkers synthesized a number of Pt(II)-terpyridine complexes (Figure 3) and subsequently tested them for in vitro antiproliferative properties against colon cancer HCT 116, colon adenocarcinoma SW480, lung cancer NCI-H460 and endometrial carcinoma SiHa cell lines (72 h incubation) [25].

Complex:	R:
1	-OH
2	-O⌒N(CH₂CH₂OH)₂
3	-O⌒N(CH₂CH₂Cl)₂
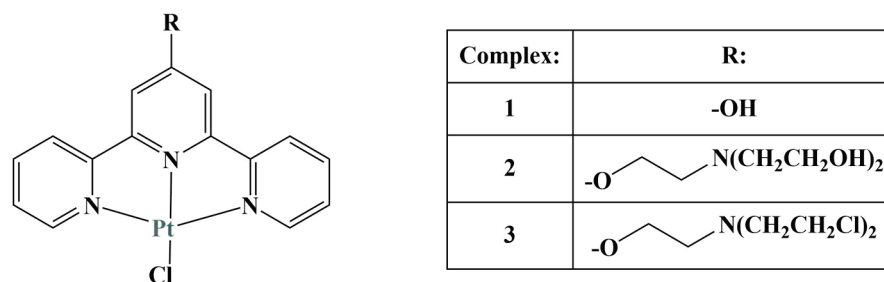
Figure 3. Three Pt(II)-terpyridine complexes, described in [25].

Substituting the hydroxyl group of complex 1 with an organic mustard-type side chain significantly increased the antiproliferative activity of the complex against all cell lines tested. IC_{50} values decreased in the following order complex 3 (IC_{50} between 0.4 and 4.0) > complex 2 (IC_{50} between 1.0 and 5.6) > complex 1(IC_{50} between 14 and 22). What should be noted is that the corresponding ligands themselves were very active in the nanomolar range. Adding Pt(II) to form complexes increased IC_{50} values more than ten-fold. Despite that, complexes 2 and 3 suppressed cancer cell growth to the same degree

or even further than the positive control cisplatin. Additional assays showed rapid binding to L-histidine, 9-ethylguanine and L-cysteine.

Another series of four platinum–terpyridine complexes [26] were studied as promising antiproliferative agents against A549, its cisplatin-resistant subline A549/DDP, epidermoid carcinoma A431, HeLa and MCF-7. Results showed that all tested substances were as active, or more active, compared to the positive control cisplatin, targeting not only DNA, but also membrane proteins. Epidermal growth factor receptor (EGFR) inhibitory activity was estimated to be higher (IC$_{50}$ about 10 μM for the complexes) than that of gefitinib (IC$_{50}$ of about 90 μM).

Kutlu and coworkers [27] synthesized two pyridine-based Pt(II) complexes (Figure 4) and tested them against the colon cancer cell line (DLD-1). After 24 h incubation, applying the MTT assay, complex 1 behaved as a stronger cytostatic (IC$_{50}$ = 25.79 μM), compared to complex 2.
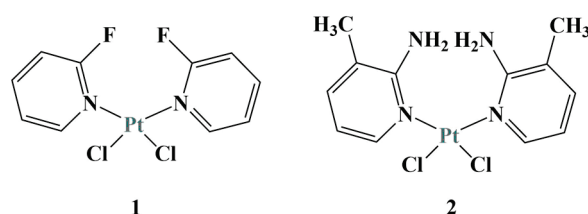
Figure 4. The pyridine-based complexes 1 and 2 described in [27].

The presence of electron-withdrawing functional groups (such as fluorine atoms in complex 1) was deemed responsible for the increased antiproliferative effect. In this case, the authors proposed that the bond between the pyridine nitrogen and the platinum ion decreases due to lower electron density, causing an effective increase in interaction with DNA. Electron donors such as the amino- and methyl- groups in complex 2 would tend to have the opposite effect.

Mbugua and coworkers [28] synthesized Pt(II) and Pd(II) complexes with pyrrole-substituted Schiff bases. The newly-generated substances were tested with the aid of the MTT test (24 h exposure) against the colorectal adenocarcinoma Caco-2, HeLa, Hep-G2, MCF-7 and bone cancer PC-3 cell lines. Non-cancerous MCF-12A was also tested. The most active Pt(II) complex (Figure 5) was extremely potent against Hep-G2, with IC$_{50}$ being in the nanomolar range (IC$_{50}$ = 0.3 μM). It also suppressed the Caco-2, MCF-7 and PC-3 (IC$_{50}$ ranging between 16 and 30 μM).
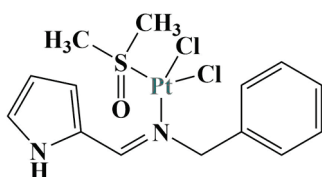
Figure 5. The most potent antiproliferative complex described in [28].

The complex manifests a strong DNA-binding ability, the authors proposed using it as a possible viable candidate for DNA intercalation. Its low toxicity against the healthy MCF-12A shows its potential as a selective molecule with anticancer activity.

Another Schiff base containing complex was synthesized, characterized and tested for antiproliferative activity against MCF-7, Hep-G2, HeLa and A549 cancer cells and non-cancerous NHDF cells [29]. The complex exhibited pronounced activity against MCF-7. Its antiproliferative behavior against the cancer cell lines was significant, though lower than that of cisplatin. On the other hand, toxicity against the healthy NHDF cells was low, showing better selectivity than the positive control. Additionally, the ligand itself was less active than the complex. Significant calf thymus DNA (CT-DNA) binding was observed.

A number of potent phenanthriplatin analogs [30] (Figure 6) with multidentate ligands have been synthesized and tested (MTT assay, 72 h) for anticancer activity against the ovarian cancer A2780, its cisplatin-resistant variant A2780cis, ovarian adenocarcinoma SKOV-3, triple-negative breast cancer MDA-MB-231 and A549 cancer cell lines. Toxicity against normal MET5A and HEK-293 cells was also measured.
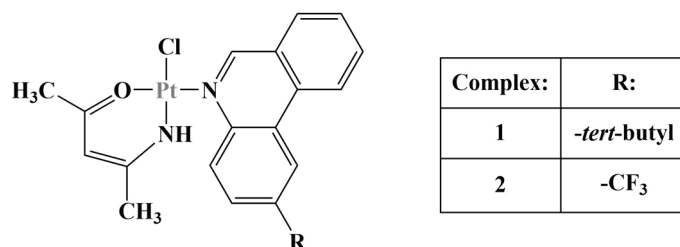

Complex:	R:
1	*-tert*-butyl
2	-CF_3

Figure 6. The complexes described in [30].

Both ligands were inactive in the absence of the Pt(II) coordination center. Complex 2 was much more effective than complex 1. After 72 h incubation, complex 2 was found to be more potent than cisplatin against all cancer cell lines, including the cisplatin-resistant A2780cis (IC_{50} = 0.55 µM). Its toxicity against normal cells was decreased compared to phenanthriplatin. Cellular uptake was also improved and apoptosis was induced.

Tham and coworkers [31] followed a novel approach in terms of Pt-based anticancer therapy. They attempted to cause immunogenic cell death by causing endoplasmic reticulum stress. The novel compounds were tested against CT26 colorectal carcinoma (IC_{50} between 1.5 and 8.8 µM). Increasing lipophilicity caused a corresponding increase in cellular uptake. The most potent complex increased intracellular ROS levels and caused endoplasmic reticulum stress. An induction in phagocytosis-related signaling was observed.

Derivatives of benzothiazole aniline [32] (a substance with known anticancer properties) were used as ligands it order to produce selective anticancer agents (Figure 7). Cell viability was measured using the cell counting kit 8 (CCK-8) method (24 h cultivation).
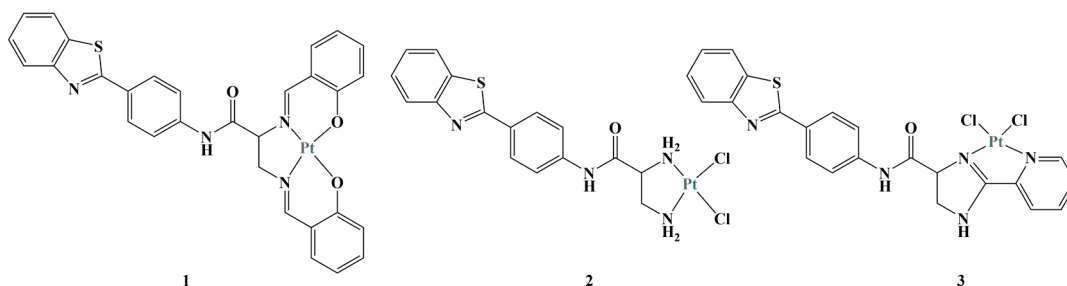
Figure 7. The complexes described in [32].

All three complexes were less active than their corresponding organic ligands, but more active that benzothiazole aniline itself. Complexes 1 and 2 were particularly effective against the Hep-G2 human hepatic carcinoma cell line (half-maximal inhibitory concentration below 30 µM). Complex 1 moderately suppressed the proliferation of rat glioma C6, HeLa, colorectal adenocarcinoma HT-29 and MCF-7 cancer cell lines (IC_{50} below 100 µM). Toxicity against a variety of non-malignant cell lines was measured, revealing good selectivity toward cancer cells. Molecular docking revealed that complex 1 acted as an intercalating agent, binding to the minor groove of DNA.

A series of pyridine co-ligand functionalized cationic complexes inhibited proliferation in MCF-7, A549 and Hep-G2 cancer cells [33]. MTT testing proved a concentration-dependent antiproliferative effect (48 h treatment). The most active complexes are displayed on Figure 8.
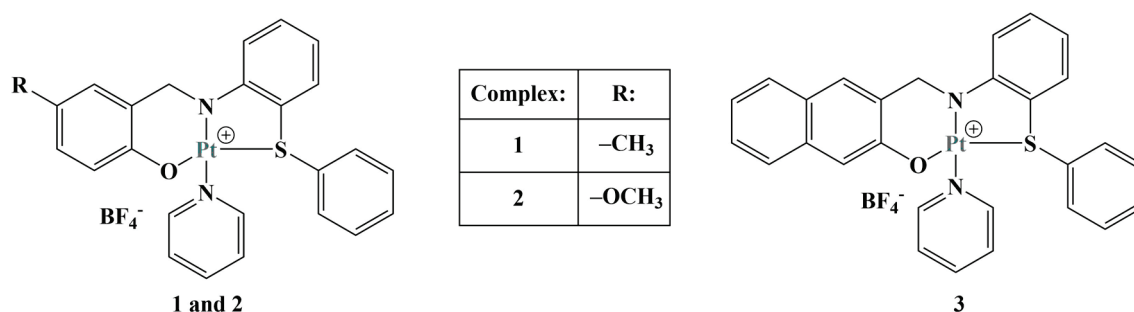
Figure 8. The complexes described in [33].

Cancer cell tests revealed complexes 1 and 2 to be more potent than the positive control oxaliplatin and as potent as cisplatin. Complex 3 was more potent than both positive controls. Clonogenic studies showed that these three complexes suppressed the clonogenic potential of the tested cell lines. Cancer cell migration, invasion and cancer stem cell spheroid formation were decreased. Complex 3 demonstrated potential to target sterol regulatory element-binding protein 1 (SREBP-1)-dependent signaling pathways, thus inhibiting lipid biogenesis.

Nadar and coworkers [34] designed radioactive platinum(II)–bisphosphonate complexes in an attempt to specifically target bone cancer. The aim was to combine the anticancer activity of Pt(II) with the good radionuclide potential of its radioactive isotope ^{195}Pt and the bone-targeting properties of bisphosphonates. This novel approach yielded promising results as Pt uptake, due to treatment of mice with the novel complex, was concentrated in the hard tissues, compared to a Pt(II) bearing, non-bisphosphonate positive control.

Pt(II), liganded with two bidentate analogs of thiourea (a known anticancer molecule) exhibited a moderate antiproliferative effect (MTT assay, 48 h) against colorectal cancer LoVo and MCF-7 with an IC$_{50}$ greater than 100 μM [35]. Interestingly, if Pt(II) was exchanged with Pd(II) as a coordination center, then antiproliferative activity dramatically improved (IC$_{50}$ between 10.44 and 62.86 μM), approaching that of cisplatin.

Mononuclear, Schiff base macrocyclic ligands were synthesized and coordinated with Pt(II) [36] (Figure 9). MTT assay (24 h incubation) was performed in order to estimate potential antiproliferative activity. Both ligands significantly suppressed the HeLa (IC$_{50}$ between 12 and 15 μM) and A549 cell lines (IC$_{50}$ = 10 μM). The addition of Pt(II) further improved the observed effect with an IC$_{50}$ between 6 and 11 μM.
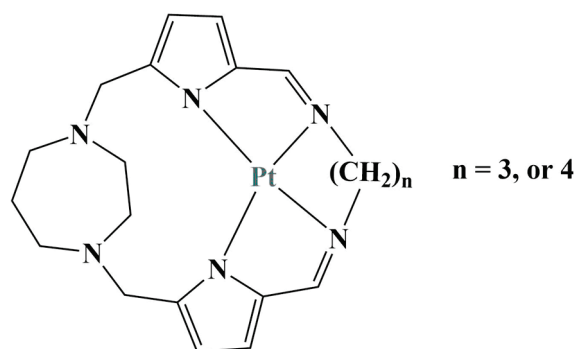
Figure 9. The macrocyclic Pt(II) complexes described in [36].

A Pt(II) complex with an ONN-"pincer" ligand [37] showed significant antiproliferative effect against Hep-G2 cells (IC$_{50}$ = 6 to 12 μM), comparable to cisplatin. Activity against normal hPBMC was very mild, where IC$_{50}$ > 200 μM.

Yambulatov and coworkers have synthesized a series of Pt(II) complexes with substituted 1,4-diaza-1,3-butadienes (redox-active, "non-innocent" ligands) [38]. They were tested for antiproliferative activity against malignant SKOV-3 and normal HDF cell lines.

One of the complexes manifested significant activity against SCOV-3, similar to cisplatin (IC$_{50}$ = 12 μM) and high toxicity against the non-cancerous cell line (IC$_{50}$ = 9 μM)

Octahedral platinum (IV) complexes with the non-steroidal anti-inflammatory drugs indomethacin and acetylsalicylic acid as axial ligands have been reported [39]. After 72 h of incubation, the MTT assay showed significant cytotoxicity against a large panel of cancer cell lines. Particularly notable was the manifested activity against ovarian A2780 and cisplatin-resistant ovarian (ADDP) cancer cell lines. Activity against HT-29 colon cancer was also significantly increased in comparison to the positive controls cisplatin, carboplatin and oxaliplatin.

Another Pt(IV) prodrug was designed with two axial maleimide moieties to facilitate albumin binding [40]. Testing was performed on an in vivo murine cancer CT26 model. Twenty days after the beginning of treatment, tumor growth was significantly suppressed compared to the positive control oxaliplatin. Survival of the test animals was prolonged, some even entered remission and one was completely cured. The authors propose the formation of a stable albumin adduct in the blood stream, followed by cellular endocytosis and subsequent reduction of Pt(IV) to active Pt(II).

A series of mono-axial octahedral diazido Pt(IV) complexes with coumarin 3-carboxylate (an anticancer agent), 4-phenylbutyrate or dichloroacetate (PDK inhibitors) and their di-axial functionalized analogs were synthesized and tested against A2780 and A549 [41]. Cytotoxicity was measured versus healthy MRC-5 fibroblasts as well. Both mono- and di-functionalized complexes manifested significant photocytotoxicity after irradiation with blue light with IC$_{50}$ values in the nanomolar range (IC$_{50}$ = 0.11–7.1 for A2780 and 1.2–51.9 for A549). At equimolar concentrations, the di-functionalized complexes caused higher platinum cell accumulation and photogenerated ROS, compared to their mono-functionalized analogs. Another diazido-Pt(IV) complex [42] (Figure 10) was unreactive in the dark, but highly cytotoxic when irradiated with visible or UV light (MTT test, 2 h exposure). It acted as a prodrug that, upon photoactivation, was reduced to square planar Pt(II) species that binds to nuclear DNA. Additionally, photoactivation causes the release of a variety of reactive species such as azidyl and hydroxyl radicals, singlet oxygen and others that further add to the cytotoxic effect and possibly cause immunogenic cell death.
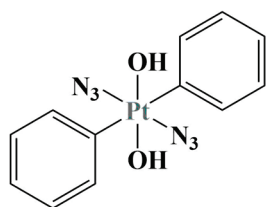
Figure 10. The diazido-complex described in [42].

When photoactivated, the complex is able to induce calreticulin exposure on the membrane of A2780 cells as well as the release of high mobility group box 1 (HMGB1) protein and ATP to the extracellular environment—known symptoms of immunogenic cell death.

Essential information on the Pt complexes' structure, type of cancer cells suppressed and biological activity has been summarized in Table 1.

Table 1. Summary of the platinum complexes presented.

Citation Number	Metal Ion/Ligand Type	Effective against	Biological Activity (If Investigated)
[22]	Pt(II), triphenylphosphonium-pyridine	A549; HL-7702	mtDNA lesions, impairment of mitochondrial membrane potential
[23]	Pt(II), triangular polynuclear complex	HMLER; HMLER-shEcad; MCF10A	DNA intercalation; DNA groove binding
[24]	Pt(II), folic acid	MCF-7	increased Bak1/Bclx ratios and Caspase-3 activity
[25]	Pt(II), terpyridine	HCT116; SW480; NCI-H460; SiHa	Binding to L-histidine, 9-ethylguanine and L-cysteine
[26]	Pt(II), terpyridine	A549; A549/DDP; A431; HeLa; MCF-7	DNA binding; EGFR inhibition
[27]	Pt(II), substituted pyridines	DLD-1	n/a
[28]	Pt(II), pyrrole-substituted Schiff bases	Caco-2; HeLa; Hep-G2; MCF-7; PC-3	DNA intercalation
[29]	Pt(II), Schiff base	MCF-7	CT-DNA binding
[30]	Pt(II), phenanthridine	A2780; A2780cis; SKOV-3; MDA-MB-231; A549	Apoptosis
[31]	Pt(II), N-heterocyclic carbene (NHC)	CT26	Induction of endoplasmic reticulum stress, increase in ROS
[32]	Pt(II), benzothiazole aniline	C6; HeLa; HT-29; MCF-7	DNA intercalation
[33]	Pt(II), pyridine cationic	MCF-7; A549; Hep-G2	sterol regulatory element-binding protein 1 (SREBP-1) targeting, lipid biogenesis inhibition
[34]	Pt(II), radioactive bisphosphonate	n/a	Theragnostic, bone accumulation in mice
[35]	Pt(II), thiourea	LoVo; MCF-7	n/a
[36]	Pt(II), macrocyclic Schiff base	HeLa; A549	n/a
[37]	Pt(II), ONN-"pincer"	Hep-G2	n/a
[38]	Pt(II), 1,4-diaza-1,3-butadiene	SCOV-3	n/a
[39]	Pt(IV), axial ligands indomethacin/ acetylsalicylic acid	A2780 ADDP	n/a
[40]	Pt(IV), axial maleamide	CT-26 (in vivo murine model)	Albumin binding enhances drug accumulation in cancer cells
[41]	Pt(IV), mono- and di-axial diazido complex	A2780; A549	Photocytotoxicity, DNA binding, ROS generation
[42]	Pt(IV), diazido complex	A2780	UV-induced photocytotoxicity, ROS generation, immunogenic cell death

2.2. Ruthenium Coordination Compounds

Platinum-based drugs are undeniably effective in the treatment of a variety of cancers. Unfortunately, they are not a "silver bullet"—limited activity against many common neoplastic diseases, significant toxicity and acquired platinum resistance [43] have all pushed the broader scientific community to look for alternatives. One such alternative is presented by another member of the transition metal family—ruthenium. It is redox-active, i.e., exists in a variety of oxidation states, the most prominent under physiological conditions being +2 and +3 (the former is considered more active) [44]. Ru(II)/(III) complexes are characterized by six-coordinated octahedral configuration, allowing for employment of biologically active ligands with different geometries. Rates of ligand exchange in Ru(II) and Ru(III) complexes are similar [45] to those of Pt(II). Ru compounds are considered less toxic than Pt. Ionic mimicry (similar ionic charge/ionic radius ratios) allows Ru to compete with Fe for binding with biomolecules, employing the transferrin pathway to specifically target cancer cells [46]. Protein and DNA binding, impairment of mitochondrial functions, cell cycle

arrest and apoptosis are frequently described. Photoactivation is also a prominent feature of Ru-complex research. It provides improved toxicity over a localized area, thus reducing systemic adverse events while promoting antiproliferative activity. Two main approaches toward synthesis of Ru-based anticancer complexes seem to prevail above all. The first one involves complexation with polypyridyl-type bi/tri-dentate ligands, employing a bipyridine, terpyridine or 1,10-phenanthroline scaffold. The second approach involves coordination with a five or six-membered arene ligand, a monodentate and a bidentate ligand. To the reader's benefit, the authors recommend a number of detailed reviews, delving deep into the subject of ruthenium complexes in anticancer therapy [43,44,47,48]. Henceforth the authors introduce some prominent samples of the vast experimental and publication efforts that have been invested over the past three years into the search for Ru-coordination compounds with anticancer activity.

A Ru(II) complex with a Schiff base and p-cymene as ligands was synthesized and tested against Caco-2 and normal mouse fibroblast L-929 strains [49]. The Schiff ligand itself and its ruthenium complex manifested low antiproliferative activity against Caco-2, the former being the less toxic of the two (IC_{50} = 803.65 and 510.26, respectively).

Cole and coworkers [50] synthesized a series of Ru complexes, two 6,6′-dimethyl-2,2′-bipyridine and an imidazo[4,5-f][1,10]phenanthroline ligand as potential photodynamic therapeutic agents (Figure 11). Cytotoxicities in dark conditions as well as photocytotoxicities were estimated using the resazurin viability assay in both hypoxic and normoxic conditions. All compounds were moderately active in dark conditions against SKMEL-28 melanoma cells (EC_{50} between 30−75 μM). Hypoxic conditions caused EC_{50} values to double, consistent with previous observations.
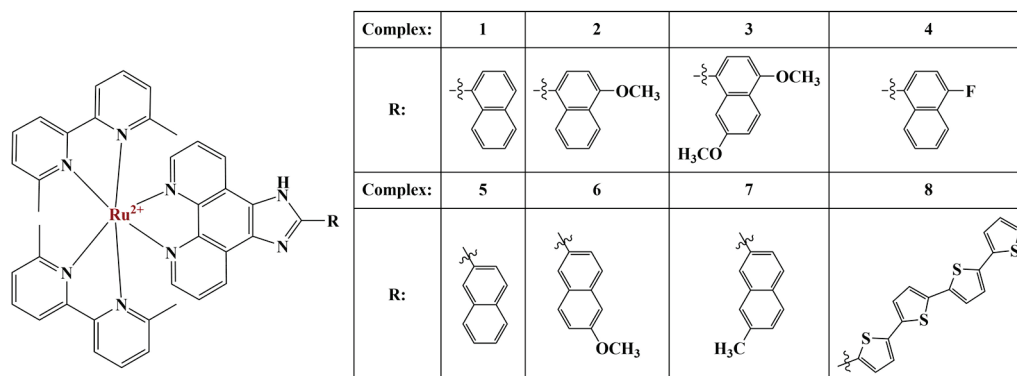
Figure 11. The complexes described by [50].

Irradiation with visible light increased cytotoxicity of compounds 1, 4, 6 and 7, dropping EC_{50} to between 2.5 to 5 μM. Compounds 1 and 7 maintained their high post-irradiation cytotoxicity even in hypoxic conditions. The authors tried irradiation with red and green light, with less success. When the substitute R was replaced by a chain of three or four thiophene rings (complex 8), the complex exhibited attomolar (in normoxia) and picomolar (in hypoxia) cytotoxicities toward SKMEL-28 cells [51]. The authors proposed the photosensitizing capacity of these complexes to be a result of efficient production of singlet oxygen and a possible involvement of triplet intra-ligand charge transfer states. Similar polypyridine ruthenium(II) complexes [52] were tested (MTT assay) against melanoma B16, Hep-G2, A549 cancer and LO2 normal cell lines. The antiproliferative effect was in the low micromolar range. Particularly against B16, the compounds performed better than cisplatin both in terms of antiproliferative effect and in terms of selectivity. Cell migration was disrupted, G0/G1 cell cycle arrest was observed and apoptosis was increased. B16 cells also experienced a significant increase in intracellular ROS. The Ru(II) complexes penetrated the mitochondrial membrane. Intracellular GSH was depleted and MDA levels were significantly increased compared to the non-treated control group.

Another novel photosensitizing polypyridyl complex incorporates the anthraquinone rhein [53] (Figure 12). The complex is lipophilic and able to penetrate the lysosomes of A549 cells.
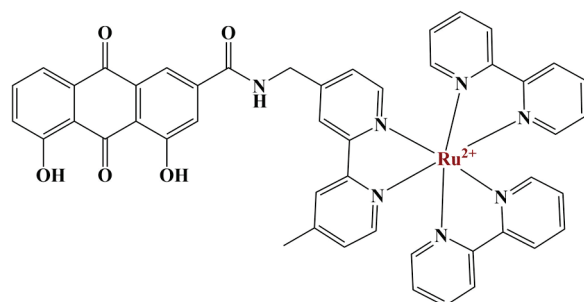

Figure 12. The complex described by [53].

In dark conditions, the complex does not generate intracellular ROS. Light irradiation causes intracellular ROS production. Cytotoxicities against MCF-7, A549, leukemia NB-4, A2780, cisplatin-resistant A2780R and normal liver cells LO2 were measured using the MTT assay in both light and dark conditions. IC$_{50}$ values against all cell lines are moderate (35 to 250 µM) after 48 h of cultivation in darkness. Furthermore, 15 min of irradiation increases toxicities dramatically (IC$_{50}$ of 35 to 25 µM). Phototoxicity indices against all cell lines are between 4 and 28.5. The authors propose the main mechanism of action in light conditions is the induction of autophagy.

Similar polypyridyl Ru(II) complexes have been synthesized, bearing a naphthoquinone moiety (plumbagin) [54]. The two most potent complexes bear two 1,10-phenanthroline plus one plumbagin ligands and two 4,7-diphenyl-1,10-phenanthroline and one plumbagin ligands. Increasing the lipophilicity of the ancillary ligands (from dimethyl sulfoxide (DMSO), through bipyridine and 1,10-phenanthroline to 4,7-dipjenyl-1,10-phenanthroline) increases biological activity against in vivo MCG-803 tumor mice model. The two most potent substances severely impair mitochondrial respiration and glycolysis, induce DNA damage and increase expression of the growth arrest and DNA damage inducible alpha (GADD45A) gene, causing G0/G1 cell cycle arrest.

Notaro and coworkers investigated a polypyridyl Ru(II) complex, incorporating a maltol ligand with the aim to improve bioavailability of the metal ion [55]. The compound was highly cytotoxic against HeLa, A2780 and its cisplatin and doxorubicin-resistant varieties A2780cis and A2780ADR, CT26, CT26LUC cancer cells and normal RPE-1 cells, manifesting no selectivity toward cancer cells. Adding the maltol moiety improved cytotoxicity of the complex (IC$_{50}$ = 0.42–2.86 µM), even though maltol itself is non-toxic. The compound induces apoptosis in HeLa cells after 4 h of incubation, cell accumulation being greater than that of cisplatin. It accumulates predominantly in the cellular nucleus. Another study [56] discovered that cellular resistance to ruthenium cyclometallated compounds depends on ABCB1 export and EGFR gene expression. Inhibiting these genes improved the biological activity.

Chen and coworkers tested a Ru(II) polypyridyl complex with intrinsic antiproliferative properties in combination with taxol [57] against HeLa and A549 cells and their taxol-resistant variants. Synergistic effects were observed, even at low dosages. Pyroptosis, caspase 1 activation, gasdermin D (GSDMD) activation and ROS increase in HeLa/Taxol cells was observed. An in vivo naked mice model also yielded promising results.

A series of N-heterocyclic carbene Ru(II) arene complexes [58] were synthesized and tested for antiproliferative activity (Figure 13).
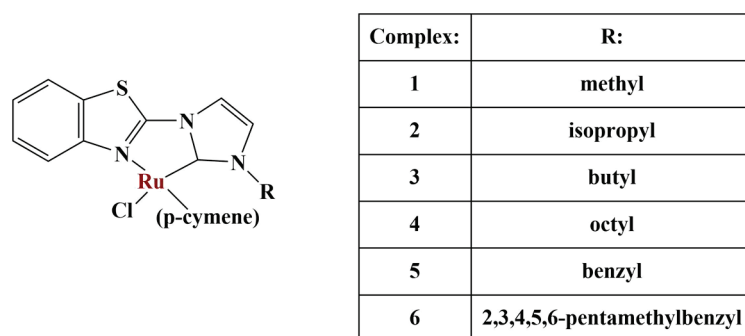
Complex:	R:
1	methyl
2	isopropyl
3	butyl
4	octyl
5	benzyl
6	2,3,4,5,6-pentamethylbenzyl

Figure 13. The complexes presented in [58].

After 48 h of exposure, results from the MTT assay demonstrated that attaching short alkyl moieties caused very low cytotoxicity. Complexes 4 and 6 had the highest lipophilicity and manifested high cytotoxicity, comparable to cisplatin, against a panel of cancer cell lines—A549, HT-29, HCT116, LoVo, HeLa and A2780 (IC$_{50}$ = 1.98−25.6). They exhibited antimigratory and proapoptotic activity against A2780 and induced mitochondrial dysfunction, releasing intracellular ROS.

Morais and coworkers tested a series of cyclopentadienyl Ru(II) complexes [59] with monodentate imidazole-based or bidentate heteroaromatic ligands. The investigated substances were very lipophilic. Binding to human serum albumin (HSA) was noted. Those that incorporate a bidentate heteroaromatic ligand manifested significant antiproliferative activity (MTT assay, 72 h) against A2780 (IC$_{50}$ = 0.20−0.45 μM), MDA-MB-231 (IC$_{50}$ = 13.4 to over 100 μM) and HT-29(IC$_{50}$ = 11.3 to over 100 μM), unlike the group with monodentate ligands.

Elsayed and coworkers [60] synthesized one Ru(II) and one Ru(III) complex, coordinated with 2-aminophenyl benzimidazole and DMSO (Figure 14-1 and -2, respectively)
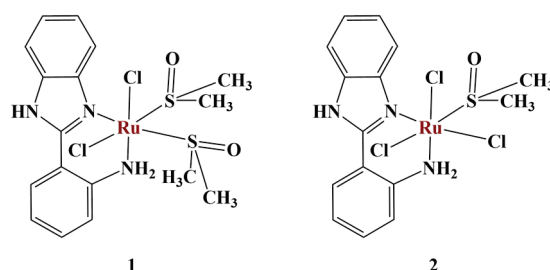
Figure 14. Complexes 1 and 2 presented in [60].

In vitro MTT assay showed that both complexes manifested moderate cytotoxicity against Caco-2 and MCF-7 (IC$_{50}$ = 230–320 μM) and very low toxicity against non-cancerous liver (THLE-2). Activity of the Ru(III) complex—complex 2—was higher than that of its Ru(II) analog. Treatment with complex 2 induced DNA laddering in both cancer cell types tested. G2/M cell cycle arrest was observed. An in vivo mouse model with Ehrlich ascites carcinoma (EAC) showed that complex 2 decreases liver damage markers in inoculated mice. The authors proposed that this complex prevented the growth of the EAC cells and caused cell death. Superoxide dismutase (SOD), catalase (CAT) and glutathione (GSH) levels increased in a dose-dependent manner compared to the non-treated group of animals.

A series of Biginelli hybrids were synthesized and liganded to Ru(II) [61]. The antiproliferative activity (MTT, 48 h exposure) against a panel of cancer cell lines of the series of ligands was moderate. Adding Ru(II) significantly increased potency. Two of the complexes (Figure 15) manifested significant cytotoxicity against HeLa, A375 and K562 cancer cells (IC$_{50}$ = 8.63−33.85 μM).
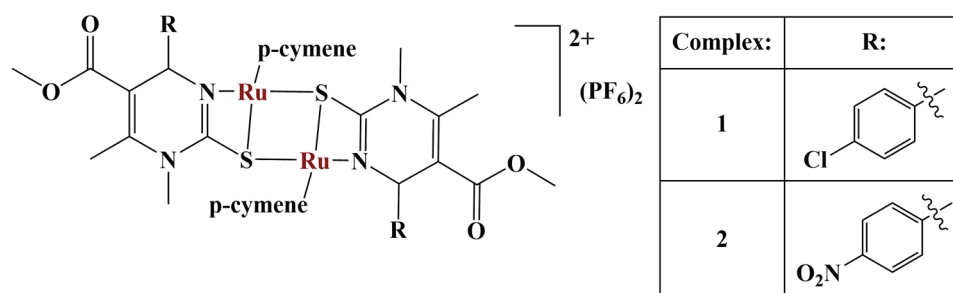
Figure 15. The complexes presented in [61].

Adding chlorine or nitro-groups to the aromatic ring seemed to increase cytotoxicity. These two complexes demonstrated pronounced antiangiogenic effects, via in vitro inhibition of endothelial cell tube formation after 48 h. Cell migration was also impeded.

A series of Ru(II)-p-cymene-imidazophenanthroline complexes [62] were synthesized and tested against the HeLa and CaCo-2 cancer cell lines and normal HEK-293 cells. CT-DNA and bovine serum albumin (BSA) binding was noted. The most prominent member (Figure 16) exhibited strong antiproliferative activity (MTT assay) at an IC_{50} of 2.0−2.5 μM. Toxicity against HEK293 was found to be low with selectivity factor of over 40.
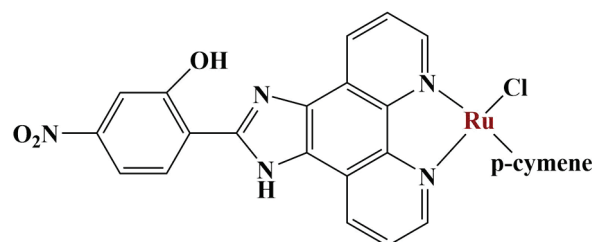
Figure 16. The most active complex presented in [62].

Strong antiproliferative activity was observed even in the presence of 1 mM GSH. Loss of activity was minimal. Adding electron-donating groups to the hydroxyphenyl moiety decreased biological activity, while addition of electron-withdrawing groups increased cytotoxicity. Similar complexes, incorporating substituted phenyl, instead of a substituted hydroxyphenyl moiety [63] were tested against the MDB-MA-231, HeLa and normal HEK293 cell lines. CT-DNA and BSA binding was noted here as well. The antiproliferative activity of the two most prominent substances toward cancer cells was similar to cisplatin (MTT assay); however, their toxicity toward the normal cell line was significantly lower—IC_{50} values of 85 and 178 against cisplatin's 64. A p-fluorophenyl moiety improved activity against HeLa and p-nitrophenyl moiety increased toxicity against MDB-MA-231.

Ru(II) complexes with diclofenac and organophosphines as ligands [64] (Figure 17) were synthesized and tested for biological activity. MTT testing revealed the compounds to be effective against A549, MDA-MB-231 and MCF-7 cancer cells, with an IC_{50} from 0.56 to 12.28 μM—similar to or lower than cisplatin.
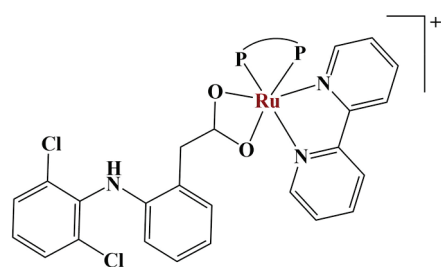
Figure 17. The complexes presented in [64].

The tested compounds were more toxic to the non-cancerous MRC-5 and MCF-10A cell lines compared to cisplatin. Interactions with BSA and CT-DNA were noted. One of the complexes induced apoptosis in MCF-7.

Two bis-aminophosphine Ru(II) complexes with p-cymene ligands [65] exhibited antiproliferative effects against A375 cells with IC_{50} values (6.72 and 8.76 μM) lower than cisplatin. Both compounds were more active than the bis-aminophosphine ligand alone. The complex, containing two units of p-cymene-Ru(II) induced apoptosis in the tested cell line.

A number of Ru(II) p-cymene complexes with cyclic/polycyclic aromatic diamine ligands [66] manifested better cytotoxic effects than cisplatin against the OVCAR-3, M-14 and HOP-62 cancer cell lines (IC_{50} = 4.31–6.31 μM). CT-DNA binding improved with the increase in the delocalization of the aromatic fragment of the ligand.

A series of dinuclear p-cymene-tetrazole-Ru(II) complexes [67] were tested against several types of cancer cell lines (MTT assay). The ligands themselves were non-cytotoxic. Two of the compounds yielded promising results against the HeLa, MCF-7 and A549 cell lines. DNA binding, bovine serum albumin binding and morphological changes indicating apoptosis were observed. G0/G1 cell cycle arrest was induced and cell migration was inhibited.

A number of half-sandwich arene chloride complexes of Ru(II) [68] were bound to CT-DNA and BSA protein. All complexes exhibited good anticancer potency against MCF-7 cells (IC_{50} = 2.64–18.21 μM).

Organometallic Ru(II)-flavone [69] complexes were synthesized and tested against the MCF-7 and MDA-MB-231 cell lines. Neither complex exhibited significant antiproliferative activity. Interestingly, one of the thioflavone ligands, containing a C=S group demonstrated very high cytotoxic activity against MCF-7. Once this functional group was engaged in complexation with Ru(III), anticancer activity was diminished, though still significant (IC_{50} = 1.2–43.06 μM). The Ru(II)-thioflavone complex was found to inhibit MCF-7 and MDA-MB-231 cell migration.

Ru(III)-pyrazolopyrimidine [70] complexes manifested stronger antiproliferative activity against SCOV-3 cells compared to cisplatin. Toxicity against normal liver cells was low. Cell invasion and proliferation were inhibited. Intracellular ROS levels increased, mitochondrial membrane potential was reduced and apoptosis was initiated.

Ru(II) complexes with biologically active aminoflavone ligands [71] were synthesized in order to overcome cisplatin resistance in a number of cell lines. The compounds (Figure 18) were tested against A2780, A2780cis, Toledo and Toledo-cis.
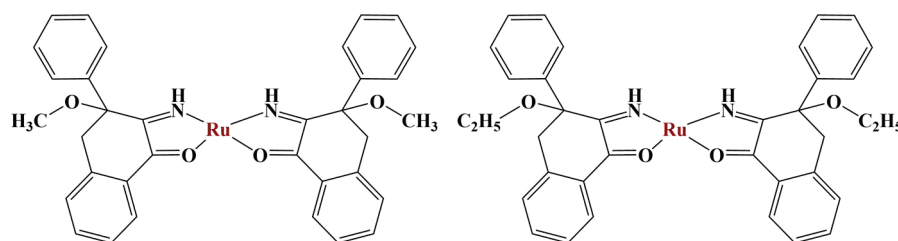

Figure 18. The complexes presented in [71].

They were effective in the low-micromolar range both against sensitive and cisplatin-resistant lines (MTT assay, IC_{50} = 0.5–4.6 μM). Mitochondrial membrane potential loss occurred in a dose-dependent manner. Apoptosis was induced due to interaction with DNA.

Conjugates containing two or three dinuclear Ru(II)–arene structures [72] have been tested against the A2780, A2780cisR (cisplatin-resistant), A24 and (D-)A24cisPt8.0 cell lines. All compounds are much more potent than cisplatin with an IC_{50} between 23 and 650 nM. Ester conjugates are more potent than amide analogs.

Qu and coworkers investigated how protonation states of ligands in Ru(II) complexes may influence photodissociation and quantum yields for singlet oxygen [73]. They observed

that deprotonation of bipyridine ligand hydroxyl groups increased quantum yield for singlet oxygen (these are reduced ten-fold by protonation) and decreased quantum yield for photodissociation products.

Oliveira et al. prepared two Ru(II)-diphosphine complexes, containing lapachol and lawsone as ligands [74]. Both complexes were highly cytotoxic against the MDA-MB-231, MCF-7, A549 and DU-145 (prostate) cancer cell lines with IC_{50} values in the low micromolar range (IC_{50} = 0.03–2.70 μM). They interacted with the minor DNA grooves and moderately with bovine serum albumin. The lapachol-containing complex was highly selective against triple-negative breast cancer (MDA-MB-231), inhibiting cell migration and colony formation. It arrested cell cycle, disrupted mitochondrial membrane potential and caused an increase in ROS.

Ru(III) coordination compounds with quinolone antibiotics [75] were tested against LoVo colon cancer in order to translate antibacterial action to anticancer activity. Complexes with levofloxacin, ciprofloxacin and ofloxacin demonstrated stronger antiproliferative effect than cisplatin. G0/G1 cell cycle arrest was observed. More Ru(III) complexes with triazolopyrimidine [76] ligands were screened on MCF-7, HeLa and normal L929 cells. Increased ROS generation was observed as well as DNA and protein binding. Increased lipophilicity of the tested substances was associated with higher antiproliferative effect (IC_{50} as low as 4 μM against MCF-7 and 5 μM against HeLa). Toxicity against L929 was lower than cisplatin's.

A Ru(III) complex with 1,4,8,11-tetraazacyclotetradecane exhibited an antiproliferative effect against SiHa cells, with an IC_{50} of 48 μM after 48 h of exposure [77]. Cell morphology changes were observed, such as nuclear fragmentation. The number of apoptotic cells increased, while the number of viable cells decreased after 24 h of exposure at 50 μM concentration.

Essential information on the Ru complexes' structure, type of cancer cells suppressed and biological activity has been summarized in Table 2.

Table 2. Summary of the ruthenium complexes presented.

Citation Number	Metal Ion/Ligand Type	Effective against	Biological Activity (If Investigated)
[49]	Ru(II), p-cymene, Shiff base	Caco-2	n/a
[50,51]	Ru(II), polypyridine, 1,10-phenanthroline	SKMEL-28	Photocytotoxicity, ROS generation
[52]	Ru(II), polypyridine	B16; HepG2; A549	Disrupted cell migration, G0/G1 cell cycle arrest, ROS generation, mitochondrial membrane penetration
[53]	Ru(II), rhein-substituted polypyridine	MCF-7; A549; NB-4; A2780; A2780R	Photocytotoxicity, autophagy
[54]	Ru(II), 1,10-phenanthroline, plumbagin	MCG-803 in vivo murine model	Mitochondrial impairment, DNA damage, G0/G1 cell cycle arrest
[55]	Ru(II), polypyridine, maltol	HeLa; A2780; A2780cis; A2780ADR; CT-26; CT-26LUC	Apoptosis
[57]	Ru(II), polypyridine,	HeLa, A549	Pyroptosis, caspase 1 activation, ROS increase
[58]	Ru(II), NHC	A549; HT-29; HCT-116; LoVo; HeLa; A2780	Mitochondrial dysfunction, apoptosis, disrupted cell migration
[59]	Ru(II), cyclopentadienyl	A2780; MDAMB231; HT29	HSA binding.
[60]	Ru(II)/(III), 2-aminophenyl benzimidazole, DMSO	Caco-2, MCF-7, EAC(in vivo)	DNA-laddering, G2/M cell cycle arrest
[61]	Ru(II), dinuclear, Biginelli hybrids	HeLa; A375; K562	Inhibited cell migration and endothelial tube formation

Table 2. *Cont.*

Citation Number	Metal Ion/Ligand Type	Effective against	Biological Activity (If Investigated)
[62]	Ru(II), p-cymene, imidazophenanthroline	HeLa; CaCo-2	CT-DNA and BSA binding
[63]	Ru(II), p-cymene, imidazophenanthroline	MDB-MA-231; HeLa	CT-DNA and BSA binding
[64]	Ru(II), diclofenac, organophosphines	A549; MDA-MB-231; MCF-7	CT-DNA and BSA binding, apoptosis
[65]	Ru(II), p-cymene, bis-aminophosphine	A375	Apoptosis
[66]	Ru(II), p-cymene, aromatic diamine	OVCAR-3; M-14; HOP-62	CT-DNA binding
[67]	Ru(II), dinuclear, p-cymene, tetrazole	HeLa; MCF-7; A549	DNA and BSA binding, G0/G1 cell cycle arrest, cell migration inhibition
[68]	Ru(II), half-sandwich arene	MCF-7	CT-DNA and BSA binding
[69]	Ru(II), flavone	MCF-7; MDA-MB-231	Cell migration inhibition
[70]	Ru(II), pyrazolopyrimidine	SCOV-3	ROS generation, mitochondrial impairment, inhibition of cell invasion and proliferation
[71]	Ru(II), aminoflavone	A2780; A2780cis; Toledo; Toledo-cis	Mitochondrial impairment, DNA interaction, apoptosis
[72]	Ru(II), dinuclear, arene	A2780; A2780cisR; A24; (D-)A24cisPt8.0	n/a
[74]	Ru(II), diphosphine, lapachol, lawsone	MDA-MB-231; MCF-7; A549; DU-145	DNA interaction. Cell cycle arrest, mitochondrial disruption, ROS increase
[75]	Ru(III), quinolone antibiotics	LoVo	G0/G1 cell cycle arrest
[76]	Ru(III), triazolopyrimidine	MCF-7, HeLa	Increased ROS generation, DNA and protein binding
[77]	Ru(III), 1,4,8,11-tetraazacyclotetradecane	SiHa	Nuclear fragmentation, apoptosis

2.3. Gallium Coordination Compounds

Gallium is a post-transition metal that exhibits a typical oxidation state of +3. In terms of ionic radius, electric charge and coordination number, Ga(III) closely resembles Fe(III) [78]. For that reason, similar to Ru, Ga compounds are able to compete for iron-occupied sites in biomolecules. This ionic mimicry is fundamental for the biological activity of Ga(III) substances. The involvement of gallium in cancer research dates back four decades [79–81]. Gallium compounds have been applied as diagnostic and therapeutic agents in oncology [79]. Rapidly proliferating malignancies have high metabolic activity and need significant iron intake. Many types of cancer are characterized with overexpression of transferrin receptors [82]. Ga(III) competes with iron for transferrin binding which allows it to penetrate "iron-hungry" cancer cells and exhibit its physiological effects—impairment of DNA synthesis, disruption of mitochondrial function, overall inhibition of iron-dependent enzymes, generation of ROS and ultimately, apoptosis [83]. As the search for novel, metal-based anticancer drugs intensifies, scientific interest into Ga(III) complexes with antiproliferative action has been revitalized over the past decade [83–89]. The relatively low number of studies, performed so far, combined with the intrinsic anticancer properties of the Ga(III) ion itself present an exciting possibility for research into novel complexes with biologically active ligands and potential antiproliferative action.

A number of gallium complexes with planar tetradentate ligands have recently been synthesized. Unlike the most prevalent six-coordinated complexes, these tend to block interactions between the metal coordination center and biomolecules to a lesser extent. In this case the vacant coordination sites may possess labile solvent molecules that would, in theory, allow for improved interaction with biomolecules by way of solvent ligand exchange.

A number of such gallium(III) salens were synthesized by Zhang and co-workers [9]. One of the complexes (Figure 19) exhibited anticancer activity against several cell lines (HeLa, Hep-G2, MCF-7, A549) within the nanomolar dosage range (IC$_{50}$ = 0.42–1.25 μM), as established using MTT assay.
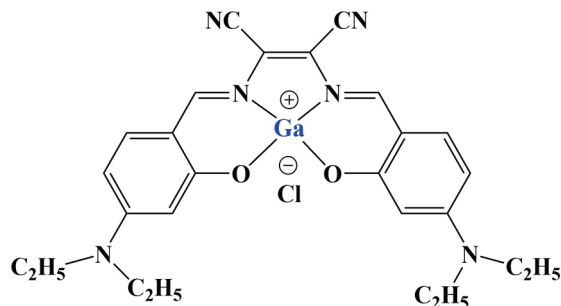

Figure 19. One of the complexes presented in [9].

Coordination with gallium(III) dramatically improved activity compared to free ligands and zinc analogs. The ethyl substituent at the amino-group turned out to be crucial, methyl and 1,4-butanediyl moieties decreased biological activity. The most prominent complex was found to enter cells through passive diffusion, being distributed mainly in mitochondria, endoplasmic reticulum and lysosomes. It was also discovered to inhibit protein disulfide isomerase in a concentration-dependent manner.

Gross and coworkers developed tetradentate metallocorroles with potential anticancer activity [90]. A variety of metal ions were coordinated with a corrole ligand. All compounds manifested moderate cytotoxicity against the DU-145, SKMEL-28, MDA-MB-231 and OVCAR-3 cell lines. Cytotoxicity increased with lipophilicity which depended on the type of liganded metal ion. The Ga(III) complex exhibited moderate antiproliferative activity (IC$_{50}$ = 129–274 μM).

A number of benzoylpyridine thiosemicarbazones were synthesized as tridentate ligands with potential antiproliferative properties [91]. After synthesis, these series of ligands were coordinated with gallium(III) in a molar ratio of 1:1. Both the ligands themselves and their complexes exhibited significant antiproliferative activity (higher than that of cisplatin) against the HepG-2 cell line. Increasing the lipophilicity of the ligands tended to improve the antiproliferative effect after 48 h of treatment. Additionally, the inclusion of gallium(III) further improved the observed action. The most potent ligand and its gallium(III) complex (Figure 20) significantly increased early and late apoptosis in that same cell line at 5μM concentrations. Mitochondrial membrane potential was decreased. Ferritin expression was downregulated, while transferrin receptor-1 expression was upregulated. Both activated caspase-3 and ROS were increased, the effect of the gallium(III) complex being significantly improved, compared to the ligand itself.
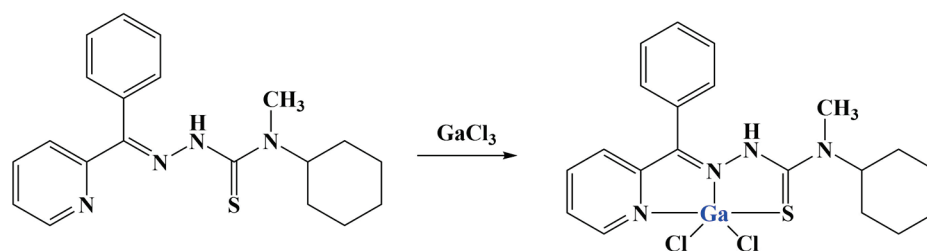
Figure 20. One of the complexes presented in [91].

Firmino and co-workers [92] synthesized two isonicotynoyl hydrazones as potential iron chelators. Generally, iron chelators tend to exert antiproliferative effects as they deprive

malignant cells of much necessary iron. Both compounds (Figure 21) were coordinated to gallium(III) at a ligand: metal ion ratio of 1:2.
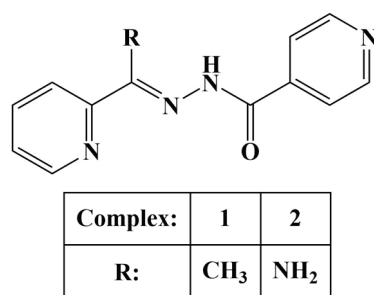
Complex:	1	2
R:	CH_3	NH_2

Figure 21. The ligands presented in [92].

The novel ligands and their gallium(III) complexes were assayed for antiproliferative action against the leukemia HL60, MCF-7, HCT116 and PC-3 cancer cell lines as well as the non-malignant HEK-293 line (MTT, 48 h). The hydrazone, containing primary amino-group (compound 2) and its gallium(III) complex did not inhibit cell viability at 10 μM concentration. When that amino-group was replaced with a methyl moiety (compound 1), cell viability in all cancer cell lines was reduced to 50% at that concentration. Clonogenicity was reduced. Increasing lipophilicity improved anticancer activity. It is noteworthy that the activity of both ligands did not differ significantly from the activity of their respective complexes. Compound 1 and its complex were further tested for cytotoxicity. Their IC_{50} values against HL60 and HCT116 were within the low micromolar range ($IC_{50} = 0.4$–2.0 μM), exhibiting at least 25-fold lesser toxicity toward the non-malignant HEK-293 line.

Two similar hydrazones were complexed with gallium(III) (Figure 22) [84] in order to test their anticancer and antitubercular activities. Both ligands and their respective complexes were tested for their impact on cell viability of cancer (MCF-7, PC-3) and non-cancerous (RWPE-1) cells with the help of the MTT test. All substances manifested cytotoxicity within the micromolar range against MCF-7, with gallium(III) complexation strengthening the observed effect. Ligands and complex 1 were inactive toward PC-3, while complex 2 has a selectivity index (related to RWPE-1) lower than 1. The improved activity of the halogenated ligand was associated with its higher lipophilicity. Its complex accumulated to a larger extent in both cancer cell strains.
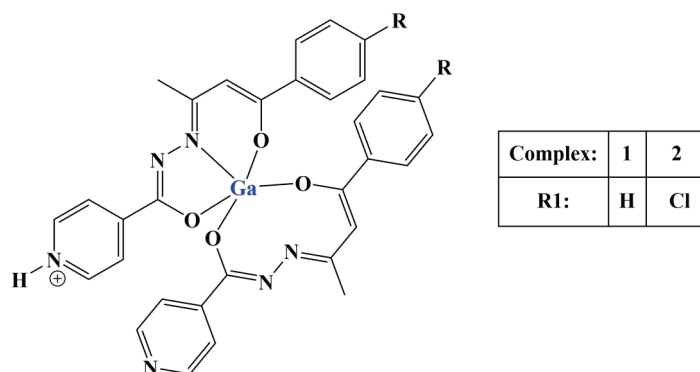
Complex:	1	2
R1:	H	Cl

Figure 22. The complexes presented in [84].

A number of octahedral gallium complexes with polypyridyl ligands (Figure 23) were tested against bulk osteosarcoma cells (OSC) and osteosarcoma stem cells (OSCs) [93]. These compounds were found to be potent at nanomolar concentrations. Anticancer potency was measured via the MTT assay ($IC_{50} = 0.07$–3.60 μM). Salinomycin, cisplatin and carboplatin were used as positive controls. IC_{50} values of all three complexes were significantly lower than those of the positive controls. Activity improved with the increase

of lipophilicity, complex 3 being active within the nanomolar range against osteosarcoma cells and osteosarcoma stem cells.
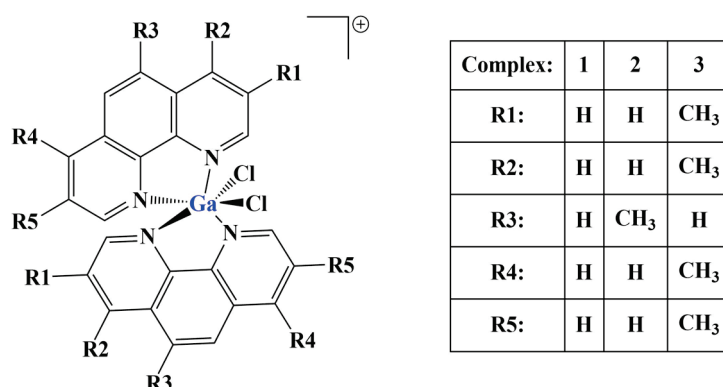
Figure 23. The complexes presented in [93].

Assays were conducted also on non-cancerous cell lines—HEK 293T, MCF710A, BEAS-2B and GMO7575. Complex 3 was significantly less potent against these. It manifested an ability to enter osteosarcoma cell nuclei with a potential to damage genomic DNA and to initiate caspase-dependent cell death.

A series of publications [85,94] describe promising antiproliferative activity of a gallium(III) complexes with substituted 8-quinolinols. They are structural analogs of tris(8-quinolinolato)gallium(III), also known as KP46 and AP-002 (Figure 24a)—a potential metallodrug, currently undergoing clinical trials [94]. Gallium complexes of four structural analogs of KP46 (Figure 24b) were tested against several cancer cell lines—A2780, MDA-MB-231 and HCT116. The non-cancerous MRC5pd30 line was also investigated.
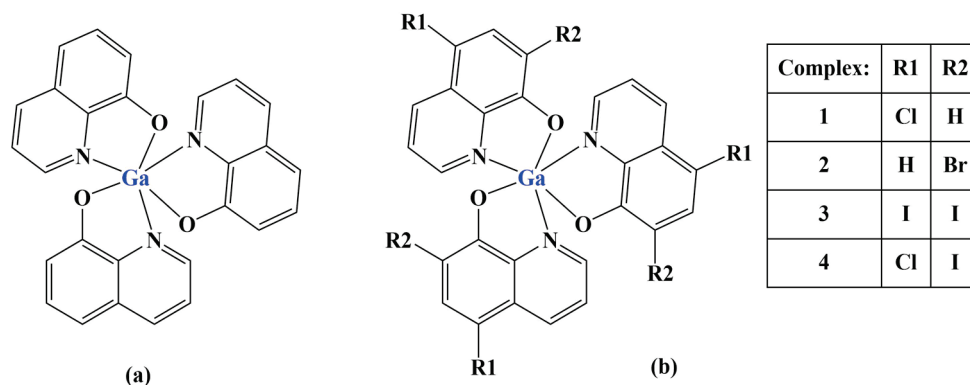
Figure 24. Structures of KP46 (**a**) and its analogues (**b**) presented in [94,95].

Complex 1 (with 5-chloro-substituted ligand) manifested the most pronounced antiproliferative effect (IC_{50} = 6.5–14.0 μM), comparable to that of the positive control cisplatin with regard to the various cell lines. Non-cancerous cells were affected at 25–65 times higher concentrations than cancer cells. The complex was significantly more active than the ligand itself.

A different study [95] focused on KP46 (Figure 24a) itself. It was tested against a variety of human cell lines: BJAB mock, including vincristine and doxorubicin-resistant; Nalm-6, including vincristine, etoposide and methotrexate-resistant strains; SK-N-AS and its vincristine-resistant subline; and K652. KP46 was found to induce apoptosis at a higher percentage than doxorubicin after 72 h of incubation. The observed activity was partially caspase-dependent, inducing processing of procaspases 3 and 9. The compound manifested a significant antiproliferative effect against BJAB and its vincristine-resistant subline, while the doxorubicin-resistant cells were unaffected. Mitochondrial membrane potential was

decreased by about 64% at a 20 µM concentration. Increased pro-apoptotic Harakiri protein expression was observed. The compound was found to possess not only intrinsic antiproliferative properties, but also to be highly effective in combination treatments with "established" anticancer agents against resistant cell lines. Synergies with cytarabine and methotrexate, causing up to a four-fold increase of apoptotic cells when treating BJAB were observed. Even a low concentration of 0.75 µM, in combination with daunorubibin, was able to overcome daunorubicin resistance in the K652 strain—increases in the number of apoptotic cells were three-fold.

Essential information on the Ga complexes' structures, type of cancer cells suppressed and biological activity has been summarized in Table 3.

Table 3. Summary of the gallium complexes presented.

Citation Number	Metal Ion/Ligand Type	Effective against	Biological Activity (If Investigated)
[9]	Ga(III), salen	HeLa, HepG 2, MCF-7, A549	Protein disulfide isomerase inhibition
[84]	Ga(III), hydrazone	MCF-7; PC-3	n/a
[90]	Ga(III), corrole	DU145; SK-MEL-28; MDA-MB-231; OVCAR-3	n/a
[91]	Ga(III), benzoylpyridine thiosemicarbazone	HepG-2	Impaired mitochondrial function, ferritin expression downregulated, transferrin receptor-1 upregulated, activated caspase-3 increased ROS
[92]	Ga(III), isonicotynoyl hydrazone	HL-60; MCF-7; HCT-116; PC3	Reduced clonogenicity.
[93]	Ga(III), polypyridine	OSC; OSCs	Damage to genomic DNA, apoptosis
[94]	Ga(III), substituted 8-quinolinol	A2780, MDA-MB-231 and HCT116	
[95]	Ga(III), 8-quinolinol	BJAB mock; Nalm-6; SK-N-AS; K652	Cell proliferation inhibition, impaired mitochondrial function, apoptosis

2.4. Gold Coordination Compounds

Gold has been used as a therapeutic since ancient times [96]. The earliest recorded use of gold as a medicine dates back 2500 years in China. Over the past two centuries in Europe, gold compounds have been used to treat "melancholy", fevers, syphilis and tuberculosis [96]. Compared to platinum-based drugs, complexes with gold tend to be less toxic. Such compounds have historically been applied with success in the treatment of rheumatoid arthritis (Myocrisin[TM], Solganol[TM], Ridaura[TM] (auranofin), etc.) and malaria [97]. Chrysotherapy (therapy with gold-containing compounds) research in the field of oncology has been ongoing for several decades now as a possible alternative to platinum-based treatments and their numerous disadvantages in terms of severe side effects and cancer cell resistance [96,98]. Gold complexes as antitumor agents tend to target thioredoxin reductase (TrxR), and in general, proteins and enzymes bearing thiol groups [99]. Similar to ruthenium and gallium, research of novel gold coordination compounds with antiproliferative properties is driven by the distinct deficiencies of modern platinum-based therapies. Alkynyl-gold complexes are currently a subject of particular interest due to the particular stability of the C-Au bond, making the gold ion more resistant to physiological reductants before reaching its target. Additionally, modifying the ancillary ligand can impact the pharmacological behavior of the investigated complex [98]. The authors would like to recommend the following detailed reviews of Au(I)/(III)-complex applications in oncology [99–101]. The most recent discoveries over the past three years are described below.

A number of halo and pseudohalo gold(I) complexes with 4,5-diarylimidazoles (Figure 25) were synthesized and tested for antiproliferative activity against hepatocellular carcinoma

strains HepG2, SMMC-7721 and Hep3B [102]. The study was an expansion on previous work with similar compounds [103].
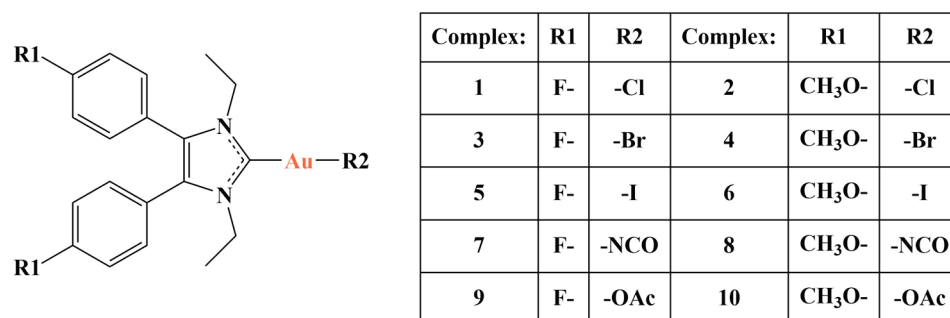

Complex:	R1	R2	Complex:	R1	R2
1	F-	-Cl	2	CH$_3$O-	-Cl
3	F-	-Br	4	CH$_3$O-	-Br
5	F-	-I	6	CH$_3$O-	-I
7	F-	-NCO	8	CH$_3$O-	-NCO
9	F-	-OAc	10	CH$_3$O-	-OAc

Figure 25. The complexes presented in [102].

MTT assay was applied to measure the antiproliferative effect with cisplatin and auranofin being used as positive controls. All investigated substances manifested antiproliferative activity similar to that of the controls (IC$_{50}$ values were up to 20µM). Complex 1 was the least active. Notably, the larger the halogen ligand (I > Br > Cl), the stronger the antiproliferative activity, a fact attributed by the authors to an increase in lipophilicity in the same order. Acetato-gold complexes were more active than cyanate-gold complexes. The most active substance 6 was found to be stable in PBS, including in the presence of high concentrations of GSH (Au prefers "soft" S-ligands). It exhibited better selectivity than the positive controls toward hepatocellular carcinoma HCC cells compared to normal LO2 and H8 cells. TrxR, a prominent target for gold, was inhibited, intracellular ROS production was increased and mitochondrial function was impaired.

Walther and coworkers [104] investigated two gold(I)-N-heterocyclic carbene complexes for anticancer activity (Figure 26).
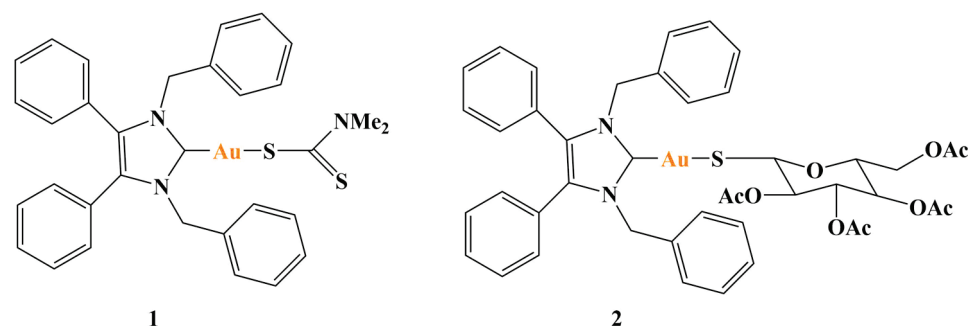
Figure 26. The complexes presented in [104].

IC$_{50}$ values were within the nanomolar range (sulforhodamine B (SRB) assay) after 48 h of incubation against OVCAR3, NCI-H522, HT29, T-47D and PC-3 lines (GI$_{50}$ = 0.26–0.79 µM). Growth of PC-3 derived xenograft tumors was inhibited, mammalian TrxR was suppressed and nuclear protein Ki67 was reduced—a marker for inhibition of cell proliferation.

Gulzar and coworkers [105] synthesized a series of NHC-gold(I)-thione complexes (Figure 27) and tested them against the HCT-15, A549 and MCF7 cancer cell lines (MTT assay, 24 h). Cisplatin was the positive standard.
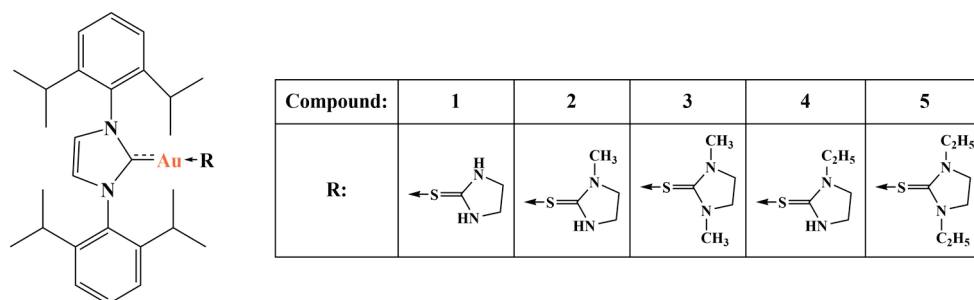
Figure 27. The complexes presented in [105].

IC$_{50}$ values (74.26 to 102.17 μM) were about 2–3 times higher than the those for cisplatin. The authors concluded that thione ligands do not contribute to the antiproliferative activity of such gold(I) complexes.

Alkynyl-gold complexes have been intensively studied in recent years for their antiproliferative effect [98]. They tend to exhibit significant anticancer effects, associated with TrxR inhibitory activity [106–109]. A number of investigations to that effect have been carried out recently.

A phenanthrene bridge was substituted with two terminal alkynyl groups in order to build potential anticancer complexes with two gold(I)-phosphine centers [110] (Figure 28). The potential antiproliferative activity of both gold complexes was assessed against the MCF-7, HEPG-2, PC-3 and MOLT-4 cancer cell lines (SRB, 72 h). The phenanthrene-ethynyl "bridging" ligand had very low activity against all tested strains. Both gold complexes behaved in a similar manner to the positive control cisplatin (IC$_{50}$ varied at 18–28 μM with all cancer cell lines). DNA binding was noted for both complexes and the ligand. The authors of the study proposed that substituting the phenanthrene skeleton at positions 9 and 10 would allow for modification of lipophilicity of the complexes improving their solubility—a common issue with alkynyl-gold compounds [111].
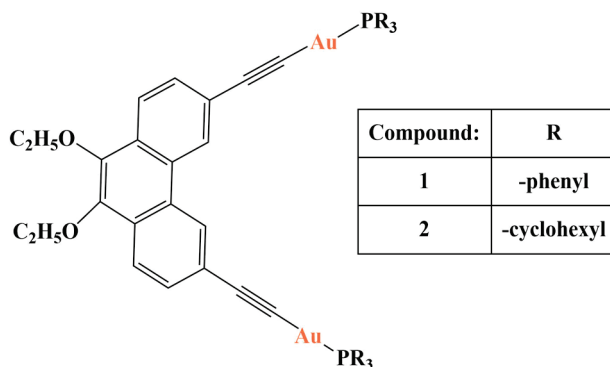
Figure 28. The complexes presented in [110].

Another study [112] evaluated a number of alkynyl-gold(I)-triphenylphosphine complexes against cancerous HT29, IGROV1, HL60 and non-malignant I407 cells. The most active substance (Figure 29) exhibited antiproliferative activity in the low-micromolar range (IC$_{50}$ = 3.3–7.9 μM), similar to that of the positive standard auranofin. It, however, turned out to be most toxic against the normal cell line (IC$_{50}$ = 1.7 μM). Two other noteworthy compounds inhibited proliferation in IGROV1 and HL60 cells, while being non-toxic to I407. Both were binuclear complexes and their thioredoxine reductase inhibitory activity was significantly stronger than in the rest of the experimental substances that were mononuclear.
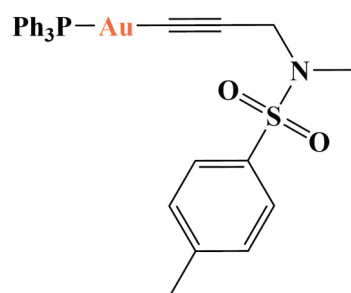
Figure 29. One of the complexes presented in [112].

Marmol and coworkers synthesized and tested alkynyl-gold(I)-substituted 3-hydroxyflavones against a series of cancer cell lines [113]. Several alkyne-substituted ligands were coordinated with Au(I), together with either triphenylphosphane (PPh_3), or 1,3,5-triaza-7-phosphaadamantane (PTA) (Figure 30). Their antiproliferative activity, expressed as IC_{50} against undifferentiated Caco-2/TC7 cells is within the micromolar range (IC_{50} = 1.5–7.68 µM, MTT assay).
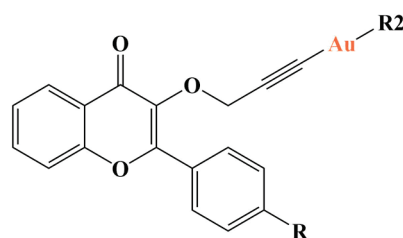
Complex:	R	R2	Complex:	R	R2
1a	H	PPh_3	2a	H	PTA
1b	Br	PPh_3	2b	Br	PTA
1c	Cl	PPh_3	2c	Cl	PTA
1d	OCH_3	PPh_3	2d	OCH_3	PTA

Figure 30. One of the complexes presented in [113].

Lipophilicity was higher in the PPh_3 compounds, compared to the PTA-containing complexes. MTT and SRB assays were both utilized to measure cytotoxicity of all eight gold complexes against MCF-7, HepG5 and Caco-2/TC7 cells. Selectivity was assessed with the help of non-cancerous differentiated Caco-2 as a model of the intestinal barrier. Cisplatin and auranofin were used as positive controls. All complexes manifested antiproliferative effects against the cancer cell lines within the micromolar range (IC_{50} is higher than auranofin and lower than cisplatin). The more lipophilic series of PPh_3-containing compounds suppressed proliferation in Caco-2/TC7 and HepG2 to a greater extent compared to the PTA series. This trend was reversed with MCF-7. Selectivity indices of the PTA complexes were similar to those of auranofin and cisplatin. Those of the PPh_3-complexes were much improved. Complexes 1b and 2c were additionally examined. Complex 1b inhibited COX-2, thioredoxine reductase, glutathione reductase, increased ROS levels and triggered apoptosis after 24 h of incubation. Complex 2c inhibited COX-1, thioredoxine reductase, glutathione reductase, increased ROS levels and triggered apoptosis after 48 h.

A series of mononuclear phosphane-Au(I)-alkynyl complexes (Figure 31) were synthesized by Babgi and coworkers [114] with the aim to elucidate the impact of phenolic Schiff base addition on biological activity, including antiproliferative (SRB assay), HSA binding and thioredoxine reductase inhibition (in silico docking).

Complex:	R	R2
1	C_6H_5-	-CHO
2	$C_6H_{11}-$	-CHO
3	C_6H_5-	![N=, OH]
4	C_6H_5-	![N=, OH]
5	$C_6H_{11}-$	![N=, OH]
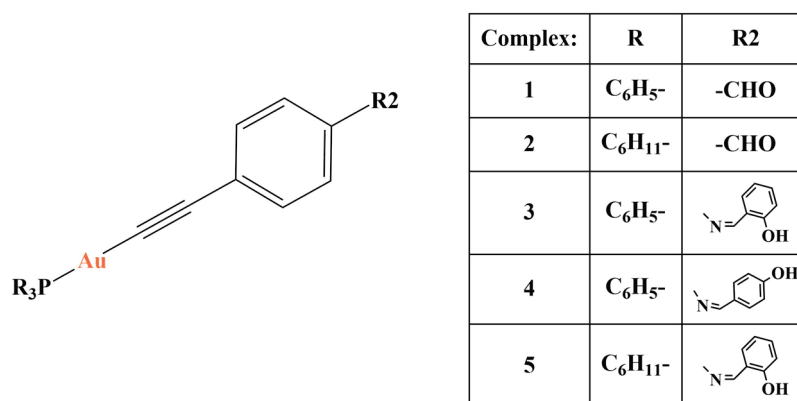
Figure 31. One of the complexes presented in [114].

The aldehyde complexes (Figure 1-1,-2) suppressed the proliferation OVCAR-3 and HOP-62 cells (IC_{50} in the 12–16 μM range). Changing the aldehyde group with a phenolic Shiff base caused dramatic improvement of cytotoxicity (IC_{50} in the 5–9 μM range). The p-hydroxy substituted complex 4 was much more effective against OVCAR-3, compared to its o-hydroxy-substituted analogs. Within the scope of this investigation, substituting the triphenylphosphine with a tricyclohexyl moiety did not impact biological activity. Molecular docking calculations showed that substituting the aldehyde group for a Schiff base may change the binding site with human thioredoxin reductase. Changing triphenylphosphine with tricyclohexanephosphine increased HSA binding. Adding a phenolic moiety had the same effect.

An alkynyl-activated quinazoline carboxamide was synthesized in order to produce a series of alkynyl-Au(I) complexes [115] (Figure 32). Quinazoline carboxamides tend to bind to translocator protein 18kDa (TSPO), situated on the outer mitochondrial membrane [116]. They could be applied as chemo-/photo-sensitizers and diagnostic agents as TSPO is overexpressed in a variety of cancer types.

Compound:	R
1	-PPh$_3$
2	-TPA
3	![imidazole structure with H3C groups]
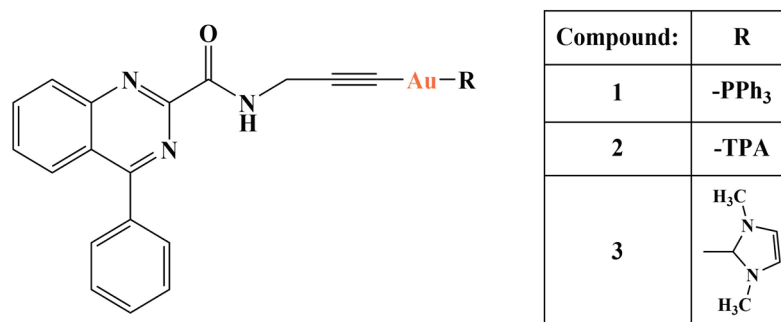
Figure 32. Some of the complexes presented in [115].

All three complexes were stable in PBS at 37 °C for over 72 h, including in culture media. Their cytotoxicities were tested with the help of the XTT assay. Bladder cancer lines 5637 and T24 were incubated with the complexes for 72 and 96 h. Compound 3 manifested modest activity against 5637 after 72 and 96 h. The IC_{50} values of complexes 1 and 2 were in the low micromolar to nanomolar ranges (IC_{50} = 0.17–12.40 μM). Complex 1 was more active than complex 2 with 5637 (72 and 96 h) and T24 (72 h). Complex 2 was more active with T24 after 96 h. Cellular uptake decreased in the following way 2 > 1 > 3. Complexes 1 and 2 activated caspases, in the case of the latter with delayed timing. Thioredoxine reductase inhibition increased in the following order 1 > 2 > 3.

Bian and coworkers [117] synthesized a series of alkyne-activated pentacyclic triterpene derivatives (betulinic acid, ursolic acid, clycyrrhetic acid and oleanolic acid). Triterpenes are known for their anticancer activity [118], attacking a multitude of targets.

The authors tested whether conjugating such substances with gold(I) and PPh$_3$ would yield complexes with varied mechanisms of action beyond the expected thioredoxine reductase inhibition. All substances were tested against the MCF-7, HT-29, HepG3 and A2780 cancer cell lines (MTT assay) and were found to manifest moderate antiproliferative activity against most cell lines, except A2780 where the impact was significant (IC$_{50}$ for A2780 was mostly between 25 and 40 µM). The oleanolic acid derivative (Figure 33) was found to have an IC$_{50}$ against A2780 in the low micromolar range (10 µM)—similar to the positive controls cisplatin and auranofin. It inhibited thioredoxine reductase (both purified enzyme and cellular-A2780) to a lesser extent than auranofin, impaired mitochondrial function, increased cellular ROS production and induced endoplasmic reticulum stress.
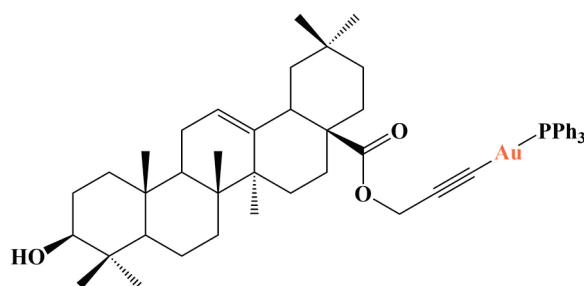
Figure 33. One of the complexes presented in [117].

Romanova and coworkers synthesized a series of gold(I) complexes with alkynyl-activated ibuprofen [119] (Figure 34) and tested them (MTT assay, 72 h) for antiproliferative activity against MCF-7, MDA-MB-231 and HT-29 cancer lines as well as MCF-10A non-cancerous cells.
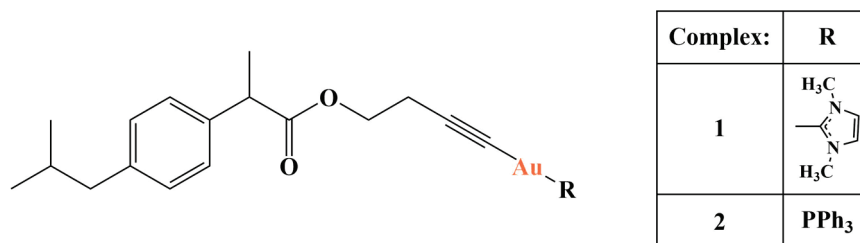
Figure 34. One of the complexes presented in [119].

The activity of both complexes was comparable to the positive controls cisplatin and auranofin, where the IC$_{50}$ was in the low micromolar range (0.98–3.42 µM), and selectivity was very much improved with regard to the non-cancerous cell line. The N-heterocyclic carbenium (NHC) complex had lower antitumor activity than the triphenylphosphine one, but manifested much better selectivity in relation to the non-neoplastic MCF-10A cells. TrxR and glutathione reductase inhibition was observed as well as an increase in ROS.

Essential information on the Au complexes' structures, type of cancer cells suppressed and biological activity has been summarized in Table 4.

Table 4. Summary of the gold complexes presented.

Citation Number	Metal Ion/Ligand Type	Effective against	Biological Activity (If Investigated)
[102]	Au(I), 4,5-diarylimidazoles	HepG2; SMMC-7721; Hep3B	TrxR inhibition, ROS increase
[104]	Au(I), NHC	OVCAR3; NCI-H522; HT29; T-47D; PC-3	TrxR inhibition, nuclear protein Ki67 reduction
[105]	Au(I), NHC	HCT-15; A549; MCF7	n/a
[110]	Au(I), phosphine, alkynylphenanthrene	MCF-7; HEPG-2; PC-3; MOLT-4	DNA binding
[112]	Au(I)-alkynyl, triphenylphosphane	HT29; IGROV1; HL60	TrxR inhibition
[113]	Au(I)-alkynyl, triphenylphosphine/ PTA	MCF-7; HepG5; Caco-2/TC7	TrxR inhibition, COX-1/2 inhibition, increased ROS
[114]	Au(I)-alkynyl, phosphane	OVCAR-3; HOP-62	HSA binding
[115]	Au(I)-alkynyl	5637; T24	TrxR inhibition
[117]	Au(I)-alkynyl-triterpene	MCF-7; HT-29; HepG3; A2780	TrxR inhibition, mitochondrial impairment, increased ROS, endoplasmic reticulum stress
[119]	Au(I)-alkynyl-ibuprofen	MCF-7; MDA-MB-231; HT-29	TrxR and glutathione reductase inhibition, increased ROS

2.5. Lanthanum Coordination Compounds

Lanthanum is the first member of the lanthanide series of *f*-transition metals. Its typical oxidation state is +3 and its coordination number can vary between 6 and 12. In terms of ionic potential La(III) resembles a multitude of "biological" ions (Fe(III), Ca(II), Zn(II), Mg(II)) and is therefore able to competitively replace them in ion-binding proteins [120]. A number of studies have related La(III) toxicity to impairment of zinc- and iron-dependent enzymatic systems, suppressing SOD, CAT and disrupting mitochondrial function [121–123]. Currently lanthanum is applied in medicine in the form of the phosphate binder lanthanum carbonate [124]. During the past decade, the popularity of La(III) complexes in cancer research has been steadily rising, mostly due to La's ability to mimic biometals and to coordinate bioactive ligands [83]. As the search for La(III) complexes suitable for cancer therapy is slowly gaining traction [125], the authors would like to introduce the most prominent studies on this subject over the past three years.

Mohammed and coworkers synthesized a series of lanthanide complexes with two ferrocene-substituted Schiff bases [126]. Both La(III) complexes with these two ligands (1:1 metal ion:ligand molar ratio) manifested moderate antiproliferative activities (IC$_{50}$ about 22 μM) against the MCF7 cell line (SRB, 48 h). Molecular docking studies suggested interaction with the 3HB5 breast cancer receptor.

A tetradentate Schiff base ligand (Figure 35) was coordinated with La(III) [127]. Both substances were tested for antiproliferative activity against MCF-7 and HepG2 (SRB, 48h exposure) and yielded promising results (IC$_{50}$ = 23–50 μM). Adding La(III) to the Schiff base decreased anticancer activity against MCF-7 and dramatically improved it against Hep-G2.
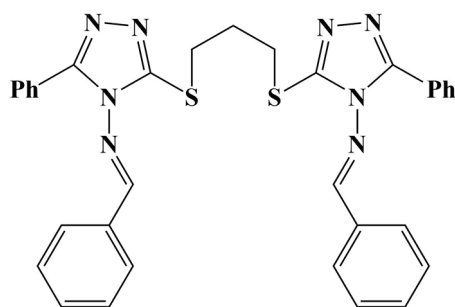
Figure 35. The ligand of the complex presented in [127].

A La(III)-5-fluorouracil complex (1:1 molar ratio) was synthesized and tested against the Caco-2 cell line (trypan blue exclusion assay). The presence of the La(III) coordination center significantly improved cytotoxicity, compared to 5-fluorouracil [128]. Molecular docking studies suggested interaction with site II of BSA.

A La(III) complex with tyrosine (metal: ligand molar ratio is 1:3) was tested against MCF-7 cells [129]. After 72 h of incubation (MTT assay), the complex manifested antiproliferative activity (IC_{50} = 21 μM) similar to the positive control cisplatin. Furthermore, the compound was found to be non-toxic to non-cancerous ADSC cells.

La(III) was complexed with N,N′-bis(2-aminoethyl)oxamide (Figure 36-1), 2,2′-bipyridine (Figure 36-2), 1,10-phenanthroline (Figure 36-3) and dipyrido(3,2-a:2′,3′-c)phenazine (Figure 36-4) [130]. Four complexes were synthesized—[La(1)$_2$(NO$_3$)$_2$](NO$_3$), [La(1)(2)](NO$_3$)$_3$, [La(1)(3)](NO$_3$)$_3$ and [La(1)$_2$(3)](NO$_3$)$_3$. All complexes manifested moderated cytotoxic activities (MTT assay against MCF-7), the highest activity being observed by [La(1)$_2$(3)](NO$_3$)$_3$, with an IC_{50} = 22 μM. The bigger the aromatic planar structure of the ligand, the greater the cytotoxicity, attributed by the authors to DNA intercalation and cleaving.
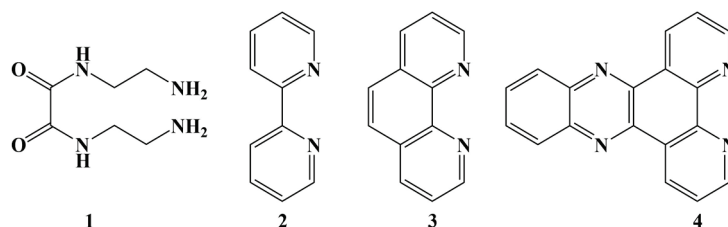
Figure 36. The ligands of the complexes presented in [130].

A mixed ligand La(III) complex with 2,2′-bipyridyl and 5,7-dibromo-8-quinolinol manifested significant activity against SK-OV-3/DDP, NCI-H460, HeLa and HL-7702 cells [131]. IC_{50} is within the low micromolar range (MTT assay). The strongest cytotoxicity was against HeLa—about 2 μM.

Two La(III) complexes (Figure 37) with pyridine-2,6-dicarboxylate were tested against the HL60, HepG2, HT29 and normal HFF cell lines [132]. Oxaliplatin was used as a positive control. The complexes were more potent than the ligands themselves.
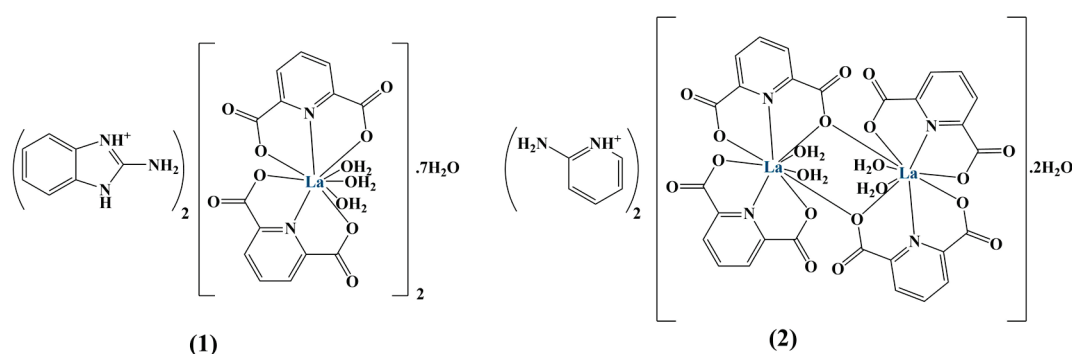
Figure 37. The ligands of the complexes presented in [132].

Complex 1 manifested a stronger antiproliferative effect compared to complex 2 against all cell lines (MTT assay). Complex 1 was particularly effective against HL60 (IC_{50} = 0.69 μM). Activity against Hep-G2 and HT-29 was moderate (IC_{50} = 20.76 and 90.34 μM, respectively). Both compounds were non-toxic against HFF. Complexes 1 and 2 increased ROS levels in HL 60 by 211% and 141%, respectively, the result being higher than that for the positive control oxaliplatin.

A La(III) complex with 2,2′-bipyridine [133] was tested against the MCF-7, A549 and the non-cancerous HFB cell lines (MTT test, 24 h). Molecular docking suggested interaction

with site III in BSA. 5-FU and methotrexate were used as positive controls. The complex manifested a promising antiproliferative effect. IC_{50} was about ten-fold lower than the positive controls (3.25-3.99 versus 27.5–47.8 μM). Additionally, cytotoxicity against the healthy cell line was about two times lower than methotrexate and 5-FU.

Essential information on the La complexes' structures, type of cancer cells suppressed and biological activity has been summarized in Table 5.

Table 5. Summary of the lanthanum complexes presented.

Citation Number	Metal Ion/Ligand Type	Effective against	Biological Activity (If Investigated)
[126]	La(III), ferrocene-substituted Schiff base	MCF-7	Molecular docking: 3HB5 breast cancer receptor
[127]	La(III), tetradentate Schiff base	MCF-7, HepG2	n/a
[128]	La(III), 5-fluorouracil	Caco2	n/a
[129]	La(III), tyrosine	MCF-7	Molecular docking: interaction with site II of BSA
[130]	La(III), polypyridine, 1,10-phenanthroline	MCF-7	DNA intercalation, DNA cleaving
[131]	La(III), bipyridyl	SK-OV-3/DDP; NCI-H460; HeLa; HL-7702	n/a
[132]	La(III), pyridine-2,6-dicarboxylate	HL60; HepG2; HT29	ROS increase
[133]	La(III), bipyridine	MCF-7; A-549	Molecular docking: interaction with site III of BSA

3. Discussion and Conclusions

Metal-based drugs are continually gaining ground in modern medicine, particularly in the field of oncology. Platinum, ruthenium, gold, lanthanum and gallium coordination compounds provide promising perspectives in the constant search for novel anticancer drugs. The research reviewed here helped the authors draw a number of conclusions:

- Depending on the element serving as coordination center, the complexes under review exhibit their antiproliferative activity via different pathways: DNA impairment via inter-/intra-strand crosslinks, mitochondrial function impairment, generation of ROS and apoptosis/necrosis. These effects result from a variety of biochemical and physico-chemical mechanisms: DNA/protein binding, ionic mimicry, competitive inhibition of enzymes and photosensitization. This multitude of possible metal-dependent modes of anticancer action allows for consideration of potential combination therapies that improve effectiveness, avoid therapy resistance and reduce systemic toxicities;
- The activities of the metal coordination centers can be modified with a suitable choice of ligands. High cytotoxicity against tumors is not enough, unless it goes hand in hand with good selectivity and/or a suitable cancer cell targeting mechanism;
- Physicochemical mechanisms such as photoactivation, as in photodynamic therapy, allow for targeting specific areas of the body with the aid of a photosensitizer with low systemic toxicity. Developing transition metal complexes with suitable photophysical properties seems to be a suitable direction, both logical and necessary, in the search of novel anticancer treatments.

Institutional Review Board Statement: Not applicable.

Informed Consent Statement: Not applicable.

Data Availability Statement: Not applicable.

References

1. Arruebo, M.; Vilaboa, N.; Sáez-Gutierrez, B.; Lambea, J.; Tres, A.; Valladares, M.; González-Fernández, Á. Assessment of the evolution of cancer treatment therapies. *Cancers* **2011**, *3*, 3279–3330. [CrossRef] [PubMed]

2. Pham, T.C.; Nguyen, V.-N.; Choi, Y.; Lee, S.; Yoon, J. Recent strategies to develop innovative photosensitizers for enhanced photodynamic therapy. *Chem. Rev.* **2021**, *121*, 13454–13619. [CrossRef] [PubMed]

3. Agostinis, P.; Berg, K.; Cengel, K.A.; Foster, T.H.; Girotti, A.W.; Gollnick, S.O.; Hahn, S.M.; Hamblin, M.R.; Juzeniene, A.; Kessel, D. Photodynamic therapy of cancer: An update. *CA Cancer J. Clin.* **2011**, *61*, 250–281. [CrossRef] [PubMed]

4. Hausinger, R.P. New metal cofactors and recent metallocofactor insights. *Curr. Opin. Struct. Biol.* **2019**, *59*, 1–8. [CrossRef] [PubMed]

5. Grass, G.; Rensing, L.; Rensing, C. Metal toxicity. *Metallomics* **2011**, *3*, 1095–1097. [CrossRef] [PubMed]

6. Lucaciu, R.L.; Hangan, A.C.; Sevastre, B.; Oprean, L.S. Metallo-Drugs in Cancer Therapy: Past, Present and Future. *Molecules* **2022**, *27*, 6485. [CrossRef]

7. Alessio, E.; Guo, Z. Metal anticancer complexes–activity, mechanism of action, future perspectives. *Eur. J. Inorg. Chem.* **2017**, *2017*, 1539–1540. [CrossRef]

8. Jakupec, M.A.; Keppler, B.K. Gallium in cancer treatment. *Curr. Top. Med. Chem.* **2004**, *4*, 1575–1583. [CrossRef]

9. Yin, H.Y.; Gao, J.J.; Chen, X.; Ma, B.; Yang, Z.S.; Tang, J.; Wang, B.W.; Chen, T.; Wang, C.; Gao, S. A gallium (III) complex that engages protein disulfide isomerase A3 (PDIA3) as an anticancer target. *Angew. Chem. Int. Ed.* **2020**, *59*, 20147–20153. [CrossRef]

10. Peng, X.X.; Gao, S.; Zhang, J.L. Gallium (III) complexes in cancer chemotherapy. *Eur. J. Inorg. Chem.* **2022**, *2022*, e202100953. [CrossRef]

11. Florea, A.-M.; Büsselberg, D. Cisplatin as an anti-tumor drug: Cellular mechanisms of activity, drug resistance and induced side effects. *Cancers* **2011**, *3*, 1351–1371. [CrossRef] [PubMed]

12. Qi, L.; Luo, Q.; Zhang, Y.; Jia, F.; Zhao, Y.; Wang, F. Advances in toxicological research of the anticancer drug cisplatin. *Chem. Res. Toxicol.* **2019**, *32*, 1469–1486. [CrossRef]

13. Ho, G.Y.; Woodward, N.; Coward, J.I. Cisplatin versus carboplatin: Comparative review of therapeutic management in solid malignancies. *Crit. Rev. Oncol. /Hematol.* **2016**, *102*, 37–46. [CrossRef] [PubMed]

14. Guo, Y.; He, Y.; Wu, S.; Zhang, S.; Song, D.; Zhu, Z.; Guo, Z.; Wang, X. Enhancing cytotoxicity of a monofunctional platinum complex via a dual-DNA-damage approach. *Inorg. Chem.* **2019**, *58*, 13150–13160. [CrossRef] [PubMed]

15. Hector, S.; Bolanowska-Higdon, W.; Zdanowicz, J.; Hitt, S.; Pendyala, L. In vitro studies on the mechanisms of oxaliplatin resistance. *Cancer Chemother. Pharmacol.* **2001**, *48*, 398–406. [CrossRef]

16. Dilruba, S.; Kalayda, G.V. Platinum-based drugs: Past, present and future. *Cancer Chemother. Pharmacol.* **2016**, *77*, 1103–1124. [CrossRef]

17. Chen, X.; Wu, Y.; Dong, H.Y.; Zhang, C.; Zhang, Y. Platinum-based agents for individualized Cancer Treatmen. *Curr. Mol. Med.* **2013**, *13*, 1603–1612. [CrossRef]

18. Rottenberg, S.; Disler, C.; Perego, P. The rediscovery of platinum-based cancer therapy. *Nat. Rev. Cancer* **2021**, *21*, 37–50. [CrossRef]

19. Han, X.; Sun, J.; Wang, Y.; He, Z. Recent advances in platinum (IV) complex-based delivery systems to improve platinum (II) anticancer therapy. *Med. Res. Rev.* **2015**, *35*, 1268–1299. [CrossRef]

20. Xu, Z.; Wang, Z.; Deng, Z.; Zhu, G. Recent advances in the synthesis, stability, and activation of platinum (IV) anticancer prodrugs. *Coord. Chem. Rev.* **2021**, *442*, 213991. [CrossRef]

21. Wang, Z.; Deng, Z.; Zhu, G. Emerging platinum (IV) prodrugs to combat cisplatin resistance: From isolated cancer cells to tumor microenvironment. *Dalton Trans.* **2019**, *48*, 2536–2544. [CrossRef] [PubMed]

22. Zhu, Z.; Wang, Z.; Zhang, C.; Wang, Y.; Zhang, H.; Gan, Z.; Guo, Z.; Wang, X. Mitochondrion-targeted platinum complexes suppressing lung cancer through multiple pathways involving energy metabolism. *Chem. Sci.* **2019**, *10*, 3089–3095. [CrossRef] [PubMed]

23. Eskandari, A.; Kundu, A.; Ghosh, S.; Suntharalingam, K. A triangular platinum (II) multinuclear complex with cytotoxicity towards breast cancer stem cells. *Angew. Chem.* **2019**, *131*, 12187–12192. [CrossRef]

24. He, C.; Majd, M.H.; Shiri, F.; Shahraki, S. Palladium and platinum complexes of folic acid as new drug delivery systems for treatment of breast cancer cells. *J. Mol. Struct.* **2021**, *1229*, 129806. [CrossRef]

25. Adams, M.; Sullivan, M.P.; Tong, K.K.; Goldstone, D.C.; Hanif, M.; Jamieson, S.M.; Hartinger, C.G. Mustards-derived Terpyridine–platinum complexes as anticancer agents: DNA alkylation vs coordination. *Inorg. Chem.* **2021**, *60*, 2414–2424. [CrossRef]

26. Li, C.; Xu, F.; Zhao, Y.; Zheng, W.; Zeng, W.; Luo, Q.; Wang, Z.; Wu, K.; Du, J.; Wang, F. Platinum (II) terpyridine anticancer complexes possessing multiple mode of DNA interaction and EGFR inhibiting activity. *Front. Chem.* **2020**, *8*, 210. [CrossRef]

27. Kutlu, E.; Emen, F.M.; Kismali, G.; Kınaytürk, N.K.; Kılıç, D.; Karacolak, A.I.; Demirdogen, R.E. Pyridine derivative platinum complexes: Synthesis, molecular structure, DFT and initial anticancer activity studies. *J. Mol. Struct.* **2021**, *1234*, 130191. [CrossRef]

28. Mbugua, S.N.; Sibuyi, N.R.; Njenga, L.W.; Odhiambo, R.A.; Wandiga, S.O.; Meyer, M.; Lalancette, R.A.; Onani, M.O. New palladium (II) and platinum (II) complexes based on pyrrole schiff bases: Synthesis, characterization, X-ray structure, and anticancer activity. *ACS Omega* **2020**, *5*, 14942–14954. [CrossRef]

29. Sankarganesh, M.; Vijay Solomon, R.; Dhaveethu Raja, J. Platinum complex with pyrimidine-and morpholine-based ligand: Synthesis, spectroscopic, DFT, TDDFT, catalytic reduction, in vitro anticancer, antioxidant, antimicrobial, DNA binding and molecular modeling studies. *J. Biomol. Struct. Dyn.* **2021**, *39*, 1055–1067. [CrossRef]

30. Lozada, I.B.; Huang, B.; Stilgenbauer, M.; Beach, T.; Qiu, Z.; Zheng, Y.; Herbert, D.E. Monofunctional platinum (ii) anticancer complexes based on multidentate phenanthridine-containing ligand frameworks. *Dalton Trans.* **2020**, *49*, 6557–6560. [CrossRef]

31. Tham, M.J.R.; Babak, M.V.; Ang, W.H. PlatinER: A highly potent anticancer platinum (II) complex that induces endoplasmic reticulum stress driven immunogenic cell death. *Angew. Chem. Int. Ed.* **2020**, *59*, 19070–19078. [CrossRef] [PubMed]

32. Islam, M.K.; Baek, A.-R.; Sung, B.; Yang, B.-W.; Choi, G.; Park, H.-J.; Kim, Y.-H.; Kim, M.; Ha, S.; Lee, G.-H. Synthesis, Characterization, and Anticancer Activity of Benzothiazole Aniline Derivatives and Their Platinum (II) Complexes as New Chemotherapy Agents. *Pharmaceuticals* **2021**, *14*, 832. [CrossRef] [PubMed]

33. Bai, X.; Ali, A.; Wang, N.; Liu, Z.; Lv, Z.; Zhang, Z.; Zhao, X.; Hao, H.; Zhang, Y.; Rahman, F.-U. Inhibition of SREBP-mediated lipid biosynthesis and activation of multiple anticancer mechanisms by platinum complexes: Ascribe possibilities of new antitumor strategies. *Eur. J. Med. Chem.* **2022**, *227*, 113920. [CrossRef]

34. Nadar, R.A.; Farbod, K.; der Schilden, K.C.-v.; Schlatt, L.; Crone, B.; Asokan, N.; Curci, A.; Brand, M.; Bornhaeuser, M.; Iafisco, M. Targeting of radioactive platinum-bisphosphonate anticancer drugs to bone of high metabolic activity. *Sci. Rep.* **2020**, *10*, 5889. [CrossRef] [PubMed]

35. Faihan, A.S.; Hatshan, M.R.; Kadhim, M.M.; Alqahtani, A.S.; Nasr, F.A.; Saleh, A.M.; Al-Jibori, S.A.; Al-Janabi, A.S. Promising bio-active complexes of platinum (II) and palladium (II) derived from heterocyclic thiourea: Synthesis, characterization, DFT, molecular docking, and anti-cancer studies. *J. Mol. Struct.* **2022**, *1252*, 132198. [CrossRef]

36. Zeynali, H.; Keypour, H.; Hosseinzadeh, L.; Gable, R.W. The non-templating synthesis of macro-cyclic Schiff base ligands containing pyrrole and homopiperazine and their binuclear nickel (II), cobalt (II) and mononuclear platinum (II) complexes: X-ray single crystal and anticancer studies. *J. Mol. Struct.* **2021**, *1244*, 130956. [CrossRef]

37. Bera, B.; Mondal, S.; Gharami, S.; Naskar, R.; Saha, K.D.; Mondal, T.K. Palladium (II) and platinum (II) complexes with ONN donor pincer ligand: Synthesis, characterization and in vitro cytotoxicity study. *New J. Chem.* **2022**, *46*, 11277–11285. [CrossRef]

38. Yambulatov, D.S.; Lutsenko, I.A.; Nikolaevskii, S.A.; Petrov, P.A.; Smolyaninov, I.V.; Malyants, I.K.; Shender, V.O.; Kiskin, M.A.; Sidorov, A.A.; Berberova, N.T. α-Diimine Cisplatin Derivatives: Synthesis, Structure, Cyclic Voltammetry and Cytotoxicity. *Molecules* **2022**, *27*, 8565. [CrossRef]

39. Khoury, A.; Sakoff, J.A.; Gilbert, J.; Scott, K.F.; Karan, S.; Gordon, C.P.; Aldrich-Wright, J.R. Cyclooxygenase-inhibiting platinum (iv) prodrugs with potent anticancer activity. *Pharmaceutics* **2022**, *14*, 787. [CrossRef]

40. Schueffl, H.; Theiner, S.; Hermann, G.; Mayr, J.; Fronik, P.; Groza, D.; van Schonhooven, S.; Galvez, L.; Sommerfeld, N.S.; Schintlmeister, A. Albumin-targeting of an oxaliplatin-releasing platinum (iv) prodrug results in pronounced anticancer activity due to endocytotic drug uptake in vivo. *Chem. Sci.* **2021**, *12*, 12587–12599. [CrossRef]

41. Shi, H.; Imberti, C.; Clarkson, G.J.; Sadler, P.J. Axial functionalisation of photoactive diazido platinum (IV) anticancer complexes. *Inorg. Chem. Front.* **2020**, *7*, 3533–3540. [CrossRef] [PubMed]

42. Novohradsky, V.; Pracharova, J.; Kasparkova, J.; Imberti, C.; Bridgewater, H.E.; Sadler, P.J.; Brabec, V. Induction of immunogenic cell death in cancer cells by a photoactivated platinum (IV) prodrug. *Inorg. Chem. Front.* **2020**, *7*, 4150–4159. [CrossRef] [PubMed]

43. Kostova, I. Ruthenium complexes as anticancer agents. *Curr. Med. Chem.* **2006**, *13*, 1085–1107. [CrossRef] [PubMed]

44. Lee, S.Y.; Kim, C.Y.; Nam, T.-G. Ruthenium complexes as anticancer agents: A brief history and perspectives. *Drug Des. Dev. Ther.* **2020**, *14*, 5375–5392. [CrossRef] [PubMed]

45. Reedijk, B.J. Metal-ligand exchange kinetics in platinum and ruthenium complexes. *Platin. Met. Rev.* **2008**, *52*, 2–11. [CrossRef]

46. Kratz, F.; Messori, L. Spectral characterization of ruthenium (III) transferrin. *J. Inorg. Biochem.* **1993**, *49*, 79–82. [CrossRef]

47. Simović, A.R.; Masnikosa, R.; Bratsos, I.; Alessio, E. Chemistry and reactivity of ruthenium (II) complexes: DNA/protein binding mode and anticancer activity are related to the complex structure. *Coord. Chem. Rev.* **2019**, *398*, 113011. [CrossRef]

48. Yan, Y.K.; Melchart, M.; Habtemariam, A.; Sadler, P.J. Organometallic chemistry, biology and medicine: Ruthenium arene anticancer complexes. *Chem. Commun.* **2005**, *14*, 4764–4776. [CrossRef]

49. Alkış, M.E.; Keleştemür, Ü.; Alan, Y.; Turan, N.; Buldurun, K. Cobalt and ruthenium complexes with pyrimidine based schiff base: Synthesis, characterization, anticancer activities and electrochemotherapy efficiency. *J. Mol. Struct.* **2021**, *1226*, 129402. [CrossRef]

50. Cole, H.D.; Roque III, J.A.; Lifshits, L.M.; Hodges, R.; Barrett, P.C.; Havrylyuk, D.; Heidary, D.; Ramasamy, E.; Cameron, C.G.; Glazer, E.C. Fine-Feature Modifications to Strained Ruthenium Complexes Radically Alter Their Hypoxic Anticancer Activity. *Photochem. Photobiol.* **2022**, *98*, 73–84. [CrossRef]

51. Roque III, J.A.; Cole, H.D.; Barrett, P.C.; Lifshits, L.M.; Hodges, R.O.; Kim, S.; Deep, G.; Francés-Monerris, A.; Alberto, M.E.; Cameron, C.G. Intraligand excited states turn a ruthenium oligothiophene complex into a light-triggered Ubertoxin with anticancer effects in extreme hypoxia. *J. Am. Chem. Soc.* **2022**, *144*, 8317–8336. [CrossRef] [PubMed]

52. Liang, L.; Wu, X.; Shi, C.; Wen, H.; Wu, S.; Chen, J.; Huang, C.; Wang, Y.; Liu, Y. Synthesis and characterization of polypyridine ruthenium (II) complexes and anticancer efficacy studies in vivo and in vitro. *J. Inorg. Biochem.* **2022**, *236*, 111963. [CrossRef]

53. Chen, J.; Tao, Q.; Wu, J.; Wang, M.; Su, Z.; Qian, Y.; Yu, T.; Wang, Y.; Xue, X.; Liu, H.-K. A lysosome-targeted ruthenium (II) polypyridyl complex as photodynamic anticancer agent. *J. Inorg. Biochem.* **2020**, *210*, 111132. [CrossRef] [PubMed]

54. Li, Y.-L.; Zhu, X.-M.; Chen, N.-F.; Chen, S.-T.; Yang, Y.; Liang, H.; Chen, Z.-F. Anticancer activity of ruthenium (II) plumbagin complexes with polypyridyl as ancillary ligands via inhibiting energy metabolism and GADD45A-mediated cell cycle arrest. *Eur. J. Med. Chem.* **2022**, *236*, 114312. [CrossRef] [PubMed]

55. Notaro, A.; Jakubaszek, M.; Koch, S.; Rubbiani, R.; Dömötör, O.; Enyedy, É.A.; Dotou, M.; Bedioui, F.; Tharaud, M.; Goud, B. A maltol-containing Ruthenium Polypyridyl Complex as a Potential Anticancer Agent. *Chem.—Eur. J.* **2020**, *26*, 4997–5009. [CrossRef] [PubMed]

56. Licona, C.; Delhorme, J.-B.; Riegel, G.; Vidimar, V.; Cerón-Camacho, R.; Boff, B.; Venkatasamy, A.; Tomasetto, C.; Gomes, P.d.S.F.C.; Rognan, D. Anticancer activity of ruthenium and osmium cyclometalated compounds: Identification of ABCB1 and EGFR as resistance mechanisms. *Inorg. Chem. Front.* **2020**, *7*, 678–688. [CrossRef]

57. Chen, D.; Guo, S.; Tang, X.; Rong, Y.; Bo, H.; Shen, H.; Zhao, Z.; Qiao, A.; Shen, J.; Wang, J. Combination of ruthenium (II) polypyridyl complex Δ-Ru1 and Taxol enhances the anti-cancer effect on Taxol-resistant cancer cells through Caspase-1/GSDMD-mediated pyroptosis. *J. Inorg. Biochem.* **2022**, *230*, 111749. [CrossRef]

58. Chen, C.; Xu, C.; Li, T.; Lu, S.; Luo, F.; Wang, H. Novel NHC-coordinated ruthenium (II) arene complexes achieve synergistic efficacy as safe and effective anticancer therapeutics. *Eur. J. Med. Chem.* **2020**, *203*, 112605. [CrossRef]

59. Morais, T.S.; Marques, F.; Madeira, P.J.A.; Robalo, M.P.; Garcia, M.H. Design and Anticancer Properties of New Water-Soluble Ruthenium–Cyclopentadienyl Complexes. *Pharmaceuticals* **2022**, *15*, 862. [CrossRef]

60. Elsayed, S.A.; Harrypersad, S.; Sahyon, H.A.; El-Magd, M.A.; Walsby, C.J. Ruthenium (II)/(III) DMSO-based complexes of 2-aminophenyl benzimidazole with in vitro and in vivo anticancer activity. *Molecules* **2020**, *25*, 4284. [CrossRef]

61. Janković, N.; Milović, E.; Jovanović, J.Đ.; Marković, Z.; Vraneš, M.; Stanojković, T.; Matić, I.; Crnogorac, M.Đ.; Klisurić, O.; Cvetinov, M. A new class of half-sandwich ruthenium complexes containing Biginelli hybrids: Anticancer and anti-SARS-CoV-2 activities. *Chem.-Biol. Interact.* **2022**, *363*, 110025. [CrossRef] [PubMed]

62. Kar, B.; Das, U.; De, S.; Pete, S.; Sharma, A.; Roy, N.; SK, A.K.; Panda, D.; Paira, P. GSH-resistant and highly cytoselective ruthenium (II)-p-cymene-(imidazo [4,5-f][1,10] phenanthrolin-2-yl) phenol complexes as potential anticancer agents. *Dalton Trans.* **2021**, *50*, 10369–10373. [CrossRef] [PubMed]

63. De, S.; Kumar, R.S.; Gauthaman, A.; Kumar, S.A.; Paira, P.; Moorthy, A.; Banerjee, S. Luminescent ruthenium (II)-para-cymene complexes of aryl substituted imidazo-1, 10-phenanthroline as anticancer agents and the effect of remote substituents on cytotoxic activities. *Inorg. Chim. Acta* **2021**, *515*, 120066. [CrossRef]

64. Oliveira, K.M.; Honorato, J.; Goncalves, G.R.; Cominetti, M.R.; Batista, A.A.; Correa, R.S. Ru (II)/diclofenac-based complexes: DNA, BSA interaction and their anticancer evaluation against lung and breast tumor cells. *Dalton Trans.* **2020**, *49*, 12643–12652. [CrossRef]

65. Engelbrecht, Z.; Roberts, K.E.; Hussan, A.; Amenuvor, G.; Cronje, M.J.; Darkwa, J.; Makhubela, B.C.; Sitole, L. Synthesis and anti-cancer activity of bis-amino-phosphine ligand and its ruthenium (II) complexes. *Bioorganic Med. Chem. Lett.* **2020**, *30*, 127492. [CrossRef]

66. Alsaeedi, M.S.; Babgi, B.A.; Abdellattif, M.H.; Jedidi, A.; Humphrey, M.G.; Hussien, M.A. DNA-binding capabilities and anticancer activities of ruthenium (II) cymene complexes with (Poly) cyclic aromatic diamine ligands. *Molecules* **2020**, *26*, 76. [CrossRef]

67. Sonkar, C.; Malviya, N.; Sinha, N.; Mukherjee, A.; Pakhira, S.; Mukhopadhyay, S. Selective anticancer activities of ruthenium (II)-tetrazole complexes and their mechanistic insights. *BioMetals* **2021**, *34*, 795–812. [CrossRef]

68. Khan, T.A.; Bhar, K.; Thirumoorthi, R.; Roy, T.K.; Sharma, A.K. Design, synthesis, characterization and evaluation of the anticancer activity of water-soluble half-sandwich ruthenium (II) arene halido complexes. *New J. Chem.* **2020**, *44*, 239–257. [CrossRef]

69. Khater, M.; Brazier, J.A.; Greco, F.; Osborn, H.M. Anticancer evaluation of new organometallic ruthenium (II) flavone complexes. *RSC Med. Chem.* **2023**. [CrossRef]

70. Gu, Y.-Q.; Shen, W.-Y.; Yang, Q.-Y.; Chen, Z.-F.; Liang, H. Ru (III) complexes with pyrazolopyrimidines as anticancer agents: Bioactivities and the underlying mechanisms. *Dalton Trans.* **2022**, *51*, 1333–1343. [CrossRef]

71. Fabijańska, M.; Kasprzak, M.M.; Ochocki, J. Ruthenium (II) and Platinum (II) Complexes with Biologically Active Aminoflavone Ligands Exhibit In Vitro Anticancer Activity. *Int. J. Mol. Sci.* **2021**, *22*, 7568. [CrossRef] [PubMed]

72. Studer, V.; Anghel, N.; Desiatkina, O.; Felder, T.; Boubaker, G.; Amdouni, Y.; Ramseier, J.; Hungerbühler, M.; Kempf, C.; Heverhagen, J.T. Conjugates containing two and three trithiolato-bridged dinuclear ruthenium (II)-arene units as in vitro antiparasitic and anticancer agents. *Pharmaceuticals* **2020**, *13*, 471. [CrossRef] [PubMed]

73. Qu, F.; Lamb, R.W.; Cameron, C.G.; Park, S.; Oladipupo, O.; Gray, J.L.; Xu, Y.; Cole, H.D.; Bonizzoni, M.; Kim, Y. Singlet Oxygen Formation vs Photodissociation for Light-Responsive Protic Ruthenium Anticancer Compounds: The Oxygenated Substituent Determines Which Pathway Dominates. *Inorg. Chem.* **2021**, *60*, 2138–2148. [CrossRef] [PubMed]

74. Oliveira, K.M.; Honorato, J.; Demidoff, F.C.; Schultz, M.S.; Netto, C.D.; Cominetti, M.R.; Correa, R.S.; Batista, A.A. Lapachol in the design of a new ruthenium (II)-diphosphine complex as a promising anticancer metallodrug. *J. Inorg. Biochem.* **2021**, *214*, 111289. [CrossRef]

75. Mihaila, M.; Hotnog, C.M.; Bostan, M.; Munteanu, A.C.; Vacaroiu, I.A.; Brasoveanu, L.I.; Uivarosi, V. Anticancer activity of some ruthenium (III) complexes with quinolone antibiotics: In vitro cytotoxicity, cell cycle modulation, and apoptosis-inducing properties in LoVo colon cancer cell line. *Appl. Sci.* **2021**, *11*, 8594. [CrossRef]

76. Fandzloch, M.; Dobrzańska, L.; Jędrzejewski, T.; Jezierska, J.; Wiśniewska, J.; Łakomska, I. Synthesis, structure and biological evaluation of ruthenium (III) complexes of triazolopyrimidines with anticancer properties. *JBIC J. Biol. Inorg. Chem.* **2020**, *25*, 109–124. [CrossRef]

77. Kanaoujiya, R.; Singh, D.; Minocha, T.; Yadav, S.K.; Srivastava, S. Synthesis, characterization of ruthenium (III) macrocyclic complexes of 1, 4, 8, 11-tetraazacyclotetradecane (cyclam) and in vitro assessment of anti-cancer activity. *Mater. Today Proc.* **2022**, *65*, 3143–3149.

78. Wadas, T.J.; Wong, E.H.; Weisman, G.R.; Anderson, C.J. Coordinating radiometals of copper, gallium, indium, yttrium, and zirconium for PET and SPECT imaging of disease. *Chem. Rev.* **2010**, *110*, 2858–2902. [CrossRef]

79. Chitambar, C.R.; Zivkovic, Z. Uptake of gallium-67 by human leukemic cells: Demonstration of transferrin receptor-dependent and transferrin-independent mechanisms. *Cancer Res.* **1987**, *47*, 3929–3934.

80. Johnston, G.S. Clinical applications of gallium in oncology. *Int. J. Nucl. Med. Biol.* **1981**, *8*, 249–255. [CrossRef]

81. Vallabhajosula, S.R.; Harwig, J.; Wolf, W. The mechanism of tumor localization of gallium-67 citrate: Role of transferrin binding and effect of tumor pH. *Int. J. Nucl. Med. Biol.* **1981**, *8*, 363–370. [CrossRef] [PubMed]

82. Bernstein, L.R. Mechanisms of therapeutic activity for gallium. *Pharmacol. Rev.* **1998**, *50*, 665–682. [PubMed]

83. Todorov, L.; Kostova, I.; Traykova, M. Lanthanum, Gallium and their Impact on Oxidative Stress. *Curr. Med. Chem.* **2019**, *26*, 4280–4295. [CrossRef] [PubMed]

84. Leitao, R.C.; Silva, F.; Ribeiro, G.H.; Santos, I.C.; Guerreiro, J.F.; Mendes, F.; Batista, A.A.; Pavan, F.R.; Maia, P.I.d.S.; Paulo, A. Gallium and indium complexes with isoniazid-derived ligands: Interaction with biomolecules and biological activity against cancer cells and Mycobacterium tuberculosis. *J. Inorg. Biochem.* **2022**, *240*, 112091. [CrossRef]

85. Hreusova, M.; Novohradsky, V.; Markova, L.; Kostrhunova, H.; Potočňák, I.; Brabec, V.; Kasparkova, J. Gallium (III) Complex with Cloxyquin Ligands Induces Ferroptosis in Cancer Cells and Is a Potent Agent against Both Differentiated and Tumorigenic Cancer Stem Rhabdomyosarcoma Cells. *Bioinorg. Chem. Appl.* **2022**, *2022*, 3095749. [CrossRef]

86. Chitambar, C.R.; Antholine, W.E. Iron-targeting antitumor activity of gallium compounds and novel insights into triapine®-metal complexes. *Antioxid. Redox Signal.* **2013**, *18*, 956–972. [CrossRef]

87. Lessa, J.A.; Parrilha, G.L.; Beraldo, H. Gallium complexes as new promising metallodrug candidates. *Inorg. Chim. Acta* **2012**, *393*, 53–63. [CrossRef]

88. Chitambar, C.R. Gallium-containing anticancer compounds. *Future Med. Chem.* **2012**, *4*, 1257–1272. [CrossRef]

89. Chitambar, C.R. Medical applications and toxicities of gallium compounds. *Int. J. Environ. Res. Public Health* **2010**, *7*, 2337–2361. [CrossRef]

90. Soll, M.; Goswami, T.K.; Chen, Q.-C.; Saltsman, I.; Teo, R.D.; Shahgholi, M.; Lim, P.; Di Bilio, A.J.; Cohen, S.; Termini, J. Cell-penetrating protein/corrole nanoparticles. *Sci. Rep.* **2019**, *9*, 2294. [CrossRef]

91. Qi, J.; Liu, T.; Zhao, W.; Zheng, X.; Wang, Y. Synthesis, crystal structure and antiproliferative mechanisms of gallium (iii) complexes with benzoylpyridine thiosemicarbazones. *RSC Adv.* **2020**, *10*, 18553–18559. [CrossRef]

92. dos SS Firmino, G.; Andre, S.C.; Hastenreiter, Z.; Campos, V.K.; Abdel-Salam, M.A.; de Souza-Fagundes, E.M.; Lessa, J.A. In vitro assessment of the cytotoxicity of Gallium (III) complexes with Isoniazid-Derived Hydrazones: Effects on clonogenic survival of HCT-116 cells. *Inorg. Chim. Acta* **2019**, *497*, 119079. [CrossRef]

93. Robin, P.; Singh, K.; Suntharalingam, K. Gallium (iii)-polypyridyl complexes as anti-osteosarcoma stem cell agents. *Chem. Commun.* **2020**, *56*, 1509–1512. [CrossRef]

94. Litecká, M.; Hreusova, M.; Kašpárková, J.; Gyepes, R.; Smolková, R.; Obuch, J.; David, T.; Potočňák, I. Low-dimensional compounds containing bioactive ligands. Part XIV: High selective antiproliferative activity of tris (5-chloro-8-quinolinolato) gallium (III) complex against human cancer cell lines. *Bioorganic Med. Chem. Lett.* **2020**, *30*, 127206. [CrossRef] [PubMed]

95. Wilke, N.L.; Abodo, L.O.; Frias, C.; Frias, J.; Baas, J.; Jakupec, M.A.; Keppler, B.K.; Prokop, A. The gallium complex KP46 sensitizes resistant leukemia cells and overcomes Bcl-2-induced multidrug resistance in lymphoma cells via upregulation of Harakiri and downregulation of XIAP in vitro. *Biomed. Pharmacother.* **2022**, *156*, 113974. [CrossRef] [PubMed]

96. Pricker, S.P. Medical uses of gold compounds: Past, present and future. *Gold Bull.* **1996**, *29*, 53–60. [CrossRef]

97. Navarro, M. Gold complexes as potential anti-parasitic agents. *Coord. Chem. Rev.* **2009**, *253*, 1619–1626. [CrossRef]

98. Yang, Z.; Jiang, G.; Xu, Z.; Zhao, S.; Liu, W. Advances in alkynyl gold complexes for use as potential anticancer agents. *Coord. Chem. Rev.* **2020**, *423*, 213492. [CrossRef]

99. Lu, Y.; Ma, X.; Chang, X.; Liang, Z.; Lv, L.; Shan, M.; Lu, Q.; Wen, Z.; Gust, R.; Liu, W. Recent development of gold (I) and gold (III) complexes as therapeutic agents for cancer diseases. *Chem. Soc. Rev.* **2022**. [CrossRef]

100. Che, C.-M.; Sun, R.W.-Y. Therapeutic applications of gold complexes: Lipophilic gold (III) cations and gold (I) complexes for anti-cancer treatment. *Chem. Commun.* **2011**, *47*, 9554–9560. [CrossRef]

101. Nardon, C.; Boscutti, G.; Fregona, D. Beyond platinums: Gold complexes as anticancer agents. *Anticancer. Res.* **2014**, *34*, 487–492. [PubMed]

102. Bian, M.; Fan, R.; Jiang, G.; Wang, Y.; Lu, Y.; Liu, W. Halo and pseudohalo gold (I)–NHC complexes derived from 4, 5-diarylimidazoles with excellent in vitro and in vivo anticancer activities against HCC. *J. Med. Chem.* **2020**, *63*, 9197–9211. [CrossRef] [PubMed]

103. Liu, W.; Bensdorf, K.; Proetto, M.; Abram, U.; Hagenbach, A.; Gust, R. NHC gold halide complexes derived from 4, 5-diarylimidazoles: Synthesis, structural analysis, and pharmacological investigations as potential antitumor agents. *J. Med. Chem.* **2011**, *54*, 8605–8615. [CrossRef] [PubMed]

104. Walther, W.; Althagafi, D.; Curran, D.; O'Beirne, C.; Mc Carthy, C.; Ott, I.; Basu, U.; Büttner, B.; Sterner-Kock, A.; Müller-Bunz, H. In-vitro and in-vivo investigations into the carbene-gold anticancer drug candidates NHC*-Au-SCSNMe2 and NHC*-Au-S-GLUC against advanced prostate cancer PC3. *Anti-Cancer Drugs* **2020**, *31*, 672–683. [CrossRef] [PubMed]

105. Gulzar, S.; Ammara, U.; Abid, Z.; Shahid, M.; Ashraf, R.S.; Baig, N.; Kawde, A.-N.; Bhatia, G.; Isab, A.A.; Altaf, M. Synthesis, in vitro anticancer activity and reactions with biomolecule of gold (I)-NHC carbene complexes. *J. Mol. Struct.* **2022**, *1255*, 132482. [CrossRef]

106. Meyer, A.; Gutiérrez, A.; Ott, I.; Rodríguez, L. Phosphine-bridged dinuclear gold (I) alkynyl complexes: Thioredoxin reductase inhibition and cytotoxicity. *Inorg. Chim. Acta* **2013**, *398*, 72–76. [CrossRef]

107. Arcau, J.; Andermark, V.; Aguiló, E.; Gandioso, A.; Moro, A.; Cetina, M.; Lima, J.C.; Rissanen, K.; Ott, I.; Rodríguez, L. Luminescent alkynyl-gold (I) coumarin derivatives and their biological activity. *Dalton Trans.* **2014**, *43*, 4426–4436. [CrossRef]

108. Rawat, A.; Reddy, A.V.B. Recent advances on anticancer activity of coumarin derivatives. *Eur. J. Med. Chem. Rep.* **2022**, 100038. [CrossRef]

109. Andermark, V.; Göke, K.; Kokoschka, M.; El Maaty, M.A.A.; Lum, C.T.; Zou, T.; Sun, R.W.-Y.; Aguilo, E.; Oehninger, L.; Rodríguez, L. Alkynyl gold (I) phosphane complexes: Evaluation of structure–activity-relationships for the phosphane ligands, effects on key signaling proteins and preliminary in-vivo studies with a nanoformulated complex. *J. Inorg. Biochem.* **2016**, *160*, 140–148. [CrossRef]

110. Alsaeedi, M.S.; Babgi, B.A.; Hussien, M.A.; Abdellattif, M.H.; Humphrey, M.G. DNA-binding and anticancer activity of binuclear gold (I) alkynyl complexes with a phenanthrenyl bridging ligand. *Molecules* **2020**, *25*, 1033. [CrossRef]

111. Chui, C.-H.; Wong, R.S.-M.; Gambari, R.; Cheng, G.Y.-M.; Yuen, M.C.-W.; Chan, K.-W.; Tong, S.-W.; Lau, F.-Y.; Bo-San Lai, P.; Lam, K.-H. Antitumor activity of diethynylfluorene derivatives of gold (I). *Bioorganic Med. Chem.* **2009**, *17*, 7872–7877. [CrossRef] [PubMed]

112. De Nisi, C.B.; Leonzio, M.; Sartor, G.; Fato, R.; Naldi, M.; Monari, M.; Calonghi, N.; Bandini, M. Synthesis, cytotoxicity and anti-cancer activity of new alkynyl-gold (i) complexes Assunta. *Dalton Trans.* **2016**, *45*, 1546–1553. [CrossRef] [PubMed]

113. Marmol, I.; Castellnou, P.; Alvarez, R.; Gimeno, M.C.; Rodríguez-Yoldi, M.J.; Cerrada, E. Alkynyl Gold (I) complexes derived from 3-hydroxyflavones as multi-targeted drugs against colon cancer. *Eur. J. Med. Chem.* **2019**, *183*, 111661. [CrossRef] [PubMed]

114. Babgi, B.A.; Alsayari, J.; Alenezi, H.M.; Abdellatif, M.H.; Eltayeb, N.E.; Emwas, A.-H.M.; Jaremko, M.; Hussien, M.A. Alteration of anticancer and protein-binding properties of gold (I) Alkynyl by phenolic Schiff bases moieties. *Pharmaceutics* **2021**, *13*, 461. [CrossRef] [PubMed]

115. Tabrizi, L.; Yang, W.S.; Chintha, C.; Morrison, L.; Samali, A.; Ramos, J.W.; Erxleben, A. Gold (I) Complexes with a Quinazoline Carboxamide Alkynyl Ligand: Synthesis, Cytotoxicity, and Mechanistic Studies. *Eur. J. Inorg. Chem.* **2021**, *2021*, 1921–1928. [CrossRef]

116. Xie, Q.; Su, M.; Liu, Y.; Zhang, D.; Li, Z.; Bai, M. Translocator protein (TSPO)-Targeted agents for photodynamic therapy of cancer. *Photodiagnosis Photodyn. Ther.* **2021**, *34*, 102209. [CrossRef]

117. Bian, M.; Sun, Y.; Liu, Y.; Xu, Z.; Fan, R.; Liu, Z.; Liu, W. A gold (i) complex containing an oleanolic acid derivative as a potential anti-ovarian-cancer agent by inhibiting trxr and activating ros-mediated ers. *Chem.–Eur. J.* **2020**, *26*, 7092–7108. [CrossRef]

118. Aminin, D.L.; Menchinskaya, E.S.; Pisliagin, E.A.; Silchenko, A.S.; Avilov, S.A.; Kalinin, V.I. Anticancer activity of sea cucumber triterpene glycosides. *Mar. Drugs* **2015**, *13*, 1202–1223. [CrossRef]

119. Tabrizi, L.; Romanova, J. Antiproliferative Activity of Gold (I) N-Heterocyclic Carbene and Triphenylphosphine Complexes with Ibuprofen Derivatives as Effective Enzyme Inhibitors. *Appl. Organomet. Chem.* **2020**, *34*, e5618. [CrossRef]

120. Evans, C.H. *Biochemistry of the Lanthanides*; Springer Science & Business Media: New York, NY, USA, 2013; Volume 8.

121. Huang, P.; Li, J.; Zhang, S.; Chen, C.; Han, Y.; Liu, N.; Xiao, Y.; Wang, H.; Zhang, M.; Yu, Q. Effects of lanthanum, cerium, and neodymium on the nuclei and mitochondria of hepatocytes: Accumulation and oxidative damage. *Environ. Toxicol. Pharmacol.* **2011**, *31*, 25–32. [CrossRef]

122. He, X.; Zhang, Z.; Zhang, H.; Zhao, Y.; Chai, Z. Neurotoxicological evaluation of long-term lanthanum chloride exposure in rats. *Toxicol. Sci.* **2008**, *103*, 354–361. [CrossRef] [PubMed]

123. Zheng, H.-L.; Zhao, Z.-Q.; Zhang, C.-G.; Feng, J.-Z.; Ke, Z.-L.; Su, M.-J. Changes in lipid peroxidation, the redox system and ATPase activities in plasma membranes of rice seedling roots caused by lanthanum chloride. *Biometals* **2000**, *13*, 157–163. [CrossRef] [PubMed]

124. Damment, S.; Beevers, C.; Gatehouse, D. Evaluation of the potential genotoxicity of the phosphate binder lanthanum carbonate. *Mutagenesis* **2005**, *20*, 29–37. [CrossRef] [PubMed]

125. Chundawat, N.S.; Jadoun, S.; Zarrintaj, P.; Chauhan, N.P.S. Lanthanide complexes as anticancer agents: A review. *Polyhedron* **2021**, *207*, 115387. [CrossRef]

126. Deghadi, G.R.; Mohamed, G.G. Can New Series of Half-sandwich Lanthanum (III), Erbium (III), and Ytterbium (III) Complexes of Organometallic Ferrocenyl Schiff Base Ligands Display Biological Activities as Antibacterial and Anticancer Drugs? *Comments Inorg. Chem.* **2022**, *42*, 368–401. [CrossRef]

127. Deghadi, R.G.; Abbas, A.A.; Mohamed, G.G. Theoretical and experimental investigations of new bis (amino triazole) schiff base ligand: Preparation of its UO2 (II), Er (III), and La (III) complexes, studying of their antibacterial, anticancer, and molecular docking. *Appl. Organomet. Chem.* **2021**, *35*, e6292. [CrossRef]

128. Abo El-Maali, N.; Wahman, A.Y.; Aly, A.A.; Nassar, A.Y.; Sayed, D.M. Anticancer activity of lanthanum (III) and europium (III) 5-fluorouracil complexes on Caco-2 cell line. *Appl. Organomet. Chem.* **2020**, *34*, e5594. [CrossRef]

129. Shahraki, S.; Shiri, F.; Heidari Majd, M.; Dahmardeh, S. Investigating the biological potency of novel lanthanum (III) amino acid complex: MCF-7 breast cancer cell line, BSA and β-LG as targets. *J. Iran. Chem. Soc.* **2019**, *16*, 301–313. [CrossRef]

130. Bhat, V.V.; Chetana, P.; Dhale, M.A.; Soman, S. Synthesis, characterization, in vitro biological evaluation and molecular docking studies of newly synthesized mononuclear lanthanum (III) complexes of N, N′-bis (2-aminoethyl) oxamide and phenanthroline bases. *J. Mol. Struct.* **2022**, *1270*, 133903. [CrossRef]

131. Qin, Q.-P.; Wang, Z.-F.; Tan, M.-X.; Huang, X.-L.; Zou, H.-H.; Zou, B.-Q.; Shi, B.-B.; Zhang, S.-H. Complexes of lanthanides (III) with mixed 2, 2′-bipyridyl and 5, 7-dibromo-8-quinolinoline chelating ligands as a new class of promising anti-cancer agents. *Metallomics* **2019**, *11*, 1005–1015. [CrossRef]

132. Abdolmaleki, S.; Aliabadi, A.; Ghadermazi, M. Two La (III) complexes containing pyridine-2, 6-dicarboxylate as in vitro potent cytotoxic agents toward human lymphocyte cells. *Inorg. Chim. Acta* **2022**, *542*, 121152. [CrossRef]

133. Aramesh-Boroujeni, Z.; Aramesh, N.; Jahani, S.; Khorasani-Motlagh, M.; Kerman, K.; Noroozifar, M. Experimental and computational interaction studies of terbium (III) and lanthanide (III) complexes containing 2, 2′-bipyridine with bovine serum albumin and their in vitro anticancer and antimicrobial activities. *J. Biomol. Struct. Dyn.* **2021**, *39*, 5105–5116. [CrossRef] [PubMed]

Article

Novel Biotinylated Cu(II)-Phenanthroline Complexes: 2D and 3D Cytotoxic Activity and Mechanistic Insight

Stephen Barrett [1,†], Michele De Franco [2], Chiara Donati [2], Cristina Marzano [2], Valentina Gandin [2,*] and Diego Montagner [1,3,*]

1   Department of Chemistry, Maynooth University, W23 NPY6 Maynooth, Ireland; stephen.barrett@mu.ie
2   Department of Pharmaceutical and Pharmacological Sciences, University of Padova, 35131 Padova, Italy; michele.defranco@phd.unipd.it (M.D.F.); chiara.donati.1@phd.unipd.it (C.D.); cristina.marzano@unipd.it (C.M.)
3   Kathleen Londsdale Institute for Human Health Research, Maynooth University, W23 F2H6 Maynooth, Ireland
*   Correspondence: valentina.gandin@unipd.it (V.G.); diego.montagner@mu.ie (D.M.)
†   S.B. dedicates this paper to Andrew Barrett RIP.

Abstract: The interest in the use of copper as a metal scaffold for the development of novel chemotherapeutics has considerably grown in recent years. This is mainly due to the relatively lower toxicity of copper complexes with respect to platinum drugs (i.e., cisplatin), the different mechanisms of action, and the cheaper cost. In the last decades, hundreds of copper-based complexes were developed and screened as anticancer agents, with the antesignanus of all compounds being copper bis-phenanthroline $[Cu(phen)_2]^{2+}$ developed by D.S. Sigman in the late 1990s. In particular, copper(phen) derivatives have been shown high interest in their capacity to interact with DNA by nucleobase intercalation. Here, we report the synthesis and chemical characterization of four novel copper(II) complexes functionalised with phenanthroline derivatives containing biotin. Biotin, also known as Vitamin B7, is involved in a series of metabolic processes, and its receptors are often overexpressed in many tumour cells. A detailed biological analysis including cytotoxicity in 2D and 3D, cellular drug uptake, DNA interaction, and morphological studies are discussed.

Keywords: copper(II) complexes; biotin; anticancer activity; 3D cell cultures

1. Introduction

Platinum(II) anticancer drugs, cisplatin, carboplatin, and oxaliplatin have displayed phenomenal clinical activity in the treatment of solid tumours in the past several decades, and are used in nearly 50% of all clinical chemotherapeutic regimens [1–3]. Platinum-derived anticancer agents deliver their cytotoxicity mainly through covalent binding to the therapeutic target DNA rather than noncovalent interaction, a behaviour that is different from most of the classical nonmetal organic drugs, therefore resulting in enhanced anticancer activity due to the amplified duration of drug action [4–6]. The drawbacks associated with the use of these drugs are the offsite interactions between the platinum and biomolecules (such as proteins, enzymes . . .), which not only lead to chronic side effects but also to decreased drug efficacy. This effect, coupled with the increasing resistance developed by cancers to platinum complexes, opens the door for the need of designing new and highly selective-based anticancer therapeutics [1]. One strategy is to exploit the overexpression of specific receptors on or within the tumour cell. The use of specific vectors that can be recognized by these overexpressed receptors is a smart strategy to increase the selectivity of metal-based drugs enhancing the accumulation inside cancer tissues [7]. This strategy, paired with the use of an endogenous metal centre like copper(II), should lead to a more selective and less-toxic alternative to a platinum-based therapeutic arsenal [8].

Biotin belongs to the family of B vitamins, and it is more specifically known as vitamin B7 or vitamin H. Biotin is involved in a huge array of metabolic processes in mammals but also in many other organisms. Mostly, it is used for the regulation of carbohydrates and amino acids [9]. Biotin is a water-soluble heterocyclic molecule formed of two condensed five-member rings (a tetrahydrothiophene ring fused to an ureido ring) and a carboxylic acid at the end of a four-carbon chain which makes it a highly attractive delivery vector (Figure 1). Recent reports have shown that the biotin-specific uptake systems are enhanced in many cancer cells, including leukaemia (L1210FR), ovarian (Ov2008, ID8), colon (Colo-26), mastocytoma (P815), lung (M109), renal (RENCA, RD0995) and breast (4T1, JC, MMT06056) cancer cell lines [10]. Biotin has been demonstrated to be very rapidly taken up into tumour cells which overexpress the biotin-related receptors on their cell surface. Studies have already shown that tagging classical metal-based chemotherapy drugs with a biotin moiety leads to very positive effects [11]. Guo et al. developed several biotinylated Pt(IV) complexes with indomethacin [12,13] and, in 2017, Wang et al. created a library of Pt(IV) complexes with biotin in an axial position [14]. Very recently, in 2022, Han et al. developed a Pt(IV) complex bearing one HDAC inhibitor (4-phenylbutyric acid) and biotin moiety attached in the axial positions [15]. In 2019, Upadhyay et al. reported the synthesis and biological evaluation of platinum(II) complexes where a biotin moiety was conjugated to a 1,10-phenanthroline scaffold [16] and biotinylated ruthenium, osmium, and copper complexes are described [17–21].
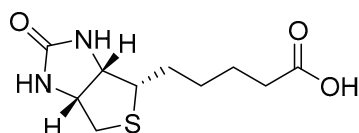
Figure 1. Structure of biotin.

Inspired by these results, we here report the synthesis, characterization, and biological application of four novel Cu(II) complexes (**1**–**4**) with two different biotin-functionalized ligands **A** and **B** (Scheme 1). The addition of the biotin to the scaffolds of phenanthroline and dafone (4,5-Diazafluoren-9-one) will enhance not only the selectivity toward tumour tissues but also the hydrophilic features of the final complexes, which is an important characteristic for biological applications. The in vitro anticancer potential of these complexes has been investigated on 2D and 3D cancer-cell models; additionally, cell-free and in-cell studies were carried out in order to elucidate their mechanism of action.
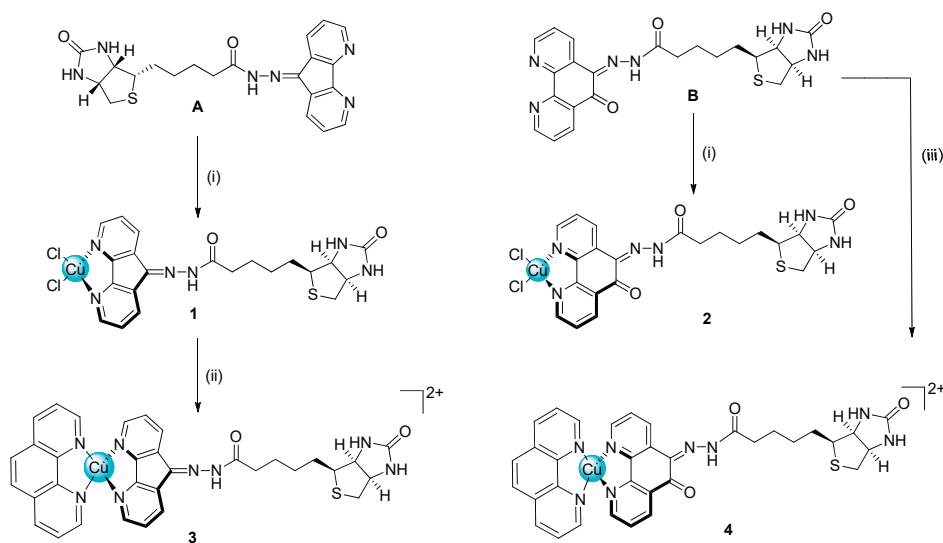
Scheme 1. Synthetic pathway for the formation of complexes **1**–**4**. (i)—CuCl$_2$/MeOH/reflux; (ii)—1,10-Phenanthroline/AgNO$_3$/DMF/r.t; (iii)—[Cu(phen)(ONO$_2$)$_2$]/DMF/40 °C.

2. Results and Discussion

2.1. Synthesis and Characterisation

Phenanthroline derivatives of Cu(II) have been historically studied as antimicrobial and anticancer compounds, with a strong ability to intercalate between the DNA nucleobases [22,23]. On these bases, we decided to modify the phenanthroline scaffold to allow functionalisation with the vector biotin. Two novel ligands (**A** and **B**) were conjugated to the Cu(II) centre, obtaining four novel complexes, two with two chlorides (**1** and **2**) and two with another phenanthroline (**3** and **4**) completing the copper coordination sphere (Scheme 1).

As described in the experimental section and in Scheme S1 (Supporting Information), biotin was transformed in the corresponding methyl ester derivative (**1**) before being functionalised with hydrazine to obtain the biotin-hydrazine derivative (**2**). Biotin-hydrazine **2** was then reacted with dafone (4,5-Diazafluoren-9-one) or phendione, obtaining the two novel ligands (**A** and **B**, respectively). The novel ligands were characterised by multinuclear NMR, IR, elemental analyses, and HR-MS (Figures S1–S6 in Supporting Information).

The synthesis of the four novel complexes **1**–**4** has been challenging and only after different attempts, the complexes were obtained in high purity for biological studies. Complexes **1** and **2** were obtained by reacting $CuCl_2$ and the corresponding ligand (**A** or **B**) in MeOH. Complex **3** was obtained from complex **1** by reaction with one equivalent of phenanthroline in the presence of $AgNO_3$. Complex **4**, finally, was obtained by direct reaction of ligand **B** with one equivalent of $[Cu(phen)(ONO_2)_2]$ in DMF. All the complexes have been characterised by IR and HR-MS and the purity was assessed by elemental analyses and HPLC (Figures S7–S13 in Supporting Information). The complexes are stable in physiological buffer solutions in the pH range of 4–9 and are stable at pH 6 for at least one week (UV-Studies, Figure S14 in Supporting Information).

2.2. Cytotoxicity

The in vitro anticancer potential of the newly developed complexes and of the ligands has been tested on six different cancer cell lines including PSN-1 (pancreatic), HCT-15 (colorectal with low sensitivity for cisplatin), 2008 (ovarian), A431 (cervical), MDA-MB-231 (breast), and U1285 (lung) cancer cells. For comparison purposes, cisplatin efficacy was assessed under the same experimental conditions. The cytotoxicity parameters, expressed in terms of IC_{50} and obtained after 72 h of drug exposure by MTT assay, are reported in Table 1.

Table 1. IC_{50} values of complexes **1**–**4** in PSN-1 (pancreatic), HCT-15 (colorectal with low sensitivity for cisplatin), 2008 (ovarian), A431 (cervical), MDA-MB-231 (breast), and U1285 (lung) cancer cells. Cells (3–$5 \times 10^3 \times$ well) were treated for 72 h with tested compounds. Cell viability was estimated by means of the MTT test. The IC_{50} values were calculated by a four-parameter (4-PL) logistic model ($p < 0.05$). S.D. = standard deviation.

Complex	PSN-1	HCT-15	2008	A431	MDA-MB-231	U-1285
1	0.6 ± 0.2	0.4 ± 0.1	4.5 ± 0.6	7.2 ± 0.6	2.1 ± 0.4	5.9 ± 0.5
2	0.4 ± 0.1	0.4 ± 0.1	1.1 ± 0.3	1.2 ± 0.5	1.4 ± 0.1	3.8 ± 0.5
3	0.7 ± 0.2	1.8 ± 0.2	3.3 ± 0.1	0.9 ± 0.2	1.4 ± 0.4	3.0 ± 0.3
4	0.6 ± 0.2	0.4 ± 0.02	0.6 ± 0.2	0.3 ± 0.03	0.6 ± 0.1	2.0 ± 0.6
A	>50	>50	>50	>50	>50	>50
B	N/A	N/A	21.48 ± 0.72	N/A	N/A	28.13 ± 2.77
Cisplatin	12.1 ± 2.9	13.9 ± 1.7	2.2 ± 1.4	2.1 ± 0.9	30.5 ± 2.6	2.1 ± 0.9

All the newly developed copper complexes showed strong cytotoxicity against most of the cell lines, with average IC_{50} values from three to fourteen times lower with respect to those elicited by the reference drug cisplatin. Ligands **A** and **B** did not show activity comparable to the complexes. Compound **4** was the most active complex in 2D assays, with an average IC_{50} value in the low micromolar range (0.8 μM) while the weakest was

complex **1** (average IC_{50} 3.4 μM). Due to note, all the complexes were very effective in the MDA-MB-231 cell line, which overexpress the SMVT (sodium-dependent multivitamin transporter) receptor, which is well known to be involved in the intracellular translocation of biotin [24].

Table 2 reported the IC_{50} values of the complexes against two types of ovarian cancer cells, one sensitive (2008) and one resistant to cisplatin (C13*). Very interesting, all complexes showed similar activity in both cell lines, indicating that they can overcome the cisplatin resistance. The resistance factor (R.F., the ratio among IC_{50} values obtained in resistant C13*cells and those calculated in the sensitive 2008 ones) calculated for all tested complexes resulted to be ≤2 (R.F. for cisplatin 11.1), strongly confirming the ability of the complexes to bypass cisplatin resistance.

Table 2. IC_{50} values of complexes **1**–**4** against 2008 and C13* ovarian cancer cell lines. Cells ($3 \times 10^3 \times$ well) were treated for 72 h with tested compounds. Cell viability was estimated by means of the MTT test. The IC_{50} values were calculated by a four-parameter (4-PL) logistic model ($p < 0.05$). S.D. = standard deviation. RF = IC_{50} resistant/IC_{50} parental cells.

Complex	2008	C13*	R.F.
1	4.5 ± 0.6	2.0 ± 0.8	0.4
2	1.1 ± 0.3	1.1 ± 0.4	1.0
3	3.3 ± 0.1	2.5 ± 0.2	0.7
4	0.6 ± 0.2	1.1 ± 0.3	1.9
Cisplatin	2.2 ± 1.4	24.1 ± 3.0	11.1

In order to preliminarily assess the possible toxic effect on noncancerous cells, we also evaluated the cytotoxic potential of the newly developed Cu(II) complexes against noncancerous CHO cells (Table 3). For all tested complexes, calculated IC_{50} values were higher than those obtained (on average) against tumour cells, thus indicating for this class of metal complexes a slightly preferential cytotoxicity against cancer cells, as attested by the calculated selectivity index values (SI = the quotient of the average IC_{50} toward normal cells divided by the average IC_{50} for the malignant cells).

Table 3. Cytotoxic potential of the developed Cu(II) complexes against noncancerous CHO cells.

Complex	CHO	S.I.
1	13.1 ± 0.9	3.9
2	5.2 ± 0.3	3.7
3	2.1 ± 0.8	1.1
4	1.8 ± 0.7	2.3
Cisplatin	24.1 ± 3.0	11.1

The most active complexes, **2** and **4**, were also screened against 3D spheroids of human pancreatic PSN-1 cancer cells to further assess their anticancer potential in a more predictive environment. The 2D cell cultures reflect only in part the morphology of human cancer cells and do not represent the complexity of the in vivo tumour microenvironment regarding morphology, growth, gene expression, and differentiation. Conversely, the 3D cell cultures (spheroids), constitute an alternative and/or parallel approach to 2D, as they more accurately mimic the tumour microenvironment, and, nowadays, they are increasingly used as preclinical tumour models in anticancer drug screenings.

The cancer spheroids were treated with tested complexes for 72 h, and the cell viability was estimated by means of a modified acid phosphatase (APH) assay. The IC_{50} values for complexes **2** and **4** in 3D PSN-1 human pancreatic adenocarcinoma-cell spheroids are shown in Table 4. Both complexes proved to be far more active than cisplatin in 3D spheroids, being about forty and eight times more effective than the reference metallodrug,

respectively. On the other hand, compared with 2D assays, complex **2** was found more cytotoxic than complex **4** in 3D studies.

Table 4. IC_{50} values of complexes **2** and **4** against human pancreatic PSN-1 cancer-cell spheroids. The cells (2.5×10^3 cells/well) were treated for 72 h with tested compounds. Cell viability was estimated by means of the APH test. IC_{50} values were calculated from the dose-response curves by a 4-PL logistic model ($p < 0.05$). S.D. = standard deviation.

Complex	PSN-1
2	1.3 ± 0.5
4	6.9 ± 1.3
Cisplatin	52.6 ± 3.8

2.3. Cellular Uptake

The ability to enter cancer cells is a very important factor to determine the biological activity of metal-based compounds. Consequently, with the aim of correlating the antiproliferative activity elicited by all the newly developed complexes and their accumulation profiles into cancer cells, the Cu content was evaluated in the SMVT overexpressing MDA-MB-231 cells. Uptake profiles were determined by treating cancer cells for 24 h with two concentrations (2 and 3 µM) of tested complexes. Results, reported in Figure 2, clearly showed that the Cu intracellular content was dose dependent and, among all, complexes which are most internalised into cancer cells are derivatives **3** and **4**. These results suggest that the role of the biotin in the cellular uptake is minimal and that complexes are mainly internalised by passive diffusion, being that complexes **3** and **4** are the most lipophilic ones (due to the presence of phenanthroline with respect to the chlorides in complexes **1** and **2**). Interestingly, a linear and direct correlation between drug uptake and 2D cytotoxicity could be drawn for all tested complexes (Figure S15 in Supporting Information).
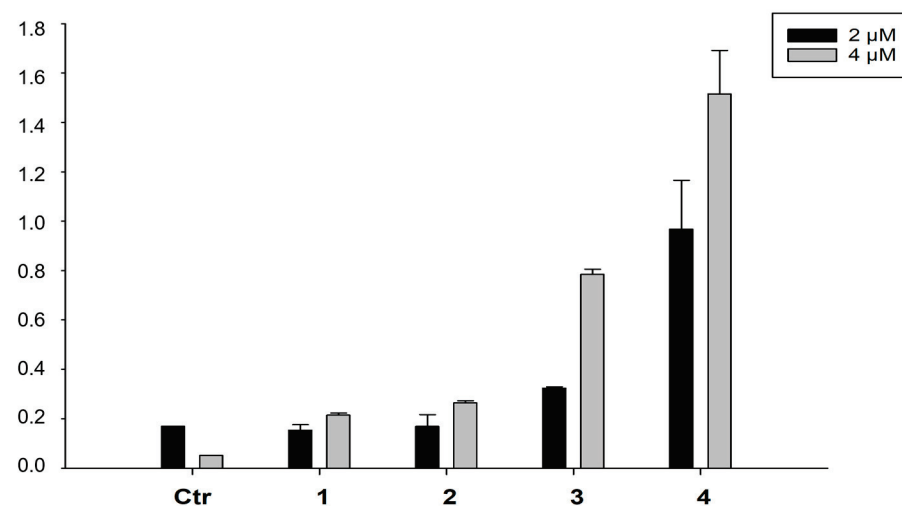
Figure 2. Cellular uptake of complexes **1**–**4** in drug-treated MDA-MB-231 human breast cancer cells. Cells were incubated for 24 h with 2 or 4 µM of tested complexes. The amount of cellular Cu was estimated by GF-AAS. Error bars are S.D.

2.4. DNA Interaction and PDI Inhibition

A number of research studies were performed on the elucidation of the mechanism of action of copper complexes in the past three decades. Despite several different molecular targets having been proposed for copper(II) complexes, DNA still represents one of the most substantiated when considering diamine ligands. On this basis, we thought it of interest to evaluate the ability of tested complexes to interact with DNA, both at molecular and cellular levels. An ethidium bromide (EB) displacement assay was used to understand

if the complexes interact with the DNA at a molecular level. Compounds **3** and **4** displayed the highest quenching values and the relative fluorescence decrease was greater than 50% with binding constants of 2.53×10^7 M(bp^{-1}) and 1.28×10^7 M(bp^{-1}) for compounds **3** and **4**, respectively (Figure 3). These values are very much in line with what was previously seen by us [25] and also very close to the reported literature values of 2.60×10^7 M(bp^{-1}) and 3.04×10^7 M(bp^{-1}) for the bis complexes of [Cu(phen)$_2$]$^{2+}$ and [Cu(DPQ)$_2$]$^{2+}$ reported by Molphy et al. [26]. Compounds **1** and **2** instead showed very small quenching and the binding constants were not determined. It is largely possible that the presence of the 1,10-phenanthroline scaffold on compounds **3** and **4** is contributing to the increased displacement of the EtBr (probably by intercalation) and leading to a more noticeable decrease in the fluorescence.
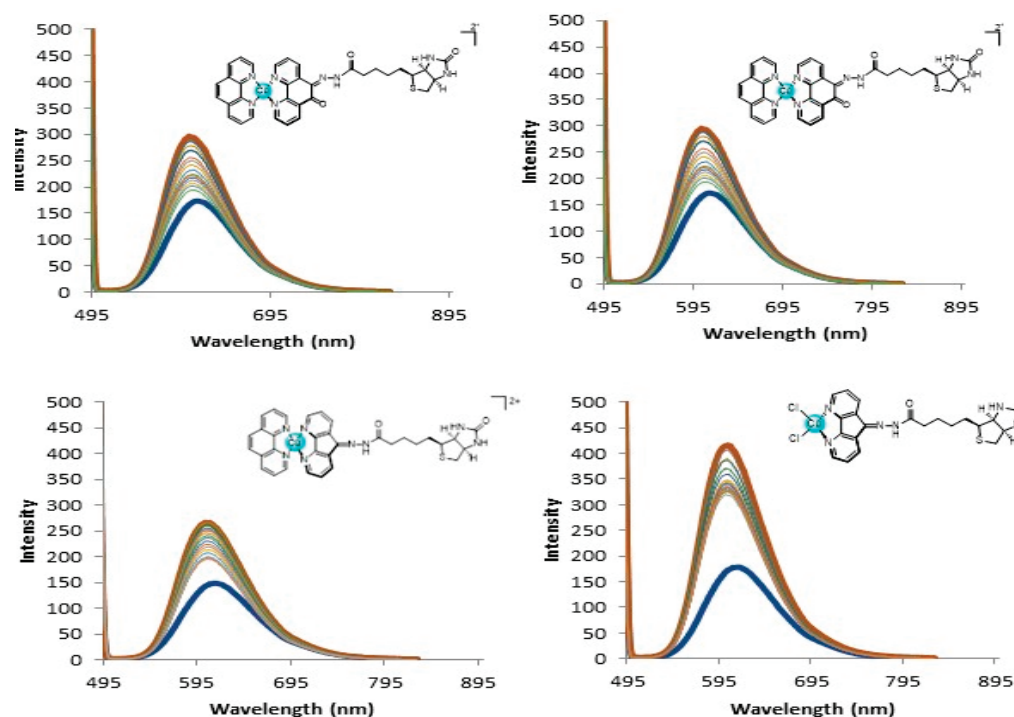
Figure 3. DNA Fluorescence quenching and relative displacement of EtBr for complexes **1**–**4**.

As proof of the principle of their DNA-targeting ability, the alkaline single-cell gel electrophoresis (Comet assay, Figure 4) assay was performed to evaluate cellular genomic DNA lesions induced by tested complexes. The most effective cytotoxic derivatives, complexes **2** and **4,** were chosen as the most representative compounds. MDA-MDB-231 cells were exposed for 3 h to 4 μM of tested compounds or 200 μM of the reference drug chlorambucil. Figure 4A depicts the relative percentage of comets and the number of cells forming a comet relative to the total number of detected cells per each condition in two randomly captured fields from two independent experiments. Comet assay studies clearly showed that at least one fourth and one third of cells treated with compounds **2** and **4**, respectively, presented lesioned genomic DNA. Interestingly, the DNA damaging efficacy of compound **4** was even much higher than that induced by the reference compound chlorambucil. On the contrary, cell metalation studies clearly showed that complexes are not able to covalently bind the DNA (Figure S16 in Supporting Information). Altogether, these data confirm that DNA is a major target for this class of complexes and the interaction is mainly by intercalation. On the other hand, some reports highlighted protein disulphide isomerase (PDI) as an emerging target for copper complexes [27]. On this basis, we also evaluated the ability of our complexes to act as PDI inhibitors. The enzyme was treated with 25 μM of complexes **2** and **4**, and the ability to hamper its activity was assessed by a biochemical colourimetric method (Proteostat kit). As shown in Figure 4B, both complexes are able to inhibit the PDI

by 45 and 15%, respectively, indicating that PDI could be a possible secondary molecular target for this class of copper(II) complexes.
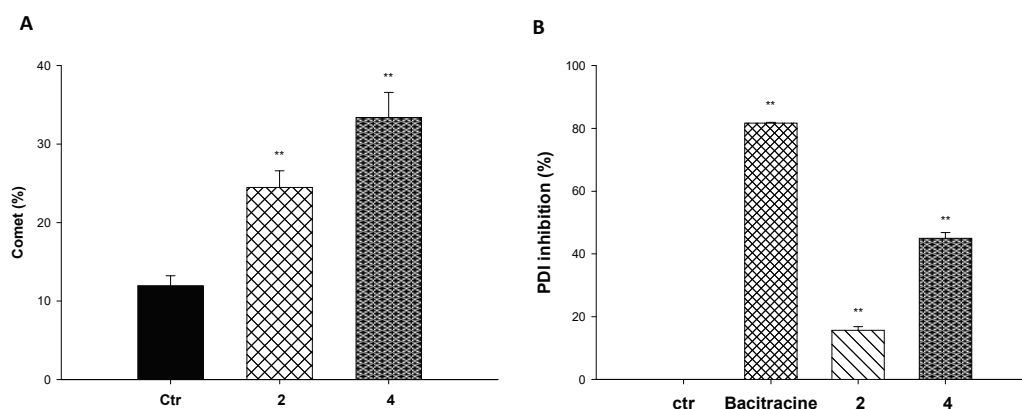
Figure 4. Mechanistic studies. (**A**) Comet assay: MDA-MDB-231 cells were treated for 3 h with 4 µM of tested compounds **2** and **4** or 200 µM of the reference drug chlorambucil. The relative percentage of comets (number of cells forming a comet/total number of cells) was detected in two randomly captured fields from two independent experiments. (**B**) PDI inhibition induced by tested compounds was measured by Proteostat PDI assay kit. The PDI inhibitor Bacitracine (0.5 mM) was used as a positive control. Error bars indicate S.D. ** $p < 0.01$ compared with control.

Transmission electron microscopy (TEM) studies were also performed to assess the eventual modification of cellular/subcellular morphological features induced by the tested complexes. Figure 5 reports the TEM images of the breast carcinoma cells MDA-MB-231 treated for 24 h with IC$_{50}$ concentrations of cisplatin or compounds **2** and **4**. Cells treated with compounds **2** and **4** showed a very different morphology with respect to the untreated cells and were characterized by a substantial enhancement of the mitochondrial dimensions (*swelling*) and a partial disruption of the cristae structures. Furthermore, an extensive increase in cytoplasmatic multivesicular bodies and in nuclear multilamellar bodies was detected. It is reported that the multivesicular bodies derive from activation of the lysosomes and, therefore, this suggests that the mechanism of action involves cytoplasmic acidic organelles.
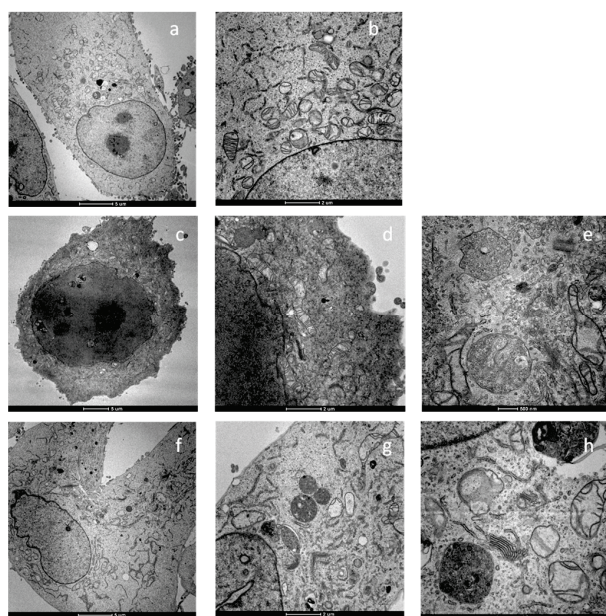
Figure 5. TEM analysis of MDA-MB-231 human breast cancer cells: (**a,b**) control cells; (**c–e**) cells treated for 24 h with IC$_{50}$ concentrations of **2**; (**f–h**) cells treated for 24 h with IC$_{50}$ concentrations of **4**.

2.5. Apoptosis and Morphological Studies

In order to assess the ability of the most representative complex **4** to induce cancer cell death by apoptosis, the Hoechst33258 assay was performed on human breast carcinoma cells MDA-MB-231. Cells were incubated with complex **4** at 3 µM for 24 and 48 h. Cells treated with derivative **4**, similar to cisplatin, presented brightly stained nuclei and morphological features typical of cells undergoing apoptosis, such as chromatin condensation and fragmentation (Figure 6) in a time-dependent manner. These results clearly indicate that the newly developed copper(II) complexes induced cancer-cell death by apoptosis.
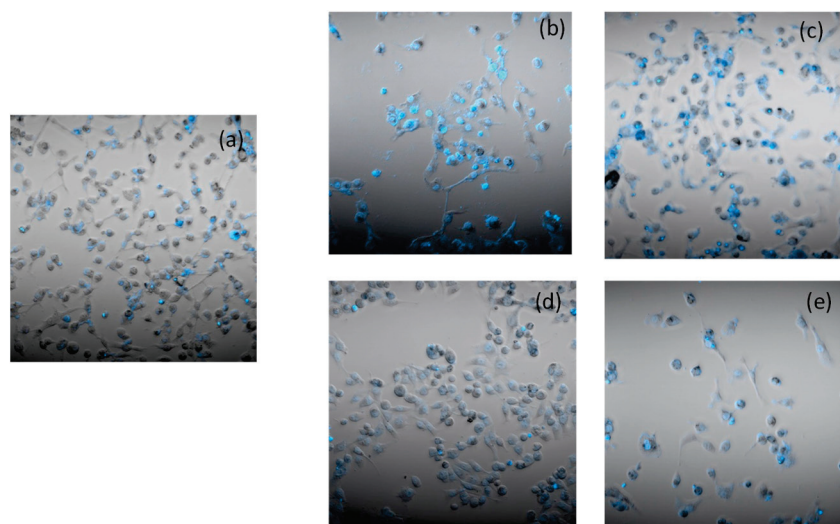
Figure 6. Hoechst staining of MDA-MB-231 cells: (**a**) control cells; cells incubated for 24 h (**b**) or 48 h (**c**) with IC$_{50}$ of cisplatin; cells incubated for 24 h (**d**) or 48 h (**e**) with IC$_{50}$ of **4**.

3. Experimental Part

3.1. Material and Methods

All reactants and reagents were purchased from commercial sources, in particular Sigma-Aldrich and Fluorochem. All solvents were used without further purification. Dafone [28], phendione [25] and [Cu(phen)(ONO$_2$)$_2$] [29] were synthesised as previously reported with minor modifications.

The description of the instruments and of the experiments to assess the purity of the samples via HPLC are described in previous papers [25,30–32].

3.1.1. Stability

The pH stability was examined over a pH range of 4–9 by preparing a 10 µM solution of each compound in H$_2$O and adjusting the pH using 0.01 mL of either NaOH 1 M or 0.1 M and HCl of the same in order to keep the volume consistent. When the desired pH was reached, the solution was allowed to stabilise for 10 min at 18 °C before it was then examined in a UV-Vis spectrometer at over a range of 200–600 nM. The stability at pH = 6 was assessed over a period of 1 week.

3.1.2. Ethidium Bromide Displacement Assay

EtBr displacement assays were performed in 10 mM phosphate buffer solution (pH 7.4) as described by Boger et al. [33] The binding values were calculated using the % relative decrease of fluorescence at 50% and the equation below.

$$E_{EB} \frac{[EtBr]}{[compound]50\%_{FI}} \tag{1}$$

3.1.3. Experiments with Cultured Human Cancer Cells

Tested compounds were dissolved in DMSO and added to the cell-growth medium to a final solvent concentration of 0.5%, which is well reported to not have cytotoxic effects on cell viability. Cisplatin (Sigma Chemical Co., St. Louis, MO, USA) was dissolved in a physiologic solution (0.9% sodium chloride).

3.1.4. Cell Cultures

Human colon (HCT-15), pancreatic (PSN-1), and breast (MDA-MB-231) carcinoma-cell lines were obtained from the American Type Culture Collection (ATCC, Rockville, MD). Human cervical carcinoma (A431) cells were kindly provided by Prof. F. Zunino (Division of Experimental Oncology B, Istituto Nazionale dei Tumori, Milan). Human ovarian carcinoma (2008) cells and their cisplatin-resistant counterpart (C13*) were kindly provided by Prof. G. Marverti (Dipartimento di Scienze Biomediche, Università di Modena University, Italy). Cell lines were cultured in RPMI-1640 or DMEM medium (Euroclone) added with 10% fetal calf serum (Euroclone, Milan, Italy), antibiotics (50 units per mL penicillin, and 50 µg mL^{-1} streptomycin), and 2 mM L-glutamine.

3.1.5. MTT Test

The growth inhibitory effect toward the tumour cell lines was evaluated by the MTT test as previously described [34].

3.1.6. Spheroid Cultures

Spheroid cultures were performed by seeding 2.5×10^3 PSN-1 cancer cells/well in spheroid-suitable tissue culture untreated 96-well plates (Greiner Bio-one, Kremsmünster, Austria) in RPMI-1640 cell culture medium without phenol red (Sigma Chemical Co., St. Louis, MO, USA) containing 10% fetal calf serum and supplemented with 20% methyl cellulose stock solution.

3.1.7. APH Assay

An established APH-modified assay was used to detect the cytotoxicity profile in 3D spheroids, as previously described. IC$_{50}$ values were calculated using a 4-PL model [35,36].

3.1.8. Copper Cellular Content

MDA-MB-231 cells (2.5×10^6) were seeded in 75 cm^2 flasks in a growth medium (20 mL). Following 24 h, cells were treated for 24 h with tested complexes and samples processed as previously described [27].

3.1.9. Comet Assay

About 3×10^4 MDA-MB-231 cells were seeded in 25 cm^2 flasks in a growth medium. After overnight incubation, cells were treated for 3 h with 2.5 µM of tested compounds and processed as previously described [27]. Pictures were captured with a Zeiss LSM-800 confocal microscope (Zeiss, Oberkochen, Germany). All photos were analyzed by the Zen 2.3 system (Zeiss, Oberkochen, Germany).

3.1.10. Protein Disulfide Isomerase (PDI) Activity

The reductase activity of PDI was assayed by measuring the PDI-catalysed reduction of insulin in the presence of increasing concentrations of the tested compounds by using the PROTEOSTAT PDI assay kit (Enzo Life Sciences, Lausen, Switzerland). Experiments were performed according to the manufacturer's instructions as previously described [27]. IC$_{50}$ values were calculated by the 4-PL model.

3.1.11. Transmission Electron Microscopy (TEM) Analyses

About 10^6 MDA-MB-231 cells were seeded in 24-well plates and, following overnight incubation, were treated with the tested compounds for 24 h. Then, cells were processed as

previously described [1]. Pictures were captured with a Hitachi H-600 electron microscope (Hitachi, Tokyo, Japan) operating at 75 kV. All photos were analyzed by using Corel Draw 11.

3.1.12. Cell Death Induction

MDA-MB-231 cells were seeded into 8-well tissue-culture slides (BD Falcon, Bedford, MA, USA) at 5×10^4 cells/well (0.8 cm^2). After overnight incubation, cells were treated with IC_{50} doses of the tested compound and processed as previously described [27].

3.1.13. Statistical Analysis

All values are the means $\pm$ SD of no less than three measurements starting from three different cell cultures. Multiple comparisons were made by ANOVA followed by the Tukey–Kramer multiple comparison test (* $p < 0.05$, ** $p < 0.01$), using GraphPad InStat software 3.10 (GraphPad Software, San Diego, CA, USA).

3.2. Synthesis and Characterisation

The ligands **A** and **B** were synthesised according to Scheme S1 in Supporting Information.

3.2.1. 1,10-Phenanthroline-5,6-dione (phendione)

The phendione was prepared using a previous method from our group [24]; 1,10-phenanthroline (2000 mg, 10 mmoles) and potassium bromide (2000 mg, 16.8 mmoles) were added to a round bottom flask containing an ice-cold mixture of H_2SO_4 (20 mL) and HNO_3 (10 mL). The solution was refluxed at 100 °C for 3 h and a dark-orange colour was observed. The solution was allowed to cool to room temperature, then slowly poured into deionised iced H_2O (200 mL). To this was added slowly a solution of NaOH (200 mL, 5 M) until a pH of ~6 was reached. The solution was then poured into a separation funnel and washed with $CHCl_3$ (2 × 50 mL). The organic phase was dried using anhydrous sodium sulphate. The solution was then filtered and reduced in vacuo. A yellow solid was recovered. The crude yellow solid was purified via recrystallization from MeOH to give yellow needles (162 mg, 77%). ^{1}H NMR (500 MHz, CDCl$_3$) δ 9.11 (dd, 2H), 8.49 (dd, 2H), 7.58 (dd, J = 7.9, 4.7 Hz, 2H). ^{13}C NMR (126 MHz, CDCl$_3$) δ 178.8, 156.5, 153.0, 137.4, 128.2, 125.7. Elemental Analysis: $C_{12}H_6N_2O$% Calculated C 68.57, H 2.88, N 13.51, % Found: C 67.97, H 3.07, N 13.14 HR-MS (+): m/z Calculated for $C_{12}H_6N_2O$ + [H$^+$] 211.0508, Found 211.0507.

3.2.2. Dafone (4,5-Diazafluoren-9-one)

Dafone was synthesised as reported in the literature with modifications [28]; 1,10-phenanthroline (1000 mg, 5.54 mmoles) and KOH (1010 g, 18.1 mmoles) were refluxed into H_2O (60 mL). In a separate flask KMnO$_4$ (2540 mg, 16.01 mmoles) was dissolved in warm H_2O (35 mL, 85 °C). The KMnO$_4$ was then added dropwise with stirring over the course of 3.5 h. It was kept at 85 °C for the duration of the addition. After the final addition, the stirring was allowed to continue for 1 h. The brown solution was gravity filtered while hot and the brown solid was washed extensively with H_2O. The orange filtrate was allowed to cool to room temperature and then extracted with $CHCl_3$ (3 × 150 mL). The organic layers were combined and washed with brine (100 mL), then dried over Na_2SO_4 anhydrous. The solvent was removed under reduced pressure to yield the crude yellow/orange solid. The crude product was purified via recrystallization from acetone to give needles (450 mg, 45%). ^{1}H NMR (500 MHz, CDCl$_3$) δ 8.80 (ddd, J = 5.0, 1.5, 1.0, 2H), 7.99 (ddd, J = 7.5, 1.5, 1.1, 2H), 7.35 (ddd, J = 7.5, 5.0, 0.8, 2H). ^{13}C NMR (126 MHz, CDCl$_3$) δ 189.7, 163.5, 155.3, 131.6, 129.4, 124.8. Elemental Analysis: $C_{11}H_6N_2O$ % Calculated: C 72.52, H 3.32, N 15.38. % Found: C 73.06, H 3.83, N 15.94. HR-MS (+): m/z Calculated for $C_{11}H_6N_2O$ + [H$^+$] 183.0482, Found 183.0561.

3.2.3. Biotin Methyl Ester (**1**)

The synthesis of biotin methyl ester was performed according to a modified protocol previously reported [37]. Biotin (300 mg, 1.23 mmoles) was suspended in dry MeOH (3 mL) and placed under N$_2$. Following this, the system was flushed entirely with N$_2$. SOCl$_2$ (0.3 mL,

4 mmoles) was then added dropwise via cannula. The solution was allowed to stir overnight at room temperature. A clear golden solution was observed. The excess $SOCl_2$ and MeOH were removed under reduced pressure. The flask was cooled in an ice bath for an hour and a crystalline solid was obtained. The white solid was taken up in $CHCl_3$ (25 mL) and washed with $NaHCO_3$ (2 × 30 mL) and then with brine (25 mL). The organic layer was dried over Na_2SO_4 (anhydrous) and the solvent was removed under reduced pressure to yield the title compound as a white solid (269 mg, 85%). ^{1}H NMR (500 MHz, DMSO-d_6) δ 6.46 (s, 1H), 6.38 (s, 1H), 4.30 (dd, J = 7.5, 5.3, 1H), 4.13 (m, 1H), 3.57 (s, 3H, O-CH_3), 3.09 (m, 1H), 2.81 (dd, J = 12.4, 5.1, 1H), 2.56 (t, J = 13.4, 1H), 2.29 (m, 2H), 1.53 (m, 4H), 1.27 (m, 2H). ^{13}C NMR (126 MHz, DMSO-d_6) δ 173.3162.7, 61.1, 59.3, 55.4, 51.2, 48.6, 33.1, 28.1, 28.0, 24.5. Elemental Analysis: $C_{11}H_{18}N_2O_3S$ % Calculated: C 51.14, H 7.02, N 10.84% Found: C 50.86, H 6.77, N 10.56.

3.2.4. Biotin Hydrazide (**2**)

Biotin-hydrazide was synthesised as reported in the literature with slight modification [38]. Biotin methyl ester (200 mg, 0.77 mmoles) was suspended in dry MeOH (10 mL) and placed under N_2. Hydrazine hydrate (210 mg, 6.77 mmoles) was added dropwise via cannula to the suspension of biotin methyl ester. The solution was warmed to 50 °C until a clear solution was observed (10–12 min). The solution was allowed to stir for 24 h at room temperature and a white precipitate was observed. The MeOH was removed under reduced pressure to yield a white solid. The crude product was taken up in warm H_2O (40 mL) and the aqueous layer was washed with $CHCl_3$ (3 × 30 mL). The aqueous layers were combined, and the H_2O was removed under reduced pressure to yield a white solid (184 mg, 92%). R_f 0.72 (DCM: MeOH 90:10). ^{1}H NMR (500 MHz, DMSO-d_6) δ = 8.93 (s, 1H, *N-H*), 6.44 (s, 1H), 6.37 (s, 1H), 4.30 (dd, 1H), 4.19 (s, 2H, N-H_2), 4.12 (m, 1H), 3.09 (m, 1H), 2.82 (dd, J = 12.4, 5.1, 1H), 2.61 (m, 1H), 2.00 (m, 2H), 1.43 (m, 6H). ^{13}C NMR (126 MHz, DMSO-d_6) δ = 175.6, 165.3, 62.0, 60.2, 55.2, 39.6, 33.3, 27.7, 27.5, 24.8. Elemental Analysis: $C_{10}H_{18}N_4O_2S$ % Calculated: C 46.49, H 7.02, N 21.69% Found: C 46.19, H 7.16, N 20.46. HR-MS (+): m/z Calculated for $C_{10}H_{18}N_4O_2S$ + [Na$^+$] 281.1047, Found 281.1049.

3.2.5. Biotin-Dafone (**A**)

Biotin hydrazide (138 mg, 0.537 mmoles), dafone (98 mg, 0.537 mmoles), and *p*-TSA (*p*-Toluenesulfonic acid 10% mol) were suspended in EtOH (20 mL). The solution was refluxed until a clear solution was observed (1–1.5 h). The solution was then allowed to stir for 24 h at room temperature. A white precipitate was observed. The white solid was collected via Buchner filtration, washed with $CHCl_3$ (2 × 30 mL) and dried under a high vacuum. No further purification was required (112 mg, 54%). ^{1}H NMR (500 MHz, DMSO-d_6) δ 11.38 (s, 1H, *H*-N-N), 8.73 (dd, J = 11.9, 7.0, 3H, Ar-H), 8.22 (s, 1H, Ar-H), 7.51 (m, 2H, Ar-H), 6.47 (d, J = 4.7, 1H, C=O-N-*H*), 6.38 (d, J = 5.2, 1H, C=O-N-*H*), 4.32 (d, J = 4.4, 1H, NC*H*), 4.12 (m, 2H, S-CH_2), 3.17 (m, 2H, SC*H* & NC*H*), 2.83 (d, broad, J = 5.0, 2H, C=O-CH_2), 1.78–1.28 (m, 6H, 3 × CH_2). ^{13}C NMR (126 MHz, DMSO-d_6) δ 162.7, 158.4, 156.7, 151.3, 140.4, 134.5, 132.4, 129.0, 124.3, 123.5, 89.8, 87.7, 61.1, 59.2, 55.4, 48.6, 40.4 (under DMSO, DEPT—135), 28.3, 28.1, 24.5, 16.9. Elemental Analysis: $C_{21}H_{22}N_6O_2S$% Calculated: C 59.70, H 5.25, N 19.89, % Found: C 59.06, H 5.16, N 19.46. HR-MS (+): m/z Calculated for $C_{21}H_{22}N_6O_2S$ + [Na$^+$] 445.1423, Found 445.1390.

3.2.6. Biotin-Phen (**B**)

Biotin hydrazide (245 mg, 0.948 mmol) was suspended in warm EtOH (20 mL, 50 °C). In a separate flask, phendione (200 mg, 0.948 mmol) was dissolved in warm EtOH (20 mL, 50 °C). The phendione was then added dropwise while stirring to the biotin hydrazine over the course of 45 min. A yellow mixture was observed. *P*-TSA (10% mol) was added and after 20 min the solution turned a clear-yellow colour. The solution was allowed to reflux for 12 h and then allowed to cool to room temperature. The EtOH was reduced under vacuum to 25% volume and the flask was placed in the fridge overnight. A

bright-yellow precipitate was observed. The yellow solid was taken up in $CHCl_3$ (20 mL), washed with brine (2 × 30 mL), and dried over Na_2SO_4. The excess $CHCl_3$ was removed under reduced pressure to yield a bright-yellow solid. The crude product was purified via silica-gel chromatography (95:5) DCM/MeOH (360 mg, 85%). R_f 0.88. ^{1}H NMR (500 MHz, DMSO-d_6) δ = 13.97 (s, 1H, N-H), 9.08 (dd, J = 4.5, 1.8, 1H, Ar-H), 8.86 (dd, J = 4.5, 1.7, 1H, Ar-H), 8.55 (m, J = 8.0, 1.7, 2H, Ar-H), 7.73 (dd, 1H, Ar-H), 7.64 (dd, J = 8.1, 4.5, 1H, Ar-H). 6.48 (s, 1H, CN-H), 6.37 (s, 1H, CN-H), 4.31 (dd, J = 7.6, 5.2, 1H, CH), 4.15 (m, 1H, CH), 3.14 (m, 2H, SCH_2), 2.83 (m, 2H, amide CH_2), 2.60 (m, 1H, SC-H), 1.71–1.52 (m, 6H, 3× CH_2). ^{13}C NMR (126 MHz, DMSO-d_6) δ = 180.8, 162.7, 155.5, 152.2, 150.6, 146.2, 135.7, 131.5, 131.4, 130.8, 128.4, 127.4, 125.0, 124.0, 79.2, 61.0, 59.2, 55.4, 54.9, 40.1 (under DMSO dept—135), 28.1, 24.1. Elemental Analysis: $C_{22}H_{22}N_6O_3S$% Calculated: C 58.65, H 4.92, N 18.65, % Found: C 58.40, H 5.11, N 18.22. HRMS (ESI +): m/z Calculated for $C_{22}H_{22}N_6O_3S$ + [Na^+] 473.1372, Found 473.1366.

3.2.7. [Cu(phen)(ONO$_2$)$_2$]

[Cu(phen)(ONO$_2$)$_2$] was synthesised as reported in the literature with slight modification [28]; 1,10-Phenanthroline (250 mg, 1.38 mmoles) was dissolved in methanol (30 mL). To this was added Copper (II) nitrate trihydrate (366 mg, 1.51 mmoles) dissolved in MeOH (5 mL). The solution was refluxed for 2 h at 80 °C. A bright-blue colour was observed. The solution was allowed to cool to room temperature. Et$_2$O (20 mL) was added while stirring continued. A blue precipitate was observed. The precipitate was collected via vacuum filtration and washed with Et$_2$O (20 mL). The blue solid was purified via recrystallization from MeOH to give bright-blue needles (225 mg, 44%). Elemental Analysis $C_{12}H_8CuN_4O_6$ + H_2O% Calculated: C 37.36, H 2.61, N 14.52, % Found: C 37.81, H 2.96, N 14.21.

3.2.8. [Cu(dafone-biotin)Cl$_2$] (**1**)

A (153 mg, 0.363 mmol) was suspended in refluxing MeOH (40 mL). CuCl$_2$.2H$_2$O (68 mg, 0.398 mmol) was added dropwise while stirring. A green suspension was observed and after 5–6 min a clear solution was observed. The solution was allowed to reflux for another 4 h at which stage a fine-green precipitate was formed. The solution was allowed to stir for a further 3 h and then was cooled at r.t. and the green solid was collected via Buchner filtration and washed with cold MeOH (98 mg, 49%). Elemental Analysis: $C_{21}H_{22}Cl_2CuN_6O_2S$% Calculated: C 45.29, H 3.98, N 15.09, % Found: C 45.88, H 3.48, N 14.80. IR (ATR): 3335, 2922, 1655, 1610, 1481, 1086, 741. cm^{-1}. HPLC (RP): CH$_3$CN: H$_2$O (80:20) RT 2.17 min 100%. HR-MS (+): m/z Calculated for $C_{21}H_{22}Cl_2CuN_6O_2S$ [M]$^+$ 555.0230, Found 555.0021.

3.2.9. [Cu(phendione-biotin)Cl$_2$] (**2**)

B (246 mg, 0.546 mmol) was suspended in MeOH (30 mL) and warmed to 50 °C and a solution of CuCl$_2$.2H$_2$O (111 mg, 0.655 mmol) in MeOH was added dropwise. The solution was refluxed. After 10–15 min a clear-green solution was observed for a brief few moments before a green precipitate began to form. The reflux was allowed to continue for a further 4 h before allowing the solution to cool to room temperature. The fine-green precipitate was collected via Buchner filtration and washed very gently with CHCl$_3$ (10 mL) to dispel any unreacted ligand. No further purification was required (148 mg, 47%). Elemental Analysis: $C_{22}H_{22}Cl_2CuN_6O_3S$% Calculated: C 45.17, H 3.79, N 14.37, % Found: C 45.78, H 3.91, N 14.76. IR (ATR): 3341, 2907, 1650, 1608, 1480, 1078, 741. cm^{-1}. HPLC (RP): CH$_3$CN: H$_2$O (80:20) RT 1.97 min 100%. HR-MS (+): m/z Calculated for $C_{22}H_{22}CuN_6O_2S$ [M$^+$] 583.0147, Found 584.0004.

3.2.10. [Cu(phen)(dafone-biotin)](NO$_3$)$_2$ (**3**)

One (104 mg, 0.180 mmol) was dissolved in anhydrous DMF (20 mL). AgNO$_3$ (61 mg, 0.36mmol) dissolved in anhydrous DMF (3 mL) was added to the solution containing [Cu(dafone-biotin)Cl$_2$] (**1**) and the solution was allowed to stir at r.t and in darkness for 4 h. An extremely

fine white precipitate was observed. The white precipitate was filtered off and 2 drops of HCl (1M) were added to the filtrate to examine for excess Ag. The filtrate was filtered a second time and the clear-green filtrate was placed back into a round bottom and protected from light. To this was added solid 1,10-phenanthroline (35 mg, 0.0180 mmol). Immediately a deep-green solution was observed. The solution was allowed to stir overnight at r.t.; the DMF was reduced in vacuo and the resulting solution precipitated into excess Et_2O. A light-green solid was observed. This solid was filtered and washed with $CHCl_3$ (20 mL) and dried under a high vacuum (108 mg, 74%). HPLC (RP): CH_3CN: H_2O (80:20) RT 3.34 min 97% 3.85 min 3%. Elemental Analysis: $C_{33}H_{30}CuN_{10}O_8S$ % Calculated: C 50.16, H 3.83, N 17.72. % Found: C 49.72, H 3.50, N 17.28.

3.2.11. [Cu(phen)(phendione-biotin)](NO₃)₂ (4)

B (73 mg, 0.162 mmol) was dissolved in DMF (15 mL); in a separate flask [Cu(phen)(ONO$_2$)$_2$] (66 mg, 0.162 mmol) was dissolved in DMF (5 mL). The copper(II) solution was then added dropwise with stirring to the solution of biotin-phen **B**. A green colour was observed. The solution was allowed to stir for 24 h at 40 °C after which a brown colour was observed. The solution was allowed to cool to room temperature and diethyl—ether (30 mL) was added. A pale precipitate was observed. The brown solid was filtered off and the filtrate was concentrated in vacuo. The remaining green concentrate was precipitated into excess Et_2O and the pale-green solid was collected. The solution was spun in the centrifuge for 10 min at 4000 rpm and a dark-green pellet was recovered. The pellet was washed gently with $CHCl_3$ (82 mg, 67%). Elemental Analysis: $C_{34}H_{30}CuN_8O_9S$% Calculated: C 49.91, H 3.70, N 17.12,% Found: C 49.42, H 3.46, N 16.82. IR (ATR): 3058, 1647,1518, 1361, 1298, 1033, 846, 718. cm^{-1}. HPLC (RP): CH_3CN: H_2O (80:20) RT, 3.23 min, 100%. HR-MS (+): m/z Calculated for $C_{34}H_{30}CuN_6O_3S$ [M-2(NO$_3$)]$^+$ 693.1442, Found 693.1444.

4. Conclusions

In this research article, we have described the synthesis and the chemical characterisation of four novel copper(II) complexes functionalised with phenanthroline derivatives containing biotin. Biotin (Vitamin B7) plays a major role in many metabolic pathways and its receptors are overexpressed in many different cancer cell types. Two of the final complexes (**1** and **2**) contain two chlorides while the other two complexes (**3** and **4**) contain a phenanthroline ligand at the completion of the coordination sphere. The complexes were found stable in physiological conditions and over the pH range of 4–9. A detailed biological screening revealed that the four complexes possess strong anticancer properties against five different cancer cells, being also effective in overpassing cisplatin resistance in C13* ovarian cancer cells. The most promising complexes **2** and **4** showed strong activity also in 3D pancreatic cancer-cell cultures. The complexes are intracellularly uptaken probably by passive diffusion, as complexes **3** and **4** containing an extra phenanthroline moiety characterized by superior lipophilicity showed the highest internalisation profiles. Mechanistically, the principal molecular targets seem to be the protein disulphide isomerase (PDI) together with the nuclear DNA (electrostatic interaction rather than covalent DNA adducts). Morphological studies of the most promising complex 4 on SMVT overexpressing human breast carcinoma cells MDA-MB-231 indicate that the newly developed copper(II) complex elicited cell death by means of apoptosis. Unfortunately, the cellular-uptake studies do not clarify if biotin is playing the role of a targeting vector, but the lower cytotoxicity shown in normal cells with respect to the tumour cells is important to pursue for research in this field. Further biotinylating strategies will be taken into account in the development of novel biotin-functionalised metal complexes.

Supplementary Materials: The following supporting information can be downloaded at: https://www.mdpi.com/article/10.3390/molecules28104112/s1, Synthetic Schemes, NMR Spectra, HPLC Chromatograms, ESI-MS, UV-pH dependance and further biological assays.

References

1. Yu, C.; Wang, Z.; Sun, Z.; Zhang, L.; Zhang, W.; Xu, Y.; Zhang, J.-J. Platinum-Based Combination Therapy: Molecular Rationale, Current Clinical Uses, and Future Perspectives. *J. Med. Chem.* **2020**, *63*, 13397–13412. [CrossRef] [PubMed]
2. Wheate, N.J.; Walker, S.S.; Craig, E.G.; Oun, R. The status of platinum anticancer drugs in the clinic and in clinical trials. *Dalton Trans.* **2010**, *39*, 8113–8127. [CrossRef] [PubMed]
3. Johnstone, T.C.; Suntharalingam, K.; Lippard, S.J. The Next Generation of Platinum Drugs: Targeted Pt(II) Agents, Nanoparticle Delivery, and Pt(IV) Prodrugs. *Chem. Rev.* **2016**, *116*, 3436–3486. [CrossRef] [PubMed]
4. Klein, A.V.; Hambley, T.W. Platinum Drug Distribution in Cancer Cells and Tumors. *Chem. Rev.* **2009**, *109*, 4911–4920. [CrossRef] [PubMed]
5. Wang, K.; Zhu, C.; He, Y.; Zhang, Z.; Zhou, W.; Muhammad, N.; Guo, Y.; Wang, X.; Guo, Z. Restraining Cancer Cells by Dual Metabolic Inhibition with a Mitochondrion-Targeted Platinum(II) Complex. *Angew. Chem. Int. Ed.* **2019**, *58*, 4638–4643. [CrossRef]
6. Huang, K.-B.; Wang, F.-Y.; Feng, H.-W.; Luo, H.; Long, Y.; Zou, T.; Chan, A.S.C.; Liu, R.; Zou, H.; Chen, Z.F.; et al. An aminophosphonate ester ligand-containing platinum(ii) complex induces potent immunogenic cell death in vitro and elicits effective anti-tumour immune responses in vivo. *Chem. Commun.* **2019**, *55*, 13066–13069. [CrossRef]
7. Harper, B.W.; Krause-Heuer, A.M.; Grant, M.P.; Manohar, M.; Garbutcheon-Singh, K.B.; Aldrich-Wright, J.R. Advances in Platinum Chemotherapeutics. *Chem. Eur. J.* **2010**, *16*, 7064–7077. [CrossRef] [PubMed]
8. Santini, C.; Pellei, M.; Gandin, V.; Porchia, M.; Tisato, F.; Marzano, C. Advances in copper complexes as anticancer agents. *Chem. Rev.* **2014**, *114*, 815–862. [CrossRef] [PubMed]
9. Maiti, S.; Paira, P. Biotin conjugated organic molecules and proteins for cancer therapy: A review. *Eur. J. Med. Chem.* **2018**, *45*, 206–223. [CrossRef]
10. Russell-Jones, G.; McTavish, K.; McEwan, J.; Rice, J.; Nowotnik, D. Vitamin-mediated targeting as a potential mechanism to increase drug uptake by tumours. *J. Inorg. Biochem.* **2004**, *98*, 1625–1633. [CrossRef]
11. Lo, K.K.-W.; Hiu, W.-K.; Chung, C.-K.; Tsang, K.H.-K.; Lee, T.K.-M.; Ng, D.C.-M. Luminescent Transition Metal Polypyridine Biotin Complexes. *J. Chin. Chem. Soc.* **2006**, *53*, 53–65. [CrossRef]
12. Zhao, J.; Hua, W.; Xu, G.; Gou, S. Biotinylated platinum(IV) complexes designed to target cancer cells. *J. Inorg. Biochem.* **2017**, *176*, 175–180. [CrossRef] [PubMed]
13. Hu, W.; Fang, L.; Hua, W.; Gou, S. Biotin-Pt (IV)-indomethacin hybrid: A targeting anticancer prodrug providing enhanced cancer cellular uptake and reversing cisplatin resistance. *J. Inorg. Biochem.* **2017**, *175*, 47–57. [CrossRef] [PubMed]
14. Muhammad, N.; Sadia, N.; Zhu, C.; Luo, C.; Guo, Z.; Wang, X. Biotin-tagged platinum(iv) complexes as targeted cytostatic agents against breast cancer cells. *Chem. Commun.* **2017**, *53*, 9971–9974. [CrossRef] [PubMed]
15. Han, W.; He, W.; Song, Y.; Zhao, J.; Song, Z.; Shan, Y.; Hua, W.; Sun, Y. Multifunctional platinum(iv) complex bearing HDAC inhibitor and biotin moiety exhibits prominent cytotoxicity and tumor-targeting ability. *Dalton Trans.* **2022**, *51*, 7343–7351. [CrossRef] [PubMed]
16. Upadhyay, A.; Gautam, S.; Ramu, V.; Kondaiah, P.; Chakravarty, A.R. Photocytotoxic cancer cell-targeting platinum(II) complexes of glucose-appended curcumin and biotinylated 1,10-phenanthroline. *Dalton Trans.* **2019**, *48*, 17556–17565. [CrossRef] [PubMed]
17. Marloye, M.; Inam, H.; Moore, C.J.; Debaille, V.; Pritchard, J.R.; Gelbcke, M.; Meyer, F.; Dufrasne, F.; Berger, G. Synthesis, structure and anticancer properties of new biotin- and morpholine-functionalized ruthenium and osmium half-sandwich complexes. *J. Biolog. Inorg. Chem.* **2021**, *26*, 535–549. [CrossRef]
18. Zhang, K.Y.; Lo, K.K.-W. Synthesis, Properties, and Live-Cell Imaging Studies of Luminescent Cyclometalated Iridium(III) Polypyridine Complexes Containing Two or Three Biotin Pendants. *Inorg. Chem.* **2009**, *48*, 6011–6025. [CrossRef]

19. Leung, C.-H.; Zhong, H.-J.; Chan, D.S.-H.; Ma, D.-L. Bioactive iridium and rhodium complexes as therapeutic agents. *Coord. Chem. Rev.* **2013**, *257*, 1764–1776. [CrossRef]

20. Kallus, S.; Uhlik, L.; Van Schoonhoven, S.; Pelivan, K.; Berger, W.; Enyedy, E.A.; Hofman, T.; Heffeter, P.; Kowol, C.R.; Keppler, B.K. Synthesis and biological evaluation of biotin-conjugated anticancer thiosemicarbazones and their iron(III) and copper(II) complexes. *J. Inorg. Biochem.* **2019**, *190*, 85–97. [CrossRef]

21. Graham, D.R.; Marshall, L.E.; Reich, K.A.; Sigman, D.S. Cleavage of DNA by coordination complexes. Superoxide formation in the oxidation of 1,10-phenanthroline-cuprous complexes by oxygen—Relevance to DNA-cleavage reaction. *J. Am. Chem. Soc.* **1980**, *102*, 5419–5542. Available online: https://pubs.acs.org/doi/pdf/10.1021/ja00536a063 (accessed on 1 July 1980). [CrossRef]

22. Musib, D.; Upadhyay, A.; Pal, M.; Kausar Raza, M.D.; Saha, I.; Kunwar, A.; Roy, M. Red light-activable biotinylated copper(II) complex-functionalized gold nanocomposite (Biotin-Cu@AuNP) towards targeted photodynamic therapy. *J. Inorg. Biochem.* **2023**, *243*, 112183. [CrossRef] [PubMed]

23. Ng, N.S.; Laverett, P.; Hibbs, D.E.; Yang, Q.; Bulanadi, J.C.; Wu, M.J.; Aldrich-Wright, J.R. The antimicrobial properties of some copper(ii) and platinum(ii) 1,10-phenanthroline complexes. *Dalton Trans.* **2013**, *42*, 3196–3209. [CrossRef]

24. Vadlapudi, A.D.; Vadlapatla, R.K.; Mitra, A.K. Sodium Dependent Multivitamin Transporter (SMVT): A Potential Target for Drug Delivery. *Curr. Drug Targets* **2012**, *13*, 994–1003. [CrossRef] [PubMed]

25. Barrett, S.; De Franco, M.; Kellett, A.; Dempsey, E.; Marzano, C.; Erxleben, A.; Gandin, V.; Montagner, D. Anticancer activity, DNA binding and cell mechanistic studies of estrogen-functionalised Cu(II) complexes. *J. Biol. Inorg. Chem.* **2020**, *25*, 49–60. [CrossRef] [PubMed]

26. Molphy, Z.; McKee, V.; Kellett, A. Copper bis-Dipyridoquinoxaline Is a Potent DNA Intercalator that Induces Superoxide-Mediated Cleavage via the Minor Groove. *Molecules* **2019**, *24*, 4301. [CrossRef]

27. Pellei, M.; Santini, C.; Bagnarelli, L.; Battocchio, C.; Lucci, G.; Venditti, I.; Meneghini, C.; Amatori, S.; Sgarbossa, P.; Marzano, C.; et al. Exploring the Antitumor Potential of Copper Complexes Based on Ester Derivatives of Bis(pyrazol-1-yl)acetate Ligands. *Int. J. Mol. Sci.* **2022**, *23*, 9397. [CrossRef]

28. Menon, S.; Rajasekharan, M.V. Bis chelate Cu(II) complexes of dafone—Synthesis, structural, EPR and optical spectral studies. *Polyhedron* **1998**, *17*, 2463–2476. [CrossRef]

29. Molphy, Z.; Prisecaru, A.; Slator, C.; Barron, N.; McCann, M.; Colleran, J.; Chandran, D.; Gathergood, N.; Kellett, A. Copper Phenanthrene Oxidative Chemical Nucleases. *Inorg. Chem.* **2014**, *53*, 5392–5404. [CrossRef]

30. Barrett, S.; Delaney, S.; Kavanagh, K.; Montagner, D. Evaluation of in vitro and in vivo antibacterial activity of novel Cu(II)-steroid complexes. *Inorg. Chim. Acta* **2018**, *479*, 261–265. [CrossRef]

31. Moynihan, E.; Bassi, G.; Ruffini, A.; Panseri, S.; Montesi, M.; Velasco-Torrijos, T.; Montagner, D. Click Pt(IV)-Carbohydrates Pro-Drugs for Treatment of Osteosarcoma. *Front. Chem.* **2021**, *9*, 795997. [CrossRef] [PubMed]

32. Moynihan, E.; Panseri, S.; Bassi, G.; Rossi, A.; Campodoni, E.; Dempsey, E.; Montesi, M.; Velasco-Torrijos, T.; Montagner, D. Development of Novel Pt(IV)-Carbohydrate Derivatives as Targeted Anticancer Agents against Osteosarcoma. *Int. J. Mol. Sci.* **2023**, *24*, 6028. [CrossRef] [PubMed]

33. Boger, D.L.; Fink, B.E.; Brunette, S.R.; Tse, W.C.; Hedrick, M.P. A simple, high-resolution method for establishing DNA binding affinity and sequence selectivity. *J. Am. Chem. Soc.* **2001**, *123*, 5878–5891. [CrossRef] [PubMed]

34. Dall'Acqua, S.; Peron, G.; Ferrari, S.; Gandin, V.; Bramucci, M.; Quassinti, L.; Mártonfi, P.; Maggi, F. Phytochemical investigations and antiproliferative secondary metabolites from Thymus alternans growing in Slovakia. *Pharm. Biol.* **2017**, *55*, 1162–1170. [CrossRef] [PubMed]

35. Harper, B.W.J.; Petruzzella, E.; Sirota, R.; Faccioli, F.F.; Aldrich-Wright, J.R.; Gandin, V.; Gibson, D. Synthesis, characterization and in vitro and in vivo anticancer activity of Pt(iv) derivatives of [Pt(1S,2S-DACH)(5,6-dimethyl-1,10-phenanthroline)]. *Dalton Trans.* **2017**, *30*, 7005–7019. [CrossRef]

36. Doboszewski, B.; Groaz, E.; Herdewijn, P. Synthesis of phosphonoglycine backbone units for the development of phosphono peptide nucleic acids. *Eur. J. Org. Chem.* **2013**, *22*, 4804–4815. [CrossRef]

37. Sittiwong, W.; Cordonier, E.L.; Zampleni, J.; Dussault, P.H. β-Keto and β-hydroxyphosphonate analogs of biotin-5'-AMP are inhibitors of holocarboxylase synthetase. *Bioorg. Med. Chem. Lett.* **2014**, *24*, 5568–5571. [CrossRef]

38. Murar, C.E.; Thuaud, F.; Bode, J.W. KAHA Ligations That Form Aspartyl Aldehyde Residues as Synthetic Handles for Protein Modification and Purification. *J. Am. Chem. Soc.* **2014**, *136*, 18140–18148. [CrossRef] [PubMed]

Screening of Specific and Common Pathways in Breast Cancer Cell Lines MCF-7 and MDA-MB-231 Treated with Chlorophyllides Composites

Keng-Shiang Huang [1] [ID], **Yi-Ting Wang** [2] [ID], **Omkar Byadgi** [3] [ID], **Ting-Yu Huang** [2], **Mi-Hsueh Tai** [2], **Jei-Fu Shaw** [2,*] [ID] **and Chih-Hui Yang** [2,4,5,*] [ID]

[1] The School of Chinese Medicine for Post-Baccalaureate, I-Shou University, No. 8, Yida Rd., Jiaosu Village Yanchao District, Kaohsiung City 82445, Taiwan; huangks@isu.edu.tw
[2] Department of Biological Science and Technology, I-Shou University, No. 8, Yida Rd., Jiaosu Village Yanchao District, Kaohsiung City 82445, Taiwan; teengina1220@isu.edu.tw (Y.-T.W.); z09170707@isu.edu.tw (T.-Y.H.); mihsueh@isu.edu.tw (M.-H.T.)
[3] International College, International Program in Ornamental Fish Technology and Aquatic Animal Health, National Pingtung University of Science and Technology, No. 1, Shuefu Road, Neipu, Pingtung 91201, Taiwan; omkarcof1@gmail.com
[4] Pharmacy Department, E-Da Hospital, No. 1, Yida Rd., Jiaosu Village Yanchao District, Kaohsiung City 82445, Taiwan
[5] Taiwan Instrument Research Institute, National Applied Research Laboratories, Taipei City 106214, Taiwan
*   Correspondence: shawjf@isu.edu.tw (J.-F.S.); chyang@isu.edu.tw (C.-H.Y.); Tel.: +886-7-6151100 (ext. 7310) (J.-F.S.); +886-7-6151100 (ext. 7312) (C.-H.Y.); Fax: +886-7-6151959 (J.-F.S. & C.-H.Y.)

Abstract: Our previous findings have shown that the chlorophyllides composites have anticancer activities to breast cancer cell lines (MCF-7 and MDA-MB-231). In the present study, microarray gene expression profiling was utilized to investigate the chlorophyllides anticancer mechanism on the breast cancer cells lines. Results showed that chlorophyllides composites induced upregulation of 43 and 56 differentially expressed genes (DEG) in MCF-7 and MDA-MB-231 cells, respectively. In both cell lines, chlorophyllides composites modulated the expression of annexin A4 (ANXA4), chemokine C-C motif receptor 1 (CCR1), stromal interaction molecule 2 (STIM2), ethanolamine kinase 1 (ETNK1) and member of RAS oncogene family (RAP2B). Further, the KEGG annotation revealed that chlorophyllides composites modulated DEGs that are associated with the endocrine system in MCF-7 cells and with the nervous system in MDA-MB-231 cells, respectively. The expression levels of 9 genes were validated by quantitative reverse transcription PCR (RT-qPCR). The expression of CCR1, STIM2, ETNK1, MAGI1 and TOP2A were upregulated in both chlorophyllides composites treated-MCF-7 and MDA-MB-231 cells. The different expression of NLRC5, SLC7A7 and PKN1 provided valuable information for future investigation and development of novel cancer therapy.

Keywords: chlorophyllides; microarray-based detection; breast cancer; MCF-7; MDA-MB-231

1. Introduction

Breast cancer is the second most likely cause of cancer-related mortality in women [1–3]. It is evident that molecular alterations or epigenetic modifications in cancerous cells leads to the formation of the malignancies [4]. Clinical classifications of breast cancers were based on the status of estrogen receptor (ER), progesterone receptor (PR) and human epidermal growth receptor 2 (HER2) [5]. Generally, MCF-7 includes ER-positive and PR-positive breast cancer cell lines [6]. MDA-MB-231 cells are triple-negative breast cancer (TNBC), which are negative for ER, PR and HER2. Morphologically, MCF-7 and MDA-MB-231 cells are both epithelial cells that are derived from mammary gland carcinoma cells. Histologically, MCF-7 is a luminal type of breast cancer, while MDA-MB-231 is a basal type.

MCF-7 cells were effectively treated with drugs, such as tamoxifen paclitaxel, docetaxel or doxorubicin. MDA-MB-231 cells (TNBC) are found to be aggressive, prone to relapse, have high metastasis rate and poor prognosis and are insensitive to treatment [7–11].

Current treatment for breast cancer is a multi-strategy approach, including chemotherapy, surgery, radiotherapy and endocrine therapy [5,12,13]. Treatment for breast cancer (stages I-III) includes surgery and radiation therapy, with chemotherapy or other drug therapies administered before (neoadjuvant) or after (adjuvant) surgery. Chemotherapy is used mainly for downstaging, shrinking of tumors or to determine the response to therapy during early-stage breast cancer and to locally advanced breast cancer [14]. Cancer can be removed by surgery, including lumpectomy and then by whole-breast irradiation or mastectomy [15]. Whole breast irradiation is relatively acceptable, but it has inevitable acute and delayed toxic effects [16,17]. Systemic chemotherapy using cytotoxic agents or endocrine therapy are the major treatment strategy for metastatic breast cancer [12]. For example, the commonly used chemotherapy drugs—paclitaxel was diterpene (C20) formed through the condensation of four isoprene molecules [18,19]. Generally, paclitaxel was applied as a first-line (adjuvant) treatment of node-positive breast cancer [20]. For the metastatic breast cancer which has failed after combination of chemotherapy or relapse of adjuvant chemotherapy (within 6 months), paclitaxel was app clied as a second line agent in breast cancer. The cytotoxic effects of paclitaxel are targeting of p53, inducing cellular apoptosis and mitotic arrest [21]. Natural compounds that are derived from plants have interesting biological activities, including antimicrobial, anti-oxidation, anti-inflammatory and cytotoxic effects [22]. The diverse range of compounds that showed potential inhibitory effects against oncogenic transcription factors in breast cancer were surveyed and reviewed, namely edomin, triterpenoids, parthenolide, vincristine, irinotecan, green tea polyphenol and several others [5,12].

Although there are several technologies for the identification of differentially expressed genes after treatment, microarray is a precise and thorough tool [23]. The advantages of microarray for gene detection are rapid, high accuracy and comprehensive detection [24,25]. Microarray technology has been used to study gene expression during the oncogenesis, metastasis or drug resistance during cancers [26–28]. Similarly, it can also be applied to the diagnosis, classification, prognosis and screening of drug targets involved in the treatment of breast cancer [29–31]. For example, microarray could be applied in cell lines with different stages of metastasis to obtain metastasis-related genes [32,33]. Further, to compare the differential expressions between different subtypes of breast cancers (e.g., MCF-7 and MDA-MB-231 cells), a large number of tumor-specific markers could be screened. Therefore, advances in microarray has made it possible and accelerated the overall study on the differentially expressed genes in breast cancer.

MDA-MB-231 cells are insensitive to conventional breast cancer treatments (e.g., chemotherapy, endocrine therapy or targeted therapy) due to drug resistance and metastasis [34–36]. The differentially expressed genes (DEGs) may be involved in signaling pathways, such as apoptosis, cell cycle and cell growth and thus have been common therapy targets in drug-resistant breast cancers. Although drugs that target important factors in signaling pathways may activate another or inhibit to resist drug effect, therapies targeting those factors have offered promising results for preventing breast cancer. Our previous studies have demonstrated that chlorophyllide composites have potential in the treatment of MDA-MB-231 cells [37,38]. However, the underlying molecular mechanisms involved have yet to be fully elucidated. Understanding the mechanisms that drive drug resistance is important to the development of novel treatment and to increase the surveillance in patients. Therefore, the main aim of this study is to characterize the effects of chlorophyllides on MCF-7 and MDA-MB-231 cells through microarray gene expression profiling. We compared the gene expression profiles among chlorophyllides composites-treated MCF-7 and MDA-MB-231 cells to exhibit the cancer-related or drug resistance-related molecular mechanism and frame a possible strategy to develop as a target of botanical drugs.

2. Materials and Methods

2.1. Materials

Ethanol and *n*-hexane were purchased from Seedchem Company Pty., Ltd. (Melbourne, Australia). 3-(4,5-dimethylthiazol-2-yl)-2,5-diphenyl tetrazolium bromide (MTT), potassium hydroxide, sodium phosphate, Triton™ X-100 and chlorophyll a/b standards were purchased from Sigma-Aldrich, Inc. (St. Louis, MO, USA). Sweet potato leaves were purchased from a local market in Kaohsiung, Taiwan. Human breast cancer cell lines (MCF-7 and MDA-MB-231) were purchased from the Bioresource Collection and Research Center (Food Industry Research and Development Institute, Taiwan). Dulbecco's modified Eagle's medium (DMEM) and fetal bovine serum (FBS) were obtained from Invitrogen (Carlsbad, CA, USA). TRIzol® reagent was purchased from Invitrogen Corp. (Carlsbad, CA, USA).

2.2. Chlorophyll Extraction and Measurement

Chlorophyll was obtained as described from the laboratory of Prof. Shaw [37]. Fresh leaf samples were washed with water and blotted. Ten grams of fresh, clean leaves were weighted and ground into powders using a mortar and pestle, with liquid nitrogen (50 mL) in the dark. Chlorophyll was extracted by immersing 1 g of leaf powder in 125 mL of ethanol. After 48 h, ethanol extract was centrifuged at $1500 \times g$ for 5 min. The chlorophyll from ethanol extracts were then sequentially extracted using *n*-hexane. After 48 h, the double extract of chlorophylls was centrifuged at $1500 \times g$ for 5 min, and purified chlorophylls from ethanol-hexane extracts were obtained. The concentrations of chlorophyll a/b were measured by UV-Vis spectrophotometer (BioTek Instruments, Inc., Winooski, VT, USA) for the absorbance at 649 and 665 nm, which are the major absorption peaks for chlorophyll *a* and *b*, respectively. The chlorophyll *a* and *b* contents of the leaves were calculated using previously devised equations [39].

2.3. Preparation of Chlorophyllides Composites by Using Chlorophyllase

Chlorophyllase was obtained as described from the laboratory of Prof. Shaw [40]. The reaction mixture contained 0.5 mg of recombinant chlorophyllase, 650 μL of the reaction buffer (100 mM sodium phosphate (pH 7.4) and 0.24% Triton X-100) and 0.1 mL of chlorophyll extracts from the sweet potato leaves (100 mM). The reaction mixture was incubated at 37 °C for 30 min in a shaking water bath, then the enzymatic reaction was stopped by adding 1 mL of 10 mM KOH. The reaction mixture was then vortexed vigorously and centrifuged at 4000 rpm for 10 min to collect chlorophyllides composites. Chlorophyllides composites were then concentrated, and the solvents were removed by evaporation under reduced pressure at 40 °C on a rotary evaporator (IKA-Werke, Germany). The concentrated composites were processed by lyophilization, weighed and stored at −80 °C for further experiments. All compounds were found to be >95% pure by HPLC analysis (Figure S1).

2.4. Total RNA Preparation for Sequencing

Breast cancer cell lines (MCF-7 and MDA-MB-231), cultured in DMEM supplemented with 10% FBS and maintained at 37 °C under a humidified atmosphere of 5% CO_2 with 5×10^4 cells/well, were treated with 100 μg/mL of prepared chlorophyllides composites [37,38] or DMSO (vehicle control). Cells were collected at 24 h after treatment and shipped using dry ice to Welgene Biotech. Co., Ltd., Taipei, Taiwan.

Total RNA was extracted using TRIzol® reagent according to the manufacturer's instructions [41]. The RNA quality was confirmed using the ratios A260/280 and A260/230 (Thermo fisher scientific Inc., Waltham, MA, USA). RNA concentration and integrity were analyzed by Bioanalyzer 2100 total RNA Nano series II chip (Agilent, Santa Clara, CA, USA).

2.5. Preparation of cDNA Library and Sequencing

RNA integrity was assessed using the RNA Nano 6000 Assay Kit on the Bioanalyzer 2100 system (Agilent Technologies, Santa Clara, CA, USA). 0.2 µg of total RNA was amplified by a Low Input Quick-Amp Labeling kit (Agilent Technologies, Santa Clara, CA, USA) and labeled with Cy3 (CyDye, Agilent Technologies, Santa Clara, CA, USA) during the in vitro transcription process. 0.6 µg of Cy3-labled cRNA was fragmented to an average size of about 50–100 nucleotides by incubation with fragmentation buffer at 60 °C for 30 min [42].

2.6. Microarray Gene Expression Profiling

Microarray profiling was performed using Agilent SurePrint Microarray (Agilent Technologies, Santa Clara, CA, USA) at 65 °C for 17 h After washing and drying by nitrogen gun blowing, microarrays were scanned with an Agilent microarray scanner (Agilent Technologies, Santa Clara, CA, USA) at 535 nm for Cy3. Scanned images were analyzed by Feature Extraction 10.7.3.1 software (Agilent Technologies, Santa Clara, CA, USA), an image analysis and normalization software was used to quantify signal and background intensity for each feature. Raw signal data was normalized by quantile normalization for differential expressed genes discovery. For functional assay, enrichment tests for gene ontology (GO) and KEGG pathway were performed for DEGs by clusterProfiler.

2.7. Quantitative Reverse Transcription PCR (RT-qPCR)

Validation of RNA-Seq data was performed by RT-qPCR. DNase I-treated total RNA from chlorophyllides composites-treated MCF-7 and MDA-MB-231 cells was subjected to cDNA synthesis using iScript™ cDNA synthesis kits (Bio-Rad, Hercules, CA, USA). PCR primers were designed based on the transcriptome sequences of annexin A4 (ANXA4), chemokine C-C motif receptor 1 (CCR1), stromal interaction molecule 2 (STIM2), ethanolamine kinase 1 (ETNK1) and member of RAS oncogene family (RAP2B) using Primer 2 Plus software (Table 1). GAPDH served as the internal control, and RT-qPCR was performed using iQSYBR Green Supermix (Bio-Rad Laboratories, Hercules, CA, USA), and each sample was run in triplicate. The thermal gradient feature (CFX96, Bio-Rad Laboratories) was used to determine the optimal annealing temperature for all primers. The real-time PCR program used was 95 °C for 3 min, followed by 40 cycles of 95 °C for 15 s, 58 °C for 15 s, and 72 °C for 35 s. Dissociation and melting curves of amplification products were performed and results were analyzed using the CFX Manager Software package (Bio-Rad Laboratories). The $2'^{\Delta\Delta Ct}$ method was chosen as the calculation method [43]. The difference in the cycle threshold (Ct) value of the target gene and its housekeeping gene (GAPDH), called ΔCt, was calculated using the following equation: $\Delta\Delta Ct$ = (ΔCt of chlorophyllides composites treatment or vehicle control group for the target gene at each time point) − (ΔCt of the initial control).

2.8. Statistical Analysis

Statistical comparisons were carried out by independent *t*-test using SPSS statistical software version 22.0 (SPSS Inc., Chicago, IL, USA). Values are shown as mean ± standard deviation. The acceptable level for statistical significance was $p < 0.05$.

Table 1. Primer name, sequence, target gene and product size used in the present study.

Name	Sequence	Target Gene	Product Size (bp)
GAPDH-F	ATCACTGCCACCCAGA AGAC	*GAPDH*	460
GAPDH-R	ATGAGGTCCACCACCCTGTT		
CCR1-F	AGAAGCCGGGATGGAAACTC	*CCR1*	165
CCR1-R	TTCCAACCAGGCCAATGACA		
STIM2-F	AGTCTTTGGGACTCTGCACG	*STIM2*	129
STIM2-R	TGTTGCCAGCGAAAAAGTCG		
ETNK1-F	CCAAAGCATGTCTGCAACCC	*ETNK1*	114
ETNK1-R	AAGCAGAAGCCTTGACCCTC		
RAP2B-F	AGCTTCCAGGACATCAAGCC	*RAP2B*	190
RAP2B-R	AGGCTTTGTTTTTGGCCGAC		
MAGIL-F	GCCTTGCACAACCCGATCT	*MAGIL*	150
MAGIL-R	GGCTTGGGTGTCCCATAATAG		
NLRC5-F	ACCTTAAGCCTGTGTCCACG	*NLRC5*	115
NLRC5-R	CTGTGAACCTGCCACAGCA		
SLC7A7-F	CTCACTGCTTAACGGCGTGT	*SLC7A7*	170
SLC7A7-R	CCAGTTCCGCATAACAAAGG		
PKN1-F	GCCATCAAGGCTCTGAAGAA	*PKN1*	136
PKN1-R	GTCTGGAAACAGCCGAAGAG		
TOP2A-F	CTTTGGCTCGATTGTTATTTCC	*TOP2A*	142
TOP2A-R	CCCAGTACCGATTCCTTCAG		

3. Results and Discussion

3.1. DEG Analysis in MCF-7 and MDA-MB-231 Cells

MCF-7 cells and MDA-MB-231 cell were subjected to chlorophyllides composites treatment, and the gene expression levels were compared. The data indicated that a total of 124 and 77 DEGs were specifically identified in MCF-7 and MDA-MB-231 cells, respectively (Figure 1A). These included 43 upregulated and 81 downregulated genes in MCF-7 and 56 upregulated and 21 downregulated genes in MDA-MB-231 cells ($\geq$2-fold change (FC), $p < 0.05$). To analyze the common and specific DEGs in the two cells, a Venn diagram was also performed. There were 118 specific DEGs for the chlorophyllides composites-treated MCF-7 cells and 71 specific DEGs for the chlorophyllides composites-treated MDA-MB-231 cells. We first identified the 6 overlapped genes were found between chlorophyllides composites-treated MCF-7 and MDA-MB-231 cells (Figure 1B). The results revealed that the significant differences in the chlorophyllides composites-treated MCF-7 and MDA-MB-231 cells as compared to their parental cells. Therefore, chlorophyllides composites targeted and affected the expression of DEGs, indicating that chlorophyllides composites specifically inhibited the proliferation of MCF-7 and MDA-MB-231 cells. This finding is consistent with our previous results [38]. Furthermore, a higher number of DEGs was found in MCF-7, indicating that chlorophyllides composites were more efficient in MCF-7 cells.
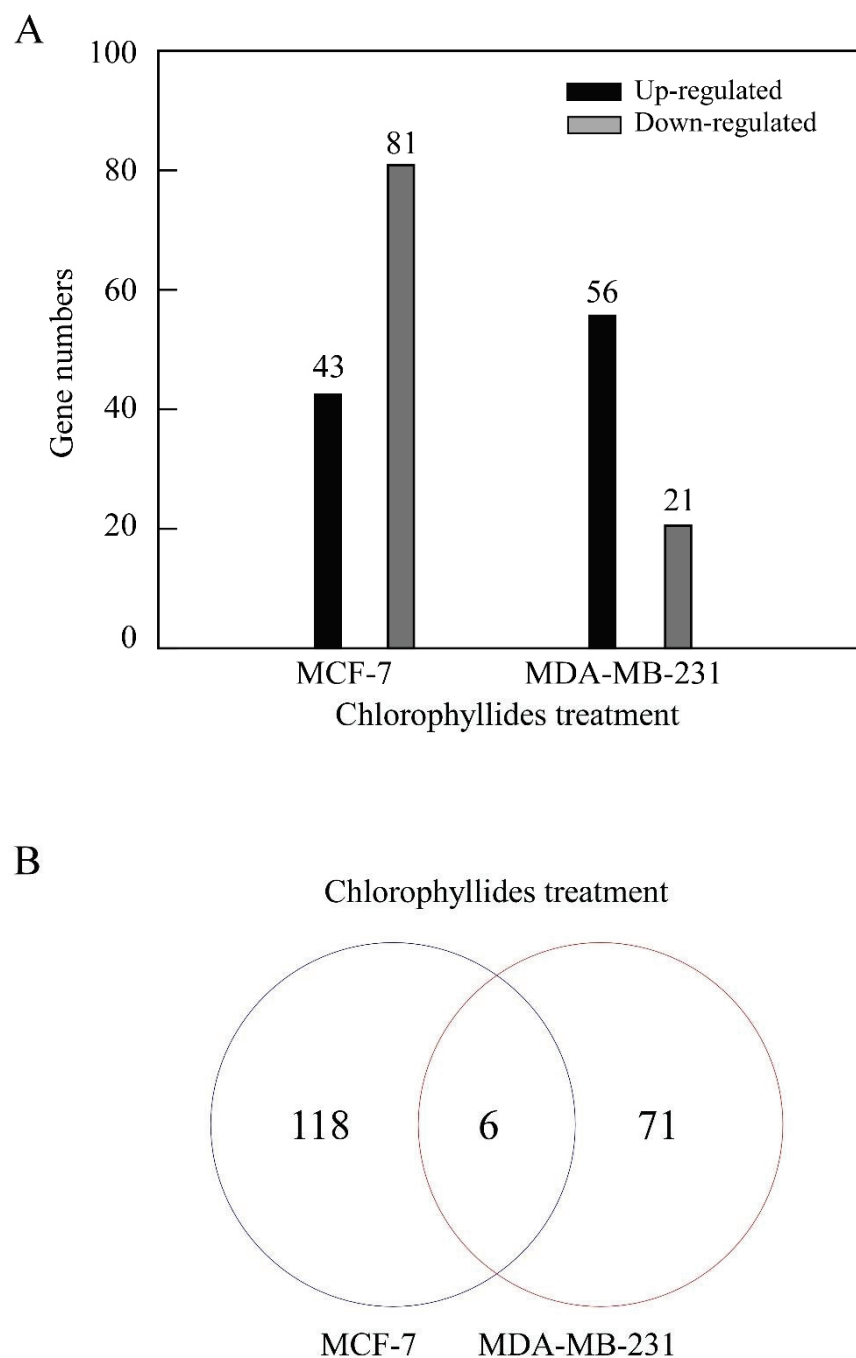
Figure 1. Comparisons of differentially expressed genes (DEGs) from MCF-7 and MDA-MD-231. (**A**) Upregulation and downregulation of DEGs in MCF-7 and MDA-MD-231 cells with chlorophyllides treatments. (**B**) Venn diagram of the overlapped DEGs between chlorophyllides-treated MCF-7 and MDA-MB-231 cells. The MCF-7 and MDA-MB-231 cells shared six genes of DEGs.

3.2. GO Annotation of Differential Expessed Genes

Comparison of gene expression levels between the MCF-7 cells, subjected to chlorophyllides composites and control cells, a total of 1383 GO terms were enriched. 29, 39 and 26 genes were clustered into three categories, namely biological process (BP), cellular component (CC) and molecular function (MF). The most enriched groups with 4 genes in MF were purine nucleoside binding and nucleoside binding. Eight groups in BP were enriched, including mesenchyme development, negative regulation of catabolic process, maintenance of location, negative regulation of cell migration, negative regulation of cell motility, nega-

tive regulation of cellular component movement, negative regulation of locomotion and muscle system process. The most enriched groups with 4 genes in CC were cell leading edge and synaptic membrane.

Comparison of gene expression levels between chlorophyllides composites-treated MDA-MB-231 cells and control cells revealed that a total of 1051 GO terms were enriched. Twenty-five, 27 and 16 genes were clustered into BP, CC, and MF. Fourteen groups in MF were enriched, such as enzyme activity, cytokine activity or receptor ligand activity. The most enriched groups with 2 genes in BP were organelle fission and response to nutrient levels. The most enriched groups in CC were tertiary granule, ficolin-1-rich granule, secretory granule membrane, postsynaptic density, asymmetric synapse, postsynaptic specialization, neuron to neuron synapse, nuclear chromatin and microtubule.

To investigate the functional roles of the DEGs, specific DEGs with chlorophyllides composites treatment were mainly functionally annotated and assigned to GO terms (Figure 2). In MCF-7 cells, specific DEGs with chlorophyllides composites treatment were assigned to 958 GO terms based on sequence homology, and a total of 21 functional groups were clustered into BP, CC and MF (Figure 2A). The unigene sequences from MF were clustered into 6 different classifications. The largest subcategory within MF was "binding", followed by "catalytic activity". Twenty genes and 11 genes were annotated for binding and catalytic activity out of total MF. In the CC, sequences were distributed into 3 classifications. The most represented subcategories were "cell", followed by "cellular anatomical entity". "Metabolic process" with 246 GO annotations was the most represented among 12 subcategories within the BP, followed by "development process" for 226 GO annotations.

In MDA-MB-231 cells, specific DEGs were annotated and shown in Figure 2B. Those DEGs with chlorophyllides composites treatment were ascribed to 590 GO terms and divided into 21 functional groups (Figure 2B). The unigene sequences from MF were clustered into 7 different classifications. The largest subcategory within MF was "catalytic activity", followed by "binding". In the CC, sequences were distributed into 3 classifications. The most represented subcategories were "cellular anatomical entity", followed by "cell". "Metabolic process" with 369 GO annotations was the most represented among 11 subcategories within the BP, followed by "cellular process" for 191 GO annotations.

It has been reported that ursolic acid, quercetin, curcumin and kaempferol are potential anti-cancer compounds in the treatment of breast cancer [44–47]. Guo et al. evaluated the anti-cancer mechanism of ursolic acid by microarray [48]. They indicated that the effects of ursolic acid were by inhibition of nuclear factor kappa-B kinase (IKK)/nuclear factor kappa-B (NF-κB) and serine/threonine kinase protein (RAF)/ERK pathways in MCF-7 cells [48]. Bachmeier et al. reported that curcumin inhibited the phosphorylation of the IKK in breast cancer cells [49]. In the present study, our results demonstrated that the group-biological process was enriched with chlorophyllides composites treatment, indicating that chlorophyllides composites treatment may affect the metabolism, cell communication, or development. Therefore, the functional annotations of unigenes according to the GO database provide ample numbers of candidate genes and valuable information of the biological activity of chlorophyllides composites treatment in MCF-7 and MDA-MB-231 cells.
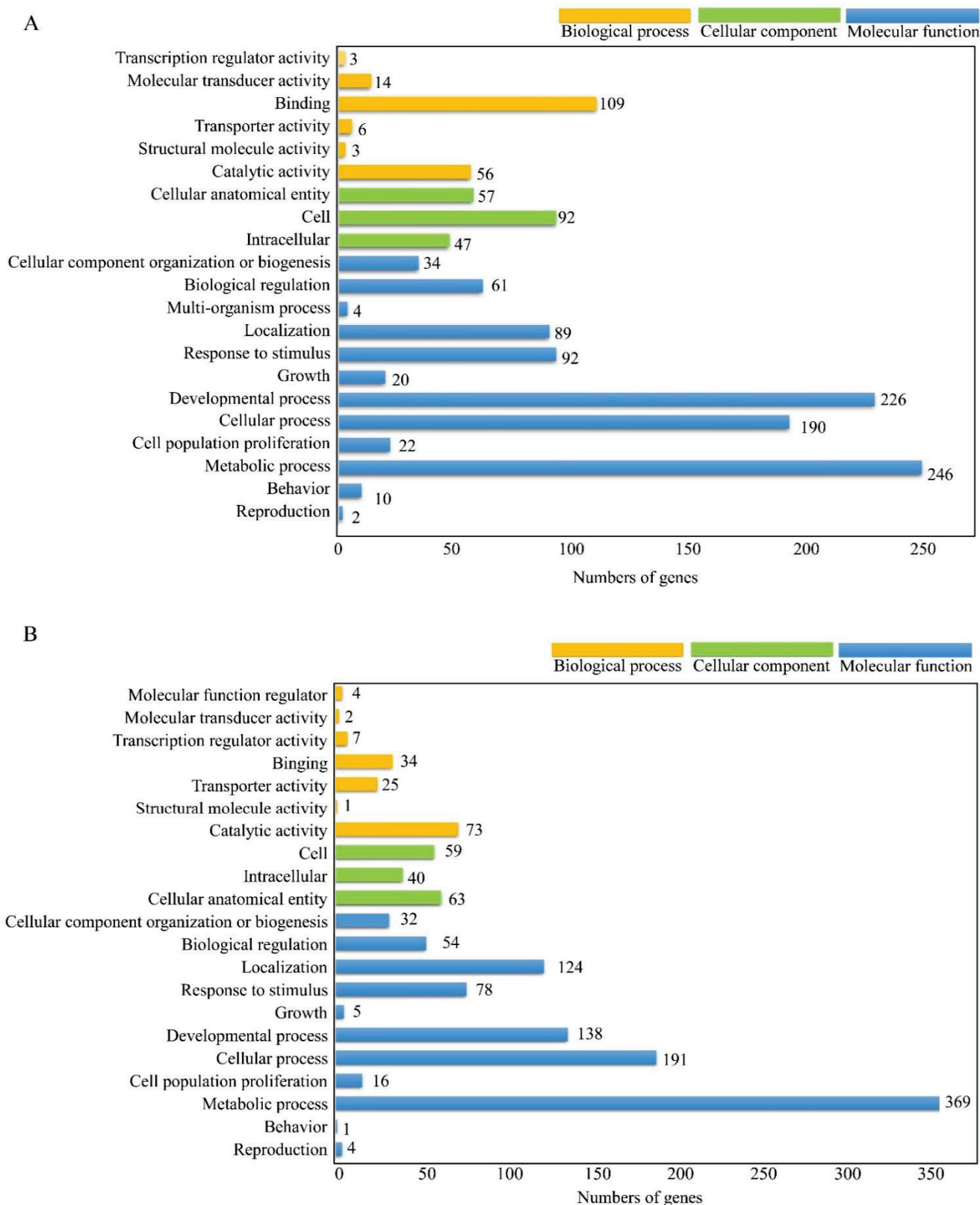
Figure 2. Functional distribution of GO annotation extracted from chlorophyllides composites treatments. (**A**) MCF-7 cells with chlorophyllides composites treatments. (**B**) MDA-MB-231 cells with chlorophyllides composites treatments. The results of GO enrichment analysis of DEGs were classified into three categories: molecular functions, cellular component and biological process. The *y*-axis is gene functional classification of GO, while *x*-axis is the corresponding number of genes.

3.3. KEGG Pathway Analysis of DEGs

Overall, specific DEGs from MCF-7 with chlorophyllides composites treatment had significant matches, which were allocated to 41 KEGG pathways classified into 6 main categories, namely metabolism, genetic information processing, environmental information processing, cellular processes, organismal systems and human diseases (Figure 3A). The highest number of genes (13 gene) categorized from KEGG analysis related to human diseases with sub-groups from viral infectious disease (3 genes), substance dependence (3 genes), cardiovascular disease (2 genes), cancer (2 genes in overview and 1 gene in specific types), neurodegenerative disease (1 gene) and endocrine and metabolic disease (1 gene). Ten genes were related to organismal systems, where the majority of the genes were categorized as endocrine system (4 genes), followed by digestive system (2 genes), sensory system (2 genes), immune system (1 gene), circulatory system (1 gene), nervous system (1 gene) and aging (1 gene). Seven genes related to environmental information processing were categorized as signal transduction (6 genes) and signaling molecules and interactions (1 gene). Six and 3 genes were related to metabolism and genetic information processing, respectively. However, no genes were categorized into cellular processes.

Moreover, DEGs from MDA-MB-231 cells with chlorophyllides composites treatment were allocated to 22 KEGG pathways (Figure 3B). The highest number of genes categorized from KEGG analysis related to organismal systems with sub-groups from the nervous or immune systems (2 genes). Seven pathways with 3 genes (RGS9, IL1B and SPl1) were related to human disease. It is interesting that IL1B was categorized into 6 pathways, including of hsa05010, hsa05321, hsa05146 and hsa05152. Three genes were allotted to metabolism with subgroups of global and overview map, carbohydrate metabolism, amino acid metabolism and glycan biosynthesis and metabolism.

It has been reported that genomic profile is substantially different between MCF-7 and MDA-MB-231 cells. In the present study, we found that only 41 and 22 KEGG pathways were annotated in MCF-7 and MDA-MB-231 cells. It is worth noting that different cell lines carried specific genomic alternations, possibly due to different response to chlorophyllides composites.
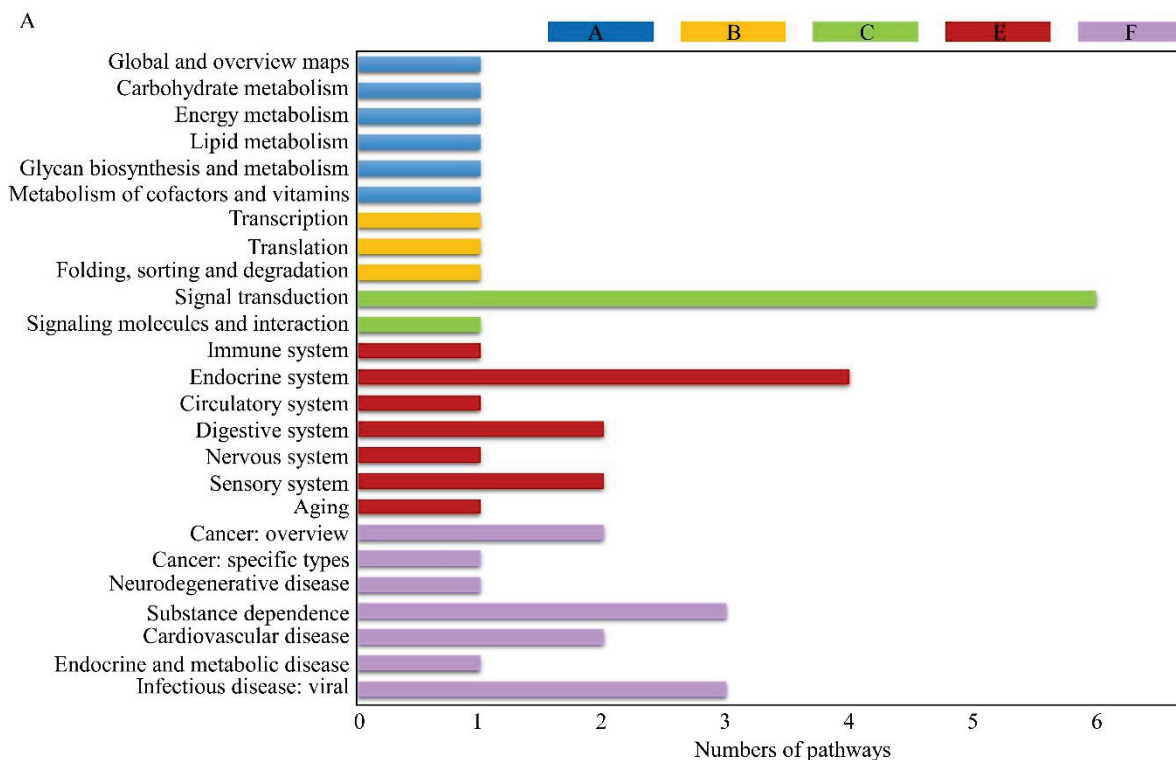
Figure 3. *Cont.*
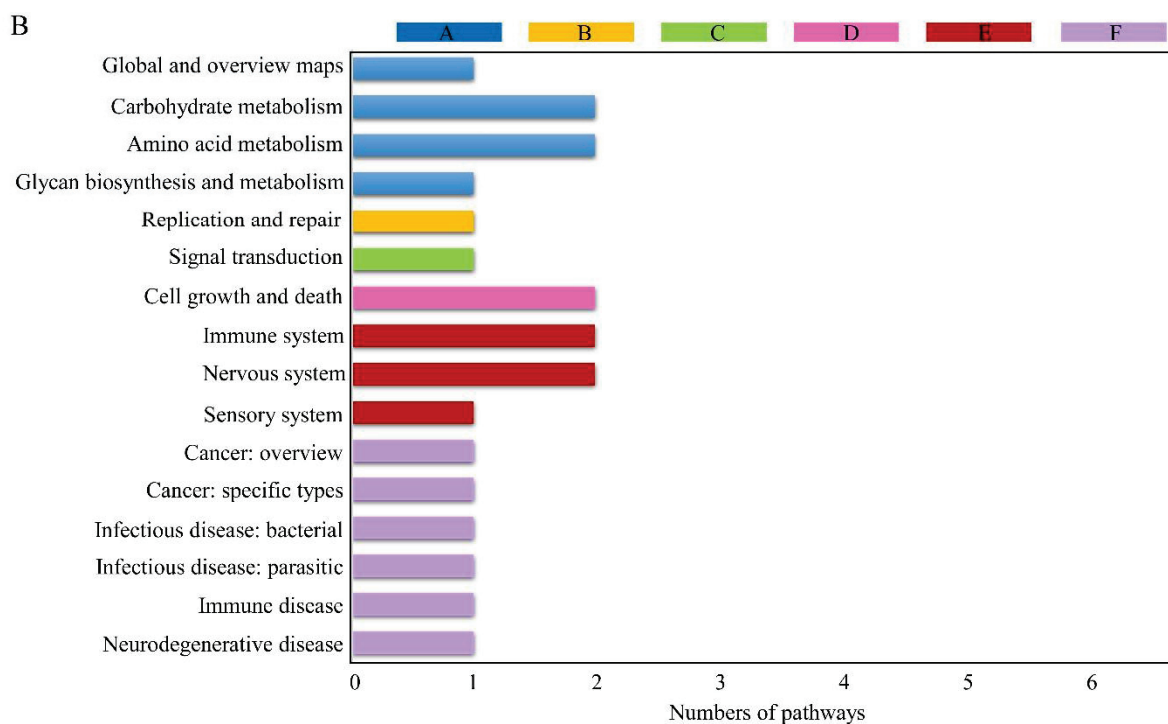
Figure 3. KEGG (Kyoto Encyclopedia of Genes and Genomes) assembled unigenes from chlorophyllides composites treatments. (**A**) MCF-7 cells; (**B**) MDA-MB-231 cells. The results were classified into six categories: A. metabolism; B. genetic information processing; C. environmental information processing; D. cellular processes; E. organismal systems; and F. human diseases. The *y*-axis is classification of KEGG, and the *x*-axis is the corresponding numbers of pathways. $p < 0.5$.

3.4. Analysis of Common KEGG Pathways

To further identify the chlorophyllides composites relevant KEGG pathways that were common in both breast cancer cell lines, we compared the KEGG pathways that were enriched in chlorophyllides composites-treated MCF-7 and MDA-MB-231 cells (Figure 4). The top 20 common KEGG pathways were shown, including the PI3K-Akt signaling pathway, MAPK pathway, Rap1 signaling pathway or human T-cell leukemia virus 1 infection. In this study, we focused more on the underlying pathways that are related to cancer or drug resistance. Hence, the differential expression involved in cancer or drug resistance was compared between MCF-7 and MDA-MB-231 cells (Tables 2 and 3). The results revealed that 23 and 4 significantly enriched KEGG pathways related to cancer and drug resistance were identified, respectively. We observed that 90, 89 and 74 DEGs were mapped to "proteoglycans in cancer" (hsa05205), "transcriptional misregulation in cancer" (hsa05202) and "viral carcinogenesis" (hsa05203) pathways (Table 2). For the chlorophyllides composites relevant pathways in drug resistance, there were 15, 38, 42 and 45 DEGs related to "antifolate resistance" (hsa01523), "platinum drug resistance" (hsa01524), "EGFR tyrosine kinase inhibitor resistance" (hsa01521) and "endocrine resistance" (hsa01522) pathways (Table 3).
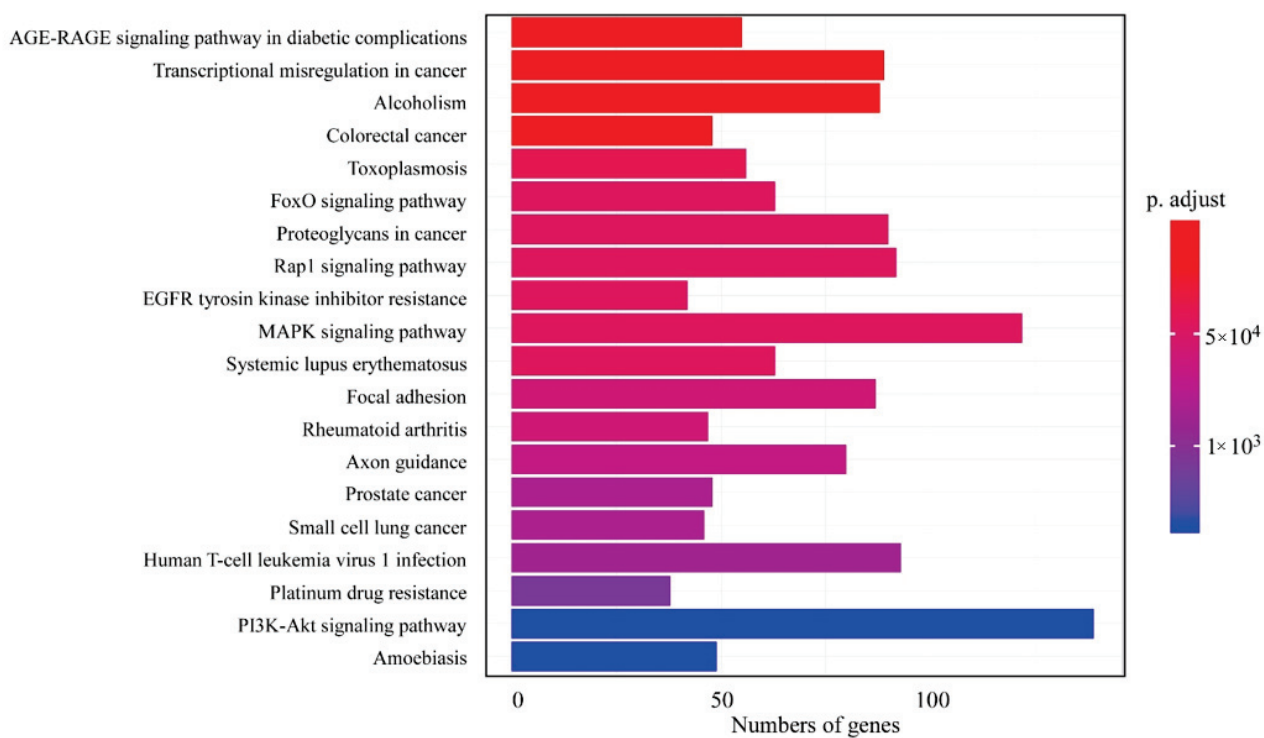
Figure 4. Common KEGG pathways in chlorophyllides composites-treated MCF-7 and MDA-MB-231 cells. The *y*-axis is classification of KEGG, and the *x*-axis is the corresponding number of genes.

Table 2. Analysis of chlorophyllides composites relevant pathway in cancers.

Pathway ID	Pathway Description	Number of DEGs			All Genes with Pathway Annotation	*q*-Value
		Up	Down	Total DEGs		
hsa05202	Transcriptional misregulation in cancer	47	42	89 (3.749%)	186 (2.347%)	1.296×10^{-5}
hsa05203	Viral carcinogenesis	34	40	74 (3.117%)	201 (2.536%)	0.0428029
hsa05205	Proteoglycans in cancer	35	55	90 (3.791%)	204 (2.574%)	0.0002796
hsa05210	Colorectal cancer	22	26	48 (2.022%)	86 (1.085%)	2.367×10^{-5}
hsa05211	Renal cell carcinoma	17	12	29 (1.222%)	69 (0.871%)	0.0433838
hsa05212	Pancreatic cancer	15	22	37 (1.559%)	69 (0.871%)	0.0021288
hsa05213	Endometrial cancer	13	14	27 (1.137%)	69 (0.871%)	0.0159683
hsa05214	Glioma	17	17	34 (1.432%)	69 (0.871%)	0.0118167
hsa05215	Prostate cancer	25	23	48 (2.022%)	97 (1.224%)	0.0005016
hsa05216	Thyroid cancer	10	11	21 (0.885%)	37 (0.467%)	0.0032991
hsa05217	Basal cell carcinoma	9	15	24 (1.011%)	63 (0.795%)	0.1293504
hsa05218	Melanoma	15	16	31 (1.306%)	72 (0.909%)	0.0298569
hsa05219	Bladder cancer	9	9	18 (0.758%)	41 (0.517%)	0.0669118
hsa05220	Chronic myeloid leukemia	14	22	36 (1.516%)	76 (0.959%)	0.0045089

Table 2. *Cont.*

Pathway ID	Pathway Description	Number of DEGs			All Genes with Pathway Annotation	q-Value
		Up	Down	Total DEGs		
hsa05221	Acute myeloid leukemia	15	16	31 (1.306%)	67 (0.845%)	0.0118167
hsa05222	Small cell lung cancer	13	33	46 (1.938%)	92 (1.161%)	0.0005016
hsa05223	Non-small cell lung cancer	13	20	33 (1.390%)	66 (0.833%)	0.0029084
hsa05224	Breast cancer	34	27	61 (2.570%)	147 (1.855%)	0.0066776
hsa05225	Hepatocellular carcinoma	32	40	72 (3.033%)	168 (2.120%)	0.0016521
hsa05226	Gastric cancer	30	28	58 (2.443%)	149 (1.880%)	0.0283904
hsa05230	Central carbon metabolism in cancer	13	17	30 (1.264%)	69 (0.871%)	0.0286728
hsa05231	Choline metabolism in cancer	20	16	36 (1.516%)	98 (1.237%)	0.1137391
hsa05235	PD-L1 expression and PD-1 checkpoint pathway in cancer	14	21	35 (1.474%)	89 (1.123%)	0.0624114

Table 3. Drug resistance pathway analysis of chlorophyllides composites.

Pathway ID	Pathway Description	Number of DEGs			All Genes with Pathway Annotation	q-Value
		Up	Down	Total DEGs		
hsa01521	EGFR tyrosine kinase inhibitor resistance	22	20	42 (1.769%)	79 (0.997%)	0.0002796
hsa01522	Endocrine resistance	24	21	45 (1.896%)	98 (1.237%)	0.0032168
hsa01523	Antifolate resistance	5	10	15 (0.632%)	31 (0.391%)	0.0464471
hsa01524	Platinum drug resistance	15	23	38 (1.601%)	73 (0.921%)	0.0006735

Li et al. identified the key genes and pathways associated with metastasis of MCF-7 and MDA-MB-231 cells [50]. Further, they identified survival-correlated genes (ALOX15, COL4A6, LMB13, MTAP, PLA2G4A, TAT) and metastasis-associated genes (SNRPN, ARNT2, HDGFRP3, ERO1LB, ERLIN2, YBX2, EBF4). They also identified signaling pathways; metabolic pathways, phagosome pathway, PI3K-AKT signaling pathway, focal adhesion, ECM-receptor interaction, pancreatic secretion and human papillomavirus infection were mainly associated with metastasis. In addition, Sun et al. screened and identified common and specific genes in breast cancer subtypes basal-like, Her2, LumA, LumB and normal-like molecular subtypes [51]. The authors identified 4 common and 34 specific DEGs in different subtypes. Similar to these studies, chlorophyllides composites treatment also affected signal transduction or metabolic progress, indicating that chlorophyllides composites may act on the genes that correlated with metastasis.

3.5. Validation of RNA Expression by RT-qPCR

The functions of upregulated and downregulated genes are correlated with chlorophyllides composites treatment. For further understanding the role of chlorophyllides composites in breast cancers and to find potential targets for chlorophyllides composites treatment, gene expression profiles between chlorophyllides composites-treated MCF-7 cells and MDA-MB-231 cells were compared. We analyzed the microarray data sets

of upregulated and downregulated genes in MCF-7 and MDA-MB-231 cells to identify specific effects of chlorophyllides composites-induced cytotoxicity. Hierarchical clustering indicated that the DEGs were detected by chlorophyllides composites treatment between MCF-7 and MDA-MB-231 cells (Figure 5). Collectively, the levels of 52 genes were differentially expressed in MCF-7 and MDA-MB-231 cells. The expression of 16 genes was upregulated in MCF-7 cells, such as annexin A4 (ANXA4), chemokine C-C motif receptor 1 (CCR1), stromal interaction molecule 2 (STIM2), ethanolamine kinase 1 (ETNK1) and member of RAS oncogene family (RAP2B). There were 36 upregulated expressed genes in MDA-MB-231 cells, such as membrane-associated guanylate kinase WW and PDZ domain containing 1 (MAGI1), NLR family CARD domain containing 5 (NLRC5), solute carrier family 7 membrane 7 (SLC7A7), protein kinase N1 (PKN1) and DNA topoisomerase II alpha 170 kDa (TOP2A). The log2 FC of CCR1, STIM2, ETNK1 and RAP2B from microarray resulted in chlorophyllides composites-treated MCF-7 cells that were 5.954, 2.783, 2.181 and 2.375, respectively. The log2 FC of MAGl1, NLRC5, SLC7A7, TOP2A and PKN1 from microarray results in chlorophyllides-treated MDA-MB-231 cells were 2.307, 5.824, 22.208, 2.52 and 2.32, respectively.
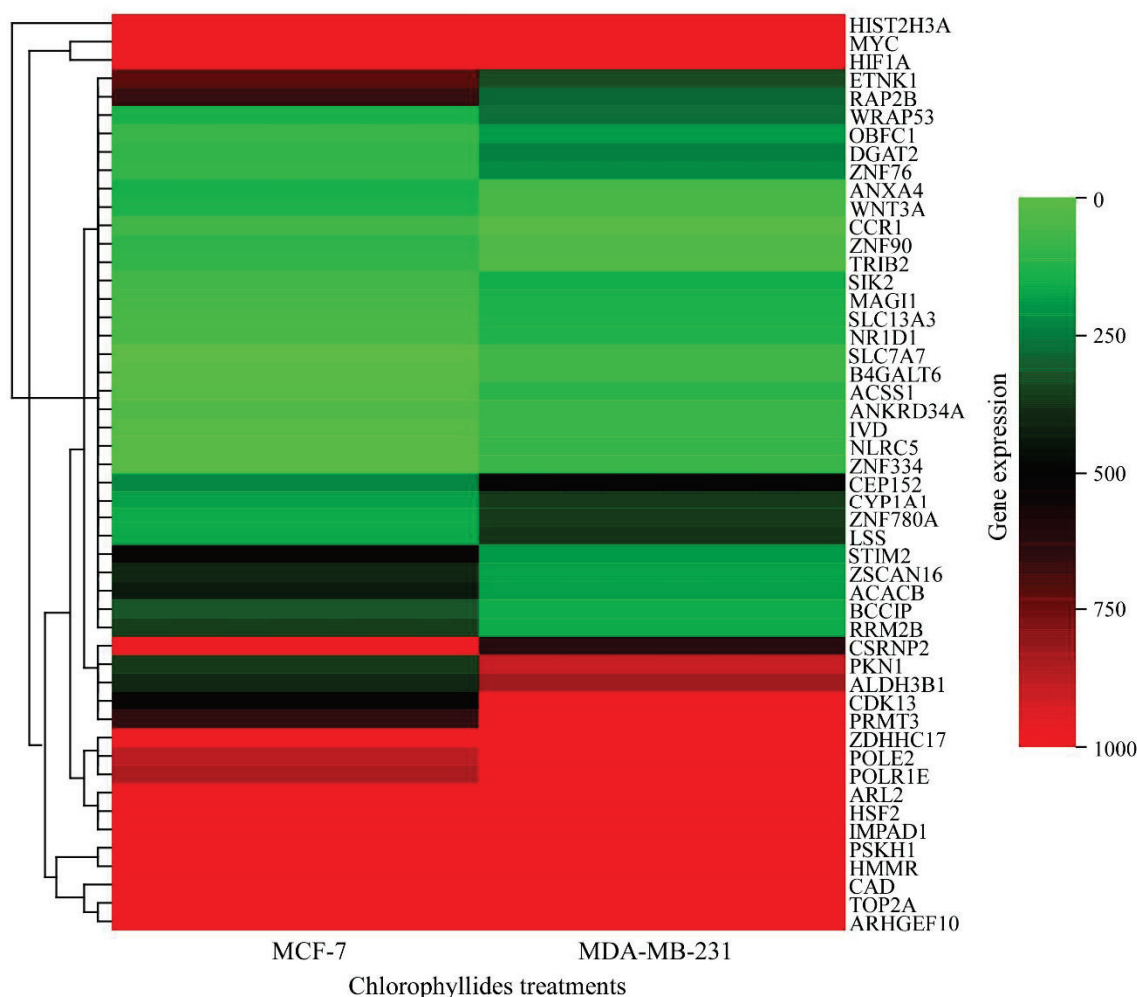
Figure 5. Identification of common DEGs between chlorophyllides composites-treated MCF-7 and MDA-MB-231 cells. Heat map showing the hierarchical cluster of differential expression levels between chlorophyllides composites-treated MCF-7 and MDA-MB-231 cells. The top 50 candidate genes were selected from chlorophyllide-treated MCF-7 and MDA-MB-231 cells. The color scale represents expression values; red indicates the high expression level, and the green refers to the low expression level.

To validate the expression level of CCR1, STIM2, ETNK1, RAP2B, MAGl1, NLRC5, SLC7A7, TOP2A and PKN1 identified in chlorophyllides composites-treated MCF-7 and MDA-MB-231 cells, we performed RT-qPCR to evaluate their expression levels of genes as mentioned above (Figure 6). Nine randomly selected genes were detected in the chlorophyllides composites-treated MCF-7 and MDA-MB-231 cells by RT-qPCR, and the primers were listed in Table 1. The FC of CCR1, STIM2, ETNK1, MAGl1 and TOP2A by RT-qPCR were 6.798, 2.687, 5.75 and 1.574, respectively. The FC of above-mentioned genes were consistent with the expression changes detected by microarray dataset. In MDA-MB-231 cells, the expression level of CCR1, STIM2, ETNK1, RAP2B, MAGl1, NLRC5, SLC7A7 and TOP2A were significantly upregulated, while PKN1 was significantly downregulated. The FC of CCR1, STIM2, ETNK1, RAP2B, NLRC5, SLC7A7 and TOP2A were 10.07, 3.508, 5.95, 3.694, 5.523, 11.015 and 1.159, respectively. The FC of STIM2, RAP2B and NLRC5 were similar to the expression changes detected by RT-qPCR and microarray dataset.
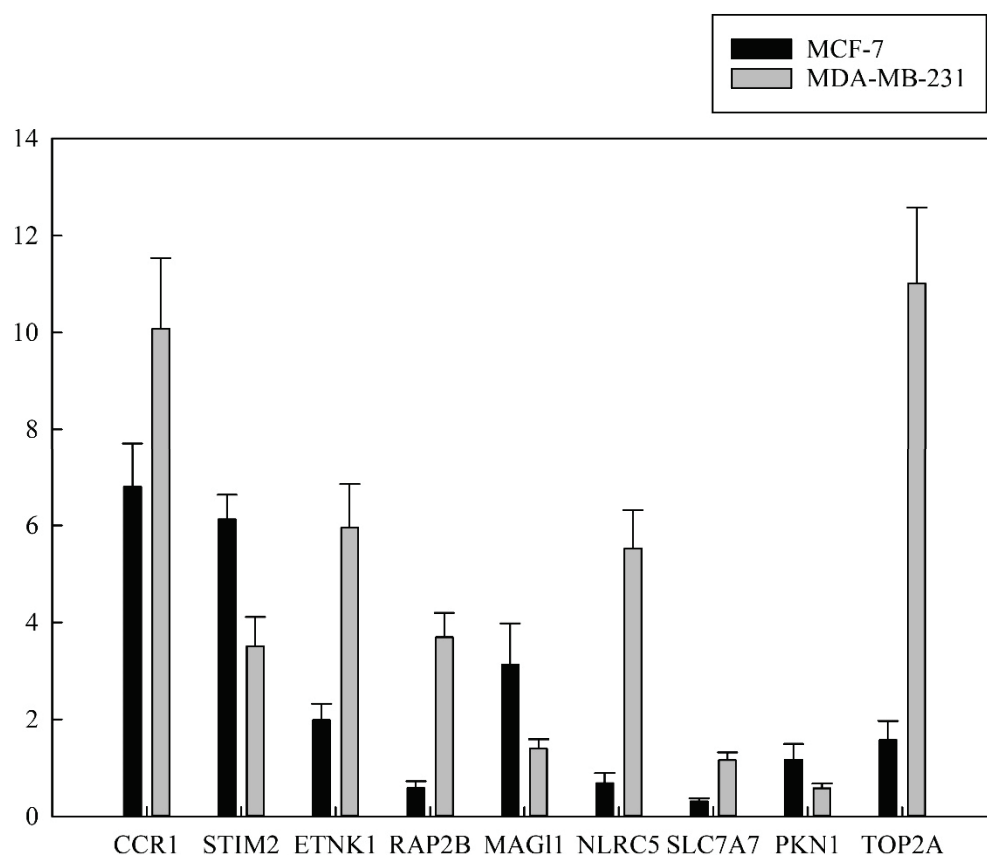
Figure 6. Validation of relative expression levels from RNA-seq and real-time polymerase chain reaction. Nine randomly selected differentially expressed genes (DEGs) were validated for the expression level from chlorophyllide-treated MCF-7 and MDA-MB-231 cells. Expression of target genes was normalized to GAPDH as a reference gene, and statistically significant differences from control are presented, with $p < 0.05$. The *x*-axis denotes nine genes. The *y*-axis refers to the relative expression level with the mean $\pm$ standard deviation of five replicates.

The genes mentioned below were identified and mapped to the KEGG database, and their association was observed (Table 4). It has been reported that the natural products from plant sources have various biological activities, such as anti-oxidation, anti-inflammation or anti-proliferation [5]. Many of the reported anti-cancer effects of natural compounds also target cellular proteins that play important roles in signal transduction, apoptosis or cell cycle arrest [52]. By the bioinformatics analysis, we found that many DEGs were enriched in signaling and cellular process, such as CCR1, STIM2, ETNK1, RAP2B, MAGI1, NLRC5, SLC7A7, PKN1 and TOP2A. Previously, we have demonstrated that purified chlorophyl-

lides composites could be a potential candidate for combination therapy to breast cancers with multiple drug resistance [38]. Therefore, we focused on several interesting factors that were differentially affected by chlorophyllides composites treatment in MCF-7 and MDA-MB-231 cells. CCR1 expression was upregulated in both MCF-7 and MDA-MB-231 cells. CCR1 belonged to the G protein-linked receptor superfamily. The expression of CCR1 has been reported on tumor cells, peripheral blood cells, immune cells and stromal cells. After the binding of CC chemokine (e.g., CCL14, CCL15, CCL16), CCR1 exhibited important roles in tumor invasion and metastasis in several cancers [53–57]. STIM2 was upregulated in both MCF-7 and MDA-MB-231 cells, and the FC in both cells was in accordance with RT-qPCR and microarray data. STIM2 is an endoplasmic reticulum-associated Ca^{2+}-sensing protein that responded to endoplasmic reticulum Ca^{2+} store depletion and transduced this cellular signal to Orai1 channel proteins [58,59]. Previous studies have demonstrated that disturbance of STIM is associated with the pathogenesis of several diseases, such as autoimmune disorders, cancer, cardiovascular disease, ageing, Alzheimer's and Huntington's diseases [60–62]. ETNK1 expression was upregulated in both MCF-7 and MDA-MB-231 cells. ETNK1 is an ethanolamine-specific kinase that catalyzes the phosphorylation of ethanolamine to generate phosphoethanolamine, which is the first step for biosynthesis of phosphatidylethanolamine. Previous studies have reported that mutations of ETNK1 may play important roles in oncogenesis [63,64]. RAP2B is a member of the Ras oncogene family that was upregulated by chlorophyllides composites in MDA-MB-231 cells. As signaling effectors of GTPase-binding protein Rap, Rap2B mediated various biological functions, including regulating the p53-mediated pro-survival function, and binding phospholipase C-ε and interferon-γ that promote the development of tumors [65].

The increased levels of MAGI1 by chlorophyllides composites was observed in the MCF-7 and MDA-MB-231 cells. MAGI1 is an important protein that is transmitted from extracellular environment to intracellular signaling pathways [66,67]. It has been reported that MAGI1 functioned as a tumor suppressor in several tumors (e.g., cervical cancer, leukemia, colorectal cancer, hepatocellular carcinoma, and gastric cancer. The expression of the NLRC5 gene was upregulated in MDA-MB-231 cells, and the relative expression between MCF-7 and MDA-MB-231 cells was strongly downregulated by more than 5.523-fold. This finding is similar to the expression levels observed in microarray data (5.824 fold). NLRC5 belongs to a large protein family that is involved in the regulation of inflammatory response in tumors. Functions of NLRC5 in tumors remain as a debate [68]. NLRC5 overexpression upregulated the MHC class I-mediated antigen presentation pathway that leads to immune escape of tumor cells. In contrast, new evidence has demonstrated that NLRC5 could promote tumor malignancy [69]. Similarly, the expression of the SLC7A7 gene was upregulated in MDA-MB-231 cells, and the relative expression between MCF-7 and MDA-MB-231 cells was strongly downregulated as observed by more than 35.4-fold. The *SLC7A7* gene encodes for the y$^+$LAT1 transporter [70,71]. The y$^+$LAT1 transporter was responsible for exchanging cationic amino acids with neutral amino acids and sodium at epithelial cells of the kidney and intestine. It has been reported that mutation in *SLC7A7* caused a rare inherited metabolic disorder of dibasic amino acid transport-lysinuric protein intolerance.

The expression levels of the PKN1 gene in MCF-7 cells were higher in comparison to MDA-MB-231 cells. PKN1 is a member of the protein kinase C superfamily. Disruption of PKN1 kinase activity is involved in several human diseases, including cancer. A previous study has demonstrated that mitotic phosphorylation is essential for PKN1's oncogenic function [72]. It was reported that PKN1 acted as a RhoA effector that transduced androgen-responsiveness to serum response factor [73]. Overexpression of PKN1 occurred during clinical castration-recurrent prostate cancer progression, stimulated tumor growth and shortened the survival of prostate cancer xenograft. Since PKN1 belongs to the kinase family, which function as signaling proteins and are identified as successful targets for cancer treatment, it is reasonable to suggest that chlorophyllides composites may interact with PKN1 or inhibit the activity of PKN1.

Table 4. Differentially expressed genes (DEGs) regulate after chlorophyllides treatment between MCF-7 and MDA-MB-231 cells.

Description	Gene Name	Log2 FC *	KEGG Pathway
Up regulation (MCF-7-chlorophyllides/MDA-MB-231-chlorophyllides)			
annexin A4	ANXA4	1.3495564	hsa04974
C-C motif chemokine receptor 1	CCR1	2.573958	ko04060, ko04061, ko04062, ko05163, ko05167
stromal interaction molecule 2	STIM2	1.4764014	hsa04020
ethanolamine kinase 1	ETNK1	1.1246655	hsa00564, hsa01100
RAP2B, member of RAS oncogene family	RAP2B	1.2477774	NA
BRCA2 and CDKN1A interacting protein	BCCIP	1.0360939	NA
ribonucleotide reductase M2 B	RRM2B	1.1502474	hsa00230, hsa00240, hsa00480, hsa00983, hsa01100, hsa04115
cysteine-serine-rich nuclear protein 2	CSRNP2	1.155312	NA
serine kinase H1	PSKH1	1.1608988	NA
zinc finger and SCAN domain containing 16	ZSCAN16	1.175633	NA
histone cluster 2, H3a	HIST2H3A	1.2060455	hsa04613, hsa05034, hsa05131, hsa05202, hsa05322
wingless-type MMTV integration site family, member 3A	WNT3A	1.2382799	hsa04150, hsa04310, hsa04390, hsa04550, hsa04916, hsa04934, hsa05010, hsa05022, hsa05165, hsa05200, hsa05205, hsa05206, hsa05217, hsa05224, hsa05225, hsa05226
acetyl-CoA carboxylase beta	ACACB	1.2477973	hsa00061, hsa00620, hsa00640, hsa01100, hsa04152, hsa04910, hsa04920, hsa04922, hsa04931
zinc finger protein 90	ZNF90	1.4318171	hsa05168
hyaluronan-mediated motility receptor	HMMR	1.4742341	ko04512
tribbles pseudokinase 2	TRIB2	1.5311222	NA
Down- regulation (MCF-7-chlorophyllides/MDA-MB-231-chlorophyllides)			
membrane associated guanylate kinase, WW and PDZ domain containing 1	MAGI1	−1.2064317	hsa04015, hsa04151, hsa04530, hsa05165
NLR family, CARD domain containing 5	NLRC5	−2.5420052	NA
solute carrier family 7 (amino acid transporter light chain, y+L system), member 7	SLC7A7	−4.4729806	hsa04974
protein kinase N1	PKN1	−1.3322328	hsa04151, hsa04621, hsa05132, hsa05135
topoisomerase (DNA) II alpha 170kDa	TOP2A	−1.1590858	hsa01524
UDP-Gal:betaGlcNAc beta 1,4-galactosyltransferase, polypeptide 6	B4GALT6	−3.2967566	ko00600, ko01100
zinc finger protein 334	ZNF334	−2.4680017	hsa05168
acyl-CoA synthetase short-chain family member 1	ACSS1	−2.1925126	hsa00010, hsa00620, hsa00630, hsa00640, hsa01100, hsa01200
isovaleryl-CoA dehydrogenase	IVD	−1.8816549	ko00280, ko01100
ADP-ribosylation factor-like 2	ARL2	−1.8091316	NA

Table 4. *Cont.*

Description	Gene Name	Log2 FC *	KEGG Pathway
Rho guanine nucleotide exchange factor 10	*ARHGEF10*	−1.9429478	ko04270, ko04611, ko04810, ko04928, ko05130, ko05135, ko05163, ko05200, ko05205, ko05417
cyclin-dependent kinase 13	*CDK13*	−1.3298924	NA
diacylglycerol O-acyltransferase 2	*DGAT2*	−1.3269336	ko00561, ko01100, ko04975
solute carrier family 13 (sodium-dependent dicarboxylate transporter), member 3	*SLC13A3*	−1.3249987	NA
nuclear receptor subfamily 1, group D, member 1	*NR1D1*	−1.2920206	ko04710
zinc finger protein 76	*ZNF76*	−1.2438793	hsa05168
ankyrin repeat domain 34A	*ANKRD34A*	−1.2280619	NA
salt-inducible kinase 2	*SIK2*	−1.2129109	ko04922
v-myc avian myelocytomatosis viral oncogene homolog	*MYC*	−1.2045108	ko04010, ko04012, ko04110, ko04151, ko04218, ko04310, ko04350, ko04390, ko04391, ko04550, ko04630, ko04919, ko05132, ko05160, ko05161, ko05163, ko05166, ko05167, ko05169, ko05200, ko05202, ko05205, ko05206, ko05207, ko05210, ko05213, ko05216, ko05219, ko05220, ko05221, ko05222, ko05224, ko05225, ko05226, ko05230
zinc finger protein 780A	*ZNF780A*	−1.1839843	hsa05168
oligonucleotide/oligosaccharide-binding fold containing 1	*OBFC1*	−1.1801386	NA
lanosterol synthase	*LSS*	−1.163355	ko00100, ko01100, ko01110, ko01130
zinc finger, DHHC-type containing 17	*ZDHHC17*	−1.1437738	NA
carbamoyl-phosphate synthetase 2, aspartate transcarbamylase, and dihydroorotase	*CAD*	−1.1388409	hsa00240, hsa00250, hsa01100, hsa01240
centrosomal protein 152kDa	*CEP152*	−1.1385807	NA
hypoxia inducible factor 1, alpha subunit	*HIF1A*	−1.0661852	ko04066, ko04137, ko04140, ko04212, ko04361 Axon regeneration ko04659, ko04919, ko05167, ko05200, ko05205, ko05211, ko05230, ko05231, ko05235
aldehyde dehydrogenase 3 family, member B1	*ALDH3B1*	−1.063386	hsa00010, hsa00340, hsa00350, hsa00360, hsa00410, hsa00980, hsa00982, hsa01100
polymerase (DNA directed), epsilon 2, accessory subunit	*POLE2*	−1.0376518	ko03030, ko03410, ko03420
arginine methyltransferase 3	*PRMT3*	−1.0357205	NA
polymerase (RNA) I polypeptide E, 53kDa	*POLR1E*	−1.0155994	ko03020
cytochrome P450, family 1, subfamily A, polypeptide 1	*CYP1A1*	−1.0129887	ko00140, ko00380, ko00830, ko00980, ko01100, ko04913, ko05204
WD repeat containing, antisense to TP53	*WRAP53*	−1.0114268	NA
heat shock transcription factor 2	*HSF2*	−1.0091325	ko03000
inositol monophosphatase domain containing 1	*IMPAD1*	−1.0071035	ko00562, ko00920, ko01100, ko01120, ko01130, ko04070

NA: not available; Log2 FC *: Log2 FC (MCF-7-chlorophyllides/MDA-MB-231-chlorophyllides).

TOP2 A was upregulated in MCF-7 and MDA-MB-231 cells. TOP2A acted as a DNA replication- and cell division-regulating enzyme. The overexpression of TOP2A was reported in several human cancers, including breast cancer and hepatocellular carcinoma [74]. Also, high levels of expression of chromatin regulatory genes (e.g., TOP2A) increased DNA accessibility and then led to greater anthracycline benefit [75]. Amplification of the *MYC* oncogene was the most common abnormality in breast cancer cells, which is similar to the previous study [50]. We also observed that *Myc* oncogenes were upregulated in chlorophyllides composites-treated MDA-MB-231 cells.

Breast cancer is regarded as a heterogeneous disease characterized by molecular aberrations and varying histologic and biological features. Microarray-based gene expression profiling had a significant impact on the understanding of breast cancers. The molecular classification system and prognostic multigene classifiers by microarrays was developed [10]. For example, correlation was found between immunohistochemistry and gene profiling of breast cancer, especially basal-like breast carcinoma. The intrinsic 40-gene set was found to classify breast cancer subtype and genes expression differentiations by microarray [76]. In addition, the gene expression profiling from triple negative breast cancer (TNBC) patients by next generation sequencing assay targeted all coding regions of 229 common cancer-related genes [77]. Genetic alterations in TNBC by next-generation sequencing assays was successfully detected [78]. Nonetheless, the functional annotation of common or specific unigenes provided ample numbers of candidate genes and valuable information about biological features of chlorophyllides composites treatment in this study.

4. Conclusions

Chlorophyllides composites could be mass manufactured from chlorophyll using chlorophyllase. In addition, chlorophyllides composites clearly exhibited amazing anti-cancer activities to breast cancer cell lines (MCF-7 or MDA-MB-231) [37]. To the best of our knowledge, this study is the first to evaluate the effects of chlorophyllides composites on MCF-7 and MDA-MB-231 cells by microarray profile. Moreover, it is also first to identify the global gene expression pattern from the chlorophyllides-treated group. Results indicated that 124 and 77 differentially expressed genes in MCF-7 cells and MDA-MB-231 cells after chlorophyllides composites treatment (A ≥ 2-fold change) was evident. Among these, it is possible to highlight that the expression of CCR1, STIM2, ETNK1, MAGl1 and TOP2A were upregulated in both chlorophyllides composites treated-MCF-7 and MDA-MB-231 cells, indicating that chlorophyllides composites may specifically target or inhibit the activity of these genes. Altogether, these results provide valuable information on the molecular mechanisms induced by chlorophyllides composites in MCF-7 and MDA-MB-231 cells. The DEGs of NLRC5, SLC7A7 and PKN1 may be used as therapy targets that facilitate the development of botanical drugs.

Institutional Review Board Statement: Not applicable.

Informed Consent Statement: Not applicable.

Data Availability Statement: Data is contained within the article or supplementary material.

Conflicts of Interest: The authors declare that there is no conflict of interest regarding the publication of this article.

Sample Availability: Samples of the compounds-chlorophyllides conpositesare available from the author (Jei-Fu Shaw).

Abbreviations

(ANXA4)	annexin A4
(BP)	biological process
(CC)	cellular component
(CCR1)	chemokine C-C motif receptor 1
(TOP2A)	DNA topoisomerase II alpha 170 kDa
(ER)	estrogen receptor
(ETNK1)	ethanolamine kinase 1
(FC)	fold change
(HER2)	human epidermal growth receptor 2
(RAP2B)	member of RAS oncogene family
(MAGI1)	membrane associated guanylate kinase WW and PDZ domain containing 1
(MF)	molecular function
(NLRC5)	NLR family CARD domain containing 5
(SLC7A7)	solute carrier family 7 membrane 7
(STIM2)	stromal interaction molecule 2
(PR)	progesterone receptor
(PKN1)	protein kinase N1
(TNBC)	triple negative breast cancer
(RT-qPCR)	quantitative reverse transcription PCR

References

1. Siegel, R.L.; Miller, K.D.; Fuchs, H.E.; Jemal, A. Cancer Statistics, 2021. *CA A Cancer J. Clin.* **2021**, *71*, 7–33. [CrossRef] [PubMed]
2. McCann, K.E.; Hurvitz, S.A.; McAndrew, N. Advances in targeted therapies for triple-begative breast cancer. *Drugs* **2019**, *79*, 1217–1230. [CrossRef] [PubMed]
3. DeSantis, C.E.; Ma, J.; Gaudet, M.M.; Newman, L.A.; Miller, K.D.; Goding Sauer, A.; Jemal, A.; Siegel, R.L. Breast cancer statistics, 2019. *CA A Cancer J. Clin.* **2019**, *69*, 438–451. [CrossRef] [PubMed]
4. Reddy, T.P.; Rosato, R.R.; Li, X.; Moulder, S.; Piwnica-Worms, H.; Chang, J.C. A comprehensive overview of metaplastic breast cancer: Clinical features and molecular aberrations. *Breast Cancer Res.* **2020**, *22*, 121. [CrossRef] [PubMed]
5. Loibl, S.; Poortmans, P.; Morrow, M.; Denkert, C.; Curigliano, G. Breast cancer. *Lancet* **2021**, *10286*, 1750–1769. [CrossRef]
6. ComŞA, Ş.; CÎMpean, A.M.; Raica, M. The Story of MCF-7 Breast Cancer Cell Line: 40 years of Experience in Research. *Anticancer Res.* **2015**, *35*, 3147.
7. Theodossiou, T.A.; Ali, M.; Grigalavicius, M.; Grallert, B.; Dillard, P.; Schink, K.O.; Olsen, C.E.; Wälchli, S.; Inderberg, E.M.; Kubin, A.; et al. Simultaneous defeat of MCF7 and MDA-MB-231 resistances by a hypericin PDT–tamoxifen hybrid therapy. *NPJ Breast Cancer* **2019**, *5*, 13. [CrossRef]
8. Yin, L.; Duan, J.J.; Bian, X.W.; Yu, S.C. Triple-negative breast cancer molecular subtyping and treatment progress. *Breast Cancer Res.* **2020**, *22*, 61. [CrossRef]
9. da Silva, J.L.; Cardoso Nunes, N.C.; Izetti, P.; de Mesquita, G.G.; de Melo, A.C. Triple negative breast cancer: A thorough review of biomarkers. *Crit. Rev. Oncol. Hematol.* **2020**, *145*, 102855. [CrossRef]
10. Reis-Filho, J.S.; Pusztai, L. Gene expression profiling in breast cancer: Classification, prognostication, and prediction. *Lancet* **2011**, *378*, 1812–1823. [CrossRef]
11. González-Martínez, S.; Pérez-Mies, B.; Carretero-Barrio, I.; Palacios-Berraquero, M.L.; Perez-García, J.; Cortés, J.; Palacios, J. Molecular Features of Metaplastic Breast Carcinoma: An Infrequent Subtype of Triple Negative Breast Carcinoma. *Cancers* **2020**, *12*, 1832. [CrossRef] [PubMed]
12. Waks, A.G.; Winer, E.P. Breast cancer treatment: A review. *JAMA* **2019**, *321*, 288–300. [CrossRef] [PubMed]
13. Montemurro, F.; Nuzzolese, I.; Ponzone, R. Neoadjuvant or adjuvant chemotherapy in early breast cancer? *Expert Opin Pharm.* **2020**, *21*, 1071–1082. [CrossRef]
14. Diaby, V.; Tawk, R.; Sanogo, V.; Xiao, H.; Montero, A.J. A review of systematic reviews of the cost-effectiveness of hormone therapy, chemotherapy, and targeted therapy for breast cancer. *Breast Cancer Res. Treat.* **2015**, *151*, 27–40. [CrossRef] [PubMed]
15. Shigematsu, H.; Fujisawa, T.; Shien, T.; Iwata, H. Omitting surgery for early breast cancer showing clinical complete response to primary systemic therapy. *Jpn. J. Clin. Oncol.* **2020**, *50*, 629–634. [CrossRef]

16. Recht, A.; McArthur, H.; Solin, L.J.; Tendulkar, R.; Whitley, A.; Giuliano, A. Contemporary guidelines in whole-breast irradiation: An alternative perspective. *Int. J. Radiat. Oncol. Biol. Phys.* **2019**, *104*, 567–573. [CrossRef]

17. Castaneda, S.A.; Strasser, J. Updates in the treatment of breast cancer with radiotherapy. *Surg. Oncol. Clin.* **2017**, *26*, 371–382. [CrossRef]

18. Lyseng-Williamson, K.A.; Fenton, C. Docetaxel: A review of its use in metastatic breast cancer. *Drugs* **2005**, *65*, 2513–2531. [CrossRef]

19. Willson, M.L.; Burke, L.; Ferguson, T.; Ghersi, D.; Nowak, A.K.; Wilcken, N. Taxanes for adjuvant treatment of early breast cancer. *Cochrane Database Syst. Rev.* **2019**, *9*, CD004421. [CrossRef]

20. Alqahtani, F.Y.; Aleanizy, F.S.; El Tahir, E.; Alkahtani, H.M.; AlQuadeib, B.T. Chapter Three—Paclitaxel. In *Profiles of Drug Substances, Excipients and Related Methodology*; Brittain, H.G., Ed.; Academic Press: Cambridge, MA, USA, 2019; Volume 44, pp. 205–238.

21. Gallego-Jara, J.; Lozano-Terol, G.; Sola-Martínez, R.A.; Cánovas-Díaz, M.; de Diego Puente, T. A compressive review about Taxol(®): History and future challenges. *Molecules* **2020**, *25*, 5986. [CrossRef]

22. Dehelean, C.A.; Marcovici, I.; Soica, C.; Mioc, M.; Coricovac, D.; Iurciuc, S.; Cretu, O.M.; Pinzaru, I. Plant-derived anticancer compounds as new perspectives in drug discovery and alternative therapy. *Molecules* **2021**, *26*, 1109. [CrossRef] [PubMed]

23. Nacht, M.; Ferguson, A.T.; Zhang, W.; Petroziello, J.M.; Cook, B.P.; Gao, Y.H.; Maguire, S.; Riley, D.; Coppola, G.; Landes, G.M.; et al. Combining serial analysis of gene expression and array technologies to identify genes differentially expressed in breast cancer. *Cancer Res.* **1999**, *59*, 5464–5470.

24. Russo, G.; Zegar, C.; Giordano, A. Advantages and limitations of microarray technology in human cancer. *Oncogene* **2003**, *22*, 6497–6507. [CrossRef] [PubMed]

25. Rao, M.S.; Van Vleet, T.R.; Ciurlionis, R.; Buck, W.R.; Mittelstadt, S.W.; Blomme, E.A.G.; Liguori, M.J. Comparison of RNA-Seq and Microarray Gene Expression Platforms for the Toxicogenomic Evaluation of Liver From Short-Term Rat Toxicity Studies. *Front. Genet.* **2019**, *9*, 636. [CrossRef] [PubMed]

26. Januchowski, R.; Sterzyńska, K.; Zawierucha, P.; Ruciński, M.; Świerczewska, M.; Partyka, M.; Bednarek-Rajewska, K.; Brązert, M.; Nowicki, M.; Zabel, M.; et al. Microarray-based detection and expression analysis of new genes associated with drug resistance in ovarian cancer cell lines. *Oncotarget* **2017**, *8*, 49944–49958. [CrossRef]

27. Sandhu, R.; Parker, J.S.; Jones, W.D.; Livasy, C.A.; Coleman, W.B. Microarray-Based Gene Expression Profiling for Molecular Classification of Breast Cancer and Identification of New Targets for Therapy. *Lab. Med.* **2010**, *41*, 364–372. [CrossRef]

28. Si, W.; Shen, J.; Zheng, H.; Fan, W. The role and mechanisms of action of microRNAs in cancer drug resistance. *Clin. Epigenetics* **2019**, *11*, 25. [CrossRef]

29. Malvia, S.; Bagadi, S.A.R.; Pradhan, D.; Chintamani, C.; Bhatnagar, A.; Arora, D.; Sarin, R.; Saxena, S. Study of Gene Expression Profiles of Breast Cancers in Indian Women. *Sci. Rep.* **2019**, *9*, 10018. [CrossRef]

30. Glinsky, G.V.; Berezovska, O.; Glinskii, A.B. Microarray analysis identifies a death-from-cancer signature predicting therapy failure in patients with multiple types of cancer. *J. Clin. Investig.* **2005**, *115*, 1503–1521. [CrossRef]

31. Yoshimaru, T.; Nakamura, Y.; Katagiri, T. Functional genomics for breast cancer drug target discovery. *J. Hum. Genet.* **2021**, *66*, 927–935. [CrossRef]

32. Kim, G.-E.; Kim, N.I.; Lee, J.S.; Park, M.H.; Kang, K. Differentially Expressed Genes in Matched Normal, Cancer, and Lymph Node Metastases Predict Clinical Outcomes in Patients With Breast Cancer. *Appl. Immunohistochem. Mol. Morphol.* **2020**, *28*, 111. [CrossRef] [PubMed]

33. Kuo, W.-H.; Chang, Y.-Y.; Lai, L.-C.; Tsai, M.-H.; Hsiao, C.K.; Chang, K.-J.; Chuang, E.Y. Molecular Characteristics and Metastasis Predictor Genes of Triple-Negative Breast Cancer: A Clinical Study of Triple-Negative Breast Carcinomas. *PLoS ONE* **2012**, *7*, e45831. [CrossRef] [PubMed]

34. Bellon, J.R.; Burstein, H.J.; Frank, E.S.; Mittendorf, E.A.; King, T.A. Multidisciplinary considerations in the treatment of triple-negative breast cancer. *CA A Cancer J. Clin.* **2020**, *70*, 432–442. [CrossRef] [PubMed]

35. Sotiriou, C.; Pusztai, L. Gene-Expression Signatures in Breast Cancer. *New Engl. J. Med.* **2009**, *360*, 790–800. [CrossRef]

36. Hortobagyi, G.N. Treatment of Breast Cancer. *N. Engl. J. Med.* **1998**, *339*, 974–984. [CrossRef] [PubMed]

37. Wang, Y.T.; Yang, C.H.; Huang, T.Y.; Tai, M.H.; Sie, R.H.; Shaw, J.F. Cytotoxic effects of chlorophyllides in ethanol crude extracts from plant leaves. *Evid Based Complement Altern. Med.* **2019**, *2019*, 9494328. [CrossRef]

38. Hsiang, Y.P.; Wang, Y.T.; Huang, K.S.; Huang, T.Y.; Tai, M.H.; Lin, Y.M.; Yang, C.H.; Shaw, J.F. Facile production of chlorophyllides using recombinant CrCLH1 and their cytotoxicity towards multidrug resistant breast cancer cell lines. *PLoS ONE* **2021**, *16*, e0250565. [CrossRef]

39. Qin, H.; Li, S.; Li, D. An improved method for determining phytoplankton chlorophyll a concentration without filtration. *Hydrobiologia* **2013**, *707*, 81–95. [CrossRef]

40. Chou, Y.L.; Ko, C.Y.; Yen, C.C.; Chen, L.F.; Shaw, J.F. A novel recombinant chlorophyllase1 from *Chlamydomonas reinhardtii* for the production of chlorophyllide derivatives. *J. Agric. Food Chem.* **2015**, *63*, 9496–9503. [CrossRef]

41. Hummon, A.B.; Lim, S.R.; Difilippantonio, M.J.; Ried, T. Isolation and solubilization of proteins after TRIzol extraction of RNA and DNA from patient material following prolonged storage. *Biotechniques* **2007**, *42*, 467–472. [CrossRef]

42. Sheu, C.C.; Tsai, M.J.; Chen, F.W.; Chang, K.F.; Chang, W.A.; Chong, I.W.; Kuo, P.L.; Hsu, Y.L. Identification of novel genetic regulations associated with airway epithelial homeostasis using next-generation sequencing data and bioinformatics approaches. *Oncotarget* **2017**, *8*, 82674–82688. [CrossRef] [PubMed]

43. Livak, K.J.; Schmittgen, T.D. Analysis of relative gene expression data using real-time quantitative PCR and the 2(-Delta Delta C(T)) Method. *Methods* **2001**, *25*, 402–408. [CrossRef]

44. Wang, Y.; Yu, J.; Cui, R.; Lin, J.; Ding, X. Curcumin in Treating Breast Cancer: A Review. *J. Lab. Autom.* **2016**, *21*, 723–731. [CrossRef] [PubMed]

45. Wang, X.; Yang, Y.; An, Y.; Fang, G. The mechanism of anticancer action and potential clinical use of kaempferol in the treatment of breast cancer. *Biomed. Pharm.* **2019**, *117*, 109086. [CrossRef] [PubMed]

46. Yin, R.; Li, T.; Tian, J.X.; Xi, P.; Liu, R.H. Ursolic acid, a potential anticancer compound for breast cancer therapy. *Crit. Rev. Food Sci. Nutr.* **2018**, *58*, 568–574. [CrossRef]

47. Ezzati, M.; Yousefi, B.; Velaei, K.; Safa, A. A review on anti-cancer properties of Quercetin in breast cancer. *Life Sci.* **2020**, *248*, 117463. [CrossRef]

48. Guo, W.; Xu, B.; Wang, X.; Zheng, B.; Du, J.; Liu, S. The Analysis of the Anti-Tumor Mechanism of Ursolic Acid Using Connectively Map Approach in Breast Cancer Cells Line MCF-7. *Cancer Manag. Res.* **2020**, *12*, 3469–3476. [CrossRef]

49. Bachmeier, B.E.; Mohrenz, I.V.; Mirisola, V.; Schleicher, E.; Romeo, F.; Höhneke, C.; Jochum, M.; Nerlich, A.G.; Pfeffer, U. Curcumin downregulates the inflammatory cytokines CXCL1 and -2 in breast cancer cells via NFkappaB. *Carcinogenesis* **2008**, *29*, 779–789. [CrossRef]

50. Li, W.; Liu, J.; Zhang, B.; Bie, Q.; Qian, H.; Xu, W. Transcriptome Analysis Reveals Key Genes and Pathways Associated with Metastasis in Breast Cancer. *OncoTargets Ther.* **2020**, *13*, 323–335. [CrossRef]

51. Sun, N.; Gao, P.; Li, Y.; Yan, Z.; Peng, Z.; Zhang, Y.; Han, F.; Qi, X. Screening and Identification of Key Common and Specific Genes and Their Prognostic Roles in Different Molecular Subtypes of Breast Cancer. *Front. Mol. Biosci.* **2021**, *8*, 619110. [CrossRef]

52. Kim, C.; Kim, B. Anti-Cancer Natural Products and Their Bioactive Compounds Inducing ER Stress-Mediated Apoptosis: A Review. *Nutrients* **2018**, *10*, 1021. [CrossRef] [PubMed]

53. Akram, I.G.; Georges, R.; Hielscher, T.; Adwan, H.; Berger, M.R. The chemokines CCR1 and CCRL2 have a role in colorectal cancer liver metastasis. *Tumor Biol.* **2016**, *37*, 2461–2471. [CrossRef] [PubMed]

54. Korbecki, J.; Kojder, K.; Barczak, K.; Simińska, D.; Gutowska, I.; Chlubek, D.; Baranowska-Bosiacka, I. Hypoxia alters the expression of CC chemokines and CC chemokine receptors in a tumor-a literature review. *Int. J. Mol. Sci.* **2020**, *21*, 5647. [CrossRef] [PubMed]

55. Krishnan, V.; Tallapragada, S.; Schaar, B.; Kamat, K.; Chanana, A.M.; Zhang, Y.; Patel, S.; Parkash, V.; Rinker-Schaeffer, C.; Folkins, A.K.; et al. Omental macrophages secrete chemokine ligands that promote ovarian cancer colonization of the omentum via CCR1. *Commun. Biol.* **2020**, *3*, 524. [CrossRef]

56. Shin, S.Y.; Lee, D.H.; Lee, J.; Choi, C.; Kim, J.Y.; Nam, J.S.; Lim, Y.; Lee, Y.H. C-C motif chemokine receptor 1 (CCR1) is a target of the EGF-AKT-mTOR-STAT3 signaling axis in breast cancer cells. *Oncotarget* **2017**, *8*, 94591–94605. [CrossRef]

57. Liu, F.; Wu, H. CC chemokine receptors in lung adenocarcinoma: The inflammation-related prognostic biomarkers and immunotherapeutic targets. *J. Inflamm. Res.* **2021**, *14*, 267–285. [CrossRef]

58. Emrich, S.M.; Yoast, R.E.; Xin, P.; Zhang, X.; Pathak, T.; Nwokonko, R.; Gueguinou, M.F.; Subedi, K.P.; Zhou, Y.; Ambudkar, I.S.; et al. Cross-talk between N-terminal and C-terminal domains in stromal interaction molecule 2 (STIM2) determines enhanced STIM2 sensitivity. *J. Biol. Chem.* **2019**, *294*, 6318–6332. [CrossRef]

59. Novello, M.J.; Zhu, J.; Feng, Q.; Ikura, M.; Stathopulos, P.B. Structural elements of stromal interaction molecule function. *Cell Calcium* **2018**, *73*, 88–94. [CrossRef]

60. Nelson, H.A.; Roe, M.W. Molecular physiology and pathophysiology of stromal interaction molecules. *Exp. Biol. Med.* **2018**, *243*, 451–472. [CrossRef]

61. Berna-Erro, A.; Jardin, I.; Salido, G.M.; Rosado, J.A. Role of STIM2 in cell function and physiopathology. *J. Physiol.* **2017**, *595*, 3111–3128. [CrossRef]

62. López, E.; Salido, G.M.; Rosado, J.A.; Berna-Erro, A. Unraveling STIM2 function. *J. Physiol. Biochem.* **2012**, *68*, 619–633. [CrossRef] [PubMed]

63. Lasho, T.L.; Finke, C.M.; Zblewski, D.; Patnaik, M.; Ketterling, R.P.; Chen, D.; Hanson, C.A.; Tefferi, A.; Pardanani, A. Novel recurrent mutations in ethanolamine kinase 1 (ETNK1) gene in systemic mastocytosis with eosinophilia and chronic myelomonocytic leukemia. *Blood Cancer J.* **2015**, *5*, e275. [CrossRef] [PubMed]

64. Fontana, D.; Mauri, M.; Renso, R.; Docci, M.; Crespiatico, I.; Røst, L.M.; Jang, M.; Niro, A.; D'Aliberti, D.; Massimino, L.; et al. ETNK1 mutations induce a mutator phenotype that can be reverted with phosphoethanolamine. *Nat. Commun.* **2020**, *11*, 5938. [CrossRef] [PubMed]

65. Qu, D.; Huang, H.; Di, J.; Gao, K.; Lu, Z.; Zheng, J. Structure, functional regulation and signaling properties of Rap2B. *Oncol. Lett.* **2016**, *11*, 2339–2346. [CrossRef] [PubMed]

66. Li, Z.Y.; Li, X.H.; Tian, G.W.; Zhang, D.Y.; Gao, H.; Wang, Z.Y. MAGI1 inhibits the proliferation, migration and invasion of glioma cells. *OncoTargets Ther.* **2019**, *12*, 11281–11290. [CrossRef] [PubMed]

67. Feng, X.; Jia, S.; Martin, T.A.; Jiang, W.G. Regulation and involvement in cancer and pathological conditions of MAGI1, a tight junction protein. *Anticancer Res.* **2014**, *34*, 3251–3256. [PubMed]

68. Shukla, A.; Cloutier, M.; Appiya Santharam, M.; Ramanathan, S.; Ilangumaran, S. The MHC Class-I Transactivator NLRC5: Implications to Cancer Immunology and Potential Applications to Cancer Immunotherapy. *Int. J. Mol. Sci.* **2021**, *22*, 1964. [CrossRef]

69. Cho, S.X.; Vijayan, S.; Yoo, J.S.; Watanabe, T.; Ouda, R.; An, N.; Kobayashi, K.S. MHC class I transactivator NLRC5 in host immunity, cancer and beyond. *Immunology* **2021**, *162*, 252–261. [CrossRef]

70. Noguchi, A.; Takahashi, T. Overview of symptoms and treatment for lysinuric protein intolerance. *J. Hum. Genet.* **2019**, *64*, 849–858. [CrossRef]

71. Bodoy, S.; Sotillo, F.; Espino-Guarch, M.; Sperandeo, M.P.; Ormazabal, A.; Zorzano, A.; Sebastio, G.; Artuch, R.; Palacín, M. Inducible Slc7a7 knockout mouse model recapitulates lysinuric protein intolerance disease. *Int. J. Mol. Sci.* **2019**, *20*, 5294. [CrossRef]

72. Zeng, R.; Wang, Z.; Li, X.; Chen, Y.; Yang, S.; Dong, J. Cyclin-dependent kinase 1-mediated phosphorylation of protein kinase N1 promotes anchorage-independent growth and migration. *Cell. Signal.* **2020**, *69*, 109546. [CrossRef] [PubMed]

73. Venkadakrishnan, V.B.; DePriest, A.D.; Kumari, S.; Senapati, D.; Ben-Salem, S.; Su, Y.; Mudduluru, G.; Hu, Q.; Cortes, E.; Pop, E.; et al. Protein Kinase N1 control of androgen-responsive serum response factor action provides rationale for novel prostate cancer treatment strategy. *Oncogene* **2019**, *38*, 4496–4511. [CrossRef] [PubMed]

74. Cai, H.; Shao, B.; Zhou, Y.; Chen, Z. High expression of TOP2A in hepatocellular carcinoma is associated with disease progression and poor prognosis. *Oncol. Lett.* **2020**, *20*, 232. [CrossRef] [PubMed]

75. Seoane, J.A.; Kirkland, J.G.; Caswell-Jin, J.L.; Crabtree, G.R.; Curtis, C. Chromatin regulators mediate anthracycline sensitivity in breast cancer. *Nat. Med.* **2019**, *25*, 1721–1727. [CrossRef]

76. Wu, Y.M.; Hu, W.; Wang, Y.; Wang, N.; Gao, L.; Chen, Z.Z.; Zheng, W.Q. Exploring novel targets of basal-like breast carcinoma by comparative gene profiling and mechanism analysis. *Breast Cancer Res. Treat.* **2013**, *141*, 23–32. [CrossRef]

77. Weisman, P.S.; Ng, C.K.Y.; Brogi, E.; Eisenberg, R.E.; Won, H.H.; Piscuoglio, S.; De Filippo, M.R.; Ioris, R.; Akram, M.; Norton, L.; et al. Genetic alterations of triple negative breast cancer by targeted next-generation sequencing and correlation with tumor morphology. *Mod. Pathol.* **2016**, *29*, 476–488. [CrossRef]

78. Dillon, J.L.; Mockus, S.M.; Ananda, G.; Spotlow, V.; Wells, W.A.; Tsongalis, G.J.; Marotti, J.D. Somatic gene mutation analysis of triple negative breast cancers. *Breast* **2016**, *29*, 202–207. [CrossRef]

Investigating the Interaction of an Anticancer Nucleolipidic Ru(III) Complex with Human Serum Proteins: A Spectroscopic Study

Claudia Riccardi [1], Antonella Campanella [1], Daniela Montesarchio [1,2], Pompea Del Vecchio [1], Rosario Oliva [1,*] and Luigi Paduano [1,3]

1   Department of Chemical Sciences, University Federico II of Napoli, Via Cintia 21, 80126 Napoli, Italy
2   CINMPIS—Consorzio Interuniversitario Nazionale di Ricerca in Metodologie e Processi Innovativi di Sintesi, Via E. Orabona 4, 70125 Bari, Italy
3   CSGI—Consorzio Interuniversitario per Lo Sviluppo dei Sistemi a Grande Interfase, Via della Lastruccia 3, 50019 Florence, Italy
*   Correspondence: rosario.oliva2@unina.it

Abstract: Ruthenium(III) complexes are very promising candidates as metal-based anticancer drugs, and several studies have supported the likely role of human serum proteins in the transport and selective delivery of Ru(III)-based compounds to tumor cells. Herein, the anticancer nanosystem composed of an amphiphilic nucleolipid incorporating a Ru(III) complex, which we named DoHuRu, embedded into the biocompatible cationic lipid DOTAP, was investigated as to its interaction with two human serum proteins thought to be involved in the mechanism of action of Ru(III)-based anticancer drugs, i.e., human serum albumin (HSA) and human transferrin (hTf). This nanosystem was studied in comparison with the simple Ru(III) complex named AziRu, a low molecular weight metal complex previously designed as an analogue of NAMI-A, decorated with the same ruthenium ligands as DoHuRu but devoid of the nucleolipid scaffold and not inserted in liposomal formulations. For this study, different spectroscopic techniques, i.e., Fluorescence Spectroscopy and Circular Dichroism (CD), were exploited, showing that DoHuRu/DOTAP liposomes can interact with both serum proteins without affecting their secondary structures.

Keywords: ruthenium(III) complexes; anticancer drugs; liposomes; serum proteins; interactions

1. Introduction

Interest in Ru-based anticancer agents has rapidly increased since the discovery of their promising anticancer activity coupled with a significantly lower toxicity compared to known Pt-containing drugs [1–7].

Three Ru(III)-containing complexes have undertaken advanced clinical trials as anticancer drugs, i.e., NAMI-A [8,9], KP1019 [10–13] and its sodium salt analogue known as NKP-1339 [14–17]. Despite their structural similarity (Supplementary Materials, Figure S1), these Ru(III) complexes significantly differ in their bioactivity [18], but share the ability to interact with plasma proteins, particularly serum albumin [19–25], by far the most abundant protein in the plasma, and human transferrin (hTf) [26–30]. In this context, particularly promising were also Ru(III) complexes bearing tetradentate N_2O_2 bis(aminophenolate) ligands, i.e., Salan-type ligands, which exhibited significant cytotoxicity against different cancer cell lines and a strong binding to serum albumin, as determined by steady-state and time-resolved fluorescence spectroscopy [31]. In addition, they were recently proved to strongly interact with lipid bilayers, mimicking mammalian plasma or cancer cell line membrane, leading to a significant increase in the permeability of the lipid vesicles without significantly affecting their structure [32].

Intrigued by the promising properties of these Ru(III)-based anticancer agents, a NAMI-A-like Ru(III) complex—first described by Attia et al. in 1993[33] and then revisited by Walsby and colleagues [34] and by some of us [35,36]—was considered a valuable

starting compound for further optimization. From a structural point of view, this low molecular weight complex, which we named AziRu (Scheme 1), has a pyridine ligand replacing the imidazole moiety of NAMI-A and sodium in place of imidazolium as the counterion. Like NAMI-A, AziRu proved to be poorly cytotoxic on various tumorigenic cells, showing lower IC_{50} values, however, on human breast MCF-7 and cervical HeLa cancer cell lines than its parent compound (Supplementary Materials, Table S1) [35,37].
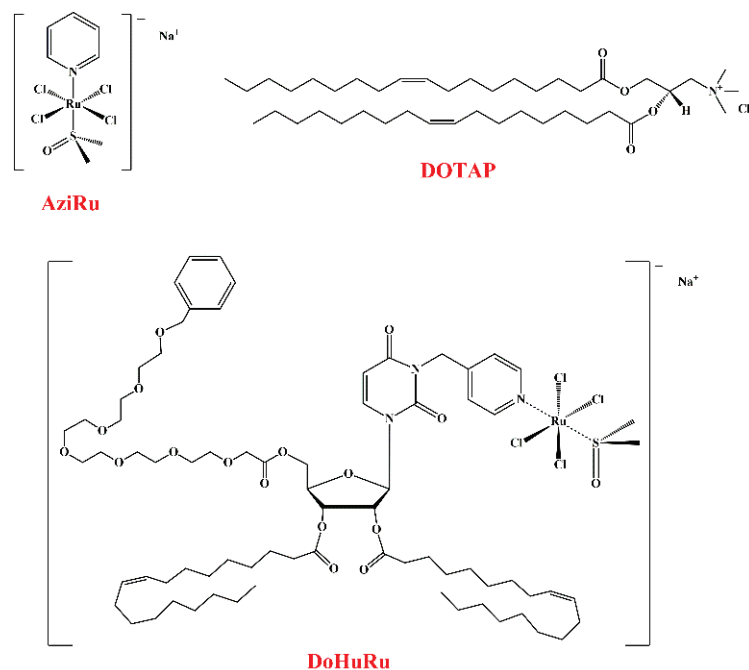
Scheme 1. Chemical structures of the Ru(III) complex AziRu, the cationic lipid DOTAP and nucleolipid-based Ru(III) complex DoHuRu, as indicated.

Analogously to NAMI-A, AziRu undergoes a hydrolysis process in aqueous solutions [38] through a ligand exchange mechanism, mainly involving the replacement of the more labile chloride ligands with water molecules or hydroxide ions, providing more reactive aquo complexes, eventually leading to poly-oxo species formation [39–43].

A detailed insight into the interaction of AziRu with proteins in the solid state could be obtained by analyzing crystals of its complexes with bovine pancreatic ribonuclease A (RNase A) [44] and hen egg white lysozyme (HEWL) [45,46]. In both cases, upon binding, the metal lost all its original ligands, as a consequence of the hydrolysis process, but the protein structure was not significantly altered by the metal complexation [44,45].

Although it is generally accepted that the hydrolysis process activates Ru(III) complexes into more reactive species effectively able to react with potential biomolecular targets, such as proteins or nucleic acids, the premature formation of aquated or poly-oxo species in the extracellular medium can deactivate, or activate too early, most of the administered drug. Thus, the hydrolysis of Ru(III) complexes must be retarded, not to be reached until at least after they are effectively internalized into cells [47].

To this end, AziRu was decorated with nucleolipid [47,48] or aminoacyl lipid scaffolds [49], and then co-aggregated with vesicle-forming lipids as the zwitterionic POPC (1-palmitoyl-2-oleoyl-sn-glycero-3-phosphocholine) or the cationic DOTAP (1,2-dioleoyl-3-trimethylammoniumpropane) (Scheme 1), providing a mini-library of various Ru(III)-loaded nanovectors [47]. The use of highly functionalized scaffolds combined with their co-formulation with biocompatible lipids proved to efficiently increase the stability of AziRu in physiological conditions, by reducing its hydrolysis rate, and also to enhance its cellular internalization [35–37,50–54]. As a major achievement, the proposed design allowed converting a weakly cytotoxic compound, i.e., AziRu, into potent antiproliferative

agents, particularly active on breast cancer cells, without showing significant toxicity on healthy cell lines [35–37,47,50–54]. These formulations proved to be effective and selective also in vivo in breast cancer xenografts mouse models [55,56].

Among the various developed systems, the nucleolipid-based Ru(III) complex called DoHuRu (Scheme 1) [35,51,52], embedded into the biocompatible lipid DOTAP (a schematic representation of the obtained liposome-based nanosystem is reported in Scheme 2) proved to have intriguing biological activity on different cancer cell lines with respect to naked AziRu (Supplementary Materials, Table S1), and was chosen here as a representative compound in the previously prepared compounds library to analyze in more detail their binding properties with serum proteins.

DoHuRu/DOTAP nanosystems
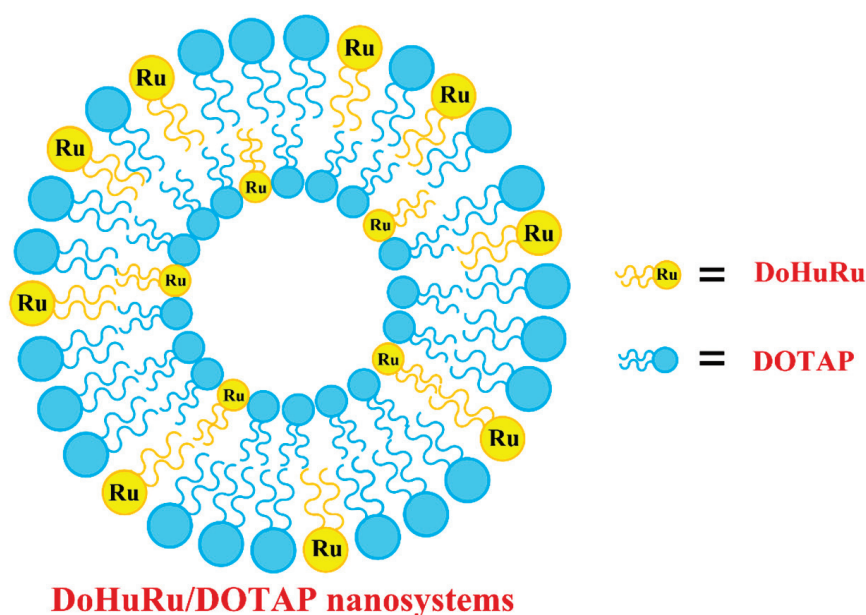
Scheme 2. Schematic representation of liposomal DOTAP-based nanoaggregates containing the nucleolipid-based Ru(III) complex DoHuRu.

Since anticancer Ru(III)-based compounds are usually administered intravenously, extensive in vivo binding to plasma proteins can have significant consequences on the biodistribution and bioavailability of these complexes [57]. These proteins can in fact behave as suitable carriers for ruthenium inside cells through permeation and/or endocytosis mechanisms, providing selective tumor targeting [58–62].

In detail, human serum albumin (HSA) is the major soluble protein constituent of the circulatory system, identified as a well-established transporter of both endogenous and exogenous species in the bloodstream, including drugs [63,64]. In addition, HSA is known to accumulate in tumors as a consequence of enhanced permeability and retention effect [60–62].

In turn, to promote their rapid growth, some malignant cells require high levels of iron(III) and for this reason upregulate the expression of transferrin receptors on their surface. In this context, human transferrin (hTf) could have a role in vivo as a natural carrier for metal complexes, and hTf receptors can be exploited to provide a privileged route for delivering drugs to tumor cells [59,65].

Considering that both albumin and transferrin are involved in the mechanism of action proposed for NAMI-A, in this work we studied the interaction of the effective anticancer DoHuRu/DOTAP formulations with HSA and hTf, using the naked AziRu complex and the pure lipid DOTAP as controls.

Aiming at obtaining precious information on the mechanism of action of the proposed liposome-containing nucleolipid-based Ru(III) complexes, fluorescence and Circular Dichroism (CD) spectroscopies data were exploited here. In detail, fluorescence spec-

troscopy was used to obtain information on the interaction between the proteins and AziRu or the Ru(III)-containing vesicles. In contrast, CD measurements were exploited to verify the effect on the secondary structures of the target proteins produced by binding with AziRu or DoHuRu/DOTAP liposomes.

2. Results and Discussion

2.1. Preparation and Characterization of Ru(III) Complexes and Liposomes

As a first step, the Ru(III) complexes AziRu [34,38] and DoHuRu [35,51,52] were synthesized following previously described procedures. Then, DoHuRu/DOTAP liposomes were prepared through the thin film protocol by dissolving known weighed amounts of both components and mixing them at the desired Ru complex: lipid 30:70 molar ratio. In parallel, also bare DOTAP liposomes were prepared as control. After preparation, as described in Material and Methods and in Mangiapia et al. [51], these liposomes were analyzed by Dynamic Light Scattering (DLS) measurements. In Supplementary Materials, Figure S2, the hydrodynamic radius distribution functions for the two preparations are shown. The hydrodynamic radius of the DOTAP and DoHuRu/DOTAP nanosystems proved to be in the 70–100 nm range, which is the typical range of unilamellar vesicles, in accordance with previous investigations [51]. DLS measurements fully confirmed a monodisperse liposome dispersion for both bare DOTAP and DoHuRu/DOTAP formulations.

2.2. Study of the Interaction of AziRu and DoHuRu/DOTAP Liposomes with Serum Proteins

Fluorescence quenching is a widely used technique to gain information on the interaction of serum proteins with drugs or small ligands [66,67]. The fluorescence emission of proteins comes from the three aromatic residues tryptophan, tyrosine, and phenylalanine. Phenylalanine has a very low quantum yield, and the fluorescence of tyrosine is almost totally quenched if it is ionized or close to an amino group, a carboxyl group, or a tryptophan. Hence, the fluorescence of proteins (and thus also of HSA and hTf) is almost exclusively due to the tryptophan emission alone. Particularly, the emission spectrum of HSA mainly derives from a single tryptophan residue located at the 214 position in the subdomain IIA, while that of hTf is essentially due to 8 Trp residues. In addition to the common sources of quenching, in the case of hTf, the two iron ions strongly affect the hTf emission spectrum [68]. Changes in the intrinsic fluorescence intensity of HSA and hTf proteins—due to spatial reorganization of the tryptophan residues—are evidenced when small molecules are bound to the proteins [69].

The nude AziRu complex has been used as a reference in this study to probe the effects of the liposomal carrier in interactions with human serum proteins. The fluorescence spectra at 20 °C of HSA and hTf in the absence and presence of AziRu are reported in Figure 1A,B, respectively.

Upon excitation at 280 nm, HSA and hTf showed strong fluorescence emission bands centered at 345 and 330 nm, respectively. On the other hand, AziRu has no intrinsic fluorescence upon excitation at the same wavelength. It is important to note that AziRu absorbs at the used excitation wavelength and, to a much lesser extent, at the wavelength of emission of the proteins (see Supplementary Materials, Figure S3 for the UV/Vis spectrum of AziRu in PBS buffer). Thus, an inner filter effect could be active and should be corrected. However, since at the used AziRu concentrations, the absorbance of the ligand is quite low, the lack of correction can lead to a slight overestimation of the binding constants. The addition of increasing amounts of AziRu (in the 5–150 μM range) to each protein, kept at a fixed concentration of 5 μM, produced a marked fluorescence quenching, that represents clear evidence of interaction. Similar outcomes were reported for several Ru complexes [70–72], and also for the binding of NAMI-A to hTf [28,29] where, in all cases, a decrease of fluorescence intensity was observed upon binding. It is important to note that the observed decrease of intensity suggests that the Trp residues are localized not far from the binding pocket of AziRu, otherwise no changes in the intensity could be observed. Finally, the binding of AziRu to both proteins did not cause any change in the emission

maximum and shape of the peaks, indicating that upon binding, the microenvironment surrounding the Trp residues was not affected by the small ligand.
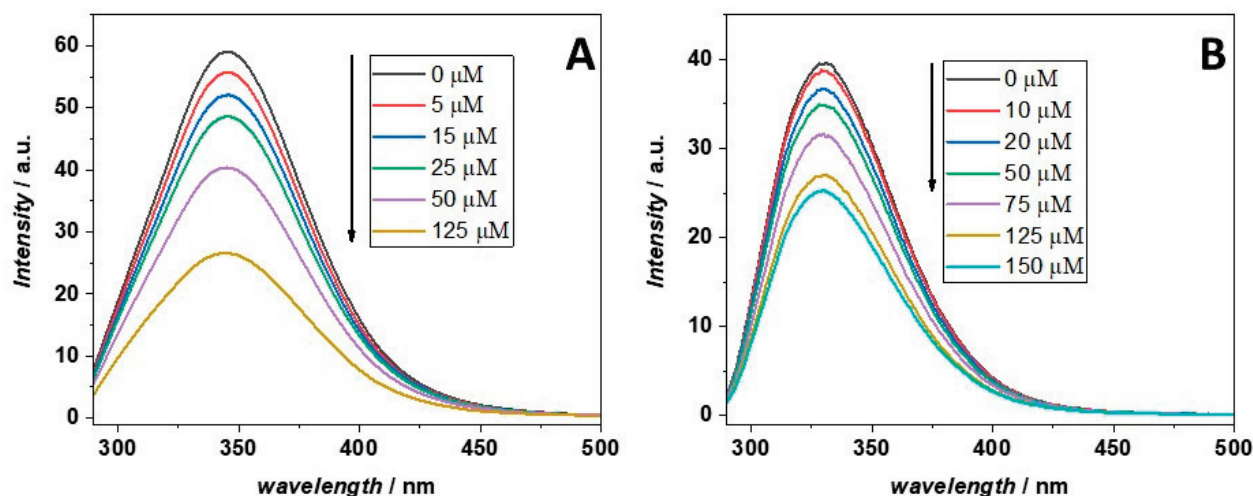
Figure 1. Fluorescence emission spectra at 20 °C of (**A**) HSA and (**B**) hTf in the absence and presence of increasing concentrations of AziRu, as reported in the legend. The spectra of the proteins in the absence of the ligand are reported in black. The concentrations of HSA and hTf were kept constant at 5 μM. The excitation wavelength was set at 280 nm. The fluorescence emission of HSA and hTf are centered at 345 and 330 nm, respectively. The arrows indicate the direction of the effects due to addition of increasing concentrations of AziRu.

To evaluate the strength of the complex formed between AziRu and each serum protein, fluorescence quenching data were analyzed by the Stern–Volmer Equation (1):

$$\frac{F_0}{F} = 1 + K_{SV}[Q] = 1 + K_S[Q] \tag{1}$$

where F_0 and F are the steady-state fluorescence intensities of the proteins in the absence and presence of the quencher AziRu, respectively. K_{SV} is the Stern–Volmer quenching constant and $[Q]$ is the concentration of the quencher, i.e., AziRu in the present case. As will be shown later, the quenching mechanism was found to be static. Thus, the Stern–Volmer constant is, in this case, a quenching constant due to a static process (i.e., complex formation) and, thus, can be indicated also as K_S (where S is for static). In Figure 2, the Stern–Volmer plots obtained at the temperature of 20 °C for the titration of a solution of HSA and hTf with a solution of AziRu are reported.
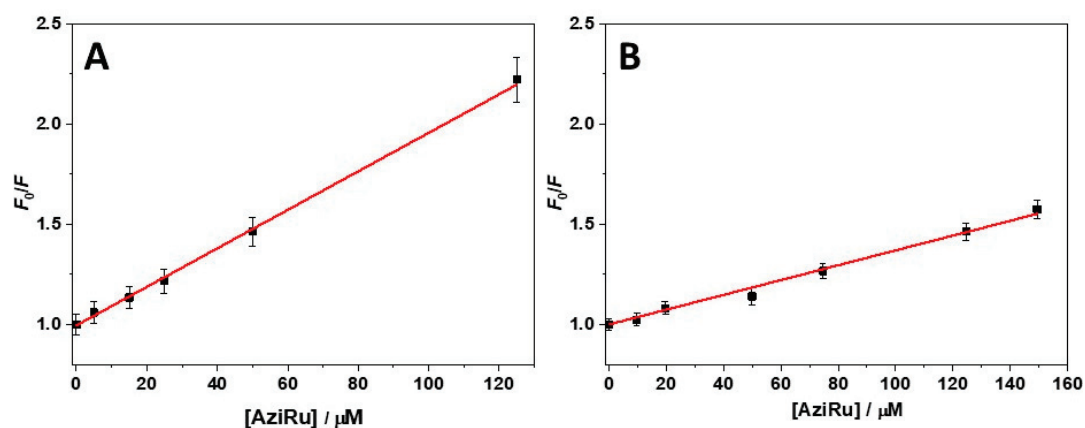
Figure 2. Stern–Volmer plots for the binding of AziRu with (**A**) HSA and (**B**) hTf at 20 °C. The red lines represent the best fit of experimental data according to equation 1 reported in the text.

As evidenced by the data reported in Figure 2, a linear plot was obtained in both cases, allowing the data fitting by using equation 1. The obtained values of K_{SV} for the interaction of AziRu with HSA and hTf are $(9.7 \pm 0.5) \times 10^3$ M^{-1} and $(3.7 \pm 0.7) \times 10^3$ M^{-1}, respectively (Table 1). These data revealed a higher ability of AziRu to quench the fluorescence of HSA than that of hTf, suggesting a higher affinity of AziRu for HSA than hTf. However, quenching due to the interaction of AziRu with proteins can be dynamic (deactivation of the excited state through collisional events) or static (complex formation in the ground state) in nature [73]. Static and dynamic quenching can be distinguished on the basis of their dependence from temperature. Higher temperatures result in faster diffusion and hence a larger amount of collisional quenching. Thus, if dynamic quenching is the only active mode, an increase in temperature should lead to an increase of the value of K_{SV}. In contrast, when the quenching is static, an increase in temperature should not favor the complex formation, and a decrease of K_{SV} is normally observed [73]. In Supplementary Materials, Figure S4, the Stern–Volmer plots recorded at 10 and 20 °C are shown. In Table 1 the corresponding values of K_{SV} are collected.

Table 1. Stern–Volmer constants for the complex formation between AziRu and serum proteins obtained at 10 °C and 20 °C.

System	T/°C	K_{SV}/M^{-1}
HSA-AziRu	10	$(1.1 \pm 0.5) \times 10^4$
HSA-AziRu	20	$(9.7 \pm 0.5) \times 10^3$
hTf-AziRu	10	$(5.1 \pm 1.0) \times 10^3$
hTf-AziRu	20	$(3.7 \pm 0.7) \times 10^3$

As reported in Table 1, the value of K_{SV} decreased on increasing the temperature for both proteins, i.e., K_{SV} (20 °C) < K_{SV} (10 °C), thus indicating that the quenching mechanism is essentially static. Finally, in supporting the static nature of the observed decrease in fluorescence, it is to be considered that the K_{SV} values for dynamic quenching are usually ~10^1 M^{-1}. In contrast, for static quenching, the constants are higher at least by one order of magnitude. Thus, one can conclude that the observed quenching is indeed due to the formation of a complex between the ligand and the proteins. Consequently, the value of K_{SV} is equivalent to the binding constant (K_b), defined as the ratio between the complex concentration and the product of the concentrations of the free ligand and free protein. Collectively, the reported data showed that AziRu had a higher affinity for HSA compared to hTf. However, it is important that both obtained K_{SV} values are quite small. This finding agrees with the hypothesized role of these proteins in serum, allowing the transport of small compounds, but also their release.

The static nature of the quenching mechanism, as demonstrated above, allows us treating the Stern–Volmer constants as binding constants for the complex formation. However, in the Stern–Volmer analysis, a 1:1 complex is assumed to be formed. The linearity of the Stern–Volmer plots reported in Figure 2 is strong evidence that the stoichiometry is effectively 1:1, otherwise deviations from linearity should be observed. However, in order to determine the binding stoichiometry (n) and further support the 1:1 complex formation, the Stern–Volmer equation can be rearranged in the following form (Equation (2)) [74]:

$$\log\left(\frac{F_0 - F}{F}\right) = \log K_b + n\log[Q] \tag{2}$$

where F_0 and F are the fluorescence intensities in the absence and presence of the ligand, respectively, $[Q]$ is the ligand concentration, K_b is the apparent binding constant, and n is the stoichiometry defined as the number of ligand molecules interacting with one molecule of protein. The calculated K_b and n at 20 °C are reported in Table 2. In turn, the corresponding plots of $\log(F_0 - F/F)$ vs. $\log[Q]$ are shown in Supplementary Materials, Figure S5.

Table 2. Values of the apparent binding constant (K_b) and stoichiometry (n) for the complex formation between AziRu and each serum protein obtained at 20 °C.

System	K_b/M^{-1}	N
HSA-AziRu	$(1.2 \pm 0.3) \times 10^4$	0.94 ± 0.20
hTf-AziRu	$(2.3 \pm 0.5) \times 10^3$	1.1 ± 0.2

The obtained values showed that both proteins formed a 1:1 complex, with obtained values of K_b in excellent agreement with the values of K_{SV} reported above, completely validating the Stern–Volmer analysis reported above [75].

Next, in order to probe specific interactions between the studied proteins and the Ru-containing vesicles, the same fluorescence analysis carried out on AziRu was performed with the DoHuRu/DOTAP liposomes. However, to take into account possible interactions between the proteins and pure DOTAP vesicles, both protein solutions were titrated first with a pure DOTAP vesicles suspension, and, after each addition, the corresponding fluorescence spectrum was acquired. The spectra obtained for HSA/DOTAP and hTf/DOTAP systems are shown in Supplementary Materials, Figure S6A and S6B, respectively.

For both proteins, a small but significant decrease of their fluorescence intensity was observed upon addition of DOTAP vesicles. In particular, at the highest DOTAP concentration tested, the fluorescence intensity drop in the case of HSA was around 16% and for hTf around 5%. In addition, no wavelength shift of the fluorescence maximum (346 nm for HSA and 332 nm for hTf) was observed. The reported data indicated that both proteins could interact with DOTAP vesicles. However, due to the low change in the fluorescence intensity, the interaction appeared overall very weak, particularly in the case of hTf.

The same titration experiments were repeated by titrating the HSA and hTf solutions with the DoHuRu/DOTAP 30:70 vesicles suspension (Figure 3A and Figure 3B, respectively).
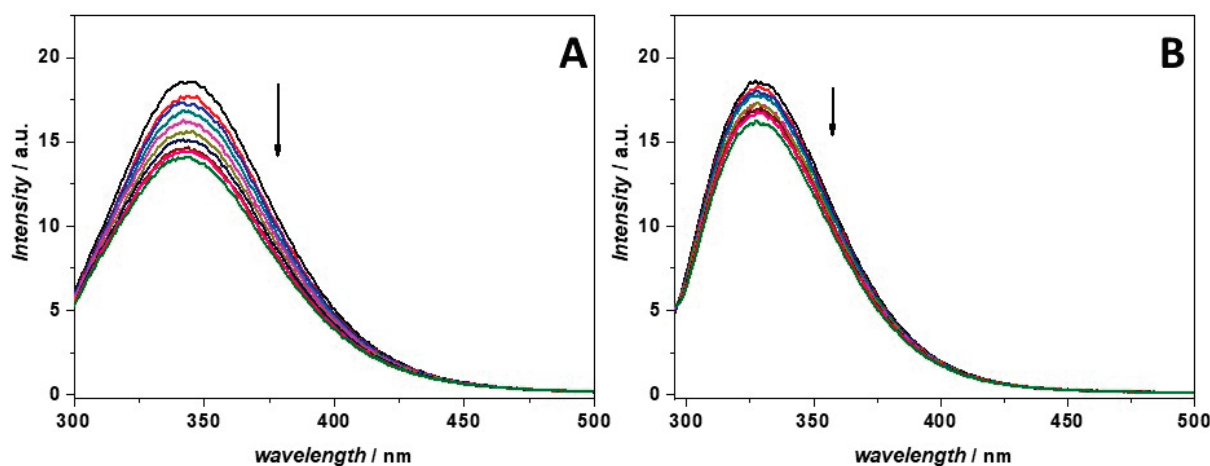
Figure 3. Fluorescence emission spectra of (**A**) HSA and (**B**) hTf in the absence (black spectra) and in the presence of increasing DoHuRu/DOTAP vesicles concentrations (colored spectra). The arrows indicate the direction of the effects due to increasing concentrations of DoHuRu/DOTAP. The excitation wavelength was set at 280 nm. All the experiments were performed in a 1-cm path length quartz cuvette at the temperature of 20 °C.

For the HSA titration (Figure 3A), a marked decrease of the fluorescence intensity upon addition of the Ru-containing vesicles was observed, reaching a 24% fluorescence intensity drop at the highest vesicle concentration explored. In contrast, the decrease in fluorescence intensity at 332 nm observed for hTf after titration with the Ru-containing vesicles was less pronounced (around 12%). The observed decrease could be due to the complex formation between the proteins and the vesicles, which affects the fluorescence emission of the

tryptophan residues. In addition, in both cases, no shift of the emission maximum was observed, indicating that the microenvironment surrounding the Trp residues was not affected by the interaction process, thus suggesting that the interaction probably occurred without any conformational change of the proteins.

In order to quantitatively describe the complex formation with the Ru-containing vesicles, these data were treated by the Stern–Volmer analysis as carried out with AziRu. The Stern–Volmer plots obtained from the titrations experiments on the serum proteins with DOTAP and DoHuRu/DOTAP are reported in Supplementary Materials, Figure S7, while the values of the corresponding Stern–Volmer constants are reported in Table 3.

Table 3. Stern–Volmer constants for the complex formation between DOTAP and DoHuRu/DOTAP vesicles with serum proteins (HSA and hTf) obtained at 20 °C.

Scheme 1	T/°C	K_{SV}/M^{-1}
HSA-DOTAP	20	$(2.9 \pm 0.7) \times 10^3$
HSA-DoHuRu/DOTAP	20	$(5.5 \pm 0.5) \times 10^3$
hTf-DOTAP	20	$(0.98 \pm 0.10) \times 10^3$
hTf-DoHuRu/DOTAP	20	$(2.3 \pm 0.6) \times 10^3$

Inspection of the data reported in Table 3 revealed that HSA is able to interact with DOTAP vesicles alone. This agrees with the known ability of serum proteins like BSA and HSA to interact with a wide variety of ligands, and primarily fatty acids [76]. When DOTAP was coformulated with the nucleolipid-based Ru(III) complex DoHuRu, an increase of the K_{SV} value was observed (from 2.9×10^3 M^{-1} to 5.5×10^3 M^{-1}), clearly demonstrating that the interaction of liposomes with proteins is enhanced when the nucleolipidic Ru complex is incorporated in the vesicles. It is interesting to note that the presence of a lipid formulation does not seem to dramatically limit the ability of HSA to interact with the Ru complex, since the K_{SV} value for DoHuRu/DOTAP vesicles is only ca. two-fold lower with respect to that found with AziRu.

As far as hTf is concerned, this protein proved to be able to interact with pure DOTAP vesicles, but with a lower affinity with respect to HSA (K_{SV} of 0.98×10^3 M^{-1} vs. 2.9×10^3 M^{-1}). Interestingly, the vesicles containing the Ru complex showed enhanced ability to interact with hTf compared to pure DOTAP liposomes, also highlighting in this case the presence of specific interactions with the Ru complex. Indeed, the value of K_{SV} for the complex between hTf and DoHuRu/DOTAP liposomes (2.3×10^3 M^{-1}) was comparable, within the experimental error, to the one obtained for AziRu (3.7×10^3 M^{-1}).

Finally, the hydrodynamic radius distribution of DOTAP and DoHuRu/DOTAP vesicles in the presence of the two serum proteins was also verified by means of dynamic light scattering experiments. In Supplementaty Materials, Figures S8 and S9 the hydrodynamic radius distribution functions for vesicles in the absence and presence of HSA and hTf are reported, respectively. HSA affects the size distribution of DOTAP and DoHuRu/DOTAP vesicles in a concentration dependent manner, leading to a broader size distribution centered at higher R_H values compared to those in the absence of the protein. Interestingly, this effect is evident for DoHuRu/DOTAP vesicles at a lower protein concentration with respect to the bare DOTAP, which could be attributable to the higher affinity of HSA for the nucleolipid Ru complex. In contrast, the size distribution of DOTAP vesicles is not affected at all by the presence of hTf. This is expected for a low affinity binding event. Surprisingly, hTf showed a marked effect on DoHuRu/DOTAP vesicles. As in the case of HSA, at the highest protein concentration used, the size distribution is centered at higher R_H values compared to those in the absence of protein, leading to bigger vesicles. However, it is remarkable that the integrity of liposomes is always preserved upon proteins binding.

2.3. Conformational Behavior of Serum Proteins in the Presence of the Ru-Containing Complexes

Changes in the protein secondary structure induced by ligand binding and/or interaction with vesicles are typically studied by recording CD spectra in the far-UV region [77].

The CD spectra of free HSA and hTf in the absence and presence of increasing concentrations of AziRu are shown in Figure 4A and Figure 4B, respectively.
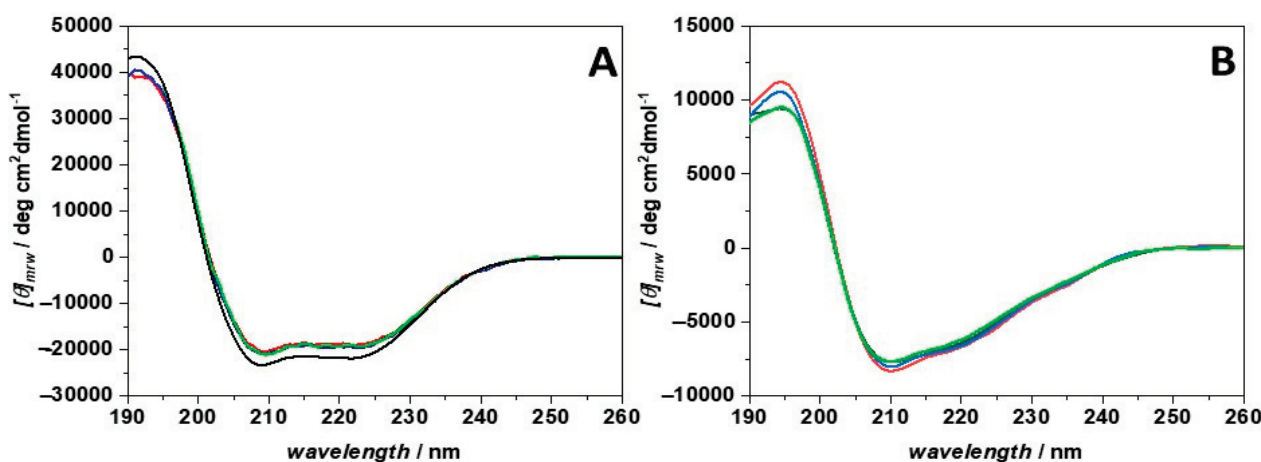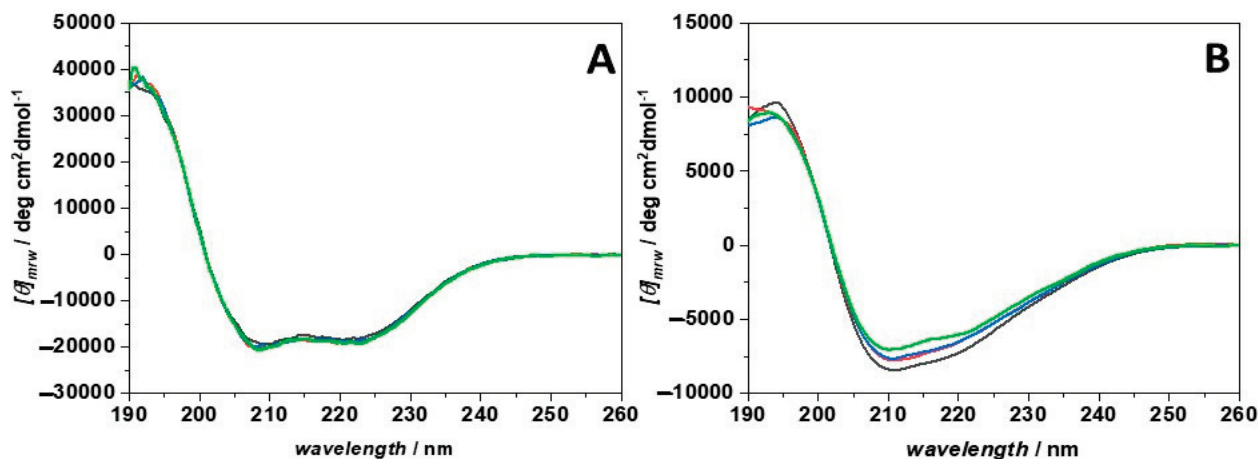

Figure 4. Far UV-CD spectra of (**A**) HSA and (**B**) hTf recorded in the absence (black spectra) and in the presence of increasing concentrations of AziRu. The concentrations of both proteins were 1.5 μM. The AziRu concentrations were: 1.5 μM (red spectra), 7.5 μM (blue spectra) and 75 μM (green spectra). The spectra were recorded at 20 °C by using a 0.1 cm path length quartz cuvette.

The CD spectrum of HSA showed two negative bands at 208 and 220 nm, and a positive band around 195 nm, indicative of the presence of an α-helix structure [77], in agreement with previously reported CD data and the deposited protein crystal structure [76,78]. Conversely, the CD spectrum of hTf showed a distinct minimum around 210 nm, a weak negative band around 220 nm, and a positive band at 195 nm. These spectral features suggested that also this protein adopts an α-helical conformation. However, the intensities of the two minima are not the same, indicating that not all the protein is folded in a helix conformation. Indeed, an inspection of the hTf crystal structure revealed the presence of a consistent portion of the protein folded in a twisted β-sheet conformation, as well as turns and disordered regions [79], thus explaining the obtained CD spectrum.

For HSA, in the presence of AziRu (at a ligand-to-protein ratio of 1:1, 5:1, and 50:1), only a modest decrease in the intensity of these negative bands occurred, suggesting that the interaction with this small ligand does not sensibly affect the overall secondary structure of the protein. Similar results were obtained for hTf. Thus, even if AziRu can bind both proteins, the integrity of their secondary structures is preserved upon complex formation.

The same experiments were also performed in the presence of the DoHuRu/DOTAP liposomes, to verify possible conformational changes of the proteins imposed by the complexation with Ru(III) containing vesicles. In Figure 5, the CD spectra of HSA (panel A) and hTf (panel B) in the absence and presence of increasing concentrations of DoHuRu/DOTAP are shown.

Interestingly, the addition of the vesicles to HSA did not affect at all the secondary structure of the protein, even at the very high vesicles/protein concentration ratio of 100:1. This result agrees with previous studies showing that the secondary structure of HSA is only slightly affected by interaction with vesicles [80,81]. In sharp contrast, the CD spectra recorded for hTf suggested that some, even if small, conformational changes are produced in the protein upon interaction with DoHuRu/DOTAP vesicles. Indeed, the intensities of the two negative bands had already decreased at the lowest vesicle concentrations investigated (1.5 and 15 μM, i.e., at a 1:1 and 10:1 vesicles/protein concentration ratio). Upon increasing the vesicles concentration at 75 μM, the changes were more evident. Conversely, the intensity of the positive band at 195 nm was not affected by the interaction process. These findings suggested that the helical content of the protein decreased upon interaction, but to a low extent. Conversely, the CD spectrum of hTf (Supplementary Materials, Figure S10) was not affected at all by the presence of DOTAP vesicles. This

result highlights the key role played by the nucleolipid-based Ru complex in driving the interaction process, inducing small conformational changes in the protein structure. In conclusion, the overall secondary structure of hTf is only marginally affected by the presence of DoHuRu/DOTAP vesicles.

Figure 5. Far UV-CD spectra of (**A**) HSA and (**B**) hTf recorded in the absence (black spectra) and in the presence of increasing concentrations of DoHuRu/DOTAP. The concentrations of both proteins were 1.5 μM. For HSA, the vesicles concentrations were 45 μM (red spectrum), 75 μM (blue spectrum), and 150 μM (green spectrum). For hTf, vesicles concentrations were 1.5 μM (red spectrum), 15 μM (blue spectrum) and 75 μM (green spectrum). The spectra were recorded at 20 °C by using a 0.1 cm path length quartz cuvette.

3. Experimental Section

3.1. Materials and Methods

The following were all purchased from Sigma Aldrich and used as received: 1,2-dioleoyl-3-trimethylammonium-propane (chloride salt) (DOTAP, MW = 698.55 g/mol, >99%); albumin from human serum (≥99%); transferrin human (≥98%); and chloroform (for HPLC, ≥99.9%). All the experiments were carried out in a pseudo-physiological phosphate buffer solution (NaCl = 137 mM, KCl = 2.7 mM, Na_2HPO_4 = 10 mM, KH_2PO_4 = 2 mM, pH = 7.4).

3.2. Synthesis of AziRu and DoHuRu Ru(III) Complexes

AziRu was prepared by reacting pyridine with Na^+ [*trans*-$RuCl_4(DMSO)_2$]$^-$ in anhydrous acetonitrile, following a previously described protocol [34,38]. The nucleolipidic ruthenium complex, named DoHuRu, was prepared by reacting in stoichiometric amounts the starting nucleolipid, named DoHu [48], with the Ru complex Na^+ [*trans*-$RuCl_4(DMSO)_2$]$^-$ following previously reported procedures [35,51,52].

The desired salt was obtained in almost quantitative yields and in pure form, as confirmed by TLC, NMR, and ESI-MS analysis, whose results were in all cases in accordance with literature data.

FTIR-ATR of AziRu: significant vibrational frequencies (cm^{-1}): 3018. 2 (w) [ν (*CH*)], 1667.1 (s) [ν (*C=N*)], 1317.2 (w) [δ (*CH*)]; 1080.3 (s) [ν (*S=O*) (*DMSO*)]; 1025.8 (s) [ρ (*CH*)]; 764.0 (s) [ν (*C-S*)].

3.3. Preparation of DOTAP and DoHuRu/DOTAP Vesicles

For the preparation of the vesicles composed of 1,2-dioleoyl-3-trimethylammonium-propane (chloride salt) (DOTAP), 0.346 mL (0.00101 mmol) of a DOTAP standard solution in chloroform (2.92 mM) was transferred in a round-bottom glass vial. A thin film was obtained through evaporation of the solvent under a gentle flow of dry N_2 for at least 24 h. The film was hydrated with the phosphate buffer and dispersed in solution through

sonication at 59 kHz at 40 °C for at least 40 min. The vesicles suspension was then extruded through polycarbonate membranes of 100 nm pore size, at least 11 times. For the preparation of vesicles composed of DoHuRu and DOTAP, 2.47 mL (0.000721 mmol) of a DoHuRu (MW = 1620 g/mol) standard solution (0.292 mM), and 0.592 mL (0.00179 mmol) of a DOTAP standard solution (3.02 mM) were introduced in a round bottom glass vial. Then, the following steps were identical to the ones used for the preparation of bare DOTAP liposomes.

3.4. Preparation of the Protein Solutions

The solutions of HSA (M.W. 66 kDa g mol^{-1}) and hTF (M.W. 80 kDa) were prepared by dissolving the lyophilized powder directly in PBS buffer, pH 7.4. Their concentrations were determined spectrophotometrically by evaluating their absorbance at 280 nm, using the following extinction coefficient at 280 nm: $\varepsilon(280) = 35700$ M^{-1} cm^{-1} and $\varepsilon(280) = 85240$ M^{-1} cm^{-1} for HSA and hTf, respectively.

3.5. Dynamic Light Scattering Experiments

Dynamic light scattering (DLS) analyses were performed with a setup composed of Photocor compact goniometer, a SMD 6000 Laser Quantum 50 mW light source operating at 5325 Å, and a PMT and correlator obtained from Correlator.com. All the measurements were performed at (25.00 + 0.05) °C by using a thermostat bath. The concentration of the used lipids was 0.5 mM in all the performed experiments. The concentrations of HSA were 0.12 μM and 0.45 μM. In turn, the concentrations of hTf were 0.15 μM and 0.45 μM. DLS measurements were performed 24 h after each addition of protein solution into the vesicles suspension.

3.6. Fluorescence Spectroscopy Experiments

The interaction between serum proteins HSA and hTf with AziRu, DOTAP and DoHuRu/DOTAP vesicles was studied by following the intrinsic fluorescence changes of proteins induced by the addition of each compound. The titrations were performed by recording spectra of a protein solution at fixed concentration (5 μM) containing increasing Ru(III) complex or DOTAP amounts ranging from 0 to ~10^{-4} M. AziRu stock solutions were prepared by weight. All the samples were prepared in a saline sodium phosphate buffer (PBS) solution at pH 7.4.

Steady state fluorescence measurements were performed by means of a FluoroMax-4 fluorescence spectrophotometer (Horiba, Edison, NJ, USA), using a quartz micro cuvette (1 cm in excitation and 0.2 cm in emission) of 400 μL volume. The excitation wavelength was 280 nm, and the emission spectra were recorded in the 290–500 nm range. The excitation and emission slits were 3 nm, and the temperature was set to 20 °C and 10 °C. All protein fluorescence spectra were corrected by subtraction of the buffer alone.

3.7. Circular Dichroism Experiments

Circular dichroism (CD) spectra were acquired in the far UV-region (190–250 nm) using a Jasco J-715 spectropolarimeter (from Jasco Corporation, Tokyo, Japan) under constant nitrogen flow. The temperature was controlled by a Peltier type temperature control system (Model PTC-348WI). The spectra were recorded in a 0.1 cm quartz cuvette, with 4 s response time, 2 nm bandwidth, and 20 nm/min scan rate. Protein concentrations between 0.05–0.1 mg/mL were typically used. The spectra were measured in the absence and presence of increasing concentrations of AziRu or DoHuRu/DOTAP vesicles in a 20 mM sodium phosphate buffer, pH 7.4. Spectra were recorded at a fixed temperature of 20 °C, averaged, and corrected for the buffer baseline.

4. Conclusions

With the aim of better understanding the mechanism of action of Ru(III)-based anticancer drugs, we herein investigated via spectroscopic measurements the interaction

occurring between the nucleolipidic Ru complex DoHuRu embedded in DOTAP liposomes and two serum proteins, i.e., HSA and hTf, using the NAMI-A-like low molecular weight complex AziRu as a reference.

Fluorescence analysis gave solid evidence of the binding of the DoHuRu/DOTAP liposomes, and of AziRu as well, with both proteins. Indeed, in all cases the addition of the Ru(III)-containing compounds to the target proteins caused a quenching of the protein intrinsic fluorescence, which increased on increasing the amount of ligand, indicative of the formation of stable ligand-protein complexes. Notably, the quantitative analysis of the fluorescence data revealed binding constants in the 10^3–10^4 M^{-1} range, indicative of a moderate affinity. This is fully consistent with the postulated behaviour of these proteins, able to sequester anticancer metal-based drugs in the bloodstream and then release them in the proximity of tumour tissues. These fluorescence analysis data were further corroborated by CD spectroscopy.

Circular dichroism spectra of the studied proteins were essentially similar in shape if registered in the absence or presence of each complex, suggesting that the binding did not alter their secondary structures.

Taken together, our results highlight the fact that DoHuRu/DOTAP liposomes can also interact extensively with serum proteins, similarly to NAMI-A-like complex AziRu and in line with other anticancer Ru(III) complexes described in the literature. This binding can have important consequences for the pharmacokinetics of these metal complexes. Indeed, the formation of Ru(III) complex/serum protein adducts is of potential pharmaceutical interest, considering the putative in vivo role of these proteins as carriers allowing the selective delivery of metal complexes to cancer cells and tissues.

References

1. Alessio, E. Thirty years of the drug candidate NAMI-A and the myths in the field of ruthenium anticancer compounds: A personal perspective. *Eur. J. Inorg. Chem.* **2017**, *2017*, 1549–1560. [CrossRef]

2. Zheng, K.; Wu, Q.; Wang, C.; Tan, W.; Mei, W. Ruthenium(II) complexes as potential apoptosis inducers in chemotherapy. *Anticancer. Agents Med. Chem.* **2017**, *17*, 29–39. [CrossRef] [PubMed]

3. Thota, S.; Rodrigues, D.A.; Crans, D.C.; Barreiro, E.J. Ru(II) compounds: Next-generation anticancer metallotherapeutics? *J. Med. Chem.* **2018**, *61*, 5805–5821. [CrossRef]

4. Meier-Menches, S.M.; Gerner, C.; Berger, W.; Hartinger, C.G.; Keppler, B.K. Structure-activity relationships for ruthenium and osmium anticancer agents-towards clinical development. *Chem. Soc. Rev.* **2018**, *47*, 909–928. [CrossRef]

5. Coverdale, J.P.C.; Laroiya-McCarron, T.; Romero-Canelón, I. Designing ruthenium anticancer drugs: What have we learnt from the key drug candidates? *Inorganics* **2019**, *7*, 31. [CrossRef]

6. Lee, S.Y.; Kim, C.Y.; Nam, T.G. Ruthenium complexes as anticancer agents: A brief history and perspectives. *Drug Des. Devel. Ther.* **2020**, *14*, 5375–5392. [CrossRef] [PubMed]

7. Ferraro, M.G.; Piccolo, M.; Misso, G.; Santamaria, R.; Irace, C. Bioactivity and development of small non-platinum metal-based chemotherapeutics. *Pharmaceutics* **2022**, *14*, 954. [CrossRef] [PubMed]

8. Rademaker-Lakhai, J.M.; Van Den Bongard, D.; Pluim, D.; Beijnen, J.H.; Schellens, J.H.M. A phase I and pharmacological study with imidazolium-trans-DMSO-imidazole-tetrachlororuthenate, a novel ruthenium anticancer agent. *Clin. Cancer Res.* **2004**, *10*, 3717–3727. [CrossRef]

9. Leijen, S.; Burgers, S.A.; Baas, P.; Pluim, D.; Tibben, M.; Van Werkhoven, E.; Alessio, E.; Sava, G.; Beijnen, J.H.; Schellens, J.H.M. Phase I/II study with ruthenium compound NAMI-A and gemcitabine in patients with non-small cell lung cancer after first line therapy. *Investig. New Drugs* **2015**, *33*, 201–214. [CrossRef] [PubMed]

10. Jakupec, M.A.; Arion, V.B.; Kapitza, S.; Reisner, E.; Eichinger, A.; Pongratz, M.; Marian, B.; BGraf von Keyserlingk, N.; Keppler, B.K. KP1019 (FFC14A) from bench to bedside: Preclinical and early clinical development- an overview. *Int. J. Clin. Pharmacol. Ther.* **2005**, *43*, 595–596. [CrossRef] [PubMed]

11. Hartinger, C.G.; Zorbas-Seifried, S.; Jakupec, M.A.; Kynast, B.; Zorbas, H.; Keppler, B.K. From bench to bedside - preclinical and early clinical development of the anticancer agent indazolium trans-[tetrachlorobis(1H-indazole)ruthenate(III)] (KP1019 or FFC14A). *J. Inorg. Biochem.* **2006**, *100*, 891–904. [CrossRef] [PubMed]

12. Hartinger, C.G.; Jakupec, M.A.; Zorbas-Seifried, S.; Groessl, M.; Egger, A.; Berger, W.; Zorbas, H.; Dyson, P.J.; Keppler, B.K. KP1019, a new redox-active anticancer agent—Preclinical development and results of a clinical phase I study in tumor patients. *Chem. Biodivers.* **2008**, *5*, 2140–2155. [CrossRef]

13. Lentz, F.; Drescher, A.; Lindauer, A.; Henke, M.; Hilger, R.A.; Hartinger, C.G.; Scheulen, M.E.; Dittrich, C.; Keppler, B.K.; Jaehde, U. Pharmacokinetics of a novel anticancer ruthenium complex (KP1019, FFC14A) in a phase I dose-escalation study. *Anticancer Drugs* **2009**, *20*, 97–103. [CrossRef]

14. Dickson, N.R.; Jones, S.F.; Burris, H.A.; Ramanathan, R.K.; Weiss, G.J.; Infante, J.R.; Bendell, J.C.; McCulloch, W.; Von Hoff, D.D. A phase I dose-escalation study of NKP-1339 in patients with advanced solid tumors refractory to treatment. *J. Clin. Oncol.* **2011**, *29*, 2607. [CrossRef]

15. Thompson, D.S.; Weiss, G.J.; Jones, S.F.; Burris, H.A.; Ramanathan, R.K.; Infante, J.R.; Bendell, J.C.; Ogden, A.; Von Hoff, D.D. NKP-1339: Maximum tolerated dose defined for first-in-human GRP78 targeted agent. *J. Clin. Oncol.* **2012**, *30*, 3033. [CrossRef]

16. Trondl, R.; Heffeter, P.; Kowol, C.R.; Jakupec, M.A.; Berger, W.; Keppler, B.K. NKP-1339, the first ruthenium-based anticancer drug on the edge to clinical application. *Chem. Sci.* **2014**, *5*, 2925–2932. [CrossRef]

17. Burris, H.A.; Bakewell, S.; Bendell, J.C.; Infante, J.; Jones, S.F.; Spigel, D.R.; Weiss, G.J.; Ramanathan, R.K.; Ogden, A.; Von Hoff, D. Safety and activity of IT-139, a ruthenium-based compound, in patients with advanced solid tumours: A first-in-human, open-label, dose-escalation phase I study with expansion cohort. *ESMO Open* **2016**, *1*, e000154. [CrossRef] [PubMed]

18. Alessio, E.; Messori, L. Anticancer drug candidates face-to-face: A case story in medicinal inorganic chemistry. *Molecules* **2019**, *24*, 1995. [CrossRef] [PubMed]

19. Messori, L.; Orioli, P.; Vullo, D.; Alessio, E.; Iengo, E. A spectroscopic study of the reaction of NAMI, a novel ruthenium(III) anti-neoplastic complex, with bovine serum albumin. *Eur. J. Biochem.* **2000**, *267*, 1206–1213. [CrossRef] [PubMed]

20. Bergamo, A.; Messori, L.; Piccioli, F.; Cocchietto, M.; Sava, G. Biological role of adduct formation of the ruthenium(III) complex NAMI-A with serum albumin and serum transferrin. *Invest. New Drugs* **2003**, *21*, 401–411. [CrossRef]

21. Bytzek, A.K.; Boeck, K.; Hermann, G.; Hann, S.; Keppler, B.K.; Hartinger, C.G.; Koellensperger, G. LC- and CZE-ICP-MS approaches for the in vivo analysis of the anticancer drug candidate sodium trans-[tetrachloridobis(1H-indazole)ruthenate(III)] (KP1339) in mouse plasma. *Metallomics* **2011**, *3*, 1049–1055. [CrossRef] [PubMed]

22. Dömötör, O.; Hartinger, C.G.; Bytzek, A.K.; Kiss, T.; Keppler, B.K.; Enyedy, E.A. Characterization of the binding sites of the anticancer ruthenium(III) complexes KP1019 and KP1339 on human serum albumin via competition studies. *J. Biol. Inorg. Chem.* **2013**, *18*, 9–17. [CrossRef]

23. Zhang, Y.; Ho, A.; Yue, J.; Kong, L.; Zhou, Z.; Wu, X.; Yang, F.; Liang, H. Structural basis and anticancer properties of ruthenium-based drug complexed with human serum albumin. *Eur. J. Med. Chem.* **2014**, *86*, 449–455. [CrossRef] [PubMed]

24. Webb, M.I.; Walsby, C.J. Albumin binding and ligand-exchange processes of the Ru(III) anticancer agent NAMI-A and its bis-DMSO analogue determined by ENDOR spectroscopy. *Dalton Trans.* **2015**, *44*, 17482–17493. [CrossRef] [PubMed]

25. Bijelic, A.; Theiner, S.; Keppler, B.K.; Rompel, A. X-ray structure analysis of indazolium trans-[tetrachlorobis(1H-indazole)ruthenate(III)] (KP1019) bound to human serum albumin reveals two ruthenium binding sites and provides insights into the drug binding mechanism. *J. Med. Chem.* **2016**, *59*, 5894–5903. [CrossRef]

26. Messori, L.; Kratz, F.; Alessio, E. The interaction of the antitumor aomplexes Na[trans-RuCl($_4$) (DMSO)(Im)] and Na[trans-RuCl($_4$)(DMSO)(Ind)] with apotransferrin: A spectroscopic study. *Met. Based Drugs* **1996**, *3*, 614045. [CrossRef]

27. Pongratz, M.; Schluga, P.; Jakupec, M.A.; Arion, V.B.; Hartinger, C.G.; Allmaier, G.; Keppler, B.K. Transferrin binding and transferrin-mediated cellular uptake of the ruthenium coordination compound KP1019, studied by means of AAS, ESI-MS and CD spectroscopy. *J. Anal. At. Spectrom.* **2004**, *19*, 46–51. [CrossRef]

28. Mazuryk, O.; Kurpiewska, K.; Lewinski, K.; Stochel, G.; Brindell, M. Interaction of apo-transferrin with anticancer ruthenium complexes NAMI-A and its reduced form. *J. Inorg. Biochem.* **2012**, *116*, 11–18. [CrossRef]

29. Spiewak, K.; Brindell, M. Impact of low- and high-molecular-mass components of human serum on NAMI-A binding to transferrin. *J. Biol. Inorg. Chem.* **2015**, *20*, 695–703. [CrossRef]

30. Ciambellotti, S.; Pratesi, A.; Severi, M.; Ferraro, G.; Alessio, E.; Merlino, A.; Messori, L. The NAMI A-human ferritin system: A biophysical characterization. *Dalton Trans.* **2018**, *47*, 11429–11437. [CrossRef] [PubMed]

31. Matos, C.P.; Valente, A.; Marques, F.; Adão, P.; Paula Robalo, M.; De Almeida, R.F.M.; Pessoa, J.C.; Santos, I.; Helena Garcia, M.; Tomaz, A.I. New polydentate Ru(III)-salan complexes: Synthesis, characterization, anti-tumour activity and interaction with human serum proteins. *Inorganica Chim. Acta* **2013**, *394*, 616–626. [CrossRef]

32. Starosta, R.; Santos, T.C.; Dinis de Sousa, A.F.; Santos, M.S.; Corvo, M.L.; Tomaz, A.I.; de Almeida, R.F. Assessing the role of membrane lipids in the action of ruthenium(III) anticancer compounds. *Front. Mol. Biosci.* **2023**, *9*, 1059116. [CrossRef]

33. Alessio, E.; Balducci, G.; Lutman, A.; Mestroni, G.; Calligaris, M.; Attia, W.M. Synthesis and characterization of two new classes of ruthenium(III)-sulfoxide complexes with nitrogen donor ligands (L): Na[trans-RuCl$_4$(R$_2$SO)(L)] and mer, cis-RuCl$_3$(R$_2$SO)(R$_2$SO)(L). The crystal structure of Na[trans-RuCl$_4$(DMSO)(NH$_3$)]·2DMSO, Na[trans-RuCl. *Inorg. Chim. Acta* **1993**, *203*, 205–217. [CrossRef]

34. Webb, M.I.; Chard, R.A.; Al-Jobory, Y.M.; Jones, M.R.; Wong, E.W.Y.; Walsby, C.J. Pyridine analogs of the antimetastatic Ru(III) complex NAMI-A targeting non-covalent interactions with albumin. *Inorg. Chem.* **2012**, *51*, 954–966. [CrossRef]

35. Mangiapia, G.; D'Errico, G.; Simeone, L.; Irace, C.; Radulescu, A.; Di Pascale, A.; Colonna, A.; Montesarchio, D.; Paduano, L. Ruthenium-based complex nanocarriers for cancer therapy. *Biomaterials* **2012**, *33*, 3770–3782. [CrossRef] [PubMed]

36. Simeone, L.; Mangiapia, G.; Vitiello, G.; Irace, C.; Colonna, A.; Ortona, O.; Montesarchio, D.; Paduano, L. Cholesterol-based nucleolipid-ruthenium complex stabilized by lipid aggregates for antineoplastic therapy. *Bioconjugate Chem.* **2012**, *23*, 758–770. [CrossRef]

37. Vitiello, G.; Luchini, A.; D'Errico, G.; Santamaria, R.; Capuozzo, A.; Irace, C.; Montesarchio, D.; Paduano, L. Cationic liposomes as efficient nanocarriers for the drug delivery of an anticancer cholesterol-based ruthenium complex. *J. Mater. Chem. B* **2015**, *3*, 3011–3023. [CrossRef] [PubMed]

38. Musumeci, D.; Rozza, L.; Merlino, A.; Paduano, L.; Marzo, T.; Massai, L.; Messori, L.; Montesarchio, D. Interaction of anticancer Ru(III) complexes with single stranded and duplex DNA model systems. *Dalton Trans.* **2015**, *44*, 13914–13925. [CrossRef] [PubMed]

39. Ravera, M.; Baracco, S.; Cassino, C.; Zanello, P.; Osella, D. Appraisal of the redox behaviour of the antimetastatic ruthenium(III) complex [ImH][RuCl$_4$(DMSO)(Im)], NAMI-A. *Dalton Trans.* **2004**, 2347–2351. [CrossRef]

40. Chen, J.; Chen, L.; Liao, S.; Zheng, K.; Ji, L. A theoretical study on the hydrolysis process of the antimetastatic ruthenium(III) complex NAMI-A. *J. Phys. Chem. B* **2007**, *111*, 7862–7869. [CrossRef]

41. Vargiu, A.V.; Robertazzi, A.; Magistrato, A.; Ruggerone, P.; Carloni, P. The hydrolysis mechanism of the anticancer ruthenium drugs NAMI-A and ICR investigated by DFT-PCM calculations. *J. Phys. Chem. B* **2008**, *112*, 4401–4409. [CrossRef]

42. Pashkunova-Martic, I.; Losantos, B.C.; Kandler, N.; Keppler, B. Studies of KP46 and KP1019 and the hydrolysis product of KP1019 in lipiodol emulsions: Preparation and initial characterizations as potential theragnostic agents. *Curr. Drug Deliv.* **2018**, *15*, 134–142. [CrossRef]

43. Pal, M.; Nandi, U.; Mukherjee, D. Detailed account on activation mechanisms of ruthenium coordination complexes and their role as antineoplastic agents. *Eur. J. Med. Chem.* **2018**, *150*, 419–445. [CrossRef] [PubMed]

44. Vergara, A.; Russo Krauss, I.; Montesarchio, D.; Paduano, L.; Merlino, A. Investigating the ruthenium metalation of proteins: X-ray structure and Raman microspectroscopy of the complex between RNase A and AziRu. *Inorg. Chem.* **2013**, *52*, 10714–10716. [CrossRef]

45. Vergara, A.; D'Errico, G.; Montesarchio, D.; Paduano, L.; Merlino, A. Interaction of anticancer ruthenium compounds with proteins high-resolution X-ray structures and raman microscopy studies of the adduct between hen egg white lysozyme and AziRu. *Inorg. Chem.* **2013**, *52*, 4157–4159. [CrossRef]

46. Caterino, M.; Herrmann, M.; Merlino, A.; Riccardi, C.; Montesarchio, D.; Mroginski, M.A.; Musumeci, D.; Ruffo, F.; Paduano, L.; Hildebrandt, P.; et al. On the pH-modulated Ru-based prodrug activation mechanism. *Inorg. Chem.* **2019**, *58*, 1216–1223. [CrossRef] [PubMed]

47. Riccardi, C.; Musumeci, D.; Irace, C.; Paduano, L.; Montesarchio, D. Ru(III) complexes for anticancer therapy: The importance of being nucleolipidic. *Eur. J. Org. Chem.* **2017**, *2017*, 1100–1119. [CrossRef]

48. Simeone, L.; Mangiapia, G.; Irace, C.; Di Pascale, A.; Colonna, A.; Ortona, O.; De Napoli, L.; Montesarchio, D.; Paduano, L. Nucleolipid nanovectors as molecular carriers for potential applications in drug delivery. *Mol. Biosyst.* **2011**, *7*, 3075–3086. [CrossRef] [PubMed]

49. Riccardi, C.; Musumeci, D.; Capuozzo, A.; Irace, C.; King, S.; Russo Krauss, I.; Paduano, L.; Montesarchio, D. "Dressing up" an old drug: An aminoacyl lipid for the functionalization of Ru(III)-based anticancer agents. *ACS Biomater. Sci. Eng.* **2018**, *4*, 163–174. [CrossRef] [PubMed]

50. Montesarchio, D.; Mangiapia, G.; Vitiello, G.; Musumeci, D.; Irace, C.; Santamaria, R.; D'Errico, G.; Paduano, L. A new design for nucleolipid-based Ru(III) complexes as anticancer agents. *Dalton Trans.* **2013**, *42*, 16697–16708. [CrossRef]

51. Mangiapia, G.; Vitiello, G.; Irace, C.; Santamaria, R.; Colonna, A.; Angelico, R.; Radulescu, A.; D'Errico, G.; Montesarchio, D.; Paduano, L. Anticancer cationic ruthenium nanovectors: From rational molecular design to cellular uptake and bioactivity. *Biomacromolecules* **2013**, *14*, 2549–2560. [CrossRef] [PubMed]

52. Irace, C.; Misso, G.; Capuozzo, A.; Piccolo, M.; Riccardi, C.; Luchini, A.; Caraglia, M.; Paduano, L.; Montesarchio, D.; Santamaria, R. Antiproliferative effects of ruthenium-based nucleolipidic nanoaggregates in human models of breast cancer in vitro: Insights into their mode of action. *Sci. Rep.* **2017**, *7*, 45236–45249. [CrossRef] [PubMed]

53. Piccolo, M.; Misso, G.; Ferraro, M.G.; Riccardi, C.; Capuozzo, A.; Zarone, M.R.; Maione, F.; Trifuoggi, M.; Stiuso, P.; D'Errico, G.; et al. Exploring cellular uptake, accumulation and mechanism of action of a cationic Ru-based nanosystem in human preclinical models of breast cancer. *Sci. Rep.* **2019**, *9*, 7006. [CrossRef] [PubMed]

54. Riccardi, C.; Musumeci, D.; Trifuoggi, M.; Irace, C.; Paduano, L.; Montesarchio, D. Anticancer ruthenium (III) complexes and Ru(III) containing nanoformulations: An update on the mechanism of action and biological activity. *Pharmaceuticals* **2019**, *12*, 146. [CrossRef] [PubMed]

55. Piccolo, M.; Ferraro, M.G.; Raucci, F.; Riccardi, C.; Saviano, A.; Russo Krauss, I.; Trifuoggi, M.; Caraglia, M.; Paduano, L.; Montesarchio, D.; et al. Safety and efficacy evaluation in vivo of a cationic nucleolipid nanosystem for the nanodelivery of a Ruthenium (III) complex with superior anticancer bioactivity. *Cancers.* **2021**, *13*, 5164. [CrossRef]

56. Ferraro, M.G.; Piccolo, M.; Misso, G.; Maione, F.; Montesarchio, D.; Caraglia, M.; Paduano, L.; Santamaria, R.; Irace, C. Breast cancer chemotherapeutic options: A general overview on the preclinical validation of a multi-target Ruthenium(III) complex lodged in nucleolipid nanosystems. *Cells* **2020**, *9*, 1412. [CrossRef]

57. Timerbaev, A.R.; Hartinger, C.G.; Aleksenko, S.S.; Keppler, B.K. Interactions of antitumor metallodrugs with serum proteins: Advances in characterization using modern analytical methodology. *Chem. Rev.* **2006**, *106*, 2224–2248. [CrossRef]

58. Mackenzie, E.L.; Iwasaki, K.; Tsuji, Y. Intracellular iron transport and storage: From molecular mechanisms to health implications. *Antioxidants Redox Signal.* **2008**, *10*, 997–1030. [CrossRef]

59. Guo, W.; Zheng, W.; Luo, Q.; Li, X.; Zhao, Y.; Xiong, S.; Wang, F. Transferrin serves as a mediator to deliver organometallic ruthenium(II) anticancer complexes into cells. *Inorg. Chem.* **2013**, *52*, 5328–5338. [CrossRef]

60. Hairat, S.; Zaki, M. Half sandwiched rutheniumII complexes: En route towards the targeted delivery by Human Serum Albumin (HSA). *J. Organomet. Chem.* **2021**, *937*, 121732. [CrossRef]

61. Spada, A.; Emami, J.; Tuszynski, J.A.; Lavasanifar, A. The uniqueness of albumin as a carrier in nanodrug delivery. *Mol. Pharm.* **2021**, *18*, 1862–1894. [CrossRef]

62. Cho, H.; Jeon, S.I.; Ahn, C.H.; Shim, M.K.; Kim, K. Emerging albumin-binding anticancer drugs for tumor-targeted drug delivery: Current understandings and clinical translation. *Pharmaceutics* **2022**, *14*, 728. [CrossRef]

63. Kratz, F. Albumin as a drug carrier: Design of prodrugs, drug conjugates and nanoparticles. *J. Control. Release* **2008**, *132*, 171–183. [CrossRef] [PubMed]

64. Elsadek, B.; Kratz, F. Impact of albumin on drug delivery - new applications on the horizon. *J. Control. Release* **2012**, *157*, 4–28. [CrossRef]

65. Johnsen, K.B.; Burkhart, A.; Melander, F.; Kempen, P.J.; Vejlebo, J.B.; Siupka, P.; Nielsen, M.S.; Andresen, T.L.; Moos, T. Targeting transferrin receptors at the blood-brain barrier improves the uptake of immunoliposomes and subsequent cargo transport into the brain parenchyma. *Sci. Rep.* **2017**, *7*, 10396. [CrossRef] [PubMed]

66. Van De Weert, M. Fluorescence quenching to study protein-ligand binding: Common errors. *J. Fluoresc.* **2010**, *20*, 625–629. [CrossRef]

67. Heller, G.T.; Aprile, F.A.; Vendruscolo, M. Methods of probing the interactions between small molecules and disordered proteins. *Cell. Mol. Life Sci.* **2017**, *74*, 3225–3243. [CrossRef]

68. James, N.G.; Byrne, S.L.; Steere, A.N.; Smith, V.C.; MacGillivray, R.T.A.; Mason, A.B. Inequivalent contribution of the five tryptophan residues in the C-Lobe of human serum transferrin to the fluorescence increase when iron is released. *Biochemistry* **2009**, *48*, 2858–2867. [CrossRef] [PubMed]

69. Neelam, S.; Gokara, M.; Sudhamalla, B.; Amooru, D.G.; Subramanyam, R. Interaction studies of coumaroyltyramine with human serum albumin and its biological importance. *J. Phys. Chem. B* **2010**, *114*, 3005–3012. [CrossRef]

70. Tan, C.; Liu, J.; Li, H.; Zheng, W.; Shi, S.; Chen, L.; Ji, L. Differences in structure, physiological stability, electrochemistry, cytotoxicity, DNA and protein binding properties between two Ru(III) complexes. *J. Inorg. Biochem.* **2008**, *102*, 347–358. [CrossRef]

71. Martínez, A.; Suárez, J.; Shand, T.; Magliozzo, R.S.; Sánchez-Delgado, R.A. Interactions of arene-Ru(II)-chloroquine complexes of known antimalarial and antitumor activity with human serum albumin (HSA) and transferrin. *J. Inorg. Biochem.* **2011**, *105*, 39–45. [CrossRef] [PubMed]

72. Riccardi, C.; Piccolo, M.; Ferraro, M.G.; Graziano, R.; Musumeci, D.; Trifuoggi, M.; Irace, C.; Montesarchio, D. Bioengineered lipophilic Ru (III) complexes as potential anticancer agents. *Biomater. Adv.* **2022**, *139*, 213016. [CrossRef] [PubMed]

73. Lakowicz, J.R. *Principles of Fluorescence Spectroscopy*; Kluwer, Ed.; Plenum: New York, NY, USA, 1999.

74. Zhou, B.; Qi, Z.D.; Xiao, Q.; Dong, J.X.; Zhang, Y.Z.; Liu, Y. Interaction of loratadine with serum albumins studied by fluorescence quenching method. *J. Biochem. Biophys. Methods* **2007**, *70*, 743–747. [CrossRef] [PubMed]

75. Yan, X.; Chen, J.Q.; Hu, M.L.; Sakiyama, H.; Muddassir, M.; Liu, J.Q. Syntheses, structures and mechanisms of interactions with DNA of two new 20-core silver(I) complexes with different ligands. *Inorganica Chim. Acta* **2023**, *546*, 121297. [CrossRef]

76. Guizado, T.R.C. Analysis of the structure and dynamics of human serum albumin. *J. Mol. Model.* **2014**, *20*, 2450. [CrossRef] [PubMed]

77. Kelly, S.M.; Jess, T.J.; Price, N.C. How to study proteins by circular dichroism. *Biochim. Biophys. Acta—Proteins Proteomics* **2005**, *1751*, 119–139. [CrossRef]

78. Kamali, A.; Jahmidi-Azizi, N.; Oliva, R.; Winter, R. Deep sea osmolytes in action: Their effect on protein–ligand binding under high pressure stress. *Phys. Chem. Chem. Phys.2* **2022**, *24*, 17966–17978. [CrossRef]

79. Adams, T.E.; Mason, A.B.; He, Q.Y.; Halbrooks, P.J.; Briggs, S.K.; Smith, V.C.; MacGillivray, R.T.A.; Everse, S.J. The position of arginine 124 controls the rate of iron release from the N-lobe of human serum transferrin: A structural study. *J. Biol. Chem.* **2003**, *278*, 6027–6033. [CrossRef]

80. Chen, R.; Choudhary, P.; Schurr, R.N.; Bhattacharya, P.; Brown, J.M.; Chun Ke, P. Interaction of lipid vesicle with silver nanoparticle-serum albumin protein corona. *Appl. Phys. Lett.* **2012**, *100*, 013703–013703-4. [CrossRef]

81. Patel, R.; Ahmad Wani, F.; Mahfooz, F.; Mishra, P.; Abrar Siddiquee, M. Interaction of human serum albumin with diclofenac incorporated in catanionic vesicles. *Mater. Today Proc.* **2019**, *36*, 736–742. [CrossRef]

82. Tan, C.; Wu, S.; Lai, S.; Wang, M.; Chen, Y.; Zhou, L.; Zhu, Y.; Lian, W.; Peng, W.; Ji, L.; et al. Synthesis, structures, cellular uptake and apoptosis-inducing properties of highly cytotoxic ruthenium-norharman complexes. *Dalton Trans.* **2011**, *40*, 8611–8621. [CrossRef]

Article

Rubus Capped Zinc Oxide Nanoparticles Induce Apoptosis in MCF-7 Breast Cancer Cells

Blassan P. George *, Naresh K. Rajendran, Nicolette N. Houreld and Heidi Abrahamse

Laser Research Centre, University of Johannesburg, Johannesburg 2028, South Africa
* Correspondence: blassang@uj.ac.za

Abstract: *Rubus fairholmianus* (RF) has widely been used to treat various ailments, including pain, diabetes, and cancer. Zinc oxide nanoparticles (ZnO NPs) have drawn attention in modern healthcare applications. Hence, we designed this study to synthesize zinc oxide (ZnO) nanoparticles using *R. fairholmianus* root extract to investigate its synergistic cytotoxic effect on MCF-7 cells and explore the possible cell death mechanism. ZnO NPs were synthesized via green synthesis using *R. fairholmianus* root extract, and the effect on MCF-7 cells was determined by looking at cellular morphology, proliferation, cytotoxicity, apoptosis, and reactive oxygen species (ROS). The results showed that cellular proliferation was reduced following treatment with *R. fairholmianus* capped zinc oxide nanoparticles (RFZnO NPs), while cytotoxicity and ROS were increased. There was also an increase in apoptosis as indicated by the significant increase in cytoplasmic cytochrome c and caspase 3/7 (markers of apoptosis), as well as increased levels of pro-apoptotic proteins (p53, Bax) and decreased levels of anti-apoptotic protein (Bcl-2). In conclusion, these results showed that RFZnO NPs induce apoptosis in breast cancer cells via a mitochondria-mediated caspase-dependent apoptotic pathway and suggest the use of acetone root extract of *R. fairholmianus* for the treatment of cancer-related ailments.

Keywords: *Rubus*; zinc oxide; nanoparticles; MCF-7; apoptosis; caspases

1. Introduction

Cancer is an abnormal and uncontrolled growth of cells resulting in an increased mass or lump of cells called tumors. Cancer is a serious health concern worldwide with significant morbidity and mortality [1]. Various well-established treatments are available to treat cancer, though the side effects and high cost make the fight against cancer difficult, particularly in developing countries. Chemotherapy is one of the effective cancer treatments, but it still displays minimal specificity and is limited by the severity of the side effects and toxicity toward healthy cells. It has become a challenge to find an effective therapy for cancer treatments [2]. Thus, traditional treatment methods need to be combined with modern drug delivery technology to enhance the treatment outcome and lessen the toxic side effects [3].

Nanomedicine is a promising anticancer niche area for developing novel diagnostic and therapeutic strategies. Green synthesis of nanoparticles (NPs) is a new strategy used for various biomedical applications. This is a cost-effective, eco-friendly, and biocompatible approach for the synthesis of NPs with varied biological properties [4]. Green synthesis uses plants and microbes and allows large-scale production of NPs without extra impurities, and such NPs show enhanced catalytic activity and limit the use of expensive and toxic chemically synthesized NPs [5]. Various plant parts (flower, leaf, stem, and root) have been used for the synthesis of NPs, and the phytocompounds in the plant extracts can act as both stabilizing and reducing agents during the process [6–8]. Recently, numerous metal oxide NPs such as copper (II) oxide (CuO), titanium (II) oxide (TiO), and zinc oxide (ZnO) have been synthesized through a green approach, and ZnO NPs have become popular in biomedical, molecular recognition, optics, and electronic applications due to the inexpensive, easy,

and safe synthetic protocols [9–11]. The United States Food and Drug Administration (FDA) has approved ZnO as a safe metal oxide which showed semiconducting, catalytic, anti-inflammatory, and wound healing properties with a large band gap and high excitation binding energy [12–14]. Zinc is also an essential micronutrient in the human body and is vital for health and disease control, bone metabolism, and immune function [15–17]. Zinc-dependent proteins also play an important role in transcriptional regulation, cell death, and DNA repair [18,19].

The diverse genus *Rubus* includes over 750 species and is found on many continents [20]. *Rubus* species have been used in folk medicine due to their varied pharmacological properties. *R. fairholmianus* is also used for various ailments by tribal people [21–23]. We have reported the in vitro cytotoxic effects of *R. fairholmianus* on colorectal, breast, and lung cancer and melanoma cells [24–26]. The apoptotic efficacy of silver NPs conjugated with *R. fairholmianus* and the bioactive compounds of *R. fairholmianus* were studied on MCF-7 breast cancer cells [27,28]. We have recently reported on the biosynthesis of ZnO NPs using *R. fairholmianus* root extract and their antibacterial effects [29]. To our knowledge, no study assessing the in vitro anticancer effects of ZnO NPs capped with *R. fairholmianus* root extract in MCF-7 breast cancer cells has been reported. The anticancer potential of RFZnO NPs in MCF-7 cells was determined by analyzing cytotoxicity, proliferation, reactive oxygen species (ROS), and apoptotic cell death.

2. Results

2.1. Morphological Assessment, Cell Proliferation, and Cytotoxicity Analysis

The changes in the shape of treated and untreated breast cancer cells were analyzed. As compared to healthy untreated breast cancer cells, treated cells showed significant morphological variations such as irregular shape and rounding, as well as detachment from the culture plate and decreased confluency. The RF- and RFZnO-treated cells showed significant morphological changes compared to ZnO NP-treated and untreated cells (Figure 1a–e). The proliferation of breast cancer cells following the treatments was evaluated using the adenosine triphosphate (ATP) proliferation assay. Cellular proliferation in control cells was higher, as was evident from the increased ATP content. Exposure of cells to RF, ZnO NPs, and RFZnO NPs led to a reduction in intracellular ATP levels, which indicates reduced cellular proliferation. Cells incubated with RFZnO NPs resulted in a significant decrease ($p < 0.01$) (Figure 2a) in cell proliferation compared to untreated cells. The cytotoxic effects of RF, ZnO NPs, and RFZnO NPs were measured using the lactate dehydrogenase (LDH) assay. The release of LDH from damaged cells (through a ruptured cell membrane) into the culture media is a direct measure of cellular toxicity. Untreated MCF-7 cells showed the least amount of LDH release (absorbance: 0.2183) compared to RF- and ZnO-treated cells (absorbance: 0.361 and 0.616, respectively). A significant 5.22-fold ($p < 0.01$) increase in toxicity (absorbance: 1.141) was observed in RFZnO NP-treated cells (Figure 2b). These results indicate that the NPs synthesized from *R. fairholmianus* decreased cellular proliferation and increased cytotoxicity in MCF-7 cells 24 h post-treatment.
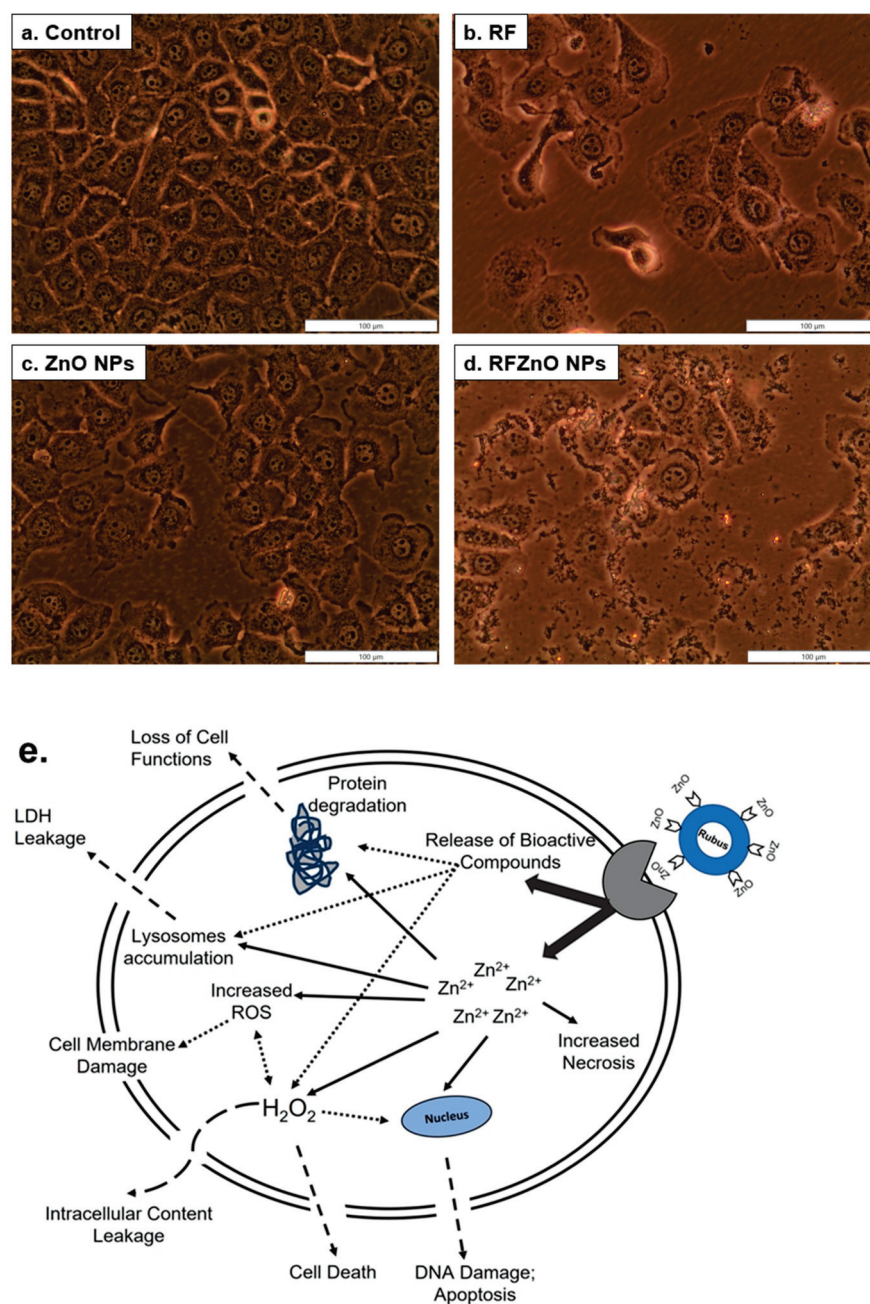
Figure 1. Morphological changes in MCF-7 breast cancer cells 24 h after treatment with *Rubus fairholmianus* (RF 10 μg/mL), zinc oxide nanoparticles (ZnO NPs 10 μg/mL), and *R. fairholmianus* capped zinc oxide nanoparticles (RFZnO NPs 10 μg/mL). Control cells did not show any sign of cell death and were found to be healthy and confluent (**a**). Treated groups showed more dead cells with loss of membrane integrity. An increased number of dead cells was seen in RF (**b**) and RFZnO NP (**d**) treatment groups compared to the control group (**a**) and cells treated with ZnO NP (**c**). (**e**) Possible cell death/cytotoxicity mechanism of action induced by RFZnO NPs.
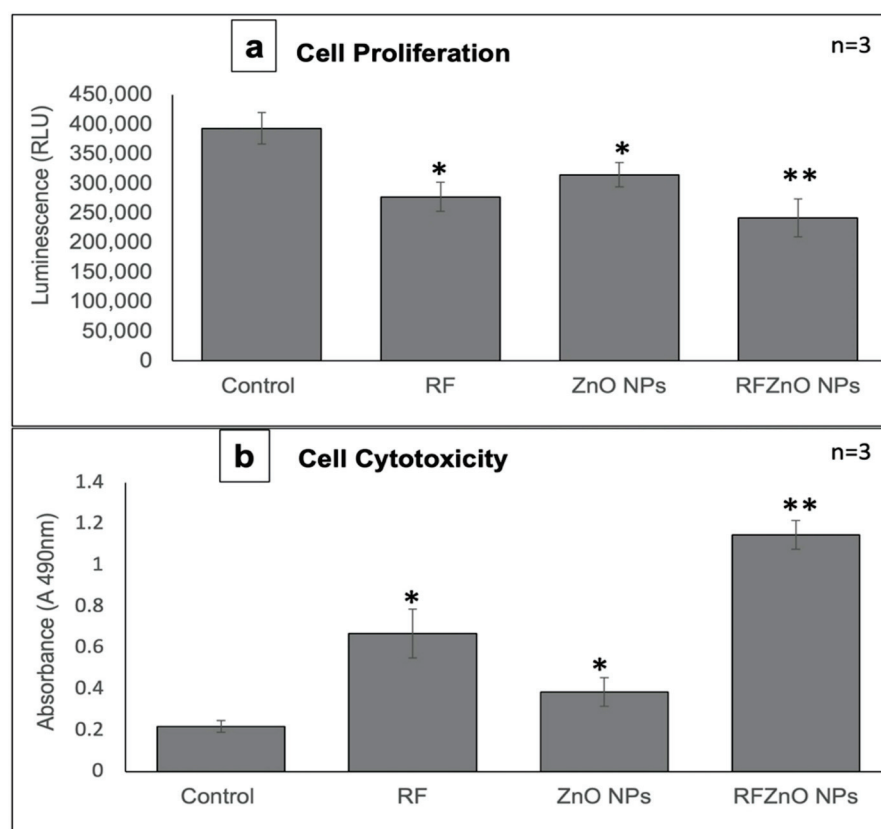
Figure 2. (**a**) Measurement of cell proliferation by adenosine triphosphate (ATP) luminescent assay. Control cells showed maximum levels of ATP. ATP levels were significantly decreased in cells treated with Rubus fairholmianus (RF 10 μg/mL), zinc oxide nanoparticles (ZnO NPs 10 μg/mL), and R. fairholmianus capped zinc oxide nanoparticles (RFZnO NPs 10 μg/mL). (**b**) Lactate dehydrogenase (LDH) was used to measure cytotoxicity. A significant increase in cytotoxicity 24 h after treatment with RF, ZnO NPs, and RFZnO NPs was observed. Significant differences are shown as * $p < 0.05$ and ** $p < 0.01$. Results represent the mean ± SE of three independent experiments.

2.2. Cytochrome C Release and Caspase 3/7 Activity

Cytochrome C (cyt c) is a water-soluble hemeprotein (~12 kDa) mainly located in the inner mitochondrial membrane. Mitochondrial release of cytotochrome c into the cytoplasm is a vital process in the execution phase of apoptosis. Cyt c functions as an electron transporter/vehicle in the respiratory chain and is then translocated to the cytosol in cells that undergo apoptosis, where it is involved in the activation of the caspase cascade signaling pathway [30]. Many apoptotic proteins induce mitochondrial damage resulting in the release of cyt c and thereby the activation of caspases. The cyt c assay results reveal that compared to the untreated cells, a significant amount of cyt c was released by treated cells (Figure 3a). A significant ($p < 0.01$) increase in cyt c release was observed in RFZnO NP-treated cells compared to untreated cells with a 4.57-fold increase. RF- and ZnO NP-treated cells showed a 2.36- and 2.20-fold increase in cyt c release, respectively.
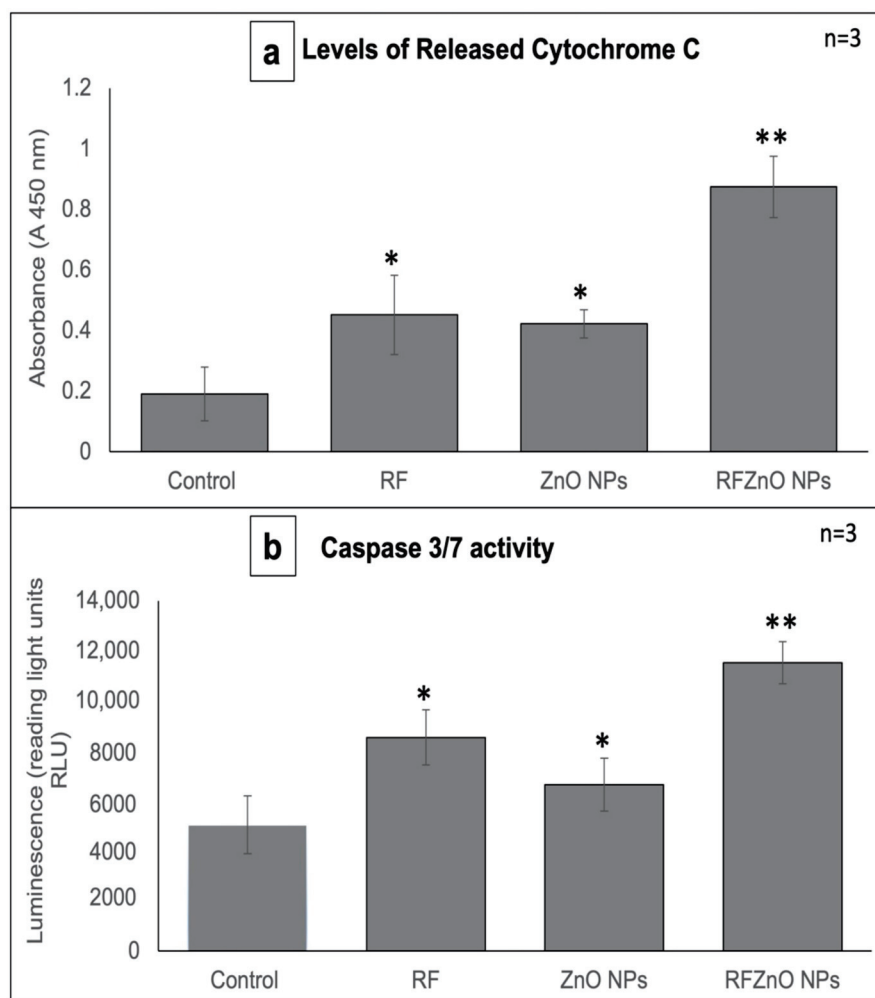
Figure 3. (**a**) Cytochrome c levels in control and treated MCF-7 cells. A significant increase in cytochrome c levels was observed in all treated cells when compared with the control. (**b**) Caspase 3/7 activity. A significant increase in caspase 3/7 activity was observed after treatments. Significant differences are shown as * $p < 0.05$ and ** $p < 0.01$. Results represent the mean $\pm$ SE of three independent experiments.

Previous studies have documented that caspase 3 is important in regulating DNA fragmentation and the initiation of apoptosis, whereas caspase 7 plays a major role in cell cycle progression and tumor growth. Based on these facts, we determined the levels of caspase 3/7 as a measure of apoptosis [31] 24 h after treatment with RF, ZnO NPs, and RFZnO NPs using the Caspase-Glo 3/7 luminescent assay kit. Caspase 3/7 levels were compared with untreated cells, and the results revealed that RFZnO NP treatment induced a noticeable increase ($p < 0.01$) in caspase 3/7 (Figure 3b).

2.3. Reactive Oxygen Species (ROS) Production and Nuclear Hoechst Staining

ROS play an important role in inducing apoptosis in cancer cells. The production of ROS was evaluated after exposure to RF, ZnO NPs, and RFZnO NPs using ELISA (Figure 4a) and qualitative fluorescence methods (Figure 4b–e), and nuclear damage was assessed qualitatively through Hoechst staining. Increased intracellular ROS levels were observed in the treated groups (RF and ZnO NPs: $p < 0.05$; *RFZnO NPs: $p < 0.01$*) (Figure 4a). The presence of red fluorescent signals in treated groups shows increased levels of ROS (Figure 4c–e). Similarly, groups incubated with RF, ZnO NPs, and RFZnO NPs showed slight nuclear damage as determined by the Hoechst stain. Untreated cells presented with homogeneously stained round nuclei, while treated cells displayed an uneven nuclear

shape and DNA condensation (Figure 4f–i). These results reflect that RFZnO NPs can induce cytosolic oxidative stress and cell death.
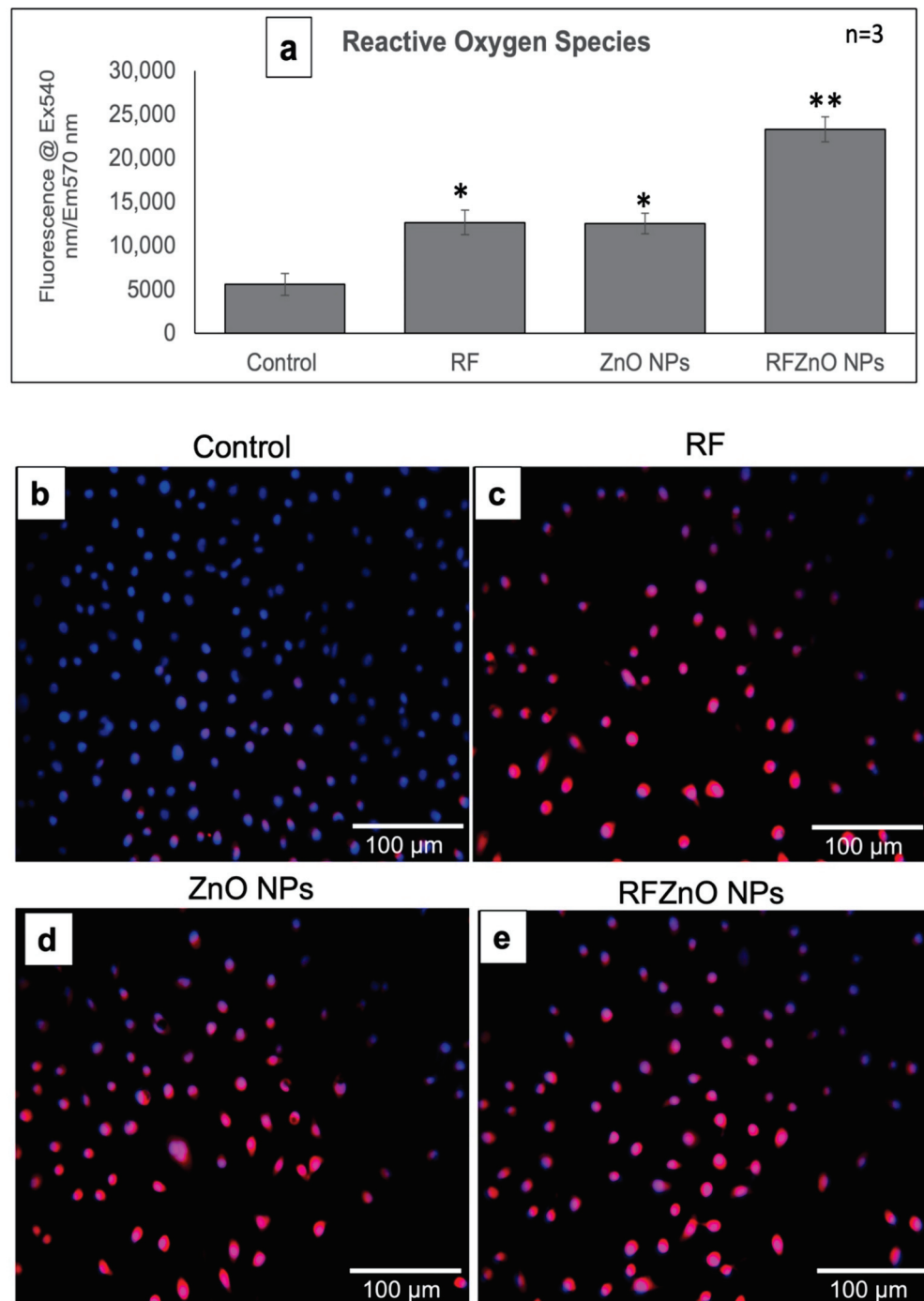
Figure 4. *Cont.*
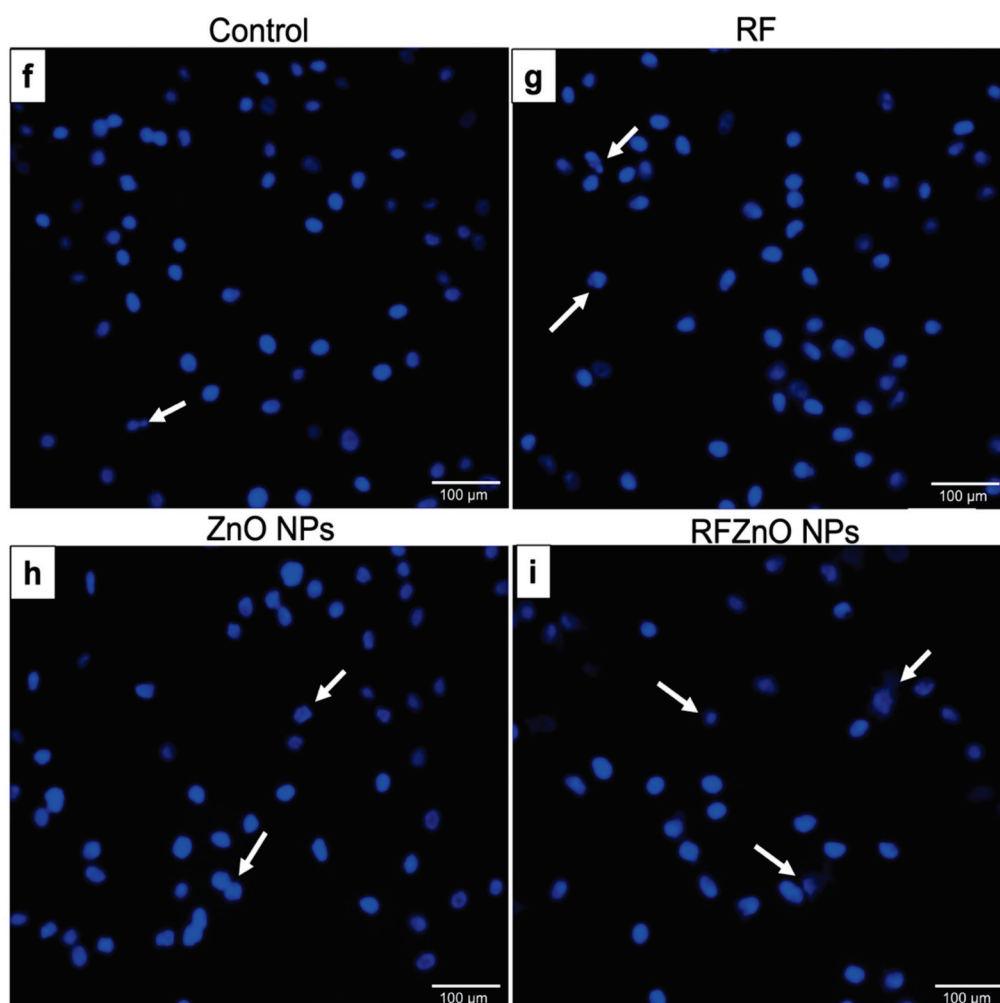
Figure 4. (**a**) Measurement of reactive oxygen species (ROS) in control and treated MCF-7 cells. There was a significant increase in ROS in *R. fairholmianus* capped zinc oxide nanoparticle (RFZnO NP)-treated groups. Significant differences are shown as * $p < 0.05$ and ** $p < 0.01$. Results represent the mean $\pm$ SE of three independent experiments. (**b–e**) Qualitative assessment of ROS: ROS are indicated by red fluorescence and nuclei are stained blue. There was increased red fluorescence, and hence increased ROS, in the treatment groups, while in the control group ROS production was lower. (**f–i**) Nuclear damage as determined by Hoechst staining. Treatments induced minor nuclear damage in MCF-7 cells; the intensity of nuclear stain was decreased, indicating nuclear disintegration (as shown by the arrows).

2.4. Immunofluorescence and Immunoblotting of p53, Bax, and Bcl-2

Apoptotic proteins were studied to determine the influence of RF, ZnO NPs, and RFZnO NPs in inducing the apoptotic pathway in breast cancer cells. From the results, apoptotic proteins Bax (Figure 5a–d) and p53 (Figure 5e–h) were found at high levels in treated groups, specifically in RFZnO NP-treated cells, while the anti-apoptotic protein Bcl-2 (Figure 5i–l) was reduced considerably in the treated groups. Following treatment, we observed activated p53 nuclear translocation, and hence more p53 was observed in the nucleus while the Bax was seen in the cytosol. Arrows in the figure indicate the presence of p53, Bax, and Bcl-2 proteins.
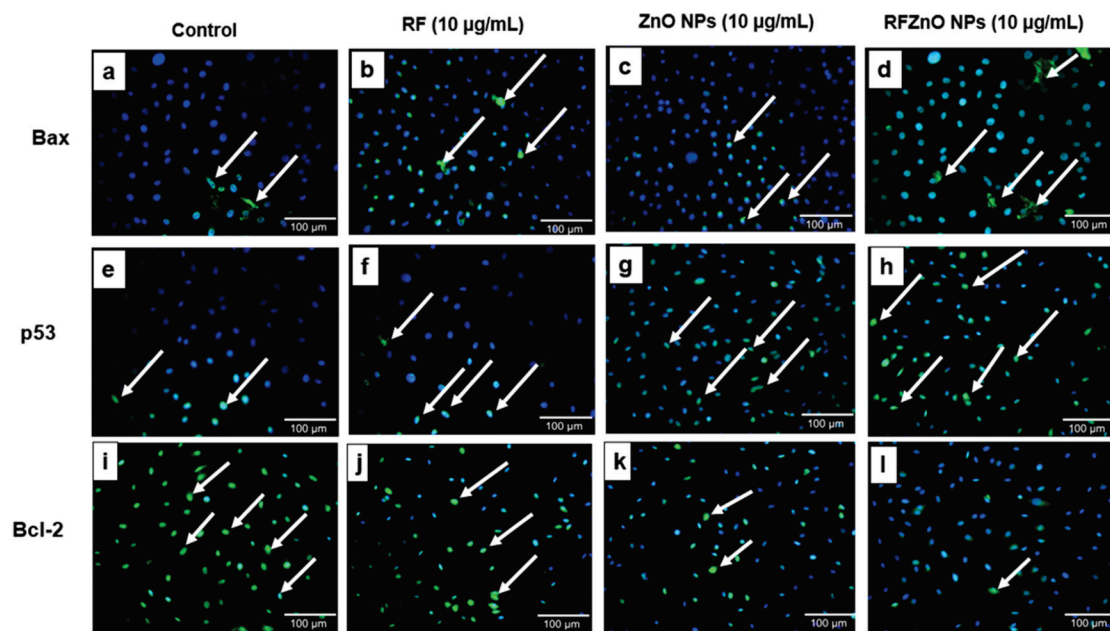
Figure 5. Immunofluorescence images of Bax (**a–d**), p53 (**e–h**), and Bcl-2 (**i–l**) in control and treated cells. Treated cells showed significant changes in the activity of apoptotic proteins. Control cells showed few p53- and Bax-positive cells and more Bcl-2-positive cells. Cells treated with Rubus fairholmianus (RF), zinc oxide nanoparticles (ZnO NPs), and R. fairholmianus capped zinc oxide nanoparticles (RFZnO NPs) showed higher levels of p53 and Bax positivity. The treatment with RF, ZnO NPs, and RFZnO NPs decreased Bcl-2. Magnification: 20X original; arrows indicate the presence of proteins p53, Bax, and Bcl-2 (FITC stained, green); nuclear stain: DAPI (blue).

We also examined the level of these proteins by Western blotting (Figure 6a,b) and observed a similar pattern. From the immunoblot results, the levels of Bax and p53 pro-apoptotic proteins were high in cells treated with RFZnO NPs, while the level of anti-apoptotic protein Bcl-2 appeared to be low. The RFZnO NP-treated groups showed significantly increased levels ($p < 0.01$) of Bax and p53, while reduced levels ($p < 0.01$) of Bcl-2 were observed. The activation of p53 and Bax leads to the loss of mitochondrial membrane potential and cyt c release, and immunofluorescence assays also support these findings.
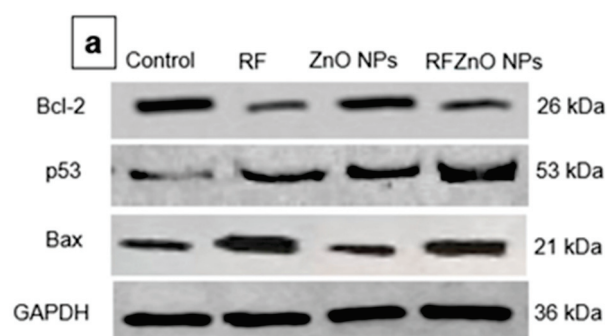
Figure 6. *Cont.*
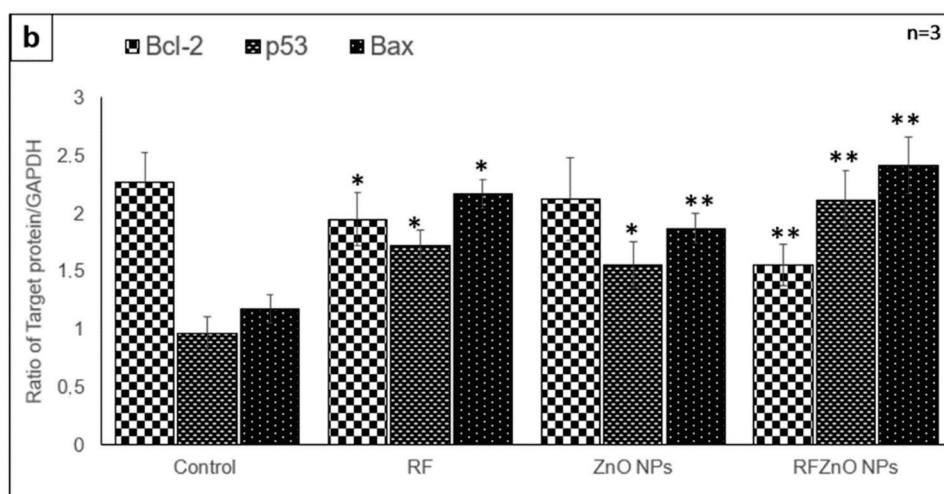
Figure 6. Effect of RFZnO NPs on the level of p53, Bax, and Bcl-2 apoptotic proteins, as determined by immunoblotting (**a**). L1: control; L2: *Rubus fairholmianus* (RF) (10 µg/mL); L3: zinc oxide nanoparticles (ZnO NPs) (10 µg/mL); L4: *R. fairholmianus* capped zinc oxide nanoparticles (RFZnO NPs) (10 µg/mL). The results showed that p53 and Bax levels were significantly increased, while the level of Bcl-2 was decreased in treated groups. Relative expression shown in a graph (**b**). Protein levels were quantified using ImageJ software and normalized to GAPDH band intensity. Significant differences are shown as * $p < 0.05$ and ** $p < 0.01$. Results represent the mean ± SE of three independent experiments.

3. Discussion

ZnO NPs are multi-faceted metal oxide NPs with diverse biological properties [32]. This study investigated the anticancer activity of green synthesized ZnO NPs against breast cancer cells. As revealed by morphological analysis by inverted microscopy, the RFZnO NP-treated MCF-7 cells showed significant morphological variations, including rounding of cells and detachment from culture plates. In addition, the ATP proliferation results displayed a significant ($p < 0.01$) decrease in proliferation after RFZnO NP treatment. However, RF- and ZnO NP-treated groups also showed decreased proliferation ($p < 0$ 05). The LDH cytotoxicity assay results were supportive of the morphology and proliferation assay results. RF, ZnO NP, and RFZnO NP treatment significantly ($p < 0.01$) induced cytotoxicity by releasing LDH into the culture media. Cytoplasmic LDH will be released into the cell culture media upon the loss of cell membrane integrity. The cytotoxicity results revealed that there is an increased cell death observed in the treated groups. This might be due to the synergistic action of *R. fairholmianus* and ZnO NPs, and it can be postulated that when cells are treated with RFZnO NPs, there will be an accumulation of Zn^{2+} in the cytosol [33] and the *Rubus* bioactive compounds will be released into the cytosol, which will result in an increased free radical production and oxidative stress which in turn might induce DNA and cell membrane damage and loss of cellular function [25,26]. The released bioactive compounds also activate apoptotic signals, resulting in cell death (Figure 1e). LDH activity is a direct measure of cellular toxicity and cell death due to cell membrane rupture and apoptosis [34]. Similarly, the cell proliferation biomarker ATP is abundant in all metabolically active viable dividing cells. Higher ATP levels indicate increased cell proliferation rates. The reduction in ATP levels is directly linked with reduced cell proliferation [35]. In this study, the data from cell morphology analysis, cytotoxicity, and proliferation assays provided evidence for the reduction in cell numbers in treated groups. Reports show that ZnO NPs induce structural changes including the loss of cell-to-cell adhesion in human cervical carcinoma cells [36].

Cyt c is a vital mitochondrial peripheral protein, and it acts as an electron shuttle and contributes to apoptosis. The intermembrane mitochondrial space (IMS) comprises a heterogeneous group of proteins that promote cell death upon release. The first molecule belonging to this group of proteins is cyt c. Upon apoptotic stimuli, cyt c is released into the

cytoplasm where it activates the adaptor molecule in the presence of ATP and generates a complex known as the apoptosome to execute apoptotic cell death [37,38]. Previous studies reported that ethanolic extracts of medicinal plants induce apoptosis via intrinsic and extrinsic pathways. The loss of mitochondrial membrane potential is a major characteristic of mitochondria-dependent apoptosis [39,40]. Hence, the analysis of mitochondrial cyt c release is an important measure of apoptotic cell death. The results (Figure 3a) show that RFZnO NPs significantly induced cyt c release ($p < 0.01$).

Apoptotic events are strongly controlled by numerous caspase proteins that ultimately mediate cell death. Caspase 3 activation occurs in the perinuclear area of the cell and is associated with mitochondrial cyt c release which can be prevented by the upregulation of Bcl-2 proteins [41]. McComb et al. reported that the stimulation of caspase 3 or 7 initiates the augmentation of the upstream apoptotic process, which is a vital feature of cell death via apoptosis. The activity of caspase 3 or 7 is essential for mitochondrial membrane depolarization, and hence cyt c release [42]. Results from this study showed that a 2-fold increase in caspase 3/7 activity was obtained (Figure 3b) after treatment with RFZnO NPs ($p < 0.01$).

Even though higher levels of ROS play a vital role in cancer incidence and progression, levels above a cytotoxic threshold lead to cancer cell death. Many commonly used anticancer therapies such as radiation, chemotherapy, and photodynamic therapy (PDT) depend on ROS production to induce cancer cell death mechanisms. Numerous reports proved that ZnO NPs exert significant antitumor activity via the generation of ROS and free radical production, and this is regarded as one of the pathways by which ZnO NPs induce cancer cell death [42,43]. Increased ROS levels lead to a decrease in antioxidant enzymes and ultimately result in cellular oxidative damage [44]. It is well proven that ROS can regulate the translocation, phosphorylation, and/or cleavage of pro-apoptotic Bcl-2 family proteins, leading to apoptosis induction [45]. Our quantitative (ELISA) (Figure 4a) and qualitative (immunofluorescence) (Figure 4b–e) experimental results showed the increased production of ROS following treatments ($p < 0.01$). Nuclear damage was assessed by Hoechst staining, which did not indicate significant nuclear damage after treatments; the control and treated cells looked similar, although minor nuclear damage was seen in treated cells (Figure 4f–i).

Further, we studied the cell death mechanism caused by ZnO NPs and RFZnO NPs using immunofluorescence and immunoblot analysis of vital apoptotic proteins (Bax, Bcl-2, and p53). Levels of pro-apoptotic proteins (Bax and p53) were increased, whereas the anti-apoptotic Bcl-2 activity was reduced. Mitochondria-mediated apoptosis requires mitochondrial membrane depolarization to release apoptotic mediators such as cyt c [38]. Tumor suppressor gene P53 is involved in the mediation of apoptosis via the regulation of BCL-2 family genes [46]. The Bcl-2 family proteins involve pro-apoptotic and anti-apoptotic members. Bcl-2 proteins are vital mediators which control the mitochondrial pores to regulate cyt c release to aid in the apoptotic process [38–40]. The anti-apoptotic Bcl-2 proteins help in cell survival by inhibiting the pro-apoptotic proteins [40]. Bax controls cell death by disrupting the mitochondria, and its activity is in turn controlled by p53 [42]. The overexpression of Bax improves mitochondrial pore opening followed by cyt c release [47]. Several studies showed that translocation of Bax without Bax/Bcl-2 ratio variation can upregulate caspase 3 to execute apoptosis [48–50]. Similar to the findings of Akhtar et al. [51] in human lung cancer cells (HepG2), our results (breast cancer cells) also reported significantly increased levels of p53 and Bax in treated cells, while there were reduced levels of Bcl-2.

The results presented show that RFZnO NPs induce p53 and Bax (pro-apoptotic); however, they did not induce anti-apoptotic Bcl-2. Furthermore, treatment with RFZnO NPs also leads to the activation of caspase 3/7, suggesting that a mitochondrial apoptotic cell death mechanism is involved in MCF-7 breast cancer. These results are also in correlation with the ROS analysis. Mohammadinejad et al. [52] reported that several kinds of oxidative stress activate intrinsic apoptosis. Our data also showed that RFZnO NPs enhanced

intracellular ROS levels, and subsequently disrupted mitochondrial function by the release of cyt c in breast cancer cells. Hence, we propose that RFZnO NP-induced apoptosis might have been caused by oxidative stress in breast cancer cells as shown in the proposed mechanism (Figure 7).
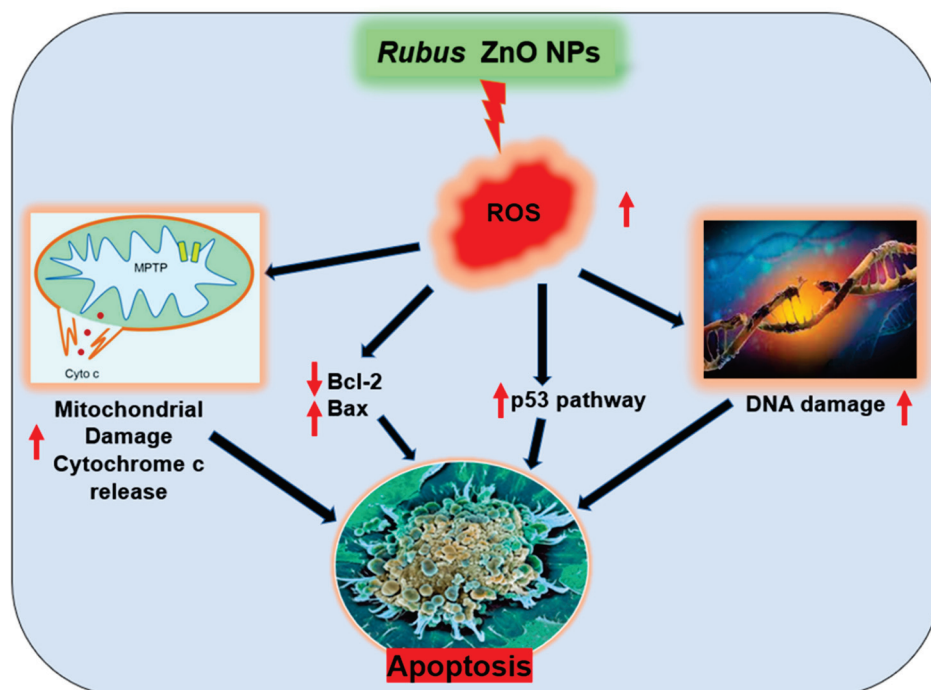

Figure 7. Proposed cell death mechanism induced by *Rubus fairholmianus* capped zinc oxide nanoparticles (RFZnO NPs). The reactive oxygen species (ROS) produced during RFZnO NP treatment induced mitochondrial cytochrome c release, induced nuclear damage, and increased the activity of p53 and Bax while reducing the activity of Bcl-2, leading to apoptotic cell death in breast cancer cells.

4. Materials and Methods

4.1. Plant Material, Collection Site, and Herbarium

Rubus fairholmianus Gard. was collected from Munnar, Kerala, India, and a herbarium sample BSI/SRC/5/23/2010-11/Tech.1657 was deposited in the Botanical Survey of India.

4.2. Extraction and Green Synthesis of ZnO NPs

The freshly collected root of *R. fairholmianus* was cleaned and shade dried. The powdered roots were used for the hot percolation Soxhlet extraction process using acetone. About 200 mg of root acetone extract was dissolved in 10 mL of 0.5% DMSO for in vitro studies.

Green synthesis of ZnO NPs: Previously we have reported on the green synthesis of ZnO NPs using R. fairholmianus root extract. The protocol explained by Rajendran et al. [29] using zinc nitrate was employed in the synthesis of ZnO NPs.

4.3. Cell Culture

Human breast adenocarcinoma cells (MCF-7, ATCC HTB-22) were used in this study. Dulbecco's modified Eagle medium (DMEM) was used for cell culture with 10% fetal bovine serum (FBS; Gibco 306.00301), 1% penicillin/streptomycin (PAA Laboratories GmbH, P11-010), and 1 μg/mL amphotericin B (PAA Laboratories GmbH, P11-001). Cells were grown at 37 °C, 5% CO_2, and 80% humidity in a CO_2 incubator. Hank's Balanced Salt Solution (HBSS, Merck, Johannesburg, South Africa) was used to wash cells when confluent. Cells were detached using 1 mL/cm^2 TryplExpress (Gibco, ThermoFischer Scientific, 12604, Johannesburg, South Africa) for subculturing. For experiments, 5×10^5 cells were seeded

in 3.5 cm diameter cell culture plates, allowed to attach for 6 h, and treated/incubated for 24 h with 10 μg/mL of RF, ZnO NPs, and RFZnO NPs for each experiment.

4.4. Morphology, Cell Proliferation, and Cytotoxicity Analysis

The morphological variations in cells after 24 h incubation with newly synthesized nanomaterials were observed using cellSens imaging software and an Olympus CKX 41 inverted light microscope (Wirsam, Johannesburg, South Africa). Treated cells were washed with HBSS before images were captured.

The CellTiter-Glo Luminescent cell viability assay (Promega, G7571, Anatech Analytical Technology, Johannesburg, South Africa) was used for the quantitative analysis of metabolic ATP contents in living cells. About 50 μL of ATP reagent and 50 μL cell suspension were incubated in the dark for 10 min at room temperature before luminescence was measured (in relative light units, RLU) on a Victor3 1420 Multilabel Counter (Perkin-Elmer, Separation Scientific, Johannesburg, South Africa). The estimation of ATP levels is a measure of cell proliferation. The CytoTox 96 Non-Radioactive Cytotoxicity Assay kit (Promega G 400, Anatech Analytical Technology, South Africa) was used to assess the cytotoxic activity of green synthesized NPs. Lactate dehydrogenase (LDH) released into the media measures the membrane integrity of the cells after treatment, which indirectly corresponds to cytotoxicity. Equal volumes (50 μL) of LDH reagent and culture medium were incubated for 30 min in the dark at room temperature and measured at 490 nm (Victor3 1420 Multilabel Counter, Perkin-Elmer, Separation Scientific).

4.5. Cytochrome C Release and Caspase 3/7 Assay

Cytochrome c is a vital factor for apoptotic events. Cytochrome c (cytoplasmic cyt c) levels were measured using the human cytochrome c Platinum ELISA assay kit (Invitrogen, KH01051, ThermoFisher Scientific, Johannesburg, South Africa), and the downstream executioner caspase 3/7 activities were measured by the Caspase-Glo 3/7 assay (Promega G8091, Anatech Analytical Technology, South Africa) according to the manufacturer's protocol [27].

4.6. Hoechst Staining and Reactive Oxygen Species (ROS) Production

ZnO NP-induced nuclear damage was studied by Hoechst nuclear staining (Hoechst 33258, H21491, Sigma-Aldrich, Johannesburg, South Africa) as explained by George et al. [19]. ROS formed in response to treatment with NPs and plant extract were analyzed using the dichlorodihydrofluorescein diacetate (DCFH-DA) assay [27]. In brief, for quantitative measurement of ROS, cells were grown in 96-well plates, and once they reached 80 to 90% confluency, they were treated for 24 h with different treatment solutions at a concentration of 10 μg/mL. After the treatment period, the medium was removed and cells were incubated with 100 μM of DCFH-DA in 100 μL of HBSS for 30 min at 37 °C. ROS generated in the cells were immediately measured at Ex: 540 nm, Em: 570 nm using the Victor3 1420 Multilabel Counter (Perkin-Elmer, Separation Scientific, South Africa). For the staining of ROS, the cells were grown on sterile coverslips in a clear-bottom 6-well plate. Once cells reached 80% confluency, they were treated similarly, i.e., 10 μg/mL treatment solutions for 24 h. After treatment, the media were replaced with fresh media and treated with 100 μM DCFH-DA for 30 min in the dark. Cells were washed once with phosphate-buffered saline (PBS) and stained with 1 μg/mL of nuclear stain (DAPI, Invitrogen, D1306, Sigma-Aldrich, South Africa). Finally, the coverslips were washed with PBS and fixed on a glass slide. Image were captured with AxioVision imaging software (Version 4) installed on a Carl Zeiss Axio Observer Z1.

4.7. Immunofluorescence and Immunoblotting

The qualitative and quantitative levels of apoptotic proteins (p53, Bax, and Bcl-2) after treatment with RFZnO NPs were determined using immunofluorescence and immunoblotting, respectively, as previously explained by George et al. [27]. The cells were cultured on

coverslips for immunofluorescence experiments, whereas for Western blotting the proteins were isolated 24 h post-treatment, separated by SDS PAGE, and transferred to a PVDF membrane. We used the primary antibodies p53 (Pab 240) (mouse monoclonal antibody, Santa Cruz Biotechnology SC-99, Anatech, Johannesburg, South Africa) Bax monoclonal antibody (2D2) (mouse monoclonal antibody, Life Technologies 336400, ThermoFisher Scientific, Johannesburg, South Africa), Bcl-2 monoclonal antibody (Bcl-2-100) (Life Technologies 13-8800), and GAPDH loading control monoclonal antibody (GA1R) (mouse monoclonal antibody, Invitrogen MA5-15738), and we used a horseradish peroxidase-conjugated secondary antibody (goat anti-mouse HRP, Santa Cruz Biotechnology SC-2005) for Western blotting and a goat anti-mouse IgG (H+L) Superclonal recombinant secondary antibody, Alexa Fluor 488 (ThermoFisher Scientific A28175), for immunofluorescence.

4.8. Statistical Analysis

The data are represented as the standard error of the mean (SEM) of three replicates (n = 3) performed in duplicate. The statistical significance was analyzed using SigmaPlot version 14.0. Untreated control cells were used to compare the statistical significance of treated cells. The differences between groups were determined using paired Student's *t* test and one-way analysis of variance (ANOVA). A *p* value less than 0.05 was considered significant.

5. Conclusions

In this study, we established that RFZnO NPs can significantly induce cytotoxicity in breast cancer cells via the induction of apoptosis and ROS production. The effect of RFZnO NPs could be directly linked with mitochondrial cyt c release to induce intrinsic apoptosis. Moreover, RFZnO NPs could increase the levels of pro-apoptotic proteins Bax and p53, eventually leading to apoptosis. Hence, the results of this study lead to the conclusion that apoptosis induction is directly linked with the toxicity of RFZnO NPs through ROS generation, increased levels of apoptotic proteins, and the release of the mitochondrial marker cyt c. The mechanisms behind the activity of RFZnO NPs necessitate an additional detailed study to validate the cell death pathway by protein and gene expression profiling.

Author Contributions: Conceptualization, and methodology, B.P.G. and N.K.R.; formal analysis, investigation, B.P.G. and N.K.R.; writing—original draft preparation, B.P.G. and N.K.R.; writing—review and editing, N.N.H. and H.A.; supervision, project administration; funding acquisition, N.N.H. and H.A. All authors have read and agreed to the published version of the manuscript.

Institutional Review Board Statement: Not applicable.

Informed Consent Statement: Not applicable.

Data Availability Statement: Not applicable.

Conflicts of Interest: The authors declare no conflict of interest.

References

1. Hassanpour, S.H.; Dehghani, M. Review of Cancer from Perspective of Molecular. *J. Cancer Res. Pract.* **2017**, *4*, 127–129. [CrossRef]
2. Fares, J.; Kanojia, D.; Rashidi, A.; Ulasov, I.; Lesniak, M.S. Landscape of Combination Therapy Trials in Breast Cancer Brain Metastasis. *Int. J. Cancer* **2020**, *147*, 1939–1952. [CrossRef] [PubMed]
3. Hanahan, D.; Weinberg, R.A. Hallmarks of Cancer: The next Generation. *Cell* **2011**, *144*, 646–674. [CrossRef] [PubMed]
4. Salam, H.A.; Sivaraj, R.; Venckatesh, R. Green Synthesis and Characterization of Zinc Oxide Nanoparticles from *Ocimum basilicum* L. Var. *purpurascens* Benth.-Lamiaceae Leaf Extract. *Mater. Lett.* **2014**, *131*, 16–18. [CrossRef]
5. Yuvakkumar, R.; Suresh, J.; Nathanael, A.J.; Sundrarajan, M.; Hong, S.I. Novel Green Synthetic Strategy to Prepare ZnO Nanocrystals Using Rambutan (*Nephelium lappaceum* L.) Peel Extract and Its Antibacterial Applications. *Mater. Sci. Eng. C Mater. Biol. Appl.* **2014**, *41*, 17–27. [CrossRef]
6. Ramesh, M.; Anbuvannan, M.; Viruthagiri, G. Green Synthesis of ZnO Nanoparticles Using Solanum Nigrum Leaf Extract and Their Antibacterial Activity. *Spectrochim. Acta Part A Mol. Biomol. Spectrosc.* **2015**, *136*, 864–870. [CrossRef]
7. Xiao, L.; Liu, C.; Chen, X.; Yang, Z. Zinc Oxide Nanoparticles Induce Renal Toxicity through Reactive Oxygen Species. *Food Chem. Toxicol. Int. J. Publ. Br. Ind. Biol. Res. Assoc.* **2016**, *90*, 76–83. [CrossRef]
8. Rajeshkumar, S. Anticancer Activity of Eco-Friendly Gold Nanoparticles against Lung and Liver Cancer Cells. *J. Genet. Eng. Biotechnol.* **2016**, *14*, 195–202. [CrossRef]
9. Sundrarajan, M.; Ambika, S.; Bharathi, K. Plant-Extract Mediated Synthesis of ZnO Nanoparticles Using Pongamia Pinnata and Their Activity against Pathogenic Bacteria. *Adv. Powder Technol.* **2015**, *26*, 1294–1299. [CrossRef]
10. Jamdagni, P.; Khatri, P.; Rana, J.S. Green Synthesis of Zinc Oxide Nanoparticles Using Flower Extract of Nyctanthes Arbor-Tristis and Their Antifungal Activity. *J. King Saud Univ.—Sci.* **2018**, *30*, 168–175. [CrossRef]
11. Taranath, T.C.; Patil, B.N. *Limonia Acidissima* L. Leaf Mediated Synthesis of Zinc Oxide Nanoparticles: A Potent Tool against Mycobacterium Tuberculosis. *Int. J. Mycobacteriol.* **2016**, *5*, 197–204. [CrossRef]
12. Pulit-Prociak, J.; Chwastowski, J.; Kucharski, A.; Banach, M. Functionalization of Textiles with Silver and Zinc Oxide Nanoparticles. *Appl. Surf. Sci.* **2016**, *385*, 543–553. [CrossRef]
13. Mirzaei, H.; Darroudi, M. Zinc Oxide Nanoparticles: Biological Synthesis and Biomedical Applications. *Ceram. Int.* **2017**, *43*, 907–914. [CrossRef]
14. Stan, M.; Popa, A.; Toloman, D.; Dehelean, A.; Lung, I.; Katona, G. Enhanced Photocatalytic Degradation Properties of Zinc Oxide Nanoparticles Synthesized by Using Plant Extracts. *Mater. Sci. Semicond. Process.* **2015**, *39*, 23–29. [CrossRef]
15. Roohani, N.; Hurrell, R.; Kelishadi, R.; Schulin, R. Zinc and Its Importance for Human Health: An Integrative Review. *J. Res. Med. Sci. Off. J. Isfahan Univ. Med. Sci.* **2013**, *18*, 144–157.
16. Ahmad, I.; Alshahrani, M.Y.; Wahab, S.; Al-Harbi, A.I.; Nisar, N.; Alraey, Y.; Alqahtani, A.; Mir, M.A.; Irfan, S.; Saeed, M. Zinc oxide nanoparticle: An effective antibacterial agent against pathogenic bacterial isolates. *J. King Saud Univ. Sci.* **2022**, *34*, 102110. [CrossRef]
17. Mishra, P.; Ahmad, A.; AI-Keridis, L.A.; Alshammari, N.; Alabdallah, N.; Muzammil, K.; Saeed, M.; Ansari, I.M. Doxorubicin-Conjugated Zinc Oxide Nanoparticles, Biogenically Synthesized Using a Fungus Aspergillus niger, Exhibit High Therapeutic Efficacy against Lung Cancer Cells. *Molecules.* **2022**, *27*, 2590. [CrossRef]
18. Zheng, J.; Lang, Y.; Zhang, Q.; Cui, D.; Sun, H.; Jiang, L.; Chen, Z.; Zhang, R.; Gao, Y.; Tian, W.; et al. Structure of Human MDM2 Complexed with RPL11 Reveals the Molecular Basis of P53 Activation. *Genes Dev.* **2015**, *29*, 1524–1534. [CrossRef]
19. Cho, J.G.; Park, S.; Lim, C.H.; Kim, H.S.; Song, S.Y.; Roh, T.-Y.; Sung, J.-H.; Suh, W.; Ham, S.-J.; Lim, K.-H.; et al. ZNF224, Krüppel like Zinc Finger Protein, Induces Cell Growth and Apoptosis-Resistance by down-Regulation of P21 and P53 via MiR-663a. *Oncotarget* **2016**, *7*, 31177–31190. [CrossRef]
20. Finn, C.E. *Rubus* spp., blackberry. In *The Encyclopedia of Fruits and Nuts*; Janick, J., Paull, R.E., Eds.; CABI: Cambridge, MA, USA, 2008; pp. 348–351.
21. Patel, A.V.; Rojas-Vera, J.; Dacke, C.G. Therapeutic Constituents and Actions of Rubus Species. *Curr. Med. Chem.* **2004**, *11*, 1501–1512. [CrossRef]
22. Das, N.J.; Saikia, S.P.; Sarkar, S.; Devi, K. Medicinal Plants of North-Kamrup District of Assam Used in Primary Healthcare System. *IJTK* **2006**, *5*, 489–493.
23. Barukial, J.; Sarmah, J.N. Ethnomedicinal Plants Used by the People of Golaghat District, Assam, India. *Int. J. Med. Aromat. Plants* **2011**, *1*, 203–211.
24. Plackal Adimuriyil George, B.; Tynga, I.M.; Abrahamse, H. In Vitro Antiproliferative Effect of the Acetone Extract of Rubus Fairholmianus Gard. Root on Human Colorectal Cancer Cells. *BioMed Res. Int.* **2015**, *2015*, 165037. [CrossRef]
25. George, B.P.; Abrahamse, H.; Parimelazhagan, T. Caspase Dependent Apoptotic Activity of Rubus Fairholmianus Gard. on MCF-7 Human Breast Cancer Cell Lines. *J. Appl. Biomed.* **2016**, *14*, 211–219. [CrossRef]
26. George, B.P.A.; Abrahamse, H.; Hemmaragala, N.M. Caspase Dependent Apoptotic Inhibition of Melanoma and Lung Cancer Cells by Tropical Rubus Extracts. *Biomed. Pharmacother.* **2016**, *80*, 193–199. [CrossRef]
27. Plackal Adimuriyil George, B.; Kumar, N.; Abrahamse, H.; Ray, S.S. Apoptotic Efficacy of Multifaceted Biosynthesized Silver Nanoparticles on Human Adenocarcinoma Cells. *Sci. Rep.* **2018**, *8*, 14368. [CrossRef]
28. George, B.P.; Abrahamse, H. Increased Oxidative Stress Induced by Rubus Bioactive Compounds Induce Apoptotic Cell Death in Human Breast Cancer Cells. *Oxid. Med. Cell. Longev.* **2019**, *2019*, 6797921. [CrossRef]

29. Rajendran, N.K.; George, B.P.; Houreld, N.N.; Abrahamse, H. Synthesis of Zinc Oxide Nanoparticles Using Rubus Fairholmianus Root Extract and Their Activity against Pathogenic Bacteria. *Molecules* **2021**, *26*, 3029. [CrossRef]

30. Eleftheriadis, T.; Pissas, G.; Liakopoulos, V.; Stefanidis, I. Cytochrome C as a potential Clinical Useful Marker of Mitochondrial and cellular Damage. *Front. Immunol.* **2016**, *7*, 279. [CrossRef]

31. Brentnall, M.; Rodriguez-Menocal, L.; De Guevara, R.L.; Enrique Cepero, E.; Boise, L.H. Caspase-9, caspase-3 and caspase-7 have distinct roles during intrinsic apoptosis. *BMC Cell Biol.* **2013**, *14*, 32. Available online: www.biomedcentral.com/1471-2121/14/32 (accessed on 9 September 2022). [CrossRef]

32. El-Shorbagy, H.M.; Eissa, S.M.; Sabet, S.; El-Ghor, A.A. Apoptosis and Oxidative Stress as Relevant Mechanisms of Antitumor Activity and Genotoxicity of ZnO-NPs Alone and in Combination with N-Acetyl Cysteine in Tumor-Bearing Mice. *Int. J. Nanomed.* **2019**, *14*, 3911–3928. [CrossRef] [PubMed]

33. Moos, P.J.; Chung, K.; Woessner, D.; Honeggar, M.; Cutler, N.S.; Veranth, J.M. ZnO Particulate Matter Requires Cell Contact for Toxicity in Human Colon Cancer Cells. *Chem. Res. Toxicol.* **2010**, *23*, 733–739. [CrossRef] [PubMed]

34. Saad, B.; Dakwar, S.; Said, O.; Abu-Hijleh, G.; Battah, F.A.; Kmeel, A.; Aziazeh, H. Evaluation of Medicinal Plant Hepatotoxicity in Co-Cultures of Hepatocytes and Monocytes. *Evid. Based Complement. Alternat. Med.* **2006**, *3*, 93–98. [CrossRef]

35. Vidau, C.; Brunet, J.-L.; Badiou, A.; Belzunces, L.P. Phenylpyrazole Insecticides Induce Cytotoxicity by Altering Mechanisms Involved in Cellular Energy Supply in the Human Epithelial Cell Model Caco-2. *Toxicol. Vitro Int. J. Publ. Assoc. BIBRA* **2009**, *23*, 589–597. [CrossRef]

36. Pandurangan, M.; Enkhtaivan, G.; Kim, D.H. Anticancer Studies of Synthesized ZnO Nanoparticles against Human Cervical Carcinoma Cells. *J. Photochem. Photobiol. B* **2016**, *158*, 206–211. [CrossRef]

37. Garrido, C.; Galluzzi, L.; Brunet, M.; Puig, P.E.; Didelot, C.; Kroemer, G. Mechanisms of Cytochrome c Release from Mitochondria. *Cell Death Differ.* **2006**, *13*, 1423–1433. [CrossRef]

38. Chota, A.; George, B.P.; Abrahamse, H. Interactions of Multidomain Pro-Apoptotic and Anti-Apoptotic Proteins in Cancer Cell Death. *Oncotarget* **2021**, *12*, 1615–1626. [CrossRef]

39. Choi, Y. Induction of apoptosis by an ethanol extract of Poria cocos Wolf. in human leukemia U937 cells. *Oncol. Rep.* **2015**, *34*, 2533–2540. [CrossRef]

40. Al-Oqail, M.M. Anticancer efficacies of Krameria lappacea extracts against human breast cancer cell line (MCF-7): Role of oxidative stress and ROS generation. *Saudi Pharm. J.* **2021**, *29*, 244–251. [CrossRef]

41. De Botton, S.; Sabri, S.; Daugas, E.; Zermati, Y.; Guidotti, J.E.; Hermine, O.; Kroemer, G.; Vainchenker, W.; Debili, N. Platelet Formation Is the Consequence of Caspase Activation within Megakaryocytes. *Blood* **2002**, *100*, 1310–1317. [CrossRef]

42. McComb, S.; Chan, P.K.; Guinot, A.; Hartmannsdottir, H.; Jenni, S.; Dobay, M.P.; Bourquin, J.-P.; Bornhauser, B.C. Efficient Apoptosis Requires Feedback Amplification of Upstream Apoptotic Signals by Effector Caspase-3 or -7. *Sci. Adv.* **2019**, *5*, eaau9433. [CrossRef]

43. Bisht, G.; Rayamajhi, S. ZnO Nanoparticles: A Promising Anticancer Agent. *Nanobiomedicine* **2016**, *3*, 9. [CrossRef]

44. Carmody, R.J.; Cotter, T.G. Signalling Apoptosis: A Radical Approach. *Redox Rep. Commun. Free Radic. Res.* **2001**, *6*, 77–90. [CrossRef]

45. Li, D.; Ueta, E.; Kimura, T.; Yamamoto, T.; Osaki, T. Reactive Oxygen Species (ROS) Control the Expression of Bcl-2 Family Proteins by Regulating Their Phosphorylation and Ubiquitination. *Cancer Sci.* **2004**, *95*, 644–650. [CrossRef]

46. Ramadan, M.A.; Shawkey, A.E.; Rabeh, M.A.; Abdellatif, A.O. Expression of P53, BAX, and BCL-2 in Human Malignant Melanoma and Squamous Cell Carcinoma Cells after Tea Tree Oil Treatment in Vitro. *Cytotechnology* **2019**, *71*, 461–473. [CrossRef]

47. Gogvadze, V.; Orrenius, S.; Zhivotovsky, B. Multiple Pathways of Cytochrome c Release from Mitochondria in Apoptosis. *Biochim. Biophys. Acta BBA—Bioenerg.* **2006**, *1757*, 639–647. [CrossRef]

48. Kumar, A.; Ghosh, S.; Chandna, S. Evidence for MicroRNA-31 Dependent Bim-Bax Interaction Preceding Mitochondrial Bax Translocation during Radiation-Induced Apoptosis. *Sci. Rep.* **2015**, *5*, 15923. [CrossRef]

49. Jia, L.; Patwari, Y.; Srinivasula, S.M.; Newland, A.C.; Fernandes-Alnemri, T.; Alnemri, E.S.; Kelsey, S.M. Bax Translocation Is Crucial for the Sensitivity of Leukaemic Cells to Etoposide-Induced Apoptosis. *Oncogene* **2001**, *20*, 4817–4826. [CrossRef]

50. Park, M.-T.; Kang, J.A.; Choi, J.-A.; Kang, C.-M.; Kim, T.-H.; Bae, S.; Kang, S.; Kim, S.; Choi, W.-I.; Cho, C.-K.; et al. Phytosphingo-sine Induces Apoptotic Cell Death via Caspase 8 Activation and Bax Translocation in Human Cancer Cells. *Clin. Cancer Res. Off. J. Am. Assoc. Cancer Res.* **2003**, *9*, 878–885.

51. Akhtar, R.S.; Geng, Y.; Klocke, B.J.; Roth, K.A. Neural Precursor Cells Possess Multiple P53-Dependent Apoptotic Pathways. *Cell Death Differ.* **2006**, *13*, 1727–1739. [CrossRef]

52. Mohammadinejad, R.; Moosavi, M.A.; Tavakol, S.; Vardar, D.Ö.; Hosseini, A.; Rahmati, M.; Dini, L.; Hussain, S.; Mandegary, A.; Klionsky, D.J. Necrotic, Apoptotic and Autophagic Cell Fates Triggered by Nanoparticles. *Autophagy* **2019**, *15*, 4–33. [CrossRef] [PubMed]

MDPI

Article

Structural Characterization of Cis– and Trans–Pt(NH₃)₂Cl₂ Conjugations with Chitosan Nanoparticles

Penparapa Chanphai, Gervais Bérubé * and Heidar-Ali Tajmir-Riahi *

Department of Chemistry, Biochemistry and Physics, University of Québec at Trois-Rivières, Trois-Rivières, QC G9A 5H7, Canada
* Correspondence: gervais.berube@uqtr.ca (G.B.); heidar-ali.tajmir-riahi@uqtr.ca (H.-A.T.-R.)

Abstract: The conjugation of chitosan 15 and 100 KD with anticancer drugs cis– and trans–Pt (NH₃)₂Cl₂ (abbreviated cis–Pt and trans–Pt) were studied at pH 5–6. Using multiple spectroscopic methods and thermodynamic analysis to characterize the nature of drug–chitosan interactions and the potential application of chitosan nanoparticles in drug delivery. Analysis showed that both hydrophobic and hydrophilic contacts are involved in drug–polymer interactions, while chitosan size and charge play a major role in the stability of drug–polymer complexes. The overall binding constants are $K_{ch-15-cis-Pt} = 1.44 \ (\pm 0.6) \times 10^5 \ M^{-1}$, $K_{ch-100-cis-Pt} = 1.89 \ (\pm 0.9) \times 10^5 \ M^{-1}$ and $K_{ch-15-trans-Pt} = 9.84 \ (\pm 0.5) \times 10^4 \ M^{-1}$, and $K_{ch-100-trans-Pt} = 1.15 \ (\pm 0.6) \times 10^5 \ M^{-1}$. More stable complexes were formed with cis–Pt than with trans–Pt–chitosan adducts, while stronger binding was observed for chitosan 100 in comparison to chitosan 15 KD. This study indicates that polymer chitosan 100 is a stronger drug carrier than chitosan 15 KD in vitro.

Keywords: chitosan; cis and trans–Pt(II); delivery; loading efficacy; thermodynamic analysis

1. Introduction

Biodegradable polymers, such as chitosan, have been extensively studied as carriers for therapeutic protein and gene delivery systems [1,2]. Chitosan (Scheme 1) is a natural polymer obtained by the deacetylation of chitin [3]. It is a non-toxic, biocompatible, and biodegradable polysaccharide. Chitosan nanoparticles have gained increased attention as drug delivery carriers because of their superior stability, low toxicity, and simpler and milder preparation method, thus providing versatile routes for the administration of drugs [4,5]. The deacetylated chitosan backbone of glucosamine units has a high density of charged amine groups, allowing strong electrostatic interactions with proteins and genes that carry an overall negative charge at neutral pH conditions [4,6]. The fast-expanding research regarding the valuable physicochemical and biological properties of chitosan has led to the recognition of this cationic polysaccharide as an important natural polymer for drug delivery [6–13]. Therefore, it was of major interest to study the conjugation of cis– and trans–Pt with chitosan and the potential application of chitosan nanoparticles in the delivery of Pt drugs.

Cisplatin has been widely used for solid tumor chemotherapy but its trans–platin isomer proved to be ineffective due to its instability and rapid deactivation by hydrolysis in the blood circulation [14–17]. It is commonly believed that the mode of action of this anticancer agent relies mainly on the formation of intrastrand cross-linked DNA adducts that block DNA replication and transcription, finally causing cancer cell death. The use of nanodelivery tools has also grown and many different strategies have been explored to deliver platinum compounds in vitro and in vivo [17,18]. Trans-Pt also causes DNA damage. It is relatively more reactive than cis–Pt and, consequently, it can be deactivated before reaching DNA. Furthermore, its trans geometry does not allow for the formation of closed di–adducts on DNA [19,20]. These facts explain the lower biological activity of trans–Pt in comparison to cis–Pt. The literature shows that trans–Pt forms different types

of DNA lesions: 35% of monofunctional adducts, 53% of intrastrand crosslinks (mainly 1,3-GXG and 1,3-AXG where X is any nucleotide), and 12% of interstrand crosslinks [21]. It is also reported that trans–Pt DNA damage can be more easily recognized and repaired than that produced by cis–Pt [22]. It is important to note that there are many platinum antitumor complexes with trans geometry possessing antitumor activity [22]. A comparative study on the interaction of cis–Pt and trans–Pt with DNA and RNA found that aggregation occurs at high concentrations and that DNA remains in the B-family conformation and RNA retains its A-family conformation [23]. It is evident that a substantial body of work was performed to study cis–Pt and trans–Pt interaction with DNA, their mechanism of action, and cell processing of platinated DNA [24,25]. However, little is known about cis–Pt and trans–Pt delivery by natural and synthetic polymers. Hence the rationale for this investigation.
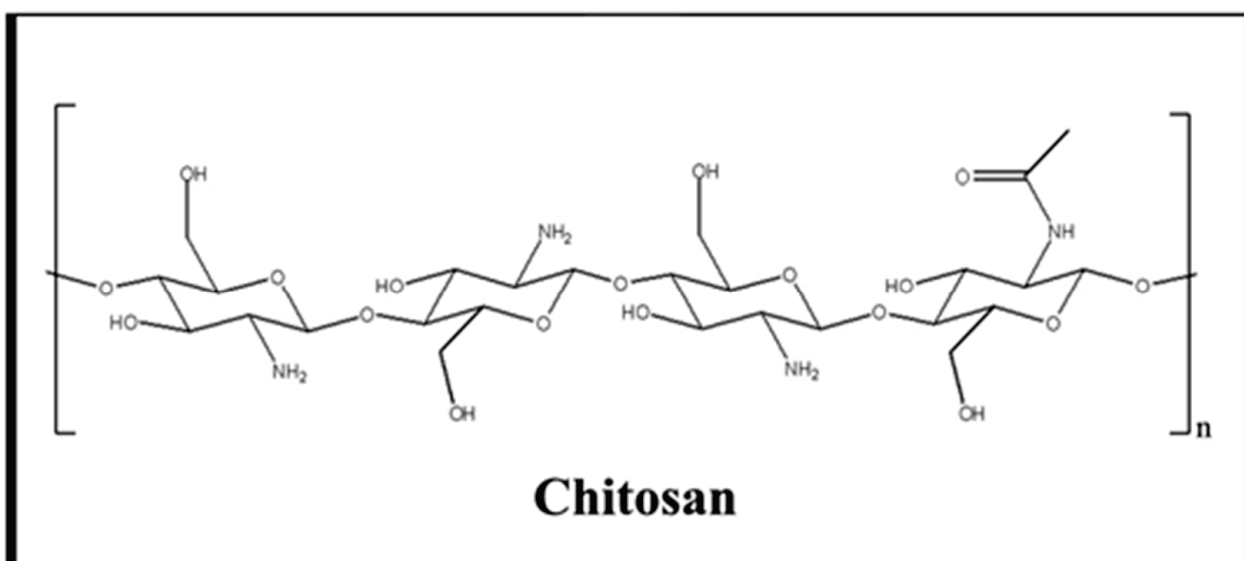
Scheme 1. Chemical structure of chitosan.

Here, we present a spectroscopic and thermodynamic analysis of the conjugation of cis– and trans–Pt with chitosan 15 and 100 KD in an aqueous solution at pH 5–6, using a constant polymer concentration and various drug contents. Structural information regarding Pt drug binding sites, binding efficacy, and the stability of Pt–chitosan complexes are discussed in this study.

2. Results and Discussion

2.1. Stability of Drug–Chitosan Complexes by UV Spectroscopy

The binding constants of cis– and trans–Pt with chitosan nanoparticles were determined as described in Section 3 [26,27]. The increasing drug concentration resulted in a constant decrease in UV light of chitosan at 270 nm (Figure 1). This is in agreement with the aggregation of chitosan upon drug interaction (Figures 1 and 2). The double reciprocal plot of $1/(A_0 - A)$ vs. $1/(\text{drug concentration})$ is linear and the binding constants (K) are estimated from the ratio of the intercept to the slope (Figures 1 and 2), where A_0 is the initial absorbance of the free polymer at 270 nm and A is the recorded absorbance of complexes at different drug concentrations. The binding constants were of Kch–15–cis–Pt = 1.44 ($\pm$0.6) $\times$ 10^5 M^{-1}, Kch–100–cis–Pt = 1.89 ($\pm$0.9) $\times$ 10^5 M^{-1} and Kch–15–trans–Pt = 9.84 ($\pm$0.5) $\times$ 10^4 M^{-1}, Kch–100–trans–Pt = 1.15 ($\pm$0.6) $\times$ 10^5 M^{-1} (Figures 1 and 2 and Table 1). Cis–Pt forms more stable complexes than trans–Pt–chitosan adducts, while stronger binding was observed for chitosan 100 in comparison to chitosan 15 KD. Thermodynamic analysis of drug–chitosan interactions with regard to hydrophobic and hydrophilic contacts are discussed below.
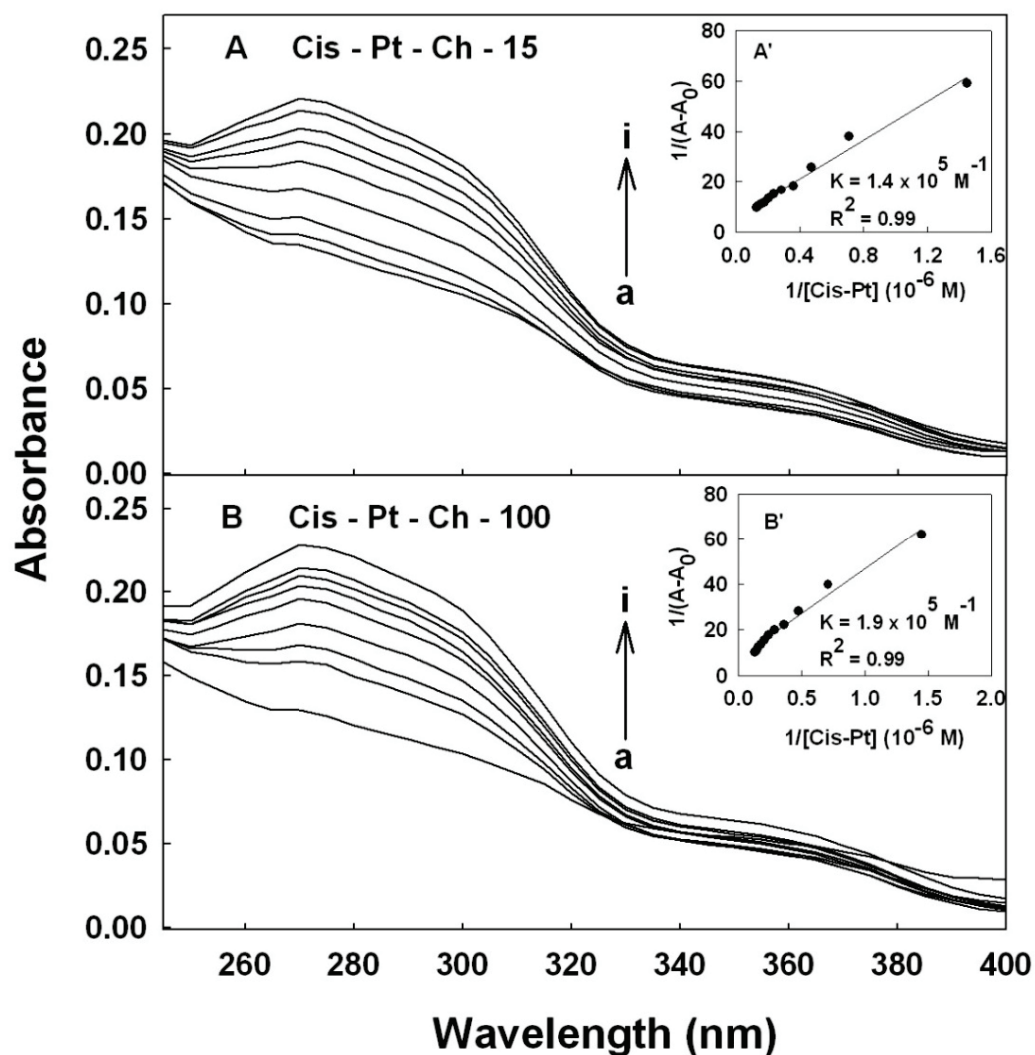
Figure 1. UV–visible spectra of chitosan nanoparticles with cis–Pt with free chitosan at 60 μM (a) and cis–Pt at 1, 5, 10, 20, 30, 40, 60, and 80 μM (b–i). Inset: plot of $1/(A_0 - A)$ vs. (1/drug concentration) and binding constant (K) for cis–Pt–polymer complexes. (**A**) Cis–Pt–Ch–15, (**B**) Cis–Pt–Ch–100.

Table 1. Variations in the binding constants for Ch–15 and Ch–100 kD with cis–Pt and trans–Pt at different temperatures.

Complexes	Temperature (K)	Binding Constant K (mol/L)$^{-1}$
Cis–Pt–Ch–15	298.15	1.44×10^5
	308.15	1.24×10^5
	318.15	1.02×10^5
Cis–Pt–Ch–100	298.15	1.89×10^5
	308.15	1.23×10^5
	318.15	9.39×10^4
Trans–Pt–Ch–15	298.15	9.84×10^4
	308.15	8.44×10^4
	318.15	7.63×10^4
Trans–Pt–Ch–100	298.15	1.14×10^5
	308.15	1.01×10^5
	318.15	8.50×10^4
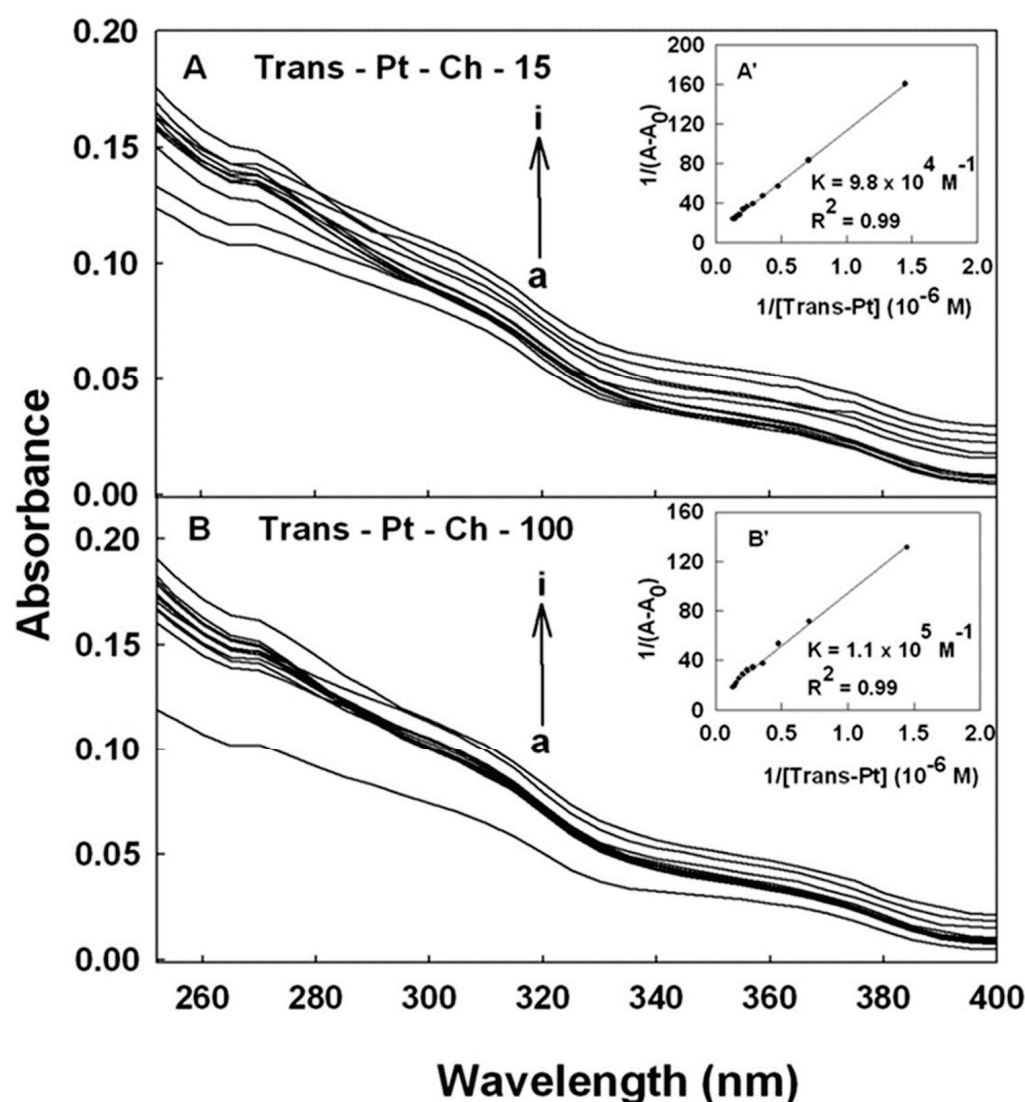
Figure 2. UV–visible spectra of chitosan nanoparticles with trans–Pt with free chitosan at 60 µM (a) and trans–Pt at 1, 5, 10, 20, 30, 40, 60, and 80 µM (b–i). Inset: plot of $1/(A_0 − A)$ vs. (1/drug concentration) and binding constant (*K*) for trans–Pt–polymer complexes. (**A**) Trans–Pt–Ch–15, (**B**) Trans–Pt–Ch–100.

2.2. Thermodynamic Analysis of Drug–Chitosan Adducts

The conjugation of Pt drugs was further analyzed by thermodynamic analysis. Based on the data of ΔH^0 and ΔS^0, the nature of drug–chitosan interactions was determined [28–31]. The thermodynamic parameters for the interaction of the Pt drugs and chitosan nanoparticles at 298.15, 308.15, and 318.15 *K* are shown in Figures 3 and 4 and Table 2. The negative sign of ΔG^0 showed that the binding process between drug and polymer is spontaneous. The drug–polymer complexes have negative ΔH^0, showing that the complex formation between the polynucleotide and the Pt drugs is an exothermic reaction. The negative ΔH^0 and positive ΔS^0 for drug adducts indicate that ionic interactions are observed in the Pt–chitosan complexation [28–31]. Therefore, the enthalpy provides more contribution to ΔG^0 than entropy, which indicates that the binding process is enthalpy driven (Table 2).
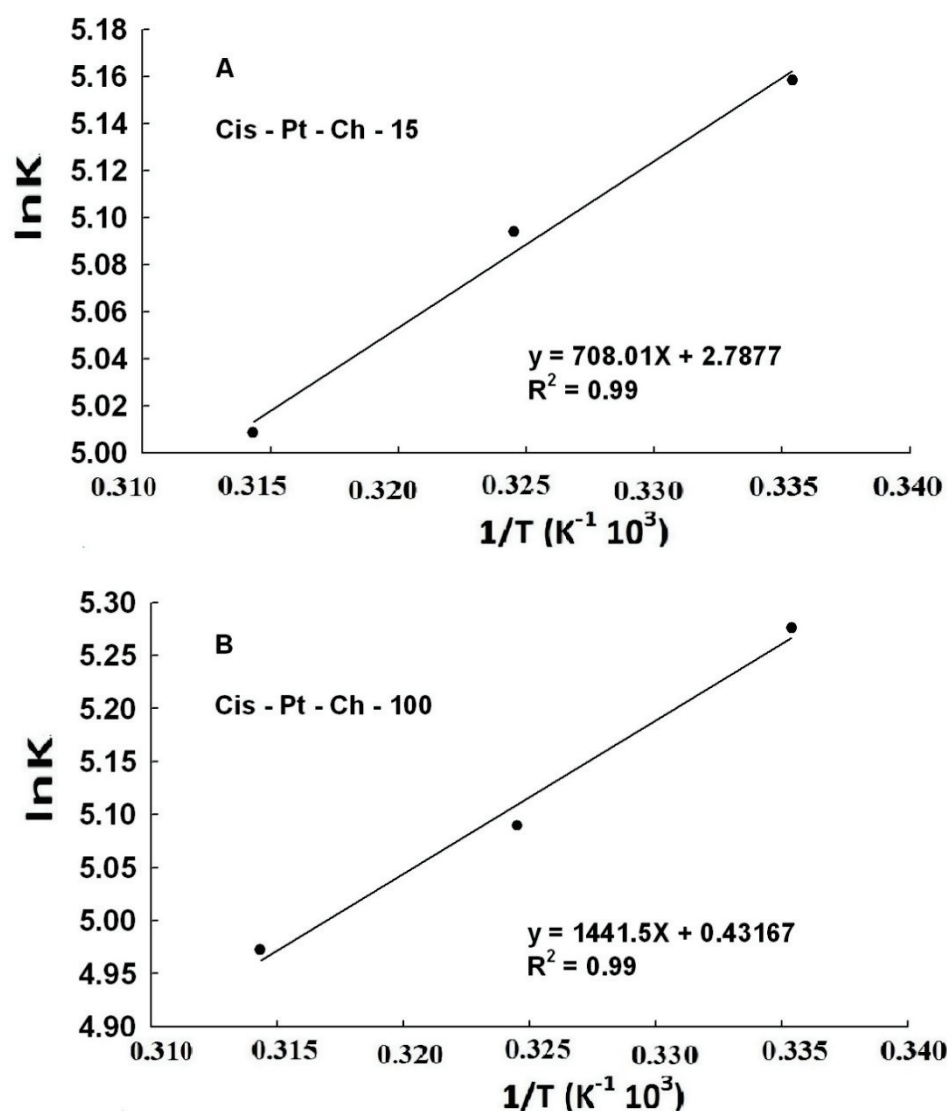
Figure 3. lnK vs. 1/T for chitosan with cis–Pt conjugates: (**A**) Cis–Pt–Ch–15; (**B**) Cis–Pt–Ch–100.

Table 2. Thermodynamic parameters for Ch–15 and Ch–100 kD with cis–Pt and trans–Pt.

Complexes	ΔH^0 (kJ. mol^{-1})	ΔS^0 (J. mol^{-1}. K^{-1})	TΔS^0 (kJ. mol^{-1})	ΔG^0 (kJ. mol^{-1})
		Thermodynamic Parameters		
Cis–Pt–Ch–15	−5.89	23.18	6.91	−12.80 (298.15 K)
			7.14	−13.03 (308.15 K)
			7.37	−13.26 (318.15 K)
Cis–Pt–Ch–100	−11.98	3.59	1.07	−13.05 (298.15 K)
			1.11	−13.09 (308.15 K)
			1.14	−13.13 (318.15 K)
Trans–Pt–Ch–15	−4.35	26.88	8.02	−12.37 (298.15 K)
			8.28	−12.64 (308.15 K)
			8.55	−12.91 (318.15 K)
Trans–Pt–Ch–100	−5.00	25.3	7.54	−12.54 (298.15 K)
			7.79	−12.80 (308.15 K)
			8.05	−13.05 (318.15 K)
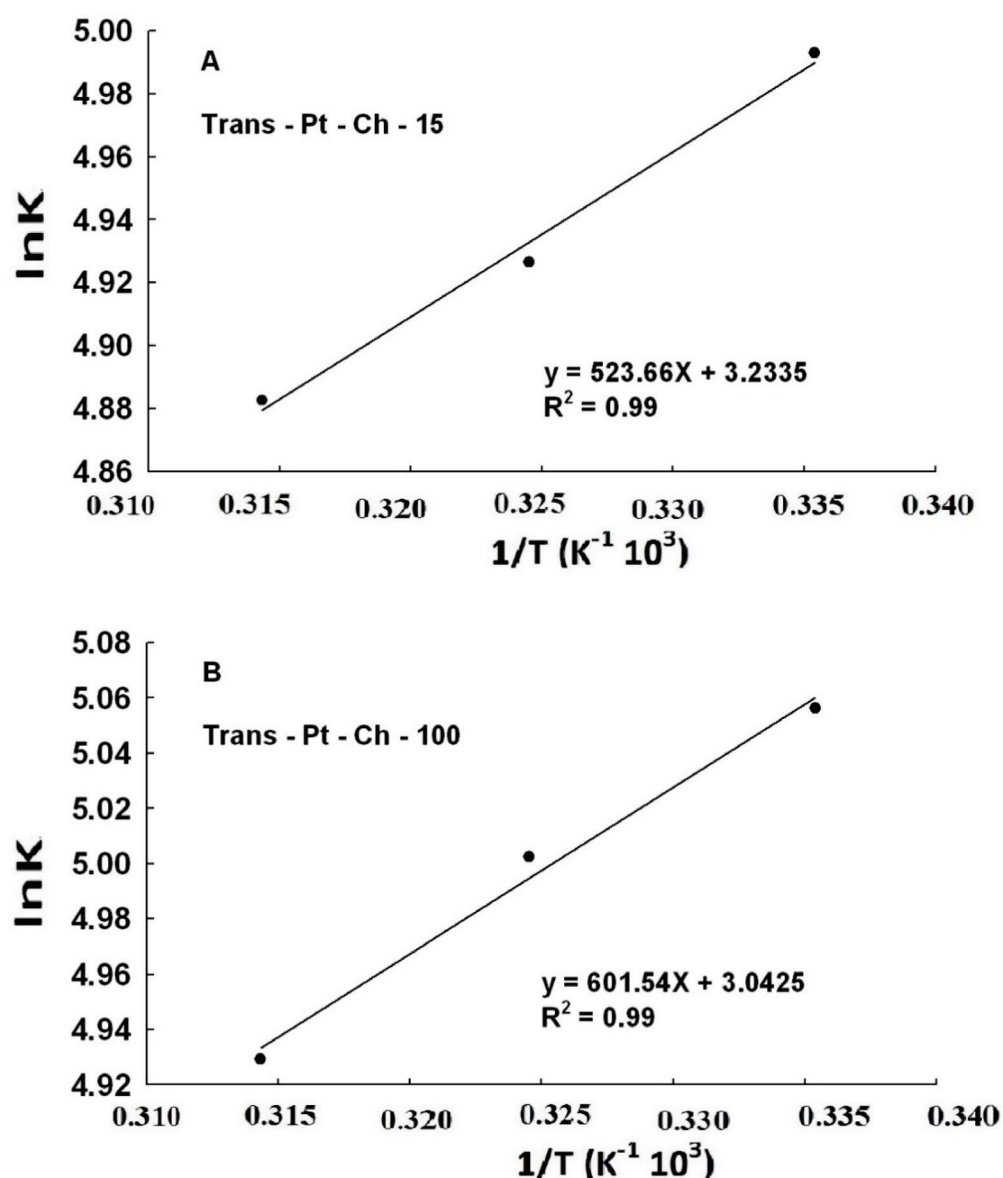
Figure 4. lnK vs. 1/T for chitosan with trans–Pt conjugates: (**A**) Trans–Pt–Ch–15; (**B**) Trans–Pt–Ch–100.

The binding efficacy for drug–chitosan conjugates was determined as reported [32]. The binding efficacy was estimated to be 75% for cis–Pt and 65% for trans–polymer complexes.

2.3. FTIR Spectra of Pt Drug–Chitosan Complexes

The chitosan interactions with cis– and trans–Pt were characterized by infrared spectroscopy and its derivative methods. The spectral shifting and intensity variations in protein and chitosan amide I band at 1656–1630 cm^{-1} (mainly C=O stretch) and amide II band at 1547–1525 cm^{-1} (C–N stretching coupled with N–H bending modes) [9,33] were monitored upon Pt interaction. The difference spectra ((chitosan solution + Pt drug solution)–(chitosan solution)) were obtained, in order to monitor the intensity variations in these vibrations and the results are shown in Figures 5 and 6.
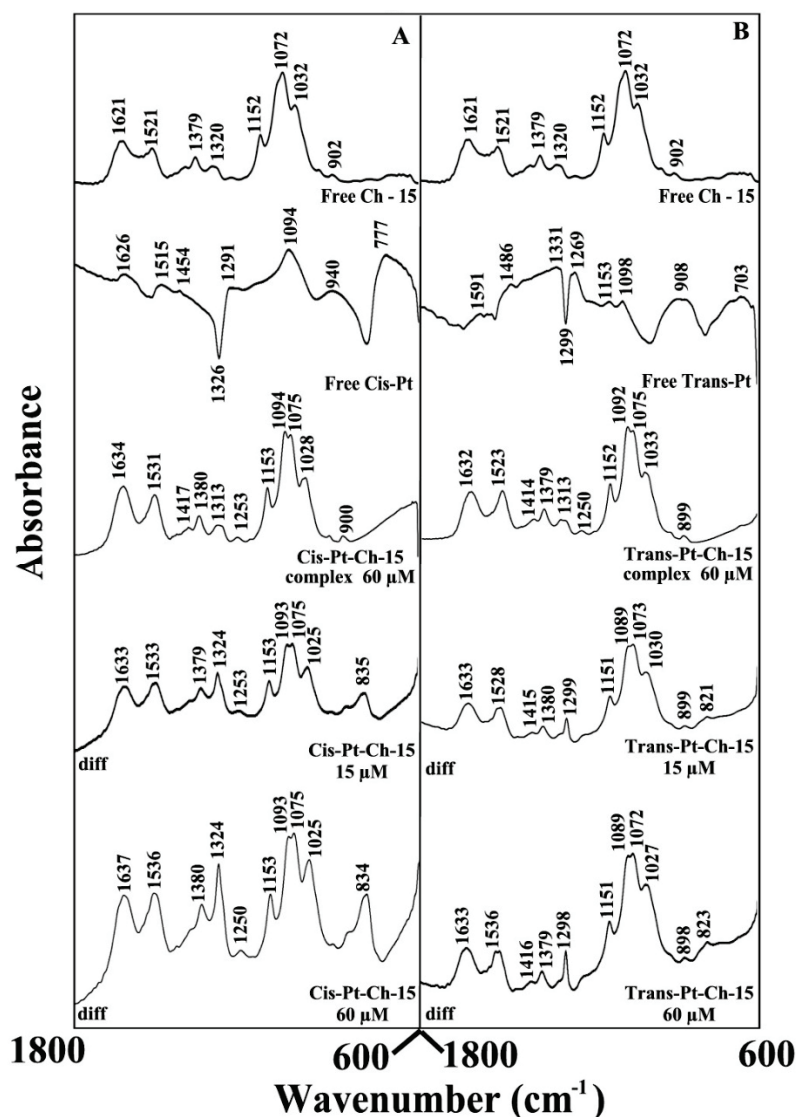
Figure 5. FTIR spectra in the region of 1800–600 cm^{-1} of hydrated films (pH 5–6) for chitosan–15 kD with cis–Pt (**A**) and trans–Pt (**B**) with chitosan (60 μM) and its Pt conjugates with difference spectra (diff.) (bottom two curves) obtained at different drug concentrations (indicated on the figure).

At a low polymer concentration (15 μM), an increase in intensity was observed for the protein amide I at 1658–1656 and amide II at 1544–1543 cm^{-1} in the difference spectra of the chitosan–cis–Pt and chitosan–trans–Pt complexes (Figures 5A,B and 6A,B, and diff., 15 μM). The positive features located in the difference spectra for the amide I and II bands at 1657, 1546 cm^{-1} (ch–15–Pt) and 1661, 1551 cm^{-1} (ch–100–Pt) are due to the increase in the intensity of chitosan amide I and amide II bands upon Pt drug interaction (Figures 5 and 6 and diffs 15 μM). This increase in the intensity for the polymer amide I and amide II bands is due to chitosan binding to Pt drug via C=O, C–N, and N–H groups (hydrophilic contacts).

As the chitosan concentration increased to 60 μM, strong positive features were observed for the amide I band at 1656, 1546 (ch–15–Pt) and 1654, 1546 (ch–100–Pt), upon chitosan complexation (Figures 5A,B and 6A,B, and diff., 60 μM). In addition, spectral shifting was observed for chitosan amide I at 1637–1632 and amide II at 1540–1526 cm^{-1} upon polymer–Pt complexation (Figures 5A,B and 6A,B, and 60 μM complexes). The observed spectral shifting and intensity variations in the amide I and amide II bands are due to chitosan binding via C–O, C–N, and NH_2 groups [9].
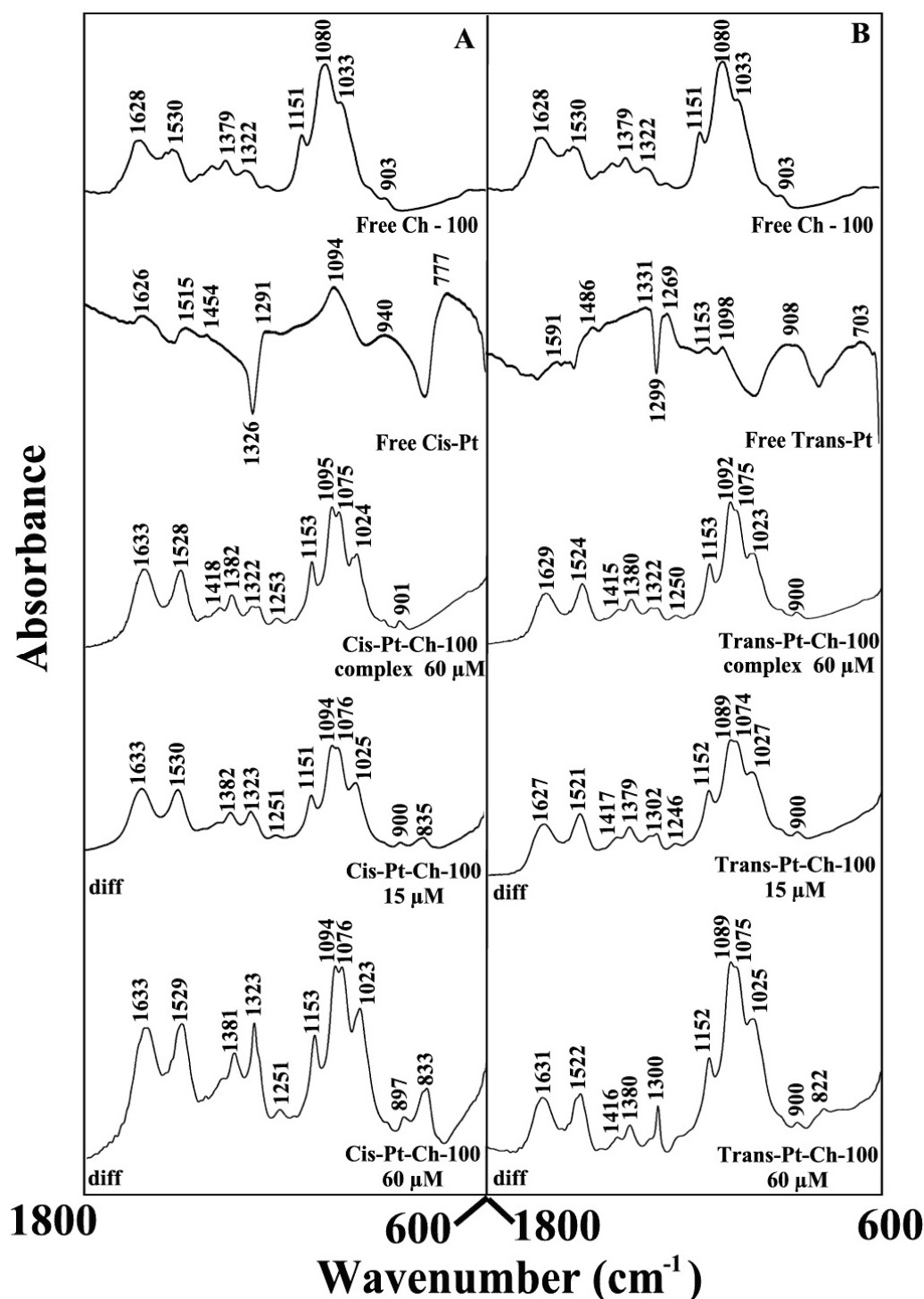
Figure 6. FTIR spectra in the region of 1800–600 cm^{-1} of hydrated films (pH 5–6) for chitosan–100 KD with cis–Pt (**A**) and trans–Pt (**B**) with chitosan (60 μM) and its Pt conjugates with difference spectra (diff.) (bottom two curves) obtained at different drug concentrations (indicated on the figure).

3. Materials and Methods

3.1. Materials

Purified chitosan 15 and 100 KD (90% deacetylated) were from Polysciences Inc. (Warrington, FL, USA) and used as supplied. Cis– and trans–Pt(NH$_3$)Cl$_2$ were purchased from Sigma Chemical Company (St. Louis, MO, USA) and used as supplied. Other chemicals were of reagent grade and used without further purification.

3.1.1. Preparation of Cis– and Trans–Pt Adducts with Chitosan Nanoparticles

Chitosan nanoparticles were prepared as reported in an earlier study [34,35]. Chitosan was dissolved in acid solution (40 mg/mL or 0.5 mM) containing 10 mM acetate buffer (pH 5–6). HCl (1 mmol) was used for this preparation. An appropriate amount of cis–Pt or trans–Pt was dissolved in water solution and diluted in Tris–HCl. Pt–chitosan complexes were characterized by UV, FTIR, and thermodynamic analysis.

3.1.2. UV–Visible Spectroscopy

The UV–Vis spectra were recorded on a Cary 60 UV–Visible spectrophotometer with a slit of 2 nm and a scan speed of 400 nm min^{-1}. Quartz cuvettes of 1 cm were utilized. The absorbance measurements were performed at pH 7.2 by keeping the concentration of chitosan constant (60 µM), while increasing drug concentrations (1 to 60 µM). The binding constants of drug–chitosan adducts were determined as reported [26].

The drug–chitosan binding constants were calculated according to the following equations:

$$\text{Chitosan + drug} \Leftrightarrow \text{Chitosan:drug} \tag{1}$$

$$K = [\text{Chitosan: drug complex}]/[\text{chitosan}]_{unc.}\,[\text{drug}]_{unc.} \tag{2}$$

wherein

drug = cis–Pt or trans–Pt and unc. stands for uncomplexed.

The values of the binding constants K were obtained from the chitosan absorption at 270 nm according to the methods published in the literature [26] where the bindings of various ligands to biomolecules were described. For weak binding affinities, the data were treated using linear reciprocal plots based on the following equation:

$$\frac{1}{A - A_0} = \frac{1}{A - A_0} + \frac{1}{K(A_\infty - A_0)} \cdot \frac{1}{C_{ligand}} \tag{3}$$

where A_0 is the absorbance of chitosan at 270 nm in the absence of ligand, A_∞ is the final absorbance of the ligated-chitosan, and A is the recorded absorbance at different ligand concentrations. The double reciprocal plot of $1/(A - A_0)$ vs. $1/C_{ligand}$ is linear and the binding constant (K) can be estimated from the ratio of the intercept to the slope [26].

3.1.3. FTIR Spectroscopy

Infrared spectra were recorded on a FTIR spectrometer (Impact 420 model), equipped with deuterated triglycine sulfate (DTGS) detector and KBr beam splitter, using AgBr windows. Solutions of drugs were added dropwise to chitosan solution with constant stirring to ensure the formation of a homogeneous solution and with drug concentrations of 15, 30, and 60 µM, and a final chitosan concentration of 60 µM. Spectra were collected after 2 h incubation of polymer with drug solution at room temperature, using hydrated films. Interferograms were accumulated over the spectral range 4000–600 cm^{-1} with a nominal resolution of 2 cm^{-1} and 100 scans. Bands from chitosan in-plane vibrational frequencies were used as standard reference in spectral subtraction [9,33].

4. Conclusions

Pt drugs bind chitosan via hydrophilic and hydrophobic contacts with more stable complexes formed for cis–Pt than for trans–Pt. Chitosan 100 forms stronger complexes with Pt than with chitosan 15 KD. As chitosan size becomes larger, protein self–aggregation occurs, which induces a major effect on polymer–drug interactions. From this study, it is established that chitosan 100 is a stronger Pt carrier than chitosan 15 KD. The former could be used to transport Pt–based drugs, potentially enhancing efficacy and drug availability in vivo.

Abbreviations

Ch	chitosan
cis– and trans–Pt	Cis– and trans–Pt(NH$_3$)$_2$Cl$_2$
FTIR	Fourier transform Infrared

References

1. Amidi, M.; Mastrobattista, E.; Jiskoot, W.; Hennink, W.E. Chitosan-based delivery systems for protein therapeutics and antigens. *Adv. Drug Deliv. Rev.* **2010**, *62*, 59–82. [CrossRef] [PubMed]
2. Gan, Q.; Wang, T. Chitosan nanaoparticles as protein delivery carrier-systematic examination of fabrication conditions for efficient loading and release. *Colloids Surf. B* **2007**, *59*, 24–34. [CrossRef] [PubMed]
3. Pacheco, N.; Garnica, G.M.; Gimeno, M.; Barzana, E.; Trombotto, S.; David, L.; Shirai, K. Structural characterization of chitin and chitosan obtained by biological and chemical methods. *Biomacromolecules* **2011**, *12*, 3285–3290. [CrossRef] [PubMed]
4. Rabea, E.I.; Badawy, M.E.T.; Stevens, C.V.; Smagghe, G.; Steurbaut, W. Chitosan as antimicrobial agent: Application and mode of action. *Biomacromolecules* **2003**, *4*, 1457–1465. [CrossRef] [PubMed]
5. Dang, J.M.; Leong, K.W. Natural polymers for gene delivery and tissue engineering. *Adv. Drug Deliv. Rev.* **2006**, *58*, 487–499. [CrossRef] [PubMed]
6. Mao, S.; Shuai, X.; Unger, F.; Simon, M.; Bi, D.; Kissel, T. The depolymerization of chitosan: Effects on physicochemical and biological properties. *Int. J. Pharm.* **2004**, *281*, 45–54. [CrossRef] [PubMed]
7. Saranya, N.; Moorthi, A.; Saravanan, S.; Pandima Devi, M.; Selvamurugan, N. Chitosan and its derivatives for gene delivery. *Int. J. Biol. Macromol.* **2011**, *49*, 234–238. [CrossRef]
8. Shu, Z.; Zhu, K.J. A Novel approach to prepare tripolyphosphate: Chitosan complex beads for controlled release drug delivery. *Int. J. Pharm.* **2000**, *201*, 51–58. [CrossRef]
9. Sanyakamdhorn, S.; Agudelo, D.; Tajmir-Riahi, H.A. Encapsulation of anitumor drug doxorubicin and its analogue by chitosan nanoparticles. *Biomacromolecules* **2013**, *14*, 557–563. [CrossRef]
10. Bowman, K.; Leong, K.W. Chitosan nanoparticles for oral drug and gene delivery. *Int. J. Nanomed.* **2006**, *1*, 117–128. [CrossRef]
11. Sultan, M.H.; Moni, S.S.; Madkhali, O.A.; Bakkari, M.A.; Alshahrani, S.; Alqahtani, S.S.; Alhakamy, N.A.; Mohan, S.; Ghazwani, M.; Bukhary, H.A.; et al. Characterization of cisplatin-loaded chitosan nanoparticles and rituximab-linked surfaces as target-specific injectable nano-formulations for combating cancer. *Sci. Rep.* **2022**, *12*, 468. [CrossRef]
12. Iqbal, H.; Khan, B.A.; Khan, Z.U.; Razzaq, A.; Khan, N.U.; Menaa, B.; Menaa, F. Fabrication, physical characterizations and in vitro antibacterial activity of cefadroxil-loaded chitosan/poly(vinyl alcohol) nanofibers against *Staphylococcus aureus* clinical isolates. *Int. J. Biol. Macromol.* **2020**, *144*, 921–931. [CrossRef]
13. Anirudhan, T.S.; Mohan, M.; Rajeev, M.R. Modified chitosan-hyaluronic acid based hydrogel for the pH-responsive co-delivery of cisplatin and doxorubicin. *Int. J. Biol. Macromol.* **2022**, *201*, 378–388. [CrossRef]
14. Johnstone, T.C.; Suntharalingam, K.; Lippard, S.J. The next generation of platinum drugs: Targeted Pt(II) agents, nanoparticle delivery, and Pt(IV) prodrugs. *Chem. Rev.* **2016**, *116*, 3436–3486. [CrossRef]
15. Butler, J.S.; Sadler, P.J. Targeted delivery of platinum-based anticancer complexes. *Curr. Opin. Chem. Biol.* **2013**, *17*, 175–188. [CrossRef]
16. Song, H.; Li, W.; Qi, R.; Yan, L.; Jing, X.; Zheng, M.; Xiao, H. Delivering a photosensitive transplatin prodrug to overcome cisplatin drug resistance. *Chem. Commun.* **2015**, *51*, 11493–11495. [CrossRef]
17. Peleg-Shulman, T.; Najajreh, Y.; Gibson, D. Interactions of cisplatin and transplatin with proteins. Comparison of binding kinetics, binding sites and reactivity of the Pt-protein adducts of cisplatin and transplatin towards biological nucleophiles. *J. Inorg. Biochem.* **2002**, *91*, 306–311. [CrossRef]

18. Aryal, S.; Hu, C.M.J.; Zhang, L. Polymer-cisplatin conjugate nanoparticles for acid-responsive drug delivery. *ACS Nano* **2010**, *26*, 251–258. [CrossRef]

19. Casini, A.; Reedijk, J. Interactions of anticancer Pt compounds with proteins: An overlooked topic in medicinal inorganic chemistry? *Chem. Sci.* **2012**, *3*, 3135–3144. [CrossRef]

20. Corinti, D.; Coletti, C.; Re, N.; Piccirillo, S.; Giamp, M.; Crestonia, M.E.; Fornarini, S. Hydrolysis of cis- and transplatin: Structure and reactivity of the aqua complexes in a solvent free environment. *RSC Adv.* **2017**, *7*, 15877–15884. [CrossRef]

21. Ferraro, G.; Massai, L.; Messorib, L.; Merlino, A. Cisplatin binding to human serum albumin: A structural study. *Chem. Commun.* **2015**, *51*, 9436–9439. [CrossRef]

22. Ahmad, S. Kinetic aspects of platinum anticancer agents. *Polyhedron* **2017**, *138*, 109–124. [CrossRef]

23. Mori, H.; Hirayama, N.; Komeiji, Y.; Mochizuki, Y. Differences in hydration between cis- and trans-platin: Quantum insights by ab initio fragment molecular orbital-based molecular dynamics (FMO–MD). *Comput. Theor. Chem.* **2012**, *986*, 30–34. [CrossRef]

24. Kartalou, M.; Essigmann, J.M. Recognition of cisplatin adducts by cellular proteins. *Mutat. Res. Fund. Mol.* **2001**, *478*, 1–21. [CrossRef]

25. Brabec, V.; Hrabina, O.; Kasparkova, J. Cytotoxic platinum coordination compounds. DNA binding agents. *Coord. Chem. Rev.* **2017**, *351*, 2–31. [CrossRef]

26. Yanat, M.; Schroën, K. Preparation methods and applications of chitosan nanoparticles; with an outlook toward reinforcement of biodegradable packaging. *React. Funct. Polym.* **2021**, *161*, 104849. [CrossRef]

27. Chanphai, P.; Tajmir-Riahi, H.A. Conjugation of tea catechins with chitosan nanoparticles. *Food Hydrocoll.* **2018**, *84*, 561–570. [CrossRef]

28. Connors, K.A. Binding constants: The measurement of molecular complex stability. *Eur. J. Med. Chem.* **1987**, *22*, 90280–90287.

29. Brugnerotto, J.; Lizardi, J.; Goycoolea, F.M.; Arguelles-Monal, W.; Desbrieres, J.; Rinaudo, M. An infrared investigation in relation with chitin and chitosan characterization. *Polymer* **2001**, *42*, 3569–3580. [CrossRef]

30. Liu, D.; Yuanan Pingjia, W.; Linbin Jiang, Y. Determination of the degree of acetylation of chitosan by UV spectrophotometry using dual standards. *Carbohydr. Res.* **2006**, *341*, 782–785. [CrossRef]

31. Ross, P.D.; Subramanian, S. Thermodynamics of protein association reactions: Forces contributing to stability. *Biochemistry* **1981**, *20*, 3096–3102. [CrossRef]

32. Bose, A. Interaction of tea polyphenols with serum albumins: A fluorescence spectroscopic analysis. *J. Lumin.* **2016**, *169*, 220–226. [CrossRef]

33. Bekale, L.; Agudelo, D.; Tajmir-Riahi, H.A. Effect of polymer molecular weight on chitosan-protein interaction. *Colloids Surf. B* **2015**, *125*, 309–317. [CrossRef]

34. Bekale, L.; Chanphai, P.; Sanyakamdhorn, S.; Agudelo, D.; Tajmir-Riahi, H.A. Microscopic and thermodynamic analysis of PEG-lactoglobulin interaction. *RSC Adv.* **2014**, *4*, 31084–31093. [CrossRef]

35. Chandra, S.; Dietrich, S.; Lang, H.; Bahadur, D. Dendrimer–doxorubicin conjugate for enhanced therapeutic effects for cancer. *J. Mater. Chem.* **2011**, *21*, 5729–5737. [CrossRef]

The Challenging Treatment of Cisplatin-Resistant Tumors: State of the Art and Future Perspectives

Giulia Coffetti, Martina Moraschi, Giorgio Facchetti *[ID] and Isabella Rimoldi *[ID]

Department of Pharmaceutical Sciences, University of Milan, Via Venezian 21, 20133 Milano, Italy
* Correspondence: giorgio.facchetti@unimi.it (G.F.); isabella.rimoldi@unimi.it (I.R.)

Abstract: One of the main problems in chemotherapy using platinum drugs as anticancer agents is the resistance phenomenon. Synthesizing and evaluating valid alternative compounds is challenging. This review focuses on the last two years of progress in the studies of platinum (II)- and platinum (IV)-based anticancer complexes. In particular, the research studies reported herein focus on the capability of some platinum-based anticancer agents to bypass resistance to chemotherapy, which is typical of well-known drugs such as cisplatin. Regarding platinum (II) complexes, this review deals with complexes in trans conformation; complexes containing bioactive ligands, as well as those that are differently charged, all experience a different reaction mechanism compared with cisplatin. Regarding platinum (IV) compounds, the focus was on complexes with biologically active ancillary ligands that exert a synergistic effect with platinum (II)-active complexes upon reduction, or those for which controllable activation can be realized thanks to intracellular stimuli.

Keywords: platinum (II) complexes; platinum (IV) complexes; anticancer agents; orphan tumors; resistance phenomena

1. Introduction

Cancer is one of the most lethal diseases, causing millions of deaths worldwide [1,2]. In particular, carcinogenesis, the process responsible for healthy cells' transformation into tumoral cells, is characterized by multi-stage evolution: initiation, promotion, and the malignant transformation of cells and progression [3–5]. During this process, some DNA mutations occur, providing the cancer with different distinctive features, such as uncontrolled cell proliferation, replicative cell immortality, the circumvention of growth suppressors (p53, RAS), the induction of angiogenesis, resistance to cell death, activation to invasion, and metastasis [6–8]. The principal cancer treatments rely on surgical resection, radiotherapy, chemotherapy, immunotherapy, and targeted therapy, but usually combined therapy is the preferred choice. Indeed, after surgery, the patient often undergoes radio- or chemotherapy [9]. The most common chemotherapeutic agents are based on platinum complexes, among which the first-in-class drug is cisplatin [10–12]. Transport across the cancer cell membrane is the first step for cisplatin therapy to be successful. Cisplatin is a highly polar species, and its cellular accumulation generally occurs at a slower rate compared with that of other small-molecule anticancer drugs. Apart from passive diffusion, other non-saturable systems, such as fluid-phase endocytosis, may be involved in platinum drug uptake, and evidence for some active or facilitated transport has been identified over the years. Moreover, several experiments have demonstrated a direct connection, with platinum-containing compounds trafficking to copper transporters [13]. Subsequent studies have highlighted the role of Ctr-1 in the uptake of cisplatin analogs. Arnesano's extensive work [14–16] showed that the role of Ctr-1 and the other proteins involved in copper metabolism is unambiguously connected to platinum drug movements across cell membranes. Upon aquation, cisplatin is activated, and it is responsible for DNA lesions due to the formation of intrastrand crosslinks; this activates signal transduction pathways,

leading to apoptosis [13,17]. On the other hand, it is also responsible for numerous side effects and, above all, drug resistance, inducing therapeutic failure despite consistent initial response rates [18,19]. Three mechanisms define cisplatin's direct involvement, demonstrating the chemo-resistant tumor cell phenotype: pre-target, on-target, and post-target resistance [20–22]. The first is characterized by reduced intracellular accumulation and increased cisplatin sequestration caused by GSH and other scavengers. For example, recent metabolomics studies have revealed that the presence of the enzyme glucose-6-phosphate dehydrogenase (G6PDH) in cisplatin-resistant ovarian cell lines is responsible for NADPH production, which maintains the GSH level and redox balance, thus reducing cisplatin's effectiveness [23]. In the second, activating particular classes of DNA polymerases removes platinum–DNA adducts that would normally generate an apoptotic signal. Moreover, multidrug resistance-associated proteins (MRPs) and ATP-binding cassette (ABC) transporters can also induce cellular resistance to cisplatin. MRP2 is mostly responsible for this effect, as its levels are overexpressed in patients with colorectal, hepatocellular, and esophageal cancer. Finally, after the interaction between cisplatin and DNA takes place, the third resistance mechanism involves defects in the signal transduction pathways that usually bring about cell death [24,25]. This is the main subject driving research toward developing new derivative complexes that can overcome these resistance mechanisms. For example, an emerging approach relies on introducing different metals. A vast library of non-platinum metal complexes has been prepared and evaluated for anticancer activities for this purpose. Ruthenium is one of the most investigated non-Pt metals for cancer treatment: Ru(III) complexes, especially NAMI-type ones, are useful for their excellent antimetastatic properties [26]. Moreover, polypyridyl Ru(II) complexes have been extensively investigated as a possible DNA "light switch", with interesting photophysical and cell migration inhibition properties [27]. Another promising strategy to improve the anticancer efficacy of platinum drugs and overcome their shortcomings is incorporating a second metal center with distinct biological targets, oxidation states, and ligand(s) of different natures into platinum complexes, which could influence their modes of action [28].

Additional studies have led to the discovery of a second and third generation of platinum complexes. Respectively, these are carboplatin, which possesses higher solubility and stability than cisplatin, and oxaliplatin, which is water-soluble and exhibits a broader spectrum of activity than other complexes.

Starting from cisplatin's structure, some ligand modifications that could improve the complex's biological properties have been introduced [29,30].

This review aims to go through all the progress of the last two years regarding the design of platinum complexes, both as Pt(II) and Pt(IV), used as anticancer agents in the treatment of cisplatin-resistant and orphan tumors (Figure 1).
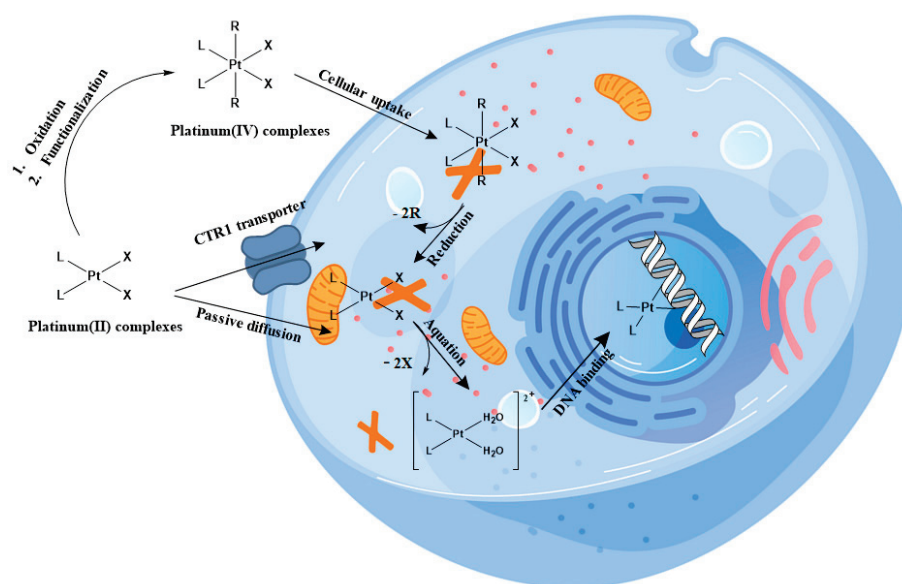
Figure 1. Pt(II) and Pt(IV) trafficking within cells.

2. Treatment of Cisplatin-Resistant Tumors: Pt(II) Complexes

2.1. Pt(II) Complexes in Trans Conformation

There are different ways to overcome cisplatin drug resistance, side effects, toxicity, and poor selectivity. One of them is related to the introduction of a trans conformation of Pt(II) complexes. The advantage of this approach is that there are different structural and DNA-binding properties in comparison with cisplatin and its derivatives, which notably possesses a cis arrangement of ligands around the metal center. For this reason, a series of trans-Pt(II) complexes (complex **1**) with heterocyclic thionate ligands has been synthesized (Figure 2) [31].
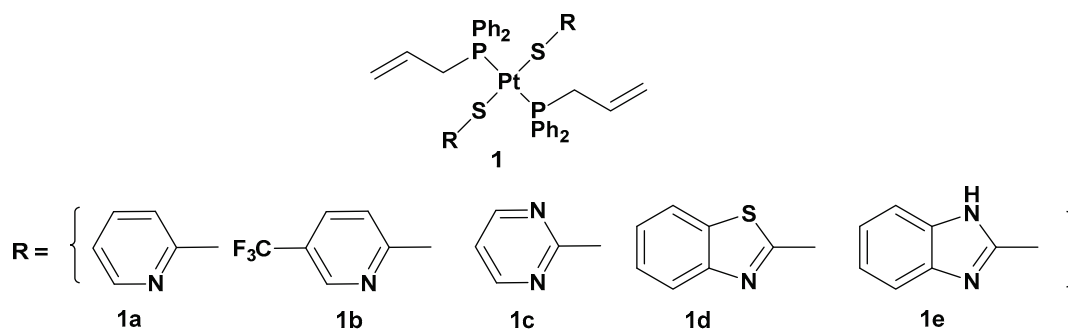
Figure 2. *Trans*-Pt(II) complexes with heterocyclic thionate ligands **1a–1e**.

All of these new complexes have been tested on three human cancer cell lines (A549 lung, SKOV3 ovarian, and MCF-7 breast cancer cell lines) and studied for their antiproliferative activities in comparison with cisplatin and complex **2**, a dichloride Pt(II) complex counterpart in a cis conformation (Figure 3).
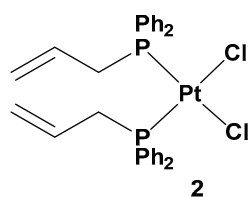
Figure 3. Dichloride *cis*-Pt(II) complex (complex **2**).

All the new complexes showed cytotoxicity in vitro against the three cancer cell lines, but only complex **1a** showed statistically significant different activity compared with cisplatin, with significantly lower IC$_{50}$ values, 4.31, 6.23, and 4.80 µM, compared with 9.71, 14.48, and 11.59 µM for cisplatin against A549, SKOV3, and MCF-7, respectively. Moreover, and most importantly, all complexes showed selectivity between tumorigenic and nontumorigenic cell lines. Interestingly, complex **2** showed lower antiproliferative activity (22.49, 34.50, and 19.01 µM against A549, SKOV3, and MCF-7, respectively) than others; complex **1b** and, above all, **1a** showed an ability to induce apoptosis in cancer cells with the highest potency, such that **1a** has been used as the representative compound of the series in further studies. In addition, **1a** can target the genomic content of MCF-7 cancerous cells and directly interact with DNA, as confirmed by comet assay. However, further studies are needed to identify the underlying mechanism of action of these platinum drugs within biological systems.

Analogously to complexes **1a–e**, trans-Pt(II) complexes with triphenylphosphine ligands have also been synthesized, and in particular, complexes **3** and **4** have been evaluated for their promising anticancer activities (Figure 4) [32]. Indeed, several analogs have been studied, starting with complexes **3** and **4,** where a triphenylphosphine ligand was substituted with a triphenylarsine ligand (complexes **5** and **6**) with the same dialkylamino ligand preserved, in addition to the two chloride ligands. For all the performed studies, cisplatin was used as a reference and **3** and **4** were used as comparisons.
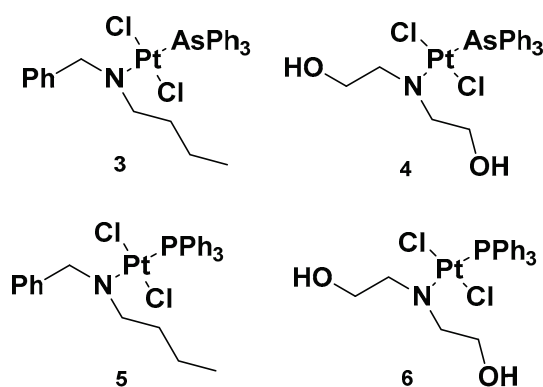
Figure 4. Complexes **3** and **4** and previously synthesized analogs **5** and **6**.

Complex **3**′s results were the most effective due to the presence of N,N-dialkylamino side chains, which contributed to an increase in lipophilicity in the complex. This is an important aspect to evaluate, as it could be useful in overcoming one of the primary issues involved in cisplatin resistance, i.e., low cellular accumulation. The Pt content found in cells incubated with **3** was found to be higher than the reference drug, suggesting the ease **3** has in crossing the cell membrane.

Furthermore, in comparison with complex **5**, complex **3** has a higher cytotoxic effect: the IC$_{50}$ values were 0.49 and 1.85 µM compared with 3.55 and 3.63 µM, seven and two times lower than complex **5** in sensitive and resistant ovarian carcinoma cells, A2780 and A2780cis, respectively. These results underline that the triphenylarsine group is more effective than the ancient triphenylphosphine group in eliciting cytotoxicity.

In studying platinum complex interactions with salmon testis DNA, complex **3** showed the ability to covalently link with the target, but to a lesser extent in comparison with the reference drug, cisplatin. In addition, this cytotoxicity was related to the ability of complex **5** and complex **3** to interfere with the activity of topoisomerase II, an important enzyme involved in DNA metabolism and correct functionality. In particular, **3** behaved as a topoisomerase II poison. This detrimental effect on topoisomerase II, along with its ability to induce transmembrane depolarization in mitochondria, is primarily responsible for the cytotoxic effect of the complex, and it can promote cell death through the apoptotic pathway.

Another trans-conformation Pt(II) complex that can be used to overcome cisplatin resistance and its side effects is an inhibitor of the Hedgehog (Hh) pathway based on GANT61 (Figure 5) [33]. The Hedgehog signaling pathway regulates cell differentiation, cell proliferation, and stem cell maintenance during embryonic development, which results in the transcription of three glioma-associated oncogene homolog (GLI) transcription factor proteins: GLI1, GLI2, and GLI3. Thus, inhibiting this pathway means targeting cancer stem cells (CSCs). GANT61 could be useful for this because it can inhibit the Hh pathway at the GLI level, and it shows antiproliferative activity in vitro and in vivo. In vivo, it undergoes hydrolysis to produce 4-pyridine carboxaldehyde (4-PCA) and the bioactive diamine derivative GANT61-D.
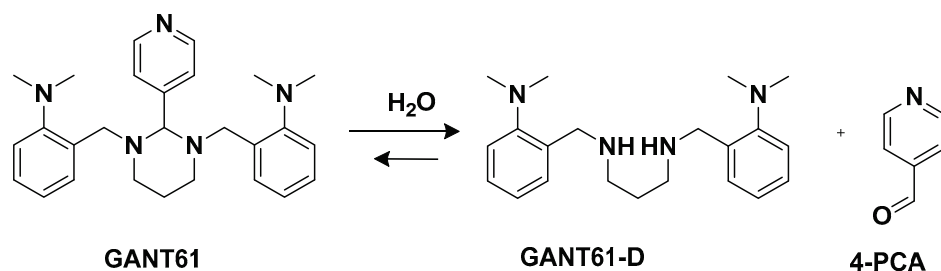
Figure 5. GANT61 hydrolysis releasing GANT61-D and 4-PCA.

Two *trans*-[Pt(II)Cl$_2$(dmso)L]-type complexes, **7** and **8**, where L represents both GANT61 and 4-PCA, have also been synthesized (Figure 6).
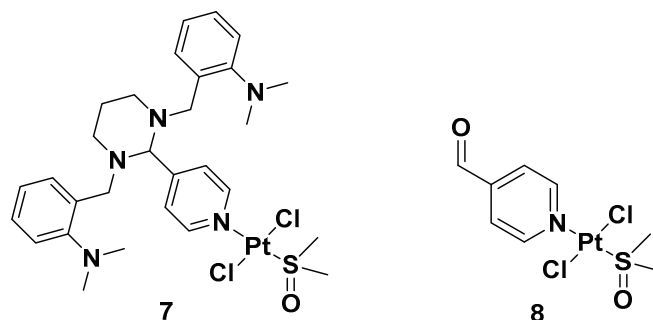
Figure 6. Complexes **7** and **8**.

Both complexes have been tested on two human mammary epithelial cell lines, HM-LER and HMLER-shEcad. This showed a larger cancer stem-like cell (CSC) population, using salinomycin as the positive control and cisplatin and carboplatin as the Pt compound control. Complex **7** showed the highest potency against both cell lines (the IC$_{50}$ values were 1.0 and 2.6 μM against HMLER and HMLER-shEcad cell lines, respectively) but without selectivity for the CSC-enriched cells and normal cells. It also showed positive activity against mammospheres, the multicellular, three-dimensional structures formed by CSCs: a significant reduction in their formation, size, and viability could be observed. Complex **7** induced apoptosis against two triple-negative breast cancer (TNBC) cell lines, MDA-MB-231, and BT549, with a potency that is, respectively, thirty and three times higher than complex **8** (IC$_{50}$ values of 3.6 and 4.0 μM for complex **7** vs. IC$_{50}$ values of >100 and 12.78 μM for complex **8** against MDA231 and BT549, respectively). A possible explanation for this activity is related to the presence of GANT61 as an N-donor ligand in complex **7**; according to the abovementioned hydrolysis process (Figure 4), it releases the bioactive Hh pathway inhibitor GANT61-D, and 4-PCA can remain bound to the Pt(II) center. In addition to inhibiting the Hh pathway, complex **7** can bind DNA, as shown by an increase in the DNA damage marker γH2AX and a reduction in the expression of GLI-1 and GLI-2, confirming the GLI function in the nucleus is blocked.

2.2. Pt(II) Complexes Carrying Biologically Active Ligands

Since the aim is to improve the anticancer effects of conventional platinum-based drugs, another possible strategy is selectively introducing structural changes around the active platinum center by choosing either carrier ligands endowed with biological activity by themselves or substituting common chloride ligands.

In this case, new platinum(II) complexes with 1-alkyl-1H-pyrazole ligands containing both iodide- and chloride-leaving groups have been synthesized (Figure 7) [34].

9a: R = CH$_3$ **10a: R = CH$_3$**
9b: R = C$_2$H$_5$ **10b: R = C$_2$H$_5$**
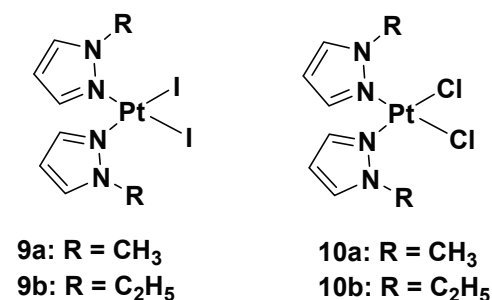
Figure 7. Platinum(II) diiodide complexes and platinum(II) dichloride complexes.

It was discovered that both iodide complexes, **9a** and **9b**, were more effective than the chloride analogs, **10a** and **10b**, and cisplatin against all cisplatin-resistant cell lines; while the chloride complexes had an effect comparable to cisplatin: 11 and 11.9 μM vs. 4 μM in the A2780 cell line; 21 and 19 μM vs. 22 μM in the A2780cisR cell line; 29 and 25 μM vs. 24 μM in the MDA-MB-231 cell line. These differences show that the mechanism of action of the new alkyl pyrazole complexes is different from that of cisplatin, thus potentially allowing the compounds to overcome the resistance mechanism. Another important aspect is that the new Pt(II) complexes are more effective in tumor cells with respect to healthy cells, thus confirming their higher selectivity toward tumor cells. Coherent with the antiproliferative effect, the intracellular Pt amount increases with lipophilicity: the most lipophilic complex causes the ethyl group to bond to the pyrazole and the iodide-leaving ligands. However, even if the amount of Pt from complexes **9a** and **b** was about ninety-fold higher than cisplatin, their effectiveness would only be five-fold higher than that of cisplatin (4.2 and 5.0 μM vs. 24 μM in the MDA-MB-231 cell line). This means that a higher amount of Pt(II) alkyl pyrazole complex is necessary to obtain a certain level of biological activity compared with cisplatin.

These data suggest a new anticancer mechanism compared with cisplatin, whose main target is nuclear DNA. Binding studies using calf thymus DNA have revealed that both chloride and iodide complexes can covalently interact with the target, but although iodide binds DNA more efficiently than its chloride analog (as demonstrated by ICP-MS), the DNA platination occurs in both to a lesser extent than cisplatin. These results suggest that DNA might not be the main target of the new complexes, **9a,b** and **10a,b**. The experimental evidence shows that the contribution exerted by the unrepaired DNA lesions (due to alkyl pyrazoles) on cytotoxicity was minimal compared with cisplatin. Conversely, it was found that the time-dependent cell response profiles (TCRPs) for complexes **9a,b** and **10a,b**, which can predict the mechanism of action in biologically active compounds, significantly differed from those typically expressed by DNA-damaging agents, such as cisplatin. Their profiles were instead superimposable on those displayed by nontubulin-targeting mitotic inhibitors toward Eg5. The mitotic tubulin Eg5 is an essential spindle motor protein, and it assembles and maintains the bipolar spindle during mitosis. When inhibited, a monoastral spindle forms, thus resulting in mitotic arrest. In the literature, it is reported that pyrazoles are important and potent inhibitors of Eg5, so analyzes have been performed to ascertain whether all the new Pt(II) complexes, **9a,b** and **10a,b**, cause a cell cycle arrest in the G2/M phase. This plausible molecular target also explains the selectivity for tumor cells exerted by these complexes, since healthy cells do not divide or only slowly proliferate tumor cells.

Concurrently, to develop platinum complexes able to hit novel molecular targets, one possible strategy relies on synthesizing Pt(II) complexes based on natural products, which have been recognized for their biological activity. Tropolone derivatives could be a significant example consistent with this idea [35]. Tropolone is a natural product isolated mostly from plants and fungi, with a seven-membered aromatic ring possessing strong activity against bacteria, antibiotic-resistant bacteria, and fungi. The different substitution groups on the aromatic ring could confer it with a plethora of different properties, such as antiviral, anti-inflammatory, and antidiabetic activities. Thus, two new complexes, [Pt(Q)(L)] (**11**) and [Pt(MQ)(L)] (**12**), were synthesized, and their cytotoxicity was evaluated, in which tropolone was combined with 8-hydroxy-quinoline (Q) or 2-methyl-8-hydroxy-quinoline (MQ), two pyridinic scaffolds known for their cytotoxic activity in different types of tumor cell lines (Figure 8).

11, R = H
12, R = Me
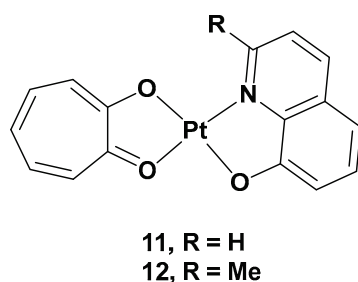
Figure 8. [Pt(Q)(L)] (**11**) and [Pt(MQ)(L)] (**12**).

The cytotoxicity was tested on different cancer cell lines: HeLa, T24, A549, NCI-H460, and MGC80-3, as well as on HL-7702 (a healthy cell line). Complex **11** showed high cytotoxicity in these cell lines, especially T24 (IC$_{50}$ = 3.6 μM), but also significant cytotoxic activity against the normal cell line, HL-7702; complex **12** showed selectivity in the tested cell lines, such as T24 and MGC80-3 (the IC$_{50}$ values were 10.3 and 5.97 μM, respectively), and lower cytotoxicity than cisplatin in the normal cell line. Overall, complex **11** showed an effect against T24, while complex **12** showed effects against both T24 and MGC80-3. The possible anticancer mechanism of both complexes, but especially complex **11**, may be the production of high ROS levels through cell mitochondria, which can damage organelles and induce severe dysfunction in the cells' machinery. In addition, complex **11** was proven to induce apoptosis by decreasing mitochondrial membrane potential, with a simultaneous increase in the Ca^{2+} level in the cells contributing to the onset of mitochondrial dysfunction, and, finally, by activating caspase-3 and caspase-9. Furthermore, complex **11** induced cell death in the G2 phase, downregulating the expression of Cdc25A, CDK1, cyclin A, and cyclin B and upregulating the expression of p27 and p21, proteins that interact with cyclin–CDK complexes within the nucleus and, hence, modify cell cycle progression. On the contrary, complex **12** induced cell arrest in the G1 phase and had similar effects to **11**, but it lacked the influence of p27 expression. Complex **11** showed a significant in vivo anticancer effect, revealed by its inhibiting effects on tumor growth in T24 xenograft mice without any renal pathological changes or influence on renal function.

Furthermore, thiosemicarbazones have shown promising activity for cancer therapy by inhibiting P-gp expression in particular. Considering the beneficial effects on both the pharmacokinetics and pharmacodynamics arising from metal coordination, their platinum complexes also possess promising biological activities, such as anticancer, antibacterial, and antiviral properties. For this reason, six novel Pt(II) complexes (**13–18**) were synthesized to overcome cisplatin resistance (Figure 9) [36].
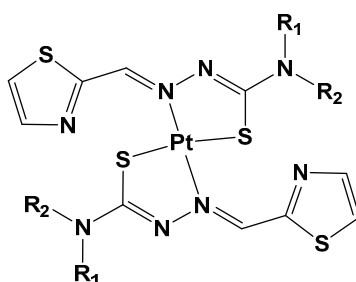
13: $R_1 = R_2 = H$ 14: $R_1 = H$, $R_2 = Me$ 15: $R_1 = H$, $R_2 = Ph$
16: $R_1 = H$, $R_2 = o$-Tol   17: $R_1 = H$, $R_2 = t$-Bu   18: $R_1 = Me$, $R_2 = Me$

**Figure 9.** Series of new Pt complexes, **13–18**.

The antiproliferative activity of **13–18** was then evaluated using an MTT assay. It was discovered that the anticancer effect was improved when R_1 was a methyl (**14**), phenyl (**15**), *o*-toluene (**16**), or tert-butyl (**17**), and the best activity occurred when both R_1 and R_2 were methyl groups. Furthermore, the different substitutions of R_1 and R_2 also influenced the accumulation of Pt agents in cancer cells, such that the anticancer activity could be modified by regulating the lipophilicity of the ligands.

To confirm the ability of these complexes to overcome cisplatin resistance, they were analyzed in comparison with cisplatin. After 48 h of incubation, the antiproliferative activity of these Pt complexes is two- to seven-fold higher than the activity of cisplatin against cisplatin-resistant lung cancer (A549cisR) cells (IC_{50} values from 5.02 to 15.32 μM vs. cisplatin value of 36.58 μM). The higher concentration of Pt inside the cells correlates with higher anticancer activity.

Both **13** and **18** can induce cell apoptosis in the depths of the 3D cell spheres, and **18** has a greater effect on metastasis than cisplatin or **13**. This means that **18** shows not only an improved tumor penetration potential, but also effectiveness in inducing cell death. Complex **18** can bind to DNA, leading to the formation of DNA-Pt adducts that can form inter-strand crosslinks, arresting DNA synthesis. It can also induce mitochondrial apoptosis and lethal autophagy.

However, the principal mechanisms by which **13** and, above all, **18** overcome cisplatin resistance rely on three different possible mechanisms: the inhibition of endogenous P-gp expression, a transporter that enables the active efflux of the drug from the cancer cells; the generation of ROS inside the cells that can reduce GSH levels, a reducing substance; and the inhibition of the MEK/ERK pathway. Another advantage of **18** is its ability to avoid important side effects in vivo, i.e., there has been no significant body weight loss observed in treated mice.

Since one of the chemoresistance mechanisms is represented by the overexpression of enzymes in the thiol redox system, such as glutathione and thioredoxin, which are generally involved in the regulation of redox balance in cells, two new Pt(II) complexes containing the triphenylphosphine moiety (widely used as a mitochondriothropic moiety), the dialkylamino group, and the bromide groups were synthesized (Figure 10) [37].
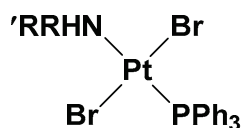
19: R = Bu, R′ = Bz
20: R = R′ = Bz

Figure 10. Pt(II) complexes **19** and **20**.

It is worth noting that the substituents of the amino group are fundamental to the cytotoxicity of both **19** and **20** in resistant cell lines, but, at the same time, complex **19** has proven to be more effective, underlying the beneficial effects of the dissymmetrical substitution pattern between these two brominated triphenylphosphine trans-platinum derivatives (the IC$_{50}$ values are three times lower than the cisplatin values, 2.15 μM vs. 6.61 μM, respectively).

While studying the mechanism of action of these two complexes, some differences with cisplatin have been found. First of all, from the cell uptake point of view, after 60 min of incubation, the amount of Pt is comparable with cisplatin and **19**; after 180 min, the uptake of cisplatin does not change, but the amount of complex **19** increases threefold. Indeed, while cisplatin probably undergoes an efflux effect, compound **19** shows a time-dependent accumulation in cells and a greater ability to cross the membrane. DNA interaction has been confirmed for both complexes due to the presence of the triphenylphosphine hydrophobic moiety and the trans geometry of bromide groups. However, this is not the only target that could explain the cytotoxic effect. Different biological assays support complex **19**′s ability to depolarize more mitochondrial membranes than cisplatin under the same concentrations and experimental conditions, thus confirming that it interferes with the cellular redox state. Both complexes **19** and **20** can decrease the total thiols in both cisplatin-resistant and -sensitive cell lines, with cisplatin influencing the thiol concentration to a lower extent and only in the sensitive cell line. In addition, another mechanism of cytotoxicity is related to its influence on thioredoxin reductase (TrxR) activity. TrxR, along with glutathione reductase (GR), is a key enzyme in redox regulation and antioxidant responses inside cells. High levels of TrxR are one of the main characteristics of cisplatin-resistant tumor cells that need to be defeated. In cisplatin-resistant cells, complexes **19** and **20** can both affect the responsivity of TrxR, resulting in a lower amount than in untreated cells.

2.3. Ionic Pt(II) Complexes

The purpose of synthesizing monofunctional cationic Pt(II) complexes is to produce substrates that benefit from binding to organic cation transporters (OTCs). This allows them to be used in the selective treatment of tumors where this transporter is overexpressed. Indeed, most of these transporters display high tissue specificity and subcellular or peculiar expressions, thus translating into specific tumor efficacy. To reach this goal, a series of cationic triamine platinum compounds have been synthesized. The general formula is [Pt(N-N′)N′Cl]X, where N–N′ is an aminomethyl–imidazole ligand, and N′ is an imidazole ring bearing the same alkyl group in the N1 position (Figure 11) [38–40].
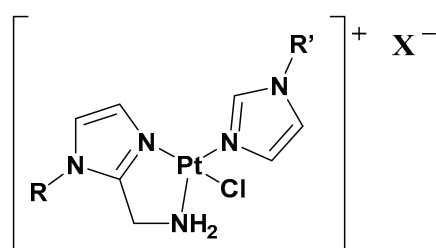
21: R = R' = CH$_3$, X = Cl$^-$
22: R = R' = CH$_3$, X = NO$_3^-$
23: R = R' = C$_4$H$_9$, X = Cl$^-$
24: R = R' = C$_6$H$_{13}$, X = Cl$^-$

Figure 11. Series of cationic platinum(II) complexes, **21–24**.

After this series, where complex **24** is more effective compared with cisplatin, other ligands have also been studied, such as 8-aminoquinoline and its chiral 5,6,7,8-tetrahydro-derivatives, also called CAMPY (Figure 12) [41].

Figure 12. Synthesis of cationic platinum(II) complexes, **25–28**.

Modifying the ligand causes a different biological effect in the corresponding cationic platinum(II) complexes. These differences are principally found in the accumulation of the complexes in different cellular phases, which results in a different effect on DNA: they seem to arrest cells into a G0/G1 phase to a greater extent; they more efficiently induce p53 mRNA; and α-tubulin and β-actin levels significantly reduce in response to new platinum(II) complexes. Furthermore, it should be highlighted that **28** is the most potent cytotoxic agent of this series against the triple-negative breast cancer MDA-MB-231, a particularly aggressive tumor still lacking effective chemotherapeutic treatments.

For this reason, **28** (**Pt-8AQ**) has been further analyzed against six tumor cell lines. Three cell lines of human glioblastoma were present, i.e., U87-MG (expressing wild-type p53), U373-MG, and U138-MG (expressing endogenous mutant p53) [42].

Complex **28** shows higher activity against glioblastoma cells compared with cisplatin, with IC_{50} values of 3.68, 11.53, and 8.05 μM against U87-MG, U373-MG, and U138-MG, respectively, compared with cisplatin, which shows IC50 values of 7.27, 22.69, and 32.1 μM against U87-MG, U373-MG, and U138-MG, respectively, while they had a similar effect on pancreatic adenocarcinoma CFPAC-1, mesothelioma MSTO-211H, and adenocarcinoma MCF-7. Furthermore, a comparison relative to the stability of the complex compared with cisplatin was made after incubating them at 37 °C for 24 h. Interestingly, **28** showed only 2.05-fold decreased activity, but significant pharmacological activity was still present. Furthermore, it was impossible to measure the IC_{50} of the cisplatin, thus indicating that the activity was completely lost after the treatment. In addition, the authors proved that even after 6 days of treatment, **28** maintained some pharmacological activity, paving the way for the development of slow-release chemotherapeutics.

To understand this new complex's mechanism of action, its interaction with some possible molecular targets and nucleophiles known to prevent platinum-based chemotherapy was studied. One of the most important factors responsible for drug resistance is glutathione (GSH) and, through ^{1}H-NMR analysis, it was possible to confirm the interaction with **28**; other factors are the membrane transporters and channels, called transportomes, in which copper transporters (CTRs) important for the cellular uptake of platinum are present. Furthermore, in this case, a monocoordinated complex with a 1:1 stoichiometry was found using ESI-MS experiments by exploiting the peptide Mets7, which mimics the methionine-rich motif involved in platinum coordination. Similarly, the interaction with

9-ethylguanine (9-EtG) was confirmed via ^{1}H-NMR, and this result highlights that DNA is the main target of this complex. Furthermore, the cytotoxicity of **28** up to a concentration of 20 µM against all three human glioblastoma cell lines is higher than that of cisplatin, whose IC$_{50}$ was undetectable. The new complex affects the cells in the G0/G1 phase, showing an earlier cell death mechanism. Since the three cell lines differ from each other regarding the genetic status of p53, the influence of **28** and cisplatin on the functional expression of this gene was evaluated, showing a different impact on the proapoptotic molecules BCL-2, BAX, PUMA, and NOXA. Both complexes downregulate p53, except in U138-MG upon treatment with **28**, and BCL-2 is downregulated by both complexes in all cells. In U87-MG, cisplatin upregulates PUMA, BAX, and NOXA. However, **28** upregulates NOXA in a more significant way, though BAX is downregulated, whereas PUMA levels remain unaltered. In U138-MG, the three genes are downregulated by cisplatin and upregulated by **28**; in U373-MG, all three genes are downregulated by both complexes.

To confirm these cytotoxic effects, photographs under a light microscope were taken and a triple staining assay was performed in one study. In cells treated with cisplatin, there were no consistent changes compared with the untreated cells, while cells treated with **28** detached from the surface and completely changed in morphology, which is typical of damaged cells. In contrast, the control cells were viable and adherent, cells treated with cisplatin were early-apoptotic, and cells treated with **28** were mostly detached and late-apoptotic. Interestingly, there were no necrotic cells, thus indicating that apoptosis is the exclusive cell death mechanism.

These experiments confirmed that **28** is a promising candidate for treating human glioblastoma, and considering its high chemical stability, it may be suitable for loading on mesenchymal stromal cells (MSCs) as a new drug delivery system [43–48]. MSCs are cells from different tissues that can uptake drugs and release them directly into the neoplastic microenvironment due to their ability to accumulate in the stroma of several primary and metastatic neoplasms. This system aims to target the tumor cells, reduce the side effects, and overcome cisplatin resistance [49].

While a plethora of cationic platinum complexes has been proposed in recent research, anionic Pt(II) complexes have never been tested for their anticancer activity. A series of complexes with the general formula NBu$_4$[(CˆN)Pt(OˆO)] has recently been synthesized and evaluated for promising TNBC activity and theranostic properties (Figure 13). The structure of this series can comprise a CˆN ligand, which is a cyclometalated form of 2-phenylpyridine (H(PhPy)); 2-thienylpyridine (H(Thpy)); or 2-benzo[h]quinoline (H(Bzq)), whereas the dioxygenated leaving group OˆO represents the dianion of tetrabromocatechol (H$_2$(BrCat)) or the dianionic form of alizarine (H$_2$(Aliz)) [50].

Alizarine moiety, because of its extended aromatic system, was chosen to introduce a labeling system to the anticancer activity, furnishing the properties of the emissive compounds so that, in principle, many biologically relevant processes could be followed in real-time by Pt-based probes. All these new complexes were tested against TNBC, an "orphan" tumor that has a negative response to currently approved drugs and hormonal therapy, as well as compounds that target HER2 protein receptors; in particular, its in vitro biological activity against the MDA-MB-231 cell line was tested.

Complexes with bromocatechol (**32–34**) showed good cytotoxic activity against MDA-MB-231 cells, which were independent of the cyclometalated ligand's nature. Complexes **29–31**, possessing alizarine as a ligand, were studied as a mixture of the two isomers, showing a different form of cytotoxic activity that depends on a different CˆN ligand. In particular, complex **29** possessed PhPy, which showed the highest cytotoxic activity (IC$_{50}$ = 1.9 µM) and selectivity between the tumoral cells and nontransformed vascular smooth cells (IC$_{50}$ = 12.5 µM vs. 1.9 µM). As to whether this activity is independent of the deoxygenated ligand, complex **35** was chosen as a test bed to confirm this hypothesis. Substituting the cyclometalated ligand with two ammonias dramatically reduced the cytotoxic activity in comparison with both its cyclometalated counterparts and cisplatin, confirming phenylpyridine and alizarine are the best matches for exerting a maximum anticancer effect.

Furthermore, studying the effect of the new complex on the cell cycle progression showed that complex **29** displays antiproliferative activity, blocking the progression of the cells through the S phase and decreasing cells in the G2/M phase.
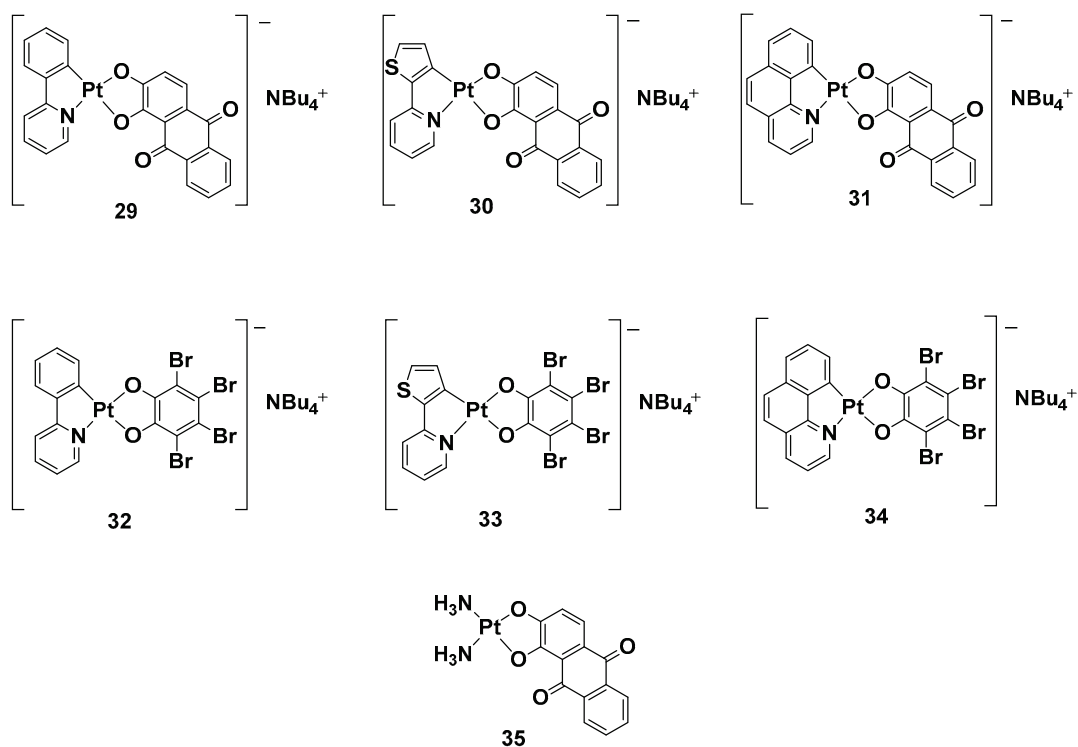
Figure 13. Anionic Pt(II) complexes, **29–35**.

In addition, even if all the anionic complexes were found to be emissive in solution in the red region of the electromagnetic spectrum in a confocal analysis, it was possible to localize complex **29** in the perinuclear region.

3. Treatment of Cisplatin-Resistant Tumor: Pt (IV) Complexes

Platinum(IV) complexes are prodrugs that have to be activated into platinum(II) complexes to act as anticancer agents. The anticancer potential of platinum(IV) agents has been known for many years, but their potential anticancer activity still needs to be elucidated and investigated; even if some complexes show encouraging pharmacological profiles, reaching different clinical phases of evaluation, they have not been approved for clinical use [51].

These new complexes are six-coordinated and possess octahedral geometry that can confer better stability than the square-planar geometries of platinum(II) complexes. Indeed, the lack of empty space within the platinum coordination sphere ideally prevents the metal in its +4 oxidation state from being attacked by nucleophilic substitution in the circulatory system, endowing Pt(IV) derivatives with an innate advantageous inertness over the Pt(II) counterparts.

The synthesis of platinum(IV) complexes instead of platinum(II) complexes could lead to further important advantages, such as lipophilicity, stability, the possibility of oral administration, cell targeting, and improved cellular uptake [52]. Another advantage is the possibility of enhancing the therapeutic effect, conjugating active biological moieties in the axial position to the center of the platinum. The ligands in the axial position have to be released to activate platinum(IV) into the reduced active form, which carries a platinum(II) center. This has a favorable synergistic effect on the tumoral cells. Octahedral platinum(IV) complexes are nontoxic to cancer cells on their own; they require a bioreduction process in their activated forms, and this is why they are considered prodrugs [53]. Some recent

examples clarifying this strategy are reported in [54]. Two Pt(IV) complexes, in which the ligands were ferulic acid (FA-COOH) and rhein (RH-COOH) and complexes **37** and **38,** were synthesized and compared with other complexes in which the ligands were benzoic acid (BA-COOH), crotonic acid (CA-COOH), and trans-cinnamic acid (TCA-COOH) and complexes **36**, **39,** and **40** (Figure 14).
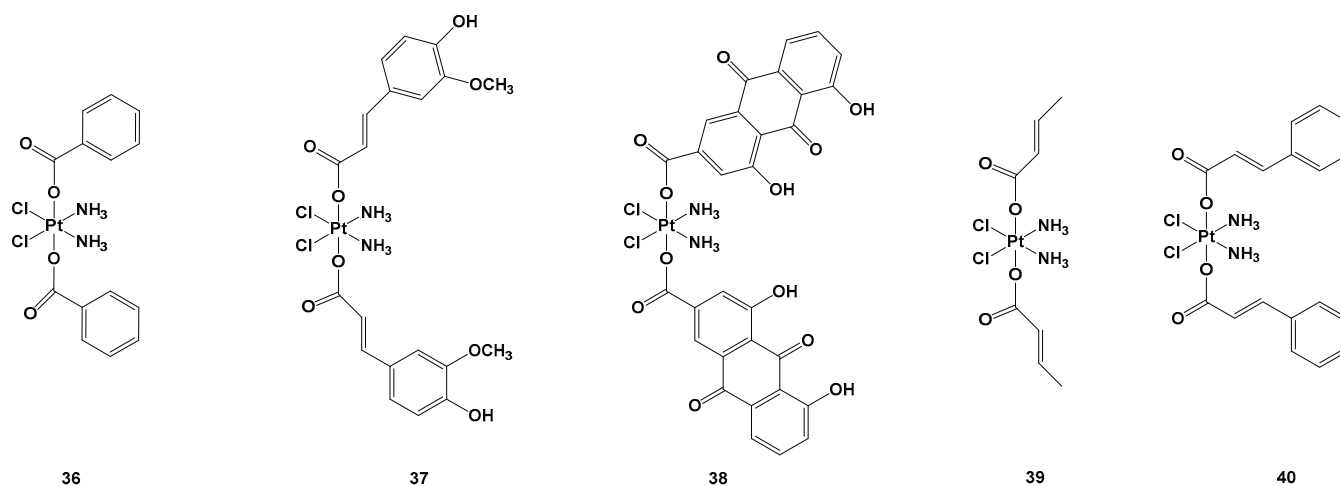
Figure 14. Pt(IV) complexes **36–40**.

Complexes **36–40** were tested against lung carcinomas A549 and A549/DDP, cisplatin-insensitive cells, and normal healthy (HL-7702) cells. In particular, complex **38** showed the highest cytotoxic activity (IC_{50} = 0.11 μM) against the A549/DDP cell line in comparison with complex **36** (IC_{50} = 3.01 μM), complex **37** (IC_{50} = 0.75 μM), complex **39** (IC50 = 3.87 μM), complex **40** (IC_{50} = 0.91 μM), and cisplatin (IC_{50} = 50.12 μM), all of which showed lower cytotoxic effects against HL-7702 compared with the standard approved regimen based on cisplatin. Complex **37** and, above all, **38,** were the most effective, but the latter led to higher activated Pt content inside the cells (probably because of its greater reduction rate), as well as inside the mitochondria, compared with complex **37** and cisplatin. To explore the mitochondrial effect caused by complexes **37** and **38**, the level of mitochondria membrane potential (MTMP) was monitored. This significantly reduced after **37** and **38** treatments, leading to cell death in lung carcinoma cancer cells due to the induction of mitochondria dysfunction. Thus, the expression levels of the apoptosis-associated proteins were evaluated to clarify their possible mode of action, and it was found that complex **38,** compared with complex **37,** exhibited higher induction in all the proteins, including cytochrome c, active-caspase-3, BAX, apaf-1, and active-caspase-9, thus providing a rational explanation of their relative IC_{50} values. Similar behavior was also observed in in vivo experiments, in which complex **38** was found to be the most cytotoxic of the series. In addition, these new compounds seem to induce minimal side effects in mice, as confirmed by the non-negligible weight loss of the animals after the treatment [53]. Another possible bioactive ligand that could be released by reducing the Pt(IV) complex is an inhibitor of glutathione (GSH) synthesis, which is generally overexpressed in cancer cells or the tumor microenvironment. For example, L-buthionine-(*S*,*R*)-sulfoximine (BSO) is a potent, specific, and irreversible inhibitor of the glutamate–cysteine ligase (GCL), as well as a rate-limiting enzyme in the synthesis of GSH; however, it also possesses antitumor activity in and of itself, although it also has a fast metabolism and excretion issues. Indeed, using this bioactive molecule in axial positions could improve pharmacokinetics and tumor selectivity, especially when used as an albumin-binding moiety, leading to a sensible decrease in GSH levels after its release.

Two Pt(IV) complexes, derivatives of oxaliplatin, have also been synthesized: BSO-OxOAc (with an inert acetate ligand) and BSO-OxMal (with the albumin-binding maleimide) (Figure 15).

41, BSO-OxOAc

42, BSO-OxMal
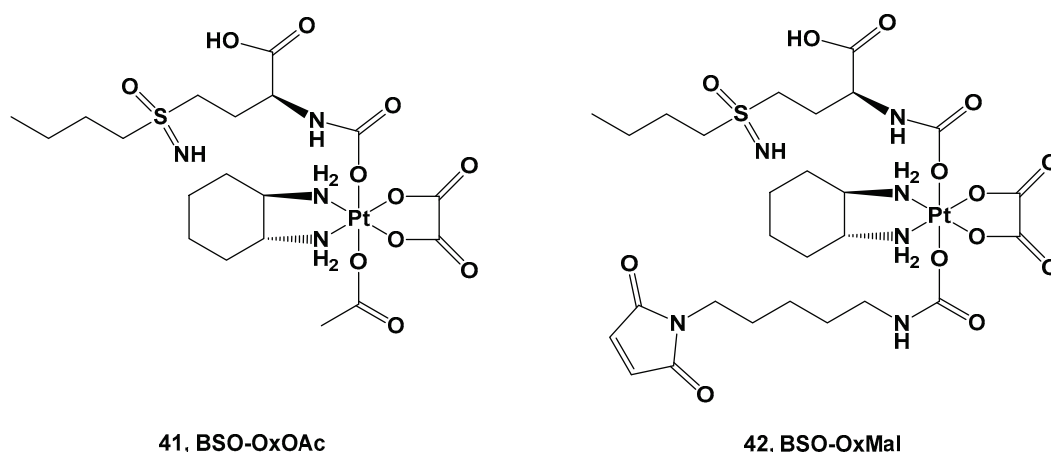
Figure 15. Pt(IV) complexes **41** and **42**.

Both complexes were tested against a human colon cancer model (HCT116), an ovarian cancer model (A2780), and their corresponding oxaliplatin (HCT116/OxR) and cisplatin-resistant models (A2780/Cis). Complex **41** was the only compound selected for the in vitro experiments, although its cytotoxicity was reduced in comparison with oxaliplatin and cisplatin in the HCT116 and A2780 cancer cell lines, with IC_{50} = 32.1 μM vs. 0.58 μM and 20.6 μM vs. 1.9 μM, respectively. As such, the resistance mechanisms of the Pt(IV) prodrug (**41**) and its toxicity against nonmalignant cell lines were demonstrated to be extremely negligible, making it a promising candidate for further investigations. For this reason, complex **41** has the advantage of a large therapeutic window but the disadvantage of needing a longer exposure time and more reducing agents to undergo the activation bioprocess.

Conversely, for in vivo experiments, only complex **42** has been explored. Pharmacokinetics studies showed that the AUC and serum half-life of complex **42** increase compared with oxaliplatin, and it is also accompanied by a significantly selective accumulation of the Pt(IV) prodrug in tumor tissue with respect to healthy tissue. Furthermore, both complexes **41** and **42** have been compared with oxaliplatin using in vivo experiments. In the first two weeks, both new complexes and oxaliplatin can reduce the tumor volume, but after this period, only complex **42** proved efficacious in stabilizing the cytotoxic effect, thus prolonging the overall survival of the mice. This higher antitumoral activity could be explained by its stronger GSH-depleting effect, increased DNA damage, and proliferation arrest in comparison with oxaliplatin. In addition, Pt(IV) prodrug did not increase DNA damage in healthy organs, thus confirming that the BSO effect is limited only to tumoral tissue.

A structure quite similar to complex **42** was retained in series **43–46**; the ligands were an albumin-targeting maleimide and 1-methyl-D-tryptophan (1-MDT) [55]. 1-MDT inhibits the indoleamine 2,3-dioxygenase (IDO) enzyme, which catabolizes tryptophan (Trp) into kynurenine (Kyn), with the binding thereof to its receptor leading to the inhibition of T-cell activation and T-cell proliferation support (Figure 16).

The four derivatives belonging to this series differ from each other in the diverse strategies applied to their synthesis and their reduction behavior.

The advantage of these new complexes seems to rely on the release of an unmodified 1-MDT ligand intracellularly, thus suggesting that coupling this ligand to a platinum(IV) center could be an effective strategy in delivering 1-MDT inside tumoral cells.

Furthermore, in vivo experiments have been performed to gain information on their pharmacokinetics and further details on their anticancer activity. The IdoEs complexes, such as **44** and **46**, show higher activity in cell cultures and lower activity in mice because of their faster reduction process, thus leading to deactivation; on the contrary, the IdoCa complexes, such as **43** and **45**, have higher cytotoxic activity in vivo because of their slower activation process, thus retaining their effects until they reach the molecular target. In addition, these experiments have confirmed that these new complexes are capable of inhibiting IDO in malignant tissue, leading to a tumor-specific change in the T-cell population [56]. The

choice to employ bioactive axial ligands in the design of platinum(IV) prodrugs could represent a valid strategy in protecting and increasing the efficacy of molecules known to be unstable or easy to deactivate under physiological conditions, thus compromising their use as active ingredients on their own. For example, chlorambucil (CLB) is a potent anticancer agent that can bind the nucleotides of DNA, such as guanine and adenine, at the N(7) and N(3) positions, thus forming DNA crosslinks. Nevertheless, its clinical use is compromised by its low bioavailability and poor selectivity, thus resulting in numerous and serious side effects. For this reason, one possibility is conjugating CLB to a platinum(IV) moiety, resulting in an advantageous delivery system for this drug (Figure 17).

43, MalCa/IdoCa

44, MalCa/IdoEs

45, MalEs/IdoCa

46, MalEs/IdoEs
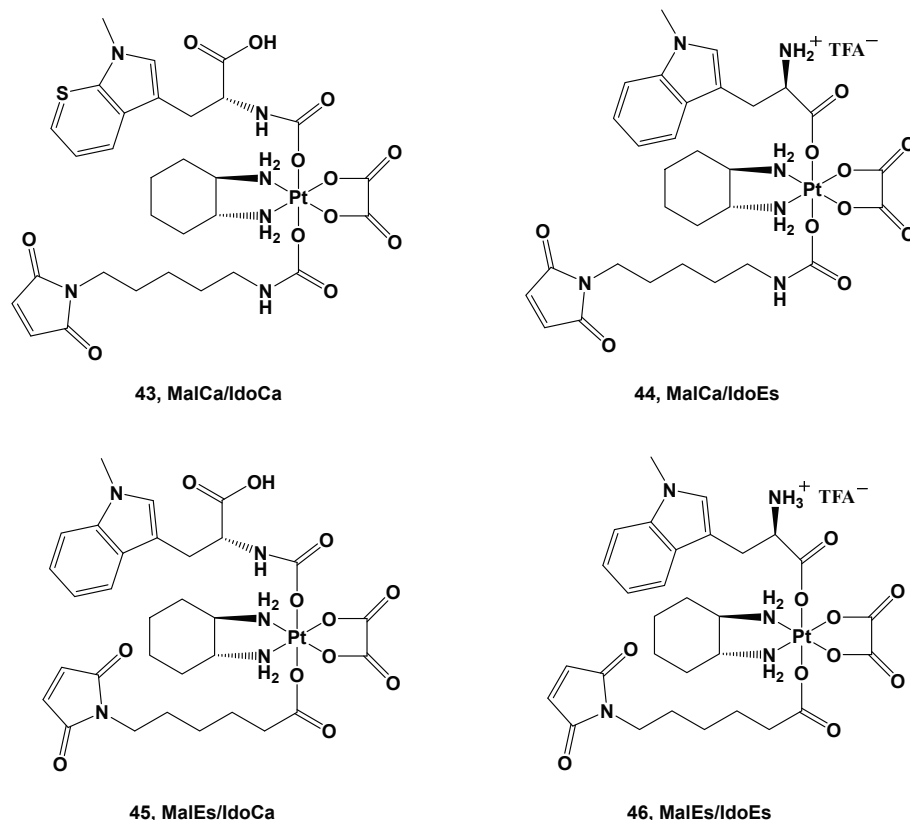
Figure 16. Pt(IV) complexes **43–46**.

PCLB, 47

5CLB, 48

56CLB, 49
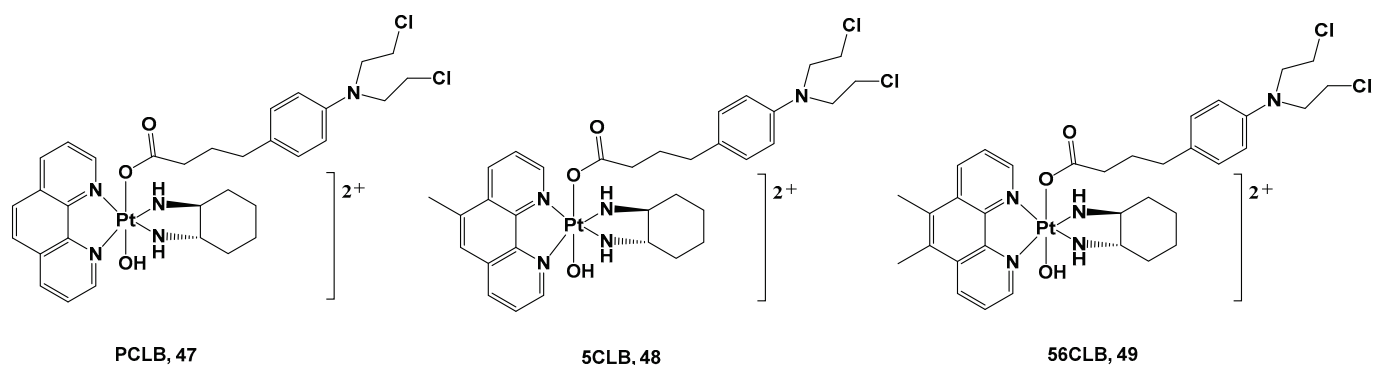
Figure 17. Pt(IV) complexes **47–49**.

All these complexes were synthesized starting with their Pt(II) precursors, PHENSS, 5MESS, and 56MESS respectively, and were tested against different cell lines and different types of tumors, such as HT29 colon, U87 glioblastoma, MCF-7 breast, A2780 ovarian, H460 lung, A431 skin, Du145 prostate, BE2-C neuroblastoma, SJ-G2 glioblastoma, MIA pancreas, ADDP ovarian (cisplatin-resistant A2780 clone), and nontumor-derived MCF10A

breast lines. The cytotoxicity data revealed that complexes **47**, **48**, and **49** exert important antitumor activity, with complex **49** being the most promising in the series. It possessed a potency similar to its Pt(II) precursor, 56MESS, toward all tested cell lines, affording it an average IC$_{50}$ of around 40 μM, but most of all, it proved to be more potent than either cisplatin or CLB. These promising results were confirmed via ^{1}H- and ^{195}Pt-NMR studies recording the reduction process of Pt(IV) complexes **47–49** 5 min after the addition of an appropriate reducing agent with the release of the CLB ligand. This confirms the validity of this synthetic strategy and represents a proof-of-concept for the development of Pt(IV) analogs. However, it is important to mention that these experiments are only approximate and do not necessarily reflect how prodrugs would behave in blood and blood serum.

In addition, complex **49**′s anticancer properties seem to be related to its ability to produce considerable amounts of ROS inside cells, thus promoting an antitumorigenic signal and triggering oxidative stress that can selectively induce cancer cell death. Finally, the presence of the two methyl groups on the phenanthroline ligand could account for the higher cytotoxicity displayed by **49** in comparison with analogs **47** and **48** as a consequence of its higher lipophilicity.

Conversely, ROS production is indeed an evident consequence of the increased respiration process, and exaggerated proliferation featuring cancer cells can be usefully exploited as a stimulus for the activation process within tumor tissue. Thus, a ROS-activated platinum (IV) prodrug bearing two boronate-ester-masked N-alkylaminoferrocene ligands has been proposed (Figure 17) [57]. Different studies have revealed that compound **50** can be selectively activated only by ROS, which is resistant to both GSH and ascorbic acid stimuli. The activation pathway presumably provided C-B oxidation, leading to the formation of two N-alkylaminoferrocenes that, once deprotected, may acquire the ability to act as electron donors for the Pt(IV) center, activating the platinum(II) drugs. This prodrug shows comparable antiproliferative activity to cisplatin (IC$_{50}$ = 2.5 μM vs. 2.1 μM) in A2780 cisplatin-resistant human ovarian carcinoma. The corresponding ROS-activated oxaliplatin analog, **51**, bears the same two boronate ester-masked N-alkylaminoferrocenes and was also proposed and evaluated for the same cancer cell line, revealing significant cytotoxicity with an IC$_{50}$ value of 0.4 μM, endowed with a 45-fold smaller effect on healthy cells (Figure 18).

50　　　　**51**
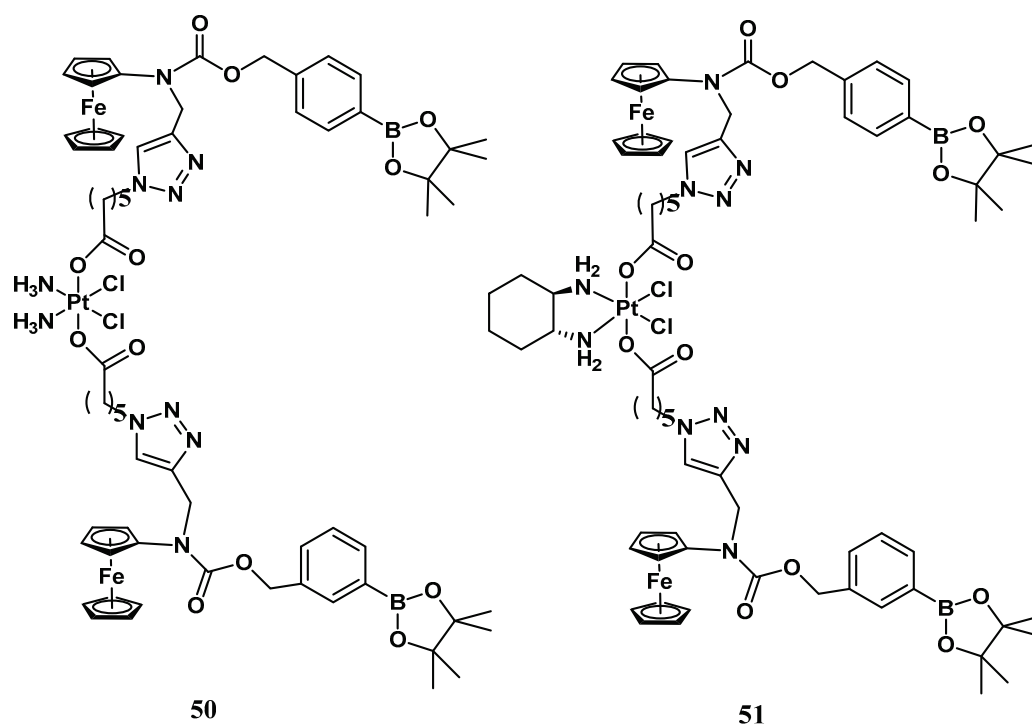
Figure 18. ROS-activated Pt(IV) complexes, **50** and **51**.

4. Conclusions and Further Perspectives

This review summarizes the recent advances in the synthesis of both platinum(II) and prodrugs platinum(IV) complexes for cisplatin-resistant cancer cell lines, whose therapeutic treatment still represents a great challenge. This can be correlated to the lack of selectivity toward the desired target and, therefore, the systemic side effects that often limit their final clinical approval. In this regard, despite continuous efforts in this direction, cisplatin remains the lead compound for so-called orphan tumors. The inability of researchers to bypass these problems can be linked to the incomplete unraveling of the mechanism of action of cisplatin, which is unknown in many ways. In recent years, [58–61] drug-delivery strategies have been developed to ameliorate the selectivity and, therefore, the systemic effects, but it will be necessary to implement and differentiate molecular targets to reverse therapeutic failure risks. As far as platinum(IV) complexes are concerned, the mechanism of activation and the consequent reduction products that form remain to be clarified. Indeed, the bioactivation in the complex biological system is far from fully addressed, as particular attention needs to be paid to the role played by the protein pool in delineating the activation pathway. Notably, most Pt(IV) prodrugs in the literature have oxygen donor ligands in axial positions, whereas only a few examples comprise different atom donors, which means that, ideally, the vast potential of platinum compounds could be explored. In this sense, a future goal can be achieved by using selective activation and drug delivery systems.

References

1. Sung, H.; Ferlay, J.; Siegel, R.L.; Laversanne, M.; Soerjomataram, I.; Jemal, A.; Bray, F. Global Cancer Statistics 2020: GLOBOCAN Estimates of Incidence and Mortality Worldwide for 36 Cancers in 185 Countries. *CA A Cancer J. Clin.* **2021**, *71*, 209–249. [CrossRef] [PubMed]
2. Collaboration, G.B.o.D.C. Cancer Incidence, Mortality, Years of Life Lost, Years Lived With Disability, and Disability-Adjusted Life Years for 29 Cancer Groups From 2010 to 2019: A Systematic Analysis for the Global Burden of Disease Study 2019. *JAMA Oncol.* **2022**, *8*, 420–444. [CrossRef]
3. Tsvetkova, D.; Ivanova, S. Application of Approved Cisplatin Derivatives in Combination Therapy against Different Cancer Diseases. *Molecules* **2022**, *27*, 2466. [CrossRef] [PubMed]
4. Peters, J.M.; Gonzalez, F.J. The Evolution of Carcinogenesis. *Toxicol. Sci.* **2018**, *165*, 272–276. [CrossRef]
5. Anderson, N.M.; Simon, M.C. The tumor microenvironment. *Curr. Biol.* **2020**, *30*, R921–R925. [CrossRef]
6. Hanahan, D.; Weinberg, R.A. Hallmarks of Cancer: The Next Generation. *Cell* **2011**, *144*, 646–674. [CrossRef] [PubMed]
7. Jia, L.-T.; Zhang, R.; Shen, L.; Yang, A.-G. Regulators of carcinogenesis: Emerging roles beyond their primary functions. *Cancer Lett.* **2015**, *357*, 75–82. [CrossRef] [PubMed]
8. Sinjab, A.; Han, G.; Wang, L.; Kadara, H. Field Carcinogenesis in Cancer Evolution: What the Cell Is Going On? *Cancer Res.* **2020**, *80*, 4888–4891. [CrossRef]
9. Caley, A.; Jones, R. The principles of cancer treatment by chemotherapy. *Surgery* **2012**, *30*, 186–190. [CrossRef]
10. Dasari, S.; Bernard Tchounwou, P. Cisplatin in cancer therapy: Molecular mechanisms of action. *Eur. J. Pharmacol.* **2014**, *740*, 364–378. [CrossRef]
11. Ali, R.; Aouida, M.; Alhaj Sulaiman, A.; Madhusudan, S.; Ramotar, D. Can Cisplatin Therapy Be Improved? Pathways That Can Be Targeted. *Int. J. Mol. Sci.* **2022**, *23*, 7241. [CrossRef] [PubMed]
12. Romani, A.M.P. Cisplatin in cancer treatment. *Biochem. Pharm.* **2022**, *206*, 115323. [CrossRef] [PubMed]
13. Ghosh, S. Cisplatin: The first metal based anticancer drug. *Bioorg. Chem.* **2019**, *88*, 102925. [CrossRef] [PubMed]

14. Arnesano, F.; Scintilla, S.; Natile, G. Interaction between Platinum Complexes and a Methionine Motif Found in Copper Transport Proteins. *Angew. Chem. Int. Ed.* **2007**, *46*, 9062–9064. [CrossRef]

15. Nguyen, T.H.; Arnesano, F.; Scintilla, S.; Rossetti, G.; Ippoliti, E.; Carloni, P.; Natile, G. Structural Determinants of Cisplatin and Transplatin Binding to the Met-Rich Motif of Ctr1: A Computational Spectroscopy Approach. *J. Chem. Theory Comput.* **2012**, *8*, 2912–2920. [CrossRef] [PubMed]

16. Ma, G.; Wu, Q.; Wu, X.; Arnesano, F.; Natile, G.; Sletten, E.; Liu, Y. The reaction of a platinated methionine motif of CTR1 with cysteine and histidine is dependent upon the type of precursor platinum complex. *J. Inorg. Biochem.* **2015**, *153*, 239–246. [CrossRef]

17. Long, D.F.; Repta, A.J. Cisplatin: Chemistry, distribution and biotransformation. *Biopharm. Drug Dispos.* **1981**, *2*, 1–16. [CrossRef]

18. Sedletska, Y.; Giraud-Panis, M.J.; Malinge, J.M. Cisplatin is a DNA-damaging antitumour compound triggering multifactorial biochemical responses in cancer cells: Importance of apoptotic pathways. *Curr. Med. Chem. Anticancer Agents* **2005**, *5*, 251–265. [CrossRef]

19. Qi, L.; Luo, Q.; Zhang, Y.; Jia, F.; Zhao, Y.; Wang, F. Advances in Toxicological Research of the Anticancer Drug Cisplatin. *Chem. Res. Toxicol.* **2019**, *32*, 1469–1486. [CrossRef]

20. Shen, D.-W.; Pouliot, L.M.; Hall, M.D.; Gottesman, M.M. Cisplatin Resistance: A Cellular Self-Defense Mechanism Resulting from Multiple Epigenetic and Genetic Changes. *Pharmacol. Rev.* **2012**, *64*, 706–721. [CrossRef]

21. Stordal, B.; Davey, M. Understanding cisplatin resistance using cellular models. *IUBMB Life* **2007**, *59*, 696–699. [CrossRef]

22. Hospers, G.A.; Mulder, N.H.; De Vries, E.G. Mechanisms of cellular resistance to cisplatin. *Med. Oncol. Tumor Pharm.* **1988**, *5*, 145–151. [CrossRef]

23. Yue, P.; Han, B.; Zhao, Y. Focus on the molecular mechanisms of cisplatin resistance based on multi-omics approaches. *Mol. Omics* **2023**, 220. [CrossRef]

24. Chen, S.-H.; Chang, J.-Y. New Insights into Mechanisms of Cisplatin Resistance: From Tumor Cell to Microenvironment. *Int. J. Mol. Sci.* **2019**, *20*, 4136. [CrossRef] [PubMed]

25. Galluzzi, L.; Senovilla, L.; Vitale, I.; Michels, J.; Martins, I.; Kepp, O.; Castedo, M.; Kroemer, G. Molecular mechanisms of cisplatin resistance. *Oncogene* **2012**, *31*, 1869–1883. [CrossRef]

26. Alessio, E.; Messori, L. NAMI-A and KP1019/1339, Two Iconic Ruthenium Anticancer Drug Candidates Face-to-Face: A Case Story in Medicinal Inorganic Chemistry. *Molecules* **2019**, *24*, 1995. [CrossRef] [PubMed]

27. Vuradi, R.K.; Nambigari, N.; Pendyala, P.; Gopu, S.; Kotha, L.R.; Sirasani, S. Study of Anti-Apoptotic mechanism of Ruthenium (II)Polypyridyl Complexes via RT-PCR and DNA binding. *Appl. Organomet. Chem.* **2020**, *34*, e5332. [CrossRef]

28. Ma, L.; Li, L.; Zhu, G. Platinum-containing heterometallic complexes in cancer therapy: Advances and perspectives. *Inorg. Chem. Front.* **2022**, *9*, 2424–2453. [CrossRef]

29. Kelland, L.R.; Sharp, S.Y.; O'Neill, C.F.; Raynaud, F.I.; Beale, P.J.; Judson, I.R. Mini-review: Discovery and development of platinum complexes designed to circumvent cisplatin resistance. *J. Inorg. Biochem.* **1999**, *77*, 111–115. [CrossRef]

30. Facchetti, G.; Rimoldi, I. Anticancer platinum(II) complexes bearing N-heterocycle rings. *Bioorg. Med. Chem. Lett.* **2019**, *29*, 1257–1263. [CrossRef] [PubMed]

31. Sakamaki, Y.; Ahmadi Mirsadeghi, H.; Fereidoonnezhad, M.; Mirzaei, F.; Moghimi Dehkordi, Z.; Chamyani, S.; Alshami, M.; Abedanzadeh, S.; Shahsavari, H.R.; Beyzavi, M.H. trans-Platinum(II) Thionate Complexes: Synthesis, Structural Characterization, and in vitro Biological Assessment as Potent Anticancer Agents. *ChemPlusChem* **2019**, *84*, 1525–1535. [CrossRef]

32. Hyeraci, M.; Agnarelli, L.; Labella, L.; Marchetti, F.; Di Paolo, M.L.; Samaritani, S.; Dalla Via, L. trans-Dichloro(triphenylarsino)(N,N-dialkylamino)platinum(II) Complexes: In Search of New Scaffolds to Circumvent Cisplatin Resistance. *Molecules* **2022**, *27*, 644. [CrossRef] [PubMed]

33. Ryan, A.L.; Northcote-Smith, J.; McKeon, A.; Roe, A.; O'Dowd, P.; Twamley, B.; Ní Chonghaile, T.; Suntharalingam, K.; Griffith, D.M. A trans-Pt(ii) hedgehog pathway inhibitor complex with cytotoxicity towards breast cancer stem cells and triple negative breast cancer cells. *Dalton Trans.* **2022**, *51*, 18127–18135. [CrossRef] [PubMed]

34. Kasparkova, J.; Kostrhunova, H.; Novohradsky, V.; Logvinov, A.A.; Temnov, V.V.; Borisova, N.E.; Podrugina, T.A.; Markova, L.; Starha, P.; Nazarov, A.A.; et al. Novel cis-Pt(II) Complexes with Alkylpyrazole Ligands: Synthesis, Characterization, and Unusual Mode of Anticancer Action. *Bioinorg. Chem. Appl.* **2022**, *2022*, 1717200. [CrossRef]

35. Mo, X.; Chen, K.; Chen, Z.; Chu, B.; Liu, D.; Liang, Y.; Xiong, J.; Yang, Y.; Cai, J.; Liang, F. Antitumor Activities for Two Pt(II) Complexes of Tropolone and 8-Hydroxyquinoline Derivative. *Inorg. Chem.* **2021**, *60*, 16128–16139. [CrossRef]

36. Jiang, M.; Yang, T.; Chu, Y.; Zhang, Z.; Sun, H.; Liang, H.; Yang, F. Design of a novel Pt(ii) complex to reverse cisplatin-induced resistance in lung cancer via a multi-mechanism. *Dalton Trans.* **2022**, *51*, 5257–5270. [CrossRef]

37. Hyeraci, M.; Scalcon, V.; Folda, A.; Labella, L.; Marchetti, F.; Samaritani, S.; Rigobello, M.P.; Dalla Via, L. New Platinum(II) Complexes Affecting Different Biomolecular Targets in Resistant Ovarian Carcinoma Cells. *ChemMedChem* **2021**, *16*, 1956–1966. [CrossRef]

38. Rimoldi, I.; Facchetti, G.; Lucchini, G.; Castiglioni, E.; Marchianò, S.; Ferri, N. In vitro anticancer activity evaluation of new cationic platinum(II) complexes based on imidazole moiety. *Bioorg. Med. Chem.* **2017**, *25*, 1907–1913. [CrossRef]

39. Rimoldi, I.; Coccè, V.; Facchetti, G.; Alessandri, G.; Brini, A.T.; Sisto, F.; Parati, E.; Cavicchini, L.; Lucchini, G.; Petrella, F.; et al. Uptake-release by MSCs of a cationic platinum(II) complex active in vitro on human malignant cancer cell lines. *Biomed. Pharmacother.* **2018**, *108*, 111–118. [CrossRef] [PubMed]

40. Sacco, F.; Tarchi, M.; Ferraro, G.; Merlino, A.; Facchetti, G.; Rimoldi, I.; Messori, L.; Massai, L. Reactions with Proteins of Three Novel Anticancer Platinum(II) Complexes Bearing N-Heterocyclic Ligands. *Int. J. Mol. Sci.* **2021**, *22*, 10551. [CrossRef]

41. Facchetti, G.; Ferri, N.; Lupo, M.G.; Giorgio, L.; Rimoldi, I. Monofunctional PtII Complexes Based on 8-Aminoquinoline: Synthesis and Pharmacological Characterization. *Eur. J. Inorg. Chem.* **2019**, *2019*, 3389–3395. [CrossRef]

42. Coccè, V.; Rimoldi, I.; Facchetti, G.; Ciusani, E.; Alessandri, G.; Signorini, L.; Sisto, F.; Giannì, A.; Paino, F.; Pessina, A. In Vitro Activity of Monofunctional Pt-II Complex Based on 8-Aminoquinoline against Human Glioblastoma. *Pharmaceutics* **2021**, *13*, 2101. [CrossRef]

43. Takayama, Y.; Kusamori, K.; Tsukimori, C.; Shimizu, Y.; Hayashi, M.; Kiyama, I.; Katsumi, H.; Sakane, T.; Yamamoto, A.; Nishikawa, M. Anticancer drug-loaded mesenchymal stem cells for targeted cancer therapy. *J. Control. Release* **2021**, *329*, 1090–1101. [CrossRef]

44. Pessina, A.; Bonomi, A.; Coccè, V.; Invernici, G.; Navone, S.; Cavicchini, L. Mesenchymal stromal cells primed with paclitaxel provide a new approach for cancer therapy. *PLoS ONE* **2011**, *6*, e28321. [CrossRef]

45. Sun, Y.; Liu, G.; Zhang, K.; Cao, Q.; Liu, T.; Li, J. Mesenchymal stem cells-derived exosomes for drug delivery. *Stem Cell Res. Ther.* **2021**, *12*, 561. [CrossRef]

46. Litvinova, L.S.; Shupletsova, V.V.; Khaziakhmatova, O.G.; Daminova, A.G.; Kudryavtseva, V.L.; Yurova, K.A.; Malashchenko, V.V.; Todosenko, N.M.; Popova, V.; Litvinov, R.I.; et al. Human Mesenchymal Stem Cells as a Carrier for a Cell-Mediated Drug Delivery. *Front. Bioeng. Biotechnol.* **2022**, *10*, 796111. [CrossRef] [PubMed]

47. Takayama, Y.; Kusamori, K.; Nishikawa, M. Mesenchymal stem/stromal cells as next-generation drug delivery vehicles for cancer therapeutics. *Expert Opin. Drug Deliv.* **2021**, *18*, 1627–1642. [CrossRef] [PubMed]

48. Babajani, A.; Soltani, P.; Jamshidi, E.; Farjoo, M.H.; Niknejad, H. Recent Advances on Drug-Loaded Mesenchymal Stem Cells With Anti-neoplastic Agents for Targeted Treatment of Cancer. *Front. Bioeng. Biotechnol.* **2020**, *8*. [CrossRef] [PubMed]

49. Pessina, A.; Leonetti, C.; Artuso, S.; Benetti, A.; Dessy, E.; Pascucci, L.; Passeri, D.; Orlandi, A.; Berenzi, A.; Bonomi, A.; et al. Drug-releasing mesenchymal cells strongly suppress B16 lung metastasis in a syngeneic murine model. *J. Exp. Clin. Cancer Res.* **2015**, *34*, 82. [CrossRef]

50. Ionescu, A.; Caligiuri, R.; Godbert, N.; Ricciardi, L.; La Deda, M.; Ghedini, M.; Ferri, N.; Lupo, M.G.; Facchetti, G.; Rimoldi, I.; et al. Cytotoxic performances of new anionic cyclometalated Pt(II) complexes bearing chelated O^O ligands. *Appl. Organomet. Chem.* **2020**, *34*, e5455. [CrossRef]

51. Ravera, M.; Gabano, E.; McGlinchey, M.J.; Osella, D. Pt(iv) antitumor prodrugs: Dogmas, paradigms, and realities. *Dalton Trans.* **2022**, *51*, 2121–2134. [CrossRef]

52. Johnstone, T.C.; Suntharalingam, K.; Lippard, S.J. The Next Generation of Platinum Drugs: Targeted Pt(II) Agents, Nanoparticle Delivery, and Pt(IV) Prodrugs. *Chem. Rev.* **2016**, *116*, 3436–3486. [CrossRef]

53. Fronik, P.; Gutmann, M.; Vician, P.; Stojanovic, M.; Kastner, A.; Heffeter, P.; Pirker, C.; Keppler, B.K.; Berger, W.; Kowol, C.R. A platinum(IV) prodrug strategy to overcome glutathione-based oxaliplatin resistance. *Commun. Chem.* **2022**, *5*, 46. [CrossRef]

54. Tan, M.-X.; Wang, Z.-F.; Qin, Q.-P.; Zou, B.-Q.; Liang, H. Complexes of oxoplatin with rhein and ferulic acid ligands as platinum(iv) prodrugs with high anti-tumor activity. *Dalton Trans.* **2020**, *49*, 1613–1619. [CrossRef] [PubMed]

55. Fronik, P.; Poetsch, I.; Kastner, A.; Mendrina, T.; Hager, S.; Hohenwallner, K.; Schueffl, H.; Herndler-Brandstetter, D.; Koel-lensperger, G.; Rampler, E.; et al. Structure–Activity Relationships of Triple-Action Platinum(IV) Prodrugs with Albumin-Binding Properties and Immunomodulating Ligands. *J. Med. Chem.* **2021**, *64*, 12132–12151. [CrossRef]

56. Aputen, A.D.; Elias, M.G.; Gilbert, J.; Sakoff, J.A.; Gordon, C.P.; Scott, K.F.; Aldrich-Wright, J.R. Potent Chlorambucil-Platinum(IV) Prodrugs. *Int. J. Mol. Sci.* **2022**, *23*, 10471. [CrossRef]

57. Chen, J.W.; Wu, T.C.; Liang, W.; Ciou, J.-J.; Lai, C.-H. Boronates as hydrogen peroxide–reactive warheads in the design of detection probes, prodrugs, and nanomedicines used in tumors and other diseases. *Drug Deliv. Transl. Res.* **2022**. [CrossRef] [PubMed]

58. Jia, C.; Deacon, G.B.; Zhang, Y.; Gao, C. Platinum(IV) antitumor complexes and their nano-drug delivery. *Coord. Chem. Rev.* **2021**, *429*, 213640. [CrossRef]

59. Phan, T.H.T.; Le, T.T.H.; Phan, K.S.; Tran, T.L.A.; Du Nguyen, H.; Le, T.T.; Bui, T.T.V.; Le, M.H.; Tran, T.H.H.; Luu, D.H.; et al. Platinum (II) complexes and their nanoformulations: Preparation, characterisation and cytotoxicity. *Adv. Nat. Sci. Nanosci. Nanotechnol.* **2021**, *12*, 025016. [CrossRef]

60. Sancho-Albero, M.; Facchetti, G.; Panini, N.; Meroni, M.; Bello, E.; Rimoldi, I.; Zucchetti, M.; Frapolli, R.; De Cola, L. Enhancing Pt (IV) complexes anticancer activity upon encapsulation in stimuli responsive nanocages. *Adv. Healthc. Mater.* **2023**, 2202932. [CrossRef] [PubMed]

61. Chen, Q.-B.; Zhou, L.-Y.; Shi, L.-X.; Cheng, Y.; Wu, K.; Yuan, Q.; Dong, Z.-J.; Gu, H.-Z.; Zhang, X.-Z.; Zou, T. Platinum(IV) Complex-Loaded nanoparticles with photosensitive activity for cancer therapy. *Coord. Chem. Rev.* **2022**, *472*, 214789. [CrossRef]

Highlights of New Strategies to Increase the Efficacy of Transition Metal Complexes for Cancer Treatments

Ester Giorgi, Francesca Binacchi, Carlo Marotta ⓘ, Damiano Cirri ⓘ, Chiara Gabbiani *ⓘ and Alessandro Pratesi *ⓘ

Department of Chemistry and Industrial Chemistry, University of Pisa, Via G. Moruzzi 13, 56124 Pisa, Italy
* Correspondence: chiara.gabbiani@unipi.it (C.G.); alessandro.pratesi@unipi.it (A.P.)

Abstract: Although important progress has been made, cancer still remains a complex disease to treat. Serious side effects, the insurgence of resistance and poor selectivity are some of the problems associated with the classical metal-based anti-cancer therapies currently in clinical use. New treatment approaches are still needed to increase cancer patient survival without cancer recurrence. Herein, we reviewed two promising—at least in our opinion—new strategies to increase the efficacy of transition metal-based complexes. First, we considered the possibility of assembling two biologically active fragments containing different metal centres into the same molecule, thus obtaining a heterobimetallic complex. A critical comparison with the monometallic counterparts was done. The reviewed literature has been divided into two groups: the case of platinum; the case of gold. Secondly, the conjugation of metal-based complexes to a targeting moiety was discussed. Particularly, we highlighted some interesting examples of compounds targeting cancer cell organelles according to a third-order targeting approach, and complexes targeting the whole cancer cell, according to a second-order targeting strategy.

Keywords: platinum compounds; gold compounds; metal-based drugs; heterobimetallic complexes; targeting strategies

1. Introduction

During the last decades, great strides have been made in the fight against cancer. The knowledge about the mechanisms of its onset and cellular resistance has notably increased, as well as the discovery of new potential therapies. Despite this, cancer remains a problematic pathology to treat due to its characteristics of aggression, ability to metastasize, resistance onset, and severe side effects of the available drugs. For these reasons, cancer is still the second leading cause of morbidity and mortality worldwide [1]. In the context of the most promising anticancer therapies developed so far, metal-based drugs have represented for several decades the cornerstone for tumour chemotherapy [2,3]. In fact, platinum complexes, such as cisplatin, oxaliplatin, and carboplatin, are still the most widely used treatments in several kinds of cancer, including testicular, cervical, ovarian, and non-small cell lung cancers. However, in several cases after a variable number of chemotherapy cycles with platinum-based complexes, tumoral cells could become less susceptible to the cytotoxic effects of the drug, thanks to the activation of a multifactorial adaptive response that involves three major components: autophagy, endoplasmic reticulum stress signalling, and senescence [4]. Thus, the majority of cisplatin-treated patients experience therapeutic failure and tumour recurrence during—or right after—the treatments [5]. In addition, there are severe side effects associated with therapeutic regimens based on platinum complexes, such as nephrotoxicity, neurotoxicity, leukopenia, thrombocytopenia, gastrointestinal issues, nausea, vomiting, and hair loss [6]. These latter are mainly due to poor drug selectivity causing the death of healthy cells together with the tumoral ones. Considering all these issues, improvements in developing new effective

therapies can indeed be pursued. These problems have prompted researchers to focus on developing a new generation of chemotherapeutics. Firstly, the research has been extended to other transition metal compounds, such as gold, ruthenium, silver, iridium, rhenium, and copper, that proved to have important cytotoxic effects on cancer cells, becoming promising potential new anticancer drugs. For example, the gold compounds' popularity increased following the idea to repurpose Auranofin, an Au(I)-based complex approved by the FDA in 1985 as an antirheumatic Au(I) agent, for the treatment of cancer [7]. In fact, several studies highlighted its promising cytotoxic properties, entering also in three separate clinical trials in the United States as an anticancer compound [8]. Additionally, for Ru-based compounds the interest of the scientific community significantly grew after the publication of NAMI-A, KP1019 and KP1339, which are three Ru(III) complexes that have entered other human clinical trials [9]. During the past years, various strategies have been explored to optimise the efficiency of metal complexes with anti-cancer activity, both in potency and selectivity, aiming to obtain the so coveted "*anticancer magic bullet*", already conceptualised in the early 1900s by Paul Ehrlich [10]. In this review, we will focus on some examples referring to two main strategies: the first one regards heterobimetallic complexes with a synergic action, while the second one refers to constructs where the metallic complex was conjugated to a targeting moiety. Starting from the promising results obtained with some monometallic complexes, a new approach was attempted combining different metal centres in one compound by forming a heterobimetallic complex able to combine the various modes of action that are typical of the constituting metal centres. The heterobimetallic compound should enhance the anticancer properties of single metallodrugs. The objective is to enlighten any possible synergistic effect due to the administration of two or more active ingredients as a single drug [11,12]. Generally, the two metal centres have a different final molecular target with diverse mechanisms of action, or they can modify different pathways in the cellular metabolism, or adjust some chemical-physical properties of the whole heterobimetallic complex, such as the solubility or lipophilicity, with different contributions [13]. The combination of different activities into one single drug should reduce the concentration needed for the therapeutic approach, and this should decrease the side effects produced by a large amount of compound needed to have a positive response to the therapy. This behaviour could be expressed in lower IC_{50} values or by overcoming the resistant problems to the current therapies. Another appealing approach involves targeting strategies, which has proved to have many advantages and potential interesting applications. Targeted anticancer agents are designed according to a strategy that aims to direct them towards cancer-specific biomarkers or biological targets which are overexpressed in cancer cells. The aim is to achieve higher selectivity than standard platinum-based therapies and, consequently, lower side effects. In fact, preferential recruitment of the drug into tumour cells results in a selective cytotoxic action that damages tumour cells more than healthy ones. After being preferentially accumulated in tumour cells, the drug interacts with specific targets by modifying or interrupting a signalling pathway that supports the evasion of apoptosis, tumour growth, and resistance in cancer cells. While in classical therapies the focus is on discovering increasingly cytotoxic and potent drugs, in targeted therapies the aim is to achieve selectivity on diseased cells, potentially leading to more significant and controlled cytotoxicity [14].

2. Heteronuclear Metal Complexes with Anticancer Activity

One of the new strategies here presented concerns the combination of two different metal centres in one single drug to build a heteronuclear metal complex. The combination of more than one metal was already used for other types of applications, such as catalysis, where electronically different metals could synergistically cooperate and have better properties compared to the monometallic precursors in a catalytic process [15]. The same approach was used more recently for potential anticancer applications. The opportunity to use different metal-based compounds, which act as anticancer but have different mechanisms of action from each other, could promote cooperative activity and synergis-

tic effects. In this review, we divided different examples into two main groups, one of platinum and one of gold. These two metal centres, as monometallic compounds, have been extensively studied and they are known to exploit their anticancer activity in different types of final targets. Platinum compounds generally act in the genomic moiety [16], while gold complexes are considered good inhibitors of thioredoxin reductase [17]. One of the most recent and interesting results of the literature concerns the combination of platinum or gold with different metal centres or a combination of them. A discussion on the possible synergistic effects of the new heteronuclear metal drugs has been done. To be sure that the enhanced anticancer activity is truly done by the cooperative action of the two metal centres, a comparison with the monometallic fragments is always needed.

2.1. The Case of Platinum

Transition metal complexes have been deeply studied for different applications, such as catalysis, antimicrobial, and also antitumoral drugs [18]. Platinum complexes are probably the most well-known and studied in the field of anticancer compounds, also thanks to the omnipresence of cisplatin and its derivatives as a starting point [19,20]. To overcome all the side effects of cisplatin such as neurotoxicity, nephro-, oto-, and gastrointestinal toxicity, alternative transition metal centres gained a place in this field [21–23]. In the last years, there are many examples of Pt(II) complexes combined with different metal centres such as Ru(II), Rh(III), Au(I), Re(I), Tc(I) [17,24–27]. Platinum-based complexes are mainly binders of genomic targets via a covalent bond between the Pt metal centre and N-7 atom of guanine base [16], even if there is also evidence of protein binding, as serum albumin [28]. Here we present the most recent and promising results of bimetallic complexes that involve different types of compounds such as photoactivable, macrocycle, or prodrugs compounds. The possible synergistic effects of two metal centres with different targets were evaluated.

Starting from the ruthenium and rhodium ones, these metal centres can form organometallic complexes usually by the coordination to nitrogen atoms or with arene ligands, making the coordination easily achievable [29]. Ruthenium-based compounds, usually considered to have antimetastatic activity, received interest as anticancer agents after the discovery of the antitumoral properties of NAMI-A, KP1019, and KP1339 mentioned above. These organometallic Ru(II)-arene derivatives have a different mechanism of action compared to cisplatin to exploit the anticancer activity, which involves the binding to the biomolecule transferrin, an iron-binding protein [30].

In 2019 Askari and co-workers published their work, where the synthesis of three heterobimetallic Pt(II)-Ru(II) and Pt(II)-Rh(III) complexes (**1–3**) (Figure 1) is described. The three bimetallic complexes **1–3** turned out to be active in the human 20S proteasome, one of the main targets for cancer therapy. Compounds **1–3** also inhibited cathepsin B and L, which take part in tumour progression and invasion. The cytotoxic activity has been evaluated also in comparison to the Pt(II)-based precursors and cisplatin. The bimetallic complexes showed a good reduction of cell viability in different tumour cell lines such as neuroblastoma SH-SY5Y, melanoma SKMel-28, hepatocellular adenocarcinoma HepG2, and colorectal adenocarcinoma Caco-2 tumour cell lines, comparable or in some cases even greater than cisplatin, while for the healthy cell line of human fibroblasts WI 38 there is no sign of cytotoxicity. The flow cytometry analyses with Annexin-V/PI staining revealed that the cell death mechanism in the SH-SY5Y line is apoptotic after 72 h of treatment. Pt(II) precursors showed no significant inhibition or antiproliferative activity, which makes them a structural feature of the proposed heterobimetallic complexes [25].
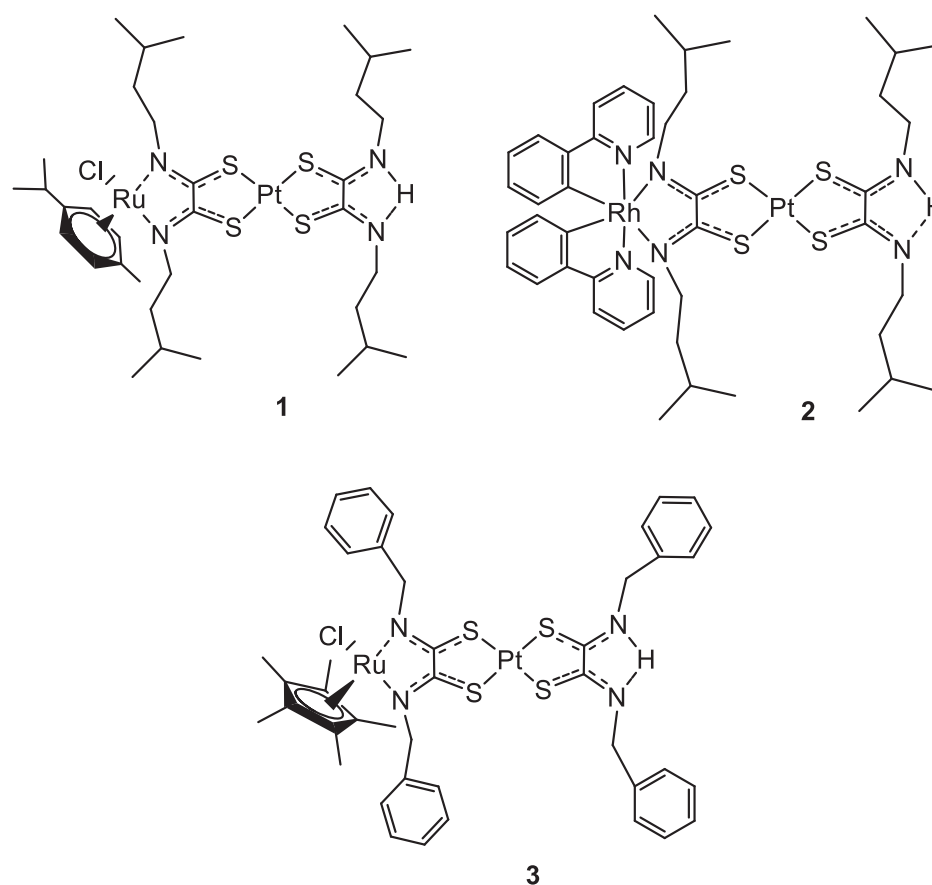
Figure 1. Molecular structure of compounds **1**–**3**.

A paper by Zheng and co-workers, published in 2018, described the synthesis and characterization of a new bimetallic Ru(II)-Pt(II) complex (Figure 2). In this case, the platinum moiety plays a pivotal role in the activity of the whole bimetallic compound improving the anticancer activity of the Ru-containing moiety. The photoactivable Ru complex **4** is combined with cis-Pt(DMSO)$_2$Cl$_2$ to obtain the heterobimetallic complex **5** through the coordination of Pt to the two free nitrogen of the bpm (2,2′-bipyrimidine) ligand. The dichloroPt(II)-containing portion could covalently bind DNA. All the tests have been performed both in dark and light conditions. The cytotoxic activity of **5** is extremely increased in light conditions and is more cytotoxic compared to **4**. These results pointed out that both complexes have overcome the cisplatin resistance of the A549R (lung cancer) cell line taking advantage of the photodamage of mtDNA. Moreover, the bimetallic complex **5** can bind to mtDNA also through the Pt centre; in fact, the impairment of the polynucleotide occurs both in the dark and upon visible light irradiation. The higher affinity of **5** to DNA is due to the double type of binding: covalent, through the Pt(II) moiety, and noncovalent, through the planar ligand of Ru(II) moiety. Under light irradiation, **5** can produce ROS inside the mitochondria, causing their dysfunction, including MMP collapse, ATP depletion, and attenuation of mitochondrial energy status (see Figure 3). Both complexes have been tested in vivo and compound **5** has shown better pharmacological properties with respect to compound **4**. In particular, **5** produced lower side effects and decreased the tumour volume without causing mouse death (Figure 4) [31].
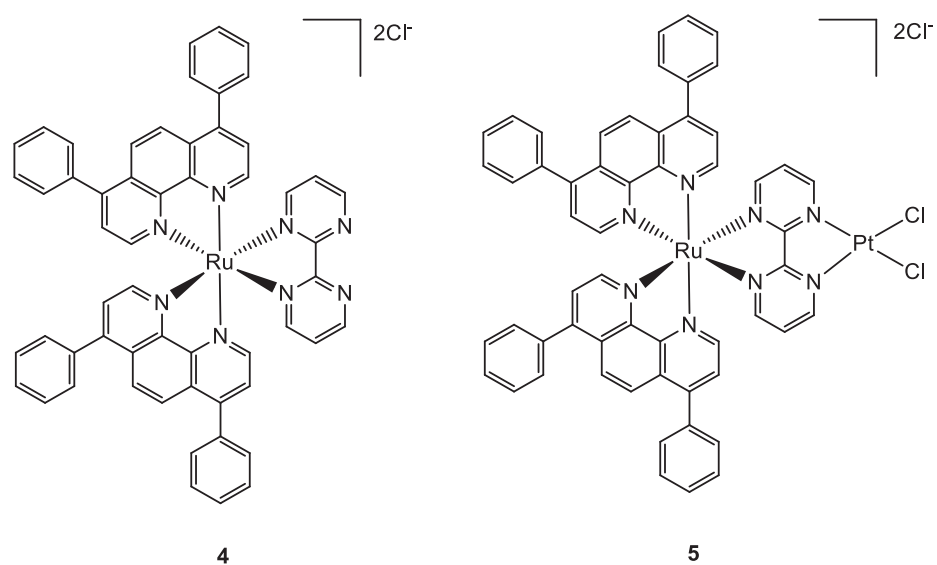
Figure 2. Molecular structure of compounds **4** and **5**.
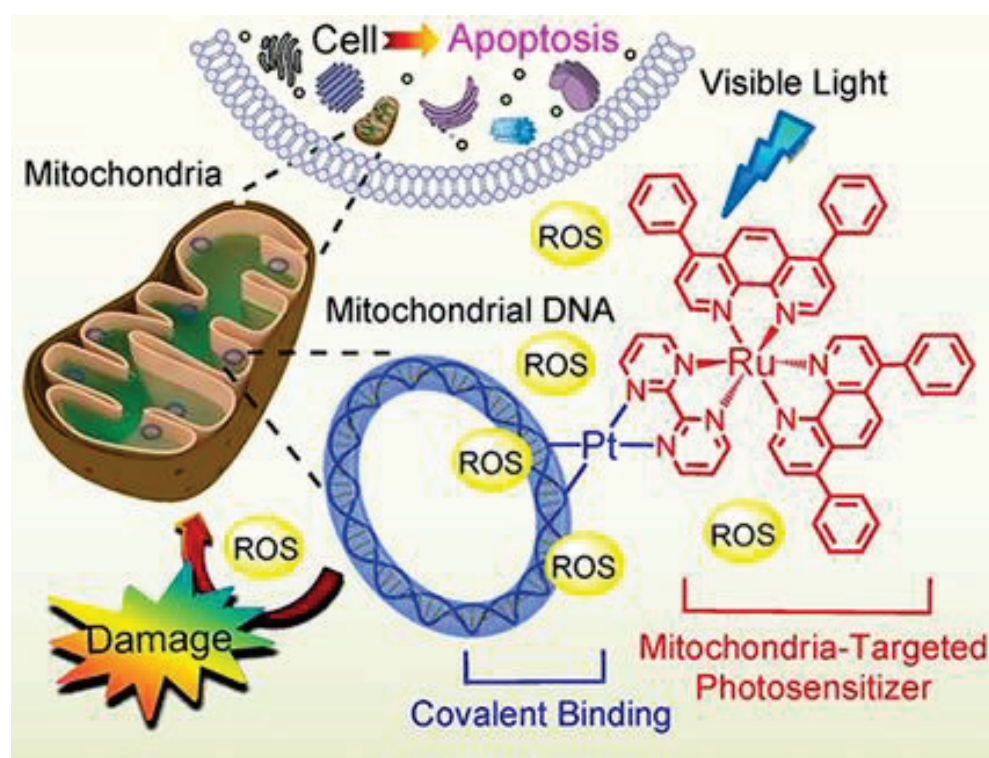
Figure 3. Representation of the mechanism of action of complex 5. (Reprinted with permission from ref. [31]. Copyright 2018 John Wiley and Sons).
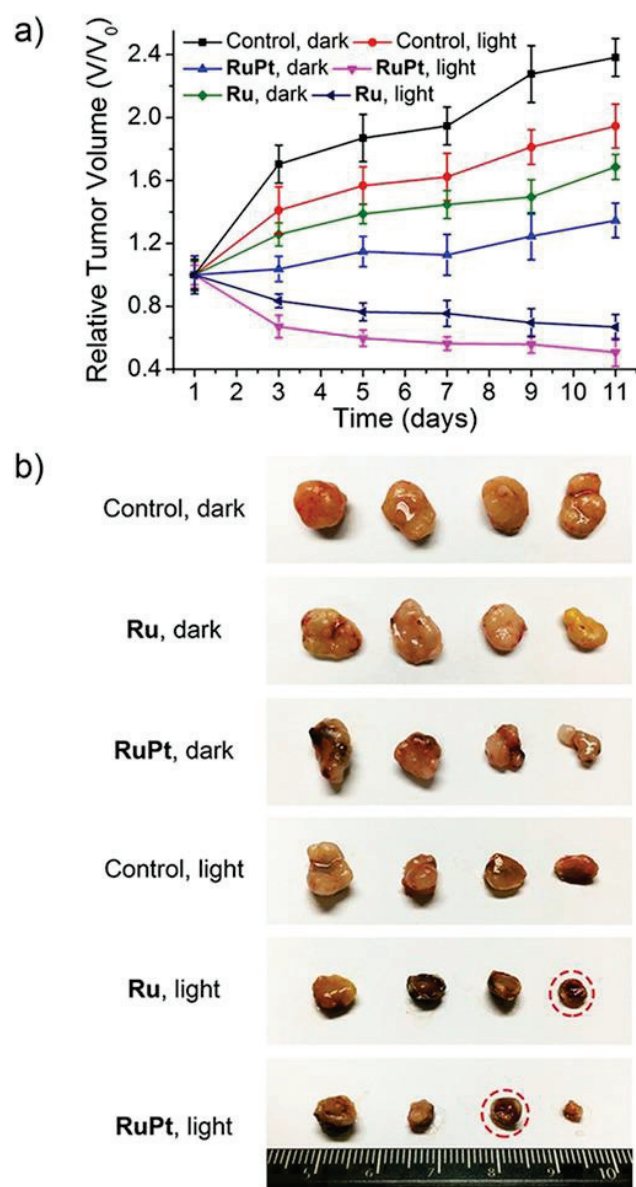
Figure 4. (**a**) Chart of the relative tumour volumes (V/V$_0$) of mice treated with PBS, **4** (Ru), and **5** (RuPt), measured for 11 days after treatment with PBS (control), under dark and light conditions. On the first and sixth days, intratumoral injections were performed. (**b**) Photo of the tumours removed from the nude mice. The completed scavenged tumours have been underlined by red dotted circles. (Reprinted with permission from ref. [31]. Copyright 2018 John Wiley and Sons).

Photoactivable systems seem to be a good alternative to overcome cisplatin toxicity and another promising new metal complex that is active upon irradiation inside the tumour cells has been studied by Zhou and co-workers [32]. The Ru–Pt complex **6** (Figure 5) has a large macrocyclic structure, and the metallacycle facilitates its cellular uptake, as confirmed by ICP-MS analyses. The uptake values for complex **6** reach 114.82 ng and 451.37 ng per million cells for Ru and Pt, while the same test with the Ru moiety alone revealed a maximum cellular Ru concentration of 2.32 ng per million cells. The study of the cytotoxic activity on the A549 cell line showed that **6** is accumulated preferentially in mitochondria and nuclei as an intact metallacycle (confirmed by confocal laser scanning microscopy analysis). Compound **6** exhibits its cytotoxic potential upon LED irradiation at 450 nm (21.8 mW cm^{-2}, 5 min), with IC$_{50}$ values of 0.71–4.4 µM, while it is extremely decreased in dark conditions, with IC$_{50}$ of 65.2–80.9 µM. Light promotes the generation of singlet oxygen specie which causes cell death producing damages concurrently in the mitochondria and

nuclei. As already observed for products **5** and **4**, also in this case the in vivo tests at low light doses obtained with a diode laser (800 nm, 50 mW, 20 s/mm), showed that **6** causes an effective tumour remission associated with low systemic toxicity.

6
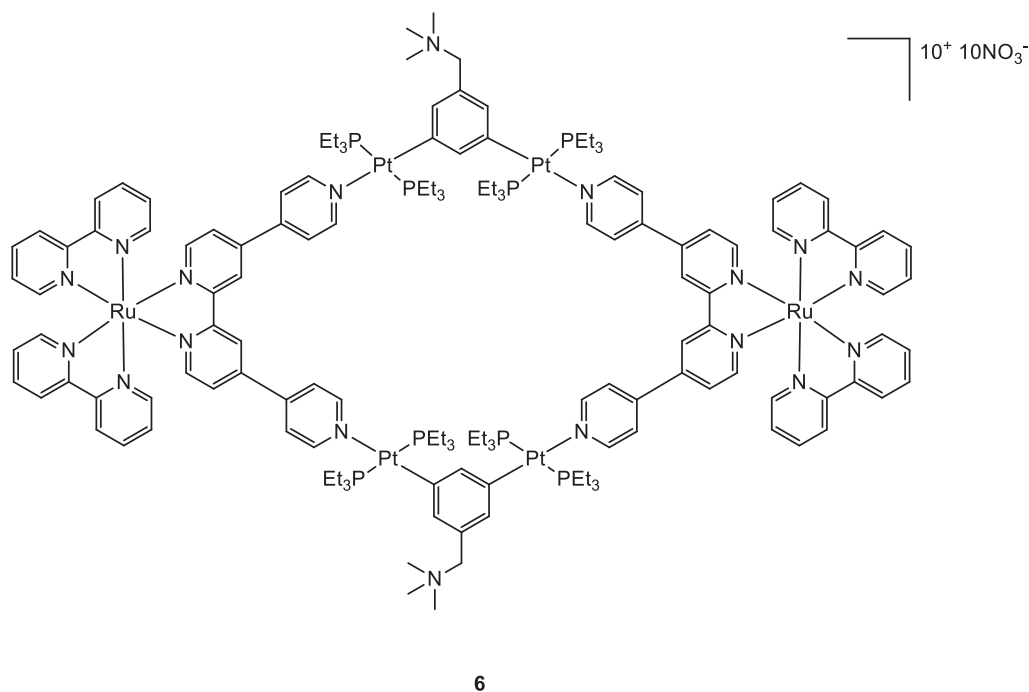
Figure 5. Molecular structure of compound **6**.

Another interesting strategy, that involves in this case the platinum moiety, is to exploit the advantage related to Pt(IV) complexes. The platinum centre in its higher oxidation state is chemically less reactive and kinetically more inert than its respective Pt(II) counterpart. This feature can be fruitfully used to prevent off-target reactions, obtaining complexes that can be considered prodrugs [33,34]. Moreover, the Pt(IV) complexes adopt the octahedral coordinative geometry, giving the opportunity to functionalise the axial positions with other biologically active molecules [35,36]. Since inside the cancer cells there is an increased reductive environment compared to the healthy ones [37], this can be exploited to obtain the selective Pt(IV) reduction inside the cancer cell, restoring the reactive Pt(II) complex with the simultaneous release of the axial ligands [38].

In this frame, the Guangyu Zhu group worked on the synthesis of new Pt(IV)–Ru(II) metal complexes (Figure 6) which combine the cytotoxic properties of cisplatin with the antimetastatic properties of ruthenium-arene complexes. They were all found to be more cytotoxic compared to cisplatin with low micromolar (**11**), sub-micromolar, and nanomolar (**7–10**) cytotoxicity in most of the human cancer cells tested. All the bimetallic complexes are effective also in cisplatin-resistant cells A2780cisR (ovarian carcinoma) and A549cisR (lung adenocarcinoma). Compounds **7–11** have a selectivity index (the ratio between the IC_{50} in MRC-5 (lung fibroblast) and the IC_{50} in A549 cells) that is nearly 10-fold higher than that of cisplatin. A direct comparison with the performances of the monometallic moieties revealed that the increased cytotoxic activity is produced by a synergistic effect between the two metal complexes [39,40].
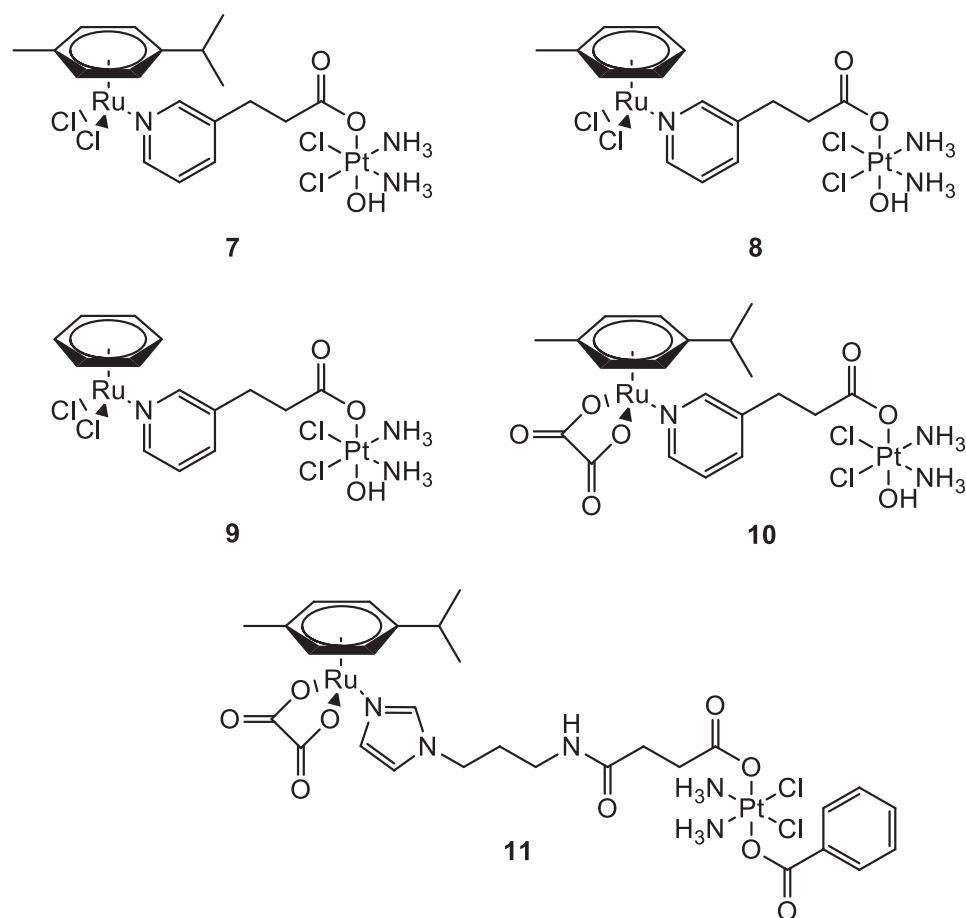
Figure 6. Molecular structure of compounds **7–11**.

Quental and co-workers investigated the combination of two different metal centres: one with therapeutic properties (i.e., Pt(II)), and the other with properties useful in diagnostics (i.e., Re(I)) to achieve a theranostic agent. The new heterobimetallic complex (**12**) (Figure 7) had indeed a rhenium moiety with photosensitizing properties and a non-classical platinum centre with intrinsic cytotoxic activity in the dark. The metalation of cellular DNA caused after the treatment with **12** both in the dark or under irradiation was investigated by employing ICP-MS analysis. After the administration of **12** in dark conditions, the polynucleotide was extracted from the cell culture and mineralised, and ICP-MS detected no presence of platinum. This agrees with gel electrophoresis experiments, where there is no modification of the mobility of the supercoiled form. On the contrary, light exposure of the cell culture treated with the studied compound increases the amount of open circular form, which is correlated to photosensitization with consequent ROS production (singlet oxygen $^1O_2$).

The Re-tricarbonyl unit in **12** could be replaced by ^{99m}Tc (**13**) (Figure 7) to allow biodistribution investigations and imaging studies in normal mice. The intensity of radioactivity was higher in the excretory organs (liver and kidney), where **13** accumulated the most [27].
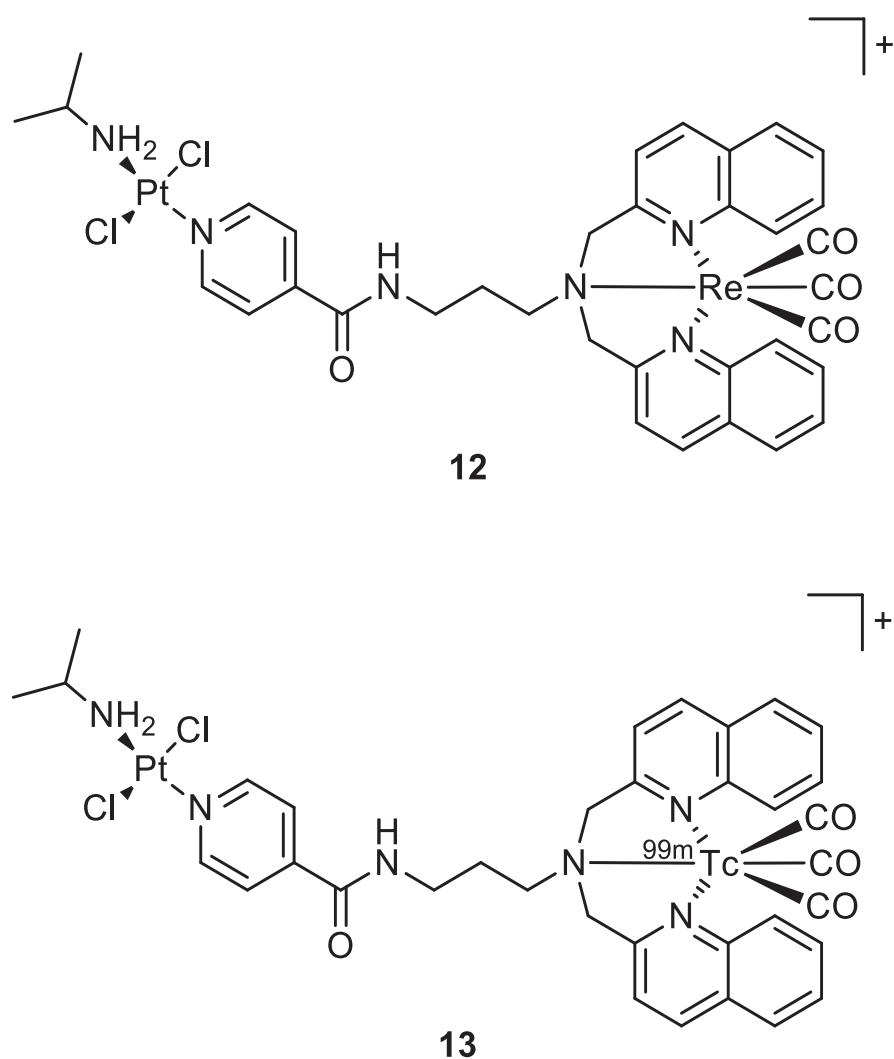
Figure 7. Molecular structure of compounds **12** and **13**.

In 2020, Bertrand and co-workers synthesised different bimetallic complexes of Pt(II)-Re(I) (**15a–d**, **16c**) starting from the Pt(II) precursors (**14a–d**) (Figure 8). The first screening was based on the MTT assay (Table 1). The most promising ones were the monometallic **14a** and the bimetallic **15a**, **15d,** and **16c** which were 10 times more cytotoxic compared to cisplatin. Additionally, **15b** and **15c** had no cytotoxic activity, while **16c** was the most cytotoxic of this group. Even those that showed good IC_{50} values on MDA-MB-231, MCF-7, and A2780 cancer cell lines all showed a very scarce selectivity when comparing the data obtained with the control healthy cells (MCF-10A). In addition, the lipophilicity of the whole complex (Table 1) was directly correlated to the ligand nature, and the bimetallic compounds **15a–d** were more lipophilic than the mono Pt counterparts, while the charged **16c** was the most hydrophilic. The amount of metal content revealed in cellular uptake experiments exactly reflected this order of lipophilicity, and it was not correlated to the cytotoxic activity. Additionally, in this case, there was no evidence of synergistic effects [24].

L = DMSO (**14a**); pyridine (**14b**)
PPh₃ (**14c**); NHC (**14d**)

L = DMSO (**15a**); pyridine (**15b**)
PPh₃ (**15c**); NHC (**15d**)

16c
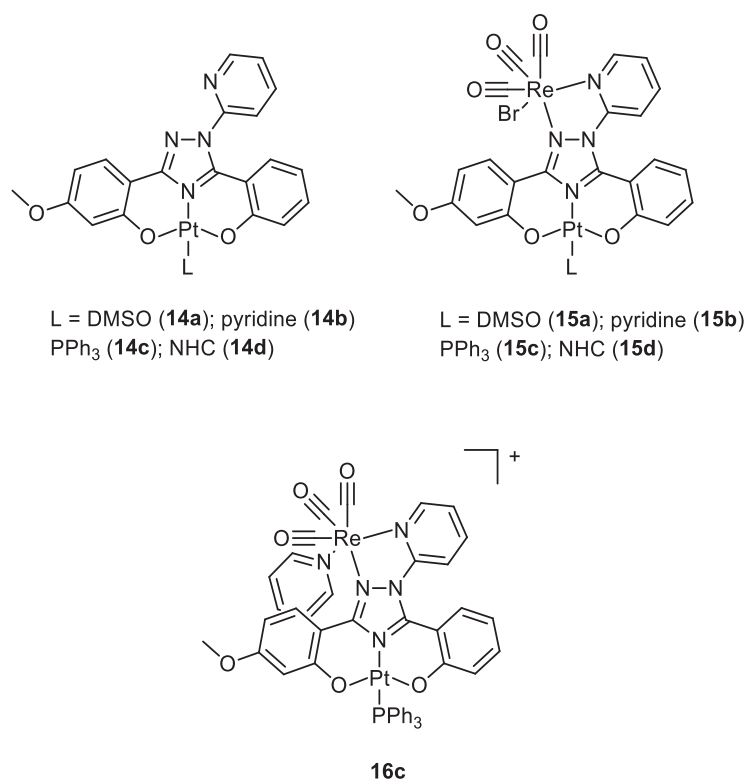
Figure 8. Molecular structure of compounds **14a–d**, **15a–d**, and **16c**.

Table 1. Antiproliferative activity of compounds **14a**, **15a**, **15d**, **16c**, and cisplatin on different cancer cell lines and the healthy cell line MCF-10F after 72 h of incubation at 37 °C. Partition coefficients of all complexes are reported as Log $P_{o/w}$. (Adapted with permission from ref. [24]. Copyright 2020 John Wiley and Sons).

Complex	$IC_{50} \pm SD$ (µM)				Log $P_{o/w}$
	MDA-MB-231	**MCF-7**	**A2780**	**MCF-10F**	
14a	3.1 ± 0.5	1.6 ± 0.9	1.5 ± 0.6	1.1 ± 0.2	3.7
14b	n. d.	n. d.	n. d.	n. d.	3.3
14c	n. d.	n. d.	n. d.	n. d.	6.9
14d	n. d.	n. d.	n. d.	n. d.	4.5
15a	2.1 ± 0.6	2.2 ± 0.4	1.5 ± 0.3	1.82 ± 0.06	3.6
15b	n. d.	n. d.	n. d.	n. d.	4.9
15c	n. d.	n. d.	n. d.	n. d.	8.1
15d	9.2 ± 3.5	20.3 ± 1.9	34.5 ± 7.2	17.4 ± 2.6	5.8
16c	$1.7 \pm 0.3.$	1.1 ± 0.4	1.3 ± 0.2	3.3 ± 0.3	2.4
cisplatin	20.4 ± 3.4	14 ± 3.5	1.0 ± 0.2	2.9 ± 0.8	−2.4 [a]

n. d. = not determined; [a] data retrieved from ref [41].

2.2. The Case of Gold

Other types of combinations involve gold compounds. Gold complexes are usually composed by the coordination of the soft metal centre with phosphine or sulphur ligands, but carbenes ligands have also gained much interest [42,43]. Gold complexes express anticancer activity by disrupting the reduction/oxidation (redox) system within the cell via the inhibition of thioredoxin reductases (TrxRs). This enzyme is present in the mitochondria and an alteration of its activity could lead to apoptosis [17,44–47]. Here we present some relevant examples of recently synthesised complexes that combine the cytotoxic potential of gold-based compounds with other metal centres which exploit their anticancer activity differently, such as Pt(II), Ru(II), Ti(IV), Ir(III), and Re(I).

To date, there are only a few examples in the literature on the combination of Au(I) and Pt(II) metal centres [13,48,49]. Some of the most promising examples are the heterometallic Pt–Au complexes depicted in Figure 9 (**18a–c**), which have shown synergistic effects by an improvement of the antiproliferative activity against A549 (lung), SKOV3 (ovarian), and MCF-7 (breast) cancer cell lines in comparison to their Pt-based precursor complexes **17a–c** and [ClAu(μ-dppm)AuCl], which are not toxic to any of the cell lines investigated. Inhibition of cell proliferation was also compared to cisplatin and Auranofin, revealing **18b** as the most promising complex, and apoptosis is the cell death mechanism in MCF-7 cancer cells in a dose-dependent manner. Furthermore, **18a** effectively internalises in MCF-7 cells, and the nucleus showed the highest accumulation of the complex, which was revealed by fluorescence microscopy, with less dispersion in the cytoplasm. Selectivity for cancer cells was investigated by comparing the IC$_{50}$ values of the healthy cell line MCF-10A (epithelial breast), with the one obtained with MCF-7. All the complexes showed good selectivity for the tumorigenic cell line, and complexes **18b** and **18c** demonstrated higher specificity for human breast cancer cells with minor damage to normal epithelial breast cells [13].

17a: C^N = bzq; Ar = C$_6$F$_5$

17b: C^N = bzq; Ar = *p*-MeC$_6$H$_4$

17c: C^N = ppy; Ar = *p*-MeC$_6$H$_4$

18a: C^N = bzq; Ar = C$_6$F$_5$

18b: C^N = bzq; Ar = *p*-MeC$_6$H$_4$

18c: C^N = ppy; Ar = *p*-MeC$_6$H$_4$
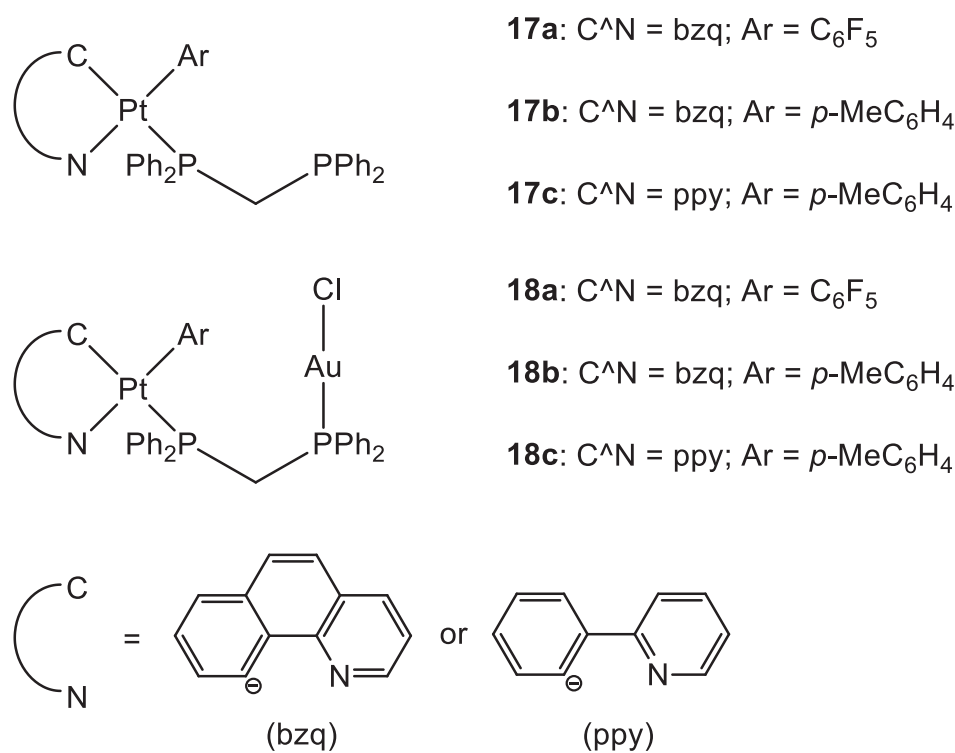
Figure 9. Molecular structure of compounds **17a–c** and **18a–c**.

In the case of the two Pt(II)-Au(I) complexes (**19, 20**) (Figure 10) proposed by Wenzel and co-workers, the new compounds exhibited great cytotoxic activity. A comparison of the IC$_{50}$ values between the ovarian cancer cell A2780 and cisplatin-resistant A2780cis showed that **19** and **20** were able to overcome possible resistance phenomena. There is no evidence of cooperative effects of the two metals, and the cytotoxicity towards a healthy cell line is comparable to the tumoral one, demonstrating a total lack of selectivity. The sugar moiety seems to improve the transport of the compound into the cells, but the phosphine ligand may counter the Pt moiety from freely binding to the double strand of DNA [49].
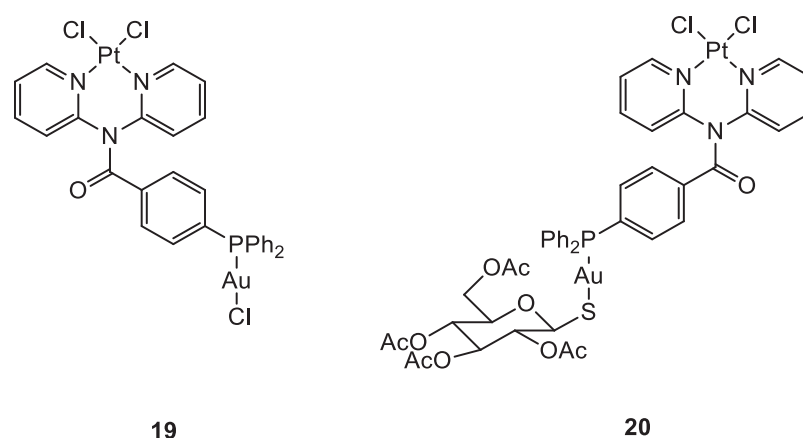
Figure 10. Molecular structure of compounds **19** and **20**.

Cinellu and co-workers compared the activity of monometallic Pt(II) complex **21** with the bimetallic Pt(II)-Au(I) complexes **22** and **23** (Figure 11). Interestingly, the heterobimetallic complex bearing the triphenylphosphine ligand (**22**) presented greater cytotoxic effects compared to the mononuclear Pt complex **21**. The IC$_{50}$ value obtained after the administration of **21** and the gold(I) precursor (AF) together in an equal amount was compared with the values obtained with the heterobimetallic complexes. The data suggested an additive rather than a synergistic effect of the platinum and gold centres in compound **21**. On the other hand, it is important that even if joined in the same molecular scaffold, the two metal complexes do not reduce their biological activity. Further, the Au(TPA) ligand decreases the antiproliferative activity of complex **23**. Moreover, compounds **21** and **22** interact with RNase A but in a different way. It seems that Rnase A shows selectivity for gold over platinum. In addition, complex **22** breakdowns in the presence of the oligonucleotide (ODN4: 5′-CGC-GCG-3′), forming different adducts with the pt fragment, [AuPPh$_3$]$^+$ and Au(I). The formation of different biomolecular adducts, which could be caused by the presence of different metal centres in the same molecule, may lead to enhanced cytotoxic effects in agreement with the observed additive effect of coupled metals [48].
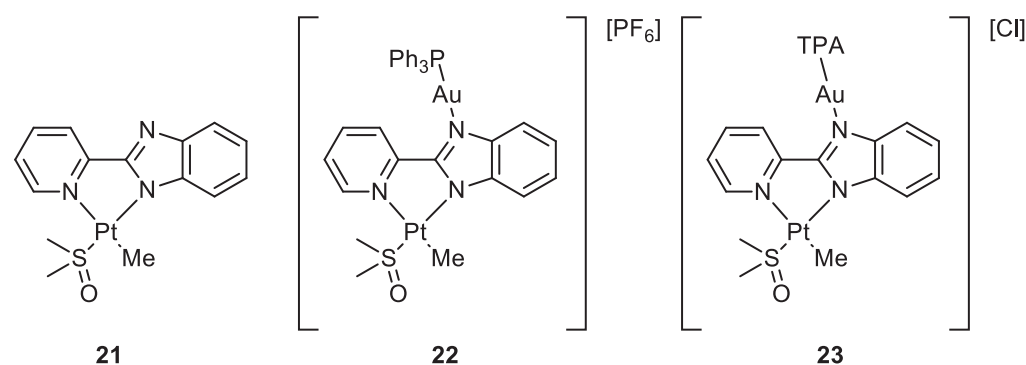
Figure 11. Molecular structure of compounds **21**–**23**.

The group of Maria Contel synthesised new heterobimetallic Ru(II)-Au(I) complexes (**25a**–**d**) (Figure 12) where the Au metal centre is coordinated to an N-heterocycle carbene. PrestoBlue assay, a resazurin-based compound which has similar behaviour to the most well-known MTT, was used to evaluate the antiproliferative activity of the complexes [50]. The bimetallic complexes are more cytotoxic compared to cisplatin and have a better selectivity toward cancer cell lines compared to the healthy ones (HEK293T). The same assay was performed with a combination of a ratio of 1:1 of the monometallic gold (**24a**–**d**) and ruthenium counterparts and they all have a lower IC$_{50}$ value compared to the corresponding heterometallic complexes. Compounds **25a**–**d** do not interact with the DNA

plasmid pBR322, so other targets may cause cell death. Complex **25a** has been tested for the inhibition of the TrxR (thioredoxin reductase) and it is more efficient than its monometallic counterparts (Figure 13). This behaviour could suggest a synergist effect of the two metal centres when present in the same compound [51]. Further inhibition studies on complex **25b** published two years after revealed as inhibited molecular targets different interleukins, metalloproteases, and cathepsins, which are important in tumour metastasis and angiogenesis [52].
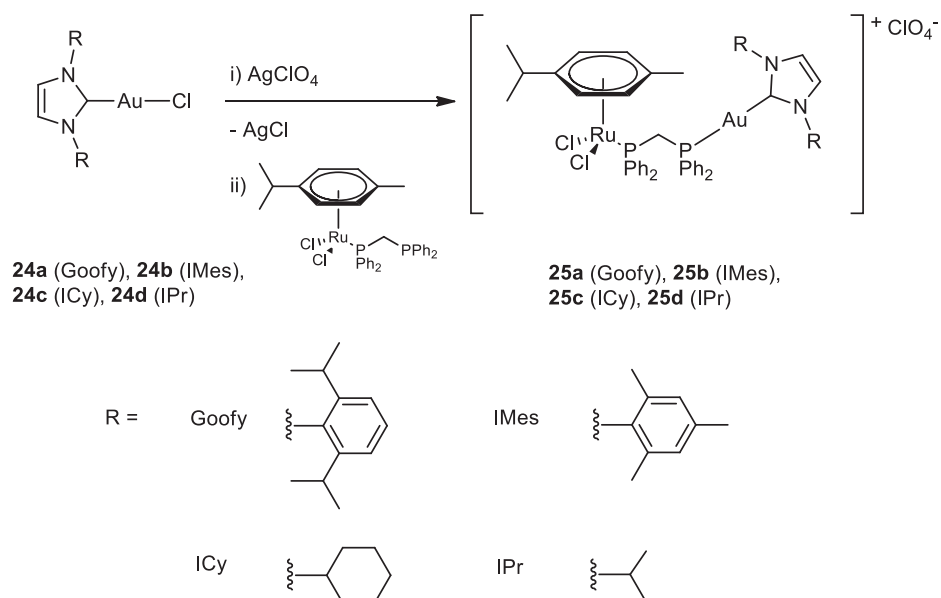
Figure 12. Molecular structure of compounds **24a–d** and **25a–d**.
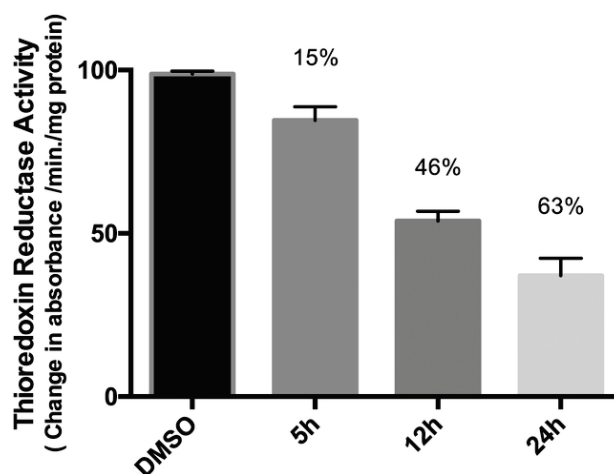
Figure 13. Activity of thioredoxin reductase of Caki-1 cells treated with 0.1% of DMSO (control) or complex **25a** (5 μM) after 5, 12, and 24 h of incubation. (Reprinted with permission from ref. [51]. Copyright 2016 Royal Society of Chemistry).

The same group worked also with heterobimetallic complexes of Ti(IV)-Au(I) (**26** and **27**) (Figure 14). The mechanism of action of **26** and **27** is different compared to cisplatin, because they do not bind DNA, but they inhibit protein kinases such as p90-RSK, AKT, MAPKAPA, and thioredoxin reductase [53,54]. The two new compounds show IC$_{50}$ values under the μM range, after 72 h of incubation, for renal cancer cell line Caki-1. Compounds **26** and **27** are more cytotoxic than the Au(I) monometallic derivatives and much more cytotoxic than the titanocene dichloride, with effective anti-migration and

anti-invasive properties, making these bimetallic compounds two promising candidates for cancer therapy [55].
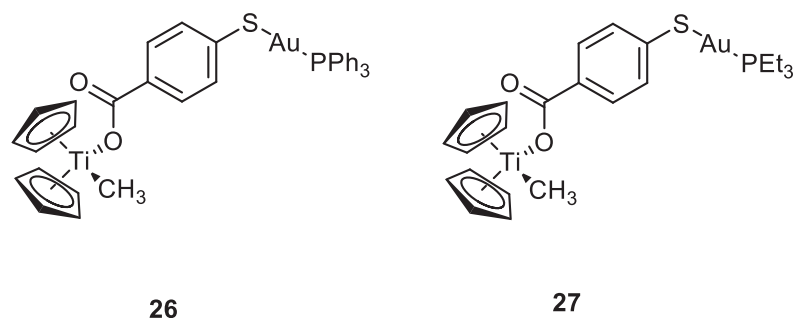
Figure 14. Molecular structure of compounds **26** and **27**.

Ir(III) complexes can form emissive phosphorescent compounds with tuneable photophysical properties. By changing the organic ligands, the wavelength of emission changes accordingly, obtaining highly pure primary colours for OLEDs (full-colour displays), or near-infrared emission for chemical sensors, bio-imaging, and telecommunication [56,57]. Only very recently have Ir(III) complexes exhibited their potency as theranostic agents. Their emission properties enable the visualisation of their cellular biodistribution and, concomitantly, Ir(III) complexes have displayed good cytotoxicity towards different cancer cells [58,59].

Three new Au(I)-Ir(III) bimetallic complexes (**29, 30,** and **31**) (Figure 15) were presented by Redrado and co-workers in 2021 and the results were compared with the monometallic precursor [Ir(N^C)$_2$(dppm)]$^+$ (**28**). All complexes induce apoptosis with the formation of cytoplasmic vacuolisation. The value of IC$_{50}$ in A549 cells ranges between 0.6 and 1.7 μM, with complex **31** being the most cytotoxic. The emission properties of Ir(III) moiety (green irradiation) allowed the investigation of cell distribution, which showed the complexes more located in the cytoplasm, and the superimposition with MitoTracker Red (MTR) emission (red irradiation), a mitochondrial selective dye used as internal standard, suggested an accumulation in the mitochondria. The presence of the gold fragment increases the generation of ROS and the inhibition of TrxR but there is no evidence of synergistic or additive effects for the heterometallic complexes [60].
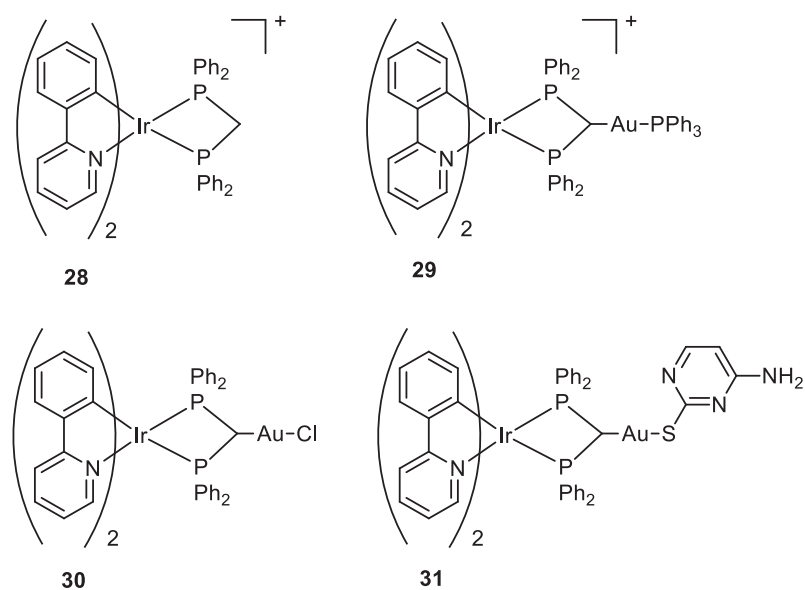
Figure 15. Molecular structure of compounds **28–31**.

Luengo and co-workers published a paper on Au(I)-Re(I) heterometallic complexes (**34a–c** and **35a–b**) (Figure 16). The antiproliferative activity has been evaluated with lung cancer cells A549 and cervix cancer cells He-La. Better results have been obtained for the cationic complexes compared to the neutral ones. The monometallic Re(I) complexes (**32, 33**) show their cytotoxic activity even at 24 h, while only the heterotrimetallic complexes reveal their selectivity towards HeLa cells after 72 h with exception of **34b**. The gold moiety is involved in the mechanism of action, even in terms of internalisation. The gold ancillary ligand guides the cellular uptake following the order -PPh$_3$>-CN^{t}Bu>-Ipr. The distribution of the heterometallic species in HeLa cells was evaluated with fluorescent microscopy, thanks to the optical properties of Re moiety. In A549 cells all the compounds precipitate and accumulate outside the cells, especially the neutral complexes **32** and **34a–c**, while in HeLa cells, the positively charged heterotrimetallic compounds **35a–b** were in the outer cellular membrane media, very close to the membrane, suggesting a possible interaction of the complexes with the membrane. These different behaviours may explain the selectivity and higher toxicity toward the HeLa cell line over A549. The monometallic Re complex **33** internalised in the cells and no precipitate was detected outside the cell membrane. This suggests that the gold moiety could be responsible for the localisation pattern, additionally with the selectivity for HeLa cells membrane over A549 one, displayed by heterometallic species [61].
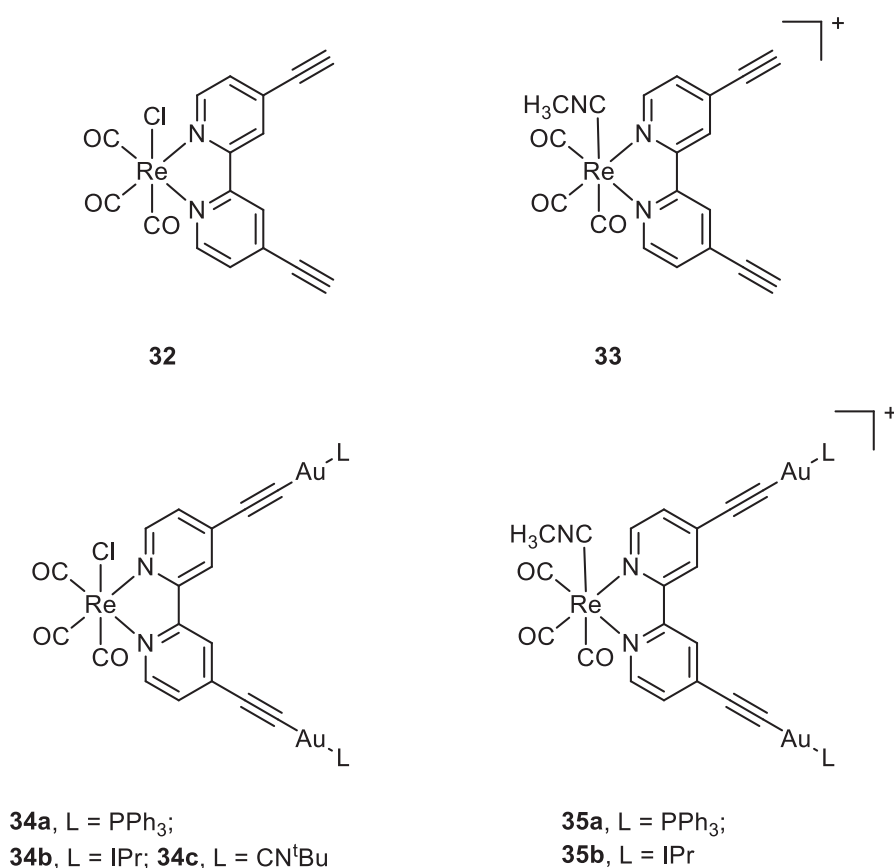
Figure 16. Molecular structure of compounds **32, 33, 34a–c**, and **35a–b**.

3. Targeting Strategies

In order to selectively accumulate metal complexes within tumour cells, two main approaches are generally used. The first is a sort of "passive targeting", where the EPR effect (Enhanced Permeability and Retention) is exploited (Figure 17) [62]. Solid tumours have a particular microenvironment characterised by rich vascularization and low lymphatic drainage, where the leaky blood vessels present several wider fenestrations than healthy

tissues [63]. While these characteristics allow the tumour to satisfy the augmented demand for nutrients necessary to support their rapid proliferation, at the same time, they allow drugs to have preferential extravasation into tumoral tissues [64]. However, they are not able to access so readily to healthy tissues, where the junctions between epithelial wall cells are tighter [64]. Anti-cancer nanomedicine is associated with finding delivery solutions, such as micelles, liposomes, and nanoparticles, that deliver the drug to tumour cells, mainly by exploiting the EPR effect [64,65]. Nevertheless, limited results have been achieved through passive targeting, due to the high heterogeneity of the tumour microenvironment, which can differ depending on the specific kind of tumour and its different stages [66]. In fact, tumours have a highly heterogeneous nature, and the intensity and nature of the EPR effect can vary [67]. Furthermore, this effect also depends on the chemical and physical characteristics of the drug, such as size, shape, and elasticity [68,69].
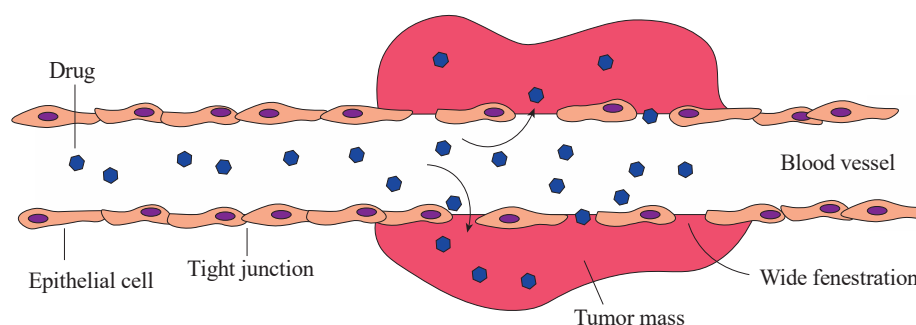
Figure 17. Schematic representation of the EPR effect.

The second approach concerns using an "active targeting strategy" that can be designed according to different methods. One of the most common approaches is the use of ligands that selectively recognise biomarkers overexpressed on tumour cells, such as receptors on the cell surface or proteins in the intracellular environment [70,71]. Otherwise, other strategies foresee the use of a prodrug, inactive in healthy cells but activated only at the site of the tumour, exploiting the unique characteristics of the tumoral microenvironment, such as the presence of high levels of ROS, low pH value, overexpression of matrix metalloprotease, or the reducing conditions [72]. There are three levels towards which active drug targeting can be directed: first-order drug targeting to a specific organ or tissue, second-order drug targeting to specific cells, and third-order drug targeting to an intracellular organelle, such as the nucleus, mitochondria, endoplasmic reticulum [73,74]. This section does not intend to make a complete and exhaustive review of all cancer-targeting metal complexes. Instead, it aims to propose an overview of some of the most significant examples of methods that have been rationally designed to obtain a preferential interaction with cancer cells, according to different active targeting strategies belonging to second and third-order types.

3.1. Organelle–Targeting Metal Complexes

Each organelle in the eukaryotic cell (Figure 18) plays a defined role, and for each organelle, a malfunction can lead to various diseases, including cancer [75]. This latter is one of the reasons why some organelles, such as mitochondria, have proved to be promising targets in anticancer therapy [76]; others are only recently emerging, such as the endoplasmic reticulum [77].

Organelle targeting can be achieved with metal complexes through two main strategies: coupling the complex to specific organelle-targeting biomolecules or finetuning of the complex's properties to satisfy the characteristics required to target that particular organelle [76].
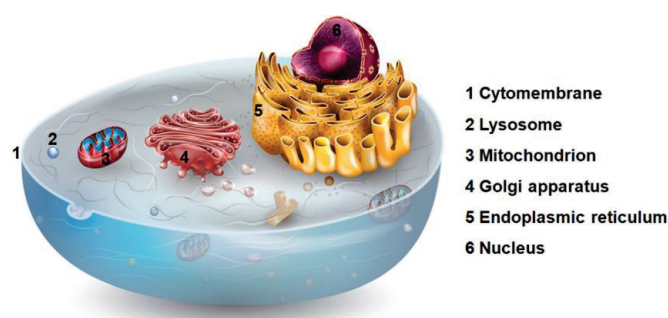
Figure 18. Representation of the most important organelles in the eukaryotic cell. (Reprinted with permission from ref. [76]. Copyright 2019 Elsevier).

3.1.1. Metal Complexes Targeting the Mitochondrion

Since discovering the critical role of mitochondria in apoptosis evasion mechanisms, these organelles have attracted much interest as potential targets in anticancer therapy [78]. Mitochondria are also called the "powerhouse of the cell" because of their role in cell energy production. However, mitochondria have many other essential roles, such as biosynthetic metabolism, regulation of cell signalling, ROS neutralization through antioxidant pathways activation, adaptive functions in response to oxidative stress, and cell death induction [79]. For these reasons, mitochondria happen to be strictly connected to many different tumorigenesis pathways [80]. Deregulation of mitochondria metabolism leads to insensitivity to anti-growth signals and consequent apoptosis evasion and uncontrolled proliferation [80]. Additionally, dysfunctions in the phenomena of mitochondrial biogenesis and mitophagy, aimed at maintaining a healthy mass turnover, seem to be involved in the activations of oncogenic pathways [80]. Therapeutic strategies that rely on mitochondrial targeting have several advantages. Among the most interesting is the opportunity to exploit the difference between the structural characteristics of the mitochondrion in healthy and diseased cells to have a drug accumulation in tumour cells. Compared to normal cells, mitochondria have different characteristics in cancer cells that can be exploited in targeting strategies to direct drugs, especially towards the tumour site. For example, the increased mitochondrial transmembrane potential ($\Delta\psi m$), which has been highlighted in many kinds of cancer, can be exploited to selectively accumulate delocalised lipophilic cations (DLCs) within mitochondria (Figure 19) [81,82]. This selectivity depends on the DLCs chemical-physical characteristics, especially the positive charge number and the lipophilicity (logP) tuning [83,84].
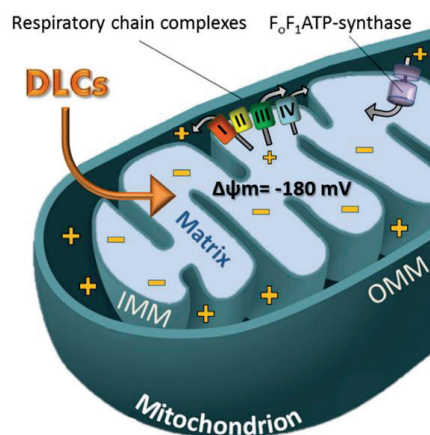
Figure 19. Uptake mechanism of DLCs in the mitochondrion. ($\Delta\psi m$: mitochondrial membrane potential; I, II, III, IV: complexes related to the mitochondrial respiratory chain; IMM: inner mitochondrial membrane; OMM: outer mitochondrial membrane). (Reprinted with permission from ref. [85]. Copyright 2018 Elsevier).

In addition, considering the central role of this organelle in tumorigenesis and in sustaining cancer cell proliferation, drugs that accumulate within the mitochondrion can inhibit its functions, cause its impairment, and activate proapoptotic signalling pathways leading to programmed cell death [86]. Beyond the issue of poor selectivity, mitochondrial targeting drugs may potentially overcome another recurring problem in classic anticancer therapy such as drug resistance. Cisplatin-induced resistance seems to depend on the action of the nucleotide excision repair (NER) machinery, which repairs alterations in DNA that prevent replication [87]. This repair pathway is only active in the nucleus while it is absent in the mitochondrion; for this reason, it is far more difficult that the damage induced by cisplatin on the mitochondrial DNA leads the onset of resistance [87]. Erxleben published an extensive review in 2019 in which 241 references regarding mitochondrion targeting metal complexes were reported [86].

In the present review, this section provides some of the most significant examples of mitochondria-targeting complexes divided by the type of metal centre.

(1). Platinum-based complexes targeting mitochondria

Although the primary target for platinum-based complexes is nuclear DNA, some studies have shown that cisplatin may have interesting direct interactions with mitochondrial DNA (mtDNA), therefore inducting apoptosis also through different mechanisms, in addition to the expected ones or also alternatively [87–89]. Intending to redirect cisplatin onto mitochondrial DNA, Wisnovsky et al. synthesised a cisplatin analogue (mtPt, **36**; Figure 20) conjugated to a peptide carrier that explicitly targets this organelle [88]. mtPt shows accumulation in the mitochondrion, cytotoxicity on HeLa cells, and damage to mtDNA without damaging nuclear DNA. Although cytotoxicity is lower than cisplatin, mtPt is also efficient in killing cisplatin-resistant ovarian A2780/CP70 cancer cells.

Dhar and collaborators used a different carrier to deliver cisplatin selectively into mitochondria [87]. They designed a cisplatin Pt(IV) prodrug that targets these organelles, Platin-M (**37**, Figure 20). Mitochondrial targeting is provided by the presence of two delocalised triphenylphosphonium cations on the Pt(IVI) complex in the axial position. Drug delivery, good pharmacokinetic, and distribution properties are achieved using biocompatible polymeric nanoparticles (NP) constituted by biodegradable poly(lactic-co-glycolic acid)-block-polyethyleneglycol, functionalised with a terminal triphenylphosphonium cation too, obtaining in this way a double targeting effect. Compared to cisplatin alone, Platin-M NPs resulted in a 30-times higher Pt concentration in mitochondria than in the nucleus. Prodrug Platin-M is locally activated by the highly reducing environment and converted into the active Pt(II) cisplatin, which was observed to form cross-links with mtDNA (Figure 21). Platin-M NPs showed 85 times higher potency than cisplatin in resistant A2780/CP70 cells, and enhanced cytotoxicity was also underlined in human neuroblastoma SH-SY5Y cells and androgen-independent Pca cells. Although the insertion of TPP moiety was successful in achieving mitochondrial targeting in the case of Platin-M, this strategy is not universally applicable; in fact, other platinum-based complexes that exhibit TPP functionalization accumulate in the nucleus [90].
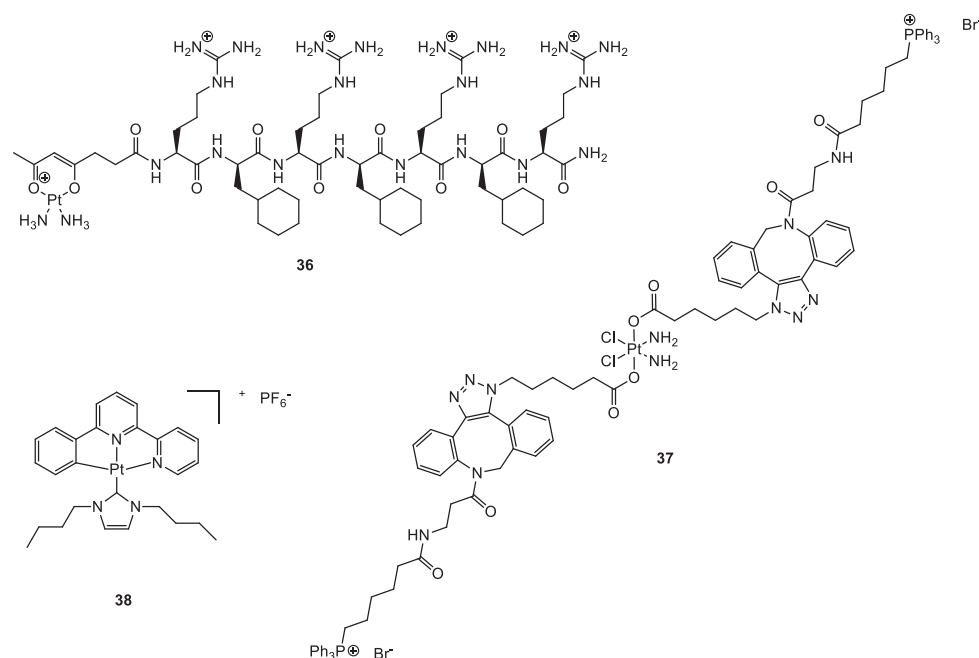
Figure 20. Structure of complexes **36**–**38**.
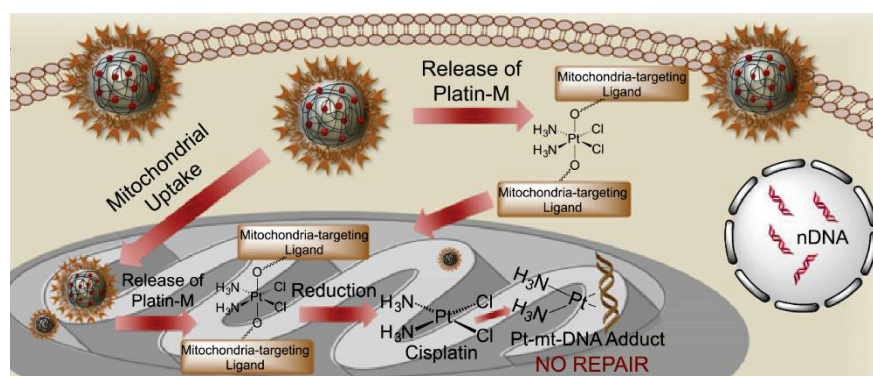
Figure 21. Mechanism of the release of Platin-M. (Reprinted from ref. [87] under the CC BY-NC-ND license, 2014).

Che and coworkers proposed a luminescent Pt(II) complex (**38**, Figure 20), that features an N-heterocyclic carbene as a ligand [91]. Given the optimal emission properties, the cellular localization of the synthesised complex was studied through fluorescence microscopy, incubating it with fluorescent dyes such as MitoTracker^TM, Hoechst 3342, and LysoTracker^TM in order to highlight the localization in mitochondria and cytoplasm, in the nucleus and lysosomes, respectively. Experiments showed that the complex is preferentially co-localised in mitochondria with MitoTracker^TM. Complex **38** was found to show promising cytotoxicity towards HeLa, HepG2, SUNE1, and CCD-19Lu cell lines (IC$_{50}$ = 0.057–0.77 µM), with a 300-fold higher potency toward HeLa than cisplatin.

(2). Gold-based complexes targeting mitochondria

The thioredoxin (Trx) system, composed of thioredoxin reductase (TrxR), thioredoxin, and NADPH, plays an essential role in regulating cellular redox balance [92]. TrxR is a ubiquitous homodimeric flavoenzyme responsible for reducing several species, including the protein thioredoxin. In mammals, two principal isoforms have been isolated, TrxR-1 (cytosolic) and TrxR-2 (mitochondrial). Cancer cell often shows TrxR overexpression, especially the isoform TrxR-2, which seems to be induced by increased levels of oxidative stress [85]. In several types of tumours, TrxR-2 has an important role in the desensitization

of cancer cells towards pro-apoptotic signals; in fact, it neutralises reactive oxygen species (ROS), which are considered important mediators of apoptosis [85,93]. As a result, TrxR has emerged as a potential target for anticancer therapies, and there has been a growing interest in metal complexes that can inhibit TrxR and induce apoptosis in cancer cells. Gold complexes have shown interesting cytotoxic activities on several tumour cell lines, and although the mechanism of action has not yet been fully elucidated, the main mechanism is explicated through the inhibition of mitochondrial thioredoxin reductase [94,95]. Regarding gold complexes, mitochondrial targeting has been achieved through two main methods. The first one, a second-order targeting, involves the conjugation of the gold complex to mitochondria-targeting carriers that allow the accumulation in the organelle. One example of carrier-conjugated gold complexes was synthesised by Köster and collaborators [96]. They exploited the mitochondrial targeting properties of di- and tetra-peptides, using them as carriers for the selective delivery of Au(I) phosphines [96]. The peptide-Au(I)phosphine conjugates (**39–40**, Figure 22) showed a cytotoxicity (2–50 μM) that seems to be correlated to their lipophilicity. This latter seems to be responsible for a higher initial uptake. Through this strategy, they could overcome the cisplatin resistance in MDA-MB231 breast cancer cells.

39a R₁=R₂=R₃=Ph
39b R₁=Ph, R₂=R₃=Et
39c R₁=R₂=R₃=Ph

40a R₁=R₂=R₃=Ph
40b R₁=Ph, R₂=R₃=Et
40c R₁=R₂=R₃=Ph
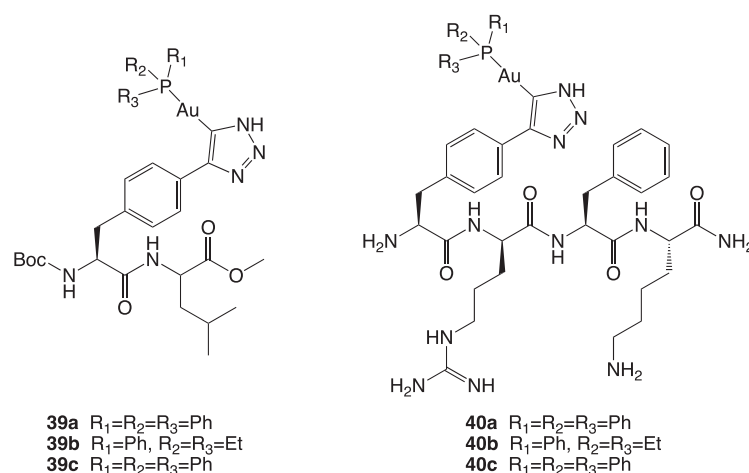
Figure 22. Structures of complexes **39a–c** and **40a–c**.

The second method involves a third-order targeting strategy: the use of complexes able to target mitochondrial proteins, the most studied of which is thioredoxin reductase in this context. Various metal-based complexes can inhibit thioredoxin reductase (e.g., complexes based on silver, copper, platinum, bismuth, palladium, antimony, iron, and ruthenium) [85]. However, gold-based complexes are still the most promising ones and seem to have the most significant potential for selective targeting strategies. Gold has a high affinity for selenium, present in the selenocysteine at the C-terminal end of the enzyme's active site [95]. This latter amino acid is relatively easy to target since, with a pKa of 5.4, it has a higher nucleophilicity than cysteine and is easily accessible on the enzyme structure [97]. Although there is an overexpression of TrxR in many tumour types, the preferential affinity of gold-based compounds for TrxR is not sufficient in most cases to ensure selective cytotoxicity on diseased cells without harming healthy cells. However, there are a few examples of gold-based compounds that showed selectivity in cancer cells. For the synthesis of gold-based complexes, N-heterocyclic carbenes ligands are particularly useful in the fine control of the complexes' lipophilicity, thanks to the structural modifications on the heterocyclic ring that can be made in a relatively easy way [98].

Hickey and collaborators designed three Au(I) N-heterocyclic carbene (Au-NHC) compounds (**41**, Figure 23) that combine TrxR inhibition and, due to their properties as DLCs, also the mitochondria targeting action [99].
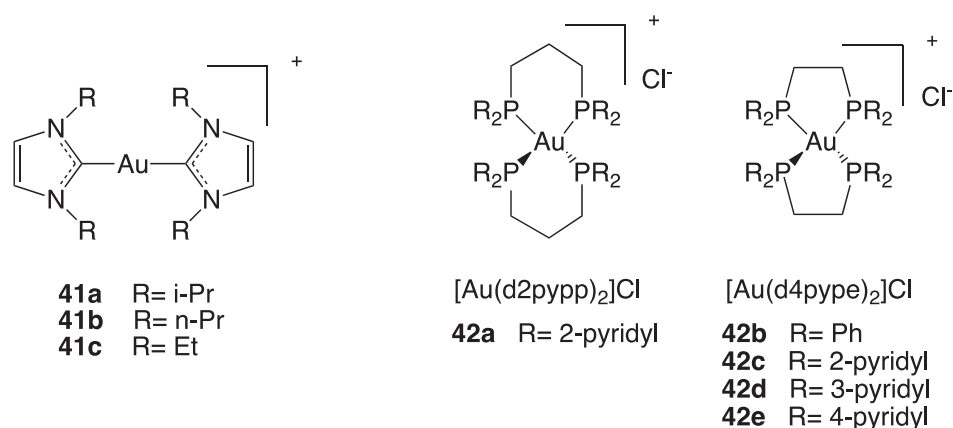
Figure 23. Structures of complexes **41a–c** and **42a–e**.

The effects of different concentrations of the three complexes were evaluated on cell growth of MDA-MB-231 and MDA-MB-468, two breast cancer cell lines, and also on HMEC, healthy human mammary epithelial cells. The three Au(I) NHC complexes have shown selective toxicity to both cancer cell lines but not to the normal cells, and the degree of selectivity is correlated with their lipophilicity. Among the three complexes, the **41a** complex, presenting an intermediate log P value, shows the best selectivity and cytotoxic potency (Figure 24).
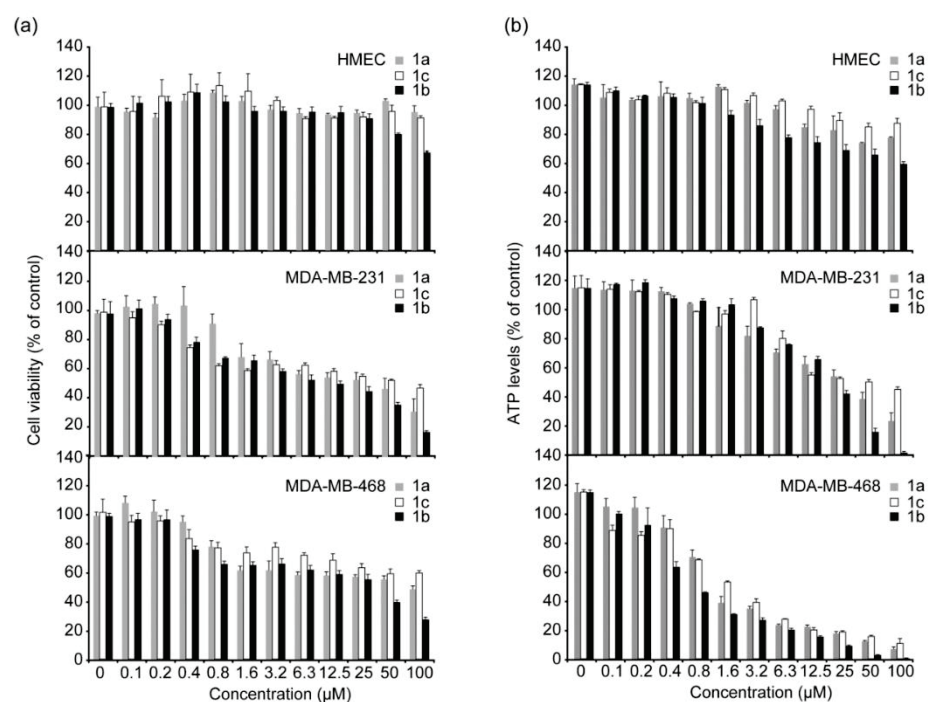
Figure 24. (Panel **a**) Cell growth measured 24 h after treatment with **6a**, **6b**, and **6c**. (Panel **b**) ATP levels of cells measured 24 h after treatment, using the ATPlite luminescence assay kit. (Reprinted with permission from ref. [99]. Copyright 2008 American Chemical Society).

In addition to carbenes, phosphines can also be used as ligands to obtain gold complexes having DLCs properties, able to target the mitochondrion. A study on the anti-cancer activity of eight bis-chelated Au(I) bidentate phosphine complexes was reported by Rackham and collaborators [100] that revealed selective anti-cancer properties of the complex [Au(d2-pypp)$_2$]Cl, presenting 1,3-bis(di-2-pyridylphosphino)propane as ligand (**42**, Figure 23). This gold complex selectively induces apoptosis in breast cancer cells MDA-

MB-468 but not in normal breast cells HMEC, at submicromolar concentrations (0.8 μM). Gold complex's accumulation in mitochondria is driven by the characteristic cancer cells' high potential difference; thus, apoptosis induction is accomplished through the mitochondrial pathway, involving mitochondrial membrane potential depolarization, depletion of the glutathione pool, and caspase-3 and caspase-9 activation.

In general, gold complexes are not able to discriminate between the two TrxR isoforms. However, there are some examples of selective inhibition of TrxR-2 [85]. The two isoforms have a high percentage of identity, and it is therefore rather difficult to achieve selectivity on either of them. However, as the two isoforms are distributed in different cell compartments, a promising way to achieve a selective inhibition of TrxR-2 is to use the mitochondrial targeting strategy so that the accumulated drug can preferentially interact with the mitochondrial isoform.

(3). Ruthenium-based complexes targeting mitochondria

Ruthenium-based complexes show promising cytotoxic activity against various cancer cell lines, including cisplatin-resistant ones, due to their ability to interact with DNA and RNA [101]. Although their primary target is generally nuclear genomic material, some examples of DLCs Ru(II) polypyridyl complexes accumulate in the mitochondrion, where they also exert their cytotoxic action [102]. A significant example is Rubb$_{16}$ (**43**, Figure 25), a dinuclear complex reported by Pisani et al., which shows an IC$_{50}$ of about 5 μM on L1210 murine leukaemia cancer cell line [103]. Even if the cytotoxicity is comparable to that of cisplatin, Rubb$_{16}$ presents 16 times higher accumulation in tumour cells than in healthy B cells. Rubb$_{16}$ is part of a series of lipophilic cations that present two metal centres connected by a flexible bridge, with the lipophilicity of the entire complex increasing as the number of methylenes in the linker rises. Using confocal microscopy and a mitochondrial tracking dye (MitoTracker Green FM), the cellular localization of the luminescent complex was highlighted in the mitochondrion, with no staining observed in the cytoplasm or other organelles. Interesting results emerged from the study on the two complexes **44a** and **44b** (Figure 25), which, despite having relatively similar molecular structures, have a considerable difference in cytotoxicity and cellular localization. Cytotoxicity was assessed in five cancer cell lines and one healthy cell line, human lung fibroblasts MRC-5. Complex **44a** had similar cytotoxicity to cisplatin but higher selectivity to diseased cells, while complex **44b** had a considerably higher IC$_{50}$. Confocal microscopy studies showed that complex **44a** is localised in the cytoplasm with a weak fluorescence in the nucleus, unlike complex **44b**, which diffuses through the whole cell, including the nucleus. Then, using high-resolution continuum source atomic absorption spectrometry (HR-CS AAS), a mitochondrial uptake of 68% of the total was measured in HeLa cells for **44a**. For these reasons, although complex **44a** interacts with isolated DNA, a mechanism of action via the mitochondrial pathway has been proposed, characterised by a perturbation of the mitochondrial membrane potential caused by the intercalation of the hydrophobic dppz moieties.
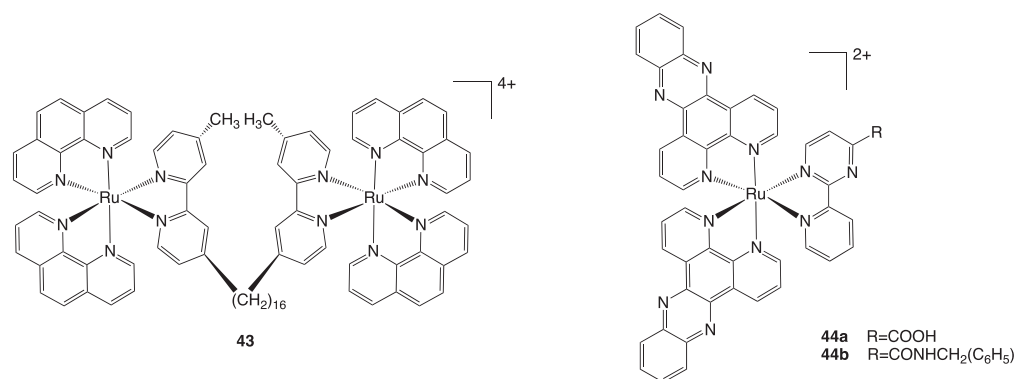
Figure 25. Structures of complexes **43** and **44a–b**.

Interestingly, the conjugation of **44a** to mitochondria-targeting or receptor-targeting peptides, performed by the same group, led to the lack of accumulation in mitochondria and, consequently, cytotoxic potency being compromised [104].

3.1.2. Metal-Based Complexes Targeting the Nucleus

The nucleus is not only the organelle that contains most of the genetic material, but it is also referred to as the "brain" of the cell, being responsible for vital cellular functions such as replication, gene expression, and cell differentiation [105]. As nuclear DNA is one of the main targets of metal-based anticancer drugs, nuclear drug delivery is crucial for optimal therapeutic efficiency. The drugs transport from the cytoplasm to the nucleus through the nuclear envelope lipidic bilayer does not take place by passive diffusion but via the nuclear pore complex (NPC), a cylindrical structure of nucleoporins that forms a hydrophilic channel through which the bidirectional transport of macromolecules between the nucleus and cytoplasm takes place [106]. Regarding NPCs, diffusion pores with an estimated diameter of 90–100 Å allow free transit of macromolecules up to 40 kDa, whereas large macromolecules with a diameter of up to 390 Å require an active transport mediated by specific receptors [107]. Nucleus-targeting metal complexes can be obtained either intrinsically or extrinsically. Intrinsic nuclear targeting complexes usually have positive charges, allowing electrostatic interaction with the phosphate groups in DNA and a planar aromatic system allowing intercalation in the double helix [76]. Conversely, extrinsic nucleus-targeting activity can be achieved by conjugating the metal complex to a nuclear localization signal (NLS), a short peptide that selectively binds the nuclear transport receptors (NTRs), that facilitate the passage across the NPCs central channel [76].

An interesting example of intrinsic targeting is [Ru(bpy)(phpy)(dppz)]$^+$ (**45**, Figure 26) [108], a Ru(II) complex that showed rapid uptake in Hela cells, with nearly 90% of the complex accumulating in the nuclei. It showed a similar distribution also in MDA-MB-231, A549, and A549/CDDP cancer cell lines, with an IC$_{50}$ value that was an order of magnitude lower than cisplatin. Further research indicated that the strong DNA binding affinity of [Ru(bpy)(phpy)(dppz)]$^+$ effectively inhibited the binding of NF-B transcription factor to DNA sequences, causing cancer cell apoptosis (Figure 27).
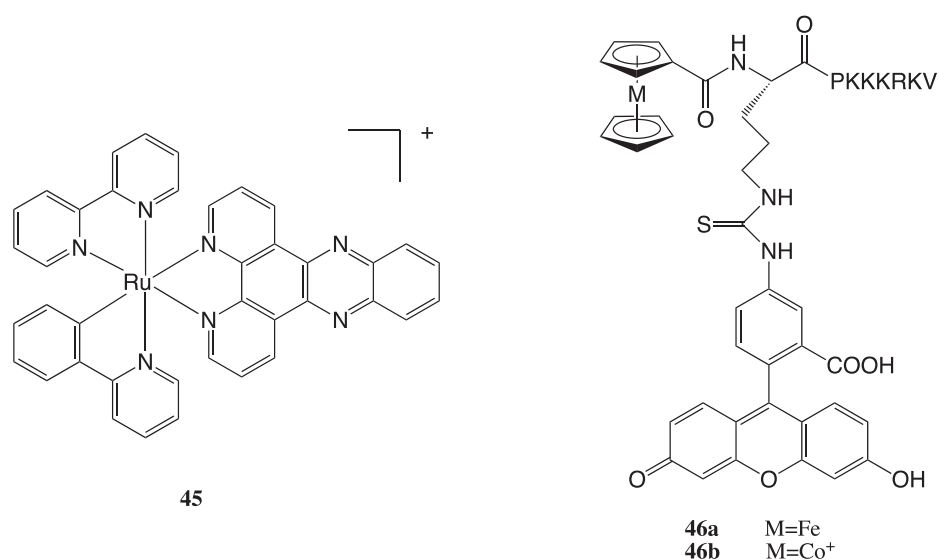
Figure 26. Structures of complexes **45** and **46a**–**b**.
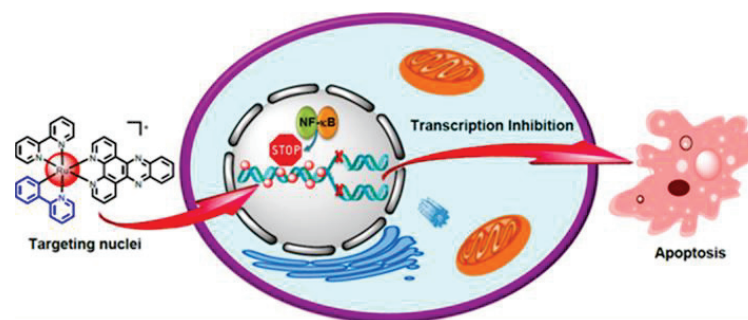
Figure 27. Representation of [Ru(bpy)(phpy)(dppz)]$^+$ nucleus-targeting activity. (Reprinted with permission from ref. [108]. Copyright 2014 American Chemical Society).

Concerning extrinsic targeting, Noor et al. synthesised a bioconjugate where an organometallic complex, a cobaltocenium cation, was linked to an NLS peptide, SV-40 T (with primary sequence H-Pro-Lys-Lys-Lys-Arg-Lys-Val-OH) [109]. The conjugate shows enhanced cellular uptake and a significant accumulation in the nucleus of HepG2 cells. The same group studied the uptake and cellular localization of some neutral ferrocene (Fe^{2+}) and positively charged Cobaltocenium (Co^{3+}) bioconjugates (**46**, Figure 26) [110], where the metal-based core was conjugated with the NLS wild-type sequence PKKKRKV. Although they did not find the complexes cytotoxic on the Hep G2 cell line, for both metal centres the fluorescence microscopy study showed significant cellular uptake and nuclear localization of the conjugates. Interestingly, the results obtained are similar for the two metal centres, thus highlighting that the positive charge may not appear decisive in nuclear targeting.

3.1.3. Metal-Based Complexes Targeting Endoplasmic Reticulum

It has been demonstrated that the endoplasmic reticulum (ER) is not just passively responsible for the transport of proteins in the intracellular or extracellular space, but it also plays a key role in regulating cellular homeostasis; in fact, the insurgence of ER stress seems to be closely related to the onset of pathological states, such as neurodegenerative disorders, diabetes, cardiac diseases, and cancer [111]. Features usually present in the tumour environment, such as low pH, lack of oxygen, strongly reducing environment, and lack of nutrients, can lead to perturbations of protein homeostasis, inducing ER stress and consequently activating signalling transduction pathways such as the unfolded protein response (UPR) [112]. This latter is an adaptive mechanism contributing to cancer growth, aggressiveness, and resistance to the treatment. For this reason, ER has attracted much interest as a promising target to address potential anticancer drugs according to a selective anticancer strategy. Notwithstanding the UPR being a key element in cancer growth and chemotherapy resistance, the promotion of ER stress induction has lately received attention as a promising anticancer technique. In particular, certain metal complexes are able to induce ER stress, which often leads to desirable immunogenic cell death. Additionally, an interesting aspect is that ER-targeting cytotoxic compounds often accomplish selectivity on cancer cells [77]. Drugs can induce ER stress through different mechanisms, such as direct contact with UPR machinery, generation of ROS, disruption of protein folding chaperones, inhibition of protein degradation, and interference with Ca^{2+} trafficking [77]. Metal complexes capable of generating ER stress in cancer cells through various mechanisms include complexes based on copper [113,114], vanadium [115], iridium [116,117], ruthenium [118,119], gold [120,121], platinum [122], palladium [123], osmium [124,125], and rhenium [126].

However, it is essential to emphasise that several mechanisms are frequently activated at the same time, and furthermore, activation of ER stress is often not the primary mechanism of action of a metal complex but rather a collateral mechanism. A promising investigated class of compounds with ER stress-inducing activities is cyclometalated cationic Ru(II) complexes. In this context, Fetzer et al. reported an interesting study on a library of 32 organoruthenium C-N, N-C-N, N-N-C cyclometalated compounds that have

been synthesised and tested for their in vitro antitumoral activity on HCT-116 colon cancer cell lines [118]. The library of compounds originates from the original lead compound RDC11 (**47**), whose structure is reported in Figure 28. Good to excellent cytotoxic properties have been found for the complexes, many of which have demonstrated an IC_{50} below the nanomolar threshold. The compounds' activity was correlated to their physicochemical properties, such as the $Ru^{III/II}$ redox potential and lipophilicity, as shown in Figure 29. Further investigation of the biological properties and cellular responses reveals that some compounds cause both DNA damage and ER stress, while others only target the ER [119].
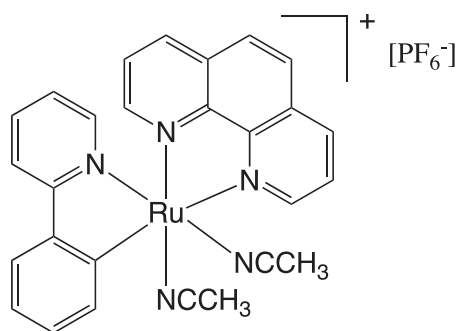
Figure 28. Structure of compound **47**.
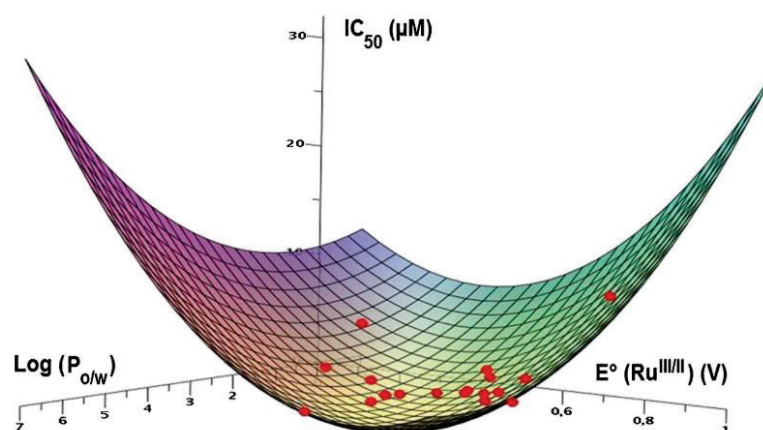
Figure 29. Three-dimensional representation of the correlation between IC_{50}, the redox potential ($E°_{RuIII/II}$) and the lipophilicity ($logP_{o/w}$). (Reprinted with permission from ref. [118]. Copyright 2011 Royal Society of Chemistry).

3.2. Cell-Targeting Metal-Based Complexes

In the human organism, cells deputed to different functions or belonging to different tissues present a heterogeneity expressed by specific biomarkers existing on the cell surface, often consisting of proteins and receptors. The same also applies to diseased cells, such as cancer cells, that usually show a cancer-specific overexpression of particular receptors [127]. In order to specifically target only cancer cells exploiting these cancer-specific biomarkers, cytotoxic compounds can be conjugated to selected ligands capable of being recognised and bound by receptors overexpressed on the cancer cell surface and then internalised via endocytosis, then released into the cytoplasm [128]. Peptides, antibodies, aptamers, or natural ligands of cell receptors can represent valuable site-selective tools to distinguish between cancer and healthy cells based on cellular surface different compositions. The most widely used and studied ligands for metal complexes delivery are the cell-penetrating homing peptides (CPHPs) [129,130]. It is necessary to specify that there are various types of peptides capable of delivering the drug to the cell, and the mode and ability to reach the

cell's interior vary greatly. Homing peptides (HP) can recognise the corresponding receptor and bind it but are not internalised within the cell, remaining on the membrane surface in the extracellular environment [129,130]. In contrast, cell-penetrating homing peptides (CPHPs) can bind the receptor and have the intrinsic ability to activate the internalization process through endocytosis. Another technique used is binding an HP, responsible for the recognition, to a cell-penetrating peptide (CPP), responsible for activating the internalization process (Figure 30) [128].
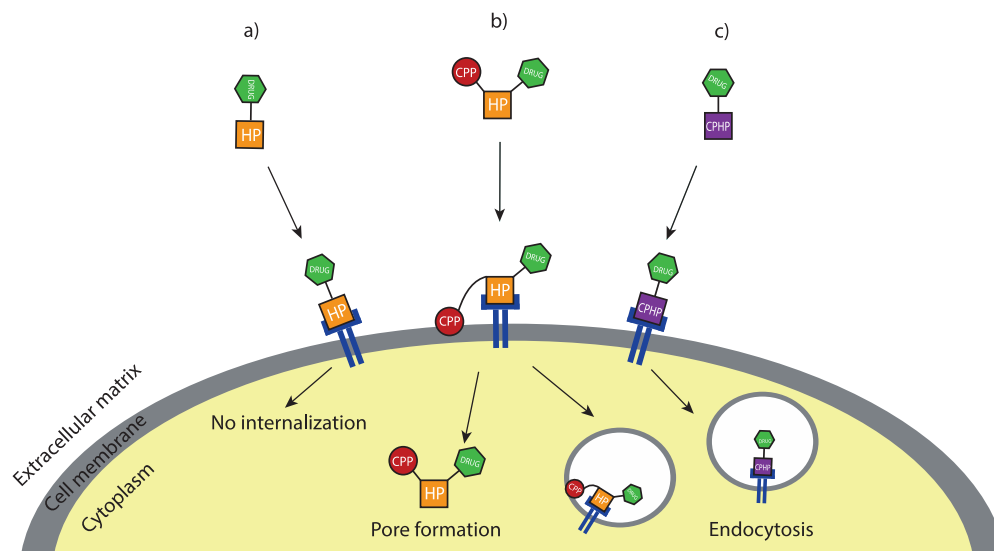
Figure 30. A representation of the three mechanisms of action of HP (**a**), CPP linked to an HP (**b**), CPHP (**c**).

Lippard and his team reported in 2007 the synthesis of a series of mono- and difunctionalised platinum(IV) complexes (**48–49**, Figure 31) conjugated to an RGD or NGR peptides [131]. These latter target $\alpha_V\beta_3/\alpha_V\beta_5$ integrins and membrane-spanning surface protein aminopeptidase N (APN), respectively, both of which are over-expressed in endothelial cells of angiogenic tumour vasculature. The HP has been conjugated by an amide linkage to the Pt(IV) centre through a succinate group. From concentration-response studies emerged that, when compared to nontargeting Pt(IV) compounds and the unconjugated targeting RGD peptide, RGD-conjugated Pt(IV) complexes are potent inhibitors of cellular growth. Although less inhibitive than their RGD counterparts, NGR conjugates were nonetheless more active than nonspecific Pt(IV)-peptide analogues.

48a X= RGD	**49a** X= RGD
48b X= NGR	**49b** X= NGR
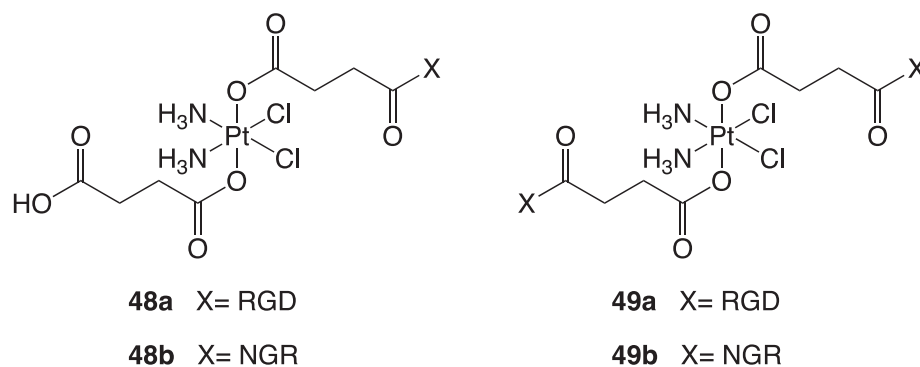
Figure 31. Structures of compounds **48a–b** and **49a–b**.

As mentioned above, in addition to peptides, other kinds of site-selective cancer-targeting molecules can also be conjugated to metal complexes to obtain a targeting activity on specific cancer cell lines. An interesting example is that of aptamers, which are short

single-stranded chains of oligonucleotides that can specifically bind their targets with high affinity, as well as being biocompatible and stable [132].

Niu et al. reported the synthesis of a bioconjugate (**50**, Figure 32) in which an NHC gold(I) complex has been linked to the sgc8c aptamer, which can selectively recognise CCRF-CEM leukaemia cells binding the protein tyrosine kinase 7(PTK-7), more abundantly expressed in cancer cells surface than in healthy ones [133].

50
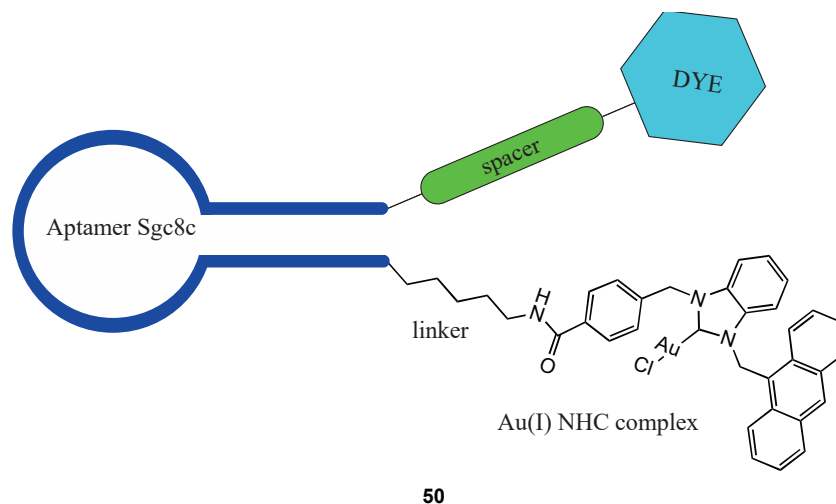
Figure 32. Structure of the bioconjugate **50**.

The bioconjugate is enriched with a double tag, making it possible to independently follow the fate of the two functional elements inside the cancer cell. An anthracenyl moiety was inserted to follow the gold complex, while the aptamer was functionalised with fluorescein isothiocyanate (FITC). Remarkably, the IC_{50} of the aptamer-functionalised complex shows higher cytotoxicity than the non-targeting complex, going from a value of 14.6 ± 1.4 μM to 0.54 ± 0.85 μM.

4. Conclusions

Inspired by the promising anticancer properties of some well-known metal-based complexes, such as auranofin, cisplatin, and NAMI, new strategies have been developed to improve the characteristics of the existing complexes and overcome the problems that they carry. Higher selectivity, lower side effects, higher potency, and the overcoming of the resistance mechanism are some of the objectives of this new generation of anticancer strategies. In this review, we focused on some interesting examples related to two main approaches: the conjugation of metal-based complexes to a targeting moiety and the synthesis of heterobimetallic complexes bearing two active molecules in just one compound. We believe this review can be a valuable tool to be used as a starting point for those researching this area, to identify the recent advances that have been made in research and to exploit the competencies to progress towards new ideas and strategies.

References

1. Bailar, J.C.; Gornik, H.L. Cancer Undefeated. *N. Engl. J. Med.* **1997**, *336*, 1569–1574. [CrossRef] [PubMed]
2. Cirri, D.; Bartoli, F.; Pratesi, A.; Baglini, E.; Barresi, E.; Marzo, T. Strategies for the Improvement of Metal-Based Chemotherapeutic Treatments. *Biomedicines* **2021**, *9*, 504. [CrossRef] [PubMed]
3. Jia, P.; Ouyang, R.; Cao, P.; Tong, X.; Zhou, X.; Lei, T.; Zhao, Y.; Guo, N.; Chang, H.; Miao, Y.; et al. Review: Recent Advances and Future Development of Metal Complexes as Anticancer Agents. *J. Coord. Chem.* **2017**, *70*, 2175–2201. [CrossRef]
4. Chern, Y.J.; Tai, I.T. Adaptive Response of Resistant Cancer Cells to Chemotherapy. *Cancer Biol. Med.* **2020**, *17*, 842–863. [CrossRef] [PubMed]
5. Galluzzi, L.; Vitale, I.; Michels, J.; Brenner, C.; Szabadkai, G.; Harel-Bellan, A.; Castedo, M.; Kroemer, G. Systems Biology of Cisplatin Resistance: Past, Present and Future. *Cell Death Dis.* **2014**, *5*, e1257. [CrossRef]
6. Mei, Y. Review of the Toxicological Mechanism of Anticancer Drug Cisplatin. *AIP Conf. Proc.* **2021**, *2350*, 020010. [CrossRef]
7. Roder, C.; Thomson, M.J. Auranofin: Repurposing an Old Drug for a Golden New Age. *Drugs RD* **2015**, *15*, 13–20. [CrossRef]
8. Abdalbari, F.H.; Telleria, C.M. The Gold Complex Auranofin: New Perspectives for Cancer Therapy. *Discov. Oncol.* **2021**, *12*, 42. [CrossRef]
9. Meier-Menches, S.M.; Gerner, C.; Berger, W.; Hartinger, C.G.; Keppler, B.K. Structure-Activity Relationships for Ruthenium and Osmium Anticancer Agents-towards Clinical Development. *Chem. Soc. Rev.* **2018**, *47*, 909–928. [CrossRef]
10. Strebhardt, K.; Ullrich, A. Paul Ehrlich's Magic Bullet Concept: 100 Years of Progress. *Nat. Rev. Cancer* **2008**, *8*, 473–480. [CrossRef]
11. van Niekerk, A.; Chellan, P.; Mapolie, S.F. Heterometallic Multinuclear Complexes as Anti-Cancer Agents-An Overview of Recent Developments. *Eur. J. Inorg. Chem.* **2019**, *2019*, 3432–3455. [CrossRef]
12. Redrado, M.; Fernández-Moreira, V.; Gimeno, M.C. Theranostics Through the Synergistic Cooperation of Heterometallic Complexes. *ChemMedChem* **2021**, *16*, 932–941. [CrossRef] [PubMed]
13. Shahsavari, H.R.; Giménez, N.; Lalinde, E.; Moreno, M.T.; Fereidoonnezhad, M.; Babadi Aghakhanpour, R.; Khatami, M.; Kalantari, F.; Jamshidi, Z.; Mohammadpour, M. Heterobimetallic PtII-AuI Complexes Comprising Unsymmetrical 1,1-Bis(Diphenylphosphanyl)Methane Bridges: Synthesis, Photophysical, and Cytotoxic Studies. *Eur. J. Inorg. Chem.* **2019**, *2019*, 1360–1373. [CrossRef]
14. Weidmann, A.G.; Komor, A.C.; Barton, J.K. Targeted Chemotherapy with Metal Complexes. *Comments Inorg. Chem.* **2014**, *34*, 114–123. [CrossRef]
15. Cooper, B.G.; Napoline, J.W.; Thomas, C.M. Catalytic Applications of Early/Late Heterobimetallic Complexes. *Catal. Rev. Sci. Eng.* **2012**, *54*, 1–40. [CrossRef]
16. Longato, B.; Bandoli, G.; Trovo, G.; Marasciulo, E.; Valle, G. Mono- and Polynuclear Guanine Complexes of Platinum(II). Syntheses and Crystal and Molecular Structures of Bis(9-Methylguanine-N(7))Bis(Trimethylphosphine)Platinum(II) Dinitrate and Cyclo-Hexakis(9-Methylguanine(-H)-N(1),N(7))Hexakis(Cis-Bis(Trimethylphosphine)Platinum(II)) Hexanitrate. *Inorg. Chem.* **1995**, *34*, 1745–1750. [CrossRef]
17. Berners-Price, S.J.; Filipovska, A. Gold Compounds as Therapeutic Agents for Human Diseases. *Metallomics* **2011**, *3*, 863–873. [CrossRef]
18. Bertrand, B.; Casini, A. A Golden Future in Medicinal Inorganic Chemistry: The Promise of Anticancer Gold Organometallic Compounds. *Dalton Trans.* **2014**, *43*, 4209–4219. [CrossRef]
19. O'Dwyer, P.J.; Stevenson, J.P.; Johnson, S.W. Clinical Status of Cisplatin, Carboplatin, and Other Platinum-Based Antitumor Drugs. *Cisplatin Chem. Biochem. Lead. Anticancer Drug* **2006**, 29–69. [CrossRef]
20. Rozencweig, M.; von Hoff, D.D.; Slavik, M.; Muggia, F.M. Cis-Diamminedichloroplatinum (II). A New Anticancer Drug. *Ann. Intern. Med.* **1977**, *86*, 803–812. [CrossRef]
21. dos Santos, N.A.G.; Ferreira, R.S.; Santos, A.C. dos Overview of Cisplatin-Induced Neurotoxicity and Ototoxicity, and the Protective Agents. *Food Chem. Toxicol.* **2020**, *136*, 111079. [CrossRef]
22. Crona, D.J.; Faso, A.; Nishijima, T.F.; McGraw, K.A.; Galsky, M.D.; Milowsky, M.I. A Systematic Review of Strategies to Prevent Cisplatin-Induced Nephrotoxicity. *The Oncologist* **2017**, *22*, 609–619. [CrossRef]
23. Manohar, S.; Leung, N. Cisplatin Nephrotoxicity: A Review of the Literature. *J. Nephrol.* **2018**, *31*, 15–25. [CrossRef]
24. Bertrand, B.; Botuha, C.; Forté, J.; Dossmann, H.; Salmain, M. A Bis-Chelating ONOˆ/NNˆ Ligand for the Synthesis of Heterobimetallic Platinum(II)/Rhenium(I) Complexes: Tools for the Optimization of a New Class of Platinum(II) Anticancer Agents. *Chem. Eur. J.* **2020**, *26*, 12846–12861. [CrossRef] [PubMed]
25. Askari, B.; Rudbari, H.A.; Micale, N.; Schirmeister, T.; Maugeri, A.; Navarra, M. Anticancer Study of Heterobimetallic Platinum(II)-Ruthenium(II) and Platinum(II)-Rhodium(III) Complexes with Bridging Dithiooxamide Ligand. *J. Organomet. Chem.* **2019**, *900*, 120918. [CrossRef]
26. Tsolis, T.; Nikolaou, N.; Ypsilantis, K.; Kougioumtzi, A.; Kordias, D.; Magklara, A.; Garoufis, A. Synthesis, Characterization, Interactions with 9-MeG and Cytotoxic Activity of Heterobimetallic RuII-PtII Complexes Bridged with 2,2′-Bipyrimidine. *J. Inorg. Biochem.* **2021**, *219*, 111435. [CrossRef]
27. Quental, L.; Raposinho, P.; Mendes, F.; Santos, I.; Navarro-Ranninger, C.; Alvarez-Valdes, A.; Huang, H.; Chao, H.; Rubbiani, R.; Gasser, G.; et al. Combining Imaging and Anticancer Properties with New Heterobimetallic Pt(II)/M(i) (M = Re, 99mTc) Complexes. *Dalton Trans.* **2017**, *46*, 14523–14536. [CrossRef]

28. Massai, L.; Pratesi, A.; Gailer, J.; Marzo, T.; Messori, L. The Cisplatin/Serum Albumin System: A Reappraisal. *Inorganica Chim. Acta* **2019**, *495*, 118983. [CrossRef]

29. Dougan, S.J.; Sadler, P.J. The Design of Organometallic Ruthenium Arene Anticancer Agents. *Chimia* **2007**, *61*, 704–715. [CrossRef]

30. Smith, C.A.; Sutherland-Smith, A.J.; Keppler, B.K.; Kratz, F.; Baker, E.N. Binding of Ruthenium(III) Anti-Tumor Drugs to Human Lactoferrin Probed by High Resolution X-Ray Crystallographic Structure Analyses. *J. Biol. Inorg. Chem.* **1996**, *1*, 424–431. [CrossRef]

31. Zheng, Y.; Zhang, D.-Y.; Zhang, H.; Cao, J.-J.; Tan, C.-P.; Ji, L.-N.; Mao, Z.-W. Photodamaging of Mitochondrial DNA to Overcome Cisplatin Resistance by a RuII–PtII Bimetallic Complex. *Chem.–Eur. J.* **2018**, *24*, 18971–18980. [CrossRef] [PubMed]

32. Zhou, Z.; Liu, J.; Rees, T.W.; Wang, H.; Li, X.; Chao, H.; Stang, P.J. Heterometallic Ru–Pt Metallacycle for Two-Photon Photodynamic Therapy. *Proc. Natl. Acad. Sci. USA* **2018**, *115*, 5664–5669. [CrossRef] [PubMed]

33. Hall, M.D.; Mellor, H.R.; Callaghan, R.; Hambley, T.W. Basis for Design and Development of Platinum(IV) Anticancer Complexes. *J. Med. Chem.* **2007**, *50*, 3403–3411. [CrossRef] [PubMed]

34. Yempala, T.; Babu, T.; Karmakar, S.; Nemirovski, A.; Ishan, M.; Gandin, V.; Gibson, D. Expanding the Arsenal of PtIV Anticancer Agents: Multi-Action PtIV Anticancer Agents with Bioactive Ligands Possessing a Hydroxy Functional Group. *Angew. Chem. Int. Ed.* **2019**, *58*, 18218–18223. [CrossRef] [PubMed]

35. Babu, T.; Sarkar, A.; Karmakar, S.; Schmidt, C.; Gibson, D. Multiaction Pt(IV) Carbamate Complexes Can Codeliver Pt(II) Drugs and Amine Containing Bioactive Molecules. *Inorg. Chem.* **2020**, *59*, 5182–5193. [CrossRef] [PubMed]

36. Harringer, S.; Hejl, M.; Enyedy, É.A.; Jakupec, M.A.; Galanski, M.S.; Keppler, B.K.; Dyson, P.J.; Varbanov, H.P. Multifunctional Pt(Iv) Prodrug Candidates Featuring the Carboplatin Core and Deferoxamine. *Dalton Trans.* **2021**, *50*, 8167–8178. [CrossRef]

37. Da Veiga Moreira, J.; Hamraz, M.; Abolhassani, M.; Bigan, E.; Pérès, S.; Paulevé, L.; Nogueira, M.L.; Steyaert, J.M.; Schwartz, L. The Redox Status of Cancer Cells Supports Me—Chanisms behind the Warburg Effect. *Metabolites* **2016**, *6*, 33. [CrossRef]

38. Johnstone, T.C.; Suntharalingam, K.; Lippard, S.J. The Next Generation of Platinum Drugs: Targeted Pt(II) Agents, Nanoparticle Delivery, and Pt(IV) Prodrugs. *Chem. Rev.* **2016**, *116*, 3436–3486. [CrossRef]

39. Ma, L.; Lin, X.; Li, C.; Xu, Z.; Chan, C.-Y.; Tse, M.-K.; Shi, P.; Zhu, G. A Cancer Cell-Selective and Low-Toxic Bifunctional Heterodinuclear Pt(IV)–Ru(II) Anticancer Prodrug. *Inorg. Chem.* **2018**, *57*, 2917–2924. [CrossRef]

40. Ma, L.; Ma, R.; Wang, Z.; Yiu, S.M.; Zhu, G. Heterodinuclear Pt(IV)-Ru(II) Anticancer Prodrugs to Combat Both Drug Resistance and Tumor Metastasis. *Chem. Commun.* **2016**, *52*, 10735–10738. [CrossRef]

41. Cirri, D.; Fabbrini, M.G.; Pratesi, A.; Ciofi, L.; Massai, L.; Marzo, T.; Messori, L. The Leading Established Metal-Based Drugs: A Revisitation of Their Relevant Physico-Chemical Data. *BioMetals* **2019**, *32*, 813–817. [CrossRef] [PubMed]

42. Marzo, T.; Cirri, D.; Gabbiani, C.; Gamberi, T.; Magherini, F.; Pratesi, A.; Guerri, A.; Biver, T.; Binacchi, F.; Stefanini, M.; et al. Auranofin, Et3PAuCl, and Et3PAuI Are Highly Cytotoxic on Colorectal Cancer Cells: A Chemical and Biological Study. *ACS Med. Chem. Lett.* **2017**, *8*, 997–1001. [CrossRef] [PubMed]

43. Binacchi, F.; Guarra, F.; Cirri, D.; Marzo, T.; Pratesi, A.; Messori, L.; Gabbiani, C.; Biver, T. On the Different Mode of Action of Au(I)/Ag(I)-NHC Bis-Anthracenyl Complexes Towards Selected Target Biomolecules. *Molecules* **2020**, *25*, 5446. [CrossRef] [PubMed]

44. Cirri, D.; Massai, L.; Giacomelli, C.; Trincavelli, M.L.; Guerri, A.; Gabbiani, C.; Messori, L.; Pratesi, A. Synthesis, Chemical Characterization, and Biological Evaluation of a Novel Auranofin Derivative as an Anticancer Agent. *Dalton Trans.* **2022**, *51*, 13527–13539. [CrossRef]

45. Menconi, A.; Marzo, T.; Massai, L.; Pratesi, A.; Severi, M.; Petroni, G.; Antonuzzo, L.; Messori, L.; Pillozzi, S.; Cirri, D. Anticancer Effects against Colorectal Cancer Models of Chloro(Triethylphosphine)Gold(I) Encapsulated in PLGA-PEG Nanoparticles. *Biometals Int. J. Role Met. Ions Biol. Biochem. Med.* **2021**, *34*, 867–879. [CrossRef]

46. Gamberi, T.; Pratesi, A.; Messori, L.; Massai, L. Proteomics as a Tool to Disclose the Cellular and Molecular Mechanisms of Selected Anticancer Gold Compounds. *Coord. Chem. Rev.* **2021**, *438*, 213905. [CrossRef]

47. Magherini, F.; Fiaschi, T.; Valocchia, E.; Becatti, M.; Pratesi, A.; Marzo, T.; Massai, L.; Gabbiani, C.; Landini, I.; Nobili, S.; et al. Antiproliferative Effects of Two Gold(I)-N-Heterocyclic Carbene Complexes in A2780 Human Ovarian Cancer Cells: A Comparative Proteomic Study. *Oncotarget* **2018**, *9*, 28042–28068. [CrossRef]

48. Serratrice, M.; Maiore, L.; Zucca, A.; Stoccoro, S.; Landini, I.; Mini, E.; Massai, L.; Ferraro, G.; Merlino, A.; Messori, L.; et al. Cytotoxic Properties of a New Organometallic Platinum(II) Complex and Its Gold(i) Heterobimetallic Derivatives. *Dalton Trans.* **2016**, *45*, 579–590. [CrossRef]

49. Wenzel, M.; Bigaeva, E.; Richard, P.; Le Gendre, P.; Picquet, M.; Casini, A.; Bodio, E. New Heteronuclear Gold(I)–Platinum(II) Complexes with Cytotoxic Properties: Are Two Metals Better than One? *J. Inorg. Biochem.* **2014**, *141*, 10–16. [CrossRef]

50. Boncler, M.; Rózalski, M.; Krajewska, U.; Podswdek, A.; Watala, C. Comparison of PrestoBlue and MTT Assays of Cellular Viability in the Assessment of Anti-Proliferative Effects of Plant Extracts on Human Endothelial Cells. *J. Pharmacol. Toxicol. Methods* **2014**, *69*, 9–16. [CrossRef]

51. Fernández-Gallardo, J.; Elie, B.T.; Sanaú, M.; Contel, M. Versatile Synthesis of Cationic N-Heterocyclic Carbene-Gold(I) Complexes Containing a Second Ancillary Ligand. Design of Heterobimetallic Ruthenium-Gold Anticancer Agents. *Chem. Commun.* **2016**, *52*, 3155–3158. [CrossRef]

52. Elie, B.T.; Pechenyy, Y.; Uddin, F.; Contel, M. A Heterometallic Ruthenium–Gold Complex Displays Antiproliferative, Antimigratory, and Antiangiogenic Properties and Inhibits Metastasis and Angiogenesis-Associated Proteases in Renal Cancer. *J. Biol. Inorg. Chem.* **2018**, *23*, 399–411. [CrossRef] [PubMed]

53. Mui, Y.F.; Fernández-Gallardo, J.; Elie, B.T.; Gubran, A.; Maluenda, I.; Sanaú, M.; Navarro, O.; Contel, M. Titanocene-Gold Complexes Containing N-Heterocyclic Carbene Ligands Inhibit Growth of Prostate, Renal, and Colon Cancers in Vitro. *Organometallics* **2016**, *35*, 1218–1227. [CrossRef] [PubMed]

54. Fernández-Gallardo, J.; Elie, B.T.; Sadhukha, T.; Prabha, S.; Sanaú, M.; Rotenberg, S.A.; Ramos, J.W.; Contel, M. Heterometallic Titanium-Gold Complexes Inhibit Renal Cancer Cells in Vitro and in Vivo. *Chem. Sci.* **2015**, *6*, 5269–5283. [CrossRef] [PubMed]

55. Elie, B.T.; Fernández-Gallardo, J.; Curado, N.; Cornejo, M.A.; Ramos, J.W.; Contel, M. Bimetallic Titanocene-Gold Phosphane Complexes Inhibit Invasion, Metastasis, and Angiogenesis-Associated Signaling Molecules in Renal Cancer. *Eur. J. Med. Chem.* **2019**, *161*, 310–322. [CrossRef]

56. Li, T.Y.; Wu, J.; Wu, Z.G.; Zheng, Y.X.; Zuo, J.L.; Pan, Y. Rational Design of Phosphorescent Iridium(III) Complexes for Emission Color Tunability and Their Applications in OLEDs. *Coord. Chem. Rev.* **2018**, *374*, 55–92. [CrossRef]

57. Wilde, A.P.; King, K.A.; Watts, R.J. Resolution and Analysis of the Components in Dual Emission of Mixed-Chelate/Ortho-Metalate Complexes of Iridium(III). *J. Phys. Chem.* **1991**, *95*, 629–634. [CrossRef]

58. Hao, L.; Li, Z.W.; Zhang, D.Y.; He, L.; Liu, W.; Yang, J.; Tan, C.P.; Ji, L.N.; Mao, Z.W. Monitoring Mitochondrial Viscosity with Anticancer Phosphorescent Ir(Iii) Complexes: Via Two-Photon Lifetime Imaging. *Chem. Sci.* **2019**, *10*, 1285–1293. [CrossRef]

59. Liu, Z.; Li, J.J.; Ge, X.X.; Zhang, S.; Xu, Z.; Gao, W. Design, Synthesis, and Evaluation of Phosphorescent Ir(III)Complexes with Anticancer Activity. *J. Inorg. Biochem.* **2019**, *197*, 110703. [CrossRef]

60. Redrado, M.; Benedi, A.; Marzo, I.; García-Otín, A.L.; Fernández-Moreira, V.; Concepción Gimeno, M. Multifunctional Heterometallic IrIII−AuI Probes as Promising Anticancer and Antiangiogenic Agents. *Chem. Eur. J.* **2021**, *27*, 9885–9897. [CrossRef]

61. Luengo, A.; Redrado, M.; Marzo, I.; Fernández-Moreira, V.; Gimeno, M.C. Luminescent Re(I)/Au(I) Species As Selective Anticancer Agents for HeLa Cells. *Inorg. Chem.* **2020**, *59*, 8960–8970. [CrossRef] [PubMed]

62. Park, J.; Choi, Y.; Chang, H.; Um, W.; Ryu, J.H.; Kwon, I.C. Alliance with EPR Effect: Combined Strategies to Improve the EPR Effect in the Tumor Microenvironment. *Theranostics* **2019**, *9*, 8073–8090. [CrossRef] [PubMed]

63. Trédan, O.; Galmarini, C.M.; Patel, K.; Tannock, I.F. Drug Resistance and the Solid Tumor Microenvironment. *J. Natl. Cancer Inst.* **2007**, *99*, 1441–1454. [CrossRef] [PubMed]

64. Subhan, M.A.; Yalamarty, S.S.K.; Filipczak, N.; Parveen, F.; Torchilin, V.P. Recent Advances in Tumor Targeting via Epr Effect for Cancer Treatment. *J. Pers. Med.* **2021**, *11*, 571. [CrossRef] [PubMed]

65. Shi, Y.; Van der Meel, R.; Chen, X.; Lammers, T. The EPR Effect and beyond: Strategies to Improve Tumor Targeting and Cancer Nanomedicine Treatment Efficacy. *Theranostics* **2020**, *10*, 8–11. [CrossRef]

66. Danhier, F. To Exploit the Tumor Microenvironment: Since the EPR Effect Fails in the Clinic, What Is the Future of Nanomedicine? *J. Control. Release* **2016**, *244*, 108–121. [CrossRef]

67. Maeda, H. Toward a Full Understanding of the EPR Effect in Primary and Metastatic Tumors as Well as Issues Related to Its Heterogeneity. *Adv. Drug Deliv. Rev.* **2015**, *91*, 3–6. [CrossRef]

68. Stylianopoulos, T. EPR-Effect: Utilizing Size-Dependent Nanoparticle Delivery to Solid Tumors. *Ther. Deliv.* **2013**, *4*, 421–423. [CrossRef]

69. Sharifi, M.; Cho, W.C.; Ansariesfahani, A.; Tarharoudi, R.; Malekisarvar, H.; Sari, S.; Bloukh, S.H.; Edis, Z.; Amin, M.; Gleghorn, J.P.; et al. An Updated Review on EPR-Based Solid Tumor Targeting Nanocarriers for Cancer Treatment. *Cancers* **2022**, *14*, 2868. [CrossRef]

70. Bazak, R.; Houri, M.; El Achy, S.; Kamel, S.; Refaat, T. Cancer Active Targeting by Nanoparticles: A Comprehensive Review of Literature. *J. Cancer Res. Clin. Oncol.* **2015**, *141*, 769–784. [CrossRef]

71. Manzari, M.T.; Shamay, Y.; Kiguchi, H.; Rosen, N.; Scaltriti, M.; Heller, D.A. Targeted Drug Delivery Strategies for Precision Medicines. *Nat. Rev. Mater.* **2021**, *6*, 351–370. [CrossRef] [PubMed]

72. Graf, N.; Lippard, S.J. Redox Activation of Metal-Based Prodrugs as a Strategy for Drug Delivery. *Adv. Drug Deliv. Rev.* **2012**, *64*, 993–1004. [CrossRef] [PubMed]

73. Zinovkin, R.A.; Zamyatnin, A.A. Mitochondria-Targeted Drugs. *Curr. Mol. Pharmacol.* **2018**, *12*, 202–214. [CrossRef] [PubMed]

74. Davis, S.S. Biomedical Applications of Nanotechnology—Implications for Drug Targeting and Gene Therapy. *Trends Biotechnol.* **1997**, *15*, 217–224. [CrossRef] [PubMed]

75. Díaz, P.; Sandoval-Bórquez, A.; Bravo-Sagua, R.; Quest, A.F.G.; Lavandero, S. Perspectives on Organelle Interaction, Protein Dysregulation, and Cancer Disease. *Front. Cell Dev. Biol.* **2021**, *9*, 613336. [CrossRef]

76. Qiu, K.; Chen, Y.; Rees, T.W.; Ji, L.; Chao, H. Organelle-Targeting Metal Complexes: From Molecular Design to Bio-Applications. *Coord. Chem. Rev.* **2019**, *378*, 66–86. [CrossRef]

77. King, A.P.; Wilson, J.J. Endoplasmic Reticulum Stress: An Arising Target for Metal-Based Anticancer Agents. *Chem. Soc. Rev.* **2020**, *49*, 8113–8136. [CrossRef]

78. Armstrong, J.S. Mitochondria: A Target for Cancer Therapy. *Br. J. Pharmacol.* **2006**, *147*, 239–248. [CrossRef]

79. McBride, H.M.; Neuspiel, M.; Wasiak, S. Mitochondria: More Than Just a Powerhouse. *Curr. Biol.* **2006**, *16*, 551–560. [CrossRef]

80. Vyas, S.; Zaganjor, E.; Haigis, M.C. Mitochondria and Cancer. *Cell* **2016**, *166*, 555–566. [CrossRef]

81. Modica-Napolitano, J.S.; Aprille, J.R. Delocalized Lipophilic Cations Selectively Target the Mitochondria of Carcinoma Cells. *Adv. Drug Deliv. Rev.* **2001**, *49*, 63–70. [CrossRef] [PubMed]

82. Zhang, B.B.; Wang, D.G.; Guo, F.F.; Xuan, C. Mitochondrial Membrane Potential and Reactive Oxygen Species in Cancer Stem Cells. *Fam. Cancer* **2015**, *14*, 19–23. [CrossRef] [PubMed]

83. Kandela, I.; Lee, W.; Indig, G.L. Effect of the Lipophilic/Hydrophilic Character of Cationic Triarylmethane Dyes on Their Selective Phototoxicity toward Tumor Cells. *Biotech. Histochem.* **2003**, *78*, 157–169. [CrossRef]

84. Trapp, S.; Horobin, R.W. A Predictive Model for the Selective Accumulation of Chemicals in Tumor Cells. *Eur. Biophys. J.* **2005**, *34*, 959–966. [CrossRef] [PubMed]

85. Scalcon, V.; Bindoli, A.; Rigobello, M.P. Significance of the Mitochondrial Thioredoxin Reductase in Cancer Cells: An Update on Role, Targets and Inhibitors. *Free Radic. Biol. Med.* **2018**, *127*, 62–79. [CrossRef]

86. Erxleben, A. Mitochondria-Targeting Anticancer Metal Complexes. *Curr. Med. Chem.* **2018**, *26*, 694–728. [CrossRef]

87. Marrache, S.; Pathak, R.K.; Dhar, S. Detouring of Cisplatin to Access Mitochondrial Genome for Overcoming Resistance. *Proc. Natl. Acad. Sci. USA* **2014**, *111*, 10444–10449. [CrossRef]

88. Wisnovsky, S.P.; Wilson, J.J.; Radford, R.J.; Pereira, M.P.; Chan, M.R.; Laposa, R.R.; Lippard, S.J.; Kelley, S.O. Targeting Mitochondrial DNA with a Platinum-Based Anticancer Agent. *Chem. Biol.* **2013**, *20*, 1323–1328. [CrossRef]

89. Cullen, K.J.; Yang, Z.; Schumaker, L.; Guo, Z. Mitochondria as a Critical Target of the Chemotheraputic Agent Cisplatin in Head and Neck Cancer. *J. Bioenerg. Biomembr.* **2007**, *39*, 43–50. [CrossRef]

90. Koo, C.K.; So, L.K.Y.; Wong, K.L.; Ho, Y.M.; Lam, Y.W.; Lam, M.H.W.; Cheah, K.W.; Cheng, C.C.W.; Kwok, W.M. A Triphenylphosphonium-Functionalised Cyclometalated Platinum(II) Complex as a Nucleolus-Specific Two-Photon Molecular Dye. *Chem. Eur. J.* **2010**, *16*, 3942–3950. [CrossRef]

91. Sun, R.W.Y.; Chow, A.L.F.; Li, X.H.; Yan, J.J.; Chui, S.S.Y.; Che, C.M. Luminescent Cyclometalated Platinum(II) Complexes Containing N-Heterocyclic Carbene Ligands with Potent in Vitro and in Vivo Anti-Cancer Properties Accumulate in Cytoplasmic Structures of Cancer Cells. *Chem. Sci.* **2011**, *2*, 728–736. [CrossRef]

92. Huang, J.; Zhong, L. Thioredoxin Reductase. *Adv. Top. Sci. Technol. China* **2012**, *8*, 41–64. [CrossRef]

93. Jia, J.J.; Geng, W.S.; Wang, Z.Q.; Chen, L.; Zeng, X.S. The Role of Thioredoxin System in Cancer: Strategy for Cancer Therapy. *Cancer Chemother. Pharmacol.* **2019**, *84*, 453–470. [CrossRef] [PubMed]

94. Pratesi, A.; Gabbiani, C.; Ginanneschi, M.; Messori, L. Reactions of Medicinally Relevant Gold Compounds with the C-Terminal Motif of Thioredoxin Reductase Elucidated by MS Analysis. *Chem. Commun.* **2010**, *46*, 7001–7003. [CrossRef] [PubMed]

95. Pratesi, A.; Gabbiani, C.; Michelucci, E.; Ginanneschi, M.; Papini, A.M.; Rubbiani, R.; Ott, I.; Messori, L. Insights on the Mechanism of Thioredoxin Reductase Inhibition by Gold N-Heterocyclic Carbene Compounds Using the Synthetic Linear Selenocysteine Containing C-Terminal Peptide HTrxR(488-499): An ESI-MS Investigation. *J. Inorg. Biochem.* **2014**, *136*, 161–169. [CrossRef]

96. Köster, S.D.; Alborzinia, H.; Can, S.; Kitanovic, I.; Wölfl, S.; Rubbiani, R.; Ott, I.; Riesterer, P.; Prokop, A.; Merz, K.; et al. A Spontaneous Gold(i)-Azide Alkyne Cycloaddition Reaction Yields Gold-Peptide Bioconjugates Which Overcome Cisplatin Resistance in a P53-Mutant Cancer Cell Line. *Chem. Sci.* **2012**, *3*, 2062–2072. [CrossRef]

97. Tolbatov, I.; Cirri, D.; Marchetti, L.; Marrone, A.; Coletti, C.; Re, N.; La Mendola, D.; Messori, L.; Marzo, T.; Gabbiani, C.; et al. Mechanistic Insights Into the Anticancer Properties of the Auranofin Analog Au(PEt3)I: A Theoretical and Experimental Study. *Front. Chem.* **2020**, *8*, 812. [CrossRef]

98. Crudden, C.M.; Allen, D.P. Stability and Reactivity of N-Heterocyclic Carbene Complexes. *Coord. Chem. Rev.* **2004**, *248*, 2247–2273. [CrossRef]

99. Hickey, J.L.; Ruhayel, R.A.; Barnard, P.J.; Baker, M.V.; Berners-Price, S.J.; Filipovska, A. Mitochondria-Targeted Chemotherapeutics: The Rational Design of Gold(I) N-Heterocyclic Carbene Complexes That Are Selectively Toxic to Cancer Cells and Target Protein Selenols in Preference to Thiols. *J. Am. Chem. Soc.* **2008**, *130*, 12570–12571. [CrossRef]

100. Rackham, O.; Nichols, S.J.; Leedman, P.J.; Berners-Price, S.J.; Filipovska, A. A Gold(I) Phosphine Complex Selectively Induces Apoptosis in Breast Cancer Cells: Implications for Anticancer Therapeutics Targeted to Mitochondria. *Biochem. Pharmacol.* **2007**, *74*, 992–1002. [CrossRef]

101. Levina, A.; Mitra, A.; Lay, P.A. Recent Developments in Ruthenium Anticancer Drugs. *Metallomics* **2009**, *1*, 458–470. [CrossRef] [PubMed]

102. Pierroz, V.; Joshi, T.; Leonidova, A.; Mari, C.; Schur, J.; Ott, I.; Spiccia, L.; Ferrari, S.; Gasser, G. Molecular and Cellular Characterization of the Biological Effects of Ruthenium(II) Complexes Incorporating 2-Pyridyl-2-Pyrimidine-4-Carboxylic Acid. *J. Am. Chem. Soc.* **2012**, *134*, 20376–20387. [CrossRef] [PubMed]

103. Pisani, M.J.; Weber, D.K.; Heimann, K.; Collins, J.G.; Keene, F.R. Selective Mitochondrial Accumulation of Cytotoxic Dinuclear Polypyridyl Ruthenium(II) Complexes. *Metallomics* **2010**, *2*, 393–396. [CrossRef] [PubMed]

104. Joshi, T.; Pierroz, V.; Ferrari, S.; Gasser, G. Bis(Dipyridophenazine)(2-(2′-Pyridyl)Pyrimidine-4-Carboxylic Acid)Ruthenium(II) Hexafluorophosphate: A Lesson in Stubbornness. *ChemMedChem* **2014**, *9*, 1419–1427. [CrossRef]

105. Lamond, A.I.; Earnshaw, W.C. Structure and Function in the Nucleus. *Science* **1998**, *280*, 547–553. [CrossRef]

106. Strambio-De-Castillia, C.; Niepel, M.; Rout, M.P. The Nuclear Pore Complex: Bridging Nuclear Transport and Gene Regulation. *Nat. Rev. Mol. Cell Biol.* **2010**, *11*, 490–501. [CrossRef]

107. Hoelz, A.; Debler, E.W.; Blobel, G. The Structure of the Nuclear Pore Complex. *Annu. Rev. Biochem.* **2011**, *80*, 613–643. [CrossRef]

108. Huang, H.; Zhang, P.; Yu, B.; Chen, Y.; Wang, J.; Ji, L.; Chao, H. Targeting Nucleus DNA with a Cyclometalated Dipyri-dophenazineruthenium(II) Complex. *J. Med. Chem.* **2014**, *57*, 8971–8983. [CrossRef]

109. Noor, F.; Wüstholz, A.; Kinscherf, R.; Metzler-Nolte, N. A Cobaltocenium-Peptide Bioconjugate Shows Enhanced Cellular Uptake and Directed Nuclear Delivery. *Angew. Chem. Int. Ed.* **2005**, *44*, 2429–2432. [CrossRef]

110. Noor, F.; Kinscherf, R.; Bonaterra, G.A.; Walczak, S.; Wölfl, S.; Metzler-Nolte, N. Enhanced Cellular Uptake and Cytotoxicity Studies of Organometallic Bioconjugates of the NLS Peptide in Hep G2 Cells. *ChemBioChem* **2009**, *10*, 493–502. [CrossRef]

111. Moenner, M.; Pluquet, O.; Bouchecareilh, M.; Chevet, E. Integrated Endoplasmic Reticulum Stress Responses in Cancer. *Cancer Res.* **2007**, *67*, 10631–10634. [CrossRef] [PubMed]

112. Schröder, M.; Kaufman, R.J. The Mammalian Unfolded Protein Response. *Annu. Rev. Biochem.* **2005**, *74*, 739–789. [CrossRef] [PubMed]

113. Gandin, V.; Tisato, F.; Dolmella, A.; Pellei, M.; Santini, C.; Giorgetti, M.; Marzano, C.; Porchia, M. In Vitro and in Vivo Anticancer Activity of Copper(I) Complexes with Homoscorpionate Tridentate Tris(Pyrazolyl)Borate and Auxiliary Monodentate Phosphine Ligands. *J. Med. Chem.* **2014**, *57*, 4745–4760. [CrossRef] [PubMed]

114. Tardito, S.; Bassanetti, I.; Bignardi, C.; Elviri, L.; Tegoni, M.; Mucchino, C.; Bussolati, O.; Franchi-Gazzola, R.; Marchiò, L. Copper Binding Agents Acting as Copper Ionophores Lead to Caspase Inhibition and Paraptotic Cell Death in Human Cancer Cells. *J. Am. Chem. Soc.* **2011**, *133*, 6235–6242. [CrossRef]

115. Banerjee, S.; Dixit, A.; Karande, A.A.; Chakravarty, A.R. Endoplasmic Reticulum Targeting Tumour SelectIVe Photocytotoxic Oxovanadium(IV) Complexes Having Vitamin-B6 and Acridinyl Moieties. *Dalton Trans.* **2016**, *45*, 783–796. [CrossRef]

116. Nam, J.S.; Kang, M.G.; Kang, J.; Park, S.Y.; Lee, S.J.C.; Kim, H.T.; Seo, J.K.; Kwon, O.H.; Lim, M.H.; Rhee, H.W.; et al. Endoplasmic Reticulum-Localized Iridium(III) Complexes as Efficient Photodynamic Therapy Agents via Protein Modifications. *J. Am. Chem. Soc.* **2016**, *138*, 10968–10977. [CrossRef]

117. Wang, L.; Guan, R.; Xie, L.; Liao, X.; Xiong, K.; Rees, T.W.; Chen, Y.; Ji, L.; Chao, H. An ER-Targeting Iridium(III) Complex That Induces Immunogenic Cell Death in Non-Small-Cell Lung Cancer. *Angew. Chem.* **2021**, *133*, 4707–4715. [CrossRef]

118. Fetzer, L.; Boff, B.; Ali, M.; Xiangjun, M.; Collin, J.-P.; Sirlin, C.; Gaiddon, C.; Pfeffer, M. Library of Second-Generation Cycloruthen-ated Compounds and Evaluation of Their Biological Properties as Potential Anticancer Drugs: Passing the Nanomolar Barrier. *Dalton Trans.* **2011**, *40*, 8869–8878. [CrossRef] [PubMed]

119. Klajner, M.; Licona, C.; Fetzer, L.; Hebraud, P.; Mellitzer, G.; Pfeffer, M.; Harlepp, S.; Gaiddon, C. Subcellular Localization and Transport Kinetics of Ruthenium Organometallic Anticancer Compounds in Living Cells: A Dose-Dependent Role for Amino Acid and Iron Transporters. *Inorg. Chem.* **2014**, *53*, 5150–5158. [CrossRef]

120. Milacic, V.; Chen, D.; Ronconi, L.; Landis-Piwowar, K.R.; Fregona, D.; Dou, Q.P. A Novel Anticancer Gold(III) Dithiocarbamate Compound Inhibits the Activity of a Purified 20S Proteasome and 26S Proteasome in Human Breast Cancer Cell Cultures and Xenografts. *Cancer Res.* **2006**, *66*, 10478–10486. [CrossRef]

121. Fiskus, W.; Saba, N.; Shen, M.; Ghias, M.; Liu, J.; Das Gupta, S.; Chauhan, L.; Rao, R.; Gunewardena, S.; Schorno, K.; et al. Auranofin Induces Lethal Oxidative and Endoplasmic Reticulum Stress and Exerts Potent Preclinical Activity against Chronic Lymphocytic Leukemia. *Cancer Res.* **2014**, *74*, 2520–2532. [CrossRef] [PubMed]

122. Wang, X.; Guo, Q.; Tao, L.; Zhao, L.; Chen, Y.; An, T.; Chen, Z.; Fu, R. E Platinum, a Newly Synthesized Platinum Compound, Induces Apoptosis through ROS-Triggered ER Stress in Gastric Carcinoma Cells. *Mol. Carcinog.* **2017**, *56*, 218–231. [CrossRef] [PubMed]

123. Wang, Y.; Hu, J.; Cai, Y.; Xu, S.; Weng, B.; Peng, K.; Wei, X.; Wei, T.; Zhou, H.; Li, X.; et al. An Oxygen-Chelate Complex, Palladium Bis-Acetylacetonate, Induces Apoptosis in H460 Cells via Endoplasmic Reticulum Stress Pathway Rather than Interacting with DNA. *J. Med. Chem.* **2013**, *56*, 9601–9611. [CrossRef] [PubMed]

124. Suntharalingam, K.; Lin, W.; Johnstone, T.C.; Bruno, P.M.; Zheng, Y.R.; Hemann, M.T.; Lippard, S.J. A Breast Cancer Stem Cell-Selective, Mammospheres-Potent Osmium(VI) Nitrido Complex. *J. Am. Chem. Soc.* **2014**, *136*, 14413–14416. [CrossRef] [PubMed]

125. Suntharalingam, K.; Johnstone, T.C.; Bruno, P.M.; Lin, W.; Hemann, M.T.; Lippard, S.J. Bidentate Ligands on Osmium(VI) Nitrido Complexes Control Intracellular Targeting and Cell Death Pathways. *J. Am. Chem. Soc.* **2013**, *135*, 14060–14063. [CrossRef]

126. King, A.P.; Marker, S.C.; Swanda, R.V.; Woods, J.J.; Qian, S.B.; Wilson, J.J. A Rhenium Isonitrile Complex Induces Unfolded Protein Response-Mediated Apoptosis in Cancer Cells. *Chem. Eur. J.* **2019**, *25*, 9206–9210. [CrossRef]

127. Akhtar, M.J.; Ahamed, M.; Alhadlaq, H.A.; Alrokayan, S.A.; Kumar, S. Targeted Anticancer Therapy: Overexpressed Receptors and Nanotechnology. *Clin. Chim. Acta* **2014**, *436*, 78–92. [CrossRef]

128. Svensen, N.; Walton, J.G.A.; Bradley, M. Peptides for Cell-Selective Drug Delivery. *Trends Pharmacol. Sci.* **2012**, *33*, 186–192. [CrossRef]

129. Soler, M.; Feliu, L.; Planas, M.; Ribas, X.; Costas, M. Peptide-Mediated Vectorization of Metal Complexes: Conjugation Strategies and Biomedical Applications. *Dalton Trans.* **2016**, *45*, 12970–12982. [CrossRef]

130. Regberg, J.; Srimanee, A.; Langel, Ü. Applications of Cell-Penetrating Peptides for Tumor Targeting and Future Cancer Therapies. *Pharmaceuticals* **2012**, *5*, 991–1007. [CrossRef]

131. Mukhopadhyay, S.; Barnés, C.M.; Haskel, A.; Short, S.M.; Barnes, K.R.; Lippard, S.J. Conjugated Platinum(IV)-Peptide Complexes for Targeting Angiogenic Tumor Vasculature. *Bioconjug. Chem.* **2008**, *19*, 39–49. [CrossRef] [PubMed]

132. Barbas, A.S.; Mi, J.; Clary, B.M.; White, R.R. Aptamer Applications for Targeted Cancer Therapy. *Future Oncol.* **2010**, *6*, 1117–1126. [CrossRef] [PubMed]

133. Niu, W.; Chen, X.; Tan, W.; Veige, A.S. N-Heterocyclic Carbene–Gold(I) Complexes Conjugated to a Leukemia-Specific DNA Aptamer for Targeted Drug Delivery. *Angew. Chem. Int. Ed.* **2016**, *55*, 8889–8893. [CrossRef] [PubMed]

Structure–Activity Relationships in NHC–Silver Complexes as Antimicrobial Agents

Luisa Ronga [1], Mario Varcamonti [2] and Diego Tesauro [3],*

[1] Institut des Sciences Analytiques et de Physico-Chimie Pour l'Environnement et les Matériaux, Université de Pau et des Pays de l'Adour, E2S UPPA, CNRS, IPREM, 64053 Pau, France; luisa.ronga@univ-pau.fr

[2] Department of Biology, University of Naples "Federico II", Via Cynthia, 80143 Naples, Italy; mario.varcamonti@unina.it

[3] Department of Pharmacy and Interuniversity Research Centre on Bioactive Peptides (CIRPeB), University of Naples "Federico II", Via Montesano, 49, 80131 Naples, Italy

* Correspondence: diego.tesauro@unina.it; Tel.: +39-0812536643

Abstract: Silver has a long history of antimicrobial activity and received an increasing interest in last decades owing to the rise in antimicrobial resistance. The major drawback is the limited duration of its antimicrobial activity. The broad-spectrum silver containing antimicrobial agents are well represented by N-heterocyclic carbenes (NHCs) silver complexes. Due to their stability, this class of complexes can release the active Ag^+ cations in prolonged time. Moreover, the properties of NHC can be tuned introducing alkyl moieties on N-heterocycle to provide a range of versatile structures with different stability and lipophilicity. This review presents designed Ag complexes and their biological activity against Gram-positive, Gram-negative bacteria and fungal strains. In particular, the structure–activity relationships underlining the major requirements to increase the capability to induce microorganism death are highlighted here. Moreover, some examples of encapsulation of silver–NHC complexes in polymer-based supramolecular aggregates are reported. The targeted delivery of silver complexes to the infected sites will be the most promising goal for the future.

Keywords: NHC silver complexes; NHCs properties; structure activity relationships (SAR); anti-bacterial compounds

1. Introduction

The fight against infections is one of the principal issues in medicinal care since the ancient eras. Although up to the XIX century microbes were not known the humankind used substances to prevent the effects of bacterial growth on food and wounds. In pharmacopeia, late-transition metal-based drugs have been played a crucial role. In old civilizations, the use of silver pots was largely diffused to avoid microbial contamination, to purify and store drinking water [1]. Metallic silver actually causes little damage to living organisms. Nevertheless, Ag^+ is the biologically active species in applications of silver-containing compounds and formulations [2]. Von Nägeli reported that 10^{-5} to 10^{-8} mol L^{-1} of Ag^+ derived from metallic silver were effective to block the growth of *A. niger* spores [3].

Silver nitrate was used in the early 1800s for the treatment of ulcers, as antiseptic in wound care and to prevent eye infections in babies [4]. The irritation and the low stability are major problems of this salt. To overcome these drawbacks, colloidal silver solutions were introduced at begin of the 20th century able to release silver cations. After the Second World War, the discovery of penicillin with its strong antimicrobial properties led to decreased interest in silver compounds. A resumption of use did not occur until the 1960s when the discovery of silver sulfadiazine allowed treating with efficacy burn wounds combining the antibiotic properties of sulfonamide with silver [5]. Silver sulfadiazine is effective against a broad range of Gram-positive and Gram-negative bacteria, and its

formulation is commercialized as topical antimicrobial cream the Silvadene[®]. The revival of silver compounds led to an increased attention of researchers to develop new compounds able to generate silver cations.

The activity of silver cations depends on their bioavailability and the delivery way [6]. It is increased by several parameters such as the presence of anions (i.e., sulfides, phosphates, chlorides) or cations (i.e., calcium and magnesium) high temperature and basic pH. For example, it was found that high concentrations of chloride anions increase the Ag^+ cation concentration; indeed, in this condition, soluble $AgCl_2^-$ anionic specie is formed rather than solid AgCl [7]. Several other factors influence the antimicrobial and antifungal activity of silver salts [8]. The mechanism of action of Ag^+ is not yet completely explicated. Silver cations target multiple sites on or within the bacterial cell. Four mechanisms have been identified as reviewed [9,10]. First, silver exhibits a strong tendency to be adsorbed to bacterial cell membranes interacting with proteins involved in cell wall synthesis as observed for the pathogen fungus *C. albicans* [11]. Inside the cell, silver cations can bind the DNA, they are able to interact with enzymes and membrane proteins and produce reactive oxygen species (ROS). Most of these mechanisms were identified detecting an increase in hydroxyl radicals generated by silver cations that cause the release of Fe^{2+} from FeS clusters [12]. Moreover, transmission electron microscopy (TEM) demonstrates morphological changes in the cell envelope. The interaction of silver ions with bacterial inner membrane is one of the most important mechanisms of Ag^+ toxicity. Jung et al. [13] proved that the accumulation of Ag^+ in the bacterial cell envelope is followed by the separation of the cytoplasmic membrane from the cell wall in both Gram-positive and Gram-negative bacteria.

Although the mechanism of damage of cell wall is still not fully understood, several hypotheses are reported in the literature. Silver ions may cause the formation of irregularly shaped pits in the outer membrane and change membrane permeability, which is caused by the progressive release of lipopolysaccharide molecules and membrane proteins. Another mechanism of bactericidal action may be based on the inhibition of cell wall synthesis interfering with the folding of involving enzymes.

Indeed, the latter mechanism can be induced by Ag^+ binding thiol of the side chain of cysteine residues due to its soft acid properties. Therefore, many protein targets have been identified. Indeed, in 2019 Wang et al. recognized 34 proteins from *E. coli* that directly bind silver using liquid chromatography (LC) combined with gel electrophoresis (GE) and inductively coupled plasma mass spectrometry (ICP-MS) [14]. Among all the metabolic ways, the glycolysis was individuated as major pathway affected leading to depleted ATP. Moreover, Ag cations can affect cell respiration, inactivating NADH and succinate dehydrogenase, transport mechanism and metabolism increasing the ROS species [15]. The crystallographic structure of urease demonstrated that the His-Cys-Met sequence in the active site binds a bimetallic cluster of Ag cation affecting a protein loop near deactivating the enzymatic function [16]. These multifaceted modes of action of silver ions justify the scarceness of reports clearly explaining the silver resistance despite its diffused use. Another point of advantage of silver ions is their broad-spectrum antibiotic activity. Indeed silver, unlike conventional organic-based antibiotics, is active against a wide range of Gram-positive and Gram-negative bacteria.

However, the activity of silver salts has a limited time of action due to their low stability; therefore, the silver complexes can overcome this drawback releasing slowly the Ag^+ cation. The choice of the ligands covalently bound to the metal center is pivotal to define the outcome of the Ag complex both in terms of its stability and in terms of its delivery on the site of action. Generally, silver(I)-S complexes show a narrower spectrum of antimicrobial activities than silver(I)-N and silver(I)-O complexes. Moreover, most of the investigated complexes with silver(I)-P bonds did not display antimicrobial activity. This evidence can be related to the high stability of their coordinative bonds and prompted researchers to explore the antibacterial properties of alternative silver ligands: i.e., N-heterocyclic carbenes (NHC). Since their discovery

by Arduengo et al. [17] NHC have become universal ligands in organometallic and inorganic coordination to transition metals in catalytic applications [18] for his versatile properties. More recently, NHC ligands have been used as carrier molecules for metals in biological applications.

The goal of this review is to report about NHC–silver complexes tested in antimicrobial applications by highlighting their structure–activity relationships (SAR). For this purpose, the presentation of silver compounds is articulated here in four sections describing NHC-silver mononuclear, binuclear and loaded on supramolecular aggregates. In particular, the section NHC–silver mononuclear complexes presents different subparagraphs detailing the design of the structures of NHCs able to tune antimicrobial activity.

2. N-Heterocyclic Carbenes (NHC) Ligands

The properties of NHC ligands to coordinate metal centers were actively studied. They are strong nucleophiles and bind both main group and transition metals often with greater stability than phosphines [19]. Their structure is based on heterocycle containing at least one nitrogen atom contiguous carbene function. This class of ligands owns peculiar steric properties and strong σ donor of the carbene C2 due to the two adjacent nitrogen lone electron pairs to the free p-orbital of the carbon atom of NHCs (see Figure 1). This consequence reduces its π-backbonding capability, even stronger than alkyl phosphines [20].
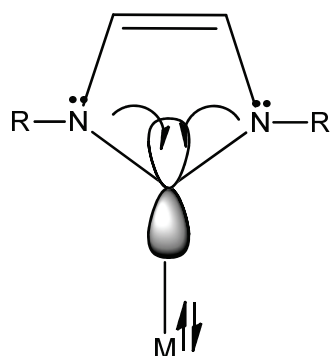
Figure 1. σ donor character of the carbene C2 due to the two adjacent nitrogen lone electron pairs to the free p-orbital.

Gusev quantified electron-donor and steric properties of a diverse group NHC with DFT calculations [21]. The σ-donor is strongly affected by substituents at C4 and C5 of the imidazole and imidazolidine rings, by the size of the N residues and by the NHC ring members (5 or 6 terms). The extended π-systems containing ligands are poor donors, whereas steric hindrance on sidechains of substituents on N do not affect bond energies. However, these substituents systematically can tune the lipophilicity.

In the literature, there are reported almost 20 types of ligands belonging to NHC class ranging from five- to seven-membered rings, but the most diffused types are: imidazolidin-2-ylidenes, imidazol-2-ylidenes and benzimidazol-2-ylidenes (see Figure 2).
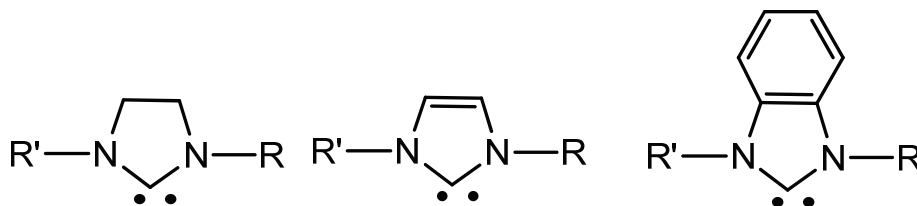
Figure 2. Structure of imidazolidin-2-ylidene (**left**), imidazol-2-ylidene (**center**) and benzimidazol-2-ylidene (**right**).

Electronic and steric properties within these three types can be tuned inducing structural changes on the side chains of nitrogens. In medical applications these features are pivotal influencing the stability and the bioavailability. Among these ligands, the benzoimidazole is a vital pharmacophore of many biologically active heterocyclic compounds with a variety of pharmacological properties, i.e., anticancer, antiviral, antibacterial, antifungal, antihelminthic, anti-inflammatory and antihistaminic [22]. Indeed, benzimidazole derivatives are used in clinical applications such as anthelmintic (albendazole, mebendazole), fungicide (benomyl, carbendazim) and antacid (omeprazole, lansoprazole) this also motivate to investigate this type of molecular scaffold. The benzimidazole fragment and some of its derivatives suppress the bacterial growth which has been explained by their competition with purines resulting in inhibition of the synthesis of microbial nucleic acids and proteins [23].

These actions are related to the structure of benzimidazoles that allows them to form strong hydrogen bonds with enzymes and biological receptors, as well as participate in hydrophobic and π–π interactions, making them ligands for a variety of metal ions.

3. NHC–Silver Mononuclear Complexes

The binding interactions between the NHCs and the silver ion produce very strong bonds. Theoretical studies on silver chlorides demonstrated that these bonds are largely attributed to Coulombic attraction between the lone-pair electrons at the ligand donor atom and the positively charged metal atoms, but covalent interactions are not negligible. The covalent contribution growths from donation of the donor lone-pair electrons to the M-Cl σ* orbital. Moreover, the benzimidazolium core-based Ag(I)–NHC can be stabilized additionally by ring π–π interactions due to the extended π-cloud system. Ag(I)–NHC complexes have been observed to be very stable to air and moisture.

Ag(I)–NHC complexes are easily synthesized in situ by deprotonation of from azolium salts (e.g., imidazole, imidazoline, benzimidazole) with basic silver precursors such as Ag_2O, Ag_2CO_3 or AgOAc. The Ag_2O favors the formation of mono NHC or bis NHC by reacting with azolium whose positive charge is neutralized by halides or non-coordinate anions respectively.

The easy synthesis of Ag(I)–NHC has been widely exploited in the context of metal transferring hence relatively few publications on silver–carbene complexes are centered on their medicinal applications.

Youngs et al. reported the first studies in 2004 [24]. In the last two decades functionalized and nonfunctionalized NHC silver complexes have been extensively designed and synthesized for biological applications. Almost hundreds of complexes were reviewed for medical applications by Patil et al. and the Young [25,26]. In this review, NHC–silver mononuclear complexes are reported in subsections on the basis of the properties of the NHC ligands. The structures of the complexes described are reported in Figures 3–11, whereas for each study the biological data of the most active complex are in the Table 1.

Roland et al. [27] carried out one of the first attempts to study antibacterial properties of a large panel of Ag(I)-NHC. They described 14 complexes designed for their catalytic properties but also with relevant antimicrobial properties. Significant changes in the activity were observed with slight differences in the NHC ligand structures. Ten of these complexes (**1–3** and **6–12**) (were found to display significant activity against *E. coli* with minimum inhibitory concentrations (MIC) ranging from 4 to 16 mgmL^{-1}. Complexes **13** and **14** were the most active with MIC values of 1–4 mgmL^{-1}, inhibiting both sensitive and resistant strains of *S. aureus* at clinically achievable concentrations. Moreover, Ag(I)–NHC s were able to reestablish the activity of Ciprofloxacin (CIP) by combining its synergistic effects.
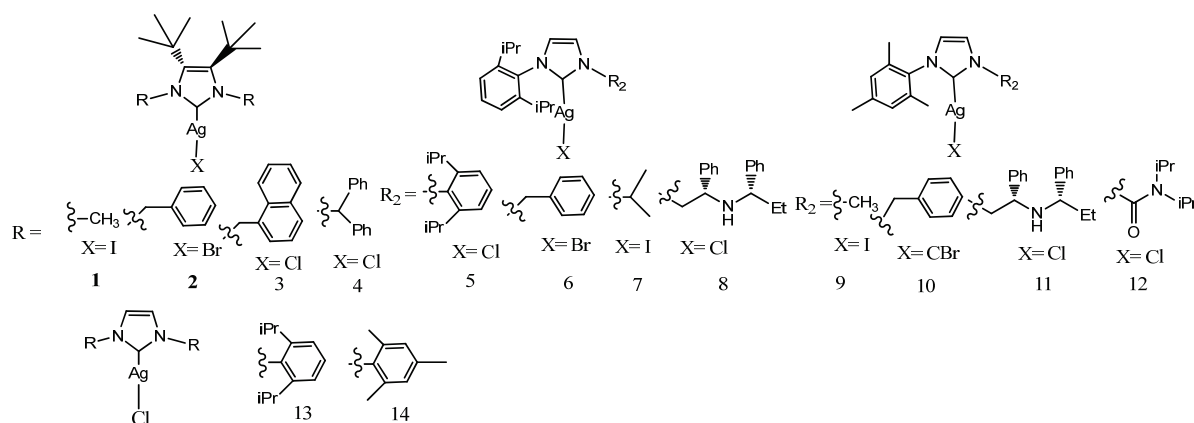
Figure 3. Structures of mononuclear NHC–silver complexes.

3.1. Benzyl-Substituted NHC–Silver Complexes

Because *p*-methoxybenzyl-substitution was successful applied in the case of the metallocene potential drugs, Tacke and coworkers designed six *p*-methoxybenzyl-substituted and benzyl-substituted Ag(I)–NHC acetate (Ac) derivatives (**15–20**) [28]. The structures of these complexes, like those of the other complexes described in this subsection, are shown in Figure 4.

To assess the antibacterial activity of compounds against both Gram-positive bacteria *Staphylococcus aureus* and Gram-negative bacteria *E. coli*, the Kirby–Bauer disk-diffusion method was applied. All imidazol-2-ylidene-Ag(I) complexes showed high antibacterial activity compared to the azolium salts and benzimidazol-2-ylidene-Ag(I) complexes that are poorly soluble. Applying the same methods in a later research study, six symmetrically substituted and non-symmetrically *p*-cyanobenzyl or benzyl substituted Ag(I)–NHC acetate derivatives (**21–26**) were tested [29].

Almost all complexes have displayed high antimicrobial activity with areas of clearance ranging from 4 to 12 mm, compared with the precursors and a marked improvement with respect to the compounds previously reported. Encouraging results pushed to study this class of compound designing other six non-symmetrically substituted and symmetrically substituted Ag(I)–NHC acetate derivatives (**27–32**) [30]. With respect to previously tested compounds, the concentration of stock solutions was reduced four-fold, and the Ag(I)–NHC complexes exhibited enhanced antibacterial activity. This achievement was due to the synergistic effects of the increased lipophilicity of the complexes. Chelation decreases the polarity of the metal ion, which further leads to the enhanced lipophilicity of the complex. The best antimicrobial activity was observed for the compound [1,3-dibenzyl-4,5-diphenylimidazol-2-ylidene]Ag(I) acetate (**32**). This complex was selected as the lead compound to carry out other assays on bacterial strains and to find the MIC [31]. The values of the MIC were observed to fall in the range 20 and 3.13 μgmL^{-1} after an incubation period of 20 h against the full bacterial panel. The activity was especially relevant against methicillin-resistant *S. aureus* (MRSA) with a MIC value of 12.5 μgmL^{-1}. MRSA has acquired resistance to almost all β-lactam antibiotics including methicillin, amoxicillin and oxacillin among others. Some years later it was demonstrated that this complex at concentration of 25 μgmL^{-1} inhibited in vitro the growth of *S. aureus* by 71.2% and *C. albicans* by 86.2% [32]. Then its antibacterial property was evaluated in vivo in larvae of Galleria mellonella. Larvae inoculated with *S. aureus* or *C. albicans* exhibited increased survival after administration of **32** (20 μL at concentration 100μg.mL^{-1}). Moreover, after the administration of **32**, the insect immune response was not observed. The lipid nature of the complex may not provoke an immune response as it may be better tolerated by the insect's immune system. As consequence, it can be concluded that the increased survival of larvae that received **32** is due to the anti-microbial properties of the compound and not to a non-specific immune response induced by the introduction of the compound. This is the first demonstration of the in vivo activity against *S. aureus* and *C. albicans* without

stimulation of non-specific immune response in larvae. Recently label-free quantitative proteomics was employed to analyze changes in protein abundance in the pathogenic yeast *C. parapsilosis* in response to treatment with **32** [33]. An increased abundance of proteins associated with detoxification and drug efflux were indicative of a cell stress response, whilst significant decreases in proteins required for protein and amino acid biosynthesis offer potential insight into the growth-inhibitory mechanisms of **32**. Achievements of proteomic findings, the prolific biofilm and adherence capabilities of *C. parapsilosis*, have demonstrated the potential of **32** to reduce epithelial cell adherence and biofilm formation and thereby decrease fungal virulence. They later investigated proteomic responses in the inhibition of growth to exposure of *S. aureus* and *P. aeruginosa* to **32** [34]. Both bacteria showed alterations in the abundance of proteins associated with the cell wall or envelope. However, in *P. aeruginosa*, a multitude of pathways was affected, including alginate biosynthesis, secretion systems, drug detoxification and anaerobic respiration. This contrasted with the response of *S. aureus*, where pathways such as protein synthesis, glucose metabolism and cell redox homeostasis were affected.

The relevant results pushed the same group to design and synthesize *p*-benzyl-substituted Ag(I)–NHC acetate compounds derived from 4,5-di-*p*-diisopropylphenyl or 4,5-di-*p*-chlorophenyl-1*H*-imidazole, (**33–42**) [35]. The complexes **34–37** were less active against both Gram-positive bacteria *S. aureus* and Gram-negative bacteria *E. coli* while **33**, **38–41** and **42** show moderate activity against *S. aureus*. However, their activity on *E. coli* remains considerably low. The introduction of isopropyl group and chlorine atom on benzoimidazole rings does not improve the antimicrobial properties observing weaker antimicrobial properties than the lead compound **32**.

Some years later Tacke et al. prepared four Ag(I)–NHC complexes substituting the acetate of the lead compound **32** with 4 substituted benzoates **43–46** [36]. These substitutions allowed the study of the effect that other ligands have on their antimicrobial activity. For instance, compounds **43–46** were screened for in vitro activity against two pathogenic bacterial strains, methicillin-resistant *S. aureus* and *E. coli*, and two fungal strains, *C. albicans* and *C. parapsilosis*. The results displayed a clear effect on the modification, with fluorine atom bearing on benzoate compound **46** showing the best inhibition against *C. parapsilosis*.

In 2017, Bhagat et al. reported in two different manuscript the synthesis of seven neutral bromide Ag(I)–NHC complexes and seven cationic NHC–Ag(I)–NHC complexes [36,37] Neutral and cationic species formation is influenced by modulating the polarity of the solvent from dichloromethane to methanol. All complexes were evaluated against one Gram-negative (*S. enterica*) and one Gram-positive (*S. aureus*). In the first paper the most potent compounds **47** and **51** inhibited the microbial growth with MIC value of 6.25 μM against *S. aureus* and **47** displayed MIC of 25 μM against *S. enterica* showing an efficient growth inhibition even up to 21 d. The treatment of bacteria with **47** and **51**, and examining cell wall appearance under SEM infers the cell wall disrupting effects of silver complexes. The factors such as hydrophobic substitutions and steric bulk affect lability of Ag-Carbene bond and thereby regulating the release of Ag^+ in an aqueous environment. The positive charge seem not to influence the silver activity in this case. In the second paper [38], the best inhibition among the six complexes, was detected with the nitrobenzyl and biphenyl carbonitrile based neutral silver **57** complex displaying MIC of 25 μM in *S. enterica* as well as in *S. aureus*. The silver complexes had higher MIC in *S. enterica* because of the resistance for silver ions. The other factors such as hydrophobic substitution and steric bulk are involved in the release of Ag^+ cations.

At the end of the last decade several groups studied the influence of substituents on benzyl moiety on imidazole ring. For instance, Haque et al. studied non-symmetrical six NHC–Ag(I)–NHC cationic complexes, **62–67** to evaluate the effect of electron-withdrawal or electron-donors on benzyl ring [39]. They introduced nitrile groups on different positions of an *N*-benzyl ring to compare the antibacterial effects with methyl groups positioned in same positions. The substitution does not induce a relevant difference in antimicrobial properties. All six complexes displayed a modest to good inhibition zone against both *E. coli*

and *S. aureus*, around 9 mm with concentration at 6 µL. Very recently Sahin et al. reported the synthesis of five neutral Ag(I)–NHC complexes bearing on imidazole benzyl ring para substituted with electron withdrawal or donor groups (**68**–**72**) [40]. All compounds were also analyzed by molecular docking methods with the potential target molecules such as N-Acyl Homoserine Lactone (AHL) Lactonase. All compounds have a high antimicrobial activity against Gram-positive and Gram-negative microorganisms but displayed the greatest effect on *C. albicans* fungi. MICs of all complexes were in the range 18–36 µM. The best inhibitor of *E. coli* biofilms was found the compound bearing the benzyl (**68**), while the bromide complex (**72**) inhibited *C. albicans* biofilm at the highest rate. In general, all reported studies indicate that the presence in different position of substituents on benzyl groups does not affect significantly the antimicrobial efficacy.
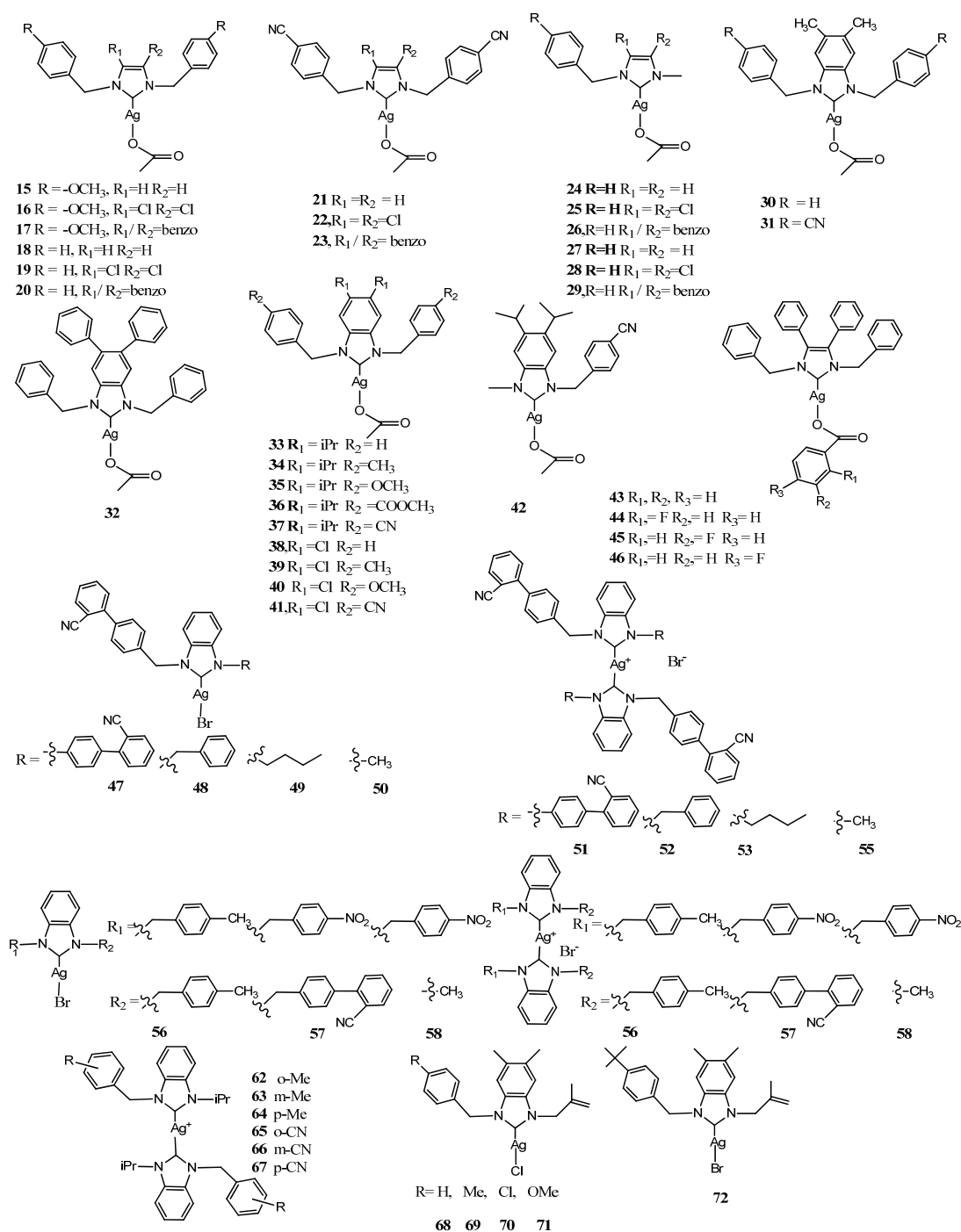
Figure 4. Structures of benzyl-substituted NHC–silver complexes.

3.2. NHC–Silver Complexes Designed with Steric Hindrance

Many attempts have been devoted to study the impact of bulky substituents on imidazole group on antimicrobial activity; the structures are reported in Figure 5. Özdemir and coworkers synthesized 10 bulky 3,5-di-*tert*-butyl substituted NHC–Ag-Br complexes (**73–82**) [41]. The evaluation was carried out against two Gram-negative bacteria (*E. coli* and *P. aeruginosa*), two Gram-positive bacteria (*S. aureus* and *E. Faecalis*) and two fungal strains (*C. albicans* and *C. tropicalis*). Reduced hindrance containing complexes (such as **81** and **82**) have less antimicrobial activity than the bulky complexes. Indeed, the bulkiest complex **77** was the most effective against all the tested microbial strains, with a MIC of 6.25 μgmL^{-1}, whereas smaller substituents bearing complex **81** exhibited an MIC from 25 to 100 μgmL^{-1}.

The influence of steric hindrance was previously studied introducing polymetyl-aryl group in seven 4-vinylbenzyl-NHC silver complexes (**83–88**) [42]. The phenyl and polymethyl aryl substituted complexes **83**, **86** and **87** showed good antibacterial activity, especially against *C tropicalis* and *C albicans* as the fungal strains. The same compounds acted in similar way against Gram-negative (*E. coli*, *P. aeruginosa*) and Gram-positive (*E. faecalis*, *S. aureus*) bacterial strains. The monosubstituted metylaryl Ag(I)-NHC complexes **84**, **85** were less active. The same group later expanded the series of the 1-(4-vinylbenzyl)benzimidazole NHC–Ag(I)-Cl complexes synthesizing alkyl functionalized ligands as well as aryl ligands (**89–95**) [43]. The antimicrobial activity was evaluated against three Gram-positive bacterial strains (*B. subtilis*, *L.monocytogenes*, *S. aureus*), seven Gram-negative bacterial strains (*E.coli*, *K. pneumoniae*, *P. mirabilis*, *P. aeruginosa*, *S. typhimurium*, *Y. enterocolitica*) and one yeast (*C. albicans*) by agar diffusion assay. In this case alkyl and aryl bearing substituents on Ag(I)–NHC complexes (**89–95**) exhibited similar inhibition zone (ZoI) between 13–19 mm without detecting very significant differences between the substituents.
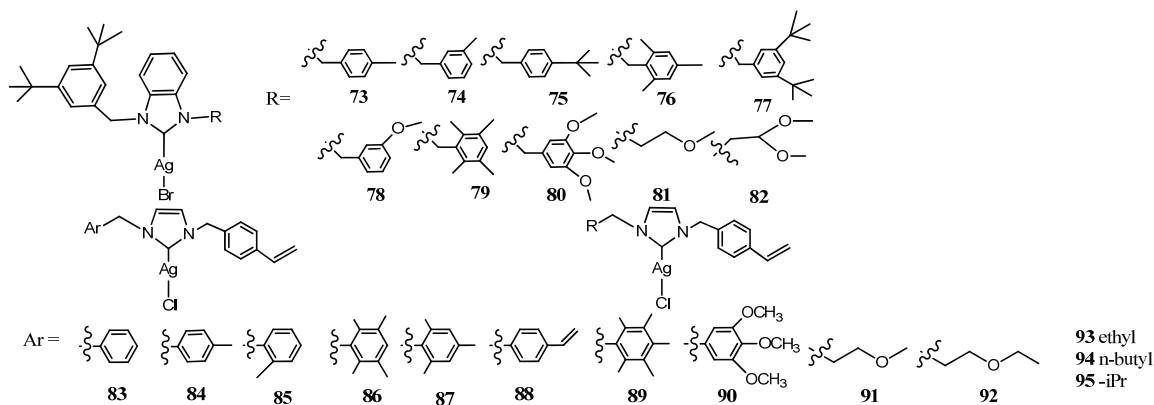
Figure 5. Structures of NHC–silver complexes designed with Steric Hindrance.

3.3. NHC–Silver Complexes Bearing p–Nitrobenzyl Group

Patil et al. studied series of NHC functionalized with *p*–nitrobenzyl (Figure 6). This moiety was selected due the relevance of the nitrobenzene derivatives, which are being used in the synthesis of many drugs acting as analgesics, antipyretics and antipsychotic. The authors reported the synthesis of eight cationic NHC–Ag–NHC complexes (**96–103**), from non-symmetrically *p*-nitrobenzyl- and *p*-cyanobenzyl-substituted salts [44]. The isopropyl (**96**) and *p*-cyanobenzyl-substituted (**100–103**) showed in the evaluation antimicrobial activity the best activity against Gram-negative (*E. coli*), whereas *i*butyl (**96**) and *p*-cyanobenzyl-substituted (**100–103**) were the most effective against Gram-positive (*S. aureus*).

Later they studied the effect of substituents on position 4 and 5 on imidazole rings synthetizing four non-symmetrically *p*-nitrobenzyl-substituted Ag(I)–NHC acetate (**104–107**) and four respective cationic NHC-Ag(I)–NHC complexes (**108–111**) [45]. In general, all of

the complexes displayed MIC ranging between 8.0 and 128 μgmL^{-1} in vitro antibacterial activity against two Gram-positive bacteria (*S. aureus* and *B. subtitis*) and four Gram-negative bacteria (*E. coli*, *P. aeruginosa*, *S. sonnei* and *S. typhi*). The more active among the Ag(I)–NHC acetate was **107** complexes with highest bioactivity against *S. aureus* and *E. coli* (MIC 8 μgmL^{-1}) whereas the more active among the NHC–Ag(I)–NHC complex was 4,5 diphenyl imidazole- Ag(I)–NHC (**110**) with the highest bioactivity against *E. coli* (MIC 8 μgmL^{-1}).

The same group followed their studies on *p*-nitrobenzyl-substituted NHC bearing alkyl chain with different length on imizole ring. They prepared five Ag– NHC acetate complexes (**112–116**) and five NHC–Ag(I)–NHC complexes (**117–121**) [46]. All these complexes were screened against the same bacterial strains. The antibacterial activity of Ag(I)-NHC acetateAc and NHC–Ag(I)–NHC complexes was comparable with the MIC ranging between 16.0 and 128 μgmL^{-1}, observing that the MIC decreases with an increase in the alkyl chain length. The increase in antibacterial activity was already detected by Asekunowo et al. in previous paper [47]. They compared three types of nonsymmetrically alkyl substituted *N*-benzyl benzimidazole NHC–Ag(I)–NHC complexes (**122–124**). The effect of the N-alkyl substitution on antibacterial activities was evaluated against two bacteria strains, the Gram-positive *S. aureus* and the Gram-negative *E. coli* with a MIC value ranging between 12.5–50 μgmL^{-1}. The complexes bearing on imidazole longer alkyl chain length displayed major activity against both bacteria strains. This suggests that in this case ligands may simply facilitate the transport of Ag(I) ions to their biological targets. Moreover, all complexes were efficient in promoting cleavage or degradation of DNA.

More recently Granillo et al. synthesized [Ag(1–methyl–3–(4–nitrobenzyl)–1H–imidazoleCl]$_2$ **125** [48]. The dimeric molecular structure of the complex was determined by single crystal X–ray diffraction. The antibacterial assays in vitro were performed against two Gram-positive (*S. aureus* and *B. subtilis*) and two Gram-negative species (*P. aeruginosa* and *E. coli*) by Kirby–Bauer's disk diffusion method. Compound exhibited moderate activity against *S. aureus* and *P. aeruginosa* when 4.31 μg of Ag were used, similar behavior was found against *B. subtilis* and *E. coli* but only when 5.74 μg of Ag were employed. The ZoI tested against *S. aureus* is comparable to other products previously reported with *p*-nitrobenzyl-substituted benzoimidazole Ag(I)-NHC **112**.
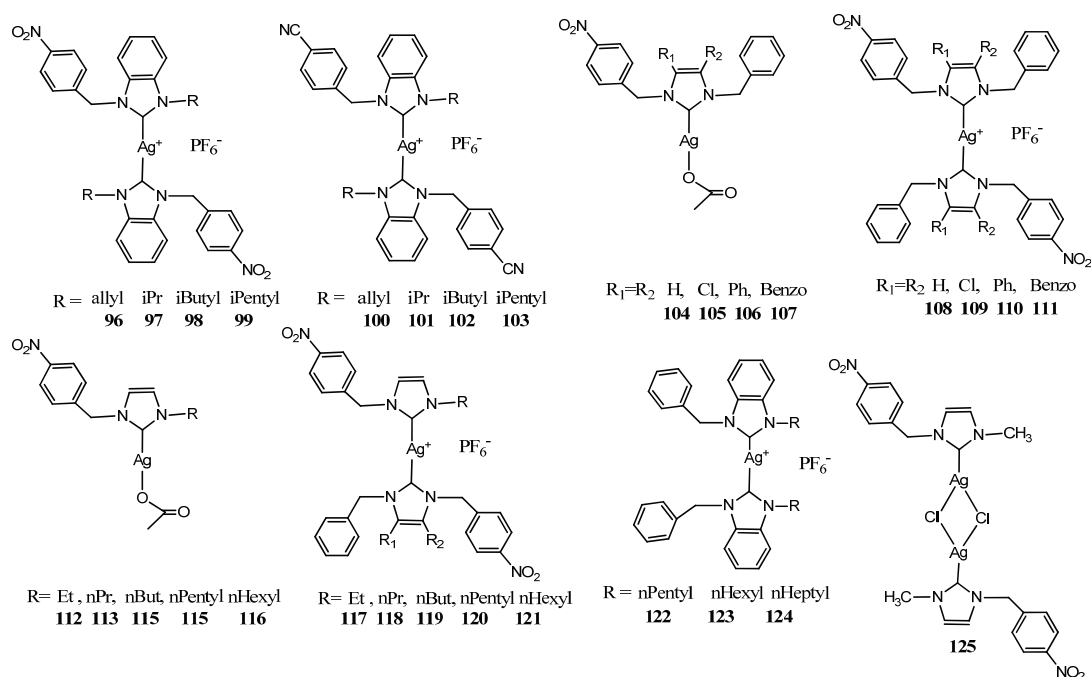
Figure 6. Structures of NHC–silver complexes bearing p–nitrobenzyl group and structures of compared complexes to them.

3.4. NHC–Silver Complexes Bearing Naphthalil Group

Ott et al. synthesized NHC–Ag acetate complexes bearing bis-1,8-naphthalimide ligands (**126**) (Figure 7). This complex combine the DNA interacting naphthalimide with a metal based mechanism of drug action [49]. The unsubstituted bis-naphthalimide Ag(I)–NHC complex **126** was evaluated against three Gram-negative bacteria (*E. coli*, *A. baumannii* and *P. aeruginosa*) and three Gram-positive bacteria (*B. subtitis* and two *S. aureus* strains, DSM 20231 and ATCC 43300). The growth of Gram-negative bacteria was not significantly affected while Gram-positive bacteria were more sensitive with the most relevant value of MIC (16 µgmL^{-1}) for *B. subtitis*. This might be due to differences in the cell envelops of Gram-positive and Gram-negative bacteria, efflux systems, and/or to metal-based inhibition of bacterial thioredoxin reductase (TrxR), which is more harmful for Gram-positive bacteria [50]. Later Gök et al. reported the synthesis of seven naphthalen-1-ylmethyl substituted Ag(I)–NHC complexes (**127–133**) [51]. These NHC–Ag-Cl complexes were screened in vitro toward four bacteria (*S. aureus*, *E. coli*, *E. faecalis* and *P. aeruginosa*) and two fungi (*C albicans* and *C tropicalis*). This research confirmed the results obtained by Ott et al. [49] finding to be effective only against Gram-positive bacteria. Indeed complex **127** is the most effective compound against *S. aureus* with a MIC of 6.25 µgmL^{-1}, and complex **128** displayed the highest activity against the fungal strains with a MIC of 6.25 µgmL^{-1}.
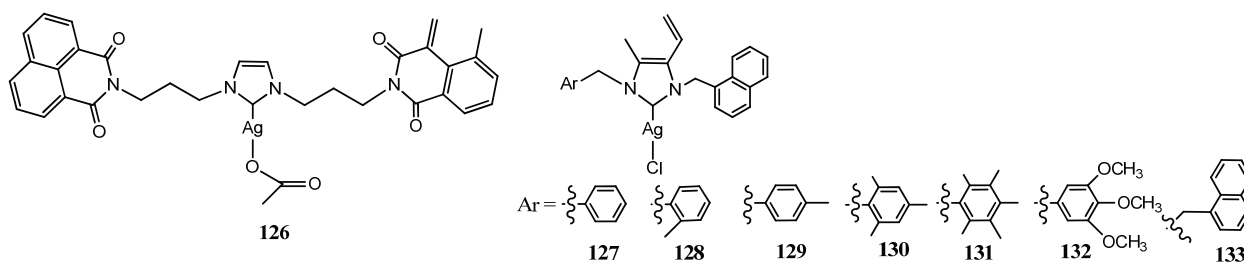
Figure 7. Structures of NHC–silver complexes bearing naphthalil group.

3.5. NHC–Silver Complexes Bearing Electron Withdrawing Substituents

Stability of Ag(I)–NHC complexes can be improved by the use of electron withdrawing groups at the 4 and 5 positions of the imidazolin-2-ylidene ligand (Figure 8). Youngs and co-workers designed three Ag(I)-NHC acetate complexes based on 4,5,6,7-tetrachlorobenzimidazole (**134–136**) [52]. The benzimidazole allows to add two more of the sigma-withdrawing π-donating chlorine atoms than imidazole increasing the stability of the NHCs. These complexes proved highly efficacious with MICs ranging from 0.25 to 6 µg mL^{-1}. The addition of a hydroxyethyl substituent in **135** increase the relative water solubility. It was the best inhibitor on growth of the silver-resistant J53 + pMG101 *E. coli* strain (MIC 8 µL) while the methylnaphthyl bearing complex **136** exhibited bactericidal activity against silver-resistant bacteria. Asekunomo et al. synthesized three NHC–Ag–NHC complexes containing either an alkyl nitrile or an aryl nitrile. (**137–139**) [53]. They detected that all complexes could effectively bind DNA. Furthermore, the complexes **137–139** in vitro were evaluated against both *E. coli* and *S. aureus* showing moderate antibacterial activity without significantly difference. Very recently, three mono butyronitrile funtionalized benzimidazole Ag(I)–NHC complexes were synthesized by Turker et al. (**140–142**) [54]. Although their antibacterial activities are moderate, they are more active higher against Gram-positive (*S. aureus*, *methicillin-resistant S aureus* and *E faecalis*) strains with MIC in ranging 12.5–100 µgmL^{-1} for **142** than against Gram-negative (*E. coli*, *K. pneumoniae*, *A. baumannii* and *P. aeruginosa*) strains. Moreover, promising results were achieved against the standard fungal *C albicans* and *C. glabrata*.

Carbonyl groups were introduced by Haque et al. that designed two Ag(I)–NHC acetate and NHC-Ag(I)–NHC complexes **143–144** bearing a keto alkyl chain to study the effect of carbonyl group against the proliferation of bacteria [55]. Biological assays results

indicate that both compounds possess a good antimicrobial activity against both *E. coli* and *S. aureus*, with an MIC of 31.25 µgmL^{-1}. Furthermore, all tested compounds cleaved DNA.

Kaloğlu et al. reported the synthesis of eight substituted *N*-(2-(2-ethoxy)phenoxyethyl) benzimidazole Ag(I)-NHC complexes (**145–152**) [56]. These complexes were studied at different temperature by NMR. These investigations have furnished evidence for ligand-exchange equilibria between neutral monocarbene complexes [AgX(NHC)] and ion pairs [Ag(NHC)$_2$][AgX$_2$] (X = halogen) through an associative mechanism. All complexes exhibited good activities against standard bacterial strains (*E. faecalis*, *S. aureus*, *E. coli* and *P. aeruginosa*) and the fungal strains (*C. albicans* and *C. tropicalis*). However, the most lipophilic complex (**151**) was found out as the most active especially against Gram-positive and fungal strains with a MIC of 6.25 µgmL^{-1}. Other most lipophilic complexes **145 148** were active with an effective concentration range of 6.25–25 µgmL^{-1}.
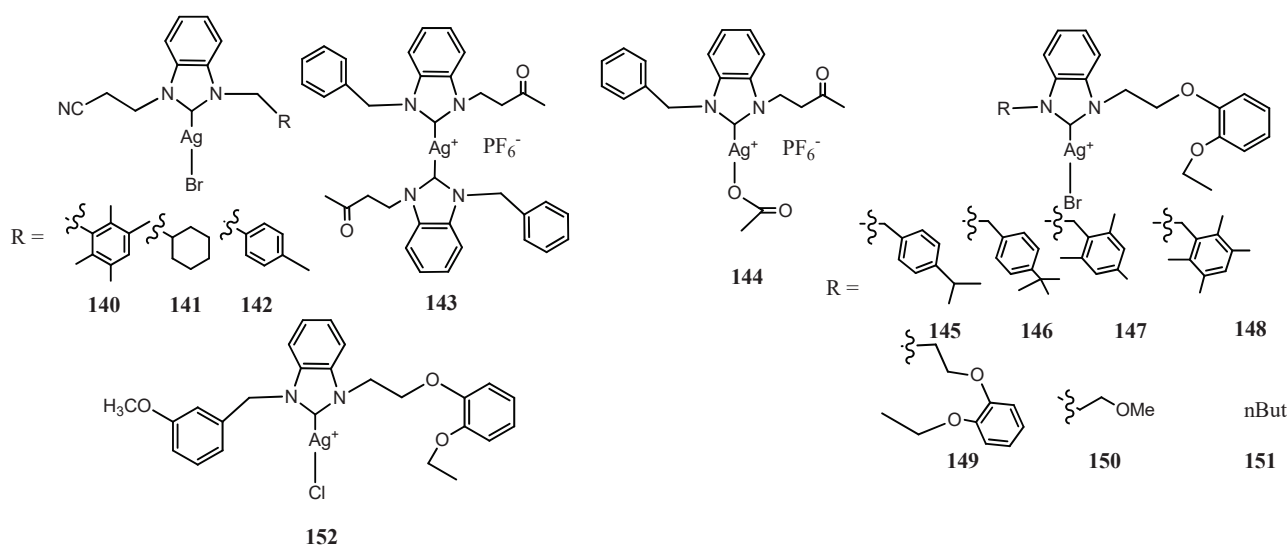
Figure 8. Structures of NHC–silver complexes bearing electron withdrawing substituents.

3.6. NHC–Silver Complexes Bearing Aliphatic Substituents

The relevance of lipophilic groups to favor antimicrobial activity pushed to synthesize a series of highly lipophilic 1-(2-Cycloheptylethyl substituted Ag(I)–NHC complexes bearing aryl and anthracene moieties (**153–156**) (Figure 9) [57]. All compounds performed similar antibacterial and antifungal properties compared to those found in the previous study (MIC: 6.25 µgmL^{-1} for Gram-positive bacteria and fungi strains).

Four allyl substituted Ag(I)–NHC complexes bearing polimethyl-aryl moieties were synthesized by Üstün et al. (**157–160**) [58]. Silver complexes showed higher antimicrobial activity against all microorganisms tested and better antifilm properties than the corresponding salts. Specifically, the **160** complex exhibited anticandidal activity similar to that of Flucanozol and reduced significantly *E. coli* and *C. albicans* biofilm zone. The best behavior of **160** can be attributed to the increase in the number of alkyl groups on benzyl moiety that increases in lipophilicity. Later Tutar et al. expanded the investigation of this class of compounds synthesizing other six allyl-substituted benzimidazole-based Ag(I)–NHC complexes (**161–166**) [59]. All tested compounds showed strong and similar activity against *E. coli* ATCC 25922 at very low concentration (≤3.9 µgmL^{-1}) as compared to ampicillin as well as they displayed the same or stronger activity against the *A. baumannii* isolate with MIC values of 15.6–31.25 µg mL^{-1}. The authors claim more efficacies of these compounds versus same strains used by Achar et al. [60]. All compounds inhibited the formation of *E. coli*, *K. pneumoniae*, *E. faecalis* and *A. baumannii* biofilms at sub-MIC concentrations in the range 30–90% and *C. albicans* biofilm formation by 38–53%. In the same year, a parallel paper reported other four 1-allyl 5,6-dimethylbenzimidazole Ag(I)–NHC complexes with methyl substituted aryls in different position compared to *t*but substituted (**167–170**) [61]. The

best performance against all microorganisms was detected for **170** with MIC < 1.9 μgmL^{-1}. Moreover, in this case NHC salts showed moderate antifungal and antibiofilm activity while the others silver complexes had anyway strong antimicrobial activity with MIC values <3.9–15.6 μgmL^{-1} without relevant difference changing the methyl position. In particular, all methyl functionalized benzoimidazole silver complex increases the activity against *C. albicans* (<1.9 μgmL^{-1}) compared with a similar compound previously reported unfunctionalized benzoimidazole silver complex (7.8 μgmL^{-1}).
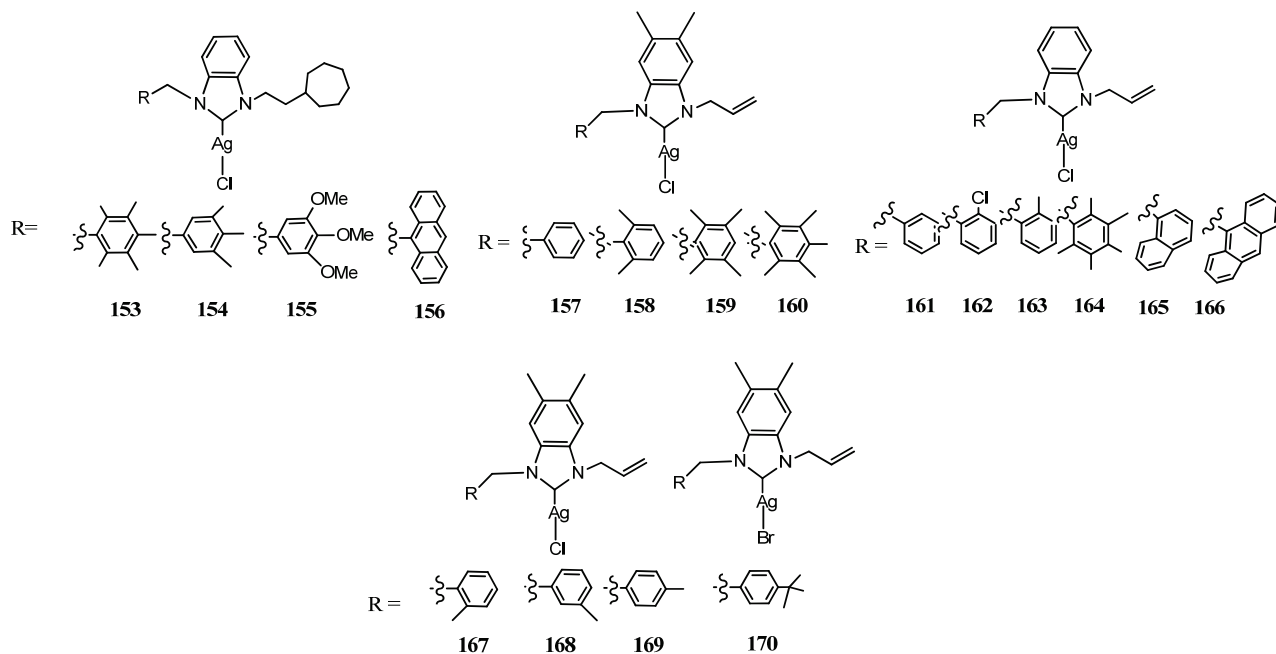
Figure 9. Structures of NHC–silver complexes bearing aliphatic substituents.

3.7. NHC–Silver Complexes with Nitrogenous Substituents

Mnasri et al. prepared silver complex functionalizing non-symmetrical benzoimidazole ring with diisopropylamino)ethyl or pyrrolidin-1-yl groups and the other nitrogen with a polymethyl substituted benzyl (**171–176**) (Figure 10) [62]. The authors designed these ligands to evaluate the effect of steric hindrance on Ag(I)-NHC complexes. It has been found that the complexes were antimicrobially active with MIC values between 0.24 and 62.5 μgmL^{-1} and showed higher activity than the free ligand. Results indicated that the presence of sterically bulky groups directly grafted on the nitrogen atom of the benzimidazol-2-ylidene ligand has a positive effect on the antimicrobial activity. In particular the silver complexes **173** and **171**, displayed inhibition of bacterial growth with MICs of 0.24 and 1.95 mgmL^{-1}, respectively, against *L. monocytogenes* ATCC 19117 and *S. typhimurium* ATCC 14028.

Recently, Muniyappan et al. synthesized silver complexes bearing picolyl and benzyl linked biphenyl NHC ligands (**177–179**) [63]. These biphenyl NHC ligands showed the inherent sigma donating properties through proton-coupled carbon NMR spectroscopy. All silver complexes showed comparable antibiotic activity against *P. aeruginosa* as that of reported antibiotic lead compound **32** and enhanced compared to previous reported *i*butyl substituted benzimidazole Ag(I)–NHC complexes and to the reported phenyl-substituted NHC precursors. All complexes showed promising antimicrobial activity against Gram-positive (*S. aureus* IE903) and Gram-negative (*P. aeruginosa* E322) bacterial strains cultured from the human clinical isolates.
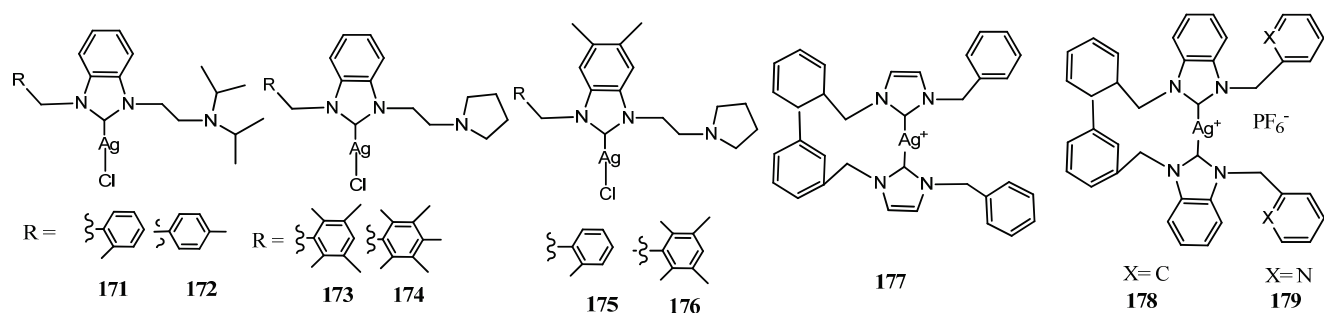
Figure 10. Structures of NHC–silver complexes with nitrogenous substituents.

3.8. Unusual NHC–Silver Complexes

Knowledges have been increased investigating non-classical NHC silver compounds in the last years. Very recently Sanchez et al. prepared {Ag[NHCMes,R]}$_n$ polymeric complexes (**180–184**) (Figure 11) [64]. In the solid state, **180** is a one-dimensional coordination polymer, in which the Ag$^+$ cation is bonded to the carbene ligand and to the carboxylate group of a symmetry-related Ag[NHCMes,H] moiety. Antimicrobial properties of these complexes were evaluated versus Gram-negative bacteria *E. coli* and *P. aeruginosa*. From observed MIC and Minimum Bactericidal Concentration (MBC) values, complex **182** showed the best antimicrobial properties (eutomer), which were significantly better than those of its enantiomeric derivative **182** (distomer). Additionally, analysis of MIC and MBC values of **182–184** reveals a clear structure–antimicrobial effect relationship. Antimicrobial activity decreases when the steric properties of the R alkyl group in {Ag[NHCMes,R]}$_n$ increase.

Di Napoli et al. synthesized five silver complexes having bidentate NHC ligands **185–189** [65]. Four of these ligands were neutral, having an alcohol group on alkyl substituent of one of the two nitrogen atoms of the heterocycle [NHC–OH], the fifth, having a ligand alkoxide, is mono-anionic [NHC–O$^-$]. All the synthesized complexes have a significant antibacterial activity against *E. coli* and *B. subtilis* (MIC 5–50 µgmL^{-1}). Probably, the pincer effect of both [NHC–OH] and [NHC–O$^-$] ligands stabilizes these compounds slowing the cation release.

Prencipe et al. tested acridine scaffold and detailed nonclassical pyrazole derived Ag(I)–NHC neutral (**190**, **192–193**) and NHC-Ag(I)–NHC cationic complexes (**191**, **194**) [66]. Their inhibitor effect on two Gram-negative bacteria: *E. coli DH5α* and *P. aeruginosa* PAOI and two Gram-positive bacteria: *S. aureus* 6538P and *B. subtilis* PY79 was evaluated. The acridine attached to imidazole core in neutral and cationic complexes has shown effectiveness at extremely low MIC values (less than ≤1 µM). Although pyrazole NHC silver complexes were less active than the acridine Ag(I)–NHC (≤50 µM), they represent the first example of this class of compounds with antimicrobial properties. Another unusual NHC ligands is derived from 1,2,4-triazoles. The presence of a third peripheral nitrogen of the heterocyclic ring induces significant differences compared to imidazole-based ligands. This modification causes dissymmetry, and reduces the strength of sigma donation whilst increasing the π-accepting properties of these ligands and increase the acidity of the pre-carbenic C5 proton.

Mather et al. synthesized a series of Ag(I) (**195–202**) complexes of 1,2,4-triazolylidene and imidazolylidene based NHC ligands [67].

The antibacterial activity has been evaluated providing a direct comparison between the influence of 1,2,4-triazolylidene versus imidazolylidene ligands on these properties. All complexes were not active against Gram-positive bacteria strains while they show antibacterial properties against Gram-negative. The lowest MIC values (2–4 µg mL^{-1} and 2 µg mL^{-1}) were found for **200** and **201** against *A. baumannii* and the magnitude of these values were similar to the antibiotic colistin (≤2 µg mL^{-1}).

The complexes bearing dimethyl and diethyl substituents **199**, **200** and **201** were found to have greater levels of antibacterial activity in comparison to the phenyl substituted

complexes **196** and **197** while the 1,2,4-triazolyle and imidazole rings do induce clear and relevant difference. Complexes **200** was investigated to determine the propensity to develop bacterial resistance, and no resistance was observed for *A. baumannii*.

Table 1. Best NHC–silver inhibitors of each reference.

Entry	N° of Tested Strains	Highest Activity Against	Concentration	ZoI or MIC or CA *	Ref.
1, 7	5	*E. coli*	4 mg mL^{-1}	MIC	[27]
14	5	*S. aureus*	1 mg mL^{-1}	MIC	[27]
32	7	*M. smegmatis*	5 mg mL^{-1}	MIC	[31]
42	2	*S. aureus*	7 mm	CA	[35]
47, 51	2	*S. aureus*	6.25 μM	MIC	[37]
57	2	*S. aureus*	25 μM	MIC	[38]
62	2	*S. aureus*	14 mm at 12 μL	ZoI	[39]
72	5	*E. faecalis–C. albicans*	14 μM	MIC	[40]
77	4	*All strains*	6.25 μg mL^{-1}	MIC	[41]
83, 86, 87	6	*C. tropicali–C. albicans*	25 μg mL^{-1}	MIC	[42]
89	11	*S. aureus*	19 mm at 50 μL	ZoI	[43]
96	2	*S. aureus*	17 mm at 2.85 nM	ZoI	[44]
102	2	*S. aureus*	17 mm at 2.85 nM	ZoI	[44]
107	6	*S. aureus–E. coli*	8 μgmL^{-1}	MIC	[45]
110	6	*E. coli*	8 μgmL^{-1}	MIC	[45]
115–116	6	*S. aureus–E. coli*	16.0 μgmL^{-1}	MIC	[46]
120–121	6	*S. aureus–E. coli*	16.0 μgmL^{-1}	MIC	[46]
123–124	2	*S. aureus*	12.5 μgmL^{-1}	MIC	[47]
125	4	*S. aureus–P. aeruginosa*	12 mm at 9 μL	ZoI	[48]
126	6	*B. subtitis*	16.0 μgmL^{-1}	MIC	[49]
127	6	*S. aureus*	6.25 μgmL^{-1}	MIC	[51]
128	6	*C. albicans–C tropicalis*	6.25 μgmL^{-1}	MIC	[51]
135	8	*E. coli J53 + pMG101*	8 μgmL^{-1}	MIC	[52]
137	2	*S. aureus*	13.5 mm at 25 μgmL^{-1}	ZoI	[53]
142	9	*S. aureus*	12.5 μgmL^{-1}	MIC	[54]
143–144	2	*S. aureus–E. coli*	31.25 μgmL^{-1}	MIC	[55]
151	6	*E. faecalis–S. aureus*	6.25μgmL^{-1}	MIC	[56]
153–156	6	*C. albicans–C tropicalis*	6.25 μgmL^{-1}	MIC	[57]
153–156	6	*E. faecalis–S. aureus*	6.25 μgmL^{-1}	MIC	[57]
158, 160	4	*E. faecalis–S. aureus–E. coli*	7.8 μgmL^{-1}	MIC	[58]
161–166	6	*E. coli*	≤3.9 μgmL^{-1}	MIC	[59]
170	5	*S. aureus*	<1.9 μgmL^{-1}	MIC	[61]
173	6	*L. monocytogenes*	0.24 mgmL^{-1}	MIC	[62]
177–179	3	*P. aeruginosa E322*	10 ppm	MIC	[63]

Table 1. *Cont.*

Entry	N° of Tested Strains	Highest Activity Against	Concentration	ZoI or MIC or CA *	Ref.
182	2	*P. aeruginosa*	39 µM	MIC	[64]
188–189	2	*E. coli–E.subtitis*	5 µgmL^{-1}	MIC	[65]
192–194	4	*All Strains*	<1µM	MIC	[66]
200–201	4	*A. baumannii*	2 µg mL^{-1}	MIC	[67]

* ZoI (inhibition zone), CA (Clearance Area), MIC (minimum inhibitory concentrations).
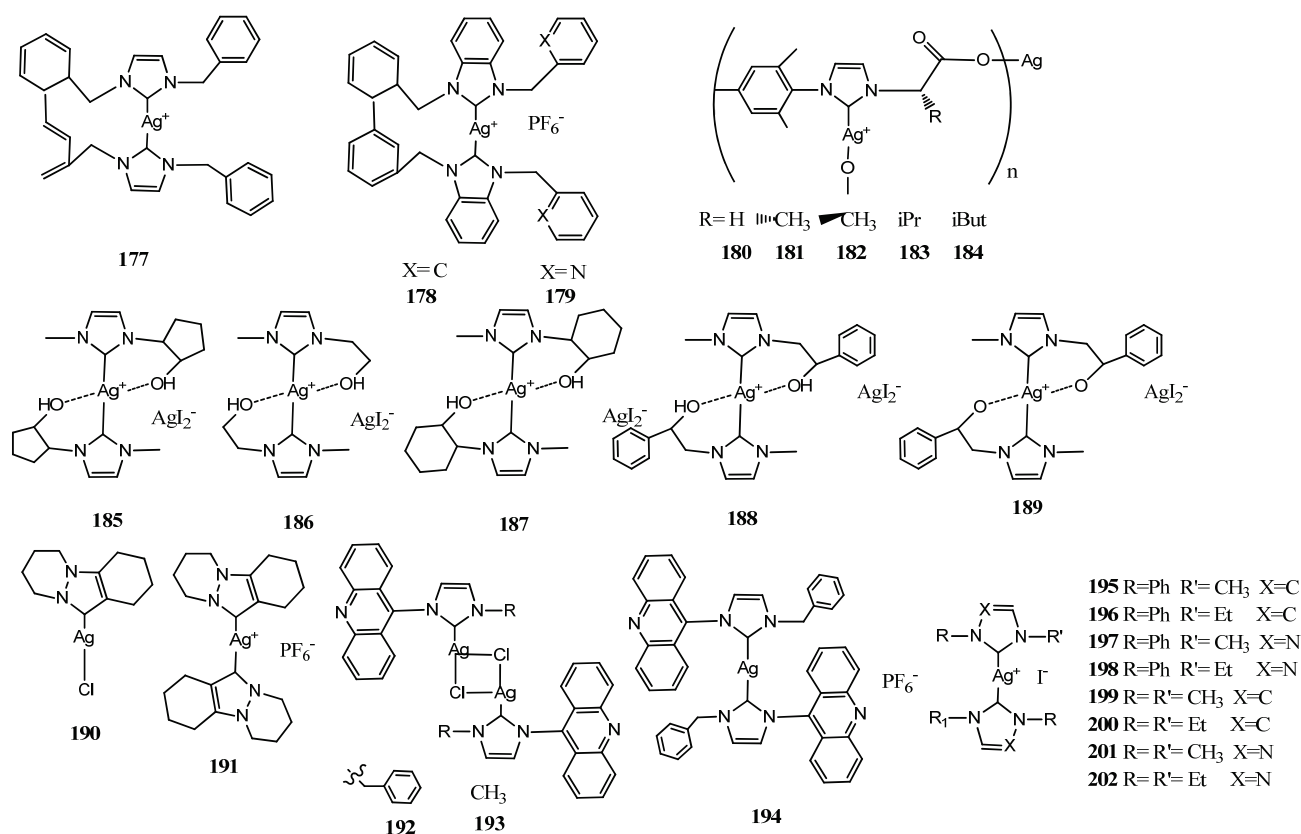
Figure 11. Structures of unusual NHC–silver complexes.

4. NHC–Silver Complex with Ligand in Dual Activity

A class of complexes was designed to exploit the synergic activity of silver cations and the ligand with antibiotic properties moiety. All structures of reviewed complexes in this section are in Figure 12 and the antimicrobial data of the most active inhibitor are in Table 2.

Table 2. Best dual target and binuclear NHC silver complexes inhibitors of each reference.

Entry	N° Strains	Highest Activity Against	Concentration	ZoI or MIC or % of G *	Ref.
203	36	*E. coli–Burkholderia*	1 µg mL^{-1}	MIC	[68]
210	6	*E. faecalis–S. aureus*	25 µgmL^{-1}	MIC	[69]
210	6	*C. albicans–C tropicalis*	25 µgmL^{-1}	MIC	[69]
212–216	6	*P. aeruginosa*	8 µgmL^{-1}	MIC	[70]

Table 2. *Cont.*

Entry	N° Strains	Highest Activity Against	Concentration	ZoI or MIC or % of G *	Ref.
212	6	*P. aeruginosa*	24 mm at 12 μL	ZoI	[70]
217, 220	6	*P. aeruginosa*	8 μgmL^{-1}	MIC	[71]
231–236	4	*S. aureus–E. coli*	16 μgmL^{-1}	MIC	[72]
243–245	2	*E. coli*	8 μgmL^{-1}	MIC	[60]
253	3	*S. aureus–E. coli*	5.85 μgmL^{-1}	MIC	[73]
255	2	*S. aureus*	6.25 μmolL^{-1}	MIC	[74]
263–264	7	*All Strains*	>95%	% of G	[75]
271, 275	5	*E. coli*	6.25 μgmL^{-1}	MIC	[76]
271	5	*P. aeruginosa*	6.25 μgmL^{-1}	MIC	[76]
278–279	2	*E. coli–S. aureus*	27.0 mm at 100μL mL^{-1}	ZoI	[77]
284	2	*E. coli–S. aureus*	12.5 μgmL^{-1}	MIC	[53]
285	8	*S. aureus–B. subtilis*	15.7 μgmL^{-1}	MIC	[78]
288–293	2	*E. coli and S. aureus*	8 ± 1 mm at 9 μL	ZoI	[79]
295–296	2	*E. coli and S. aureus*	13 ± 0.6 mm at 6 μL	ZoI	[80]
302	2	*E. coli–S. aureus*	12.5 μM	MIC	[81]
305	4	*M. brunensis*	15 ± 0.9 μgmL^{-1}	MIC	[82]
308	3	*S. aureus*	2.09 μM	MIC	[83]
310	2	*S. aureus*	0.382 μgmL^{-1}	MIC	[84]
316	2	*S. aureus*	20 ± 1 mm at 12 μL	ZoI	[85]
317	2	*E. coli*	1.56 μM	MIC	[86]
322	2	*S. aureus*	20 ± 1 mm at 12 μL	ZoI	[86]

* Percentage of growth.

Caffeine is a xanthine derivative; it is a good candidate as carrier molecule for the delivery of silver cations to the lungs. Young and co-workers introduced a methyl group in the structure of imidazole moiety of caffeine to synthesize NHC [68]. This complex **203** exhibited high in vitro antimicrobial efficacy against a broad spectrum of highly resistant respiratory pathogens including members of the *Burkholderia cepacia* complex and against *E. coli* with MIC values as low as 1 μgmL^{-1}. The addition of hydroxyl such as a hydroxyethyl group on methylcaffeine appears to greatly enhance the water solubility of the resulting silver carbene complex favoring the use in spray for future treatment of virulent and multidrug-resistant (MDR) pulmonary infection [87]. The coumarin derivative class is possible to evaluate for their antibiotic properties. Antimicrobial coumarin derivatives, such as novobiocin, clorobiocin and coumermycin A$_1$, exert their antibacterial activity by inhibition of the type II DNA topoisomerase DNA gyrase [88]. Karatas et al. synthesized eight Ag(I) complexes coordinate by NHC ligands which tethered coumarin group (**204–211**) [69]. The cationic NHC–Ag–NHC complexes have a structure such as [AgL$_2$]$^+$[AgCl$_2$]$^-$. The salts and the silver complexes were evaluated against two Gram-negative bacteria (*E. coli* and *P. aeruginosa*), two Gram-positive bacteria (*S. aureus* and *E. faecalis*) and two fungal stains (*C. albicans* and *C. tropicalis*). The results of this study displayed that addition of coumarin to the NHC scaffold did not increase antibacterial and antifungal activities significantly. More relevant is the presence of naphthyl group (**210**) that induces the highest activity with an MIC of 25 μgmL^{-1} for Gram-positive and fungal strains. After this disheartening result Achar et al. studied the behavior of five 6-chlorocoumarin NHC–Ag–NHC complexes,

with different *N*-alkyl groups (**212–216**) [70]. The complexes were evaluated against two Gram-positive bacteria (*S. aureus* and *B.subtitis*) and four Gram-negative bacteria (*E. coli*, *P. aeruginosa*, *S. typhi* and *S. sonnei*). Against these bacterial strains, salts did not show any activity with a MIC above $128 \mu gmL^{-1}$. However, the corresponding silver complexes demonstrated moderate to high antibacterial activity in the range 7 ± 1–12 ± 1 and 7 ± 1–25 ± 2 mm diameter of zone of bacterial growth inhibition against *S. aureus* and *E. coli*, respectively. This activity of complexes in the case of *E. coli* is almost two-fold higher than the antibacterial potentials of benzimidazolium salts. The complex with an isopropyl moiety attached to imidazole **212** core exhibited the highest bioactivity against *P. aeruginosa* (MIC = 8 μgmL^{-1} and ZoI= 24 ± 1 mm). In a following study fourteen 6-methylcoumarin-substituted NHC–Ag–NHC (**217–223**) and 6-methylcoumarin-substituted Ag(I)-NHC acetate (**224–230**) complexes, with different *N*-alkyl groups attached to their imidazole core, were synthesized [71]. Tested against the same strains, all the complexes were found inactive in the case of *B. subtilis*, *S. typhi* and *S. sonnei*. However, it was found that methyl and butyl bearing imidazole NHC–Ag–NHC complexes (**217**, **220**) showed exceptional activity against *P. aeruginosa* with a MIC of 8 μgmL^{-1}. This activity is comparable to that displayed by the 6-chlorocoumarin. Furthermore, no correlation could be drawn with increasing steric bulk on the NHC donors and the observed activity. However, NHC–Ag–NHC complexes displayed better results than their acetate counterparts. To explore the impact of different coumarin substituted NHC ligand backbones, the same authors synthesized silver complexes with a series of structurally related ether–functionalized imidazolium and benzimidazolium hexafluorophosphate salts bearing 6–methylcoumarin, 6–chlorocoumarin and 5,6–benzannulated coumarin substituents (**231–242**) [72]. In antibacterial evaluations, silver complexes displayed promising activity with the MIC values in the range 8–64 μgmL^{-1} against *S. aureus*, *B. subtilis*, *E. coli* and *S. typhi*, while the corresponding salts were almost no activity. Note that no appreciable differences were detected tuning the substituents on coumarin whereas generally the cationic complexes (**231–236**) were more active than Ag(I)–NHC complexes (**237–242**). The same group, following their studies on coumarin derivatives, prepared two different series of pro-ligands using 2–bromomethylbenzonitrile and substituted 4–bromomethylcoumarin derivatives to functionalize the imidazole and benzoimidazole ring. (**243–250**) [60]. The pro-ligands and the corresponding silver complexes were evaluated for antibacterial activity against Gram-positive (*S. aureus*) and Gram-negative bacteria (*E. coli*). In these series the salts were totally inactive against both the bacterial strains tested with the MIC being more than 128 μgmL^{-1}, whereas corresponding Ag(I)–NHC complexes exhibited against *E. coli* very significantly value of MIC of 8 μgmL^{-1} except for 7,8 benzosubstituted. Conversely, benzimidazole derived silver complexes having methyl– and chloro–coumarin substituents displayed MIC of 32 μgmL^{-1} against *S. aureus*. Interestingly, all benzimidazole derived silver complexes demonstrated a potential antibacterial activity against *E. coli* with a MIC of 8 μgmL^{-1}.

Yildirim et al. functionalized NHC ring tethering a morpholinoethyl moiety [73]. The morpholine ring is present in many antibiotics such as linezolid used for treating infections caused by Gram-positive bacteria, and other derivatives are tested, such as antibacterial [89]. The NHC salts were functionalized with three N-alkyl groups with different steric hindrance and electro-donating and H-bonding properties. The three Ag(I)–NHC complexes (**251–253**) were screened against *E. coli*, *S. aureus* and *C. albicans* with a MIC ranging from 5.85 to 44.4 μgmL^{-1}. These values were comparable with those recorded treating with imidazole salts. The lowest MIC values were found against bacteria strains for 3-hydroxypropyl substituted imidazole ring whereas the bulkiest imidazole ring showed the best activity *C. albicans*. These outcomes suggest that the alkyl groups, which contain bulky (isopropyl), electro-donating (propyl) and

H-bonding (hydroxypropyl) wingtip on the imidazole ring, may play an important role in the antimicrobial activity.

Aher et al. tested morpholine containing silver complexes tuning the side chain to evaluate the possible changes in antimicrobial effects. (**254–258**) [74]. The compounds **256** and **255** with butyl and methyl side chain in addition to the morpholine moiety more than other compounds inhibited the bacterial growth with MIC of 12.5 and 6.25 μmolL^{-1} against *S. aureus*, respectively, and 50 μM against *S. enterica* with an efficient growth inhibition up to 21 days with disruption of cell wall as monitored by SEM analysis. The Ag–NHC had shown enhanced bactericidal effects due to the synergistic effects of NaCl which increase solubility product for anionic AgCl$_2$$^-$.

Recently Belhi et al. synthesized four novel morpholinethyl Ag(I)–NHC complexes (**259–262**) [90]. The MIC of the 1,3-dialkyl-5,6-dimethyl-benzimidazolium salts and their complexes was determined for *E. coli*, *P. aeruginosa*, *S. aureus*, *C. glabrata* and *C. albicans* in vitro through BMD (Broth Microdilution). Although all Ag(I)-NHC complexes were active, the complex **262** exhibited a significant broad-spectrum antimicrobial activity.

Patil et al. selected 1,3–benzoxazole and 1,3–dioxolane as substituent on N atom to a series of NHC–precursors and their corresponding Ag(I) complexes [75]. Both 1,3–benzoxazole and 1,3–dioxolane derivatives have been previously studied for their pharmaceutical role as moiety present in wide number of drugs. Four dioxolane **263–266** and four benzoxazole **267–270** derivatives silver carbene were synthesized. The benzoxazole group in NHC-Ag(I)–NHC was able to coordinate with his nitrogen another Ag cation producing a binuclear silver complex (**269–270**). This structure was confirmed by X-ray crystallography. Antimicrobial properties were evaluated against four Gram-negative bacteria (*E. coli*, *K. pneumoniae*, *A. baumannii* and *P. aeruginosa*), one Gram-positive bacteria (*S. aureus*) and two fungi (*C. albicans* and *Cryptococcus neoformans*). The benzimidazolium hexafluorophosphate salts and the silver(I) complexes showed comparable antimicrobial activity in the range 0.2–26.90% of bacterial growth inhibition and fungal growth inhibition in the range 126.30–49.70%. However, the 1,3–dioxolane Ag(I)-NHC acetate **263–264** complexes achieved extraordinarily growth inhibition of all the bacterial (>95%) and fungi (>97) strains.

More recently, Lasmari et al. synthesized six 1,3–dioxolane NHC derivatives functionalizing the benzoimidazole ring with substituted benzyl (**271–276**) [76]. All complexes were screened for their antibacterial, antifungal and anti-cholinesterase activities exhibiting moderate antibacterial and antifungal activities, generally more active than corresponding NHC salts. The best inhibitor of bacterial growth was found the compound **275** bearing the anthracen-9-ylmethyl functionalized ligand with a value of MIC ranging between 6.25–12.5 μgmL^{-1}. Furthermore, the complex **271** was 2 times more active against *P. aeruginosa* than the standard drug Ampicillin with MIC value 6.25 μgmL^{-1}. The compounds **272** and **273** gave the best inhibitory activity against *C. albicans* fungi with MIC values 12.5–25 μgmL^{-1}. The results proved that the compounds indicated moderate to excellent activity against both acetylcholinesterase (AChE) and butyrylcholinesterase (BuChE). It was found that most of the complexes displayed good AChE and BuChE inhibitory activities. In particular, **273** and **275** complexes were the most powerful inhibitors with IC$_{50}$ values of 8.56 $\pm$ 1.17 μM and 5.05 $\pm$ 0.30 μM against AChE and BChE, respectively. Docking studies exposed that these compounds bind manly to the catalytic anionic site (CAS) of the AChE and BChE, respectively.
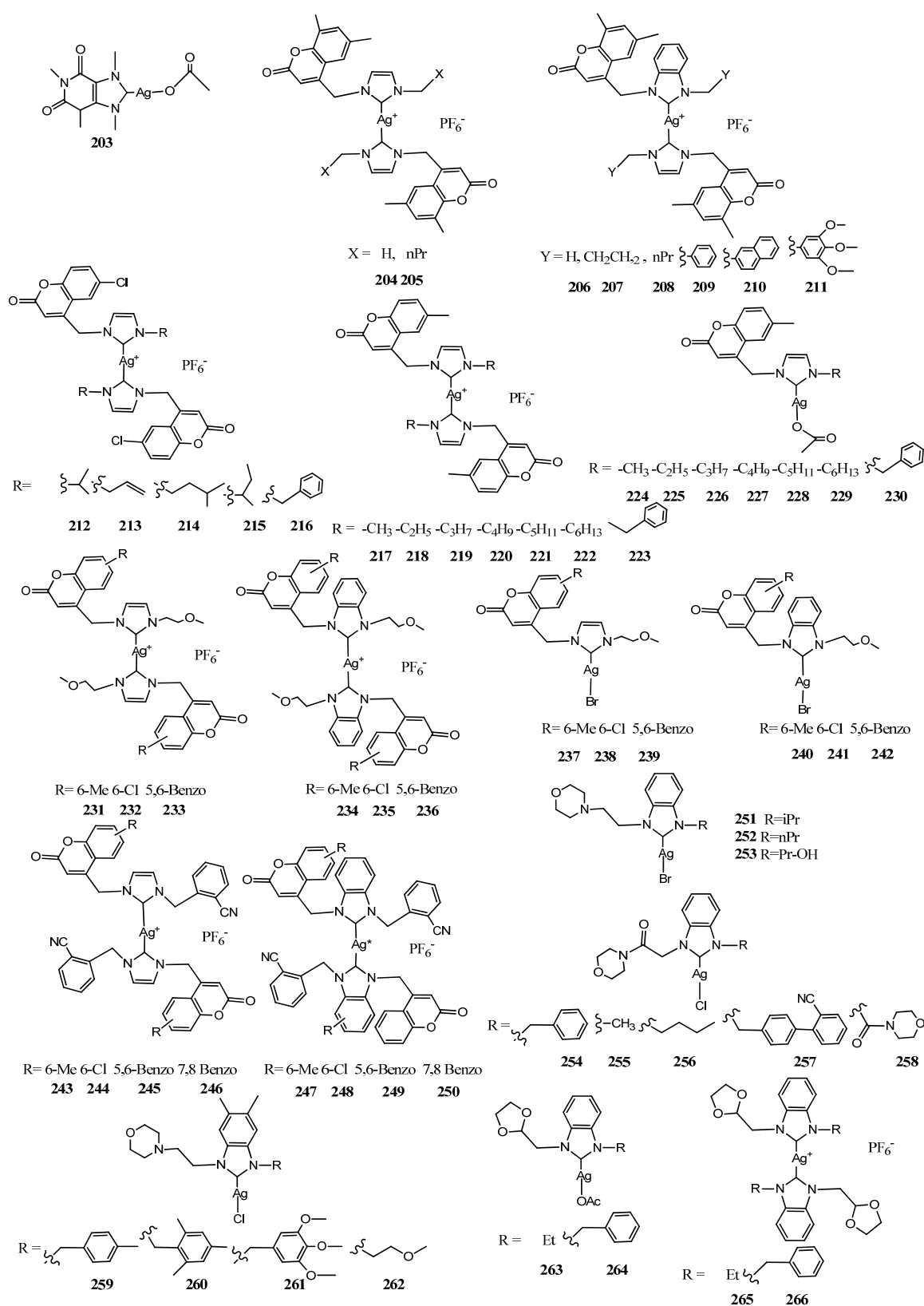
Figure 12. Structures of NHC–silver complexes coordinated by ligands with dual activity.

5. Binuclear NHC–Silver Complexes

In the last decade, ligands bearing two imidazole moieties were designed to coordinate two metal center. These complexes should exhibit higher effectiveness than mononuclear

complexes due to the presence of two metal center. All structures of reviewed complexes in this section are in Figures 13 and 14 and the antimicrobial data of the most active inhibitor are in Table 2. In a first attempt, Haque et al. synthesized a binuclear silver(I) complexes (**277–280**) of allyl and/or alkyl substituted imidazole core of NHCs [77]. The imidazole rings were linked through p-xylyl/2,6-lutidinyl group. The complexes were tested against *E. coli* and *S. aureus* bacterial strains in vitro. The complexes bearing pentyl and hexyl substitution on imidazole (**278–279**), have the major antibacterial activity than propagyl substitution (**277**) with 25.6 ± 0.5, 27.0 ± 0.7 and 26.0 ± 0.8, 27.5 ± 2.0 mm of ZoI against both tested bacteria, respectively with 5 µL solution of 100 µgmL^{-1} concentration. The authors compared to a series of mono-nuclear complexes (**281–283**) [91] exhibiting threefold lesser activity at the same biological conditions against the same bacterial strains. The enhanced activity of binuclear complexes could be ascribed to the higher stability of the complexes due to the presence of two metal centers. This event allows the slow release of silver ions at required sites.

The higher activity of binuclear complexes was demonstrated by Asekunowo et al. [53]. The binuclear Ag(I)-NHC complex **284** complex was compared to **137–139** showing a better binding ability for DNA (Kb = 3.627×10^6). Furthermore, the complex **284** was the most active among the tested complexes on mosquitocidal activity against the dengue vector *Aedes albopictus* affecting the developmental progression from larvae to adult stage. Moreover, binuclear complex **284** outperformed the rest, with the lowest MIC value (12.5 µgmL^{-1}) against both *E. coli* and *S. aureus*.

In 2016, Nomiya et al. reported the synthesis, characterization and the structure–activity relationship of three dinuclear Ag(I)–NHC complexes (**285–287**) [78]. Each of the three complexes contains four imidazole rings that are linked by either an *ortho*-xylene or a *para*-biphenyl, which induce stability to the final dinuclear silver complexes in both solution and solid state. The antibacterial activity was not as high as expected. Indeed, the binuclear complexes were evaluated against two Gram-negative bacteria (*E. coli* and *P. aeruginosa*) and two Gram-positive bacteria (*S. aureus* and *B. subtitis*), as well as four fungi (*C. albicans*, *S. cerevisiae*, *A. brasiliensis [niger]* and *P. citrium*), with MIC ranging from 15.7 to >1000 µgmL^{-1}. The most effective binuclear Ag(I)-NHC compound **285** was the complex with a planar central spacer unit with MIC ranging from 15.7 to 125 µgmL^{-1}. Therefore, the activity is dependent on the molecular structure suggesting a SAR.

In the same year, Rizali and co-workers reported six binuclear Ag(I)–NHC complexes liked through an *n*-butyl chain with disappointing biological results, (**288–293**) [79]. Indeed all complexes screened against *E. coli* and *S. aureus*, showed activity minor the ampicillin, observing ZoI for *E. coli* and *S. aureus* was approximately 8 ± 1 mm using 9 µL of solution.

The same group designed eight more binuclear Ag(I)–NHC complexes **294–301**, shorting the *n*-butyl chain to an ethyl chain and using *N*-alkyl chain to functionalize instead of *N*-benzyl group to improve the effectiveness [80]. In this case, these small variations induce only a slight increase in the antibacterial activity of the complexes compared to the previously studied compounds. For instance, complex **288** exhibited ZoI of 7 ± 1 mm versus 11 ± 1 mm for complex **298**, when screened against *E. coli*.

In the same year, Rizali and coworkers described the synthesis of three more binuclear Ag(I)–NHC complexes (**302–304**) [81]. The effect of the length of the alkyl linker chain was investigated, using either an ethyl, propyl or butyl chain. The antibacterial activities against *E. coli* and *S. aureus* showed a decreasing pattern with the increasing of the chain length in the bridging subunit. The complex **302** exhibited against both strains a lower MIC value (12.5 µM). This indicates that longer alkyl chain results in less stable complexes probably due to the weaker argentophilic interaction.
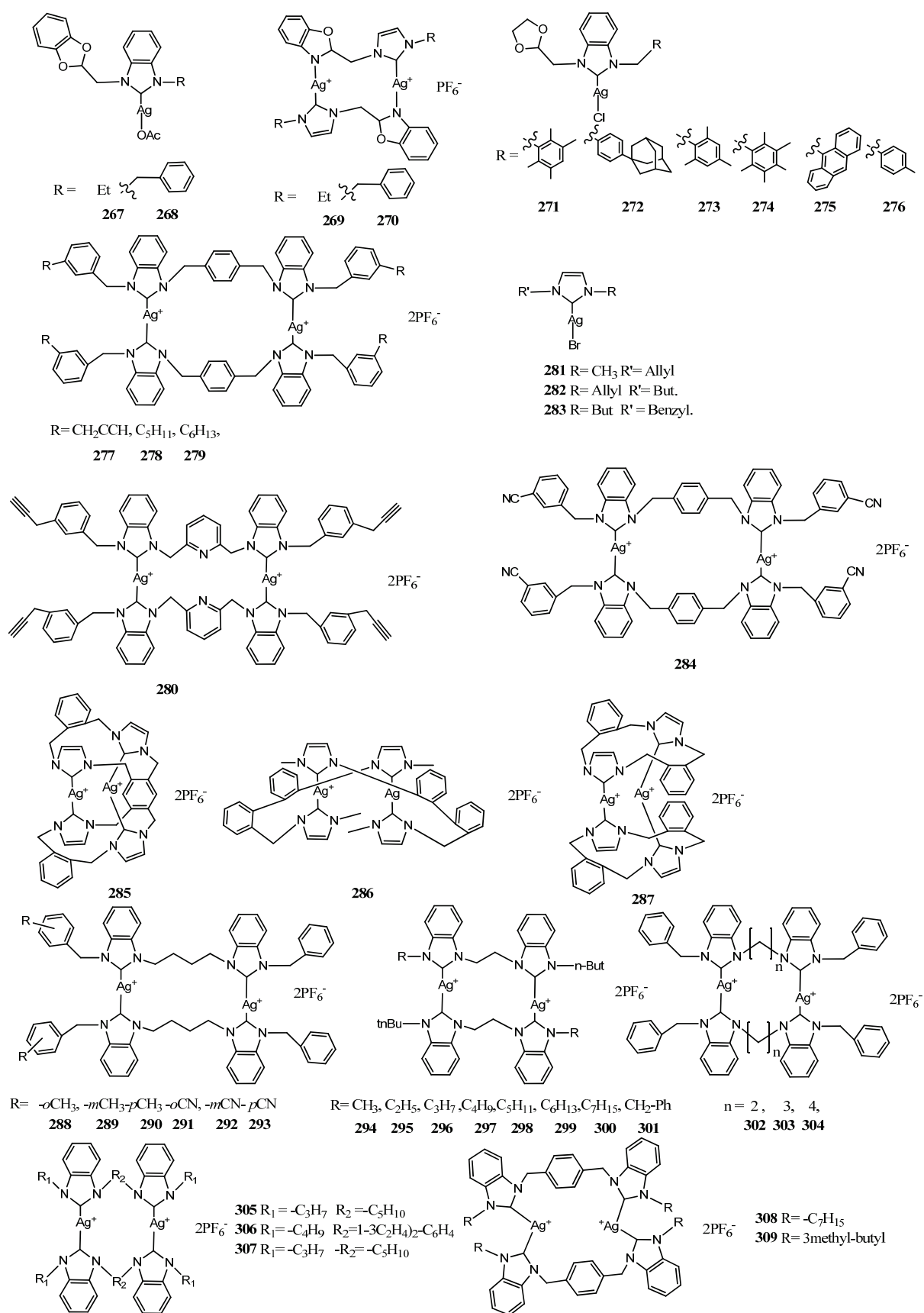
Figure 13. Structures of binuclear NHC–silver complexes.
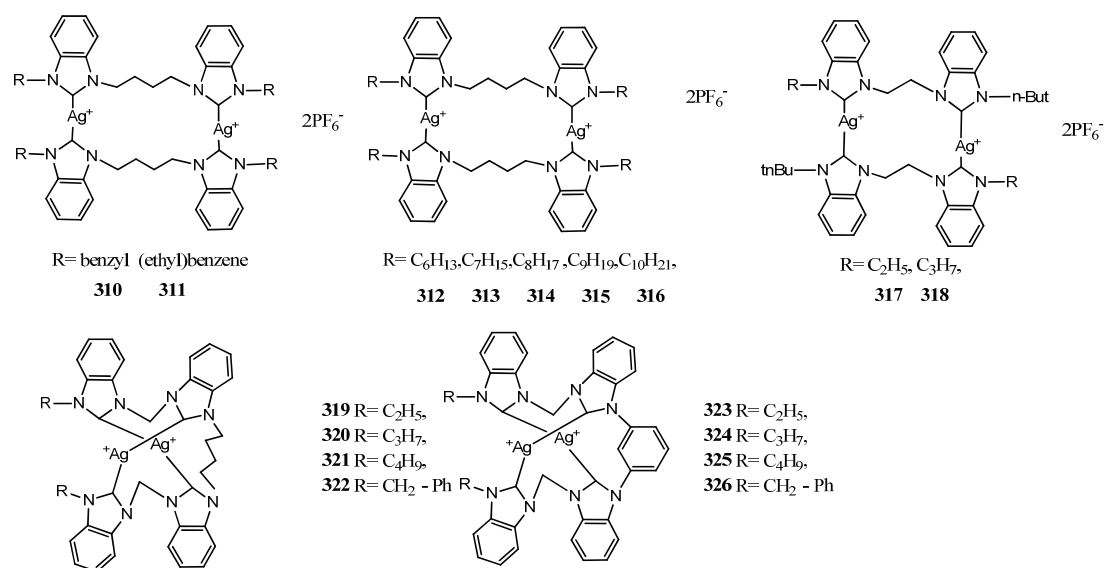
Figure 14. Structures of binuclear NHC–silver complexes.

Iqbal and coworkers designed binuclear Ag(I)–NHC (**305–307**) linked with a longer or branched alkyl chain [82]. The bis Ag(I)–NHC complex in the test in vitro against three bacterial strains (*B. subtillis*, *B. cereus* and *M. brunensis*) showed an increase in the ZoI with values ranging ZoI of 17 ± 1 mm–28 ± 1 mm and MIC 15 ± 0.1–27 ± 1 values compared to their respective ligands as well as standard drug Ciprofloxacin. In general, complexes were more effective against *B. cereus* as compared to *B.subtillis* and *M.brunensis*. All the compounds presented low hemolytic activity (0.51–8.09%) toward erythrocytes therefore they can be employed in preclinical trials resulting no-hazardous for mouse blood cells. Subsequently, expanding the same class, alkyl linkers were substituted with an aryl link [83]. Both synthesized bis Ag(I)–NHC complexes (**308–309**) were tested against three bacterial strains (*S. aureus* and *S. pneumonia* and *E. coli*) finding the MIC value in the range of 2.09–2.35 μg mL^{-1} which was almost in level to broad spectrum standard drug ciprofloxacin and very much better than silver sulfadiazine. More recently, two aryl-substituted bis-benzimidazole binuclear Ag(I)–NHC complexes (**310–311**) were described [84]. Both complexes showed ZoI for the Gram-positive (*S. Aureus*) and Gram-negative (*E. coli*) strains, i.e., 18.67 ± 0.58 and 19.83 ± 0.29 mm and 12.5 ± 0.5 and 14.33 ± 0.58 mm for *E. coli*, respectively. Moreover, they show higher ability than their respective salts to inhibit the growth of bacteria at low concentration 0.765 and 0.382 μgmL^{-1} for *S. Aureus* and 3.06 and 1.53 μgmL^{-1} for *E. coli*.

Hussaini et al. synthesized binuclear Ag(I)-NHC (**312–316**)) bearing n-alkyl homologous series with propylene spacers to investigate the effect of lipophilicity [85]. The Ag(I)-NHC complexes exhibit activities with ZoI of 11 ± 1–20 ± 1mm and 9 ± 0–16 ± 1mm using 12 μL of solution against *E. coli* and *S. aureus* respectively. In comparative studies, it was observed that the lipophilicity and biological activities of complexes are in positive correlation for both bacterial strains.

Umie et al. reported two bisbenzimidazol2-ylidenes Ag(I)–NHC and eight open chain tetrabenzimidazol-2-ylidenes Ag(I)–NHC complexes (**317–326**) [86]. All complexes exhibited against *E. coli* (ATCC 25,922) and *S. aureus* (ATCC 12,600) medium to higher ZoI compared to the standard antibiotic, Ampicillin, without enormous differences. There were no obvious difference between the activity of Ag(I)-NHC complexes compared to the silver-tetra-NHC complexes bearing both two Ag$^+$ cations per molecule. Compared to the mononuclear Ag(I)–NHC complexes, they displayed higher activities due to the higher number of Ag$^+$ per molecule, as previously demonstrated. Based on obtained data, *E. coli* depicted the highest resistance against **323** while **322** shows the highest antibacterial activity against *S. aureus*.

6. Encapsulated Nanosystems Silver–NHC Complexes

The controlled and specific release of drugs plays a pivotal role in different medical applications, often avoiding harmful high concentrations and allowing chemicals to carry out their task for a prolonged period. Targeted release of silver cations at infection site for application in vivo is crucial. Despite this consideration, few publications are reported until today. Although the promise results were obtained in vitro against different strains of bacteria, two concerns may arise: the presence of chloride anions and sulfur containing proteins in the bloodstream. The chloride anions may in some cases improve the bioavailability of Ag forming $AgCl_2^-$ more soluble than silver chloride, but in other cases destabilize the complexes favoring the silver chloride precipitation. The thiol group of cysteine can bind the silver preventing to reach the site of infection and macrophages that capture the Ag(I)–NHC. All of these drawbacks can be overcome by encapsulating the complexes in nanosystems. Pulmonary drug delivery is one of the goals. For this purpose, Young and coworkers formulated L-tyrosine polyphosphate nanoparticles LTP NPs [92] (Figure 15). Although the **327** Ag(I)–NHC displayed very low MIC (1 μgmL^{-1}) against *P aeruginosa* and *E. coli* **327**-loaded into LTP NPs still exhibits excellent antimicrobial activity in vitro and in vivo against chronically infected lungs of cystic fibrosis (CF) relevant bacteria *P aeruginosa* with an MIC value of 4 μgmL^{-1}. These nanosystems provide sustained release of the Ag$^+$ cations over the course of several days providing significant survival advantage in mouse infection models with only two doses. Surfactant and polymer micelles have been demonstrated to be an excellent system to deliver hydrophobic drugs forward a precision medicine [93]. The same authors exploited this opportunity [94]. They encapsulated the **327** compound and silver nitrate into the hydrophobic core domain of micelles obtained assembling amphiphilic block copolymers, poly(acrylic acid)-*b*-polystyrene (PAA-*b*-PS). These systems release 50% of silver within ca. 1 day and ca. 80% within 2 days and achieved a plateau with full release by ca. 4 days, a period that would provide a desired effect for therapeutic delivery. Moreover, degradable acetalated dextran (Ac-DEX) nanoparticles were prepared and loaded by a single-emulsion process with **328 [95]**. The bacterial growth kinetics, linked to release silver kinetics from the particles, demonstrated that Ac-DEX- nanoparticle formulations were active against all bacterial strains including the silver-resistant strain, *E. coli J53 + pMG101*. Compared to the free drug, the Ac-DEX nanoparticles were much more easily suspended in an aqueous phase and subsequently aerosolized, thus providing an effective method for pulmonary drug delivery.

A series of anionic dNPs from block copolymers having polyphosphoester (PPE) and poly(l-lactide) (PLLA) block segment were designed and formulated specifically for silver loading into the hydrophilic shell and/or the hydrophobic core as potential delivery carriers for silver acetate or **327** and **135** for applications in direct epithelial treatment and in urinary tract [96]. The complexes were loaded following three different ways: (1) electrostatic interaction with carboxylate groups within the hydrophilic corona; (2) coordination with the two sulfur atoms of the 1,2-dithioether moieties on the side chains of the PPE block segment; and (3) encapsulation by hydrophobic interactions with the hydrophobic PLLA core of the nanoparticle (Figure 15).

The release kinetics of silver-bearing dNPs revealed 50% release at ca. 2.5–5.5 h depending on the type of silver compound. The Ag(I)–NHC in the dNP-based delivery system improved MIC up to 70%, compared with the free complexes, as detected in vitro against 10 contemporary epidemic strains of *S. aureus* and eight uropathogenic strains of *E. coli*.
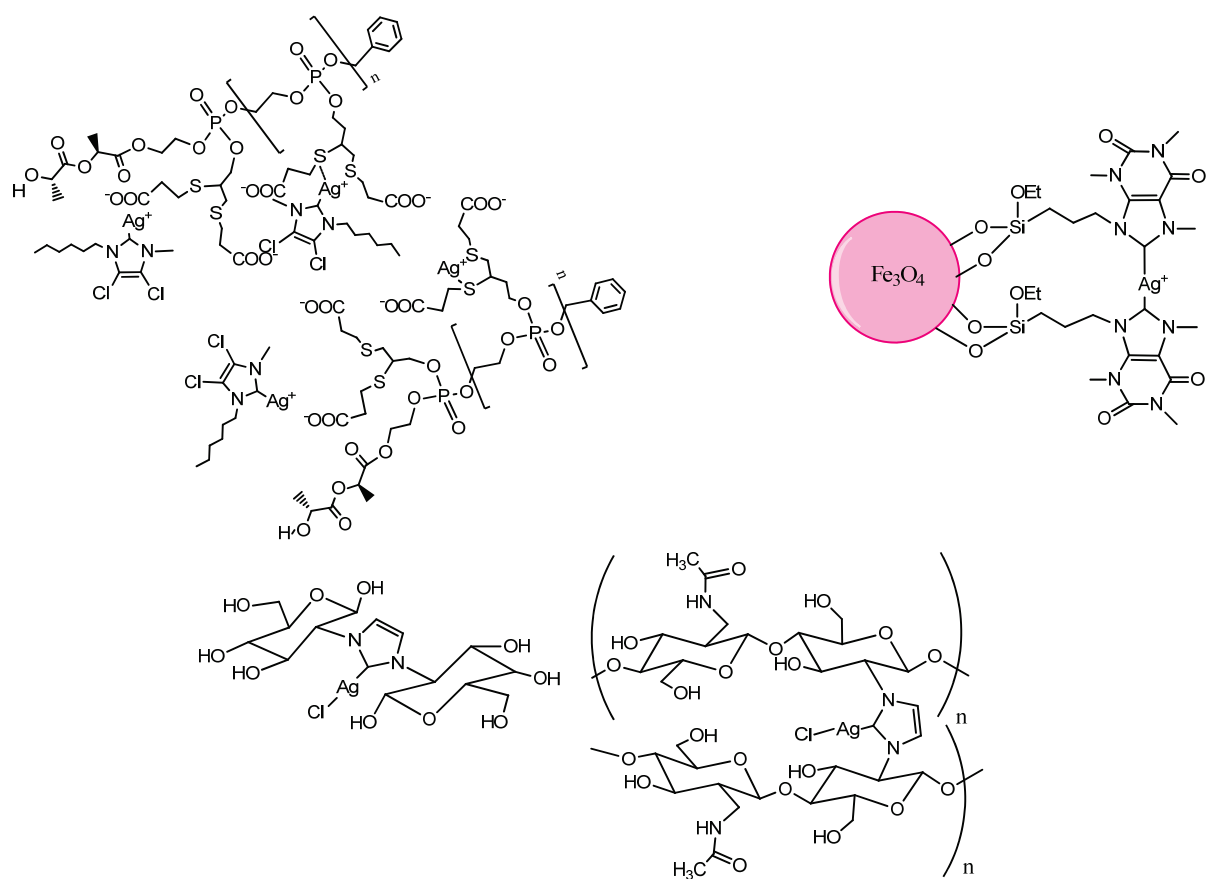
Figure 15. Structures of encapsulated NHC–Silver complexes.

More recently, Necol et al. selected chitooligosaccharides (COS) and its monomer *D*-glucosamine to bind Ag^+ through the NHC bond (Figure 15) [97].

The deacetylation of the starting material is a limiting factor for the synthesis of NHC-Ag-COS, since free amino groups are required for the synthesis of the NHC and consequent introduction of silver. The binding silver to chitosan oligomers and monomer holds and eventually improves the activity of silver in vitro. The activities were compared with that of silver nitrate and the antiseptic polyvinylpyrrolidone iodine (PVP iodine), carrying the active iodine. Based on these results, the use of NHC chitooligosaccharides is a promising approach for improving silver selectivity, achieving a consequent reduction in its toxicity and thus providing better silver formulations for clinical practice.

Very recently a Caffeine based Ag(I)–NHC complex anchored on magnetic nanoparticles (MNP-Caff-NHC@Ag complex) has been prepared by covalent grafting of caffeine on the surface of chloro-functionalized Fe_3O_4 magnetic nanoparticles followed by complexation with silver (I) acetate (Figure 15) [98]. The MNP-Caff-NHC@Ag complex displayed significant antibacterial activity against *E. coli* (NCIM-2832), *S. aureus* (NCIM-2654) and *B. cereus* (NCIM-2703) with zone of clearance between 7 mm and 17 mm.

7. Perspective and Conclusions

After the discovery of penicillin, it seemed that microbial infections would have been outdated. However, the emergence of the resistance to antibiotics has revived the fight against these pathologies. Silver can play a pivotal role in this field. Bioavailability and delivery of silver cations as active specie is the goal of scientists. The exploration of silver complexes is a valid alternative to silver nanoparticles. Complexes may enhance the efficiency by releasing the metal ions into the targeted area of the cell membrane and retain the activity over a long period. Many silver complexes were tested in medicinal applications, but the vast majority contained the NHC system. Some examples of carboxyl complexes,

as well as nitrogen complexes, are reported in the literature [99,100]. Nomiya et al. [99] suggested a mechanism for the antimicrobial activity, mainly determined by solubility, silver transport phenomena and ligand exchange equilibria rather than carboxylic acids coordination. Therefore, NHC ligands were privileged for their versatility, synthetic accessibility and stability.

More of three hundred complexes of NHCs were designed and tested in the last twenty years. The factors affecting antimicrobial activity are identified in Figure 16 as most critical (green), relevant (yellow) and least effective (red).
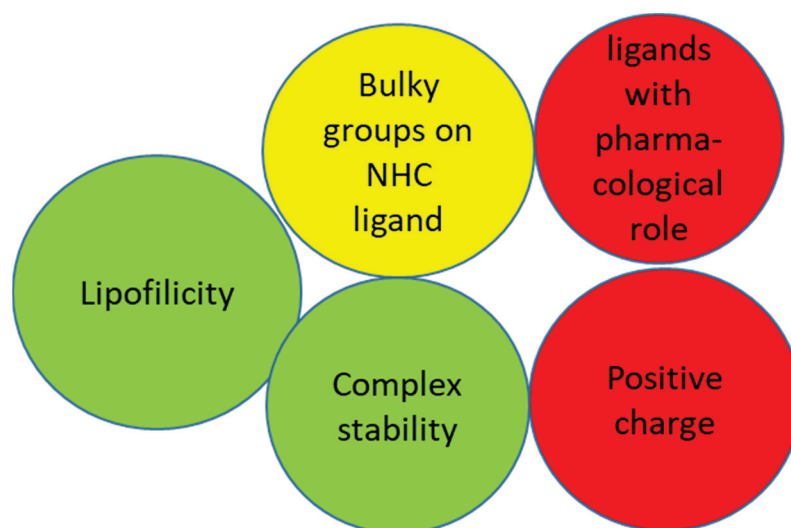
Figure 16. In green: most critical factors, in yellow: the relevant factors and in red: the least effective factors affecting antimicrobial activity.

All achievements agree that complexes must meet two requirements: they should retain their ligands releasing silver cation over prolonged time and ligands should guarantee sufficient lipophilicity. As a lipid membrane surrounds the microbial cell wall, which favors the pathway of fat-soluble materials, the increase in lipophilicity allows penetration of the complex into and across the membrane. Inside the cell they deactivate the active enzyme sites of the microorganisms.

The structure–activity relationships (SAR) are related to the substituents on imidazole or benzoimidazole rings at all positions. Electronic stability and steric hindrance of NHC stabilize the metal-NHC complexes for better bioactivity. The strength of Ag–NHC bond is influenced by the presence of substituent on 4 and 5 imidazole position. However, the presence of electron donor or withdrawal group does not induce significant variations on effectiveness. The lipophilicity can be fine-tuned by a structural versatile substituent attached to the benzimidazole or imidazole ring. Nitrogen's substituents as aryl and alkyl chain length are known to have a noteworthy effect on the bioactivity. All reported assays are in agreement that the amount of complex penetrating into the lipid bilayer is directly proportional to the increase in ligand carbon chain length. Furthermore, the presence of aromatic ring of benzimidazole further enhances their activity due to increased lipophilicity disrupting the function of cellular organelles which consequently results in the obstruction of respiratory and metabolic mechanisms of microbes. Although benzimidazole derivative molecules effectively interact with microbial targets, these ligands seem not play a specific role in antibacterial activity.

After membrane penetration, broad antimicrobial spectrum of Ag(I)–NHC complexes with large number of targets might be attributed to ligand exchange phenomenon with S-(thiols), N-or O-donors at their potential target points.

Therefore, in last years, molecular docking analysis were carried out to predict possible interactions of silver complexes with specific protein targets. These studies provide both

detailed analysis and foresight about the designing of new molecules. The interaction with proteins such as AHL Lactonase, Malate Synthase with the catalytic anionic site (CAS) of the AChE, and BChE can be tested to screen active compounds. However few X-ray or ESI-MS studies are reported on interaction between these targets and Ag(I)–NHC.

Almost all studies confirmed the effectiveness based on silver, whereas azolium salts are inactive. Although many ligands bearing naphthalene or anthracene group are able to intercalate between DNA base, they are inactive, and the efficiency is attributed to silver cation. Moreover, ligands moiety which play pharmacological role such as coumarin or morpholine seemed not significantly increase the antimicrobial properties.

As the type of bacterial strains affects antimicrobial activity in addition to the nature of silver complexes, so general conclusions about the structure–activity relationship to display antimicrobial potential cannot be drawn.

Although few example of silver complexes encapsulation in supramolecular aggregates are reported, this technology can help application in vivo. The high lipophilicity of silver complexes allows polymeric micelles to be loaded into hydrophobic compartment Moreover, these systems can protect the integrity of the complexes avoiding interaction with other proteins in vivo. They allow a slow controlled release to care wounds prolonging the effect of the drug. These achievements are promising for future applications in the fight against microorganism.

References

1. Russell, A.D.; Path, F.R.C.; Hugo, W.B. Antimicrobial Activity and Action of Silver. *Prog. Med. Chem.* **1994**, *31*, 351–370. [CrossRef] [PubMed]
2. Fong, J.; Wood, F. Nanocrystalline silver dressings in wound management: A review. *Int. J. Nanomed.* **2006**, *1*, 441–449. [CrossRef]
3. Von Nägeli, V. Über oligodynamische Erscheinungen in lebenden Zellen. *Deut. Schr. Schweiz. Naturforsch. Ges.* **1893**, *33*, 174–182.
4. Lansdown, A.B.G. A review of the use of silver in wound care: Facts and fallacies. *Br. J. Nurs.* **2004**, *13*, S6. [CrossRef]
5. Fox, C.L., Jr. Silver Sulfadiazine—A New Topical Therapy for Pseudomonas in Burns Therapy of *Pseudomonas* Infection in Burns. *Arch. Surg.* **1968**, *96*, 184–188. [CrossRef] [PubMed]
6. Silver, S. Bacterial silver resistance: Molecular biology and uses and misuses of silver compounds. *FEMS Microbiol. Rev.* **2003**, *27*, 341–353. [CrossRef]
7. Gupta, A.; Maynes, M.; Silver, S. Effects of Halides on Plasmid-Mediated Silver Resistance in *Escherichia coli*. *Appl. Environ. Microbiol.* **1998**, *64*, 5042–5045. [CrossRef] [PubMed]
8. Lansdown, A.B.G. Silver I: Its antibacterial properties and mechanism of action. *J. Wound Care* **2002**, *11*, 125–130. [CrossRef] [PubMed]
9. Eckhardt, S.; Brunetto, P.S.; Gagnon, J.; Priebe, M.; Giese, B.; Fromm, K.M. Nanobio silver; its interactions with peptides and bacteria, and its use in medicine. *Chem. Rev.* **2013**, *33*, 139–148. [CrossRef]
10. Duran, N.; Durán, M.; Bispo de Jesus, M.; Seabra, A.B.; Fávaro, W.J.; Nakazato, G. Silver nanoparticles; a new view on mechanistic aspects on antimicrobial activity. *Nanomed. Nanotechnol. Biol. Med.* **2016**, *12*, 789–799. [CrossRef]
11. Wells, T.N.C.; Scully, P.; Paravicini, G.; Proudfoot, A.E.I.; Payton, M.A. Mechanism of Irreversible Inactivation of Phosphomannose Isomerases by Silver Ions and Flamazine. *Biochemistry* **1995**, *34*, 7896–7903. [CrossRef] [PubMed]
12. Morones Ramirez, J.R.; Winkler, J.A.; Spina, C.S.; Collins, J.J. Silver enhances antibiotic activity against Gram-negative bacteria. *Sci. Trans. Med.* **2013**, *5*, 190ra181. [CrossRef] [PubMed]
13. Jung, W.K.; Koo, H.C.; Kim, K.W.; Shin, S.; Kim, S.H.; Park, Y.H. Antibacterial Activity and Mechanism of Action of the Silver Ion in *Staphylococcus aureus* and *Escherichia coli*. *Appl. Environ. Microbiol.* **2008**, *74*, 2171–2178. [CrossRef]

14. Wang, H.; Yan, A.; Liu, Z.; Yang, X.; Xu, Z.; Wang, Y.; Wang, R.; Koohi-Moghadam, M.; Hu, L.; Xia, W.; et al. Deciphering molecular mechanism of silver by integrated omic approaches enables enhancing its antimicrobial efficacy in *E. coli*. *PLoS Biol.* **2019**, *17*, e3000292. [CrossRef] [PubMed]

15. Graham, C. The role of silver in wound healing. *Br. J. Nurs.* **2005**, *14*, S22–S28. [CrossRef] [PubMed]

16. Mazzei, L.; Cianci, M.; Gonzales Vara, A.; Ciurli, S. The structure of urease inactivated by Ag(I): A new paradigm for enzyme inhibition by heavy metals. *Dalton Trans* **2018**, *47*, 8240–8247. [CrossRef]

17. Arduengo, A.J., III; Harlow, R.L.; Kline, M. A Stable crystalline carbene. *J. Am. Chem. Soc.* **1991**, *113*, 361–363. [CrossRef]

18. de Frémont, P.; Marion, N.; Nolan, S.P. Carbenes: Synthesis, properties, and organometallic chemistry. *Coord. Chem. Rev.* **2009**, *253*, 862–892. [CrossRef]

19. Bourissou, D.; Guerret, O.; Gabbaï, F.P.; Bertrand, G. Stable Carbenes. *Chem. Rev.* **2000**, *100*, 39–92. [CrossRef]

20. Fantasia, S.; Petersen, J.L.; Jacobsen, H.; Cavallo, L.; Nolan, S.P. Electronic Properties of N-Heterocyclic Carbene (NHC) Ligands: Synthetic, Structural, and Spectroscopic Studies of (NHC)Platinum(II) Complexes. *Organometallics* **2007**, *26*, 5880–5889. [CrossRef]

21. Gusev, D.G. Electronic and Steric Parameters of 76 N-Heterocyclic Carbenes in Ni(CO)$_3$(NHC). *Organometallics* **2009**, *28*, 6458–6461. [CrossRef]

22. Satija, G.; Sharma, B.; Madan, A.; Iqubal, A.; Shaquiquzzaman, M.; Akhter, M.; Parvez, S.; Khan, M.A.; Alam, M.M. Benzimidazole based derivatives as anticancer agents: Structure activity relationship analysis for various targets. *J. Heter. Chem.* **2022**, *59*, 22–66. [CrossRef]

23. Song, D.; Ma, S. Recent Development of Benzimidazole-Containing Antibacterial Agents. *ChemMedChem* **2016**, *16*, 646–659. [CrossRef] [PubMed]

24. Melaiye, A.; Simons, R.S.; Milsted, A.; Pingitore, F.; Wesdemiotis, C.; Tessier, C.A.; Youngs, W.J. Formation of water-soluble pincer silver(I)-carbene complexes: A novel antimicrobial agent. *J. Med. Chem.* **2004**, *47*, 973–977. [CrossRef]

25. Patil, S.A.; Patil, S.A.; Patil, R.; Keri, R.S.; Budagumpi, S.; Balakrishna, G.R.; Tacke, M. N-heterocyclic carbene metal complexes as bioorganometallic antimicrobial and anticancer drugs. *Future Med. Chem.* **2015**, *7*, 1305–1333. [CrossRef]

26. Kascatan-Nebioglu, A.; Panzner, M.J.; Tessier, C.A.; Cannon, C.L.; Youngs, W.J. N-Heterocyclic carbene–silver complexes: A new class of antibiotics. *Coord. Chem. Rev.* **2007**, *251*, 884–895. [CrossRef]

27. Roland, S.; Jolivalt, C.; Cresteil, T.; Eloy, L.; Bouhours, P.; Hequet, A.; Mansuy, V.; Vanucci, C.; Paris, J.M. Investigation of a series of Silver-N-heterocyclic carbenes as antibacterial agents: Activity, synergistic effects, and cytotoxicity. *Chem. Eur. J.* **2011**, *17*, 1442–1446. [CrossRef]

28. Patil, S.; Claffey, J.; Deally, A.; Hogan, M.; Gleeson, B.; Miguel, L.; Méndez, M.; Müller-Bunz, H.; Paradisi, F.; Tacke, M. Synthesis, cytotoxicity and antibacterial studies of p-methoxybenzylsubstituted and benzyl-substituted N-heterocyclic carbene–silver complexes. *Eur. J. Inorg. Chem.* **2010**, *7*, 1020–1031. [CrossRef]

29. Patil, S.; Deally, A.; Gleeson, B.; Müller-Bunz, H.; Paradisi, F.; Tacke, M. Synthesis, cytotoxicity and antibacterial studies of symmetrically and non-symmetrically benzyl- or p-Cyanobenzyl-substituted N-heterocyclic Carbene–Silver complexes. *Appl. Organomet. Chem.* **2010**, *24*, 781–793. [CrossRef]

30. Patil, S.; Deally, A.; Gleeson, B.; Müller-Bunz, H.; Paradisi, F.; Tacke, M. Novel benzyl-substituted *N*-heterocyclic carbene–silver acetate complexes: Synthesis, cytotoxicity and antibacterial studies. *Metallomics* **2011**, *3*, 74–88. [CrossRef]

31. Sharkey, M.A.; O'Gara, J.P.; Gordon, S.V.; Hackenberg, F.; Healy, C.; Paradisi, F.; Patil, S.; Schaible, B.; Tacke, M. Investigations into the Antibacterial Activity of the Silver-Based Antibiotic Drug Candidate SBC3. *Antibiotics* **2012**, *1*, 25–28. [CrossRef]

32. Browne, N.; Hackenberg, F.; Streciwilk, W.; Tacke, M.; Kavanagh, K. Assessment of in vivo antimicrobial activity of the carbene silver(I) acetate derivative SBC3 using Galleria mellonella larvae. *Biometals* **2014**, *27*, 745–752. [CrossRef] [PubMed]

33. Piatek, M.; O'Beirne, C.; Beato, Z.; Tacke, M.; Kavanagh, K. Exposure of Candida parapsilosis to the silver (I) compound SBC3 induces alterations in the proteome and reduced virulence. *Metallomics* **2022**, *14*, mfac046. [CrossRef] [PubMed]

34. Piatek, M.; O'Beirne, C.; Beato, Z.; Tacke, M.; Kavanagh, K. Pseudomonas aeruginosa and Staphylococcus aureus Display Differential Proteomic Responses to the Silver(I) Compound, SBC3. *Antibiotics* **2023**, *12*, 348. [CrossRef] [PubMed]

35. Streciwilk, W.; Cassidy, J.; Hackenberg, F.; Müller-Bunz, H.; Paradisi, F.; Tacke, M. Synthesis, cytotoxic and antibacterial studies of p-benzyl-substituted NHC-silver(I) acetate compounds derived from 4,5-di-pdiisopropylphenyl-or 4,5-di-p-chlorophenyl-1H-imidazole. *J. Organomet. Chem.* **2014**, *749*, 88–99. [CrossRef]

36. O'Beirne, C.; Alhamad, N.F.; Ma, Q.; Müller-Bunz, H.; Kavanagh, K.; Buder, G.; Zhu, X.; Tacke, M. Synthesis, structures and antimicrobial activity of novel NHC* and Ph3P-Ag(I)-benzoate derivatives. *Inorg. Chim. Acta* **2019**, *486*, 294–303. [CrossRef]

37. Aher, S.; Das, A.; Muskawar, P.; Osborne, J.; Bhagat, P. Silver (I) complexes of imidazolium based N-heterocyclic carbenes for antibacterial applications. *J. Mol. Liq.* **2017**, *231*, 396–403. [CrossRef]

38. Aher, S.; Das, A.; Muskawar, P.; Osborne, J.; Bhagat, P. Synthesis, sharacterization and antimicrobial properties of methylbenzyl and nitrobenzyl containing imidazolium-based silver N-heterocyclic carbenes. *J. Mol. Liq.* **2017**, *233*, 270–277. [CrossRef]

39. Haque, R.A.; Haziz, U.F.M.; Abdullah, A.A.; Shaheeda, N.; Razali, M.R. New non-functionalized and nitrile-functionalized benzimidazolium salts and their silver(I) complexes: Synthesis, crystal structures and antibacterial studies. *Polyhedron* **2016**, *109*, 208–217. [CrossRef]

40. Sahin, N.; Üstün, E.; Tutar, U.; Çelik, C.; Gürbüz, N.; Özdemir, I. Antimicrobial activity, inhibition of biofilm formation, and molecular docking study of novel Ag-NHC complexes. *J. Organomet. Chem.* **2021**, *954–955*, 122082. [CrossRef]

41. Kaloğlu, N.; Özdemir, I.; Günal, S.; Özdemir, I. Synthesis and antimicrobial activity of bulky 3,5-di-*tert*-butyl substituent-containing silver–N-heterocyclic carbene complexes. *Appl. Organomet. Chem.* **2017**, *31*, e3803. [CrossRef]

42. Gök, Y.; SarJ, Y.; Akkoç, S.; Özdemir, E.; Günal, S. Antimicrobial Studies of N-Heterocyclic Carbene Silver Complexes Containing Benzimidazol-2-ylidene Ligand. *Int. J. Inorg. Chem.* **2014**, *2014*, 191054. [CrossRef]

43. Gök, Y.; Akkoc, S.; Erdoğan, H.; Albayrak, S. In Vitro antimicrobial studies of new benzimidazolium salts and silver N-heterocyclic carbene complexes. *J. Enzyme Inhib. Med. Chem.* **2016**, *31*, 1322–1327. [CrossRef] [PubMed]

44. Subramanya Prasad, T.V.; Shahini, C.R.; Patil, S.A.; Huang, X.; Bugarin, A.; Patil, S.A. Non-symmetrically *p*-nitrobenzyl- and *p*-cyanobenzyl-substituted N-heterocyclic carbene-silver(I) complexes: Synthesis, characterization and antibacterial studies. *J. Coord. Chem.* **2017**, *70*, 600–614. [CrossRef]

45. Shahini, C.R.; Achar, G.; Budagumpi, S.; Tacke, M.; Patil, S.A. Non-symmetrically *p*-nitrobenzyl-substituted N-heterocyclic carbene-silver(I) complexes as metallopharmaceutical agents. *Appl. Organomet. Chem.* **2017**, *31*, e3819. [CrossRef]

46. Shahini, C.R.; Achar, G.; Budagumpi, S.; Tacke, M.; Patil, S.A. Synthesis, structural investigation and antibacterial studies of non-symmetrically *p*–nitrobenzyl substituted benzimidazole N-heterocyclic carbene-silver(I) complexes. *Inorg. Chim. Acta* **2017**, *466*, 432–441. [CrossRef]

47. Asekunowo, P.O.; Haque, R.A.; Razali, M.R. Sterically modulated silver(I) complexes of N-benzyl-substituted N-heterocyclic carbenes: Synthesis, crystal structures and bioactivity. *Transit. Met. Chem.* **2015**, *40*, 79–88. [CrossRef]

48. Carpio-Granillo, M.; Zuno-Cruz, F.J.; Sanchez-Cabrera, G.; Rojo-Gomez, E.G.; Gonzalez-Abrego, D.O.; Coronel-Olivares, C.; Caviedes, M.F.; Andrade-Lopez, N.; Rosales-Hoz, M.J.; Leyva, M.A. p-Nitrobenzyl-substituted N–heterocyclic carbene in Silver(I) and Gold(I) complexes and their antibacterial activities. *Polyhedron* **2022**, *217*, 115726. [CrossRef]

49. Streciwilk, W.; Terenzi, A.; Lo Nardo, F.; Prochnow, P.; Bandow, J.E.; Keppler, B.K.; Ott, I. Synthesis and biological evaluation of organometallic complexes bearing bis-1,8-naphthalimide ligands. *Eur. J. Inorg. Chem.* **2018**, *26*, 3104–3112. [CrossRef]

50. Lu, J.; Vlamis-Gardikas, A.; Kandasamy, K.; Zhao, R.; Gustafsson, T.N.; Engstrand, L.; Hoffner, S.; Engman, L.; Holmgren, A. Inhibition of bacterial thioredoxin reductase: An antibiotic mechanism targeting bacteria lacking glutathione. *FASEB J.* **2013**, *27*, 1394–1403. [CrossRef]

51. Gök, Y.; Akkoç, S.; Çelikal, Ö.Ö.; Özdemir, I.; Günal, S. In Vitro antimicrobial studies of naphthalen-1-ylmethyl substituted silver N-heterocyclic carbene complexes. *Arab. J. Chem.* **2019**, *12*, 2513–2518. [CrossRef]

52. Wright, B.D.; Shah, P.N.; McDonald, L.J.; Shaeffer, M.L.; Wagers, P.O.; Panzner, M.J.; Smolen, J.; Tagaev, J.; Tessier, C.A.; Cannon, C.L.; et al. Synthesis, characterization, and antimicrobial activity of silver carbene complexes derived from 4,5,6,7-tetrachlorobenzimidazole against antibiotic resistant bacteria. *Dalton Trans.* **2012**, *41*, 6500–6506. [CrossRef] [PubMed]

53. Asekunowo, P.O.; Haque, R.A.; Razali, M.R.; Avicor, S.W.; Wajidi, M.F.F. Synthesis and characterization of nitrile functionalized silver(I)-N-heterocyclic carbene complexes: DNA binding, cleavage studies, antibacterial properties and mosquitocidal activity against the dengue vector, aedes albopictus. *Eur. J. Med. Chem.* **2018**, *150*, 601–615. [CrossRef]

54. Türker, D.; Üstün, E.; Günal, S.; Yıldız, H.; Düşünceli, S.D.; Özdemir, İ. Cyanopropyl functionalized benzimidazolium salts and their silver N-heterocyclic carbene complexes: Synthesis, antimicrobial activity, and theoretical analysis. *Arch. Pharm.* **2022**, *355*, e2200041. [CrossRef]

55. Haque, R.A.; Iqbal, M.A.; Mohamad, F.; Razali, M.R. Antibacterial and DNA cleavage activity of carbonyl functionalized N-heterocyclic carbene-silver(I) and selenium compounds. *J. Mol. Struct.* **2018**, *1155*, 362–370. [CrossRef]

56. Kaloğlu, M.; Kaloğlu, N.; Özdemir, İ.; Günal, S.; Özdemir, İ. Novel benzimidazol-2-ylidene carbene precursors and their silver(I) complexes: Potential antimicrobial agents. *Bioorg. Med. Chem.* **2016**, *24*, 3649–3656. [CrossRef]

57. Karataş, M.O.; Günal, S.; Mansur, A.; Alıcı, B.; Çetinkaya, E. Synthesis and antimicrobial properties of cycloheptyl substituted benzimidazolium salts and their silver(I) carbene complexes. *J. Heter. Commun.* **2016**, *22*, 357–361. [CrossRef]

58. Üstün, E.; Şahin, N.; Çelik, C.; Tutar, U.; Özdemir, N.; Gürbüz, N.; Özdemir, İ. Synthesis, characterization, antimicrobial and antibiofilm activity, and molecular docking analysis of NHC precursors and their Ag-NHC complexes. *Dalton Trans.* **2021**, *50*, 15400–15412. [CrossRef]

59. Tutar, U.; Celik, C.; Sahin, N. Allyl Functionalized Benzimidazolium-Derived Ag(I)-N-Heterocyclic Carbene Complexes: Anti-Biofilm and Antimicrobial Properties. *Pharm. Chem. J.* **2022**, *56*, 54–60. [CrossRef]

60. Achar, G.; Hokrani, P.P.; Brinda, K.N.; Małecki, J.G.; Budagumpi, S. Synthesis, characterization, crystal structure and antibacterial properties of N– and O–functionalized (benz)imidazolium salts and their N–heterocyclic carbene silver(I) complexes. *J. Mol. Struct.* **2019**, *1196*, 627–636. [CrossRef]

61. Çelik, C.; Üstün, E.; Şahin, N.; Tutar, U. Antimicrobial and antibiofilm activities and bovine serum albumin binding properties of benzimidazolium derivative NHC salts and their Ag(I)-NHC complexes. *Appl. Organomet. Chem.* **2022**, *36*, e6891. [CrossRef]

62. Mnasri, A.; Mejri, A.; Al-Hazmy, S.M.; Arfaoui, Y.; Özdemir, I.; Gürbüz, N.; Hamdi, N. Silver–N-heterocyclic carbene complexes-catalyzed multicomponent reactions: Synthesis, spectroscopic characterization, density functional theory calculations, and antibacterial study. *Arch. Pharm.* **2021**, *354*, e2100111. [CrossRef]

63. Muniyappan, N.; Advaya, G.R.; Sujitha, E.; Sabiah, S. Picolyl and benzyl functionalized biphenyl NHC carbenes and their silver complexes: Sigma donating and antimicrobial properties. *J. Organomet. Chem.* **2021**, *954–955*, 122075. [CrossRef]

64. Sánchez, A.; Carrasco, C.J.; Montilla, F.; Álvarez, E.; Galindo, A.; Pérez-Aranda, M.; Pajuelo, E.; Alcudia, A. Antimicrobial Properties of Amino-Acid-Derived N-Heterocyclic Carbene Silver Complexes. *Pharmaceutics* **2022**, *14*, 748. [CrossRef] [PubMed]

65. Di Napoli, M.; Saturnino, C.; Cianciulli, E.I.; Varcamonti, M.; Zanfardino, A.; Tommonaro, G.; Longo, P. Silver (I) N-heterocyclic carbene complexes: Synthesis, characterization and antibacterial activity. *J. Organomet. Chem.* **2013**, *725*, 46–53. [CrossRef]

66. Prencipe, F.; Zanfardino, A.; Di Napoli, M.; Rossi, F.; D'Errico, S.; Piccialli, G.; Mangiatordi, G.F.; Saviano, M.; Ronga, L.; Varcamonti, M.; et al. Silver (I) N-Heterocyclic Carbene Complexes: A Winning and Broad Spectrum of Antimicrobial Properties. *Int. J. Mol. Sci.* **2021**, *22*, 2497. [CrossRef]

67. Mather, J.C.; Wyllie, J.A.; Hamilton, A.; Soares da Costa, T.P.; Barnard, P.J. Antibacterial silver and gold complexes of imidazole and 1,2,4-triazole derived N-heterocyclic carbenes. *Dalton Trans.* **2022**, *51*, 12056. [CrossRef] [PubMed]

68. Kascatan-Nebioglu, A.; Melaiye, A.; Hindi, K.; Durmus, S.; Panzner, M.J.; Hogue, L.A.; Mallett, R.J.; Hovis, C.E.; Coughenour, M.; Crosby, S.D.; et al. Synthesis from Caffeine of a Mixed N-Heterocyclic Carbene–Silver Acetate Complex Active against Resistant Respiratory Pathogens. *J. Med. Chem.* **2006**, *49*, 6811–6818. [CrossRef] [PubMed]

69. Karatas, M.O.; Olgundeniz, B.; Günal, S.; Özdemir, İ.; Alıcı, B.; Çetinkaya, E. Synthesis, characterization and antimicrobial activities of novel silver(I) complexes with coumarin substituted N-heterocyclic carbene ligands. *Bioorg. Med. Chem.* **2016**, *24*, 643–650. [CrossRef]

70. Achar, G.; Uppendranath, K.; Ramya, V.C.; Biffis, A.; Keri, R.S.; Budagumpi, S. Synthesis, characterization, crystal structure and biological studies of silver(I) complexes derived from coumarin-tethered N-heterocyclic carbene ligands. *Polyhedron* **2017**, *123*, 470–479. [CrossRef]

71. Achar, G.; Shahini, C.R.; Patil, S.A.; Budagumpi, S. Synthesis, structural characterization, crystal structures and antibacterial potentials of coumarin-tethered N-heterocyclic carbene silver(I) complexes. *J. Organomet. Chem.* **2017**, *833*, 28–42. [CrossRef]

72. Achar, G.; Agarwal, P.; Brinda, K.N.; Małecki, J.G.; Keri, R.S.; Budagumpi, S. Ether and coumarin–functionalized (benz)imidazolium salts and their silver(I)–N–heterocyclic carbene complexes: Synthesis, characterization, crystal structures and antimicrobial studies. *J. Organomet. Chem.* **2018**, *854*, 64e75. [CrossRef]

73. Yıldırım, I.; Aktaş, A.; Celepci, D.B.; Kırbağ, S.; Kutlu, T.; Gök, T.; Aygün, M. Synthesis, characterization, crystal structure, and antimicrobial studies of 2-morpholinoethyl-substituted benzimidazolium salts and their silver(I)-N-heterocyclic carbene complexes. *Res. Chem. Intermed.* **2017**, *43*, 6379–6393. [CrossRef]

74. Aher, S.; Das, A.; Muskawar, P.; Osborne, J.; Bhagat, P. In Vitro antimicrobial evaluation, effects of halide concentration and hemolysis study of silver-N-heterocyclic carbene complexes. *Res. Chem. Intermed.* **2018**, *44*, 2099–2110. [CrossRef]

75. Shahini, C.R.; Achar, G.; Budagumpi, S.; Müller-Bunz, H.; Tacke, M.; Patil, S.A.L. Benzoxazole and dioxolane substituted benzimidazole-based N-heterocyclic carbine-silver(I) complexes: Synthesis, structural characterization and In Vitro antimicrobial activity. *J. Organomet. Chem.* **2018**, *868*, 1–13. [CrossRef]

76. Lasmari, S.; Ikhlef, S.; Boulcina, R.; Mokrani, E.H.; Bensouici, C.; Gürbüz, N.; Dündar, M.; Karcıı, H.; Özdemir, I.; Koç, A.; et al. New silver N–heterocyclic carbenes complexes: Synthesis, Molecular docking study and biological activities evaluation as cholinesterase inhibitors and antimicrobials. *J. Mol. Struct.* **2021**, *1238*, 130399. [CrossRef]

77. Haque, R.A.; Asekunowo, P.O.; Budagumpi, S. Binuclear silver(I) complexes of p-xylyl/2,6-lutidinyl linked bis-N heterocyclic carbene ligands: Synthesis, crystal structures and biological evaluation. *Inorg. Chem. Commun.* **2014**, *47*, 56–59. [CrossRef]

78. Sakamoto, R.; Morozumi, S.; Yanagawa, Y.; Toyama, M.; Takayama, A.; Kasuga, N.C.; Nomiya, K. Synthesis, characterization, and structure–activity relationship of the antimicrobial activities of dinuclear N-heterocyclic carbene (NHC)-silver(I) complexes.l *J. Inorg. Biochem.* **2016**, *163*, 110–117. [CrossRef]

79. Haziz, U.F.M.; Haque, R.A.; Amirul, A.A.; Shaheeda, N.; Razali, M.R. Synthesis, structures and antibacterial studies of non-functionalized and nitrile-functionalized bis-benzimidazolium salts and respective dinuclear silver(I)-N-heterocyclic carbene complexes. *Polyhedron* **2016**, *117*, 628–636. [CrossRef]

80. Haziz, U.F.M.; Haque, R.A.; Amirul, A.A.; Aidda, O.N.; Razali, M.R. New class of non-symmetrical homo-dibenzimidazolium salts and their dinuclear silver(I) di-NHC complexes. *J. Organomet. Chem.* **2019**, *899*, 120914. [CrossRef]

81. Loh, Y.L.; Haziz, U.F.M.; Haque, R.A.; Amirul, A.A.; Aidda, O.N.; Razali, M.R. The effect of short alkane bridges in stability of bisbenzimidazole-2-ylidene silver(I) complexes: Synthesis, crystal structure and antibacterial activity. *J. Coord. Chem.* **2019**, *72*, 894–907. [CrossRef]

82. Habib, A.; Iqbal, M.A.; Bhatti, H.N.; Kamal, A.; Kamal, S. Synthesis of alkyl/aryl linked binuclear silver(I)-N-Heterocyclic carbene complexes and evaluation of their antimicrobial, hemolytic and thrombolytic potential. *Inorg. Chem. Commun.* **2020**, *111*, 107670. [CrossRef]

83. Ashraf, R.; Bhatti, H.N.; Iqbal, M.A.; Jamil, Y. Synthesis of aryl linked complexes, DNA interaction study and biological potentials. *Inorg. Chem. Commun.* **2020**, *119*, 108077. [CrossRef]

84. Nadeem, R.Y.; Yaqoob, M.; Yam, W.; Haque, R.A.; Iqbal, M.A. Synthesis, characterization and biological evaluation of Bis-benzimidazolium salts and their silver(I)-N-heterocyclic carbene complexes. *Med. Chem. Res.* **2022**, *31*, 1783–1791. [CrossRef]

85. Hussaini, S.Y.; Haque, R.A.; Haziz, U.F.M.; Amirul, A.A.; Razali, M.R. Dinuclear silver(I) and gold(I) N-heterocyclic carbene complexes of N-alkyl substituted bis-benzimidazol-2-ylidenes with aliphatic spacer: Synthesis, characterizations and antibacterial studies. *J. Mol. Struct.* **2021**, *1246*, 131187. [CrossRef]

86. Haziz, U.F.M.; Haque, R.A.; Amirul, A.A.; Razali, M.R. Synthesis, Structural Analysis and Antibacterial Studies of Bis and Open Chain Tetra N-Heterocyclic Carbene Dinuclear Silver(I) Complexes. *J. Mol. Struct.* **2021**, *1236*, 130301. [CrossRef]

87. Panzner, M.J.; Hindi, K.M.; Wright, B.D.; Taylor, J.B.; Han, D.S.; Youngs, W.J.; Cannon, C.L. A theobromine derived silver N-heterocyclic carbene: Synthesis, characterization, and antimicrobial efficacy studies on cystic fibrosis relevant pathogens. *Dalton Trans.* **2009**, *35*, 7308–7313. [CrossRef]

88. Maxwell, A. The interaction between coumarin drugs and DNA gyrase. *Mol. Microbiol.* **1993**, *9*, 681–686. [CrossRef]

89. Kaczor, A.; Witek, K.; Podlewska, S.; Sinou, V.; Czekajewska, J.; Żesławska, E.; Doroz-Płonka, A.; Lubelska, A.; Latacz, G.; Nitek, W.; et al. Molecular Insights into an Antibiotic Enhancer Action of New Morpholine-Containing 5-Arylideneimidazolones in the Fight against MDR Bacteria. *Int. J. Mol. Sci.* **2021**, *22*, 2062. [CrossRef]

90. Belhi, Z.; Karci, H.; Dündar, M.; Gürbüz, N.; Özdemir, İ.; Koç, A.; Cheriti, A.; Özdemir, İ. Novel benzimidazolium salts and their silver(I)-N-heterocyclic carbene complexes: Synthesis, characterization and their biological properties. *J. Coord. Chem.* **2023**, *76*, 120–133. [CrossRef]

91. Haque, R.A.; Salman, A.W.; Budagumpi, S.; Abdullah, A.A.; Abdul Majid, A.M.S. Sterically tuned Ag(I)- and Pd(II)- N-heterocyclic carbene complexes of imidazol-2-ylidenes: Synthesis, crystal structures, and in vitro antibacterial and anticancer studies. *Metallomics* **2013**, *5*, 760–769. [CrossRef] [PubMed]

92. Hindi, K.M.; Ditto, A.J.; Panzner, M.J.; Medvetz, D.A.; Han, D.S.; Hovis, C.E.; Hilliard, J.K.; Taylor, J.B.; Yun, Y.H.; Cannon, C.L.; et al. The antimicrobial efficacy of sustained release silver–carbene complex-loaded L-tyrosine polyphosphate nanoparticles: Characterization, in vitro and in vivo studies. *Biomaterials* **2009**, *30*, 3771–3779. [CrossRef] [PubMed]

93. Prencipe, F.; Diaferia, C.; Rossi, F.; Ronga, L.; Tesauro, D. Forward Precision Medicine: Micelles for Active Targeting Driven by Peptides. *Molecules* **2021**, *26*, 4049. [CrossRef]

94. Li, Y.; Hindi, K.; Watts, K.M.; Taylor, J.B.; Zhang, K.; Li, Z.; Hunstad, D.A.; Cannon, C.L.; Youngs, W.J.; Wooley, K.L. Shell crosslinked nanoparticles carrying silver antimicrobials as therapeutics. *Chem. Commun.* **2010**, *46*, 121–123. [CrossRef]

95. Ornelas-Megiatto, C.; Shah, P.N.; Wich, P.R.; Cohen, J.L.; Tagaev, J.A.; Smolen, J.A.; Wright, B.D.; Panzner, M.J.; Youngs, W.J.; Fréchet, J.M.J.; et al. Aerosolized Antimicrobial Agents Based on Degradable Dextran Nanoparticles Loaded with Silver Carbene Complexes. *Mol. Pharm.* **2012**, *9*, 3012–3022. [CrossRef]

96. Lim, Y.H.; Tiemann, K.M.; Heo, G.S.; Wagers, P.O.; Rezenom, Y.H.; Zhang, S.; Zhang, F.; Youngs, W.J.; Hunstad, D.A.; Wooley, K.L. Preparation and In Vitro Antimicrobial Activity of Silver-Bearing Degradable Polymeric Nanoparticles of Polyphosphoester-block-Poly(l-lactide). *ACS Nano* **2015**, *9*, 1995–2008. [CrossRef]

97. Necola, M.R.; Gurovic, M.S.V.; Ruiz Díaz, S.; Silbestri, G.F. Binding silver to chitooligosaccharides through N-heterocyclic carbenes: Synthesis and antimicrobial activity. *Carbohydrate Res.* **2019**, *471*, 6–12. [CrossRef]

98. Gajare, S.P.; Bansode, P.A.; Patil, P.V.; Patil, A.D.; Pore, D.M.; Sonawane, K.D.; Dhanavade, M.J.; Khot, V.M.; Rashinkar, G.S. Anticancer, Antibacterial and Hyperthermia Studies of a Caffeine-Based N-Heterocyclic Carbene Silver Complex Anchored on Magnetic Nanoparticles. *Chem. Select* **2021**, *6*, 1958–2019. [CrossRef]

99. Tsyba, I.; Bun-kit Mui, B.; Bau, R.; Noguchi, R.; Nomiya, K. Synthesis and Structure of a Water-Soluble Hexanuclear Silver(I) Nicotinate Cluster Comprised of a "Cyclohexane-Chair"-Type of Framework, Showing Effective Antibacterial and Antifungal Activities: Use of "Sparse Matrix" Techniques for Growing Crystals of Water-Soluble. Inorganic Complexes. *Inorg. Chem.* **2003**, *42*, 8028–8032. [CrossRef]

100. Stenger-Smith, J.; Chakraborty, I.; Sameera, W.M.C.; Mascharak, P.K. Antimicrobial silver (I) complexes derived from aryl-benzothiazoles as turn-on sensors: Syntheses, properties and density functional studies. *Inorg. Chim. Acta* **2018**, *471*, 326–335. [CrossRef]

Green Extracellular Synthesis of Silver Nanoparticles by *Pseudomonas alloputida*, Their Growth and Biofilm-Formation Inhibitory Activities and Synergic Behavior with Three Classical Antibiotics

Carlos Pernas-Pleite, Amparo M. Conejo-Martínez, Irma Marín * and José P. Abad *

Department of Molecular Biology, Faculty of Sciences, Biology Building, Autonomous University of Madrid, Cantoblanco, 28049 Madrid, Spain
* Correspondence: irma.marin@uam.es (I.M.); josep.abad@uam.es (J.P.A.)

Abstract: Bacterial resistance to antibiotics is on the rise and hinders the fight against bacterial infections, which are expected to cause millions of deaths by 2050. New antibiotics are difficult to find, so alternatives are needed. One could be metal-based drugs, such as silver nanoparticles (AgNPs). In general, chemical methods for AgNPs' production are potentially toxic, and the physical ones expensive, while green approaches are not. In this paper, we present the green synthesis of AgNPs using two *Pseudomonas alloputida* B003 UAM culture broths, sampled from their exponential and stationary growth phases. AgNPs were physicochemically characterized by transmission electron microscopy (TEM), total reflection X-ray fluorescence (TXRF), infrared spectroscopy (FTIR), dynamic light scattering (DLS), and X-ray diffraction (XRD), showing differential characteristics depending on the synthesis method used. Antibacterial activity was tested in three assays, and we compared the growth and biofilm-formation inhibition of six test bacteria: *Bacillus subtilis*, *Escherichia coli*, *Klebsiella pneumoniae*, *Pseudomonas aeruginosa*, *Staphylococcus aureus*, and *Staphylococcus epidermidis*. We also monitored nanoparticles' synergic behavior through the growth inhibition of *E. coli* and *S. aureus* by three classical antibiotics: ampicillin, nalidixic acid, and streptomycin. The results indicate that very good AgNP activity was obtained with particularly low MICs for the three tested strains of *P. aeruginosa*. A good synergistic effect on streptomycin activity was observed for all the nanoparticles. For ampicillin, a synergic effect was detected only against *S. aureus*. ROS production was found to be related to the AgNPs' antibacterial activity.

Keywords: antibacterial activity; antibiotics; antimicrobial activity; green synthesis; nanoparticles; *Pseudomonas alloputida*; ROS; silver; synergy

1. Introduction

The antibiotic resistance of pathogenic bacteria is one of the most pressing problems that humanity will have to deal with in the coming years [1], and is already considered a silent pandemic [2] that will cause an estimated 10 million deaths per year by 2050 [3]. Therefore, action should be taken to address this situation as soon as possible. Since not many new antibiotics are coming out, other alternatives should be studied. One of the most promising ones is the use of metal-based drugs, particularly metallic nanoparticles [4], even though some possible drawbacks also need to be studied [5]. Among metallic nanoparticles, ones based on silver are the most studied. Silver has long been known to be a good antibacterial agent in the form of monovalent silver salts, but its use in the form of nanoparticles seems to be more convenient and it has been studied extensively [6,7].

A huge number of methods have been described for the synthesis of silver nanoparticles (AgNPs), based on chemical, physical, or biological approaches. The use of chemical or physical methods usually produces a more regular shape and size of individual nanoparticles than biological methods [8–10]. However, for use as antimicrobial drugs, that may

be irrelevant in most cases. The biological methods employ extracts or culture broths containing reducing and protecting agents generating silver nanomaterials, whose activity depends on the method and the biological material used [11–16]. Since no toxic chemicals are used and the biological material is usually not expensive nor requires sophisticated equipment, biological methods are considered more convenient and greener. Most of these employ extracts of different plant parts such as seeds, leaves, flowers, etc. [11,16,17], but animal blood serum [18], invertebrates [19], algae [20], lichens [21], fungi [22], and bacteria [11,23,24] have been used as well. Different organisms may provide different physicochemical characteristics and biological properties to the nanoparticles.

Microorganisms are the second more frequently used source for the biogenic synthesis of AgNPs, especially bacteria. In these cases, intracellular and extracellular methods have been described that use extracts or culture broths of a wide diversity of bacteria, such as *Paenarthrobacter nicotinovorans* [24], *Klebsiella pneumoniae* [25], various *Pseudomonas* species [26,27], actinobacteria [28], psychrophilic bacteria [29], and even an endophytic *Bacillus cereus* [30], among many others. Using various biological materials increases the possibility of producing AgNPs with different properties. Though plants have most often been used to produce AgNPs, microorganisms are much more phylogenetically diverse and would require less physical space and growth time than plants for producing biological material in better controlled and reproducible growth conditions. So, research on new species of bacteria able to produce AgNPs could be a good approach to obtain ones with different properties, which would then allow us to select the most appropriate ones for each application. Additionally, using different media [31,32] for culturing the same bacteria or cultures from different growth phases may provide additional possibilities for generating AgNPs with different properties.

One of the main problems with using AgNPs as antimicrobial agents is the possible cytotoxicity. However, diverse studies have described different levels of toxicity of several AgNPs produced by different methods [33], from no toxicity [34,35] to high toxicity [36]. Thus, new approaches for AgNP synthesis, particularly when employing diverse biological materials, would eventually produce AgNPs that could be used in clinic. In this sense, if AgNPs show antimicrobial activity at lower concentrations than those in which they produce significant toxicity, a high possibility exists that they could be used as antibacterial agents, as several authors have claimed [33,37,38].

Another possibility is for AgNPs to be used for fighting infections in combination with classical antibiotics. This would allow us, if synergy occurs, to use lower concentrations of antibiotics and AgNPs than when they are used alone [39,40]. Moreover, recent studies have shown that AgNPs can be used to recover the use of certain classical antibiotics not regularly used because of their toxic effects or resistance [41,42].

The objectives of this study were to synthesize new types of AgNPs by a green method using *Pseudomonas alloputida*, a species never before used for AgNP production, and to determine their structural characteristics as well as their properties as antibacterial agents. As stated above, biological diversity could be helpful for producing new and different AgNPs with distinct properties. Thus, we wanted to determine if the same bacterium could also be employed to produce several types of AgNPs by using broths sampled in two growth phases, exponential (bacteria actively growing) and stationary (arrested growth), and using two media, one with and another without NaCl. Structural differences between the various AgNPs produced, as well as their antibacterial activity, would tell us if the AgNPs are different, and what their potential to be used as antibacterial agents is. Among the possible antibacterial tests, we were interested in performing quantitative determinations of the growth and biofilm-formation inhibition of various Gram-positive and Gram-negative bacteria. One of the most interesting putative applications of AgNPs is as helpers of classic antibiotics in a synergistic way, and we also wanted to evaluate this possibility for our AgNPs. Finally, we wanted to test if the AgNPs produce reactive species of oxygen (ROS) and their correlation with the antibacterial activity parameters to advance the study of their mechanism of action.

2. Results and Discussion

The work presented here addresses the production of AgNPs by biological means, to be used as antimicrobial agents. We used a *Pseudomonas* strain that had been isolated from the Tinto River estuary (Huelva, Spain) in a previous study on bacterial antibiotic resistance in this environment [43]. Before using this isolate, it was phylogenetically identified as follows.

2.1. Phylogenetic Ascription of the Bacterial Strain Used in AgNP Synthesis

Identification of the species to which this isolate belongs was performed based on a two-locus analysis with concatenated sequences of 16S rDNA and the *rpo*D gene. A neighbor-joining phylogenetic tree showed maximum proximity to the type-strain of *P. alloputida* (Figure 1). This was corroborated by the percentages of sequence similarity for both genes. A sequence of 1383 nucleotides of the 16S rDNA and one of 688 of the *rpo*D gene were used, obtaining 99.85% and 98.20% similarity, respectively. Even though the 16S rDNA is not considered discriminative enough for *Pseudomonas* species, the similarity of the analyzed sequence of *rpo*D gene was over the minimum required to identify our isolate as *P. alloputida* [44,45]. *Pseudomonas* is an interesting genus because of its biotechnological potential [46], and applications for *P. alloputida* have been described [47,48]. As far as we know, this species has not previously been used for AgNP synthesis.
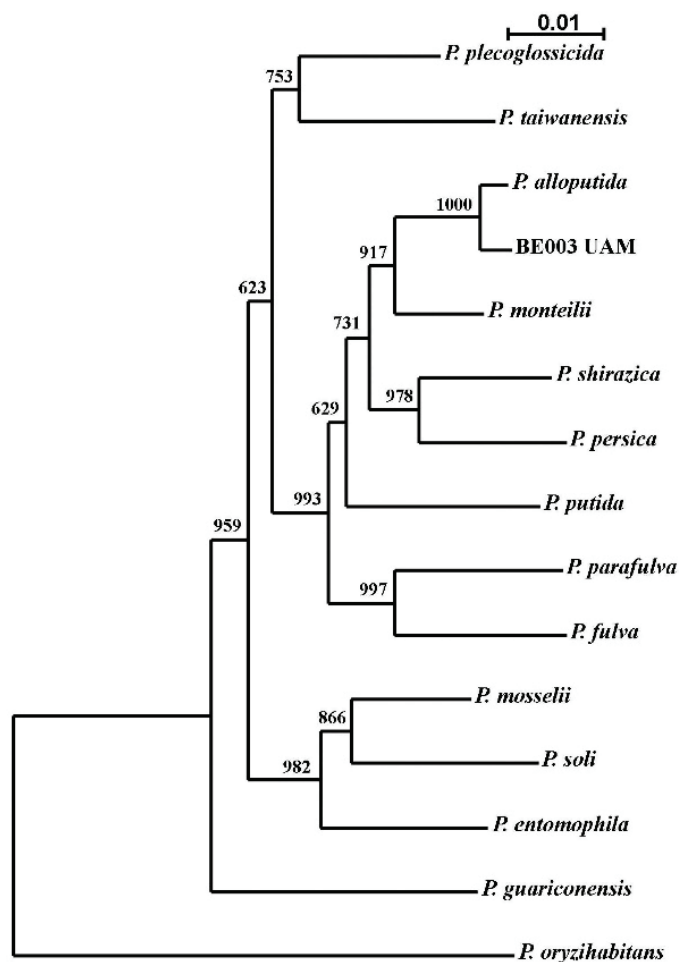
Figure 1. Neighbor-joining phylogenetic tree for assignment of the isolate B003 UAM to *Pseudomonas alloputida* species. Sequences from the type strains of each species were used. Numbers are bootstrap values of the corresponding branching points. The bar indicates the scale of phylogenetic distances of the branches.

2.2. *Pseudomonas alloputida B003 UAM Cultures and Growth Curves*

The growth of the bacterium was tested in a regular nutritive medium or a NaCl-deprived one, as the presence of this salt is known to affect AgNP synthesis [29,49] and could induce the production of different types of AgNPs. Growth curves showed that the bacterium grows faster in a regular medium (Figure S1, Supplementary Materials), indicating different behavior depending on the medium used, which might affect the broth composition and properties. As another variable to produce different AgNPs, cultures were sampled at exponential and stationary phases from each medium. We have not found reports of using bacterial broths from different growth phases for producing different types of AgNPs, but we considered this a good way to obtain different biological materials since, in the exponential phase, bacteria are in active growth, producing many different compounds, while in the stationary phase only maintenance processes are taking place.

2.3. *AgNPs Biosynthesis*

AgNPs syntheses were followed spectrophotometrically (Figure 2). The highest absorbances were observed at about 40–60 h of synthesis for the AgNPsExpCl and AgNPsStaCl (see Section 3.3 for the naming of the AgNPs), 60–80 h for AgNPsExp, and 180–200 h for the AgNPsSta. With longer reaction times, a decrease in the absorbance at λ_{max} and an increase at higher wavelengths (>550 nm) was observed, indicating rearrangement or aggregation of the AgNPs (this can be seen in Figure 2 for the longer reaction times, mainly for the AgNPs from a regular medium). For all our structural and antibacterial activity determinations, AgNPs were collected from the synthesis reactions before any sign of aggregation occurred. After the washing steps, spectra were registered to determine the integrity of the AgNPs. We observed no significant changes (Figure S2), which indicated the conservation of the structure of all AgNPs during this process.
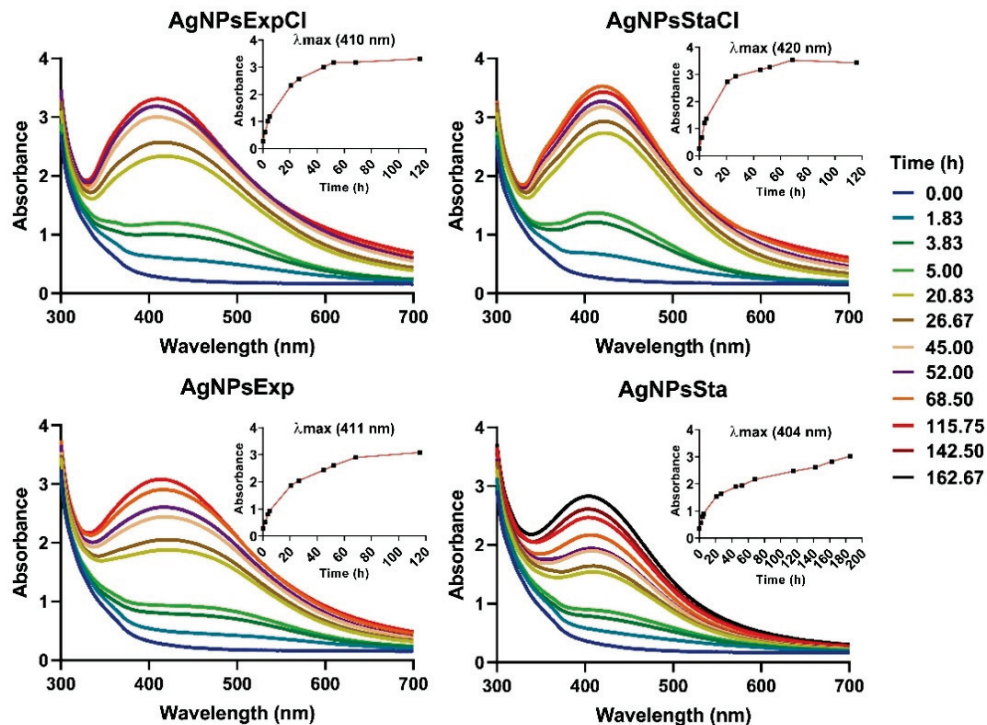
Figure 2. UV-Vis spectra of AgNPs over time during their synthesis. The inset figures in the upper right corner of each panel show the kinetics of synthesis from the increase in absorbance at the corresponding λ_{max}.

The results showed differences in the speed of synthesis depending on the NaCl content of the broths used and the growth phases from which the broths were taken.

Synthesis of AgNPs using media with NaCl was faster with no dependence on the growth phase. However, syntheses were slower when a NaCl-deprived medium was used and, in this case, different speeds were observed depending on the growth phase. The slowest were those from the stationary one. The presence of NaCl in the broth seems to facilitate nanosilver production, but we cannot determine if this effect is due to NaCl itself or the presence of different compounds in the broths, with or without NaCl, as the different growth of the bacterium in the two media may indicate. As some authors have suggested [29,49], the presence of Cl$^-$ could lead to the formation of AgCl crystals. Due to the low solubility of this compound, it may precipitate forming crystals that could have a nucleation effect on the synthesis of AgNPs, thus accelerating this process. Since the XRD analyses, which will be described later, have shown that AgNPs synthesized in the presence of NaCl contain AgCl crystals, we can guess that these were nucleating the AgNPs. In the literature, a wide range of synthesis rates for silver nanoparticles has been reported depending on the biological material used or the synthesis method and conditions, such as pH [50], temperature [29,50], or NaCl presence [29,49]. In previous work by our group [29], the presence of NaCl did not speed up AgNP synthesis; the contrary was true. This may indicate that the effect of NaCl could also be related to the bacteria used in the AgNP synthesis. The time needed for the green synthesis of AgNPs has been reported as rapid—a few minutes, as described by Mokhtari et al. (2009) [25] to hours [26]—or longer, taking days [28,36] or even several weeks, as, for instance, was described by Javani et al. (2015) [29]. In our case, the maximum production was achieved in an intermediate time.

To check the reproducibility of the synthesis, three batches of AgNPsSta and Ag-NPsStaCl were prepared as models and their kinetics compared (Figure S3), also checking the stability of the nanoparticles at 4 °C over the two weeks after synthesis and washing. Structural stability was evaluated by the UV-Vis spectra, and the conservation of antimicrobial activity by comparison of the minimal inhibitory and bactericidal concentrations (MIC and MBC) (Figure S4). The results indicated the good reproducibility of the kinetics of synthesis, stability of the spectra, and conservation of antibacterial activity. These results allow us to use each AgNP batch for at least two weeks after synthesis, when conserved at 4 °C. Nevertheless, each batch was kept at 4 °C and used for no more than one week after synthesis; spectra were rechecked just before use in each physicochemical analysis or antimicrobial activity test. The preparation of several batches of each type of AgNPs was needed during this study, and the kinetics of each were routinely checked to ensure repeatability. Once the reproducibility of the synthesis and spectra were checked, physicochemical and antibacterial activity characterization of the AgNPs was performed.

As a test to determine if the broths used once for AgNP generation still have the capability to synthesize AgNPs without deleterious consequences on the AgNPs produced, the broth used to prepare the AgNPsStaCl was reused for a new synthesis. This was performed two consecutive times without apparent changes in the kinetics of synthesis and obtained nanoparticles with the same UV-Vis spectra (Figure S5). This allows the synthesis of several batches from the same broth stock, decreasing the production costs. As far as we know, this is the first time that reusing biological material for producing consecutive batches of AgNPs has been reported.

2.4. Characterization of Biosynthesized AgNPs

2.4.1. UV-Visible Spectrophotometry

AgNPs showed typical UV-Vis spectra, as can be seen in Figure 2, with some differences in λ_{max} for nanoparticles synthesized from the stationary phase of regular medium with the largest value (420 nm). A lower, but similar, λ_{max} value was found for the AgNPs prepared with exponential broths (410–411 nm), while for those from the stationary phase a clear difference was observed, with the lowest value for AgNPsSta (404 nm). These values correlate with the AgNP sizes observed by TEM (see below), which agrees with the clear relationship between the λ_{max} and the AgNP size claimed by other authors [51].

2.4.2. Elemental Composition of AgNPs by Total Reflection X-ray Fluorescence (TXRF)

TXRF was used to determine the elemental composition of the AgNPs and the silver concentration of nanoparticle suspensions. AgNPs were mainly made of silver, with insignificant amounts of some other elements, except for Cl. Silver appeared as two adjacent peaks in the 3 KeV region, and close to them was a small one at 2.6 KeV corresponding to chlorine (Figure 3). AgNPs prepared from regular nutritive broths contained a higher proportion of Cl.
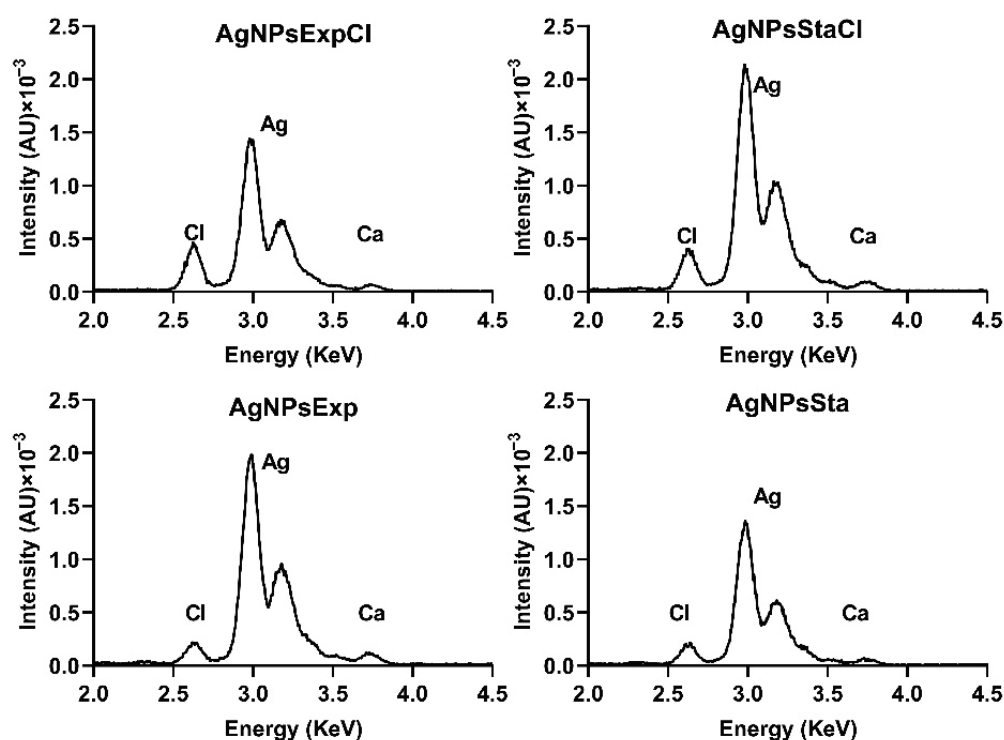
Figure 3. TXRF analysis of elemental composition of AgNPs around the silver peaks. AU: arbitrary units.

The chlorine present in the AgNPs prepared in a medium without added NaCl could come from the residual chloride salts in the extracts used in the preparation of the culture media. The low, but significant, amounts of Cl in the AgNPs prepared with a NaCl-containing medium come from the Cl provided by this salt, as found in other reports [52,53].

2.4.3. Crystallinity by Powder X-ray Diffraction (XRD)

The results of XRD for all nanoparticles tested showed peaks in 2θ values around 38.22, 44.01, 64.58, 77.53, and 81.33 degrees, corresponding to the (111), (200), (229), (311), and (222) planes, respectively, of the face-centered cubic structure of metallic silver crystals (Joint Committee on Powder Diffraction Standards (JCPDS) file 04-0783) (Figure 4). Those nanoparticles prepared with broths from a regular nutritive medium showed additional peaks at 27.89, 32.25, 46.26, 54.86, and 57.52 degrees, corresponding to the same planes, associated with a face-centered cubic structure of AgCl crystals (JCPDS file 31-1238), indicating a detectable amount of this compound in these nanoparticles.

XRD analysis of the AgNPs showed some differences between AgNPs produced in regular or NaCl-deprived media. Those produced in a medium with NaCl contained detectable amounts of AgCl crystals, as their specific peaks were observed. AgNPs synthesized in a medium without NaCl only showed detectable peaks corresponding to Ag^0 crystals, even though a smaller amount of chlorine was also detected in their TXRF analyses. Several articles have described the detection of AgCl in the XRDs of their silver nanoparticles [52,53], attributing it to the presence of NaCl in the broths used in their synthesis [52].

The presence of this quite water-insoluble material in the AgNPs could affect their activity because of the difficulty of releasing silver ions and may be one of the factors responsible for the lower antibacterial activity showed by AgNPsExtCl and AgNPsStaCl. However, the nanoparticles of AgCl (AgClNPs) described in the literature still show antibacterial activity [52,53]. It is quite curious that the synthesis of AgNPs in media containing NaCl can produce materials in which the AgNPs are predominant versus the AgClNPs (this paper), or in which AgClNPs predominate [52,53]. Since the same concentration of NaCl is present in these cases, this cannot be the determining factor in the predominant chemical form, Ag^0 or AgCl, in which silver is found in these nanomaterials. Other factors such as the composition of reducing and protecting agents in the broths, or the methodological conditions, should have some influence on this. Perhaps the concentrations of reducing and capping agents in the biological material used for synthesis could be involved in this phenomenon. If high concentrations are present, they could, totally or partially, prevent the formation of AgCl crystals, nucleating and capping the Ag^0 cores. However, if the concentrations are low, the formation of AgCl crystals before most of the silver is reduced and cores capped could occur.
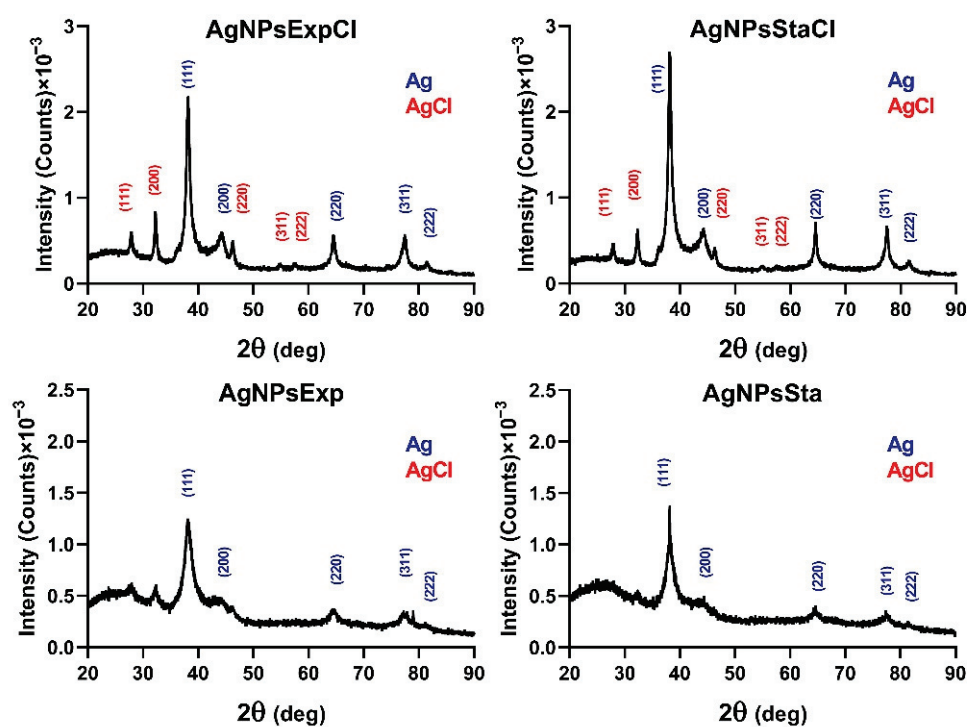
Figure 4. Nanoparticles' crystallinity determination. XRD patterns of the AgNPs with the indicated planes of Ag^0 (blue) and AgCl (red) crystals.

2.4.4. AgNPs' Core Shape and Size, as Determined by Transmission Electron Microscopy (TEM)

TEM images show the electrodense core of the AgNPs, from which their shape and size can be determined (Figure 5). The four types of AgNPs presented mostly quasi-spherical shapes, but other shapes were also found in a few nanoparticles. In some particles, higher electron density structures arranged in parallel lines were observed (examples are shown in the inset images in the lower-right corners of the panels in Figure 5).

From the analysis of several TEM images for each type of AgNPs, the average diameter of the AgNPs' cores and the polydispersity of their sizes were determined (Table 1). Average sizes were quite similar for all the AgNPs, except for AgNPsStaCl, which was almost double the size of the others. Size distributions were also assessed (Figure 6), allowing us to determine the AgNPs-cores' size polydispersity (Table 1).
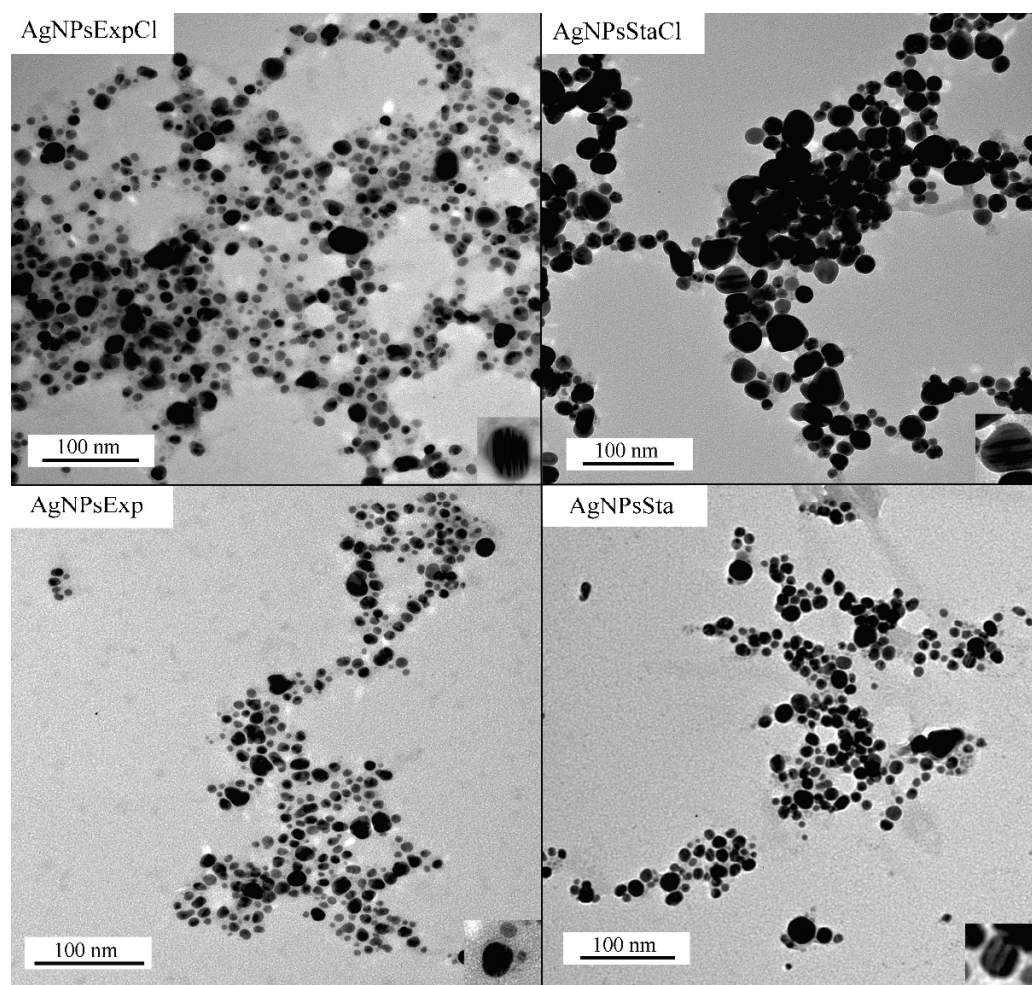
Figure 5. TEM representative images of AgNPs. Lower-right corner insets in each panel show an amplified image of a nanoparticle with internal parallel patterns.

Table 1. Summary of the AgNPs' characterization.

(AgNPs)	Z-Potential (mV)	Diameter (nm) (DLS)	PDI (DLS)	Diameter (nm) (TEM)	PDI (TEM)
AgNPsExpCl	−35.260 ± 3.295	41.760 ± 0.392	0.305 ± 0.001	9.290 ± 4.530	0.238
AgNPsStaCl	−19.850 ± 0.523	48.900 ± 1.746	0.343 ± 0.051	19.160 ± 9.450	0.243
AgNPsExp	−30.980 ± 5.893	28.780 ± 0.149	0.455 ± 0.001	8.301 ± 3.777	0.207
AgNPsSta	−23.500 ± 2.898	62.750 ± 0.918	0.304 ± 0.001	7.336 ± 5.875	0.415

The polydispersity index (PDI) values are quite similar for the various types of AgNPs, except for AgNPsSta, which is higher. In most cases, they correspond to moderate polydisperse suspensions following the nomenclature described in [54].

Recent reviews on the green synthesis of AgNPs show that a wide range of nanoparticle sizes and polydispersity can be found in the literature [9,12,13], with spherical shape being the most frequent. For instance, in the articles published from 2015 to 2021 that were summarized by Vishwanath and Negi (2021) [9], AgNPs with sizes from 2 to 200 nm, some over the limit of the nanoparticle scale, were reported. In this range, we could say that our AgNPs are rather small. Polydispersity of the AgNPs' sizes is also quite variable between reports, with monodispersity or low dispersity being scarce.
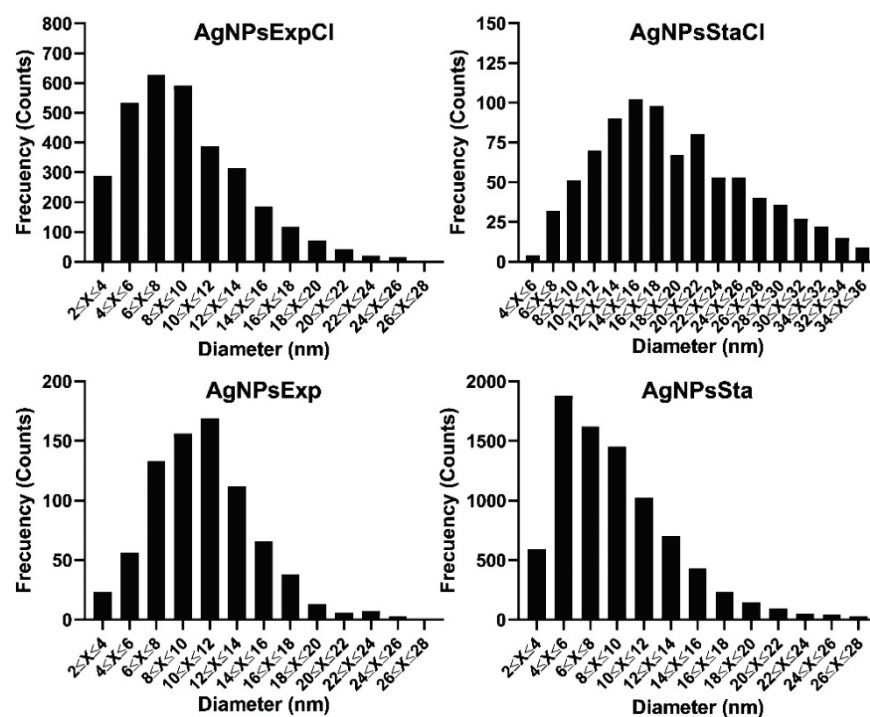
Figure 6. Distribution of AgNPs' core diameters.

2.4.5. Zeta-Potential and Hydrodynamic Diameter of AgNPs by Dynamic Light Scattering (DLS)

All the AgNPs presented a negative Z-potential, with higher values for nanoparticles synthesized using exponential phase broths, around −31 to −35 mV, than for those from stationary phases with values around −20 to −23.5 mV (Table 1). These results suggest the moderate to high stability of these materials, especially for those from exponential phase broths, assuming the generally considered relationship between Z-potential absolute values and the stability of colloids. However, such a direct relationship may not exist in many cases, as reported by Bhattacharjee (2017) [55]. No significant differences were observed based on the presence or absence of NaCl in the broths. Our test for the stability of AgNPs, prepared with stationary phase broths and based on UV-Vis spectra and antibacterial activity determination, also indicated good stability in water at 4 °C for at least two weeks, as has been indicated above.

Some authors have claimed a relationship between Z-potential and the antimicrobial activity of nanoparticles [56], suggesting that more negative values would correspond to AgNPs exhibiting reduced activity, because the repulsion of negatively charged bacterial envelopes would make it difficult to approach them. This is not the case for our AgNPs, as will be discussed below.

The average hydrodynamic diameters of the AgNPs (Table 1) were significantly different for the four types of AgNPs, with the smallest being that of AgNPsExp and the largest that of AgNPsSta. More similar were those of the AgNPs prepared with a regular nutritive medium. The size polydispersities were similar, around 0.30–0.34, indicating a moderate level for most AgNPs; the exception was AgNPsExp with a value of 0.45, slightly above the limit of moderate dispersity. Hydrodynamic diameters, as measured by DLS, show larger values than the core sizes, as can be expected. However, no correlation exists between these two sizes. We could speculate that media from the stationary phase may have higher concentration of compounds than those from the exponential phase, or different or additional ones, that may interact, producing a thicker corona. The presence of NaCl might regulate the addition of compounds on the AgNP cores, homogenizing the hydrodynamic size on cores of different size. Moreover, in [57], the authors found that NaCl can affect the hydrodynamic size, which may help to explain the findings of this study.

2.4.6. Corona Composition by Fourier Transform Infrared Spectroscopy (FTIR)

FTIR spectra showed almost no differences between the broths before and after the AgNP synthesis, with or without NaCl, but some differences could be detected among the various AgNPs and with the corresponding broths (Figure 7). In general, the infrared bands of the nanoparticles were thinner than those of the broths, indicating a simpler composition of the AgNPs' coronas. Moreover, differences in the fingerprint region can be observed between the various AgNPs, indicating their differential composition. In this region, a particular pattern is observed for each AgNP, but similarities can be observed between those coming from the same phase, from cultures with or without NaCl. Thus, the bands at around 1630 cm^{-1} are more intense that the triplet bands around 1060 cm^{-1} in the case of stationary phase AgNPs, and of similar intensity to those from the exponential one. The spectra of the two AgNPs from the stationary phase show differences in the bands around 1380–1400 cm^{-1} between those produced in a medium with NaCl or without it, with a higher intensity in the AgNPs from a medium with NaCl. Differences in this region between the AgNPs from exponential phase cultures are much less evident. These observations indicate a different composition among the four types of nanoparticles' coronas, with those obtained from the same growth phase being more similar, and less significant differences related to the presence of NaCl. The main bands of the AgNPs' IR spectra would correspond to vibrations of protein bonds (3430–3440 cm^{-1} and 1631–1635 cm^{-1} regions) and carbohydrates (1023–1106 cm^{-1} region), with minor contributions of other biomolecules. We used the barcode signals reported in [58] to ascribe the main FTIR bands to each type of biomolecule.
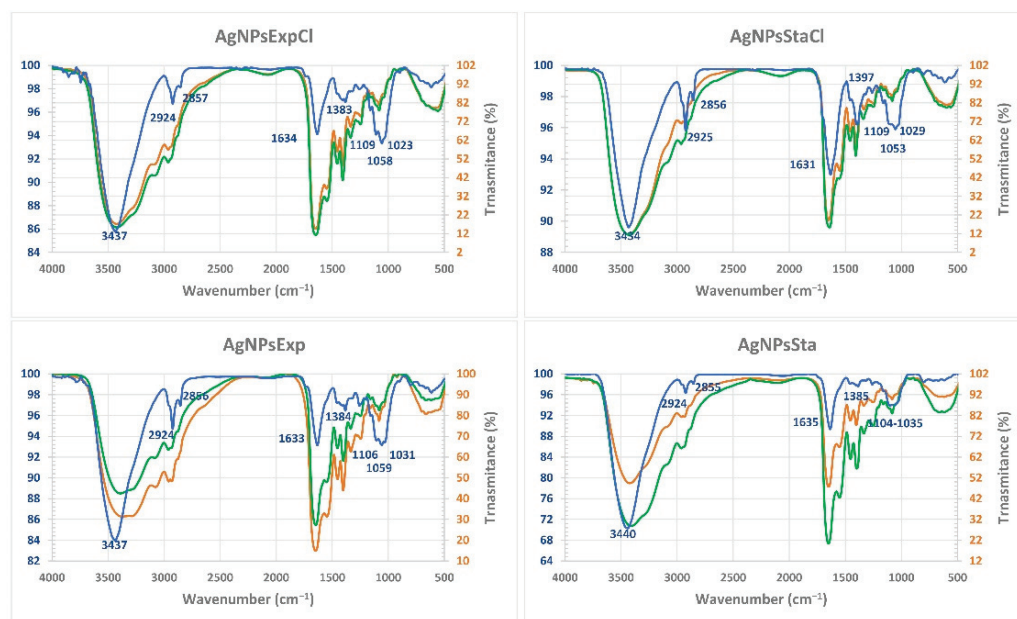
Figure 7. Characterization of the corona components of AgNPs and broths. AgNPs' spectra are shown in blue; the broths before synthesis are in orange and after synthesis in green. The wavenumber of the principal bands of AgNPs are indicated.

These results suggest that, although different conditions of synthesis are used, AgNPs tend to be surrounded by the same kind of organic compounds. Probably, differences in corona components exist, in terms of the proportion of each type of a particular compound, producing properties that may diversify its functionality. The absence of easily detectable differences in the FTIR spectra of the broth before and after synthesis tells us that most of the components detected were in high amounts, but only a small portion of them was used and attached to the silver core of the AgNPs. This agrees with the ability of the used broth to produce nanoparticles in at least two successive batches, as indicated above. The

differences between the broth and AgNPs' spectra indicate a selection during their synthesis of the components of the broth that remain on the corona. In the FTIR studies of other green synthesized AgNPs, different types of compounds have been reported; thus, for instance, Kumar and Mamidyala (2011) [26] determined the presence of proteins and lipids in the AgNPs produced by a supernatant of *Pseudomonas aeruginosa*, or in other cases, different spectra were reported [27,28,30], in most cases detecting the presence of proteins and other not well identified compounds. These different results would be related to the composition of the biological materials used in the biosynthesis and reinforce the possibility of obtaining AgNPs with different composition and properties based on biological diversity.

2.5. Antibacterial and Antibiofilm Activity of AgNPs

We evaluated each type of AgNPs for the growth inhibition of three Gram-negative bacteria and three Gram-positive ones by the microdilution method. The antibacterial activity parameters minimal inhibitory concentration (MIC), minimal bactericidal concentration (MBC), inhibitory concentration of 50% growth (IC_{50}), and inhibitory concentration of 50% biofilm formation (ICb_{50}) were also calculated (Table 2). Overall, the MIC values ranged between 0.24 and 9.68 μg of Ag/mL, depending on the AgNP type and bacterium tested. All the AgNPs showed a good activity (MIC < 10 μg of Ag/mL), with very low values for the four parameters against all bacteria. A recent review on the antibacterial activity of AgNPs described, for most of them, higher MICs values than those determined for our AgNPs [59]. For none of our AgNPs do the values of the antimicrobial activity parameters differentiate between Gram-negative and Gram-positive bacteria, but differences were observed among individual species.

Table 2. Antimicrobial and antibiofilm activity.

Test Bacteria	AgNPs	MIC (μg/mL)	MBC (μg/mL)	IC_{50} (μg/mL)	ICb_{50} (μg/mL)
E. coli ATCC 25922	AgNPsExpCl	1.01	1.34	0.12 ± 0.07 **	0.40 ± 0.05 **/##
	AgNPsStaCl	4.84	4.84	1.46 ± 0.34 **/#	2.75 ± 0.84 **/#
	AgNPsExp	0.49	0.49	0.02 ± 0.00 ***	0.14 ± 0.01 ***/##
	AgNPsSta	1.08	1.08	0.57 ± 0.05 ***/#	0.67 ± 0.03 ***/#
K. pneumoniae ATCC 29665	AgNPsExpCl	2.01	2.01	0.57 ± 0.16 */##	1.02 ± 0.91 *
	AgNPsStaCl	9.68	9.68	1.85 ± 0.73 */#	3.65 ± 0.54 */##
	AgNPsExp	0.97	0.97	0.06 ± 0.03 */##	0.54 ± 0.10 **
	AgNPsSta	1.08	1.08	0.48 ± 0.19 */#	1.13 ± 0.16 **/##
P. aeruginosa CECT 108	AgNPsExpCl	1.01	2.01	0.09 ± 0.04 */#	0.55 ± 0.03 ***/###
	AgNPsStaCl	2.42	4.84	0.55 ± 0.24 */#	1.31 ± 0.09 ***/###
	AgNPsExp	0.24	0.97	0.01 ± 0.00 **/#	0.13 ± 0.01 ***/###
	AgNPsSta	0.54	1.08	0.16 ± 0.0 2**/#	0.35 ± 0.03 ***/###
P. aeruginosa PA01	AgNPsExpCl	-	-	-	-
	AgNPsStaCl	-	-	-	-
	AgNPsExp	-	-	-	-
	AgNPsSta	0.54	1.08	0.09 ± 0.01	0.32 ± 0.05
P. aeruginosa PA14	AgNPsExpCl	-	-	-	-
	AgNPsStaCl	-	-	-	-
	AgNPsExp	-	-	-	-
	AgNPsSta	0.54	1.08	0.08 ± 0.04	0.25 ± 0.03
S. aureus CECT 794	AgNPsExpCl	4.03	4.03	0.58 ± 0.15 **/##	0.60 ± 0.34 ***
	AgNPsStaCl	9.68	9.68	4.64 ± 1.05 **/##	6.19 ± 0.08 ***/###
	AgNPsExp	1.94	3.89	0.06 ± 0.01 ***/##	1.05 ± 0.43
	AgNPsSta	1.44	2.15	0.82 ± 0.15 ***/##	1.14 ± 0.10 ###
S. epidermidis ATCC 12228	AgNPsExpCl	0.51	4.03	0.25 ± 0.05 ***/##	0.40 ± 0.24 **
	AgNPsStaCl	4.84	9.68	0.72 ± 0.02 ***/###	1.90 ± 0.25 **/###
	AgNPsExp	0.49	1.94	0.01 ± 0.00 **/##	0.23 ± 0.09 *
	AgNPsSta	1.08	4.31	0.29 ± 0.06 **/###	0.54 ± 0.09 */###

Table 2. *Cont.*

Test Bacteria	AgNPs	MIC (μg/mL)	MBC (μg/mL)	IC$_{50}$ (μg/mL)	ICb$_{50}$ (μg/mL)
B. subtilis 168	AgNPsExpCl	1.01	1.01	0.40 ± 0.08 **/##	0.24 ± 0.07 ***/#
	AgNPsStaCl	3.23	3.23	2.47 ± 0.65 **/##	0.70 ± 0.09 **/#
	AgNPsExp	0.48	0.49	0.02 ± 0.01 **/##	0.10 ± 0.03 #
	AgNPsSta	1.08	1.08	0.53 ± 0.15 **/##	0.50 ± 0.08 **/#

Antibacterial activity parameters are indicated as Ag concentrations; * indicates significant differences between AgNPs prepared from the same medium but different growth phase; # indicates significant differences between AgNPs from the same growth phase but from different media. *p*-value: <0.05 (*) or (#); <0.01 (**) or (##); <0.001 (***) or (###).

The highest MICs were for AgNPsStaCl, which ranged between 2.42 μg of Ag/mL for *P. aeruginosa* to 9.68 for *K. pneumoniae* and *S. aureus*, while, except for *S. aureus*, the most active was AgNPsExp, with values from 0.24 μg of Ag/mL for *P. aeruginosa* to 1.94 for *S. aureus*. Similar results were obtained for MBC and for IC$_{50}$ and ICb$_{50}$. The most susceptible bacterium to all AgNPs was *P. aeruginosa*, with MICs depending on AgNP type from 0.24 to 2.42 μg of Ag/mL and lower for *S. aureus* at 1.44–9.68 μg of Ag/mL. The results obtained indicated a higher activity for all the synthesized AgNPs against *P. aeruginosa* CECT 108, so we decided to include in the study two more strains of *P. aeruginosa*, from different origins, strains PA01 and PA14, to assess whether the lower values of the inhibitory concentrations were due to the species or the strain used. We chose AgNPsSta for this experiment because they have intermediate efficacy. The three strains showed similarly high susceptibility, suggesting that these AgNPs are especially active against this species. Some AgNPs have also been described as highly effective against *Pseudomonas*; for instance, AgNPs producing 99.9% of bacteria death at 5 μg/mL have been reported [60], and a 1 μg/mL MIC on *P. aeruginosa* ATCC 10145 has been described for other AgNPs, which required 4 μg/mL for inhibiting biofilm production [61]. However, very different levels of susceptibility have been reported for different strains, depending on the AgNPs used, with MICs from 1 μg/mL to 1 mg/mL [62].

In general, MIC and MBC values of the AgNPs were the same or MBC ≤ 4 × MIC, revealing a bactericidal mode of action in all bacteria evaluated for most of the AgNPs, as suggested in [63].

Physicochemical characteristics such as the shape, size, and Z-potential of AgNPs have been correlated with their antimicrobial activity. Thus, several reports have shown the effect of AgNPs shape on antimicrobial activity, sometimes with contradictory results. In some cases, a cubic shape seems to be more active than a spherical one [64]; in others, a triangular shape seems to be the most active [65]; in others still, the spherical shape has been found to be more active than triangular or others [66]. All our AgNPs were mostly spherical; moreover, good antimicrobial activity was found. Considering the AgNPs' sizes, the smallest have been associated with the best antimicrobial activity, due to their greater surface area [51,59,67,68]. In this report, the less active of our AgNPs had the largest core, while a range of higher activities was observed for the other three with similarly small sizes. This indicates a certain correlation between core size and antibacterial activity. However, the activities of the smaller AgNPs show larger differences than the sizes themselves. Probably, differences in the corona composition also have an effect on the observed antibacterial activity, as suggested by other reports in which a correlation of size and activity has not been found [29,69]. With respect to the Z-potential, more negatively charged particles have been suggested to be less active because of the eventual repulsion of the bacterial cell envelopes, also negatively charged [56]. However, in our case, the most negatively charged AgNPs are the AgNPsExpCl and the AgNPsExp, which, according to their MICs, are not less active; moreover, the AgNPsExp are the most active against most of the tested bacteria. The less charged ones are the AgNPsStaCl, but they are also less active. The effect of the Z-potential on AgNP activity is probably modulated by other factors in a still unknown way. For instance, the sign of the Z-potential can even change depending on

different factors such as pH [55]. Probably, for AgNPs that are chemically or physically produced, with low-complexity coronas, this correlation may be appropriate, but because of the high complexity of the green synthesized AgNPs, other factors may be acting to prevent such correlation.

The formation of biofilms by bacteria is usually a form of protection. It is known that the difficult penetration of substances in these structures is a way to diminish the action of antibacterial drugs [70,71]. Due to their sizes and surface properties, AgNPs have been evaluated as antibiofilm agents [72,73]. We have determined this activity of the AgNPs reported here and express it as ICb_{50} values (Table 2). These are all low, indicating the good ability of these materials to inhibit biofilm formation. In general, the comparison of ICb_{50} with IC_{50} shows the higher values of the former, indicating that these AgNPs are less active against biofilm formation than at inhibiting the growth of planktonic cells, but still showed good antibiofilm activity ($ICb_{50} < 6.20$ μg of Ag/mL). In other studies, some AgNPs have been shown to prevent the formation of biofilms by various bacteria; thus, for instance, it has been described that some commercial AgNPs were able to produce around 50% inhibition of biofilm formation at concentrations about 50 ppm for *E. coli* and a little higher for *S. aureus*, when MIC values were 6.25 and 12.5 ppm [73], respectively, showing quite a lower efficiency than our AgNPs.

2.6. Synergy of AgNPs with Classic Antibiotics by the Checkerboard Assay

Several studies have shown the ability of AgNPs to act synergistically with other drugs, such as antibiotics, in the inhibition of bacterial growth [74]. Therefore, we evaluated the possible synergy between our AgNPs and three classic antibiotics by the checkerboard assay [75,76]. The results of this analysis were analyzed based on the fractional inhibitory concentration index (FICI) [75–77] and the modulatory factor (MF) [40], for each antibiotic and AgNP combination (Table 3). A strong synergistic effect was observed between any of the AgNPs and streptomycin against *E. coli* and *S. aureus* (FICI ≤ 0.5; MF = 16–32). Synergy was also detected with ampicillin, but only against *S. aureus* (FICI ≤ 0.5; MF = 2–4). Moreover, additive activity (0.5 < FICI ≤ 1; MF = 1–2) was shown by AgNPsExp, Ag-NPsExpCl, or AgNPsStaCl in combination with nalidixic acid against *E. coli*. Indifferent effects were observed for all AgNPs with ampicillin against *E. coli*, as well as nalidixic acid against *S. aureus* and for AgNPsSta against *E. coli* (1 < FICI ≤ 2; MF = 1). No antagonistic effect (FICI ≥ 4) was detected. Using a stricter interpretation of FICI [75], a synergistic effect can be considered for all AgNPs with streptomycin against both bacteria and with ampicillin against *S. aureus*. The synergy observed by other authors was dependent on the AgNPs used, bacterial species tested, strains, and antibiotic. In previous studies recently reviewed by Ribeiro et al. [74], the most tested antibiotic was ampicillin, followed by streptomycin, while nalidixic acid was scarcely evaluated, and *E. coli* and *S. aureus* were the most frequently used bacteria. Depending on the study and the AgNPs used, positive or no synergy with ampicillin was reported; sometimes synergy of the same AgNPs was observed against either *E. coli* or *S. aureus*, both, or neither. For streptomycin, in most cases *E. coli* and *S. aureus* were synergistically inhibited by AgNPs, and only in a few cases was synergy only observed against *E. coli*. This illustrates the different behavior of various AgNPs depending on the method of synthesis and their physicochemical characteristics, though a correlation between the synergistic effects and any of the AgNP characteristics has not been described. The combined use of AgNPs and classic antibiotics may help to decrease the concentrations needed and perhaps the cytotoxic effects, as shown in [78]. This can also be useful for the recovering of antibiotics not used because of high levels of pathogen resistance, toxic effects on bacterial hosts, and perhaps the impossibility of reaching sufficient concentrations in the host's fluids or tissues for effective activity [39,41,42,79]. Mechanisms involved in AgNPs–antibiotic synergy have not been extensively studied, but some authors have correlated this phenomenon with the existence of an interaction between both components, which generates complexes that interact better with the bacterial envelopes and produce a higher release of Ag^+ from the AgNPs [80], but the possibility of

other mechanisms involving the proprietary mechanisms of each of the agents should not be ignored.

Table 3. Synergy effects of the AgNPs in combination with classic antibiotics against *E. coli* and *S. aureus*.

(AgNPs)	Test Bacteria	Ampicillin		Nalidixic Acid		Streptomycin	
		FICI	MF	FICI	MF	FICI	MF
AgNPsExpCl	*E. coli* ATCC 25922	2.000	1	0.750	2	0.047	32
	S. aureus CECT 794	0.500	2	2.000	1	0.047	16
AgNPsStaCl	*E. coli* ATCC 25922	2.000	1	1.000	1	0.180	32
	S. aureus CECT 794	0.375	4	2.000	1	0.125	16
AgNPsExp	*E. coli* ATCC 25922	2.000	1	0.625	2	0.094	32
	S. aureus CECT 794	0.375	4	2.000	1	0.078	16
AgNPsSta	*E. coli* ATCC 25922	2.000	1	2.000	1	0.039	32
	S. aureus CECT 794	0.375	4	2.000	1	0.039	32

2.7. Reactive Oxygen Species (ROS) Production

The production of reactive oxygen species (ROS) is generally considered one of the main mechanisms for AgNPs' antibacterial activity. However, this is controversial and Krce et al. (2020) [81] have claimed that it is not the case, and rather that the effect on the membrane's permeability is the main mechanism of antibacterial activity. However, the possibility still exists of ROS being one of the factors leading to the antibacterial activity of AgNPs. We have carried out a preliminary study on the production of ROS by the method generally used: measurement of fluorescence generated by the ROS effect on the structure of DCFH-DA, following an increase in fluorescence over time for several hours. The fluorescence increased over time for each AgNP in a dose-dependent way (Figure 8). For the analysis of ROS production by different nanoparticles, depending on the bacterial species used and AgNP concentrations, fluorescence produced after 6 h of incubation for each tested AgNP concentration was plotted on a graph (Figure 9). Fluorescence signals were not saturated at that time. A decrease in fluorescence was detected at the higher AgNP concentrations in all cases. This effect may be due to a methodological problem consisting of fluorescence shielding by the increased AgNP concentrations, as claimed in [81], or perhaps to other as yet unknown reasons. When considering that the AgNP concentrations producing the maximum fluorescence, differences were observed that may be related to their antibacterial activity parameters. The higher concentrations corresponded to the AgNPsStaCl, which also showed the highest MIC for *E. coli*. For *S. aureus*, the AgNPs showing the highest MIC also needed more concentration for maximum ROS production, even though in this case it was less clear. For the other AgNPs, for which MIC values were smaller and more similar, lower concentrations were needed for maximum ROS production and the differences between them were smaller, as also seen for the antibacterial activity parameters. These results support the idea that, in the two tested bacteria, the ROS production of our AgNPs is related to the efficiency of their antibacterial activity. However, more, and more precise studies of this relationship should be undertaken. Nevertheless, such a correlation does not clarify the cause–effect mechanism of the antibacterial activity. It is possible that the ROS produced by the AgNPs damages cellular components, leading to cell envelopes' disruption and cell death, or the AgNPs first damage the envelopes, which causes the observed ROS increase, with the consecutive cellular damage that leads to the cells' death. These two controversial models still need to be elucidated. The use of structurally related AgNPs with different antibacterial activities might help us to understand

the involvement of ROS production, and other possible factors, such as envelope damage, in the antibacterial activity of AgNPs, in experiments that we would like to perform soon.

This work focused on determining the antibacterial properties of the synthesized AgNPs, but many other applications for these nanomaterials may be possible, such as biomedical ones related to antiviral, antifungal and anticancer activities as well as biosensing and photo-thermal therapies, and in other fields such as optoelectronics, bioremediation, etc. [8], which may be explored in the future.
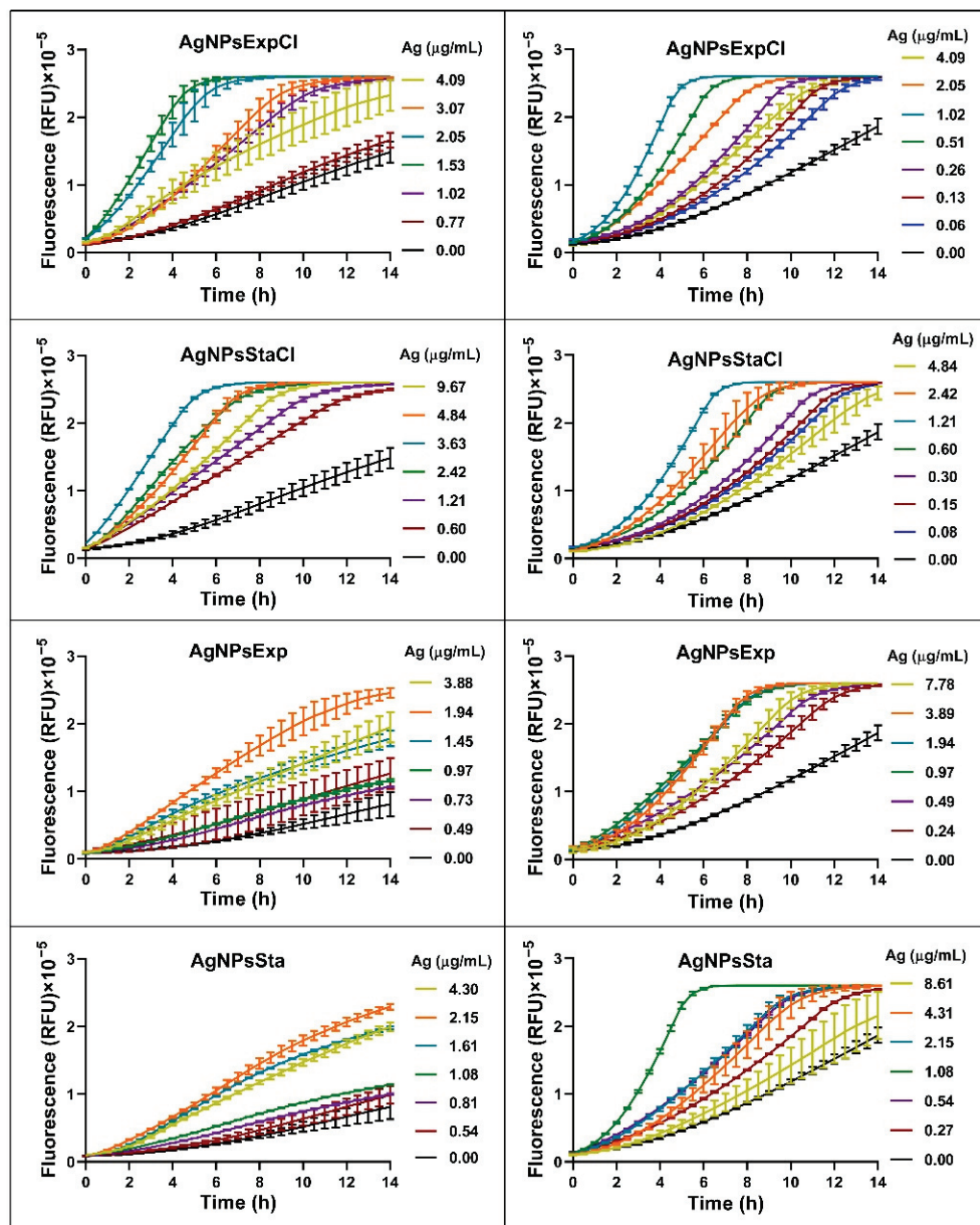
Figure 8. Kinetics of ROS production over time by cultures of *E. coli* ATCC 25922 (**left panels**) and *S. aureus* CECT 794 (**right panels**) in the presence of AgNPs. RFU: relative fluorescence units.
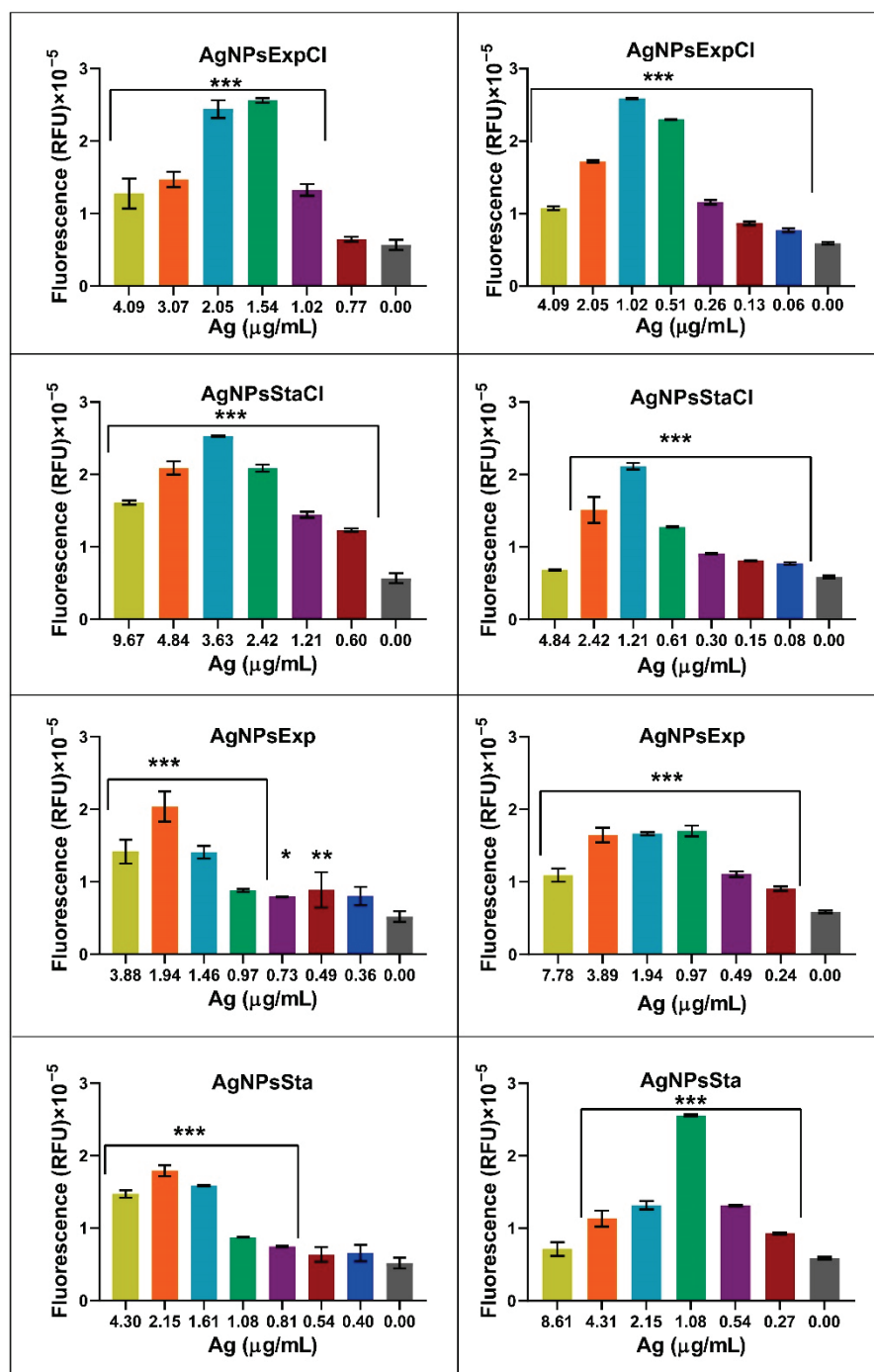
Figure 9. Production of ROS by cultures of *E. coli* ATCC 25922 (**left panels**) and *S. aureus* CECT 794 (**right panels**) after 6 h of incubation with AgNPs. RFU: relative fluorescence units. *p*-value: <0.05 (*), <0.01 (**), and <0.001 (***).

3. Materials and Methods

3.1. Microorganisms and Culture Media

The bacterium used to prepare AgNPs was previously isolated from the Tinto River estuary (Huelva, Spain) [43]. Phylogenetic ascription of the isolate was performed based on sequence analyses of the 16S rRNA and *rpo*D genes as follows.

Genomic DNA was extracted from cells obtained by culture on nutritive agar medium and using the protocol of the Ultraclean Microbial DNA Isolation Kit (MOBIO laboratories Inc., Carlsbad, CA, USA). From the DNA obtained, PCR amplifications of 16S rDNA (primers 27F and 1492R [82] and *rpo*D (primers PsEG30F and PsEG790R [44]) were

carried out in an Applied Biosystems 2720 (Applied Biosystems, Waltham, MA, USA) thermocycler. PCR reactions, in a final volume of 50 μL, contained template DNA, (1X) PCR buffer, 3 mM MgCl$_2$, 0.25 μM (each) dNTPs, 0.50 μM (each) primers, and 2.5 U Taq polymerase (NZYTech, Portugal). After an initial denaturation step at 94 °C for 5 min, 30 cycles of 94 °C for 1 min, 54 °C for 1 min, and 72 °C for 1.5 min were performed, and the reaction was finished with a 10-min extension at 72 °C. For the *rpo*D amplification primers, annealing was performed at 52 °C. Amplicons were visualized by electrophoresis in a 1% agarose gel, to guarantee the quality of the DNA, and purified by the polyethylene glycol–NaCl method [83]. Finally, the DNA samples were sequenced by Macrogen (Amsterdam, The Netherlands). The GenBank accession numbers are OP422521 (16S rRNA) and OP434430 (*rpo*D). Sequences were analyzed using FinchTV 1.4.0 (https://digitalworldbiology.com/FinchTV (accessed 2 November 2022)) for sequencing chromatograms, clustal X2 (http://www.clustal.org/clustal2/ (accessed 2 November 2022) for sequence alignment and neighbor-joining tree building, and njplot (https://njplot.software.informer.com/download/ (accessed 2 November 2022)) for visualizing the phylogenetic tree. Sequences from 16S rRNA of type strains of *Pseudomonas* species used in the phylogenetic analysis were obtained from the RDP Release 11 database (http://rdp.cme.msu.edu/ (accessed 2 November 2022)). Sequences of *rpo*D genes were obtained from GenBank.

Bacterial strains used for antibacterial activity testing were the Gram-negative bacteria *E. coli* ATCC 25922, *K. pneumoniae* ATCC 2966 and *P. aeruginosa* CECT 108, PA01, and PA14, and the Gram-positive ones *B. subtilis* 168, *S. aureus* CECT 794, and *S. epidermidis* ATCC 12228.

Culture media used were nutritive broth (3 g/L meat extract (Merck Millipore, Darmstadt, Germany), 5 g/L bacteriological peptone (Condalab, Torrejón de Ardoz, Spain), 5 g/L NaCl (Merck), nutritive agar (additional 15 g/L European bacteriological agar (Condalab)), and NaCl-deprived nutritive broth. Cultures were performed at 30 °C to grow *P. alloputida* and at 37 °C to grow the test bacteria.

3.2. Cell-Free Broth Preparation

P. alloputida cultures were set in 1-L Erlenmeyer flasks containing 400 mL of medium, with or without NaCl, in a Gyrotory® Water Bath Shaker model G76 (New Brunswick Scientific Co., Inc., Edison, NJ, USA) at 30 °C with shaking at 150 rpm. Exponential and stationary growth phases were sampled from both cultures. Cell-free broths were prepared by centrifugation in a Sorvall RC-5 Superspeed Floor Model Centrifuge (DuPont Instruments, Wilmington, DE, USA) at 22,200× *g* during 30 min and filtration of the supernatant through 0.22-μm pore size Millex® filters (Merck-Millipore, Cork, Ireland). Samples were kept at −20 °C until use.

3.3. Biosynthesis of AgNPs

For AgNP biosynthesis, a 20 mM AgNO$_3$ (Merck) solution in Milli-Q® water, obtained with a Simplicity® model of water purification system (Merck-Millipore) was added to the cell-free broths up to a 1 mM AgNO$_3$ final concentration. The reaction mixture was kept at 22 °C under fluorescent light tubes (three Sylvania 18 W tubes 15 cm above the sample). Depending on the growth phase and the broth used, nanoparticles were identified as AgNPsExpCl and AgNPsStaCl, for exponential and stationary phases, respectively, of regular nutritive medium cultures (containing NaCl), and AgNPsExp and AgNPsSta, for exponential and stationary phases, respectively, for NaCl-deprived nutritive medium cultures. Color changes of the mixtures to yellow-brown indicated nanoparticle production. UV-Vis spectra (300–700 nm) of the mix were used for spectrophotometric characterization of the AgNPs over time during their synthesis for kinetics determination. After reaching maximum absorbance without aggregation, the AgNPs were purified from the rest of the mix components by centrifugation in an Eppendorf 5430 model centrifuge (Eppendorf, Hamburg, Germany) at 20,800× *g* four times, first for 15 min, and then three times for

30 min each. Afterwards, the collected pellets were mixed and washed four times with Milli-Q water, recovering AgNPs by centrifugation in the same conditions. The final pellets were resuspended in Milli-Q water at a tenth of the initial reaction volume and kept at 4 °C, for not more than one week, until use.

3.4. Characterization of Biosynthesized AgNPs

3.4.1. UV-Visible Spectrophotometry

Formation of AgNPs, kinetics of synthesis, and final spectra of the purified Ag-NPs were followed by UV-Vis spectroscopy from 300–700 nm at 1 nm resolution using a microtiter plate incubator/reader model FLUOStar® Omega (BMG Labtech, Offenburg, Germany).

3.4.2. Transmission Electron Microscopy (TEM) of AgNPs

The shape and size of the AgNPs were determined by transmission electron microscopy (TEM) at the Centro de Biología Molecular Severo Ochoa (Madrid, Spain) using a JEM1400 JEOL microscope (Tokio, Japan) with a Oneview (Gatan Inc.-Ametek, Berwyn, PA, USA) CCD camera with a 4 K × 4 K sensor. Five microliters of a 1/50 dilution in Milli-Q water of the AgNPs stock were deposited on collodion-covered copper grids shaded with carbon, and dried before use in a Concentrator plus/Vacufuge® plus (Eppendorf)) without centrifugation. Grids were kept at room temperature and protected from light. At least 500 particles of every AgNP type were analyzed with the program ImageJ64 (https://imagej.nih.gov/ij/download.html (accessed 2 November 2022)) to determine nanoparticles' diameters. Microsoft Excel (Microsoft, Redmond, WA, USA) was used to calculate the average size and polydispersity index (PDI) using the formula PDI = $(\sigma/\gamma)^2$, where σ indicates the standard deviation of the diameter size of the nanoparticles and γ their mean [84].

3.4.3. Fourier Transform Infrared Spectroscopy (FTIR) of AgNPs

Fourier Transform Infrared Spectroscopy (FTIR) was performed at the Servicio Interdepartamental de Investigación (SIdI) of the Universidad Autónoma de Madrid (UAM). The wavenumber range was 4000–500 cm^{-1} with a 0.05 × 0.05 mm slit. Spectra were taken on a Spectrum Two (Perkin-Elmer, Waltham, MA, USA) for macro analysis (for AgNPs) or a Spotlight 200 (Perkin-Elmer) (for broths), on samples deposited on KBr pellets and dried in a vacuum. When broths of the reaction mixtures after synthesis were measured, a microanalysis was performed, centered on the clear zone of the prepared pellets to prevent the interference of residual nanoparticles.

3.4.4. X-ray Diffraction of AgNPs

X-ray diffraction (XRD) analysis was performed at the SIdI of the UAM, using a model X'Pert PRO theta/2theta X-ray diffractometer (Malvern Panalytical, Malvern, UK), with a primary germanium monochromator (monochromator Johansson) and an X'Celerator fast detector.

3.4.5. Total Reflection X-ray Fluorescence (TXRF)

This technique was used for determining AgNPs' composition and the silver concentration of AgNP suspensions at the SIdI of the UAM, using a S2 PicoFox TXRF spectrometer (Bruker, Ettlingen, Germany), equipped with a Mo X-ray source working at 50 kV and 600 μA, a multilayer monochromator with 80% reflectivity at 17.5 keV (Mo K), and an XFlash SDD detector with an effective area of 30 mm^2 and an energy resolution of better than 150 eV for 5.9 keV (Mn Kα). For deconvolution and integration, the commercial software package Spectra v. 7.5.3 (Bruker) was used.

3.4.6. Zeta Potential and Hydrodynamic Diameter of AgNPs

These parameters were measured by dynamic light scattering (DLS) using a Zetasizer Ultra (Malvern Panalytical, Malvern, UK), at the Dept. of Material Physics of the UAM, using samples diluted in Milli-Q water.

3.5. *Antibacterial Activity of AgNPs*

3.5.1. Microdilution Method

Cultures in nutritive medium were set in 96-well microplates (Sarstedt, Nümbrecht, Germany), with a final volume of 200 μL per well. The test bacteria were adjusted to 5×10^5 CFU/mL, and 1/2 serial dilutions of the stock suspensions of the AgNPs were distributed in the wells. The corresponding negative controls were also set. Microplates were incubated overnight at 37 °C, in the same microtiter plate incubator/reader indicated above. Absorbance at 660 nm was registered every hour, after 20 s shaking. All samples were implemented at least in triplicate. MIC was determined as the AgNPs concentration in the well with no apparent growth. For MBC determination, 50-μL aliquots of cultures in the wells corresponding to the MIC and two concentrations immediately above were plated in nutritive agar in duplicate. After overnight incubation at 37 °C, the MBC was calculated after colony counting and determination of the concentration of AgNPs corresponding to a killing of at least 99.9% of the original viable bacteria. IC_{50} values were calculated using GraphPad Prism VIII (GraphPad software, San Diego, CA, USA) from the growth inhibition data corresponding to the incubation times in which the growth controls reached the early stationary phase.

3.5.2. Antibiofilm Assay

Biofilm formation was evaluated by a crystal violet assay [85] with some modifications. The broths in the microplates, used for growth inhibition activity determination, were replaced with 200 μL of methanol (Honeywell, Seelze, Germany) and the microplates incubated for 20 min at RT to fix biofilms. Subsequently, methanol was replaced with 200 μL of a crystal violet (Sigma-Aldrich, St. Louis, MO, USA) 0.5% solution in Milli-Q water and the plates incubated for 20 min. After removing the colorant solution, the biofilm was washed four times with 300 μL of distilled water to remove the excess dye and dried at RT. To dissolve the dye that adhered to the biofilm, 200 μL of 96% (*v/v*) ethanol (VWR® Chemicals, Ronsy-sous-Bois, France) were added. Measurement of the dissolved crystal violet was performed at 590 nm after 30 min and after 24 h of incubation. The highest of the two readings was considered.

3.6. *Synergy of AgNPs with Classic Antibiotics in Growth Inhibition*

A checkerboard type of assay [76] was used. Test bacteria for these assays were *E. coli* ATCC 25922 and *S. aureus* CECT 794. Three classical antibiotics with different cellular targets were chosen: ampicillin, nalidixic acid, and streptomycin. The assays were carried out in 96-well microplates. The MIC of each antibiotic for each microorganism was determined previously by microdilution. Half dilutions of each antibiotic and AgNPs were prepared and distributed throughout the plate. In each well, 90 μL of bacterial culture at 1×10^6 CFU/mL were added, together with 90 μL of fresh nutritive broth, 10 μL of AgNP dilutions, and 10 μL of the corresponding antibiotic diluted solutions. Negative controls, and AgNPs and antibiotics alone, were included in the microplates. Experiments were performed in duplicate. Microplates were incubated at 37 °C for 24 h. The MIC of each antibiotic and AgNP were confirmed in the same plate as their combinations. The fractional inhibitory concentration index (FICI) [75,76] was calculated, as well as the modulatory factor (MF) [40].

3.7. *Reactive Oxygen Species (ROS) Detection*

ROS production tests were carried out with 2′-7′-dichlorodihydrofluorescein diacetate (DCFH-DA) (Sigma-Aldrich), based on the protocols described [81,86], using *E. coli* ATCC

25922 and *S. aureus* CECT 794. Bacterial cultures in the exponential phase were pelleted at $9400\times g$ and resuspended in a PBS buffer. Bacteria at 7.5×10^7 CFU/mL and DCFH-DA at a 5 μM final concentration were mixed in 96-well microplates. To the 190 μL of mixture, 10 μL of AgNPs at different concentrations, above and below their MICs, were added. Milli-Q water was used as a negative control and 0.33 mM H_2O_2 as a positive one. Plates were incubated aerobically at 37 °C for 14 h, measuring every half hour, with prior agitation at 300 rpm, using an excitation of 485–12 nm and an emission of 520 nm. The fluorescence produced after 6 h of incubation was used to compare ROS production in the presence of the different AgNPs.

3.8. Statistical Analysis

The values of IC_{50} and ICb_{50} against each bacterium were analyzed using a two-tailed unpaired *t*-test with a *p*-value of 0.05. Values for AgNPs were tested to determine differences between those prepared with the same type of broth, presence or not of NaCl, and growth phase origin. The results of ROS detection were analyzed using a two-way ANOVA and Dunnett's multiple comparison, with a *p*-value = 0.05 to detect significant differences between the negative control and the presence of different concentrations of AgNPs.

4. Conclusions

In this work, four types of AgNPs were produced by a green method, based on the use of broths from exponential and stationary growth phases of *P. alloputida* cultures in media with or without NaCl, reusing the broths for three successive batches. These AgNPs were shown to be good metal-based antibacterial drugs, especially against *P. aeruginosa* strains. These AgNPs can perform synergistically with classic antibiotics, decreasing the concentrations needed of both agents in the inhibition of bacterial growth, which may be of interest for fighting infections and lowering toxicity against the bacterial hosts. We have also shown that the ROS production promoted by these nanomaterials is related to their antibacterial activity, suggesting that they can be useful tools for studying the mechanisms involved in the antibacterial activity of Ag-based drugs.

Conflicts of Interest: The authors declare no conflict of interest.

Sample Availability: Samples of *P. alloputida* B003 UAM are available from the authors.

References

1. World Health Organization. *Antimicrobial Resistance and Primary Health Care: Brief*; World Health Organization: Geneva, Switzerland, 2018.
2. Mahoney, A.R.; Safaee, M.M.; Wuest, W.M.; Furst, A.L. The Silent Pandemic: Emergent Antibiotic Resistances Following the Global Response to SARS-CoV-2. *iScience* **2021**, *24*, 102304. [CrossRef] [PubMed]
3. O'Neill, J. *Tackling Drug-Resistant Infections Globally: Final Report and Recommendations*; The Review on Antimicrobial Resistance; HM Government and the Wellcome Trust: London, UK, 2016.
4. Rudramurthy, G.R.; Swamy, M.K.; Sinniah, U.R.; Ghasemzadeh, A. Nanoparticles: Alternatives Against Drug-Resistant Pathogenic Microbes. *Molecules* **2016**, *21*, 836. [CrossRef] [PubMed]
5. Amaro, F.; Morón, Á.; Díaz, S.; Martín-González, A.; Gutiérrez, J.C. Metallic Nanoparticles—Friends or Foes in the Battle against Antibiotic-Resistant Bacteria? *Microorganisms* **2021**, *9*, 364. [CrossRef] [PubMed]
6. Kędziora, A.; Speruda, M.; Krzyżewska, E.; Rybka, J.; Łukowiak, A.; Bugla-Płoskońska, G. Similarities and Differences between Silver Ions and Silver in Nanoforms as Antibacterial Agents. *Int. J. Mol. Sci.* **2018**, *19*, 444. [CrossRef]
7. Gordienko, M.G.; Palchikova, V.V.; Kalenov, S.V.; Belov, A.; Lyasnikova, V.N.; Poberezhniy, D.Y.; Chibisova, A.V.; Sorokin, V.V.; Skladnev, D.A. Antimicrobial Activity of Silver Salt and Silver Nanoparticles in Different Forms against Microorganisms of Different Taxonomic Groups. *J. Hazard. Mater.* **2019**, *378*, 120754. [CrossRef]
8. Lee, S.H.; Jun, B.-H. Silver Nanoparticles: Synthesis and Application for Nanomedicine. *Int. J. Mol. Sci.* **2019**, *20*, 865. [CrossRef]
9. Vishwanath, A.; Negi, B. Conventional and Green Methods of Synthesis of Silver Nanoparticles and Their Antimicrobial Properties. *Curr. Res. Green Sustain. Chem.* **2021**, *4*, 100205. [CrossRef]
10. Prasher, P.; Sharma, M. Synthesis of Silver Nanoparticles. In *Silver Nanoparticles: Synthesis, Functionalization and Applications*; Bentham books: Singapore, 2022; pp. 22–44. [CrossRef]
11. Singh, P.; Kim, Y.-J.; Zhang, D.; Yang, D.-C. Biological Synthesis of Nanoparticles from Plants and Microorganisms. *Trends Biotechnol.* **2016**, *34*, 588–599. [CrossRef]
12. Prasad, S.R.; Teli, S.B.; Ghosh, J.; Prasad, N.R.; Shaikh, V.S.; Nazeruddin, G.M.; Al-Sehemi, A.G.; Patel, I.; Shaikh, Y.I. A Review on Bio-Inspired Synthesis of Silver Nanoparticles: Their Antimicrobial Efficacy and Toxicity. *Eng. Sci.* **2021**, *16*, 90–128. [CrossRef]
13. Huq, M.A.; Ashrafudoulla, M.; Rahman, M.M.; Balusamy, S.R.; Akter, S. Green Synthesis and Potential Antibacterial Applications of Bioactive Silver Nanoparticles: A Review. *Polymers* **2022**, *14*, 742. [CrossRef]
14. Nadaf, S.J.; Jadhav, N.R.; Naikwadi, H.S.; Savekar, P.L.; Sapkal, I.D.; Kambli, M.M.; Desai, I.A. Green Synthesis of Gold and Silver Nanoparticles: Updates on Research, Patents, and Future Prospects. *OpenNano* **2022**, *8*, 100076. [CrossRef]
15. Remya, R.R.; Julius, A.; Suman, T.Y.; Aranganathan, L.; Stalin Dhas, T.; Mohanavel, V.; Karthick, A.; Muhibbullah, M. Biofab-rication of Silver Nanoparticles and Current Research of Its Environmental Applications. *J. Nanomater.* **2022**, *2022*, 2670429. [CrossRef]
16. Salnus, S.; Wahab, W.; Arfah, R.; Zenta, F.; Natsir, H.; Muri, M.; Fatimah, F.; Rajab, A.; Armah, Z.; Irfandi, R. A Review on Green Synthesis, Antimicrobial Applications and Toxicity of Silver Nanoparticles Mediated by Plant Extract. *Indones. J. Chem.* **2022**, *22*, 1129–1143. [CrossRef]
17. Akintelu, S.A.; Bo, Y.; Folorunso, A.S. A Review on Synthesis, Optimization, Mechanism, Characterization, and Antibacterial Application of Silver Nanoparticles Synthesized from Plants. *J. Chem.* **2020**, *2020*, 3189043. [CrossRef]
18. Kakakhel, M.A.; Sajjad, W.; Wu, F.; Bibi, N.; Shah, K.; Yali, Z.; Wang, W. Green Synthesis of Silver Nanoparticles and Their Shortcomings, Animal Blood a Potential Source for Silver Nanoparticles: A Review. *J. Hazard. Mater. Adv.* **2021**, *1*, 100005. [CrossRef]
19. Han, L.; Kim, Y.S.; Cho, S.; Park, Y. Invertebrate Water Extracts as Biocompatible Reducing Agents for the Green Synthesis of Gold and Silver Nanoparticles. *Nat. Prod. Commun.* **2013**, *8*, 1149–1152. [CrossRef]
20. Jacob, J.M.; Ravindran, R.; Narayanan, M.; Samuel, S.M.; Pugazhendhi, A.; Kumar, G. Microalgae: A Prospective Low-Cost Green Alternative for Nanoparticle Synthesis. *Curr. Opin. Environ. Sci. Health* **2021**, *20*, 100163. [CrossRef]
21. Rattan, R.; Shukla, S.; Sharma, B.; Bhat, M. A Mini-Review on Lichen-Based Nanoparticles and Their Applications as Antimicrobial Agents. *Front. Microbiol.* **2021**, *12*, 633090. [CrossRef]
22. Guilger-Casagrande, M.; de Lima, R. Synthesis of Silver Nanoparticles Mediated by Fungi: A Review. *Front. Bioeng. Biotechnol.* **2019**, *7*, 287. [CrossRef]
23. Tsekhmistrenko, S.I.; Bityutskyy, V.S.; Tsekhmistrenko, O.S.L.; Horalskyi, P.; Tymoshok, N.O.; Spivak, M.Y. Bacterial Synthesis of Nanoparticles: A Green Approach. *Biosyst. Divers.* **2020**, *28*, 9–17. [CrossRef]
24. Huq, A.; Akter, S. Bacterial Mediated Rapid and Facile Synthesis of Silver Nanoparticles and Their Antimicrobial Efficacy against Pathogenic Microorganisms. *Materials* **2021**, *14*, 2615. [CrossRef]
25. Mokhtari, N.; Daneshpajouh, S.; Seyedbagheri, S.; Atashdehghan, R.; Abdi, K.; Sarkar, S.; Minaian, S.; Shahverdi, H.R.; Shahverdi, A.R. Biological Synthesis of Very Small Silver Nanoparticles by Culture Supernatant of *Klebsiella pneumonie*: The Effects of Visible-Light Irradiation and the Liquid Mixing Process. *Mater. Res. Bull.* **2009**, *44*, 1415–1421. [CrossRef]

26. Kumar, C.G.; Mamidyala, S.K. Extracellular Synthesis of Silver Nanoparticles Using Culture Supernatant of *Pseudomonas aeruginosa*. *Colloids Surf. B* **2011**, *84*, 462–466. [CrossRef] [PubMed]

27. Hossain, A.; Hong, X.; Ibrahim, E.; Li, B.; Sun, G.; Meng, Y.; Wang, Y.; An, Q. Green Synthesis of Silver Nanoparticles with Culture Supernatant of a Bacterium *Pseudomonas rhodesiae* and Their Antibacterial Activity against Soft Rot Pathogen *Dickeya dadantii*. *Molecules* **2019**, *24*, 2303. [CrossRef] [PubMed]

28. Otari, S.V.; Patil, R.M.; Ghosh, S.J.; Thorat, N.D.; Pawar, S.H. Intracellular Synthesis of Silver Nanoparticle by Actinobacteria and Its Antimicrobial Activity. *Spectrochim. Acta A Mol. Biomol. Spectrosc.* **2015**, *136*, 1175–1180. [CrossRef]

29. Javani, S.; Marín, I.; Amils, R.; Abad, J.P. Four Psychrophilic Bacteria from Antarctica Extracellularly Biosynthesize at Low Temperature Highly Stable Silver Nanoparticles with Outstanding Antimicrobial Activity. *Colloids Surf. A: Physicochem. Eng. Asp.* **2015**, *483*, 60–69. [CrossRef]

30. Mujaddidi, N.; Nisa, S.; Al Ayoubi, S.; Bibi, Y.; Khan, S.; Sabir, M.; Zia, M.; Ah-mad, S.; Qayyum, A. Pharmacological Properties of Biogenically Synthesized Silver Nanoparticles Using Endophyte *Bacillus cereus* Extract of *Berberis lyceum* against Oxidative Stress and Pathogenic Multidrug-Resistant Bacteria. *Saudi J. Biol. Sci.* **2021**, *28*, 6432–6440. [CrossRef]

31. Luo, K.; Jung, S.; Park, K.-H.; Kim, Y.-R. Microbial Biosynthesis of Silver Nanoparticles in Different Culture Media. *J. Agric. Food Chem.* **2018**, *66*, 957–962. [CrossRef]

32. Baltazar-Encarnación, E.; Escárcega-González, C.E.; Vasto-Anzaldo, X.G.; Cantú-Cárdenas, M.E.; Morones-Ramírez, J.R. Silver Nanoparticles Synthesized through Green Methods Using *Escherichia coli* Top 10 (Ec-Ts) Growth Culture Medium Exhibit Antimicrobial Properties against Nongrowing Bacterial Strains. *J. Nanomater.* **2019**, *2019*, 4637325. [CrossRef]

33. Mateo, E.M.; Jiménez, M. Silver Nanoparticle-Based Therapy: Can It Be Useful to Combat Multi-Drug Resistant Bacteria? *Antibiotics* **2022**, *11*, 1205. [CrossRef]

34. Mussin, J.; Robles-Botero, V.; Casañas-Pimentel, R.; Rojas, F.; Angiolella, L.; San Martín-Martínez, E.; Giusiano, G. Antimicrobial and Cytotoxic Activity of Green Synthesis Silver Nanoparticles Targeting Skin and Soft Tissue Infectious Agents. *Sci. Rep.* **2021**, *11*, 14566. [CrossRef] [PubMed]

35. Skóra, B.; Krajewska, U.; Nowak, A.; Dziedzic, A.; Barylyak, A.; Kus-Liśkiewicz, M. Noncytotoxic Silver Nanoparticles as a New Antimicrobial Strategy. *Sci. Rep.* **2021**, *11*, 13451. [CrossRef] [PubMed]

36. Skanda, S.; Bharadwaj, P.S.J.; Datta Darshan, V.M.; Sivaramakrishnan, V.; Vijayakumar, B.S. Proficient Mycogenic Synthesis of Silver Nanoparticles by Soil Derived fungus *Aspergillus melleus* SSS-10 with Cytotoxic and Antibacterial Potency. *J. Microbiol. Methods* **2022**, *199*, 106517. [CrossRef] [PubMed]

37. Helmlinger, J.; Sengstock, C.; Groß-Heitfeld, C.; Mayer, C.; Schildhauer, T.A.; Köller, M.; Epple, M. Silver Nanoparticles with Different Size and Shape: Equal Cytotoxicity, but Different Antibacterial Effects. *RSC Adv.* **2016**, *6*, 18490–18501. [CrossRef]

38. Bamal, D.; Singh, A.; Chaudhary, G.; Kumar, M.; Singh, M.; Rani, N.; Mundlia, P.; Sehrawat, A.R. Silver Nanoparticles Biosynthesis, Characterization, Antimicrobial Activities, Applications, Cytotoxicity and Safety Issues: An Updated Review. *Nanomaterials* **2021**, *11*, 2086. [CrossRef] [PubMed]

39. Lopez-Carrizales, M.; Velasco, K.; Castillo, C.; Flores, A.; Magaña, M.; Martinez-Castanon, G.; Martinez-Gutierrez, F. In Vitro Synergism of Silver Nanoparticles with Antibiotics as an Alternative Treatment in Multiresistant Uropathogens. *Antibiotics* **2018**, *7*, 50. [CrossRef]

40. Allend, S.O.; Garcia, M.O.; da Cunha, K.F.; de Albernaz, D.T.F.; da Silva, M.E.; Ishikame, R.Y.; Panagio, L.A.; Nakazaro, G.; Reis, G.F.; Pereira, D.B.; et al. Biogenic Silver Nanoparticle (Bio-AgNP) Has an Antibacterial Effect against Carbapenem-resistant *Acinetobacter baumannii* with Synergism and Additivity When Combined with Polymyxin B. *J. Appl. Microbiol.* **2022**, *132*, 1036–1047. [CrossRef]

41. Malawong, S.; Thammawithan, S.; Sirithongsuk, P.; Daduang, S.; Klaynongsruang, S.; Wong, P.T.; Patramanon, R. Silver Nanoparticles Enhance Antimicrobial Efficacy of Antibiotics and Restore That Efficacy against the Melioidosis Pathogen. *Antibiotics* **2021**, *10*, 839. [CrossRef]

42. Garibo Ruiz, D.; Nefedova, E.; Shkil, N.N.; Shkil, N.A.; Vazquez-Gomez, R.L.; Pestryakov, A.; Bogdanchikova, N. Silver Nanoparticles Targeting the Drug Resistance Problem of *Streptococcus dysgalactiae:* Susceptibility to Antibiotics and Efflux Effect. *Inter. J. Mol. Sci.* **2022**, *23*, 6024. [CrossRef]

43. Eduardo-Correia, B.; Morales-Filloy, H.; Abad, J.P. Bacteria from the Multi-Contaminated Tinto River Estuary (SW, Spain) Show High Multi-Resistance to Antibiotics and Point to *Paenibacillus* spp. as Antibiotic-Resistance-Dissemination Players. *Front. Microbiol.* **2020**, *10*, 3071. [CrossRef]

44. Mulet, M.; Bennasar, A.; Lalucat, J.; García-Valdés, E. An *rpo*D-Based PCR Procedure for the Identification of *Pseudomonas* Species and for their Detection in Environmental Samples. *Mol. Cell. Probes* **2009**, *23*, 140–147. [CrossRef] [PubMed]

45. Sánchez, D.; Matthijs, S.; Gomila, M.; Tricot, C.; Mulet, M.; García-Valdés, E.; Lalucat, J. *rpo*D Gene Pyrosequencing for the Assessment of *Pseudomonas* Diversity in a Water Sample from the Woluwe River. *Appl. Environ. Microbiol.* **2014**, *80*, 4738–4744. [CrossRef] [PubMed]

46. Poblete-Castro, I.; Becker, J.; Dohnt, K.; dos Santos, V.M.; Wittmann, C. Industrial Biotechnology of *Pseudomonas putida* and Related Species. *Appl. Microbiol. Biotechnol.* **2012**, *93*, 2279–2290. [CrossRef] [PubMed]

47. Rojas, A.; Duque, E.; Mosqueda, G.; Golden, G.; Hurtado, A.; Ramos, J.L.; Segura, A. Three Efflux Pumps are Required to Provide Efficient Tolerance to Toluene in *Pseudomonas putida* DOT-T1E. *J. Bacteriol.* **2001**, *183*, 3967–3973. [CrossRef]

48. Sharma, P.K.; Fu, J.; Zhang, X.; Fristensky, B.; Sparling, R.; Levin, D.B. Genome Features of *Pseudomonas putida* LS46, a Novel Polyhydroxyalkanoate Producer and its Comparison with other *P. putida* Strains. *AMB Express* **2014**, *4*, 37. [CrossRef]

49. Gebauer, J.S.; Treuel, L. Influence of Individual Ionic Components on the Agglomeration Kinetics of Silver Nano-particles. *J. Colloid Interface Sci.* **2011**, *354*, 546–554. [CrossRef]

50. Alves, M.F.; Murray, P.G. Biological Synthesis of Monodisperse Uniform-Size Silver Nanoparticles (AgNPs) by Fungal Cell-Free Extracts at Elevated Temperature and pH. *J. Fungi* **2022**, *8*, 439. [CrossRef]

51. Agnihotri, S.; Mukherji, S.; Mukherji, S. Size-controlled Silver Nanoparticles Synthesized over the Range 5–100 nm Using the Same Protocol and their Antibacterial Efficacy. *RSC Adv.* **2014**, *4*, 3974–3983. [CrossRef]

52. Abd Alamer, I.S.; Tomah, A.A.; Ahmed, T.; Li, B.; Zhang, J. Biosynthesis of Silver Chloride Nanoparticles by Rhizospheric Bacteria and Their Antibacterial Activity against Phytopathogenic Bacterium *Ralstonia Solanacearum*. *Molecules* **2021**, *27*, 224. [CrossRef]

53. Ghiuta, I.; Croitoru, C.; Kost, J.; Wenkert, R.; Munteanu, D. Bacteria-Mediated Synthesis of Silver and Silver Chloride Nanoparticles and Their Antimicrobial Activity. *Appl. Sci.* **2021**, *11*, 3134. [CrossRef]

54. Nobbmann, U.L. Polydispersity—What Does It Mean for DLS and Chromatography? Available online: https://www.materials-talks.com/polydispersity-what-does-it-mean-for-dls-and-chromatography/ (accessed on 17 October 2022).

55. Bhattacharjee, S. DLS and Zeta Potential—What They Are and What They Are Not? *J. Control. Release* **2016**, *235*, 337–351. [CrossRef] [PubMed]

56. Badawy, A.M.E.; Silva, R.G.; Morris, B.; Scheckel, K.G.; Suidan, M.T.; Tolaymat, T.M. Surface Charge-Dependent Toxicity of Silver Nanoparticles. *Environ. Sci. Technol.* **2011**, *45*, 283–287. [CrossRef] [PubMed]

57. Bélteky, P.; Rónavári, A.; Igaz, N.; Szerencsés, B.; Tóth, I.Y.; Pfeiffer, I.; Kiricsi, M.; Kónya, Z. Silver Nanoparticles: Aggregation Behavior in Biorelevant Conditions and Its Impact on Biological Activity. *Int. J. Nanomed.* **2019**, *14*, 667–687. [CrossRef] [PubMed]

58. Ferro, L.; Gojkovic, Z.; Gorzsás, A.; Funk, C. Statistical Methods for Rapid Quantification of Proteins, Lipids, and Carbohydrates in Nordic Microalgal Species Using ATR-FTIR Spectroscopy. *Molecules* **2019**, *24*, 3237. [CrossRef]

59. Crisan, C.M.; Mocan, T.; Manolea, M.; Lasca, L.I.; Tabaran, F.-A.; Mocan, L. Review on Silver Nanoparticles as a Novel Class of Antibacterial Solutions. *Appl. Sci.* **2021**, *11*, 1120. [CrossRef]

60. Salomoni, R.; Léo, P.; Montemor, A.F.; Rinaldi, B.G.; Rodrigues, M. Antibacterial Effect of Silver Nanoparticles in *Pseudomonas aeruginosa*. *Nanotechnol. Sci. Appl.* **2017**, *10*, 115–121. [CrossRef]

61. Markowska, K.; Grudniak, A.M.; Krawczyk, K.; Wróbel, I.; Wolska, K.I. Modulation of Antibiotic Resistance and Induction of a Stress Response in *Pseudomonas aeruginosa* by Silver Nanoparticles. *J. Med. Microbiol.* **2014**, *63*, 849–854. [CrossRef]

62. de Lacerda, C.D.; de Souza, J.B.; Bueno, E.V.; Medeiros, S.M.F.R.D.S.; Cavalcanti, I.D.L.; Cavalcanti, I.M.F. Antibacterial and Antibiofilm Potential of Silver Nanoparticles against Antibiotic-sensitive and Multidrug-resistant *Pseudomonas aeruginosa* Strains. *Braz. J. Microbiol.* **2021**, *52*, 267–278. [CrossRef]

63. Levison, M.E. Pharmacodynamics of Antimicrobial Drugs. *Infect. Dis. Clin. N. Am.* **2004**, *18*, 451–465. [CrossRef]

64. Hong, X.; Wen, J.; Xiong, X.; Hu, Y. Shape Effect on the Antibacterial Activity of Silver Nanoparticles Synthesized Via a Microwave-assisted Method. *Environ. Sci. Pollut. Res. Int.* **2016**, *23*, 4489–4497. [CrossRef]

65. Pal, S.; Tak, Y.K.; Song, J.M. Does the Antibacterial Activity of Silver Nanoparticles Depend on the Shape of the Nanoparticle? A study of the Gram-negative Bacterium *Escherichia coli*. *Appl. Environ. Microbiol.* **2007**, *73*, 1712–1720. [CrossRef] [PubMed]

66. Cheon, J.Y.; Kim, S.J.; Rhee, Y.H.; Kwon, O.H.; Park, W.H. Shape-dependent Antimicrobial Activities of silver nanoparticles. *Int. J. Nanomed.* **2019**, *14*, 2773–2780. [CrossRef] [PubMed]

67. Dakal, T.C.; Kumar, A.; Majumdar, R.S.; Yadav, V. Mechanistic Basis of Antimicrobial Actions of Silver Nanoparticles. *Front. Microbiol.* **2016**, *7*, 1831. [CrossRef] [PubMed]

68. Morones, J.R.; Elechiguerra, J.L.; Camacho, A.; Holt, K.; Kouri, J.B.; Ramírez, J.T.; Yacaman, M.J. The Bactericidal Effect of Silver Nanoparticles. *Nanotechnology* **2005**, *16*, 2346–2353. [CrossRef] [PubMed]

69. Matzke, M.; Jurkschat, K.; Backhaus, T. Toxicity of Differently Sized and Coated Silver Nanoparticles to the Bacterium *Pseudomonas putida*: Risks for the Aquatic Environment? *Ecotoxicology* **2014**, *23*, 818–829. [CrossRef]

70. Babapour, E.; Haddadi, A.; Mirnejad, R.; Angaji, S.-A.; Amirmozafari, N. Biofilm Formation in Clinical Isolates of Nosocomial *Acinetobacter baumannii* and its Relationship with Multidrug Resistance. *Asian Pac. J. Trop. Biomed.* **2016**, *6*, 528–533. [CrossRef]

71. Nourbakhsh, F.; Nasrollahzadeh, M.S.; Tajani, A.S.; Soheili, V.; Hadizadeh, F. Bacterial Biofilms and Their Resistance Mechanisms: A Brief Look at Treatment with Natural Agents. *Folia Microbiol.* **2022**, *67*, 535–554. [CrossRef]

72. Hetta, H.F.; Al-Kadmy, I.M.S.; Khazaal, S.S.; Abbas, S.; Suhail, A.; El-Mokhtar, M.A.; Ellah, N.H.A.; Ahmed, E.A.; Abd-ellatief, R.B.; El-Masry, E.A.; et al. Antibiofilm and Antivirulence Potential of Silver Nanoparticles against Multidrug-Resistant *Acinetobacter baumannii*. *Sci. Rep.* **2021**, *11*, 10751. [CrossRef]

73. Lange, A.; Grzenia, A.; Wierzbicki, M.; Strojny-Cieslak, B.; Kalińska, A.; Gołębiewski, M.; Radzikowski, D.; Sawosz, E.; Jaworski, S. Silver and Copper Nanoparticles Inhibit Biofilm Formation by Mastitis Pathogens. *Animals* **2021**, *11*, 1884. [CrossRef]

74. Ribeiro, A.I; Dias, A.M.; Zille, A. Synergistic Effects Between Metal Nanoparticles and Commercial Antimicrobial Agents: A Review. *ACS Appl. Nano Mater.* **2022**, *5*, 3030–3064. [CrossRef]

75. Odds, F.C. Synergy, Antagonism, and What the Chequerboard Puts Between Them. *J. Antimicrob. Chemother.* **2003**, *52*, 1. [CrossRef] [PubMed]

76. Pillai, S.K.; Moellering, R.C., Jr.; Eliopoulos, G.M. Antimicrobial Combinations. In *Antibiotics in Laboratory Medicine*, 5th ed.; Lorian, V., Ed.; Lippincott Williams & Wilkins: Philadelphia, PA, USA, 2005.

77. Gómara, M.; Ramón-García, S. The FICI Paradigm: Correcting Flaws in Antimicrobial in Vitro Synergy Screens at Their Inception. *Biochem. Pharmacol.* **2019**, *163*, 299–307. [CrossRef] [PubMed]

78. Panáček, A.; Smékalová, M.; Kilianová, M.; Prucek, R.; Bogdanová, K.; Večeřová, R.; Kolář, M.; Havrdová, M.; Płaza, G.; Chojniak, J.; et al. Strong and Nonspecific Synergistic Antibacterial Efficiency of Antibiotics Combined with Silver Nanoparticles at Very Low Concentrations Showing No Cytotoxic Effect. *Molecules* **2015**, *21*, 26. [CrossRef] [PubMed]

79. Sun, W.; Sanderson, P.E.; Zheng, W. Drug Combination Therapy Increases Successful Drug Repositioning. *Drug Discov. Today* **2016**, *21*, 1189–1195. [CrossRef] [PubMed]

80. Deng, H.; McShan, D.; Zhang, Y.; Sinha, S.S.; Arslan, Z.; Ray, P.C.; Yu, H. Mechanistic Study of the Synergistic Antibacterial Activity of Combined Silver Nanoparticles and Common Antibiotics. *Environ. Sci. Technol.* **2016**, *50*, 8840–8848. [CrossRef] [PubMed]

81. Krce, L.; Šprung, M.; Rončević, T.; Maravić, A.; Čikeš Čulić, V.; Blažeka, D.; Krstulović, N.; Aviani, I. Probing the Mode of Antibacterial Action of Silver Nanoparticles Synthesized by Laser Ablation in Water: What Fluorescence and AFM Data Tell Us. *Nanomaterials* **2020**, *10*, 1040. [CrossRef]

82. Lane, D.J. 16S/23S rRNA Sequencing. In *Nucleic Acid Techniques in Bacterial Systematics*; Stackebrandt, E., Goodfellow, M., Eds.; John Wiley and Sons: Chichester, UK, 1991; pp. 115–175.

83. Schmitz, A.; Riesner, D. Purification of Nucleic Acids by Selective Precipitation with Polyethylene Glycol 6000. *Anal. Biochem.* **2006**, *354*, 311–313. [CrossRef]

84. Malvern Instruments. Frequently Asked Questions. Available online: https://www.materials-talks.com/wp-content/uploads/2017/10/What-does-polydispersity-mean.pdf (accessed on 29 September 2022).

85. Azeredo, J.; Azevedo, N.F.; Briandet, R.; Cerca, N.; Coenye, T.; Costa, A.R.; Desvaux, M.; Di Bonaventura, G.; Hébraud, M.; Jaglic, Z.; et al. Critical Review on Biofilm Methods. *Crit. Rev. Microbiol.* **2017**, *43*, 313–351. [CrossRef]

86. Ong, K.S.; Cheow, Y.L.; Lee, S.M. The Role of Reactive Oxygen Species in the Antimicrobial Activity of Pyochelin. *J. Adv. Res.* **2017**, *8*, 393–398. [CrossRef]

Synthesis and Antiparasitic Activity of New Trithiolato-Bridged Dinuclear Ruthenium(II)-arene-carbohydrate Conjugates

Isabelle Holzer [1]**, Oksana Desiatkina** [1]**, Nicoleta Anghel** [2]**, Serena K. Johns** [1,3]**, Ghalia Boubaker** [2]**, Andrew Hemphill** [2,*]**, Julien Furrer** [1,*] **and Emilia Păunescu** [1,*]

[1] Department of Chemistry, Biochemistry and Pharmaceutical Sciences, University of Bern, Freiestrasse 3, 3012 Bern, Switzerland
[2] Institute of Parasitology Vetsuisse Faculty, University of Bern, Länggass-Strasse 122, 3012 Bern, Switzerland
[3] School of Chemistry, Cardiff University, Park Place, Cardiff CF103AT, UK
[*] Correspondence: andrew.hemphill@unibe.ch (A.H.); julien.furrer@unibe.ch (J.F.); paunescu_emilia@yahoo.com (E.P.)

Abstract: Eight novel carbohydrate-tethered trithiolato dinuclear ruthenium(II)-arene complexes were synthesized using CuAAC 'click' (Cu(I)-catalyzed azide-alkyne cycloaddition) reactions, and there in vitro activity against transgenic *T. gondii* tachyzoites constitutively expressing β-galactosidase (*T. gondii* β-gal) and in non-infected human foreskin fibroblasts, HFF, was determined at 0.1 and 1 μM. When evaluated at 1 μM, seven diruthenium-carbohydrate conjugates strongly impaired parasite proliferation by >90%, while HFF viability was retained at 50% or more, and they were further subjected to the half-maximal inhibitory concentration (IC$_{50}$) measurement on *T. gondii* β-gal. Results revealed that the biological activity of the hybrids was influenced both by the nature of the carbohydrate (glucose vs. galactose) appended on ruthenium complex and the type/length of the linker between the two units. **23** and **26**, two galactose-based diruthenium conjugates, exhibited low IC$_{50}$ values and reduced effect on HFF viability when applied at 2.5 μM (**23**: IC$_{50}$ = 0.032 μM/HFF viability 92% and **26**: IC$_{50}$ = 0.153 μM/HFF viability 97%). Remarkably, compounds **23** and **26** performed significantly better than the corresponding carbohydrate non-modified diruthenium complexes, showing that this type of conjugates are a promising approach for obtaining new antiparasitic compounds with reduced toxicity.

Keywords: ruthenium(II)-arene complexes; bioorganometallic; carbohydrates; CuAAC reactions; antiparasitic; *Toxoplasma gondii*; human foreskin fibroblasts; auxotrophy; toxicity

1. Introduction

The interest in the development of metal complexes for medicinal applications increased in the middle of the 20th century after the discovery of the anticancer properties of cisplatin [1,2]. Metal-based drugs are attractive due to their great versatility in terms of metal center, oxidation state, coordination number, in addition to the nature and geometric orientation of the ligands [3]. As the use of platinum-based drugs is limited due to shortcomings like the occurrence of chemoresistance and side effects associated to their high toxicity [4,5], this encouraged the research of compounds based on other metals as alternative to platinum anticancer therapeutics [1,6–8]. Parallel investigations aimed to enlarge the purpose of metal complexes with the identification of additional pharmacological properties, such as antibiotic [9,10] and antiparasitic [11–16].

Ruthenium complexes were identified amid the most promising non-platinum chemotherapeutic alternatives [17,18]. The ruthenium(II)-arene scaffold has been declined in a myriad of compounds aimed to improve anticancer activity and selectivity [19–25], but also targeting other therapeutic applications [11,13,16,26].

A particular class of compounds containing this unit are the trithiolato-bridged dinuclear ruthenium(II)-arene complexes (**A**–**C** in Figure 1), which show not only high antiproliferative activity against cancer cells [27], but also promising antiparasitic properties [28,29]. The structure of these complexes is based on a trigonal bipyramidal Ru_2S_3 framework, with two ruthenium(II)-arene half-sandwich units. Two types of complexes can be distinguished, "mixed" (at least one of the bridge thiols is different, **A** in Figure 1) and "symmetric" (the three bridge thiols are identical, **B** and **C** in Figure 1) [27]. Former studies on *Toxoplasma gondii* [28], *Neospora caninum* [29] and *Trypanosoma brucei* [30] identified high antiparasitic activity for some of these diruthenium compounds. For example, compounds **A**–**C** (Figure 1) inhibit *T. gondii* tachyzoites proliferation with IC_{50} values in nanomolar range (down to 1.2 nM for **A**).
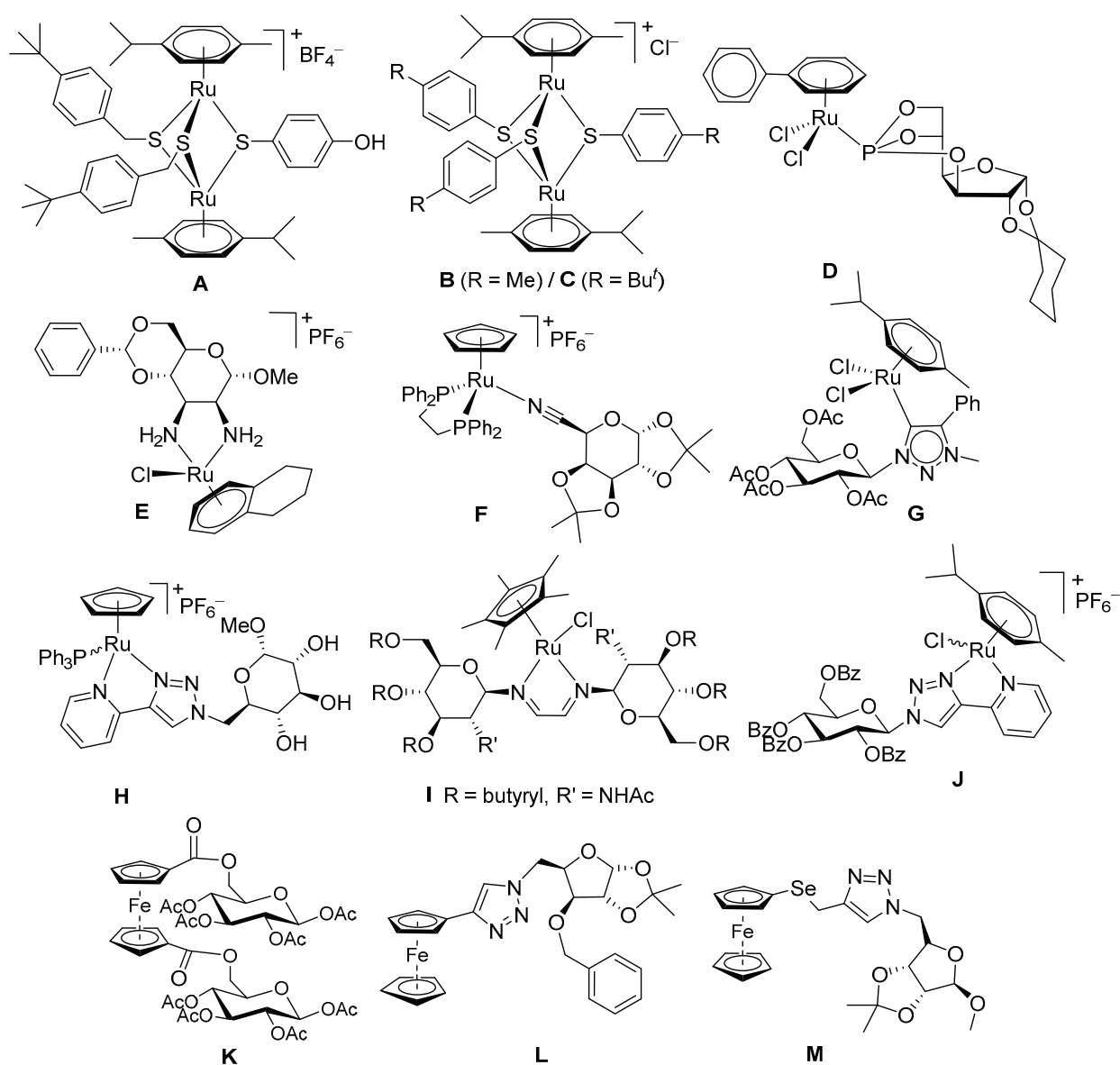
Figure 1. Structures of dinuclear thiolato-bridged ruthenium(II)-arene complexes (**A**–**C**) active against *T. gondii*, of various ruthenium(II)-arene complexes presenting carbohydrate functionalized ligands and anticancer activity (**D**–**J**), and of ferrocene-carbohydrate conjugates exhibiting antimalarial, antibacterial, and anticancer properties (**K**–**M**).

T. gondii is an obligate intracellular protozoan parasite of the phylum Apicomplexa that causes infections of medical and veterinary significance in humans and animals [31,32].

Infection is usually asymptomatic in immunocompetent individuals, but it may cause severe complications or even be fatal in immunocompromised patients [33]. Current common treatments for toxoplasmosis are not specific, require prolonged courses and have toxic side effects, and consequently, new therapeutic solutions are needed [33–36]. Unlike other pathogens, *T. gondii* has adapted to replicate in all nucleated cells of a wide range of vertebrates, regardless of their cellular metabolism, and thus displays an exceptional metabolic robustness [37,38]. *T. gondii* is auxotrophic for several metabolites including purines, polyamines, cholesterol and choline [37]. Accordingly, tackling the parasite auxotrophies and metabolic peculiarities can constitute an interesting therapeutic strategy [37].

Carbohydrates contribute to cell-cell recognition and adhesion, have a crucial role in cellular energy supply, and can bind to specific proteins (e.g., lectins, glucose transporters, and glycoenzymes). Consequently, their conjugation to metal complexes appears as a rational choice for drug design as it can promote biocompatibility and increase water solubility. Carbohydrate-metal hybrids show promise not only in medicinal chemistry [39–41] but also in catalysis [42,43]. Apart the metal, its oxidation state and coordination mode [44–46], various structural adjustments were considered as the type of the carbohydrate [47–51], its substitution position [52], and the presence and nature of the protecting groups [53–55]. The cancer cells glucose metabolism can be exploited for targeted therapy [56], and consequently, glycoconjugates of various metal complexes were explicitly designed for selective uptake by cells overexpressing glucose transporters [57–59]. In this context, the potential of ruthenium complexes containing carbohydrate-functionalized ligands has been extensively studied especially on cancer cells [60–73], and some representative examples are presented in Figure 1. Apart cancer-specific treatment [39–41,60,74–77], alternative utilizations of metal-carbohydrate hybrids, as for example antiparasitic therapy, also received a lot of interest [78–80] (Figure 1).

For example Ru(II)-arene complexes as **D** [65,66], with a carbohydrate-derived phosphorus-containing ligand, **E** [67] bearing a mannose fragment as a diamino-bidentate leg ligand, **F** [68,69], with a galactose fragment *N*-coordinated via a nitrile group, and **G** [71], containing a glucosyl functionalized 1,2,3-triazolylidene *N*-heterocyclic carbene ligand, exhibited promising antiproliferative activity on various cancer cells. Complexes like **H** [72], with methyl mannose or glucose units attached to a pyridyl-2-triazole bidentate ligand, were shown to exploit the glucose transporters for cellular uptake in cancer cells. For Ru(II) half-sandwich complexes like **I** [70] and **J** [73], the presence and nature of the protective groups proved to be essential for the biological activity. The high affinity of the malaria parasite for glucose was targeted using the ferrocenyl-glucose conjugate **K** [79], with moderate antimalarial activity in vitro in both *Plasmodium falciparum* chloroquine-resistant and non-resistant strains. Carbohydrate-ferrocenyltriazole conjugate **L** [81], exhibited antibacterial activity against both Gram-positive and Gram-negative pathogens, and triazole bridged ferrocene-selenoribose conjugate **M** [82] was cytotoxic on cancer cells.

This study continues the quest for trithiolato-bridged dinuclear ruthenium(II)-arene compounds as potential anti-*Toxoplasma* compounds with improved therapeutic value (in terms of antiparasitic efficacy/host cell toxicity balance) by exploiting the conjugate strategy and the parasite auxotrophies and specific metabolic needs. The investigation of carbohydrate metabolism in *T. gondii* has received a lot of interest [83–86] and considering the high energetic demand accompanying parasite growth and proliferation, carbohydrates can constitute an appealing choice among the metabolites able to promote the internalization of the organometallic unit in the parasite.

The synthesis of trithiolato diruthenium complexes is generally straightforward and efficient [87–89], this scaffold being robust to chemical modification and easily adaptable to the conjugate strategy as demonstrated by the various series of hybrids with peptides [90], drugs [91,92], fluorophores [89,93] or metabolites [93]. Ester and amide couplings [89,94], but also CuAAC (Cu(I)-catalyzed azide-alkyne cycloaddition) click reactions [92,93] proved to be useful tools for the functionalization of the diruthenium trithiolato unit at the level of the bridge thiols. CuAAC offer the advantage of mild reaction conditions, compatible

with various ligands [44,46,71–73,95–97] but also with organometallics [81,98–102], and enables the construction of libraries of compounds [103–105]. Additionally, trithiolato diruthenium(II)-arene compounds suitably substituted with alkyne or azide groups were already used in CuAAC reactions for obtaining conjugates with molecules of interest e.g., various nucleic bases or drugs [92,93].

The nature of the carbohydrate (acetyl protected glucose or galactose) and the type and length of the linker between the two units were addressed as sources of variability. The new diruthenium hybrids and intermediates were screened in vitro against *T. gondii* tachyzoites expressing β-galactosidase (*T. gondii* β-gal) grown in human foreskin fibroblasts (HFF) with complementary assessment of HFF host cells viability. Compounds with promising antiparasitic activity and selectivity were then subjected to dose-response (IC$_{50}$) determination on *T. gondii* β-gal and toxicity assessment on HFF at 2.5 M concentration.

2. Results and Discussions

2.1. Synthesis

2.1.1. Synthesis of the Dinuclear Ruthenium(II)-arene Intermediates **2–9**

Alkyne and azide partners are needed for the CuAAC reactions, and when appropriately substituted, both the diruthenium moiety and the carbohydrate can play either role. With this aim, various diruthenium and carbohydrate intermediates were synthesized.

The dithiolato derivative **1** [106] (obtained from the ruthenium dimer ([(η^6-p-MeC$_6$H$_4$Pr^i) RuCl]$_2$Cl$_2$) and 4-*tert*-butylbenzenemethanethiol) was reacted with a second thiol (4-mercaptophenol, 4-aminobenzenthiol, 2-(4-mercaptophenyl)acetic acid, and 2-mercapto-benzyl alcohol, respectively) to provide the trithiolato-bridged dinuclear ruthenium compounds **2–5**, as previously reported (Scheme 1) [87–89].

2, XH = *p*-OH (EtOH)
3, XH = *p*-NH$_2$ (EtOH)
4, XH = *p*-CH$_2$CO$_2$H (CH$_2$Cl$_2$, (CH)$_3$CO)
5, XH = *o*-CH$_2$OH (EtOH)
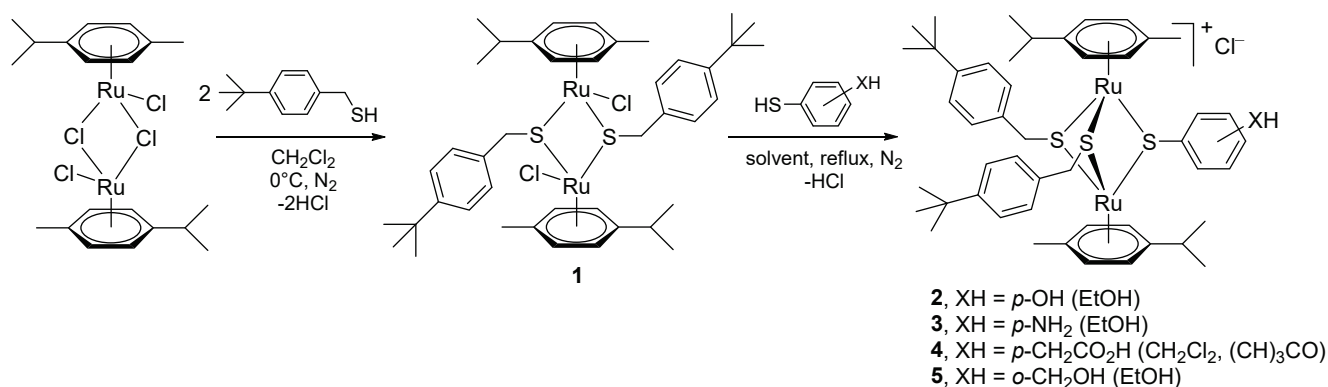
Scheme 1. Synthesis of the diruthenium intermediates bearing OH (**2**), NH$_2$ (**3**) CH$_2$CO$_2$H (**4**), and CH$_2$-OH (**5**) groups on one of the bridge thiols.

Intermediates **2–4** can be modified using ester and amide coupling reactions as previously described [89,92–94]. The alkyne ester **6** was obtained in moderate yield (47%) by reacting **2** with 5-hexynoic acid using EDCI (*N*-(3-dimethylaminopropyl)-*N'*-ethylcarbodiimide hydrochloride) as coupling agent, in basic conditions (DMAP, 4-(dimethylamino)-pyridine) (Scheme 2, top). 5-Hexynoic acid was also reacted with the amino diruthenium derivative **3** using EDCI and HOBt (1-hydroxybenzotriazole) as coupling agents, in basic conditions (DIPEA, *N*,*N*-diisopropylethylamine), to afford the amido alkyne compound **7** as reported [93] (Scheme 2, top). Similar reaction conditions were used for the synthesis of amide **8** from carboxylic acid diruthenium derivative **4** and propargylic amine as formerly described (Scheme 2, bottom) [92,93].
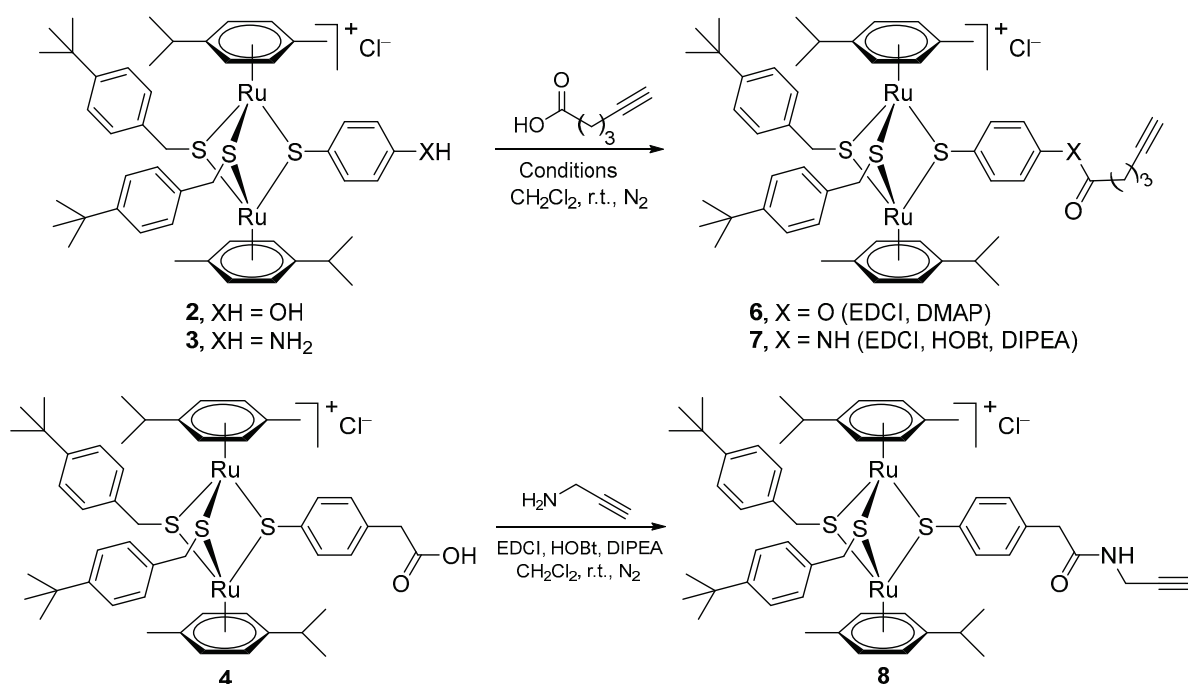
Scheme 2. Synthesis of the alkyne functionalized ester and amide diruthenium compounds **6**, **7** and **8**.

The azide trithiolato diruthenium derivative **9** (Scheme 3), was obtained following a two steps pathway starting from alcohol **5** using a reported protocol [93]. First, the hydroxy group was activated by mesylation (MsCl, methanesulfonyl chloride) in basic conditions (TEA, triethylamine), followed by the nucleophilic substitution with azide (NaN$_3$).
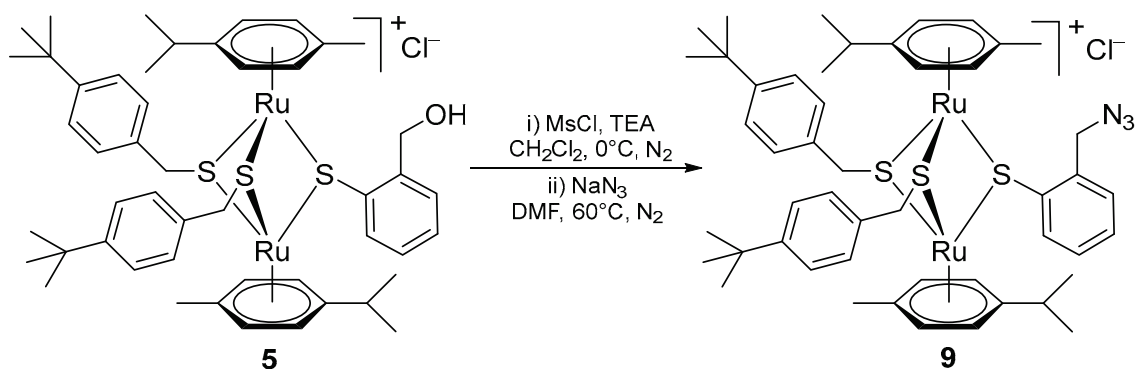
Scheme 3. Synthesis of the azide functionalized diruthenium complex **9**.

2.1.2. Synthesis of the Azide and Alkyne Functionalized Carbohydrate Intermediates **10–18**

Appropriate carbohydrate derivatives bearing azide and alkyne groups were also synthesized (Schemes 4 and 5). Azido glucose compound **10** (2,3,4,6-tetra-O-acetyl-β-D-glucopyranosyl azide), was synthesized from commercially available 2,3,4,6-tetra-O-acetyl-β-D-glucopyranosyl bromide following a literature protocol (Scheme 4) [107]. The reaction was realized with TMS-N$_3$ (trimethylsilylazide) in THF in the presence of TBAF (tetrabutylammonium fluoride) in catalytic amounts, and **10** was isolated in moderate yield (51%).
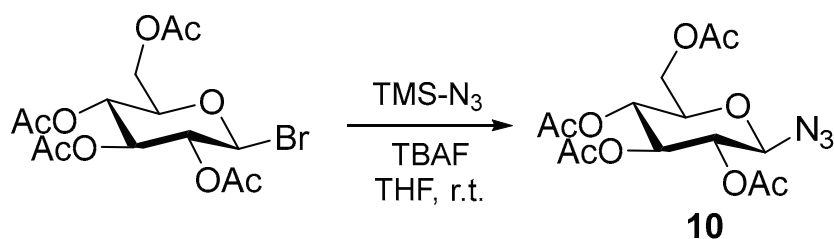
Scheme 4. Synthesis of the azido glucose derivative **10**.
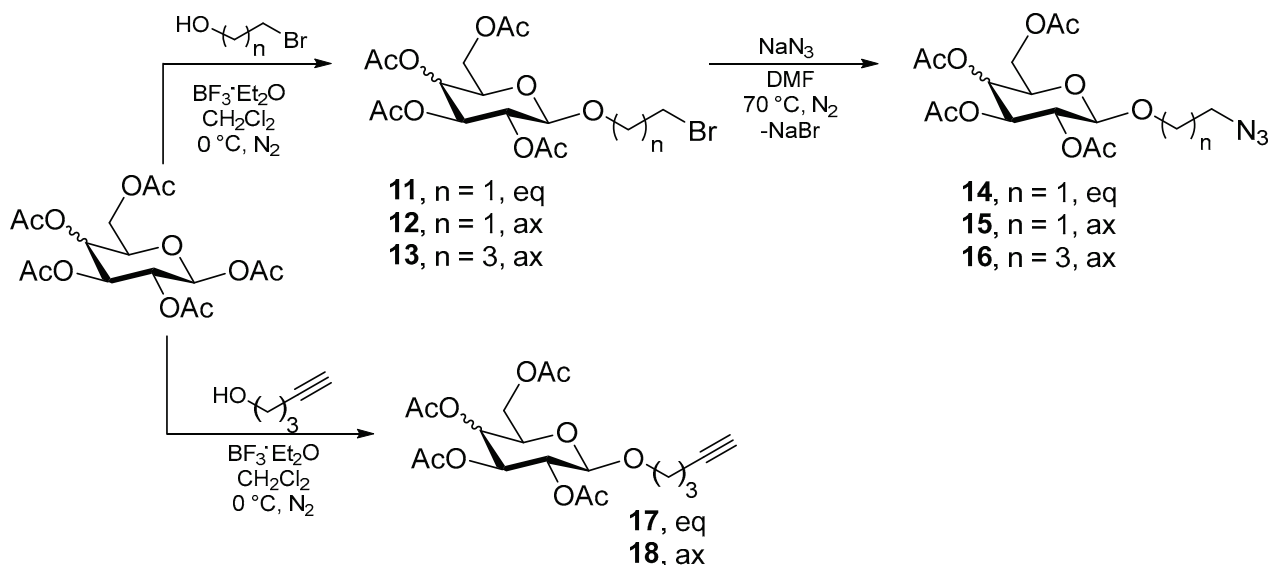
Scheme 5. Synthesis of the glucose and galactose azide **14–16**, and alkyne **17** and **18** derivatives (eq = equatorial, ax = axial).

The azide compounds **14–16** were obtained following a two-step procedure previously described [52,55,108] (Scheme 5, top). First, *β*-D-glucose pentaacetate and *β*-D-galactose pentaacetate were glycosylated with 2-bromoethanol and 4-bromo-1-butanol. The reactions were realized in the presence of BF$_3$·Et$_2$O (boron trifluoride diethyl etherate) as Lewis acid catalyst [52] and afforded the ether glycosides **11–13** in low to moderate yields (32, 41, and 47%, respectively). In the second step the bromine atom on the pending chain of **11–13** was substituted with azide (NaN$_3$) [55,108], derivatives **14–16** being isolated in 47, 74% and quantitative yields, respectively.

The alkyne functionalized carbohydrates **17** and **18** were synthesized (Scheme 5, bottom) from *β*-D-glucose pentaacetate and, respectively, from *β*-D-galactose pentaacetate and 4-pentyn-1-ol in the presence of BF$_3$·Et$_2$O [109] and were isolated in medium yields (64 and 46%).

2.1.3. Synthesis of the Carbohydrate Functionalized Trithiolato-Bridged Dinuclear Ruthenium(II)-arene Complexes **19–26**

The carbohydrate units were attached to the trithiolato diruthenium scaffold via click 1,3-dipolar cycloadditions using adapted protocols [110–112], in the presence of CuSO$_4$ as catalyst and sodium ascorbate as a reducing agent, in DMF under inert conditions. Complexes **6–9**, bearing either alkyne or azide pendant group, were reacted with the appropriately functionalized carbohydrate derivatives **10** and **14–18** (Schemes 6–9) affording eight new trithiolato diruthenium conjugates **19–26**.
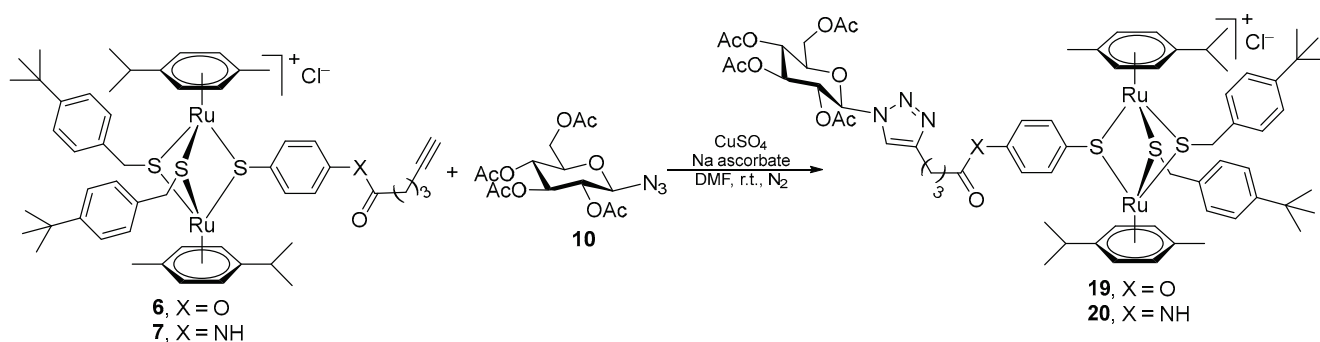
Scheme 6. Synthesis of the diruthenium glucose conjugates **19** and **20** from the alkyne ester and amide derivatives **6** and **7**.
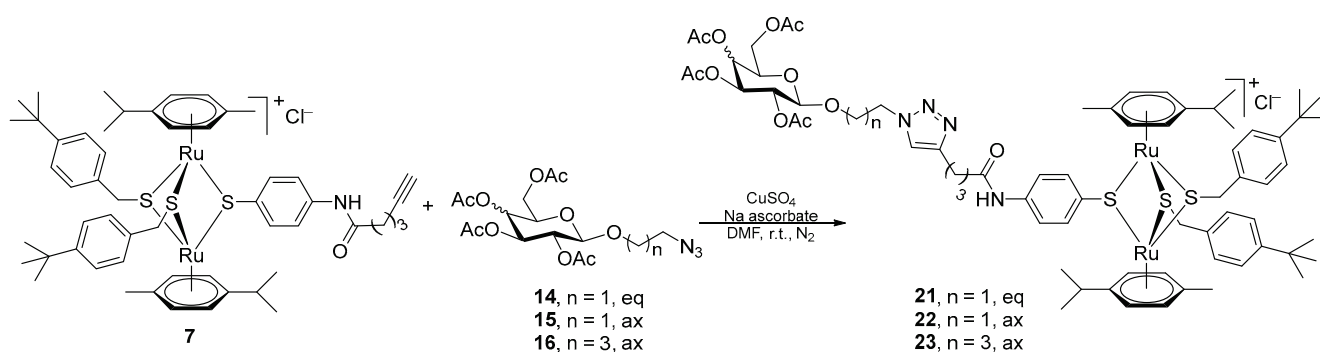
Scheme 7. Synthesis of the glucose **21**, and galactose **22** and **23** diruthenium conjugates.
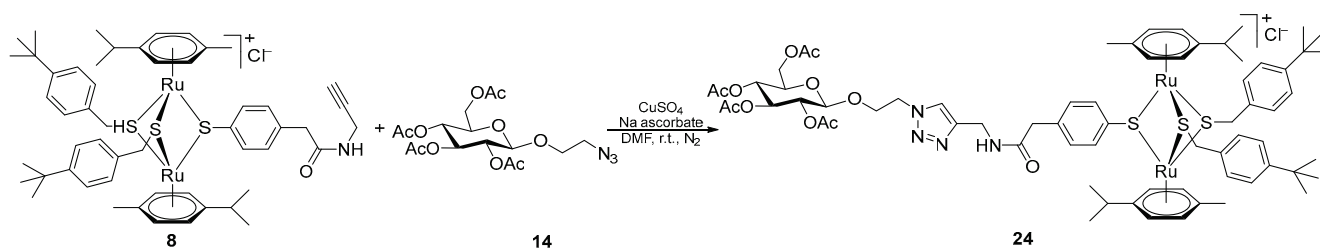
Scheme 8. Synthesis of the diruthenium glucose conjugate **24**.
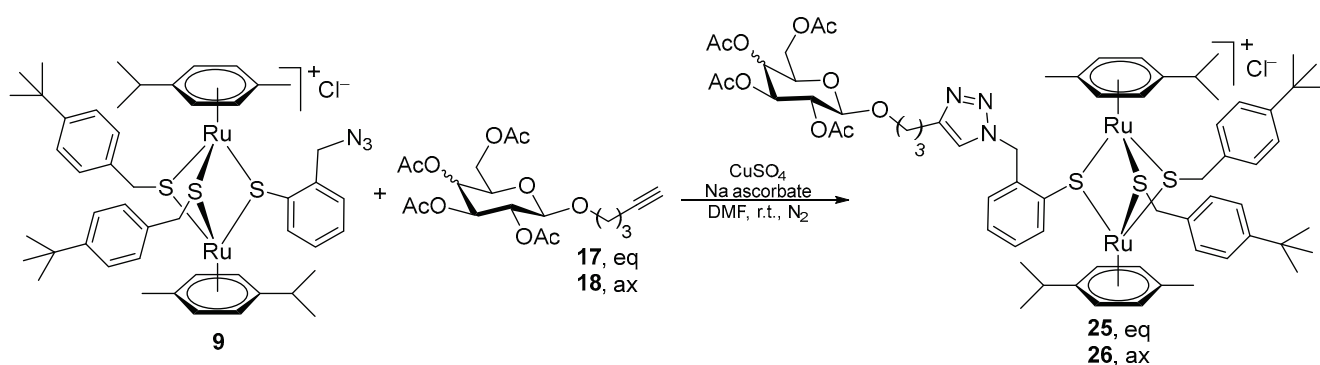
Scheme 9. Synthesis of the glucose and galactose diruthenium conjugates **25** and **26**.

Thus, alkyne functionalized diruthenium compounds **6** and **7** were reacted with glucose derivative **10** presenting an azide group directly anchored to the glucopyranosyl ring (Scheme 6). Amide conjugate **20** was isolated in good yield (72%), while difficulties were encountered in the purification of ester analogue **19** which was recovered in poorer yield (28%).

Other glycoconjugates were synthesized using alkyne intermediate **7** (Scheme 7) and two types of modifications were envisioned: (i) the nature of the carbohydrate (glucose in **21** vs. galactose in **22**), and (ii) the presence of spacers of different length between the azide group and the glucopyranosyl ring (galactose derivatives **22** and **23**). Conjugates **21–23** were isolated in good yields of 66, 65 and 74%, respectively. Neither the steric hindrance nor the nature of the carbon atom on which the azide group was anchored (**10** vs. **14**) play a key role on the yield (**20** vs. **21–23**). Similarly, the reaction of the diruthenium propargyl amide derivative **8** with galactose azide **14** afforded conjugate **24** in 75% yield (Scheme 8).

The trithiolato dinuclear intermediate **9**, presenting an azide in benzylic position on one of the bridge thiols, was reacted with glucose and galactose alkyne derivatives **17** and **18** (Scheme 9), affording carbohydrate conjugates **25** and **26** isolated in moderate yields of 51 and 63%, respectively.

All compounds were fully characterized by ^{1}H, ^{13}C nuclear magnetic resonance (NMR) spectroscopy, high resolution electrospray ionization mass spectrometry (HR ESI-MS) and elemental analysis (see Supplementary Materials). The obtainment of the triazole connector between the diruthenium unit and the carbohydrates was undoubtedly demonstrated by the ^{1}H and ^{13}C NMR spectra of the conjugates 19–26 by the signals corresponding to the proton of the triazole cycle at 7.74–8.66 ppm and of the corresponding carbon at 120.3–124.6 ppm. The absence of the signals corresponding to the proton of the mono-substituted alkyne (at 1.93–2.49 in compounds 6–8, 17 and 18) in the ^{1}H NMR spectra of conjugates 19–26 further confirm the obtainment of the hybrid molecules. Mass spectrometry corroborated the spectroscopic data with the trithiolato diruthenium glucose and galactose conjugates **19–26** showing molecular ion peaks corresponding to [M-Cl]$^+$ ions.

2.1.4. Stability of the Compounds

For the assessment of the biological activity, the compounds were prepared as stock solutions in dimethylsulfoxide (DMSO). Similar to former reports [88,89,94], the ^{1}H NMR spectra of the functionalized diruthenium complexes **6**, **7**, **20**, **22**, **25** and **26** in DMSO-d_6, recorded at 25 °C 5 min and more than 1 month after sample preparation showed no significant modifications (see Figure S1 in the Supplementary Materials), demonstrating a very good stability of the compounds in this highly complexing solvent.

Compound **19** has an ester linker that can potentially be hydrolyzed in cell growth media. Comparable conjugates with fluorophores (coumarin and BODIPY) linked through ester bonds to the trithiolato diruthenium unit were recently studied [89,93]. Only very limited solvolysis of the ester bonds was noticed after 168 h for some compounds, and it was concluded that the fluorophore diruthenium conjugates exhibit high stability in the conditions used for the biological evaluations. Therefore, it was assumed that compound **19** is appropriately stable for the first in vitro biological activity evaluation.

2.2. Assessment of the In Vitro Activity against T. Gondii β-gal and Human Foreskin Fibroblast Host Cells

2.2.1. Primary Screening

The biological activity of the carbohydrate azides and alkyne derivatives **14–16** and, respectively, **17** and **18** was not measured as these compounds were not isolated pure. Glucose and galactose conjugates **19–26**, glucose azide derivative **10** and diruthenium alkyne intermediate **6** were assessed for their in vitro biological activity in inhibiting proliferation of *T. gondii* β-gal, a transgenic strain that constitutively expresses β-galactosidase, and for toxicity to HFF (human foreskin fibroblast) used as host cells. The compounds were applied to infected or non-infected HFF cultures for 72 h and at concentrations of 0.1 and 1 μM, the results being summarized in Table 1 and Figure 2. The viability of treated HFF was measured by the alamarBlue metabolic assay, and the proliferation of *T. gondii* β-gal was quantified by the β-galactosidase colorimetric test. In both cases, results are expressed as percentage (%) compared to control parasitic and host cells treated with 0.1% DMSO for which proliferation and viability were set to 100% (Table 1).

Table 1. Results of the primary efficacy/cytotoxicity screening of the azide derivative **10** and of trithiolato diruthenium compounds **2–9** and **19–26** in non-infected HFF cultures and *T. gondii* β-gal tachyzoites cultured in HFF. Non-infected HFF monolayers treated only with 0.1% DMSO exhibited 100% viability and 100% proliferation was attributed to *T. gondii* β-gal tachyzoites treated with 0.1% DMSO only. The compounds selected for determination of IC$_{50}$ values against *T. gondii* β-gal are tagged with *. For each assay, standard deviations were calculated from triplicates.

Compound	R	HFF Viability (%)		*T. Gondii* β-gal Growth (%)	
		0.1 μM	1 μM	0.1 μM	1 μM
Diruthenium intermediates					
2 [a],*		76 ± 6	46 ± 6	66 ± 14	2 ± 0
3 [a],*		74 ± 2	48 ± 1	57 ± 1	2 ± 0
4 [a]		91 ± 4	73 ± 1	114 ± 2	110 ± 2
5 [a],*		80 ± 1	69 ± 6	2 ± 0	1 ± 0
Alkyne and azide functionalized diruthenium compounds					
6 *		101 ± 1	100 ± 1	4 ± 0	0 ± 0
7 [a],*		101 ± 0	96 ± 0	21 ± 2	0 ± 0
8 [a]		71 ± 2	46 ± 6	52 ± 13	3 ± 1
9 [a],*		96 ± 1	64 ± 1	9 ± 1	1 ± 1
Azido glucose derivative					
10		98 ± 1	99 ± 0	101 ± 1	99 ± 0
Diruthenium—glucose conjugates					
19 *		102 ± 1	97 ± 1	9 ± 1	0 ± 0
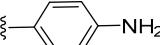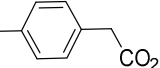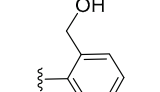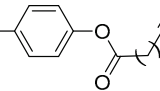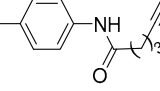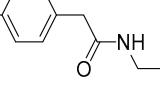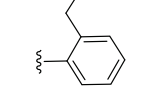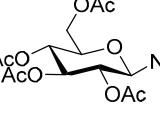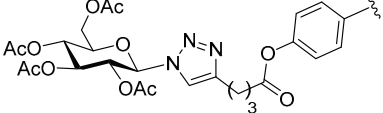
Table 1. *Cont.*

Compound	R	HFF Viability (%)		*T. Gondii* β-gal Growth (%)	
		0.1 µM	1 µM	0.1 µM	1 µM
20 *		98 ± 1	99 ± 0	100 ± 1	1 ± 2
21 *		100 ± 1	101 ± 0	87 ± 1	1 ± 0
24 *		99 ± 1	98 ± 0	66 ± 2	3 ± 0
25		98 ± 1	97 ± 1	75 ± 2	27 ± 0
Diruthenium—galactose conjugates					
22 *		100 ± 0	101 ± 0	73 ± 1	2 ± 0
23 *		99 ± 1	101 ± 1	85 ± 1	1 ± 0
26 *		98 ± 1	99 ± 1	89 ± 1	0 ± 0
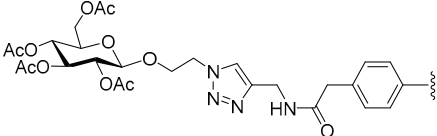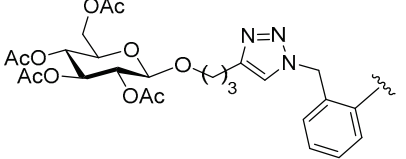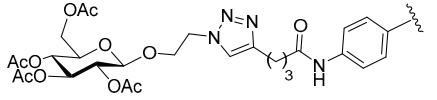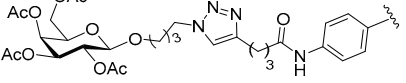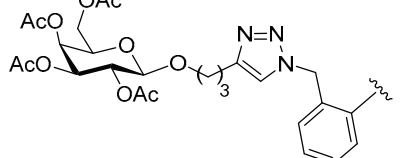
[a] Compounds reported previously [88,89,92,93].

The trithiolato diruthenium complexes **2–5** and **9**, and alkyne intermediates **7** and **8** were evaluated previously against *T. gondii* β-gal under similar conditions [88,89,92,93], and the corresponding values are shown in Table 1 and Figure 2 for comparison. The new alkyne ester derivative **6** impacted *T. gondii* proliferation but affected significantly less the viability of HFF compared to its diruthenium hydroxy intermediates **2**. The glucose azide derivative **10** exhibited neither antiparasitic activity nor host cell toxicity at both tested concentrations.

In the first screening, the eight carbohydrate conjugates **19–26,** applied at 1 µM, did not impair host cell viability. Apart from glucose conjugate **25**, all the dyads nearly abolished

parasite proliferation when applied at 1 µM. Though, apart from glucose conjugate **19**, all hybrid molecules had only a limited effect on *T. gondii* β-gal at 0.1 µM.

Both the type of carbohydrate and the nature and length of the linker influenced the antiparasitic efficacy and cytotoxicity of the conjugates, but no clear straightforward trends could be identified regarding the relationship between the structural elements and biological activity. For example, when the conjugates are applied at 0.1 µM, some differences in anti-*Toxoplasma* efficacy are observed. For instance, glucose ester derivative **19** is significantly more active on *T. gondii* compared to the amide analogue **20**. Galactose functionalized compound **22** is more efficient in inhibiting the parasite proliferation compared to the corresponding glucose derivative **21**, while for the same carbohydrate an increase of the linker length has a negative effect on the antiparasitic activity (galactose conjugates **22** and **23**).
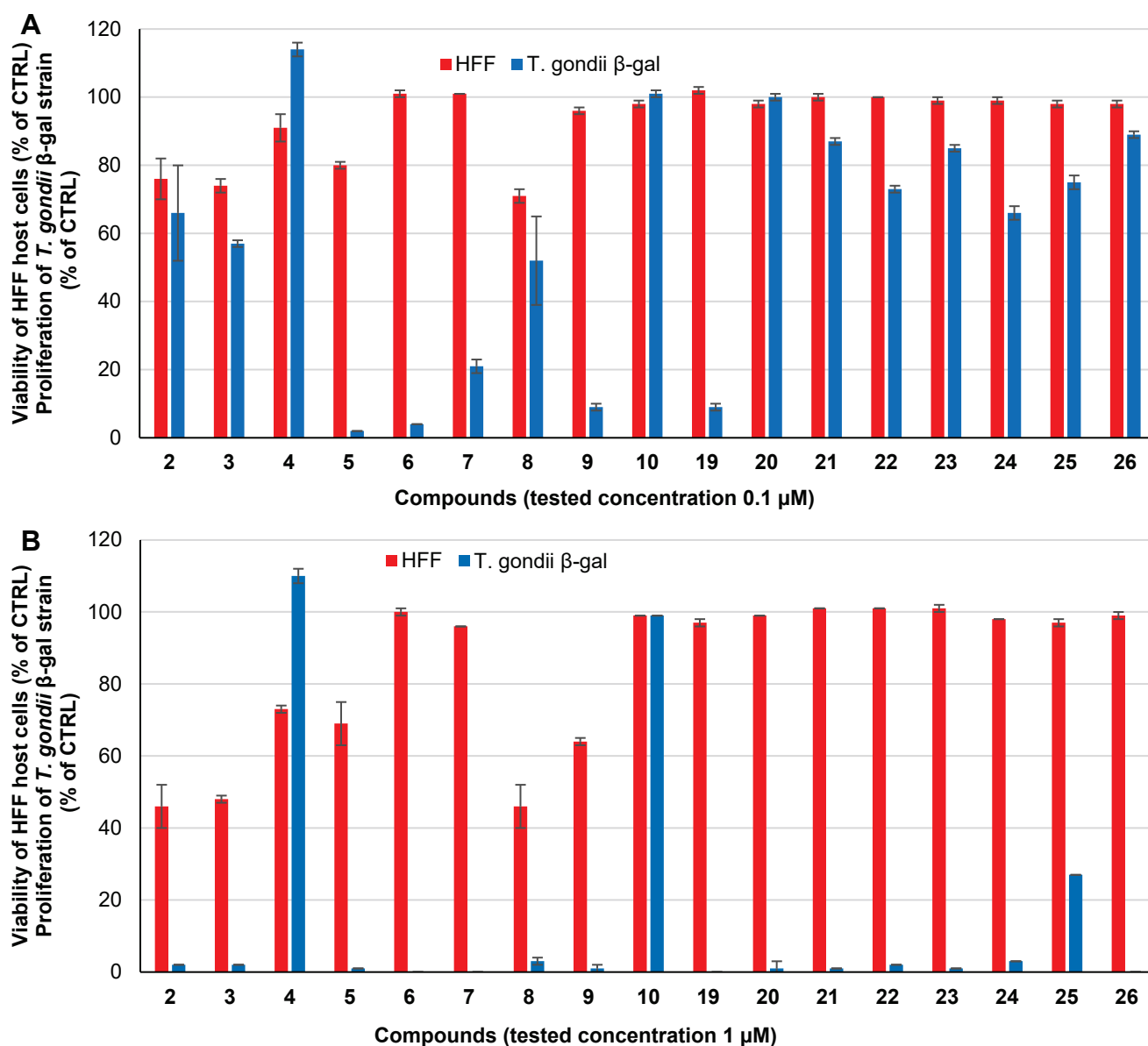
Figure 2. Clustered column chart showing the in vitro activities at 1 (**A**) and 0.1 (**B**) µM of the azide derivative **10** and of trithiolato diruthenium compounds **2–9** and **19–26** on HFF viability and *T. gondii* β-gal proliferation. For each assay, standard deviations were calculated from triplicates and are displayed on the graph. Data for compounds **2–5** and **7–9** were previously reported [88,89,92,93].

2.2.2. IC$_{50}$ Values against *T. gondii* β-gal Tachyzoites and HFF Toxicity at 2.5 μM

For a compound to be selected for the second screening, two criteria had to be met simultaneously: (i) when the compound was applied at 1 μM, *T. gondii* β-gal growth was inhibited by 90% or more compared to control treated with 0.1% DMSO only, and (ii) HFF host cell viability was not impaired by more than 50% for a compound applied at 1 μM. Based on the results of the primary screening, glucose and galactose dyads **19–24** and **26** were selected. Pyrimethamine, currently used for the treatment of toxoplasmosis, and which inhibited the proliferation of *T. gondii* β-gal tachyzoites with an IC$_{50}$ value of 0.326 μM and did not affect HFF viability at 2.5 μM (Table 2), was used as reference compound. The selection also included the diruthenium intermediate compounds **2**, **3** and **5** with free OH or NH$_2$ groups, along with two diruthenium alkyne ester and amide compounds **6** and **7**, and diruthenium azide **9**. The results are summarized in Table 2.

Table 2. Half-maximal inhibitory concentration (IC$_{50}$) values (μM) on *T. gondii* β-gal for 15 selected compounds and pyrimethamine (used as standard), and their effect at 2.5 μM on HFF viability.

Compound	R	IC$_{50}$ *T. Gondii* β-gal (μM)	[LS; LI] [b]	SE [c]	HFF Viability at 2.5 μM (%) [d]	SD [e]
Pyrimethamine [a]		0.326	[0.396; 0.288]	0.051	99	6
Diruthenium intermediates						
2 [a]		0.117	[0.139; 0.098]	0.051	56	6
3 [a]		0.153	[0.185; 0.127]	0.049	51	5
5 [a]		0.038	[0.023; 0.060]	0.110	4	2
Alkyne and azide functionalized diruthenium compounds						
6		0.023	[0.030; 0.018]	0.503	7	1
7 [a]		0.038	[0.050; 0.029]	0.063	34	1
9 [a]		0.048	[0.058; 0.040]	0.139	11	1
Diruthenium-glucose conjugates						
19		0.018	[0.031; 0.011]	0.387	29	3

Table 2. *Cont.*
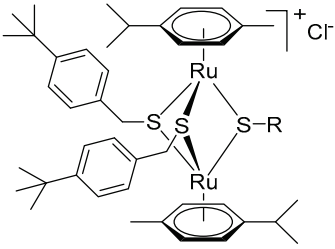
Compound	R	IC$_{50}$ *T. Gondii* β-gal (μM)	[LS; LI] [b]	SE [c]	HFF Viability at 2.5 μM (%) [d]	SD [e]
20		0.110	[0.151; 0.080]	0.416	77	1
21		0.087	[0.135; 0.056]	0.274	0	0
24		0.328	[0.437; 0.247]	0.339	66	2
	Diruthenium-galactose conjugates					
22		0.298	[0.364; 0.244]	0.066	73	1
23		0.032	[0.044; 0.023]	0.278	92	2
26		0.153	[0.178; 0.132]	0.476	97	2
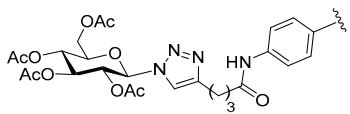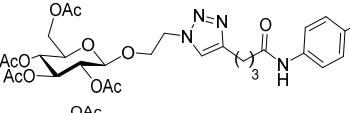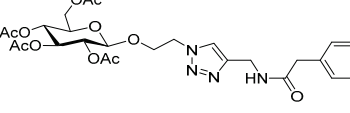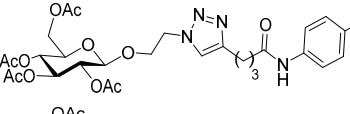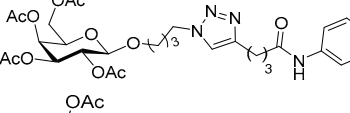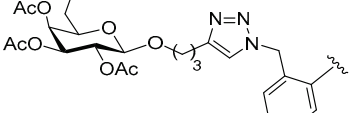
[a] Data for pyrimethamine, and compounds **2**, **3**, **5**, **7** and **9** were previously reported [88,89,92,93]. **2** and **3** did not fulfil the first screening selection criteria, but the IC$_{50}$ values and viability of HFF at 2.5 μM were determined for comparison purpose. [b] Values at 95% confidence interval (CI); LS is the upper limit of CI and LI is the lower limit of CI. [c] The standard error of the regression (SE), represents the average distance that the observed values fall from the regression line. [d] Control HFF cells treated only with 0.25% DMSO exhibited 100% viability. [e] The standard deviation of the mean (three replicate experiments).

The IC$_{50}$ values and the cytotoxicity of the diruthenium compounds **2**, **3**, **5**, **7** and **9** were measured previously [88,89,92,93]. For these diruthenium intermediates the IC$_{50}$ values ranged from 0.025 μM (**6**) to 0.153 μM (**3**). However, all intermediates also strongly affected the viability of HFF when applied at 2.5 μM, the most cytotoxic being compounds **5**, **6** and **9**.

Glucose conjugates **19** and **21** exhibited low IC$_{50}$ values (0.018 and 0.087 μM, respectively), but were toxic to host cells at 2.5 μM (HFF viability was reduced to 29% for **19** and abolished for **21**). Glucose hybrid **20** exhibited antiparasitic activity (IC$_{50}$ = 0.110 μM) but also medium cytotoxicity (HFF viability of 77%). Galactose and glucose dyads **22** and **24** had only modest antiparasitic activity (IC$_{50}$ values of 0.294 and 0.328 μM, respectively, comparable with those obtained for pyrimethamine) while being moderately toxic to HFF at 2.5 μM (73 and 66%, significantly more cytotoxic compared to the standard pyrimethamine).

Galactose conjugates **23** and **26** were the most promising of the series exhibiting not only high efficacy in inhibiting *T. gondii* β-gal proliferation (IC$_{50}$ values of 0.032 and

0.153 μM, 10-fold and 2-fold lower compared to pyrimethamine, IC_{50} = 0.326 μM), but also low cytotoxicity on the host cells when applied at 2.5 μM (HFF viability 92 and 97%, respectively).

Interestingly, both glucose and galactose hybrids **20** and **23** affected the HFF viability less than the diruthenium alkyne intermediate **7** from which they were obtained by click reactions. A similar result was also obtained for the galactose conjugate **26** compared to the diruthenium azide parent **9**.

The number of conjugates considered in this study is too limited to allow proper SAR observations. Nevertheless, apart from the conjugation with protected carbohydrates, other structural features of the dyads (as the nature and length of the linker between the two units), appear to strongly influence the biological activity, and a fine structural tuning is needed to obtain compounds with good pharmacological properties in terms of safety/anti-toxoplasma efficacy balance.

Further studies are necessary for the identification of the mode of action of trithiolato diruthenium compounds. For some other types of dinuclear Ru(II)-arene complexes reported in the literature, interactions with DNA and oligonucleotide sequences were identified [113–118]. However, unlike other Ru(II)-arene complexes presenting labile chlorine, carboxylate or monodentate N-coordinated ligands, the trithiolato diruthenium complexes do not hydrolyze and are stable in the presence of most biomolecules such as amino acids and DNA [27]. Furthermore, a recent study revealed only weak interactions via H-bonding nucleobase-pairing between trithiolato diruthenium nucleobase conjugates and the respective complementary nucleic bases [93]. In the presence of some trithiolato diruthenium complexes the oxidation of cysteine (Cys) and glutathione (GSH) to form cystine and GSSG, respectively, was observed [119,120]. TEM (transmission electron microscopy) studies of different protozoan parasites (*Toxoplasma gondii*, *Neospora caninum*, *Trypanosoma brucei*) treated with trithiolato dinuclear ruthenium(II)-arene complexes revealed alterations in the mitochondrial ultrastructure indicating this parasite organelle as potential target [29]. Noteworthy, trithiolato diruthenium conjugates with coumarin and BODIPY fluorophores [89,121] induced analogous outcome on parasite mitochondrion.

3. Materials and Methods

3.1. Chemistry

The chemistry experimental part, with full description of synthetic procedures and characterization data for all compounds are presented in the Supplementary Materials.

3.2. Biological Evaluation

3.2.1. Cell and Parasite Culture

All tissue culture media were purchased from Gibco-BRL, and biochemical agents from Sigma-Aldrich. Human foreskin fibroblasts (HFF) were obtained from the American Type Culture Collection (ATCC) and maintained in complete culture medium consisting in DMEM (Dulbecco's Modified Eagle's Medium) supplemented with 10% fetal calf serum (FCS, Gibco-BRL, Waltham, MA, USA) and antibiotics as previously described [122]. Transgenic *T. gondii* β-gal tachyzoites (expressing the β-galactosidase gene from Escherichia coli) from RH strain were kindly provided by Prof. David Sibley (Washington University, St. Louis, MO, USA) and were maintained by passages in HFF cultures as previously described [122,123].

3.2.2. In Vitro Activity Assessment against *T. Gondii* Tachyzoites and Human Foreskin Fibroblasts

The screening sequence for the compounds was described in previous reports [88]. All compounds were prepared as 1 mM stock solutions from powder in dimethyl sulfoxide (DMSO, Sigma, St. Louis, MO, USA). For in vitro activity and cytotoxicity assays, HFF were seeded at 5×10^3/well in 96 well plates and allowed to grow to confluence in complete culture medium at 37 °C and 5% CO_2. Transgenic *T. gondii* β-gal tachyzoites were freshly

isolated from infected cultures as described [122], and 96-well plates containing HFF monolayer were infected with 1×10^3 tachyzoites/well.

In a primary screening, each compound was evaluated at two concentrations 0.1 and 1 μM and added to the media prior to the infection as previously described [94]. Control non-infected non-treated HFF cultures and *T. gondii* β-gal infected but not-treated cultures were cultivated in complete medium containing 0.01 or 0.1% DMSO. The 96-well plates were incubated for 72 h at 37 °C/5% CO_2 as previously described [94].

For the IC_{50} determination on *T. gondii* β-gal, eight serial concentrations ranging from 7 nM to 1 μM were tested for each selected compound as previously described [89,92,93] and the β-galactosidase assay was performed as reported [122]. Briefly, infected HFF cultures in 96-well plates were lysed with PBS containing 0.05% Triton X-100. Then the substrate chlorophenolred-β-D-galactopyranoside (CPRG; Roche Diagnostics, Rotkreuz, Switzerland) was added in a final concentration of 0.5 mM. Absorption was measured at 570 nm wavelength using an EnSpire® multimode plate reader (PerkinElmer, Inc., Waltham, MA, USA).

All calculations were performed using the corresponding software tool contained in the Excel software package (Microsoft, Redmond, WA, USA). Cytotoxicity assays using uninfected confluent HFF host cells were performed by the alamarBlue assay as previously reported [124]. Confluent HFF monolayers in 96-well plates were exposed to 0.1, 1 and 2.5 μM of each compound and incubated for 72 h at 37 °C/5% CO_2. Then the medium was removed, the plates were washed once with PBS and 200 μL of resazurin (1:200 dilution in PBS) were added to each well. Plates were measured at excitation wavelength 530 nm and emission wavelength 590 nM using an EnSpire® multimode plate reader (PerkinElmer, Inc.). Fluorescence was measured at two different time points: T_0 as starting timepoint and T_{5h} as at 5 h later. Relative fluorescence units were calculated from time points with linear increases.

4. Conclusions

This study was focused on the synthesis and in vitro anti-*Toxoplasma* activity evaluation of eight new trithiolato-bridged arene-ruthenium(II) carbohydrate conjugates. Acetyl protected glucose and galactose moieties were pended on the diruthenium unit on one of the bridging thiols using CuAAC click reactions and connectors of several types and lengths to obtain the carbohydrate dyads. In the first screening, none of the conjugates affected the validity of host cells at 1 μM, suggesting reduced toxicity, and seven carbohydrate-diruthenium hybrids applied at 1 μM inhibited *T. gondii* β-gal growth by more than 90%. The second screening (IC_{50} values and toxicity to HFF after exposure to 2.5 μM) led to the identification of two promising acetyl protected galactose functionalized compounds **23** and **26**. Both conjugates not only exceeded (up to 10-fold) the anti-*Toxoplasma* efficacy of the standard drug pyrimethamine for similar level of toxicity to HFF, but also exhibited a significantly better antiparasitic activity/cytotoxicity balance compared to the corresponding carbohydrate non-modified diruthenium complexes.

The type and length of the linker between the diruthenium core and the carbohydrate unit significantly influenced the biological activity, and fine structural adjustments could further increase the anti-*Toxoplasma* efficacy of this type of carbohydrate conjugates. In addition, the nature of the carbohydrate and the presence/absence of protecting groups is known to strongly affect the biological activity of conjugates carbohydrate-organometallic complex [53,70,73]. Thus, the use of other carbohydrates bearing, or no protective groups is also considered.

This study showed that carbohydrate conjugation to trithiolato-diruthenium complexes is a promising strategy for obtaining novel organometallic compounds with high antiparasitic efficacy and reduced host cell cytotoxicity.

References

1. Muhammad, N.; Guo, Z. Metal-based anticancer chemotherapeutic agents. *Curr. Opin. Chem. Biol.* **2014**, *19*, 144–153. [CrossRef] [PubMed]
2. Farrell, N. Metal complexes as drugs and chemotherapeutic agents. In *Comprehensive Coordination Chemistry II*; Elsevier: Amsterdam, The Netherlands, 2004; Volume 9, pp. 809–840.
3. Ndagi, U.; Mhlongo, N.; Soliman, M.E. Metal complexes in cancer therapy–an update from drug design perspective. *Drug Des. Devel. Ther.* **2017**, *11*, 599–616. [CrossRef] [PubMed]
4. Makovec, T. Cisplatin and beyond: Molecular mechanisms of action and drug resistance development in cancer chemotherapy. *Radiol. Oncol.* **2019**, *53*, 148–158. [CrossRef] [PubMed]
5. Galluzzi, L.; Senovilla, L.; Vitale, I.; Michels, J.; Martins, I.; Kepp, O.; Castedo, M.; Kroemer, G. Molecular mechanisms of cisplatin resistance. *Oncogene* **2012**, *31*, 1869–1883. [CrossRef]
6. Karges, J.; Stokes, R.W.; Cohen, S.M. Metal complexes for therapeutic applications. *Trends Chem.* **2021**, *3*, 523–534. [CrossRef]
7. Ong, Y.C.; Gasser, G. Organometallic compounds in drug discovery: Past, present and future. *Drug Discov. Today Technol.* **2020**, *37*, 117–124. [CrossRef]
8. de Oliveira Silva, D. Ruthenium compounds targeting cancer therapy. In *Frontiers in Anti-Cancer Drug Discovery*; Atta-ur-Rahman, I., Choudhary, M., Eds.; Bentham Science: Sharjah, United Arab Emirates, 2014; Volume 4, pp. 88–156.
9. Frei, A.; Zuegg, J.; Elliott, A.G.; Baker, M.; Braese, S.; Brown, C.; Chen, F.; Dowson, C.G.; Du, G. Metal complexes, an untapped source of antibiotic potential? *Antibiotics* **2020**, *9*, 90. [CrossRef]
10. Frei, A.; Zuegg, J.; Elliott, A.G.; Baker, M.; Braese, S.; Brown, C.; Chen, F.; Dowson, C.G.; Dujardin, G.; Jung, N.; et al. Metal complexes as a promising source for new antibiotics. *Chem. Sci.* **2020**, *11*, 2627–2639. [CrossRef]
11. Gambino, D.; Otero, L. Design of prospective antiparasitic metal-based compounds including selected organometallic cores. *Inorg. Chim. Acta* **2018**, *472*, 58–75. [CrossRef]
12. Gambino, D.; Otero, Á.L. Metal compounds in the development of antiparasitic agents: Rational design from basic chemistry to the clinic. *Met. Ions Life Sci.* **2019**, *19*, 331–358. [CrossRef]
13. Mbaba, M.; Golding, T.M.; Smith, G.S. Recent advances in the biological investigation of organometallic platinum-group metal (Ir, Ru, Rh, Os, Pd, Pt) complexes as antimalarial agents. *Molecules* **2020**, *25*, 5276. [CrossRef] [PubMed]
14. Sánchez-Delgado, R.A.; Anzellotti, A. Metal complexes as chemotherapeutic agents against tropical diseases: Trypanosomiasis, malaria and leishmaniasis. *Mini Rev. Med. Chem.* **2004**, *4*, 23–30. [CrossRef] [PubMed]
15. Navarro, M.; Gabbiani, C.; Messori, L.; Gambino, D. Metal-based drugs for malaria, trypanosomiasis and leishmaniasis: Recent achievements and perspectives. *Drug Discov. Today* **2010**, *15*, 1070–1078. [CrossRef] [PubMed]
16. Ong, Y.C.; Roy, S.; Andrews, P.C.; Gasser, G. Metal compounds against neglected tropical diseases. *Chem. Rev.* **2019**, *119*, 730–796. [CrossRef] [PubMed]

17. Bergamo, A.; Gaiddon, C.; Schellens, J.H.M.; Beijnen, J.H.; Sava, G. Approaching tumour therapy beyond platinum drugs: Status of the art and perspectives of ruthenium drug candidates. *J. Inorg. Biochem.* **2012**, *106*, 90–99. [CrossRef] [PubMed]

18. Alessio, E.; Messori, L. NAMI-A and KP1019/1339, two iconic ruthenium anticancer drug candidates face-to-face: A case story in medicinal inorganic chemistry. *Molecules* **2019**, *24*, 1995. [CrossRef] [PubMed]

19. Weiss, A.; Berndsen, R.H.; Dubois, M.; Müller, C.; Schibli, R.; Griffioen, A.W.; Dyson, P.J.; Nowak-Sliwinska, P. In vivo antitumor activity of the organometallic ruthenium(II)-arene complex [Ru(η^6-*p*-cymene)Cl$_2$(pta)] (RAPTA-C) in human ovarian and colorectal carcinomas. *Chem. Sci.* **2014**, *5*, 4742–4748. [CrossRef]

20. Aird, R.E.; Cummings, J.; Ritchie, A.A.; Muir, M.; Morris, R.E.; Chen, H.; Sadler, P.J.; Jodrell, D.I. In vitro and in vivo activity and cross resistance profiles of novel ruthenium(II) organometallic arene complexes in human ovarian cancer. *Br. J. Cancer* **2002**, *86*, 1652–1657. [CrossRef]

21. Su, W.; Tang, Z.; Li, P. Development of arene ruthenium antitumor complexes. *Mini Rev. Med. Chem.* **2016**, *16*, 787–795. [CrossRef]

22. Su, W.; Li, Y.; Li, P. Design of Ru-arene complexes for antitumor drugs. *Mini Rev. Med. Chem.* **2018**, *18*, 184–193. [CrossRef]

23. Golbaghi, G.; Castonguay, A. Rationally designed ruthenium complexes for breast cancer therapy. *Molecules* **2020**, *25*, 265. [CrossRef] [PubMed]

24. Biersack, B. Anticancer activity and modes of action of (arene) ruthenium(II) complexes coordinated to C-, N-, and O-ligands. *Mini Rev. Med. Chem.* **2016**, *16*, 804–814. [CrossRef] [PubMed]

25. Zheng, K.; Wu, Q.; Ding, Y.; Mei, W. Arene ruthenium(II) complexes: The promising chemotherapeutic agent in inhibiting the proliferation, migration and invasion. *Mini-Rev. Med. Chem.* **2016**, *16*, 796–803. [CrossRef] [PubMed]

26. Laurent, Q.; Batchelor, L.K.; Dyson, P.J. Applying a Trojan horse strategy to ruthenium complexes in the pursuit of novel antibacterial agents. *Organometallics* **2018**, *37*, 915–923. [CrossRef]

27. Furrer, J.; Süss-Fink, G. Thiolato-bridged dinuclear arene ruthenium complexes and their potential as anticancer drugs. *Coord. Chem. Rev.* **2016**, *309*, 36–50. [CrossRef]

28. Basto, A.P.; Müller, J.; Rubbiani, R.; Stibal, D.; Giannini, F.; Süss-Fink, G.; Balmer, V.; Hermphill, A.; Gasser, G.; Furrer, J. Characterization of the activities of dinuclear thiolato-bridged arene ruthenium complexes against Toxoplasma gondii. *Antimicrob. Agents Chemother.* **2017**, *61*, e01031-17. [CrossRef]

29. Basto, A.P.; Anghel, N.; Rubbiani, R.; Müller, J.; Stibal, D.; Giannini, F.; Süss-Fink, G.; Balmer, V.; Gasser, G.; Furrer, J.; et al. Targeting of the mitochondrion by dinuclear thiolato-bridged arene ruthenium complexes in cancer cells and in the apicomplexan parasite Neospora caninum. *Metallomics* **2019**, *11*, 462–474. [CrossRef]

30. Jelk, J.; Balmer, V.; Stibal, D.; Giannini, F.; Süss-Fink, G.; Bütikofer, P.; Furrer, J.; Hemphill, A. Anti-parasitic dinuclear thiolato-bridged arene ruthenium complexes alter the mitochondrial ultrastructure and membrane potential in Trypanosoma brucei bloodstream forms. *Exp. Parasitol.* **2019**, *205*, 107753. [CrossRef]

31. Hill, D.; Dubey, J.P. Toxoplasma gondii: Transmission, diagnosis and prevention. *Clin. Microbiol. Infect.* **2002**, *8*, 634–640. [CrossRef]

32. Tenter, A.M.; Heckeroth, A.R.; Weiss, L.M. Toxoplasma gondii: From animals to humans. *Int. J. Parasitol.* **2000**, *30*, 1217–1258. [CrossRef]

33. Konstantinovic, N.; Guegan, H.; Stäjner, T.; Belaz, S.; Robert-Gangneux, F. Treatment of toxoplasmosis: Current options and future perspectives. *Food Waterborne Parasitol.* **2019**, *15*, e00036. [CrossRef]

34. Alday, P.H.; Doggett, J.S. Drugs in development for toxoplasmosis: Advances, challenges, and current status. *Drug Des. Dev. Ther.* **2017**, *11*, 273–293. [CrossRef]

35. Deng, Y.; Wu, T.; Zhai, S.Q.; Li, C.H. Recent progress on anti-Toxoplasma drugs discovery: Design, synthesis and screening. *Eur. J. Med. Chem.* **2019**, *183*, 111711. [CrossRef] [PubMed]

36. Antczak, M.; Dzitko, K.; Dlugonska, H. Human toxoplasmosis-Searching for novel chemotherapeutics. *Biomed. Pharmacother.* **2016**, *82*, 677–684. [CrossRef]

37. Coppens, I. Exploitation of auxotrophies and metabolic defects in Toxoplasma as therapeutic approaches. *Int. J. Parasitol.* **2014**, *44*, 109–120. [CrossRef] [PubMed]

38. Blume, M.; Seeber, F. Metabolic interactions between Toxoplasma gondii and its host. *F1000Research* **2018**, *7*, 1719. [CrossRef] [PubMed]

39. Kenny, R.G.; Marmion, C.J. Toward multi-targeted platinum and ruthenium drugs—A new paradigm in cancer drug treatment regimens? *Chem. Rev.* **2019**, *119*, 1058–1137. [CrossRef]

40. Bononi, G.; Iacopini, D.; Cicio, G.; Di Pietro, S.; Granchi, C.; Di Bussolo, V.; Minutolo, F. Glycoconjugated metal complexes as cancer diagnostic and therapeutic agents. *ChemMedChem* **2021**, *16*, 30–64. [CrossRef]

41. Pettenuzzo, A.; Pigot, R.; Ronconi, L. Metal-based glycoconjugates and their potential in targeted anticancer chemotherapy. *Metallodrugs* **2015**, *1*, 36–61. [CrossRef]

42. Byrne, J.P.; Musembi, P.; Albrecht, M. Carbohydrate-functionalized N-heterocyclic carbene Ru(II) complexes: Synthesis, characterization and catalytic transfer hydrogenation activity. *Dalton Trans.* **2019**, *48*, 11838–11847. [CrossRef]

43. Pretorius, R.; Olguín, J.; Albrecht, M. Carbohydrate-functionalized 1,2,3-triazolylidene complexes for application in base-free alcohol and amine oxidation. *Inorg. Chem.* **2017**, *56*, 12410–12420. [CrossRef] [PubMed]

44. Cucciolito, M.E.; D'Amora, A.; De Feo, G.; Ferraro, G.; Giorgio, A.; Petruk, G.; Monti, D.M.; Merlino, A.; Ruffo, F. Five-coordinate platinum(II) compounds containing sugar ligands: Synthesis, characterization, cytotoxic activity, and interaction with biological macromolecules. *Inorg. Chem.* **2018**, *57*, 3133–3143. [CrossRef] [PubMed]

45. Annunziata, A.; Cucciolito, M.E.; Esposito, R.; Ferraro, G.; Monti, D.M.; Merlino, A.; Ruffo, F. Five-coordinate platinum(II) compounds as potential anticancer agents. *Eur. J. Inorg. Chem.* **2020**, *2020*, 918–929. [CrossRef]

46. Annunziata, A.; Liberti, D.; Bedini, E.; Cucciolito, M.E.; Loreto, D.; Monti, D.M.; Merlino, A.; Ruffo, F. Square-planar vs. trigonal bipyramidal geometry in Pt(II) complexes containing triazole-based glucose ligands as potential anticancer agents. *Int. J. Mol. Sci.* **2021**, *22*, 8704. [CrossRef]

47. Patra, M.; Johnstone, T.C.; Suntharalingam, K.; Lippard, S.J. A potent glucose-platinum conjugate exploits glucose transporters and preferentially accumulates in cancer cells. *Angew. Chem. Int. Ed. Engl.* **2016**, *55*, 2550–2554. [CrossRef]

48. Gao, X.; Liu, S.; Shi, Y.; Huang, Z.; Mi, Y.; Mi, Q.; Yang, J.; Gao, Q. Mechanistic and biological characteristics of different sugar conjugated 2-methyl malonatoplatinum(II) complexes as new tumor targeting agents. *Eur. J. Med. Chem.* **2017**, *125*, 372–384. [CrossRef]

49. Wu, M.; Li, H.; Liu, R.; Gao, X.; Zhang, M.; Liu, P.; Fu, Z.; Yang, J.; Zhang-Negrerie, D.; Gao, Q. Galactose conjugated platinum(II) complex targeting the Warburg effect for treatment of non-small cell lung cancer and colon cancer. *Eur. J. Med. Chem.* **2016**, *110*, 32–42. [CrossRef]

50. Quan, L.; Lin, Z.; Lin, Y.; Wei, Y.; Lei, L.; Li, Y.; Tan, G.; Xiao, M.; Wu, T. Glucose-modification of cisplatin to facilitate cellular uptake, mitigate toxicity to normal cells, and improve anti-cancer effect in cancer cells. *J. Mol. Struct.* **2020**, *1203*, 127361. [CrossRef]

51. Wang, H.; Yang, X.; Zhao, C.; Wang, P.G.; Wang, X. Glucose-conjugated platinum(IV) complexes as tumor-targeting agents: Design, synthesis and biological evaluation. *Bioorg. Med. Chem.* **2019**, *27*, 1639–1645. [CrossRef]

52. Patra, M.; Awuah, S.G.; Lippard, S.J. Chemical approach to positional isomers of glucose–platinum conjugates reveals specific cancer targeting through glucose-transporter-mediated uptake in vitro and in vivo. *J. Am. Chem. Soc.* **2016**, *138*, 12541–12551. [CrossRef]

53. Ma, J.; Liu, H.; Xi, Z.; Hou, J.; Li, Y.; Niu, J.; Liu, T.; Bi, S.; Wang, X.; Wang, C.; et al. Protected and de-protected platinum(IV) glycoconjugates with GLUT1 and OCT2-mediated selective cancer targeting: Demonstrated enhanced transporter-mediated cytotoxic properties in vitro and in vivo. *Front. Chem.* **2018**, *6*, 386. [CrossRef] [PubMed]

54. Ma, J.; Wang, Q.; Yang, X.; Hao, W.; Huang, Z.; Zhang, J.; Wang, X.; Wang, P.G. Glycosylated platinum(IV) prodrugs demonstrated significant therapeutic efficacy in cancer cells and minimized side-effects. *Dalton Trans.* **2016**, *45*, 11830–11838. [CrossRef] [PubMed]

55. Ma, J.; Yang, X.; Hao, W.; Huang, Z.; Wang, X.; Wang, P.G. Mono-functionalized glycosylated platinum(IV) complexes possessed both pH and redox dual-responsive properties: Exhibited enhanced safety and preferentially accumulated in cancer cells in vitro and in vivo. *Eur. J. Med. Chem.* **2017**, *128*, 45–55. [CrossRef] [PubMed]

56. Calvaresi, E.C.; Hergenrother, P.J. Glucose conjugation for the specific targeting and treatment of cancer. *Chem. Sci.* **2013**, *4*, 2319–2333. [CrossRef]

57. Medina, R.A.; Owen, G.I. Glucose transporters: Expression, regulation and cancer. *Biol. Res.* **2002**, *35*, 9–26. [CrossRef]

58. Macheda, M.L.; Rogers, S.; Best, J.D. Molecular and cellular regulation of glucose transporter (GLUT) proteins in cancer. *J. Cell. Physiol.* **2005**, *202*, 654–662. [CrossRef] [PubMed]

59. Szablewski, L. Expression of glucose transporters in cancers. *Biochim. Biophys. Acta* **2013**, *1835*, 164–169. [CrossRef]

60. Fernandes, A.C. Synthesis, biological activity and medicinal applications of ruthenium complexes containing carbohydrate ligands. *Curr. Med. Chem.* **2019**, *26*, 6412–6437. [CrossRef]

61. Iacopini, D.; Biancalana, L.; Di Pietro, S.; Marchetti, F.; Di Bussolo, V. Stereoselective synthesis of new glycoconjugated ruthenium(II)-arene complexes as potential anticancer agents. In Proceedings of the EuroCarb XX, Leiden, The Netherlands, 30 June–4 July 2019.

62. D'Amora, A.; Cucciolito, M.E.; Iannitti, R.; Morelli, G.; Palumbo, R.; Ruffo, F.; Tesauro, D. Pyridine ruthenium(III) complexes entrapped in liposomes with enhanced cytotoxic properties in PC-3 prostate cancer cells. *J. Drug Deliv. Sci. Technol.* **2019**, *51*, 552–558. [CrossRef]

63. Valente, A.; Garcia, M.H.; Marques, F.; Miao, Y.; Rousseau, C.; Zinck, P. First polymer "ruthenium-cyclopentadienyl" complex as potential anticancer agent. *J. Inorg. Biochem.* **2013**, *127*, 79–81. [CrossRef]

64. Lamač, M.; Horáček, M.; Červenková Šťastná, L.; Karban, J.; Sommerová, L.; Skoupilová, H.; Hrstka, R.; Pinkas, J. Harmless glucose-modified ruthenium complexes suppressing cell migration of highly invasive cancer cell lines. *Appl. Organometal. Chem.* **2019**, *34*, e5318. [CrossRef]

65. Hanif, M.; Meier, S.M.; Nazarov, A.A.; Risse, J.; Legin, A.; Casini, A.; Jakupec, M.A.; Keppler, B.K.; Hartinger, C.G. Influence of the π-coordinated arene on the anticancer activity of ruthenium(II)carbohydrate organometallic complexes. *Front. Chem.* **2013**, *1*, 27. [CrossRef]

66. Berger, I.; Hanif, M.; Nazarov, A.A.; Hartinger, C.G.; John, R.O.; Kuznetsov, M.L.; Groessl, M.; Schmitt, F.; Zava, O.; Biba, F.; et al. In vitro anticancer activity and biologically relevant metabolization of organometallic ruthenium com plexes with carbohydrate-based ligands. *Chem. Eur. J.* **2008**, *14*, 9046–9057. [CrossRef] [PubMed]

67. Böge, M.; Fowelin, C.; Bednarski, P.; Heck, J. Diaminohexopyranosides as ligands in half-sandwich ruthenium(II), rhodium(III), and iridium(III) complexes. *Organometallics* **2015**, *34*, 1507–1521. [CrossRef]

68. Florindo, P.; Marques, I.J.; Nunes, C.D.; Fernandes, A.C. Synthesis, characterization and cytotoxicity of cyclopentadienyl ruthenium(II) complexes containing carbohydrate-derived ligands. *J. Organomet. Chem.* **2014**, *760*, 240–247. [CrossRef]

69. Florindo, P.R.; Pereira, D.M.; Borralho, P.M.; Rodrigues, C.M.P.; Piedade, M.F.M.; Fernandes, A.C. Cyclopentadienyl–ruthenium(II) and iron(II) organometallic compounds with carbohydrate derivative ligands as good colorectal anticancer agents. *J. Med. Chem.* **2015**, *58*, 4339–4347. [CrossRef]

70. Hamala, V.; Martišová, A.; Červenková Šťastná, L.; Karban, J.; Dančo, A.; Šimarek, A.; Lamač, M.; Horáček, M.; Kolářová, T.; Hrstka, R.; et al. Ruthenium tetrazene complexes bearing glucose moieties on their periphery: Synthesis, characterization, and in vitro cytotoxicity. *Appl. Organomet. Chem.* **2020**, *34*, e5896. [CrossRef]

71. Kilpin, K.J.; Crot, S.; Riedel, T.; Kitchen, J.A.; Dyson, P.J. Ruthenium(II) and osmium(II) 1,2,3-triazolylidene organometallics: A preliminary investigation into the biological activity of 'click' carbene complexes. *Dalton Trans.* **2014**, *43*, 1443–1448. [CrossRef]

72. Florindo, P.R.; Pereira, D.M.; Borralho, P.M.; Costa, P.J.; Piedade, M.F.M.; Rodrigues, C.M.P.; Fernandes, A.C. New [(η^5-C$_5$H$_5$)Ru(N–N)(PPh$_3$)][PF$_6$] compounds: Colon anticancer activity and GLUT-mediated cellular uptake of carbohydrate-appended complexes. *Dalton Trans.* **2016**, *45*, 11926–11930. [CrossRef]

73. Kacsir, I.; Sipos, A.; Ujlaki, G.; Buglyó, P.; Somsák, L.; Bai, P.; Bokor, É. Ruthenium half-sandwich type complexes with bidentate monosaccharide ligands show antineoplastic activity in ovarian cancer cell models through reactive oxygen species production. *Int. J. Mol. Sci.* **2021**, *22*, 10454. [CrossRef]

74. Hartinger, C.G.; Nazarov, A.A.; Ashraf, S.M.; Dyson, P.J.; Keppler, B.K. Carbohydrate-metal complexes and their potential as anticancer agents. *Curr. Med. Chem.* **2008**, *15*, 2574–2591. [CrossRef]

75. Wang, X.; Guo, Z. Targeting and delivery of platinum-based anticancer drugs. *Chem. Soc. Rev.* **2013**, *42*, 202–224. [CrossRef] [PubMed]

76. Fu, J.; Yang, J.; Seeberger, P.H.; Yin, J. Glycoconjugates for glucose transporter-mediated cancer-specific targeting and treatment. *Carbohydr. Res.* **2020**, *498*, 108195. [CrossRef] [PubMed]

77. Franconetti, A.; López, Ó.; Fernandez-Bolanos, J.G. Carbohydrates: Potential sweet tools against cancer. *Curr. Med. Chem.* **2020**, *27*, 1206–1242. [CrossRef]

78. Roux, C.; Biot, C. Ferrocene-based antimalarials. *Future Med. Chem.* **2012**, *4*, 783–797. [CrossRef]

79. Ferreira, C.L.; Ewart, C.B.; Barta, C.A.; Little, S.; Yardley, V.; Martins, C.; Polishchuk, E.; Smith, P.J.; Moss, J.R.; Merkel, M.; et al. Synthesis, structure, and biological activity of ferrocenyl carbohydrate conjugates. *Inorg. Chem.* **2006**, *45*, 8414–8422. [CrossRef]

80. Reddy, A.; Sangenito, L.S.; Guedes, A.A.; Branquinha, M.H.; Kavanagh, K.; McGinley, J.; Dos Santos, A.L.S.; Velasco-Torrijos, T. Glycosylated metal chelators as anti-parasitic agents with tunable selectivity. *Dalton Trans.* **2017**, *46*, 5297–5307. [CrossRef]

81. Trivedi, R.; Deepthi, S.B.; Giribabu, L.; Sridhar, B.; Sujitha, P.; Kumar, C.G.; Ramakrishna, K.V.S. Synthesis, crystal structure, electronic spectroscopy, electrochemistry and biological studies of ferrocene-carbohydrate conjugates. *Eur. J. Inorg. Chem.* **2012**, *2012*, 2267–2277. [CrossRef]

82. Panaka, S.; Trivedi, R.; Jaipal, K.; Giribabu, L.; Sujitha, P.; Kumar, C.G.; Sridhar, B. Ferrocenyl chalcogeno (sugar) triazole conjugates: Synthesis, characterization and anticancer properties. *J. Organomet. Chem.* **2016**, *813*, 125–130. [CrossRef]

83. Coppens, I.; Asai, T.; Tomavo, S. Chapter 8-Biochemistry and Metabolism of Toxoplasma gondii: Carbohydrates, Lipids and Nucleotides. In *Toxoplasma Gondii. In the Model Apicomplexan-Perspectives and Methods*, 2nd ed.; Weiss, L.M., Kim, K., Eds.; Academic Press: Cambridge, MA, USA, 2014; pp. 257–295. [CrossRef]

84. Fleige, T.; Fischer, K.; Ferguson, D.J.; Gross, U.; Bohne, W. Carbohydrate metabolism in the Toxoplasma gondii apicoplast: Localization of three glycolytic isoenzymes, the single pyruvate dehydrogenase complex, and a plastid phosphate translocator. *Eukaryot. Cell* **2007**, *6*, 984–996. [CrossRef]

85. Coppin, A.; Dzierszinski, F.; Legrand, S.; Mortuaire, M.; Ferguson, D.; Tomavo, S. Developmentally regulated biosynthesis of carbohydrate and storage polysaccharide during differentiation and tissue cyst formation in Toxoplasma gondii. *Biochimie* **2003**, *85*, 353–361. [CrossRef] [PubMed]

86. Blume, M.; Rodriguez-Contreras, D.; Landfear, S.; Fleige, T.; Soldati-Favre, D.; Lucius, R.; Gupta, N. Host-derived glucose and its transporter in the obligate intracellular pathogen Toxoplasma gondii are dispensable by glutaminolysis. *Proc. Natl. Acad. Sci. USA* **2009**, *106*, 12998–13003. [CrossRef] [PubMed]

87. Giannini, F.; Furrer, J.; Süss-Fink, G.; Clavel, C.M.; Dyson, P.J. Synthesis, characterization and in vitro anticancer activity of highly cytotoxic trithiolato diruthenium complexes of the type [(η^6-*p*-MeC$_6$H$_4$^{i}Pr)$_2$Ru$_2$(μ_2-SR^1)$_2$(μ_2-SR^2)]$^+$ containing different thiolato bridges. *J. Organomet. Chem.* **2013**, *744*, 41–48. [CrossRef]

88. Păunescu, E.; Boubaker, G.; Desiatkina, O.; Anghel, N.; Amdouni, Y.; Hemphill, A.; Furrer, J. The quest of the best—A SAR study of trithiolato-bridged dinuclear ruthenium(II)-arene compounds presenting antiparasitic properties. *Eur. J. Med. Chem.* **2021**, *222*, 113610. [CrossRef] [PubMed]

89. Desiatkina, O.; Paunescu, E.; Mosching, M.; Anghel, N.; Boubaker, G.; Amdouni, Y.; Hemphill, A.; Furrer, J. Coumarin-tagged dinuclear trithiolato-bridged ruthenium(II)arene complexes: Photophysical properties and antiparasitic activity. *ChemBioChem* **2020**, *21*, 2818–2835. [CrossRef]

90. Giannini, F.; Bartoloni, M.; Paul, L.E.H.; Süss-Fink, G.; Reymond, J.L.; Furrer, J. Cytotoxic peptide conjugates of dinuclear areneruthenium trithiolato complexes. *MedChemComm* **2015**, *6*, 347–350. [CrossRef]

91. Stíbal, D.; Therrien, B.; Süss-Fink, G.; Nowak-Sliwinska, P.; Dyson, P.J.; Čermáková, E.; Řezáčová, M.; Tomšík, P. Chlorambucil conjugates of dinuclear p-cymene ruthenium trithiolato complexes: Synthesis, characterization and cytotoxicity study in vitro and in vivo. *J. Biol. Inorg. Chem.* **2016**, *21*, 443–452. [CrossRef]

92. Desiatkina, O.; Johns, S.K.; Anghel, N.; Boubaker, G.; Hemphill, A.; Furrer, J.; Păunescu, E. Synthesis and antiparasitic activity of new conjugates-organic drugs tethered to trithiolato-bridged dinuclear ruthenium(II)-arene complexes. *Inorganics* **2021**, *9*, 59. [CrossRef]

93. Desiatkina, O.; Mösching, M.; Anghel, N.; Boubaker, G.; Amdouni, Y.; Hemphill, A.; Furrer, J.; Păunescu, E. New nucleic base-tethered trithiolato-bridged dinuclear ruthenium(II)-arene compounds: Synthesis and antiparasitic activity. *Molecules* **2022**, *27*, 8173. [CrossRef]

94. Studer, V.; Anghel, N.; Desiatkina, O.; Felder, T.; Boubaker, G.; Amdouni, Y.; Ramseier, J.; Hungerbuhler, M.; Kempf, C.; Heverhagen, J.T.; et al. Conjugates containing two and three trithiolato-bridged dinuclear ruthenium(II)-arene units as in vitro antiparasitic and anticancer agents. *Pharmaceuticals* **2020**, *13*, 471. [CrossRef]

95. Renfrew, A.K.; Juillerat-Jeanneret, L.; Dyson, P.J. Adding diversity to ruthenium(II)–arene anticancer (RAPTA) compounds via click chemistry: The influence of hydrophobic chains. *J. Organomet. Chem.* **2011**, *696*, 772–779. [CrossRef]

96. Mandal, S.; Das, R.; Gupta, P.; Mukhopadhyay, B. Synthesis of a sugar-functionalized iridium complex and its application as a fluorescent lectin sensor. *Tetrahedron Lett.* **2012**, *53*, 3915–3918. [CrossRef]

97. Schmollinger, D.; Kraft, J.; Ewald, C.; Ziegler, T. Synthesis of ruthenium and palladium complexes from glycosylated 2,20-bipyridine and terpyridine ligands. *Tetrahedron Lett.* **2017**, *58*, 3643–3645. [CrossRef]

98. Mede, T.; Jager, M.; Schubert, U.S. "Chemistry-on-the-complex": Functional Ru(II) polypyridyl-type sensitizers as divergent building blocks. *Chem. Soc. Rev.* **2018**, *47*, 7577–7627. [CrossRef] [PubMed]

99. Cisnetti, F.; Gibard, C.; Gautier, A. Post-functionalization of metal–NHC complexes: A useful toolbox for bioorganometallic chemistry (and beyond)? *J. Organomet. Chem.* **2015**, *782*, 22–30. [CrossRef]

100. van Hilst, Q.V.C.; Lagesse, N.R.; Preston, D.; Crowley, J.D. Functional metal complexes from CuAAC "click" bidentate and tridentate pyridyl-1,2,3-triazole ligands. *Dalton Trans.* **2018**, *47*, 997–1002. [CrossRef]

101. Casas-Solvas, J.M.; Ortiz-Salmeron, E.; Gimenez-Martinez, J.J.; Garcia-Fuentes, L.; Capitan-Vallvey, L.F.; Santoyo-Gonzalez, F.; Vargas-Berenguel, A. Ferrocene-carbohydrate conjugates as electrochemical probes for molecular recognition studies. *Chem. Eur. J.* **2009**, *15*, 710–725. [CrossRef]

102. Casas-Solvas, J.M.; Vargas-Berenguel, A.; Capitan-Vallvey, L.F.; Santoyo-Gonzalez, F. Convenient methods for the synthesis of ferrocene-carbohydrate conjugates. *Org. Lett.* **2004**, *6*, 3687–3690. [CrossRef]

103. Meldal, M.; Tornoe, C.W. Cu-catalyzed azide-alkyne cycloaddition. *Chem. Rev.* **2008**, *108*, 2952–3015. [CrossRef]

104. Kolb, H.C.; Finn, M.G.; Sharpless, K.B. Click chemistry: Diverse chemical function from a few good reactions. *Angew. Chem. Int. Ed. Engl.* **2001**, *40*, 2004–2021. [CrossRef]

105. Singh, M.S.; Chowdhury, S.; Koley, S. Advances of azide-alkyne cycloaddition-click chemistry over the recent decade. *Tetrahedron* **2016**, *72*, 5257–5283. [CrossRef]

106. Ibao, A.F.; Gras, M.; Therrien, B.; Süss-Fink, G.; Zava, O.; Dyson, P.J. Thiolato-bridged arene-ruthenium complexes: Synthesis, molecular structure, reactivity, and anticancer activity of the dinuclear complexes [(arene)$_2$Ru$_2$(SR)$_2$Cl$_2$]. *Eur. J. Inorg. Chem.* **2012**, *2012*, 1531–1535. [CrossRef]

107. Soli, E.D.; DeShong, P. Advances in glycosyl azide preparation via hypervalent silicates. *J. Org. Chem.* **1999**, *64*, 9724–9726. [CrossRef]

108. Paterson, S.M.; Clark, J.; Stubbs, K.A.; Chirila, T.V.; Baker, M.V. Carbohydrate-based crosslinking agents: Potential use in hydrogels. *J. Polym. Sci. A Polym. Chem.* **2011**, *49*, 4312–4315. [CrossRef]

109. Mereyala, H.B.; Gurrala, S.R. A highly diastereoselective, practical synthesis of allyl, propargyl 2,3,4,6-tetra-O-acetyl-β-d-gluco, β-d-galactopyranosides and allyl, propargyl heptaacetyl-β-d-lactosides. *Carbohydr. Res.* **1998**, *307*, 351–354. [CrossRef]

110. Roy, B.; Dutta, S.; Choudhary, A.; Basak, A.; Dasgupta, S. Design, synthesis and RNase A inhibition activity of catechin and epicatechin and nucleobase chimeric molecules. *Bioorg. Med. Chem. Lett.* **2008**, *18*, 5411–5414. [CrossRef]

111. Wang, X.; Zhu, M.; Gao, F.; Wei, W.; Qian, Y.; Liu, H.K.; Zhao, J. Imaging of a clickable anticancer iridium catalyst. *J. Inorg. Biochem.* **2018**, *180*, 179–185. [CrossRef]

112. Zabarska, N.; Stumper, A.; Rau, S. CuAAC click reactions for the design of multifunctional luminescent ruthenium complexes. *Dalton Trans.* **2016**, *45*, 2338–2351. [CrossRef]

113. Wu, Q.; Liu, L.Y.; Li, S.; Wang, F.X.; Li, J.; Qian, Y.; Su, Z.; Mao, Z.W.; Sadler, P.J.; Liu, H.K. Rigid dinuclear ruthenium-arene complexes showing strong DNA interactions. *J. Inorg. Biochem.* **2018**, *189*, 30–39. [CrossRef]

114. Zhao, J.; Li, S.; Wang, X.; Xu, G.; Gou, S. Dinuclear organoruthenium complexes exhibiting antiproliferative activity through DNA damage and a Reactive-Oxygen-Species-mediated endoplasmic reticulum stress pathway. *Inorg. Chem.* **2019**, *58*, 2208–2217. [CrossRef]

115. Murray, B.S.; Menin, L.; Scopelliti, R.; Dyson, P.J. Conformational control of anticancer activity: The application of arene-linked dinuclear ruthenium(II) organometallics. *Chem. Sci.* **2014**, *5*, 2536–2545. [CrossRef]

116. Chen, H.; Parkinson, J.A.; Novakova, O.; Bella, J.; Wang, F.; Dawson, A.; Gould, R.; Parsons, S.; Brabec, V.; Sadler, P.J. Induced-fit recognition of DNA by organometallic complexes with dynamic stereogenic centers. *Proc. Natl. Acad. Sci. USA* **2003**, *100*, 14623–14628. [CrossRef] [PubMed]

117. Wang, H.-Y.; Qian, Y.; Wang, F.-X.; Habtemariam, A.; Mao, Z.-W.; Sadler, P.J.; Liu, H.-K. Ruthenium(II)–arene metallacycles: Crystal structures, interaction with DNA, and cytotoxicity. *Eur. J. Inorg. Chem.* **2017**, *2017*, 1792–1799. [CrossRef]

118. Pettinari, C.; Pettinari, R.; Xhaferai, N.; Giambastiani, G.; Rossin, A.; Bonfili, L.; Eleuteri, A.M.; Cuccioloni, M. Binuclear 3,3′,5,5′-tetramethyl-1H,H-4,4′-bipyrazole Ruthenium(II) complexes: Synthesis, characterization and biological studies. *Inorg. Chim. Acta* **2020**, *513*, 119902. [CrossRef]

119. Giannini, F.; Furrer, J.; Ibao, A.F.; Suss-Fink, G.; Therrien, B.; Zava, O.; Baquie, M.; Dyson, P.J.; Stepnicka, P. Highly cytotoxic trithiophenolatodiruthenium complexes of the type [(η^6-*p*-MeC$_6$H$_4$Pr^i)$_2$Ru$_2$(SC$_6$H$_4$-p-X)$_3$]$^+$: Synthesis, molecular structure, electrochemistry, cytotoxicity, and glutathione oxidation potential. *J. Biol. Inorg. Chem.* **2012**, *17*, 951–960. [CrossRef] [PubMed]

120. Giannini, F.; Suss-Fink, G.; Furrer, J. Efficient oxidation of cysteine and glutathione catalyzed by a dinuclear areneruthenium trithiolato anticancer complex. *Inorg. Chem.* **2011**, *50*, 10552–10554. [CrossRef]

121. Desiatkina, O.; Boubaker, G.; Anghel, N.; Amdouni, Y.; Hemphill, A.; Furrer, J.; Paunescu, E. Synthesis, photophysical properties and biological evaluation of new conjugates BODIPY–dinuclear trithiolato-bridged ruthenium(II)-arene complexes. *ChemBioChem* **2022**, *23*, e202200536. [CrossRef]

122. Barna, F.; Debache, K.; Vock, C.A.; Kuster, T.; Hemphill, A. In vitro effects of novel ruthenium complexes in Neospora caninum and Toxoplasma gondii tachyzoites. *Antimicrob. Agents Chemother.* **2013**, *57*, 5747–5754. [CrossRef]

123. McFadden, D.C.; Seeber, F.; Boothroyd, J.C. Use of Toxoplasma gondii expressing beta-galactosidase for colorimetric assessment of drug activity in vitro. *Antimicrob. Agents Chemother.* **1997**, *41*, 1849–1853. [CrossRef]

124. Muller, J.; Aguado-Manser, A.; Manser, V.; Balmer, V.; Winzer, P.; Ritler, D.; Hostettler, I.; Arranz-Solis, D.; Ortega-Mora, L.; Hemphill, A. Buparvaquone is active against Neospora caninum in vitro and in experimentally infected mice. *Int. J. Parasitol. Drugs Drug. Resist.* **2015**, *5*, 16–25. [CrossRef]

125. Fulmer, G.R.; Miller, A.J.M.; Sherden, N.H.; Gottlieb, H.E.; Nudelman, A.; Stoltz, B.M.; Bercaw, J.E.; Goldberg, K.I. NMR chemical shifts of trace impurities: Common laboratory solvents, organics, and gases in deuterated solvents relevant to the organometallic chemist. *Organometallics* **2010**, *29*, 2176–2179. [CrossRef]

126. Ogawa, T.; Nakabayashi, S.; Shibata, S. Synthetic studies on nephritogenic glycosides. Synthesis of N-(β-l-Aspartyl)-α-d-glucopyranosylamine. *Agric. Biol. Chem.* **1983**, *47*, 281–285. [CrossRef]

Multispectral and Molecular Docking Studies Reveal Potential Effectiveness of Antidepressant Fluoxetine by Forming π-Acceptor Complexes

Ahmed Gaber [1,2,*], Walaa F. Alsanie [2,3], Majid Alhomrani [2,3], Abdulhakeem S. Alamri [2,3], Hussain Alyami [4], Sonam Shakya [5], Hamza Habeeballah [6], Heba A. Alkhatabi [7,8,9], Raed I. Felimban [7,10], Abdulwahab Alamri [11], Abdulhameed Abdullah Alhabeeb [12], Bassem M. Raafat [13] and Moamen S. Refat [14,*]

[1]   Department of Biology, College of Science, Taif University, P.O. Box 11099, Taif 21944, Saudi Arabia
[2]   Centre of Biomedical Sciences Research (CBSR), Deanship of Scientific Research, Taif University, P.O. Box 11099, Taif 21944, Saudi Arabia
[3]   Department of Clinical Laboratories Sciences, The Faculty of Applied Medical Sciences, Taif University, P.O. Box 11099, Taif 21944, Saudi Arabia
[4]   College of Medicine, Taif University, P.O. Box 11099, Taif 21944, Saudi Arabia
[5]   Department of Chemistry, Faculty of Science, Aligarh Muslim University, Aligarh 202002, India
[6]   Department of Medical Laboratory Technology, Faculty of Applied Medical Sciences in Rabigh, King Abdulaziz University, P.O. Box 80203, Jeddah 21589, Saudi Arabia
[7]   Department of Medical Laboratory Sciences, Faculty of Applied Medical Sciences, King Abdulaziz University, P.O. Box 80203, Jeddah 21589, Saudi Arabia
[8]   Center of Excellence in Genomic Medicine Research (CEGMR), King Abdulaziz University, P.O. Box 80203, Jeddah 21589, Saudi Arabia
[9]   King Fahd Medical Research Centre, Hematology Research Unit, King Abdulaziz University, P.O. Box 80203, Jeddah 21589, Saudi Arabia
[10]   Center of Innovation in Personalized Medicine (CIPM), 3D Bioprinting Unit, King Abdulaziz University, P.O. Box 80203, Jeddah 21589, Saudi Arabia
[11]   Department of Pharmacology and Toxicology, College of Pharmacy, University of Hail, P.O. Box 2240, Hail 55476, Saudi Arabia
[12]   National Centre for Mental Health Promotion, P.O. Box 95459, Riyadh 11525, Saudi Arabia
[13]   Department of Radiological Sciences, College of Applied Medical Sciences, Taif University, P.O. Box 11099, Taif 21944, Saudi Arabia
[14]   Department of Chemistry, College of Science, Taif University, P.O. Box 11099, Taif 21944, Saudi Arabia
*   Correspondence: a.gaber@tu.edu.sa (A.G.); moamen@tu.edu.sa (M.S.R.)

Abstract: Poor mood, lack of pleasure, reduced focus, remorse, unpleasant thoughts, and sleep difficulties are all symptoms of depression. The only approved treatment for children and adolescents with major depressive disorder (MDD) is fluoxetine hydrochloride (FXN), a serotonin selective reuptake inhibitor antidepressant. MDD is the most common cause of disability worldwide. In the present research, picric acid (PA); dinitrobenzene; p-nitro benzoic acid; 2,6-dichloroquinone-4-chloroimide; 2,6-dibromoquinone-4-chloroimide; and 7,7′,8,8′-tetracyanoquinodimethane were used to make 1:1 FXN charge-transfer compounds in solid and liquid forms. The isolated complexes were then characterized by elemental analysis, conductivity, infrared, Raman, and ^{1}H-NMR spectra, thermogravimetric analysis, scanning electron microscopy, and X-ray powder diffraction. Additionally, a molecular docking investigation was conducted on the donor moiety using FXN alone and the resulting charge transfer complex [(FXN)(PA)] as an acceptor to examine the interactions against two protein receptors (serotonin or dopamine). Interestingly, the [(FXN)(PA)] complex binds to both serotonin and dopamine more effectively than the FXN drug alone. Furthermore, [(FXN)(PA)]–serotonin had a greater binding energy than [FXN]–serotonin. Theoretical data were also generated by density functional theory simulations, which aided the molecular geometry investigation and could be beneficial to researchers in the future.

---

1. Introduction

Depression is a common mental illness that affects almost 300 million people of all ages around the world [1]. Depression's effects can last a long time or recur, and they can have a substantial influence on a person's ability to function and live a happy life. Major depressive disorder (MDD) is the primary cause of disability worldwide. At least one distinct depressive episode lasting at least two weeks, as well as evident changes in mood, interests, and pleasure, cognitive changes, and vegetative symptoms, characterize this severe condition. Girls are more likely than boys to be affected by MDD, with a global incidence of 3.0% and 1.8%, respectively [2].

MDD is the second leading cause of chronic illness among all medical diseases according to the years lived with disability [3]. Additionally, MDD is associated with a higher risk of contracting diseases, such as diabetes, heart disease, and stroke, which ultimately enhances the severity of the disease [4]. Notably, death by suicide can be induced by MDD. It is estimated that up to 50% of around 800,000 suicides committed annually around the world take place during a depressed episode [5], and MDD patients are approximately 20-fold more likely than the general population to commit suicide [6].

Fluoxetine hydrochloride (FXN) was first described as a selective serotonin (5-HT)-uptake inhibitor in 1974 [7] and was the initial representative of a new group of antidepressant medications identified as selective serotonin reuptake inhibitors. In fact, FXN was the first of this class to be released in the United States. Notably, inhibitors of this class are still among the most often prescribed antidepressants today [8]. Moreover, FXN is the only approved treatment for pediatric and adolescent patients with MDD [9].

Charge transfer (CT), which involves an electron donor interacting with several acceptors, is now a significant factor in the study of drug–receptor binding mechanisms [10] and several biological fields [11]. As a result, CT interactions of some acceptors have been successfully used in pharmacokinetic analysis [12], with extensive studies conducted on CT–receptor compounds for broad applications [13].

Chemists, biologists, and pharmacists are all interested in the chemistry of CT interactions and complex building, particularly when it comes to pharmaceuticals. Their interest in CT complexes is related to their high value and numerous uses in a variety of industries and technological, chemical, biological, and pharmaceutical fields. For instance, CT complexes have been employed in biological, electrical, optical, and magnetic experiments, as well as in investigations of pharmaceutical receptor-binding mechanisms [14–16]. The development of quick, dependable, and straightforward techniques for the qualitative and quantitative detection of drugs in bulk and/or pharmaceutical dose forms was also based on the production of CT complexes [17,18].

In pharmaceutical formulations, π-acceptors were employed in the spectrophotometric examination of numerous medicines [19–25]. Recent studies have demonstrated the potential efficacy of using π-acceptors to boost antidepressant drug levels [26–28].

In the current study, the CT complexes of FXN with six different types of π-acceptors were synthesized and thoroughly characterized at different levels in both solid and liquid forms. The interactions between two protein receptors (serotonin or dopamine) and ligands were also examined by molecular docking using Autodock Vina software. To understand how receptor–ligand interactions work, several molecular dynamic simulations were run. Multiple degrees of comparisons were made between CT complexes of FXN and the FXN drug alone against the serotonin receptor.

2. Results and Discussion

2.1. Multispectroscopic Studies

Recently, there has been a lot of focus on the development of stable CT complexes that come from the interaction of electron acceptors with chemical or biological molecules. The important physical and chemical characteristics of these complexes are the source of this interest. Compared with the methods of drug determination described previously in the literature, the CT complexation is an important approach that is less complicated, more affordable, and more effective [29]. Understanding the interactions between medications and receptors as well as the mechanisms behind drug action may be possible through the study of drug CT complexes [30].

In the present research, a molar ratio of 1:1 was used for the elemental analyses of all synthesized FXN-CT complexes, which are easily soluble in dimethylformamide and dimethylsulfoxide. The molar conductance values of the CT complexes of FXN revealed a slightly electrolytic nature (37–56 Ω^{-1} cm^{-1} mol^{-1}) upon the creation of positive and negative datives anions owing to hydrogen bonding.

The infrared spectrum of FXN had different stretching vibration bands at 3500 cm^{-1} (N–H stretching), 3200–3000 cm^{-1} (C–H stretching), 1600–1400 cm^{-1} (C=C stretching), 1300 cm^{-1} (C–O stretching), and 1200–1000 cm^{-1} (C–F stretching) [31]. After CT complexation, the υ(N–H) band was absent, and the δ(NH) band shifted to lower wavenumbers (1611–1629 cm^{-1}). These alterations could result from a single pair of -NH electrons interacting with the six acceptors. The n–π* CT transitions caused the C=C stretching frequency to decrease from 1590 cm^{-1} to 1569–1537 cm^{-1}. In addition, the stretching vibration of υ(C–N) shifted to 1349–1324 cm^{-1} in all six acceptors with the FXN drug complexes according to the interaction between –NH and the acceptors (Figure 1).
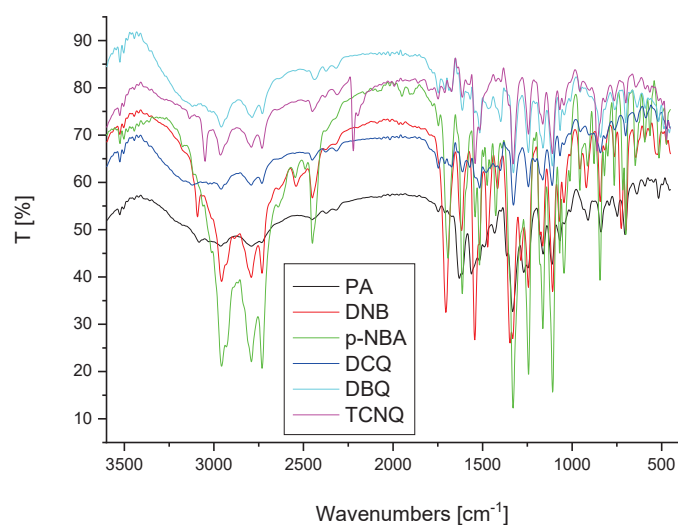
Figure 1. FTIR spectra analysis of FXN drug generated with six π-acceptors.

Few bands were observed from 2373–2452 cm^{-1} due to intermolecular hydrogen bonding between the basic nitrogen of FXN as an n-donor (D) and the π-acceptor (A), resulting in CT complexes of the n-π type (D–A) (Figure 2) [32].
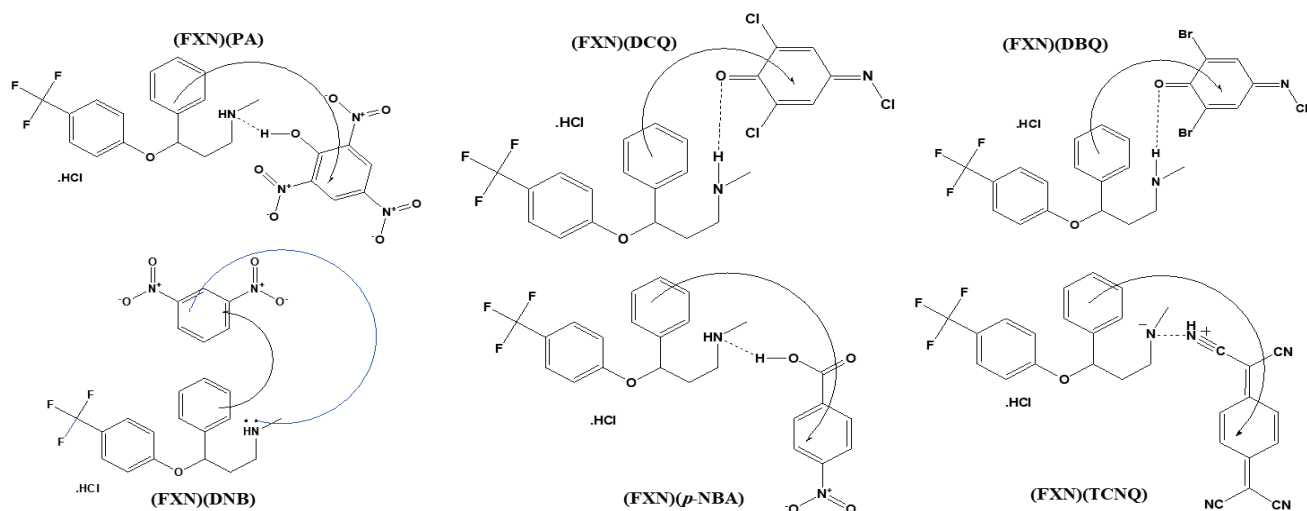
Figure 2. Molecular structures between FXN and the six π-acceptors.

^{1}HNMR spectra of the FXN with the six π-acceptors complexes are shown in Figure 3. The –NH peak of the secondary amine of FXN shifted to a lower field (9.11–9.58 ppm) due to the involvement of the -NH proton on the receptor fragment (FXN). Aromatic protons also shifted downfield in the spectra of the FXN complexes. Such a result strengthens the transfer of electrons from the lone electron pair on the nitrogen atom of the secondary amine group –NH to the acceptors and aromatic rings of the FXN donor via intermolecular hydrogen bonding.
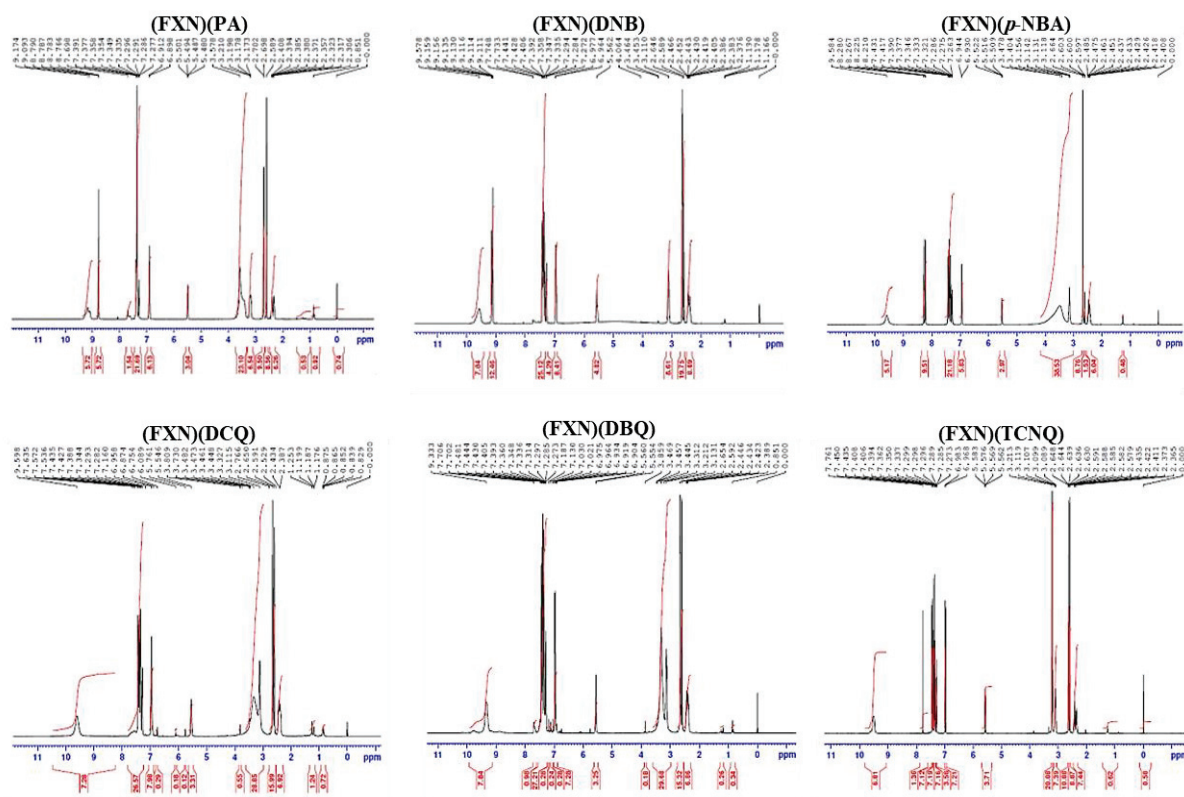
Figure 3. ^{1}HNMR spectra of the six ligand complexes.

The form of the different (FXN)(π-acceptors) is dependent on the current acceptor according to electron micrographs due to the varying chemical compositions. EDX spectra confirm the existence of carbon, oxygen, and halogens (chlorine and fluorine) in the FXN

complexes (Figure 4). The homogeneity and consistency of particle morphologies in synthesized FXN CT complexes imply that the morphological phases of the [(FXN)(π-acceptor)] complexes have a consistent matrix, with particle sizes ranging from 50 to 500 μm (Figure 4).
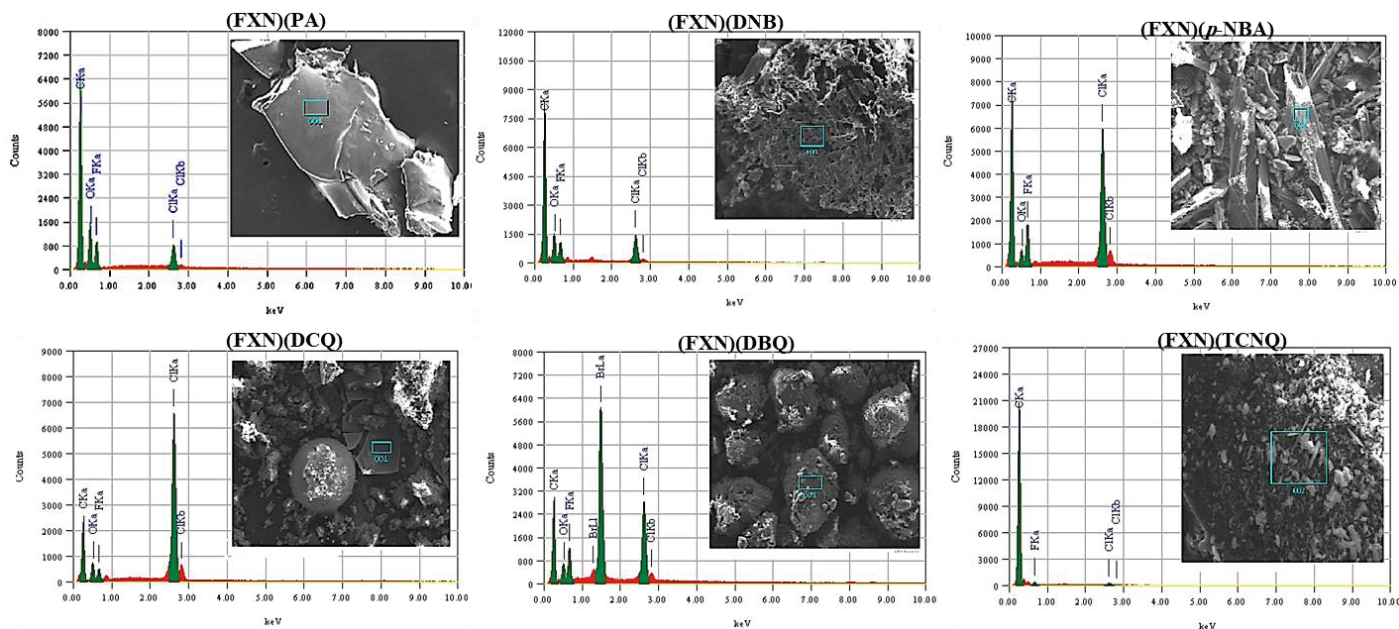
Figure 4. SEM images and EDX spectra of six ^{1}HNMR spectra of six ligand complexes.

2.2. Molecular Docking Studies

Serotonin 5-HT2A (PDB ID: 6A94) and dopamine (PDB ID: 6CM4) protein receptors were docked against all synthesized CT complexes, resulting in the optimum docking pose. For comparison reasons, FXN was utilized as control. Interestingly, five of six CT complexes showed higher docking scores than that of FXN alone at both receptors (Table 1).

Table 1. Docking score of all [(FXN)(π-acceptor)] complexes and FXN drug alone into two protein receptors [serotonin (PDB ID: 6A94) and dopamine (PDB ID: 6CM4)].

Ligands	Docking Score (kcal/mol)	
	PDB ID: 6A94	**PDB ID: 6CM4**
FXN-TCNQ	−7.8	−7.4
FXN-*p*NBA	−6.2	−5.9
FXN-DNB	−7.6	−7.1
FXN-DBQ	−8.1	−7.9
FXN-DCQ	−7.8	−7.2
FXN-PA	−9.5	−8.8
FXN	−8.5	−7.9

Table 1 shows [(FXN)(PA)] had the best docking scores out of all the [(FXN)(π-acceptor)] tested. Theoretically, [(FXN)(PA)] and serotonin have a binding energy of −9.5 kcal/mol, while dopamine has −8.8 kcal/mol. Interestingly, the [(FXN)(PA)]–serotonin (CTpS) complex interacts more strongly than dopamine due to its greater binding-energy values.

The interaction data and best docking pose of [(FXN)(PA)]–serotonin and (FXN)–serotonin are displayed in Figure 5 and Table 2.
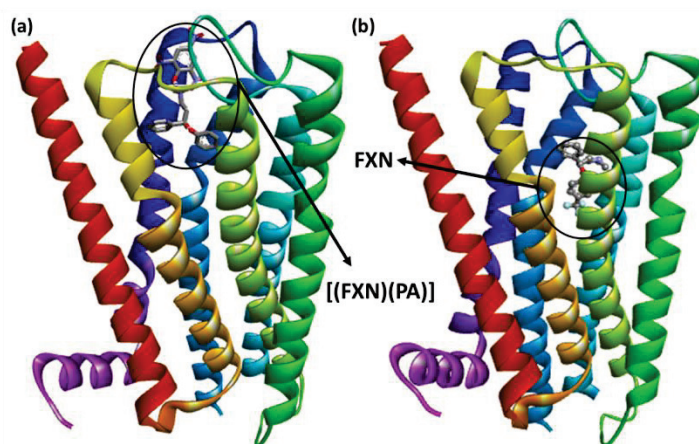
Figure 5. Best-docked pose showing a helical model of (**a**) [(FXN)(PA)]–serotonin; (**b**) (FXN)–serotonin.

Table 2. Interaction data of [(FXN)(PA)]–serotonin and (FXN)–serotonin (PDB ID: 6A94).

Ligands	Docking Score (kcal/mol)	Interactions	
		H-Bond	Others
[(FXN)(PA)]–serotonin	−9.5	Asn363	Val7.38, Leu45.52, Phe6.51(π-Alkyl); Asp3.32(π-Anion)
(FXN)–serotonin	−8.5		Phe5.47, Phe6.44(π-Alkyl); Phe6.52, Trp6.48 (π-Stacked); Asp3.32(π-Anion); Ser5.46, Ser3.36 (Halogen-Fluorine)

The 3D illustrations of the interactions between [(FXN)(PA)]–serotonin or (FXN)–serotonin are presented in Figure 6a,b.
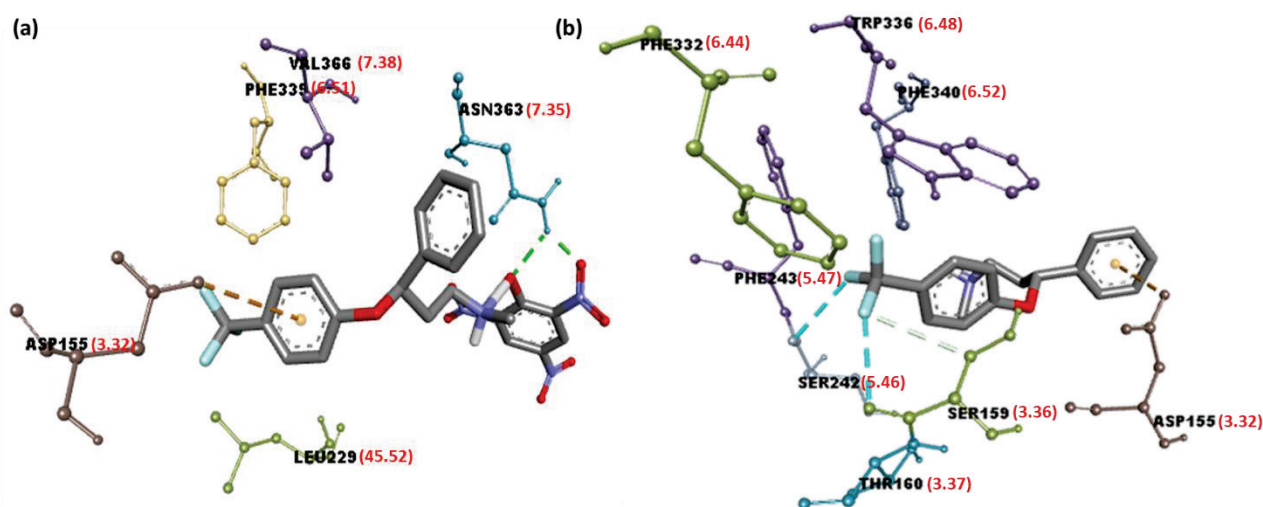
Figure 6. Three-dimensional illustrations of interactions of (**a**) [(FXN)(PA)]–serotonin and (**b**) (FXN)–serotonin, representing Ballesteros–Weinstein nomenclature in red brackets.

As shown in Figure 6a, in the [(FXN)(PA)]–serotonin complex, the amino acid residue Asn363 is responsible for the hydrogen-bond interactions. Additionally, Val366 (7.38;

Ballesteros–Weinstein nomenclature), Leu229 (45.52), Phe339 (6.51) (π-Alkyl), and Asp115 (3.32) (π-Anion) interactions were present (Table 2) [33,34]. Similarly, in the [(FXN)(TCNQ)]–serotonin complex, the amino acid residue Leu80 with halogen–fluorine; and Trp367, Val364, Val84, and Ala360 with π-Alkyl interactions, can be seen. The [(FXN)(pNBA)]–serotonin complex; the amino acid residue Val251 with π-Sigma; Gly326 and Lya323 with halogen–fluorine; and Ile327 and Leu247 with π-Alkyl interactions are also present. Additionally, there are the [(FXN)(DNB)]–serotonin complex, the amino acid residue Ile152 and Asp155 with halogen–fluorine; and Val156, Val366, and Leu229 with π-Alkyl interactions. In the [(FXN)(DBQ)]–serotonin complex, the amino acid residue Asn363 with halogen–fluorine, as well as Leu80 with π-Alkyl interactions, can be seen. The other complexes with lower scores than [(FXN)(PA)] show no hydrogen bonding with serotonin receptors, as shown in Figure S1. FXN has theoretical binding energies of −8.5 and −7.9 kcal/mol when docked with serotonin and dopamine receptors, respectively. Therefore, (FXN)–serotonin (FXNS) has a larger docking score than dopamine, indicating that FXN has a stronger interaction with serotonin. On other hand, Phe243 (5.47), Phe332 (6.44) (π-Alkyl); Phe340 (6.52), Trp336 (6.48) (π-Stacked); Asp155 (3.32) (π-Anion); and Ser242 (5.46), Ser159 (3.36) (halogen–fluorine) interactions can be seen (Table 2). This indicates that [(FXN)(PA)] has the highest docking score value and binds to both receptors more effectively than the reactant donor (FXN) alone. When a substance docks or binds with a receptor, docking scores show how much energy is released. A ligand with a higher docking score, or one that is more negative, might be able to block one with a lower docking score or one that is less negative. Figure 7 displays 2D illustrations of the interactions between the ligand and receptor. Other details (name, distance, category, and type) of the interactions are illustrated in Tables S1 and S2.
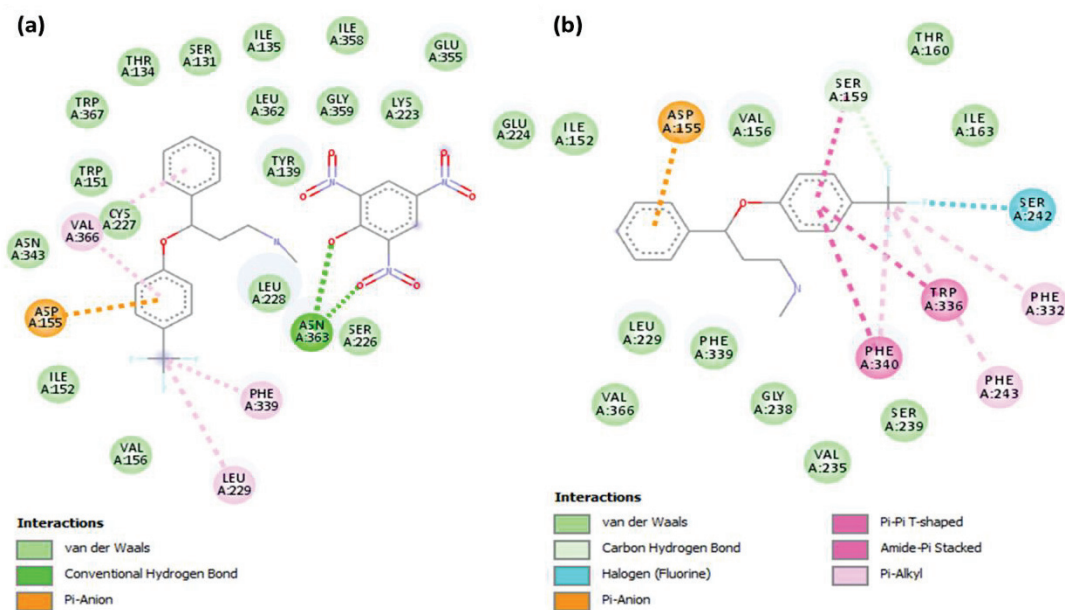
Figure 7. Two-dimensional illustration of interactions of (**a**) [(FXN)(PA)]–serotonin or (**b**) (FXN)–serotonin.

2.3. Hydrogen Bonds, Ionizability, Hydrophobicity, and Aromatic Surfaces

The ligand–receptor complexes were assessed using DiscoveryStudio (DS) software. Mutual interactions were explored, and different surfaces were created around the ligands [35]. Figures 8 and 9 display several molecular docking data at the interaction site of [(FXN)(PA)]–serotonin and (FXN)–serotonin, respectively.
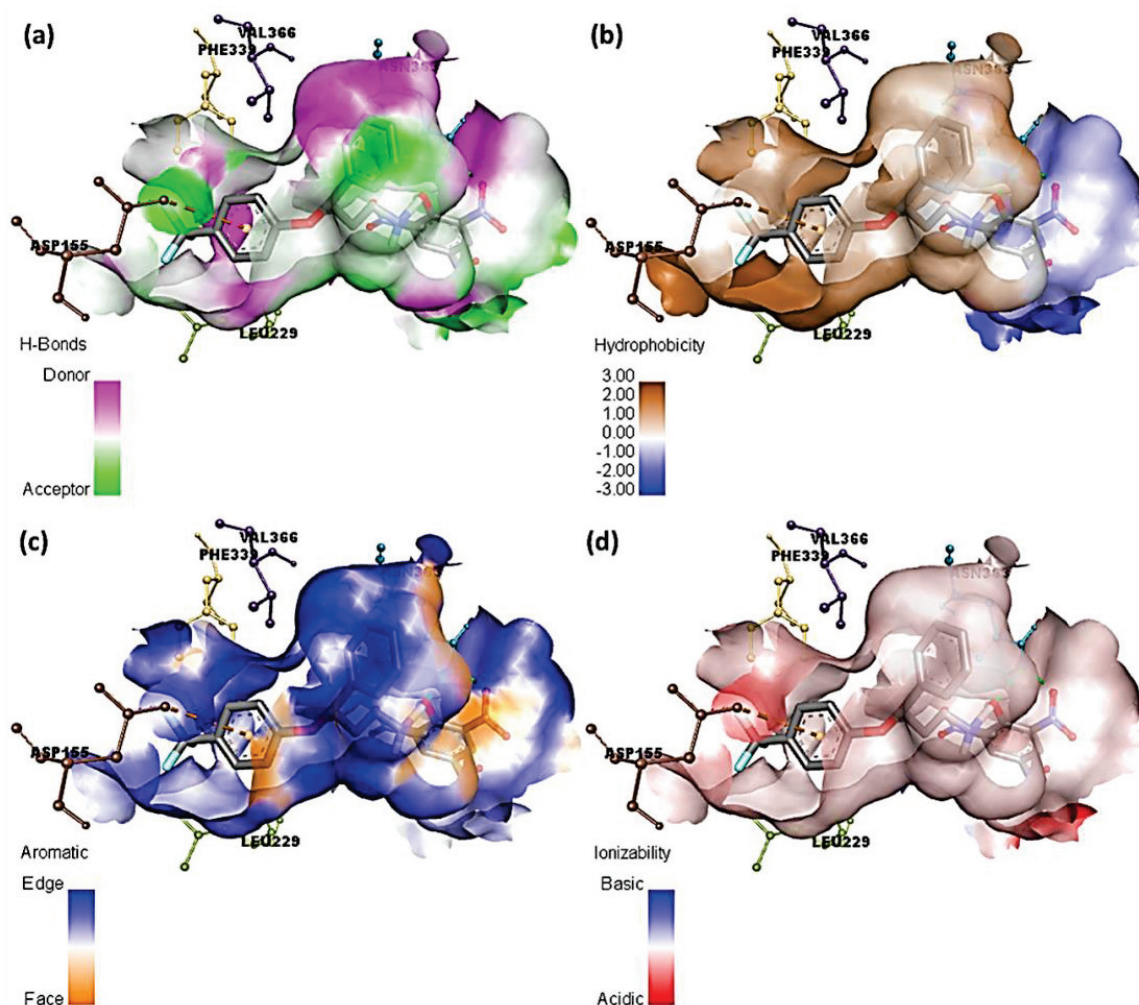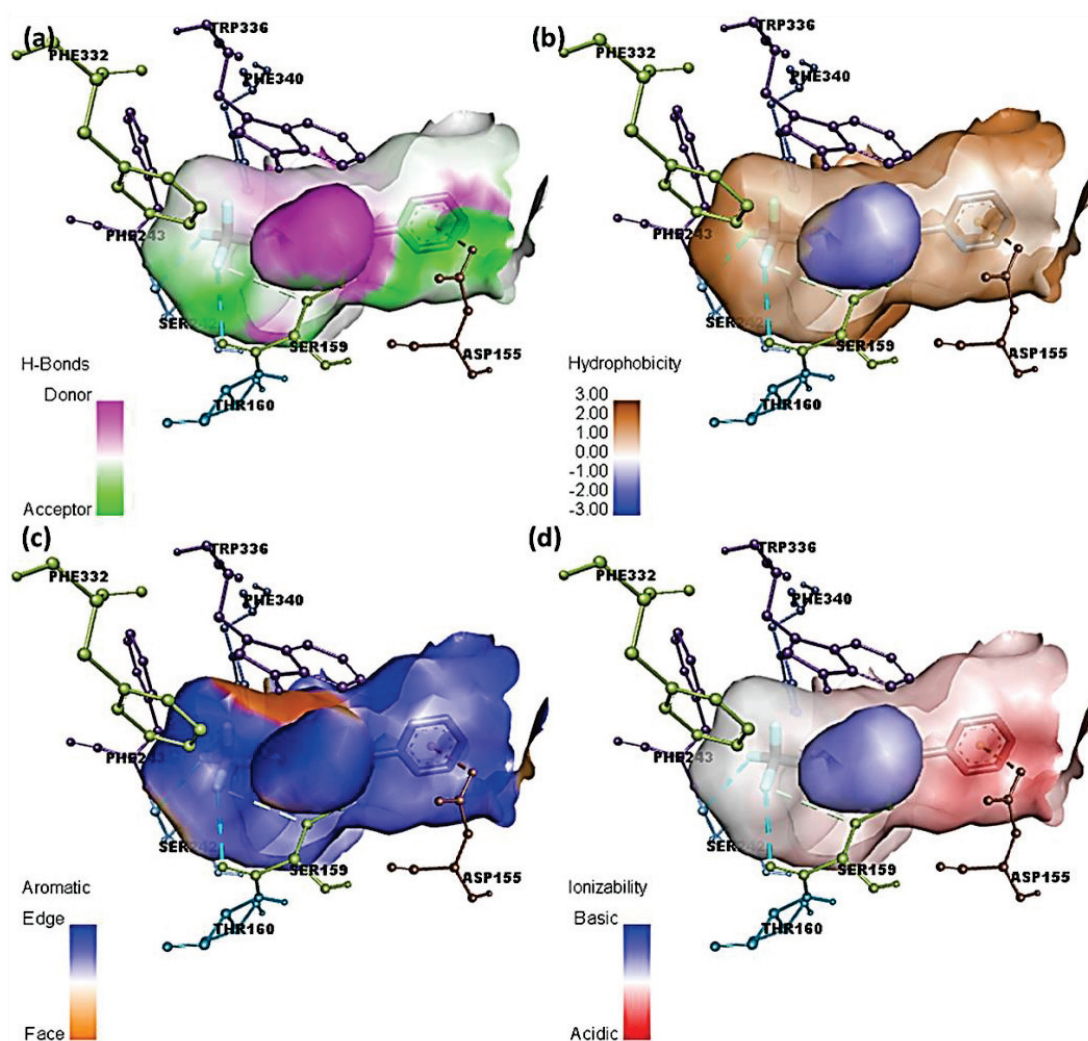
Figure 8. Molecular docking data of [(FXN)(PA)]–serotonin complex; (**a**) bonding surface of hydrogen bonds, (**b**) hydrophobic surfaces, (**c**) aromatic surface, and (**d**) ionizability surface.

Herein, fluorine atoms play a significant role in hydrogen-bond formation. The hydrogen-atom acceptor area is indicated in green, and the donor area is indicated in pink for the amino acid residues at the hydrogen-bond surface in Figure 8a and Figure S1a. The presence of the hydrophilicity features of the receptor around the ligand is confirmed by the hydrophobicity surface (Figure 8b and Figure S1b). Further, the aromatic face/edge surface (Figure 8c and Figure S1c, orange/blue = face/edge) was revealed using the docking outputs. The ionization surface reflected the acidic and basic propensity (Figure 8d and Figure S1d, blue color = basic and red color = acidic) [36].

2.4. MD Simulation and Structural Stability Analysis upon Ligand Binding

The highest docking scores from CTpS and FXNS were used as the starting structures to achieve the MD simulation at a time of 100 ns (Figure 10). The best-docked result was used to investigate the binding process at the receptor's active region in well-defined water environments. MD simulation data were processed for structural stability studies by determining the root mean square deviation (RMSD). As demonstrated in the RMSD graphic, both CTpS and FXNS achieved steady conformation after ~55 ns, with suitable RMSDs of 2.01 Å and 2.21 Å, respectively (Figure 10).

Figure 9. Molecular docking data of (FXN)–serotonin complex; (**a**) bonding surface of hydrogen bonds, (**b**) hydrophobic surfaces, (**c**) aromatic surface, and (**d**) ionizability surface.
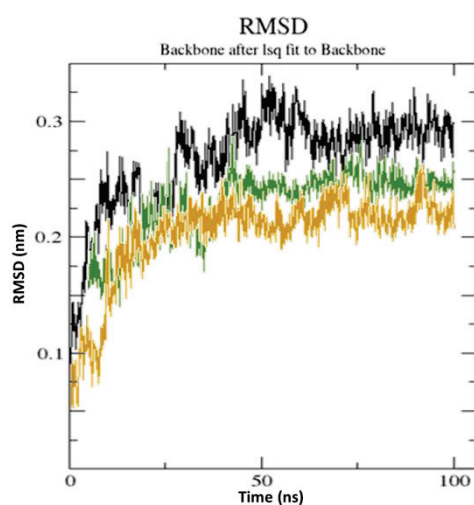
Figure 10. RMSD data of unbound serotonin receptor (black), (FXN)–serotonin (green), and [(FXN)(PA)]–serotonin (brown) at 100 ns.

An RMSD value of <3.0 Å is widely considered to be the most acceptable and implies that the complex is suitably stable [37]. Lower RMSD values for CTpS and FXNS suggest

that the ligand reduces protein flexibility, which blocks a conformational change, indicating that CTpS develops a more stable combination. The results are consistent with the theory that ligand–receptor interactions reduce the distance between protein chains and bring them closer together (Figure 11) [38].
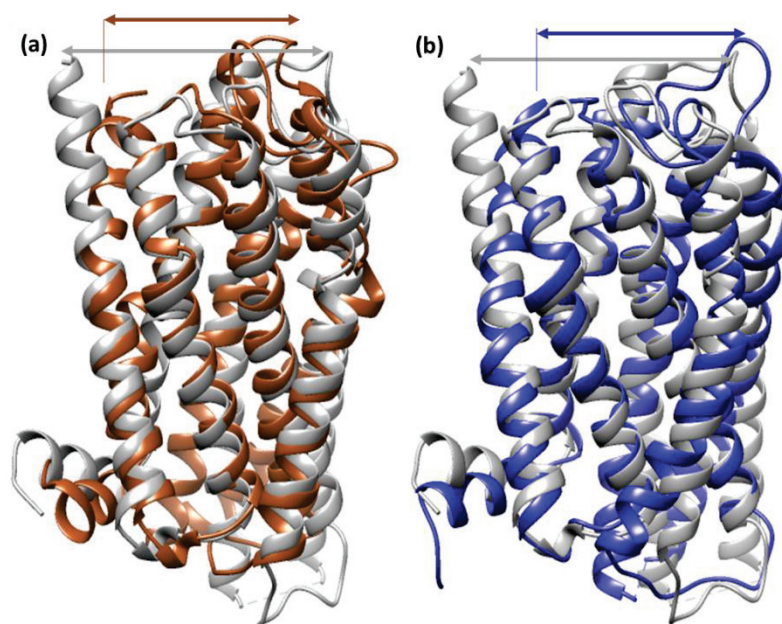
Figure 11. Superimposed simulation structure of (**a**) unbounded serotonin receptor (gray) and [(FXN)(PA)]–serotonin (brown); (**b**) unbounded serotonin receptor (gray) and (FXN)–serotonin (blue).

The standard deviation and average distance between each pair of amino acids for each conformation were displayed using RR distance maps (Figure 12) [39,40].
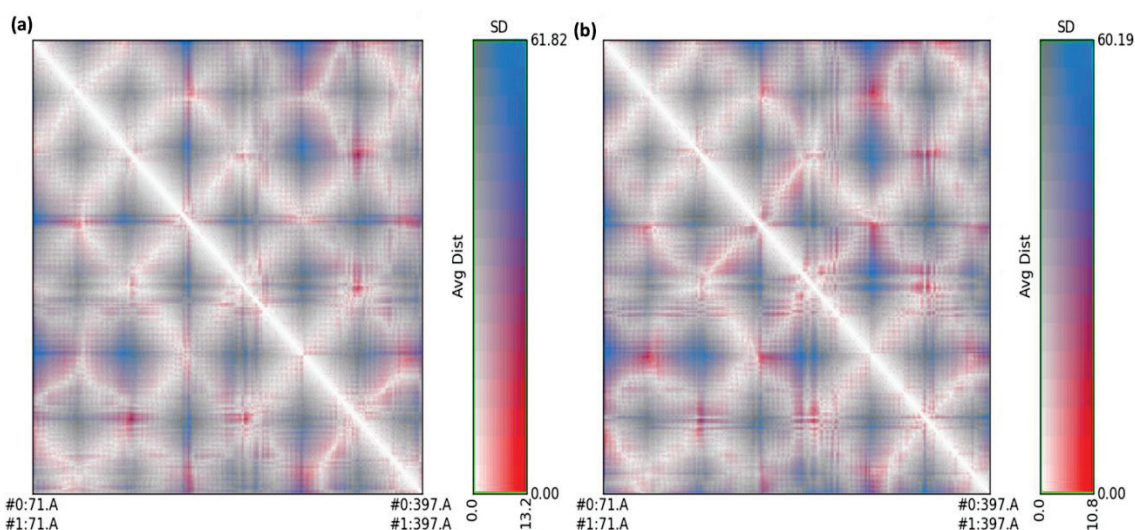
Figure 12. RR distance map between (**a**) unbounded serotonin and [(FXN)(PA)]–serotonin after simulation; (**b**) unbounded serotonin and (FXN)–serotonin after simulation. Average distance and standard deviation were included and calculated for all amino acid pairs.

The red and blue parts depict residue pairings through the highest distance differences between two amino acids, while the white diagonal represents residue pairings with a distance of zero (Figure 12). The radius of gyration (Rg) values for CTpS and FXNS were

25.62 and 26.12, respectively. The Rg for CTpS and FXNS declined during the simulation, indicating that the structures were becoming further compressed (Figure 13).
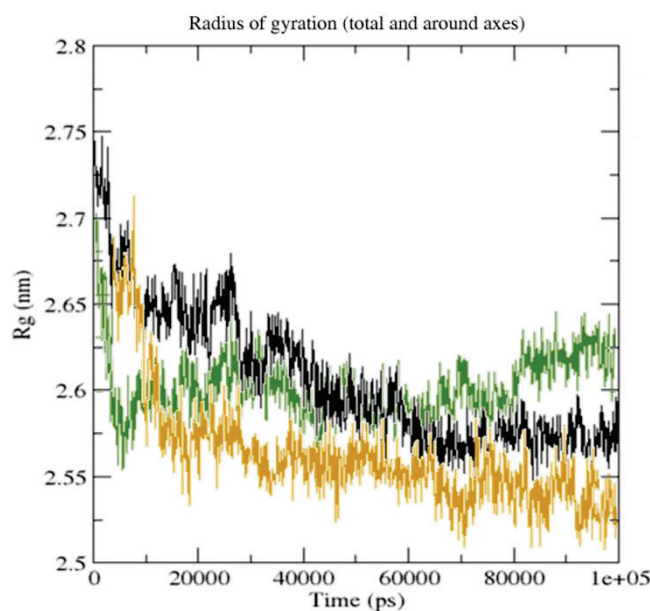
Figure 13. Radius of gyration of unbound serotonin alone (black), FXN–serotonin complex (green), and [(FXN)(PA)]–serotonin complex (brown) during 100 ns simulation.

2.5. Hydrogen-Bond Analysis

The amount of hydrogen-bond interactions that have arisen in ligand–receptor combinations (FXNS and CTpS) were plotted against time using a grid-search at grid = $25 \times 11 \times 14$ and rcut = 0.35 (Figure 14).
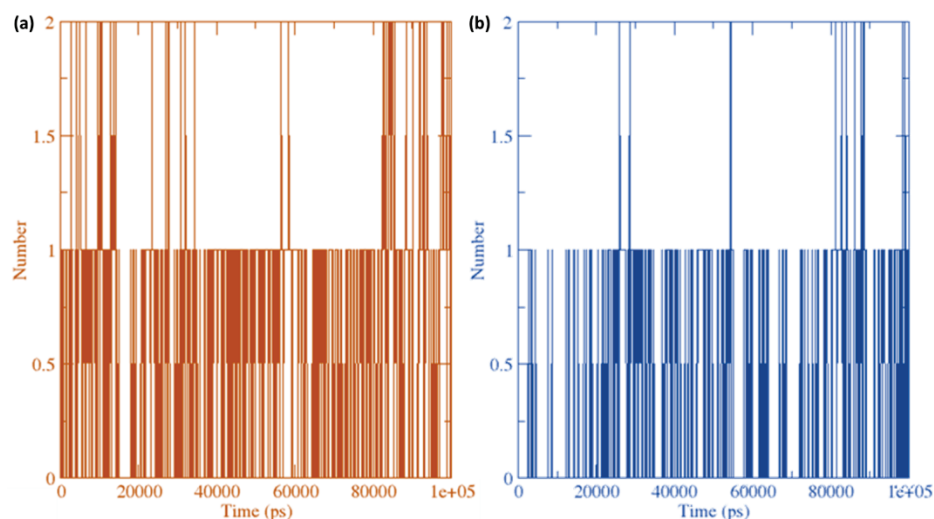
Figure 14. Average hydrogen bonding interactions between (**a**) [(FXN)(PA)]–serotonin and (**b**) (FXN)–serotonin at 100 ns simulation.

The hydrogen bonds between ligands (FXN) or [(FXN)(PA)] with serotonin receptors were calculated (Figure 14). The average number of H-bonds per timeframe was 0.656 of 252,486 for FXN–serotonin complex and was 0.216 of 252,466 for [(FXN)(PA)]–serotonin complex. Overall, the receptor–ligand interaction was found to markedly enhance the H-bonds, with more bonds in [(FXN)(PA)]–serotonin than FXN–serotonin.

2.6. Solvent Accessibility Surface Area Analysis

The solvent accessibility surface area (SASA) was found to change because of the binding of ligand to receptor (Figure 15).
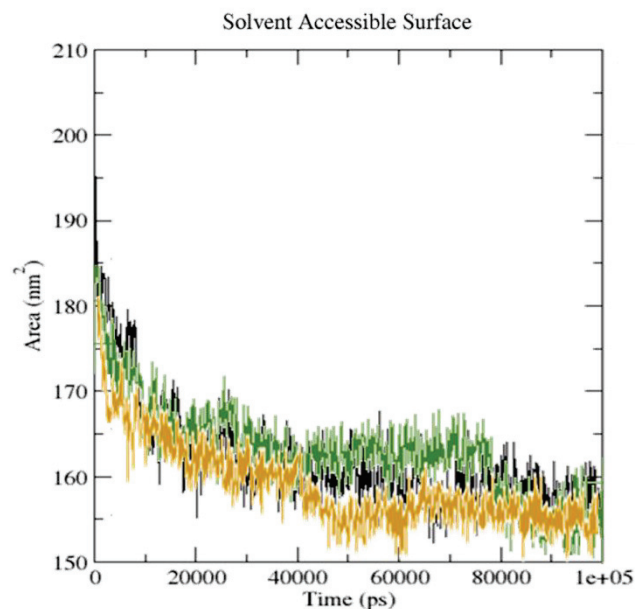
Figure 15. SASA analysis for unbound serotonin (black), [(FXN)(PA)]–serotonin (brown), and FXN–serotonin (green) during the 100 ns MD simulation.

A reduced SASA value for the serotonin upon binding to [(FXN)(PA)] suggests an adjustment in the configuration of the protein structure and a decrease in pocket size, with increased hydrophobicity around it [41].

2.7. DFT Studies

The CT complexes [(FXN)(PA)], [(FXN)(DCQ)], [(FXN)(DBQ)], [(FXN)(DNB)], [(FXN)(pNBA)], and [(FXN)(TCNQ)] were optimized using the B3LYP/6-311G++ level theory, and their binding energies were calculated and obtained as -637.49, -18.38, -25.01, -104.91, -87.31, and -332.74 kcal/mol, respectively.

The optimized geometry of CT complexes [(FXN)(PA)], [(FXN)(DCQ)], [(FXN)(DBQ)], [(FXN)(DNB)], [(FXN)(pNBA)], and [(FXN)(TCNQ)] with Mulliken at-atomic coordinates and strain-free lattice constants is presented in Figure S1. The obtained bond lengths from the optimized structure of [(FXN)(PA)] are shown in Figure S2. Bond angles and lengths are presented in Tables S3 and S4. Mulliken charges of the complex were also obtained and are provided in Table S5. The strength of the electrostatic potentials of [(FXN)(PA)] is depicted in molecular electrostatic potential (MEP) surface map (Figure 16).
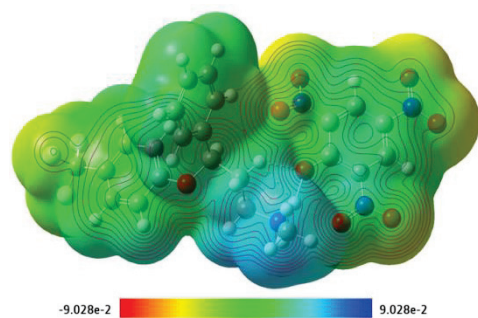
Figure 16. Molecular electrostatic potential surface map of [(FXN)(PA)] complex with respective color scales.

Blue represents the electropositive region, while red represents electronegative areas. These findings point to the molecule's preferred binding sites for electrophilic and nucleophilic charges [42]. The MEP surface is mapped with the color scale from deep red (-9.028×10^{-2}) to deep blue ($+9.028 \times 10^{-2}$) (Figure 16) [43].

TD-DFT was used to examine the nature of electronic transitions in water. The TD-DFT yielded two electronic absorption bands at 436 and 451 nm. HOMO $\rightarrow$ LUMO and HOMO-1 $\rightarrow$ LUMO were allocated at 451 and 436 nm, respectively. The electron acceptors were mainly LUMO and electron donors were HOMO, as observed in the FXN moiety of the CT complex [(FXN)(PA)]. Figure 17 represents the HOMO and LUMO spatial arrangements and their gaps and associated energies.
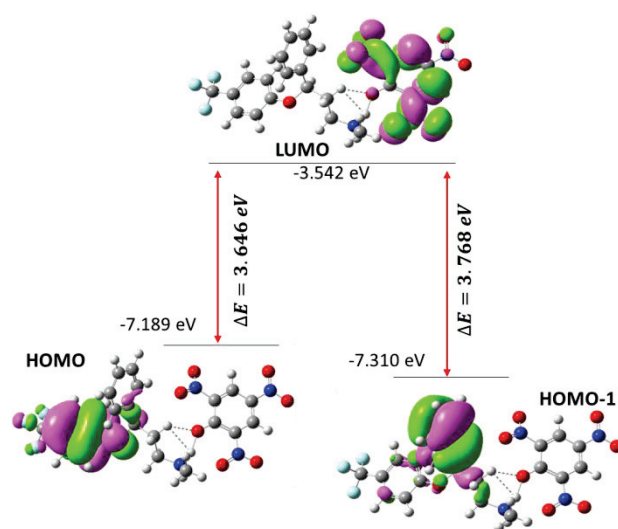
Figure 17. The energy gaps and spatial plot of HOMO and LUMO.

The molecular orbital energy level diagram of the CT complex [(FXN)(PA)] is presented in Figure 18.
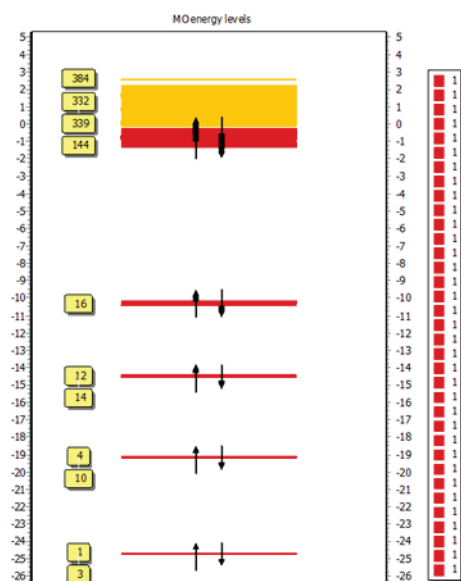
Figure 18. MO energy-level diagram of the CT complex [(FXN)(PA)].

The HOMO–LUMO and HOMO-1–LUMO gaps (ΔE) for [(FXN)(PA)] were 3.646 and 3.768 eV, respectively [44]. Based on these DFT results, some theoretical molecular parameters related to chemical reactivity in water as solvent are presented in Table 3 [45,46].

Table 3. Theoretical molecular characteristics and components of CT complex [(FXN)(PA)].

Parameters.	RB3LYP/6-311G++
Minimum SCF energy (a.u.)	−2008.551032
Polarizability (α) (a.u.)	302.014352
Dipole Moment (Debye)	9.730154
Zero-point vibrational energy (kcal/mol)	248.24365
Total thermal energy (kcal/mol)	251.492
Electronic spatial extent (a.u.)	29,874.6801
Frontier MO energies (eV)	
LUMO	−3.542
HOMO	−7.189
HOMO-1	−7.310
Gap (LUMO–HOMO)	3.646
Gap (LUMO–HOMO-1)	3.768

DFT calculations were employed to explain the stability of the CT complex [(FXN)(PA)] (Figure 19). To study the effect of the aromatic residues (indole, tyrosine, and tryptophan) of the protein on the CT complex [(FXN)(PA)], the HOMO LUMO energy and band gap were calculated for indole, tyrosine, tryptophan, FXN, PA, and [(FXN)(PA)] (Figure 19). The energy difference between HOMO and LUMO has an impact on how chemically stable molecules are. As previously reported, ligands with a smaller band gap are soft in nature, have low kinetic stability, and higher chemical reactivity [47]. The opposite is true for ligands with a wide energy gap, which are harder by nature, more unstable, and more chemically reactive [45,47]. The band gap energy of [(FXN)(PA)] is calculated as 3.646 eV, which is the smallest among all of the complexes, suggesting higher stability. On the other hand, the obtained energy of LUMO = −4.494 eV and HOMO = −8.524 eV for PA, and LUMO = −3.746 eV and HOMO = −7.849 eV for FXN (Table 4), validates the easy transfer of electrons from HOMO of FXN to LUMO of PA, and results in the formation of a stable CT complex with a smaller band gap [(FXN)(PA)]. Furthermore, the calculated LUMO energies of the aromatic residues (indole, tyrosine, and tryptophan) of the protein were not in the sequence (close enough) to dissociate the charge transfer bond between FXN and PA, ensuring the stability of the [(FXN)(PA)] complex [42,44,48,49].
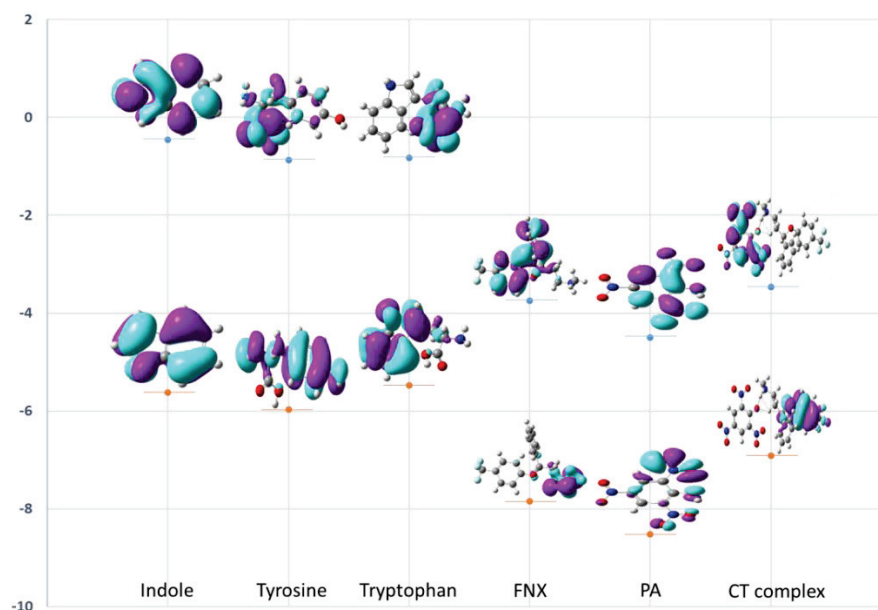
Figure 19. HOMO and LUMO energy levels of the molecular orbitals for indole, tyrosine, tryptophan, FXN, PA, and [(FXN)(PA)].

Table 4. HOMO and LUMO energies calculated for tyrosine, tryptophan, FXN, PA, and [(FXN)(PA)] at B3LYP/6-311G++ levels of theory.

	Indole	**Tyrosine**	**Tryptophan**	**FXN**	**PA**	**[(FXN)(PA)]**
LUMO (eV)	−0.456	−0.872	−0.827	−3.746	−4.494	−3.542
HOMO (eV)	−5.617	−5.974	−5.451	−7.847	−8.524	−7.189
Band gap (eV)	5.160	5.102	4.653	4.101	4.029	3.646

3. Materials and Methods

3.1. Preface

We purchased all chemicals from Aldrich and Fluka Chemicals. We utilized FXN drug and the six π-acceptors without additional purification: picric acid (PA); p-nitro benzoic acid (p-NBA); 2,6-dichloroquinone-4-chloroimide (DCQ); 2,6-dibromoquinone-4-chloroimide (DBQ); dinitrobenzene (DNB); and 7,7′,8,8′-tetracyanoquinodimethan (TCNQ) (Figure 20).
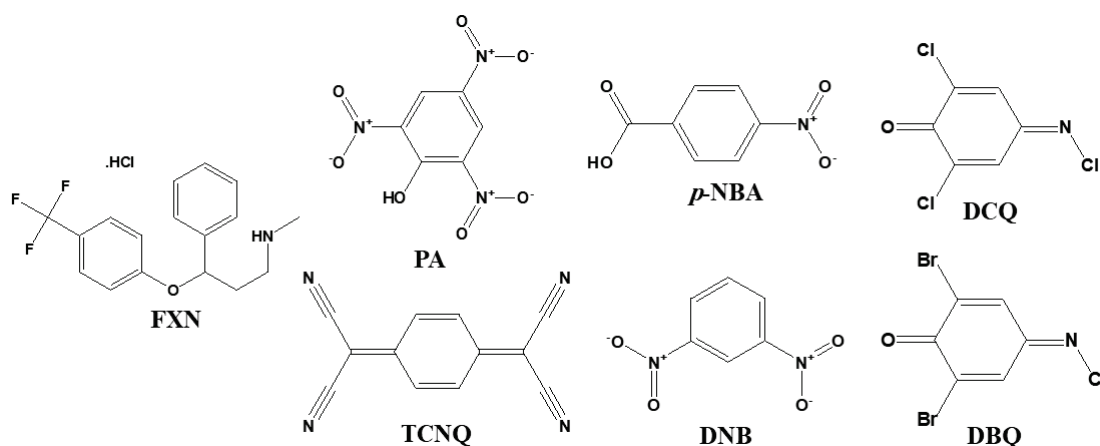
Figure 20. Structures of fluoxetin HCl (FXN) and six π-acceptors.

In order to make the solid CT complexes, we mixed 0.309 gm (1 mmol) fluoxetin hydrochloride with 1 mmol of each π-acceptor in 20 mL of chloroform solvent [50].

At room temperature, we mixed all of the combinations for 1 h. We used filtering to remove the solid products, subsequently washed the sample with minimal volumes of chloroform, then dehydrated under vacuum with CaCl$_2$.

3.2. Molecular Docking

We used OpenBabelIGUI software version 2.4.1 [51] to obtain the structure of FXN and the six CT complexes in PDBQT format. We used MMFF94 force field and conjugate gradient optimization algorithm to diminish the energy of the structures [52]. We used the conjugate gradient optimization algorithm using PyRx-Python prescription 0.8 for 500 steps. We employed the RCSB protein data repository to obtain the 3D crystal structures of serotonin 5-HT2A (PDB ID: 6A94) and dopamine (PDB ID: 6CM4) [53]. To add polar hydrogen atoms to the receptors and determine their Kollman charges, we utilized the Autodock Tool [54]. To assign partial charges, we employed the Geistenger approach. We used Autodock Vina to carry out the docking calculations [55]. We used a grid of 54 × 40 × 42 and center x = 13.562, center y = 0.255, center z = 61.097 with an exhaustiveness value of 8. We selected the docked positions on the basis of good docking scores and examined the interactions using DS Visualizer.

3.3. MD Simulation Study

We accomplished the MD simulation using the best-docked complexes of the receptor and ligand with a high docking score for FXN alone and [(FXN)(PA)]. We attained the topologies and parameters of the ligands by CGenFF with CHARMM-GUI [56,57]. We used online server CHARMM-gui to insert the DPPC (dipalmitoylphosphatidylcholine) membrane. We added lower- and upper leaflet with 72 DPPC molecules. We used SPC water models that extended 10 Å from the receptor to examine the receptor–ligand configurations in a rectangular box [58]. We administered 52 K^+ and 57 Cl^- ions (0.15 M salt) to neutralize the systems and reproduce physiological salt concentrations (Figure 21). In the NPT/NVT equilibration run, we subjected both systems to periodic boundary conditions at constant temperature (300 K) and pressure (1.0 bar) using Leap-frog MD integrator for 100 ns simulation time [59].
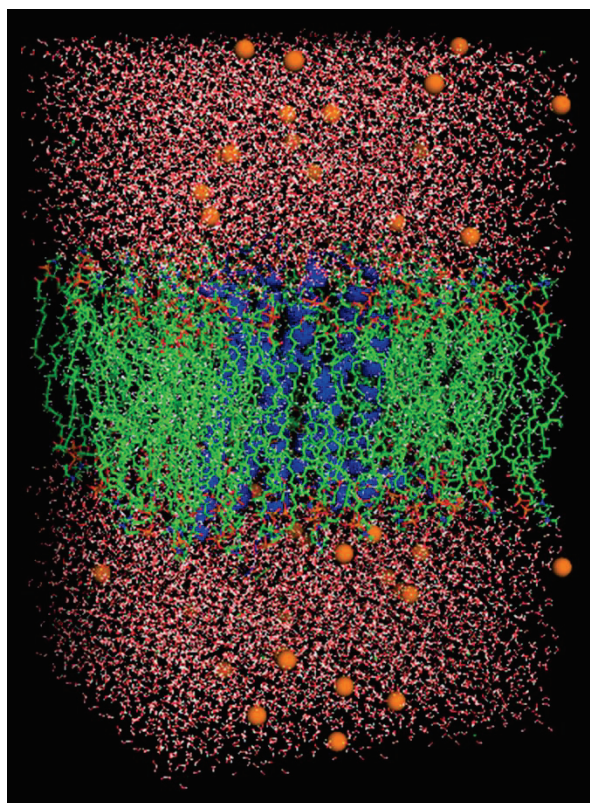
Figure 21. Lateral view of [(FXN)(PA)] complex incorporated in dipalmitoylphosphatidylcholine (DPPC) membrane in rectangular box solvated with water molecules and neutralized with 52 K^+ and 57 Cl^- ions (0.15 M salt).

To remove inappropriate links inside the system, we reduced energy using the steepest descent approach with 5000 steps [60]. We employed the GROMACS program to accomplish the trajectory investigation [61].

We assessed the root mean square deviation by gmx rms tool. We studied hydrogen bonding by Gmxhbond instrument. We used the gmx gyrate and gmxsasa tools to calculate the gyration radius and solvent-accessible surface area. We created plots with Grace Software and created pictures with Polo/VMD [62,63].

3.4. Density Functional Theory

We performed DFT analysis by Gaussian 09RevD.01 package [64]. We used the calculations to obtain a stable molecular geometry and study the electronic transitions in the CT complex [(FXN)(PA)] from a theoretical perspective. Furthermore, we applied B3LYP/6-311G++ basic to obtain the optimized structure of the CT complexes [65]. Then,

we assessed the electrostatic potential map (MEP), LUMO, and HOMO spatial plots of the [(FXN)(PA)] complex [66]. The system's chemical stability is partly determined by the boundary molecular orbitals. We also investigated several structure-based molecular properties. We also used this theory to calculate structure-based molecular parameters, such as bond lengths, angles, atomic charges, total energy, electronic properties, and protein stability. We used ChemCraft 1.5 software for visualization [67].

4. Conclusions

We evaluated the 1:1 complexes of FXN with six π-acceptor complexes in both solid and liquid phases. Several spectroscopic analyses were used to characterize the isolated complexes. Additionally, molecular docking demonstrated that [(FXN)(PA)] has the maximum immunomolecular docking score towards the serotonin [5-HT2A (PDB ID: 6A94)] receptor, and was more effective than the FXN reactant donor alone. It was also found that at 100 ns MD simulation, [(FXN)(PA)]–serotonin was more stable than (FXN)–serotonin. Furthermore, the theoretical data from the DFT calculations helped to explore the molecular geometry of the CT complexes along with their important physical parameters. The stability of the CT complex [(FXN)(PA)] was also studied by DFT calculations.

References

1. Smith, K. Mental health: A world of depression. *Nature* **2014**, *515*, 181. [CrossRef]
2. Vos, T.; Lim, S.S.; Abbafati, C.; Abbas, K.M.; Abbasi, M.; Abbasifard, M.; Bhutta, Z.A.; Ziapour, A.; Zimsen, S.R.M.; Naghavi, M.; et al. Global burden of 369 diseases and injuries in 204 countries and territories, 1990–2019: A systematic analysis for the Global Burden of Disease Study 2019. *Lancet* **2020**, *396*, 1204–1222. [CrossRef]
3. Vos, T.; Allen, C.; Arora, M.; Barber, R.M.; Bhutta, Z.A.; Brown, A.; Liang, X.; Kawashima, T.; Coggeshall, M.; Zhu, J.; et al. Global, regional, and national incidence, prevalence, and years lived with disability for 301 acute and chronic diseases and injuries in 188 countries, 1990–2013: Asystematic analysis for the Global Burden of Disease Study 2013. *Lancet* **2015**, *386*, 743–800. [CrossRef]
4. Whooley, M.A.; Wong, J.M. Depression and cardiovascular disorders. *Annu. Rev. Clin. Psychol.* **2013**, *9*, 327–354. [CrossRef] [PubMed]
5. World Health Organization. Suicide. WHO. Available online: http://www.who.int/topics/suicide/en/ (accessed on 1 March 2022).

6. Chesney, E.; Goodwin, G.M.; Fazel, S. Risks of allcause and suicide mortality in mental disorders: Ameta-review. *World Psychiatry* **2014**, *13*, 153–160. [CrossRef]

7. Wong, D.T.; Horng, J.S.; Bymaster, F.P.; Hauser, K.L.; Molloy, B.B. A selective inhibitor of serotonin uptake: Lilly 110140, 3-(p-trifluoromethylphenoxy)-N-methyl-3- phenylpropylamine. *Life Sci.* **1974**, *15*, 471–479. [CrossRef]

8. Bauer, M.; Monz, B.U.; Montejo, A.L.; Quail, D.; Dantchev, N.; Demyttenaere, K.; GarciaCebrian, A.; Grassi, L.; Perahia, D.G.S.; Reed, C.; et al. Prescribing patterns of antidepressants in europe: Results from the Factors Influencing Depression Endpoints Research (FINDER) study. *Eur. Psychiatry* **2008**, *23*, 66–73. [CrossRef]

9. National Institute for Health and Care Excellence, NICE. *Depression in Children and Young People: Identification and Management NICE Guideline [NG134]*; NICE: London, UK, 2019.

10. Korolkovas, A. *Essentials of Medical Chem*, 2nd ed.; Wiley: New York, NY, USA, 1998; Chapter 3.

11. Slifkin, A.M. *Charge-Transfer Interaction of Biomolecules*; Academic Press: New York, NY, USA, 1971.

12. Abou Attia, F.M. Use of charge-transfer complex formation for the spectrophotometric determination of nortriptyline. *Farmaco* **2000**, *55*, 659. [CrossRef]

13. Basavaiah, K. Determination of some psychotropic phenothiazine drugs by charge-transfer complexation reaction with chloranilic acid. *Farmaco* **2004**, *59*, 315. [CrossRef]

14. Liu, H.; Liu, Z.; Jiang, W.; Fu, H. Tuning the charge transfer properties by optimized donor–acceptor cocrystal for FET applications: From P type to N type. *J. Solid State Chem.* **2019**, *274*, 47–51. [CrossRef]

15. Murugesan, V.; Saravanabhavan, M.; Sekar, M. Synthesis, spectral, structural analysis and biological evaluation of a new hydrogen-bonded charge-transfer complex: 2,3-dimethylquinoxalinium-p-toluenesulfonate. *J. Photochem. Photobiol. B* **2014**, *140*, 20–27. [CrossRef] [PubMed]

16. Singh, N.; Khan, I.M.; Ahmad, A.; Javed, S. Preparation, spectral investigation and spectrophotometric studies of proton transfer complex of 2,2′-bipyridine with 3,5-dinitrobenzoic acid in various polar solvents. *J. Mol. Struct.* **2014**, *1065–1066*, 74–85. [CrossRef]

17. Darwish, I.A.; Wani, T.A.; Khalil, N.Y.; Abdel-Rahman, H.M. High throughput microwell spectrophotometric assay for olmesartanmedoxomil in tablets based on its charge-transfer reaction with DDQ. *Acta Pharm.* **2014**, *64*, 63–75. [CrossRef] [PubMed]

18. Khalil, N.Y.; Wani, T.A.; Darwish, I.A.; Assiri, I. Charge-transfer reaction of cediranib with 2,3-dichloro-3,5-dicyano-1,4-benzoquinone: Spectrophotometric investigation and use in development of microwell assay for cediranib. *Trop. J. Pharm. Res.* **2015**, *14*, 1667–1672.17. [CrossRef]

19. Refat, M.S.; Ibrahim, O.B.; Saad, H.A.; Adam, A.M.A. Usefulness of charge–transfer complexation for the assessment of sympathomimetic drugs: Spectroscopic properties of drug ephedrine hydrochloride complexed with some π-acceptors. *J. Mol. Struct.* **2014**, *1064*, 58–69. [CrossRef]

20. Eldaroti, H.H.; Gadir, S.A.; Refat, M.S.; Adam, A.M.A. Charge-transfer interaction of drug quinidine with quinol, picric acid and DDQ: Spectroscopic characterization and biological activity studies towards understanding the drug–receptor mechanism. *J. Pharm. Anal.* **2014**, *4*, 81–95. [CrossRef]

21. El-Habeeb, A.A.; Al-Saif, F.A.; Refat, M.S. Charge-transfer interactions of metoclopramide nausea drug against six kind of π-acceptors: Spectral and thermal discussions. *Spectrochim. Acta Part A* **2014**, *123*, 455–466. [CrossRef]

22. Elqudaby, H.M.; Mohamed, G.G.; El-Din, G.M.G. Analytical studies on the charge transfer complexes of loperamide hydrochloride and trimebutine drugs. Spectroscopic and thermal characterization of CT complexes. *Spectrochim. Acta Part A* **2014**, *129*, 84–95. [CrossRef]

23. Eldaroti, H.H.; Gadir, S.A.; Refat, M.S.; Adam, A.M.A. Spectroscopic investigations of the charge-transfer interaction between the drug reserpine and different acceptors: Towards understanding of drug–receptor mechanism. *Spectrochim. Acta Part A* **2013**, *115*, 309–323. [CrossRef]

24. El-Habeeb, A.A.; Al-Saif, F.A.; Refat, M.S. Spectroscopic and thermal investigations on the charge transfer interaction between risperidone as a schizophrenia drug with some traditional π-acceptors: Part 2. *J. Mol. Struct.* **2013**, *1036*, 464–477. [CrossRef]

25. El-Habeeb, A.A.; Refat, M.S. Charge transfer complexes beneficial method for determination of fluoxetine HCl pure drug: Spectroscopic and thermal analyses discussions. *Russ. J. Gen. Chem.* **2014**, *84*, 1810–1818. [CrossRef]

26. Alhomrani, M.; Alsanie, W.F.; Alamri, A.S.; Alyami, H.; Habeeballah, H.; Alkhatabi, H.A.; Felimban, R.I.; Haynes, J.M.; Shakya, S.; Raafat, B.M.; et al. Enhancing theAntipsychotic Effect of Risperidoneby Increasing Its Binding Affinity toSerotonin Receptor via Picric Acid: A Molecular Dynamics Simulation. *Pharmaceuticals* **2022**, *15*, 285. [CrossRef] [PubMed]

27. Alsanie, W.F.; Alamri, A.S.; Alyami, H.; Alhomrani, M.; Shakya, S.; Habeeballah, H.; Alkhatabi, H.A.; Felimban, R.I.; Alzahrani, A.S.; Alhabeeb, A.A.; et al. Increasing the Efficacy of Seproxetine as an Antidepressant Using Charge-Transfer Complexes. *Molecules* **2022**, *27*, 3290. [CrossRef] [PubMed]

28. Alamri, A.S.; Alhomrani, M.; Alsanie, W.F.; Alyami, H.; Shakya, S.; Habeeballah, H.; Alamri, A.; Alzahrani, O.; Alzahrani, A.S.; Alkhatabi, H.A.; et al. Enhancement of Haloperidol Binding Affinity to Dopamine Receptor via Forming a Charge-Transfer Complex with Picric Acid and 7,7,8,8-Tetracyanoquinodimethane for Improvement of the Antipsychotic Efficacy. *Molecules* **2022**, *27*, 3295. [CrossRef]

29. Darwish, I.A.; Khalil, N.Y.; Alsaif, N.A.; Herqash, R.N.; Sayed, A.Y.A.; Abdel-Rahman, H.M. Charge-Transfer Complex of Linifanib with 2,3-dichloro-3,5-dicyano-1,4-benzoquinone: Synthesis, Spectroscopic Characterization, Computational Molecular Modelling and Application in the Development of Novel 96-microwell Spectrophotometric Assay. *Drug Des. Dev. Ther.* **2021**, *15*, 1167–1180. [CrossRef]

30. He, S.; Wu, L.; Li, X.; Sun, H.; Xiong, T.; Liu, J.; Huang, C.; Xu, H.; Sun, H.; Chen, W.; et al. Metal-organic frameworks for advanced drug delivery. *Acta Pharm. Sin. B* **2021**, *11*, 2362–2395. [CrossRef]

31. Bellamy, L.J. *The Infrared Spectra of Complex Molecules*; Chapman & Hall: London, UK, 1975.

32. Foster, R. *Organic Charge-Transfer Complexes*; Academic Press: New York, NY, USA, 1969.

33. Akram, M.; Lal, H.; Shakya, S.; Din, K.U. Multispectroscopic and Computational Analysis Insight into the Interaction of Cationic Diester-Bonded Gemini Surfactants with Serine Protease α-Chymotrypsin. *ACS Omega* **2020**, *5*, 3624–3637. [CrossRef]

34. Khan, I.M.; Shakya, S.; Islam, M.; Khan, S.; Najnin, H. Synthesis and spectrophotometric studies of CT complex between 1, 2-dimethylimidazole and picric acid in different polar solvents: Exploring antimicrobial activities and molecular (DNA) docking. *Phys. Chem. Liq.* **2021**, *59*, 753–769. [CrossRef]

35. Krivák, R.; Jendele, L.; Hoksza, D. Peptide-Binding Site Prediction from Protein Structure via points on the Solvent Accessible Surface. In Proceedings of the 2018 ACM International Conference on Bioinformatics, Computational Biology, and Health Informatics, Washington, DC, USA, 29 August–1 September 2018. [CrossRef]

36. Ranjbar, A.; Jamshidi, M.; Torabi, S. Molecular modelling of the antiviral action of Resveratrol derivatives against the activity of two novel SARS CoV-2 and 2019-nCoV receptors. *Eur. Rev. Med. Pharm. Sci.* **2020**, *24*, 7834. [CrossRef]

37. Kufareva, I.; Abagyan, R. Methods of protein structure comparison. *Methods Mol. Biol.* **2012**, *857*, 231–257.

38. Wu, S.; Zhang, Y. A comprehensive assessment of sequence-based and template-based methods for protein contact prediction. *Bioinformatics* **2008**, *24*, 924–931. [CrossRef] [PubMed]

39. Marks, D.S.; Colwell, L.J.; Sheridan, R.; Hopf, T.A.; Pagnani, A.; Zecchina, R.; Sander, C. Protein 3D structure computed from evolutionary sequence variation. *PLoS ONE* **2011**, *6*, e28766. [CrossRef] [PubMed]

40. Kavitha, R.; Nirmala, S.; Nithyabalaji, R.; Sribalan, R. Biological evaluation, molecular docking and DFT studies of charge transfer complexes of quinaldic acid with heterocyclic carboxylic acid. *J. Mol. Struct.* **2020**, *1204*, 127508. [CrossRef]

41. Akram, M.; Lal, H.; Shakya, S.; Varshney, R. Molecular engineering of complexation between RNA and biodegradable cationic gemini surfactants: Role of the hydrophobic chain length. *Mol. Syst. Des. Eng.* **2022**, *7*, 487–506. [CrossRef]

42. Shakya, S.; Khan, I.M.; Ahmad, M. Charge transfer complex based real-time colorimetric chemosensor for rapid recognition of dinitrobenzene and discriminative detection of Fe_2^+ ions in aqueous media and human hemoglobin. *J. Photochem. Photobiol. A Chem.* **2020**, *392*, 112402. [CrossRef]

43. Islam, M.R.; Shakya, S.; Selim, A.; Alam, M.S.; Ali, M. Solvatochromic Absorbance and Fluorescence Probe Behavior within Ionic Liquid+ γ-Butyrolactone Mixture. *J. Chem. Eng. Data* **2019**, *64*, 4169–4180. [CrossRef]

44. Khan, I.M.; Shakya, S. Exploring Colorimetric Real-Time Sensing Behavior of a Newly Designed CT Complex toward Nitrobenzene and Co2+: Spectrophotometric, DFT/TD-DFT, and Mechanistic Insights. *ACS Omega* **2019**, *4*, 9983–9995. [CrossRef]

45. Refat, M.S.; Saad, H.A.; Gobouri, A.A.; Alsawat, M.; Adam, A.M.A.; Shakya, S.; Gaber, A.; Alsuhaibani, A.M. El-Megharbel, S.M. Synthesis and spectroscopic characterizations of nanostructured charge transfer complexes associated between moxifloxacin drug donor and metal chloride acceptors as a catalytic agent in a recycling of wastewater. *J. Mol. Liq.* **2022**, *349*, 118121. [CrossRef]

46. Flores-Holguín, N.; Frau, J.; Glossman-Mitnik, D. Virtual Prospection of Marine Cyclopeptides as Therapeutics by Means of Conceptual DFT and Computational ADMET. *Pharmaceuticals* **2022**, *15*, 509. [CrossRef]

47. Murugavel, S.; Ravikumar, C.; Jaabil, G.; Alagusundaram, P. Synthesis, crystal structure analysis, spectral investigations (NMR, FT-IR, UV), DFT calculations, ADMET studies, molecular docking and anticancer activity of 2-(1-benzyl-5-methyl-1H-1,2,3-triazol-4-yl)-4-(2-chlorophenyl)-6-methoxypyridine–a novel potent human topoisomerase IIα inhibitor. *J. Mol. Struct.* **2019**, *1176*, 729–742.

48. Khan, M.S.; Khalid, M.; Ahmad, M.S.; Shahid, M.; Ahmad, M. Three-in-one is really better: Exploring the sensing and adsorption properties in a newly designed metal–organic system incorporating a copper (II) ion. *Dalton Trans.* **2019**, *48*, 12918–12932. [CrossRef] [PubMed]

49. Shakya, S.; Khan, I.M. Charge transfer complexes: Emerging and promising colorimetric real-time chemosensors for hazardous materials. *J. Hazard. Mater.* **2021**, *403*, 123537. [CrossRef] [PubMed]

50. El-Habeeb, A.A.; Refat, M.S. Synthesis and spectroscopic characterizations of n–π* ion radical and π–π* transitions in situ charge transfer complexes between trazodone hydrochloride and different type of π–acceptors. *Russ. J Gen. Chem.* **2015**, *85*, 951–958. [CrossRef]

51. O'Boyle, N.M.; Banck, M.; James, C.A.; Morley, C.; Vandermeersch, T.; Hutchison, G.R. Open Babel: An open chemical toolbox. *J. Cheminform.* **2011**, *3*, 33. [CrossRef]

52. *PyRx-Python Prescription v. 0.8*; The Scripps Research Institute: San Diego, CA, USA, 2008.

53. Chu, C.-H.; Li, K.-M.; Lin, S.-W.; Chang, M.D.-T.; Jiang, T.-Y.; Sun, Y.-J. Crystal structures of starch binding domain from Rhizopus oryzae glucoamylase in complex with isomaltooligosaccharide: Insights into polysaccharide binding mechanism of CBM21 family. *Proteins Struct. Funct. Bioinform.* **2014**, *82*, 1079–1085. [CrossRef]

54. Morris, G.M.; Goodsell, D.S.; Halliday, R.S.; Huey, R.; Hart, W.E.; Belew, R.K.; Olson, A.J. Automated docking using a Lamarckian genetic algorithm and an empirical binding free energy function. *J. Comput. Chem.* **1998**, *19*, 1639–1662. [CrossRef]

55. Trott, O.; Olson, A.J. AutoDock Vina: Improving the speed and accuracy of docking with a new scoring function, efficient optimization, and multithreading. *J. Comput. Chem.* **2010**, *31*, 455–461. [CrossRef]

56. Vanommeslaeghe, K.; Hatcher, E.; Acharya, C.; Kundu, S.; Zhong, S.; Shim, J.; Darian, E.; Guvench, O.; Lopes, P.; Vorobyov, I.; et al. CHARMM general force field: A force field for drug-like molecules compatible with the CHARMM all-atom additivebiological force fields. *J. Comput. Chem.* **2010**, *31*, 671–690. [CrossRef]

57. Yu, W.; He, X.; Vanommeslaeghe, K.; MacKerell, A.D., Jr. Extension of the CHARMM General Force Field to sulfonylcontaining compounds and its utility in biomolecular simulations. *J. Comput. Chem.* **2012**, *33*, 2451–2468. [CrossRef]

58. Jorgensen, W.L.; Chandrasekhar, J.; Madura, J.D.; Impey, R.W.; Klein, M.L. Comparison of Simple Potential Functions for Simulating Liquid Water. *J. Chem. Phys.* **1983**, *79*, 926–935. [CrossRef]

59. Allen, M.P.; Tildesley, D.J. *Computer Simulations of Liquids*; Clarendon Press: Oxford, UK, 1987.

60. Essmann, U.; Perera, L.; Berkowitz, M.L.; Darden, T.; Lee, H.; Pedersen, L.G. A Smooth Particle Mesh Ewald Method. *J. Chem. Phys.* **1995**, *103*, 8577–8593. [CrossRef]

61. Steinbach, P.J.; Brooks, B.R. New Spherical-Cutoff Methods for Long-Range Forces in Macromolecular Simulation. *J. Comput. Chem.* **1994**, *15*, 667–683. [CrossRef]

62. Humphrey, W.; Dalke, A.; Schulten, K. VMD: Visual molecular dynamics. *J. Mol. Graph.* **1996**, *14*, 28–33. [CrossRef]

63. DeLano, W.L. *PyMOL*; DeLano Scientific: San Francisco, CA, USA, 2002.

64. Frisch, M.J.; Trucks, G.W.; Schlegel, H.B.; Scuseria, G.E.; Robb, M.A.; Cheeseman, J.R.; Scalmani, G.; Barone, V.; Petersson, G.A.; Nakatsuji, H.; et al. *Gaussian 09, Revision E.01*; Gaussian, Inc.: Wallingford, CT, USA, 2009.

65. Becke, A.D. Density-functional thermochemistry. III. The role of exact exchange. *J. Chem. Phys.* **1993**, *98*, 5648. [CrossRef]

66. Hariharan, P.C.; Pople, J.A. The effect of d-functions on molecular orbital energies for hydrocarbons. *Chem. Phys. Lett.* **1972**, *16*, 217–219. [CrossRef]

67. Zhurko, G.A.; Zhurko, D.A. *Chemcraft-Graphical Program for Visualization of Quantum Chemistry Computations*, Academic Version 1.5 (2004); Ivanovo, Russia; 2004. Available online: https://www.chemcraftprog.com/ (accessed on 5 September 2022).

Spectroscopic and Molecular Docking Studies of Cu(II), Ni(II), Co(II), and Mn(II) Complexes with Anticonvulsant Therapeutic Agent Gabapentin

Moamen S. Refat [1,*] , **Ahmed Gaber** [2,3,*] , **Yusuf S. Althobaiti** [4,5] , **Hussain Alyami** [6] , **Walaa F. Alsanie** [3,7] , **Sonam Shakya** [8] , **Abdel Majid A. Adam** [1] , **Mohamed I. Kobeasy** [1] and **Kareem A. Asla** [9]

1   Department of Chemistry, College of Science, Taif University, P.O. Box 11099, Taif 21944, Saudi Arabia; majidadam@tu.edu.sa (A.M.A.A.); m.kobeasy@tu.edu.sa (M.I.K.)
2   Department of Biology, College of Science, Taif University, P.O. Box 11099, Taif 21944, Saudi Arabia
3   Centre of Biomedical Sciences Research (CBSR), Deanship of Scientific Research, Taif University, P.O. Box 11099, Taif 21944, Saudi Arabia; w.alsanie@tu.edu.sa
4   Department of Pharmacology and Toxicology, College of Pharmacy, Taif University, P.O. Box 11099, Taif 21944, Saudi Arabia; ys.althobaiti@tu.edu.sa
5   Addiction and Neuroscience Research Unit, Taif University, P.O. Box 11099, Taif 21944, Saudi Arabia
6   College of Medicine, Taif University, P.O. Box 11099, Taif 21944, Saudi Arabia; hmyami@tu.edu.sa
7   Department of Clinical Laboratories Sciences, the Faculty of Applied Medical Sciences, Taif University, P.O. Box 11099, Taif 21944, Saudi Arabia
8   Department of Chemistry, Faculty of Science, Aligarh Muslim University, Aligarh 202002, India; sonamshakya08@gmail.com
9   Department of Chemistry, Faculty of Science, Zagazig University, Zagazig 44519, Egypt; kareemnano2014@gmail.com
*   Correspondence: moamen@tu.edu.sa (M.S.R.); a.gaber@tu.edu.sa (A.G.)

Abstract: New Cu(II), Ni(II), Co(II), and Mn(II) complexes of the gabapentin (Gpn) bidentate drug ligand were synthesized and studied using elemental analyses, melting temperatures, molar conductivity, UV–Vis, magnetic measurements, FTIR, and surface morphology (scanning (SEM) and transmission (TEM) electron microscopes).The gabapentin ligand was shown to form monobasic metal:ligand (1:1) stoichiometry complexes with the metal ions Cu(II), Ni(II), Co(II), and Mn(II). Molar conductance measurements in dimethyl-sulfoxide solvent with a concentration of 10^{-3} M correlated to a non-electrolytic character for all of the produced complexes. A deformed octahedral environment was proposed for all metal complexes. Through the nitrogen atom of the $–NH_2$ group and the oxygen atom of the carboxylate group, the Gpn drug chelated as a bidentate ligand toward the Mn^{2+}, Co^{2+}, Ni^{2+}, and Cu^{2+} metal ions. This coordination behavior was validated by spectroscopic, magnetic, and electronic spectra using the formulas of the $[M(Gpn)(H_2O)_3(Cl)] \cdot nH_2O$ complexes (where n = 2–6).Transmission electron microscopy was used to examine the nanostructure of the produced gabapentin complexes. Molecular docking was utilized to investigate the comparative interaction between the Gpn drug and its four metal [Cu(II), Ni(II), Co(II), and Mn(II)] complexes as ligands using serotonin (6BQH) and dopamine (6CM4) receptors. AutoDock Vina results were further refined through molecular dynamics simulation, and molecular processes for receptor–ligand interactions were also studied. The B3LYP level of theory and LanL2DZ basis set was used for DFT (density functional theory) studies. The optimized geometries, along with the MEP map and HOMO → LUMO of the metal complexes, were studied.

Keywords: gabapentin; transition metals; spectroscopic; FTIR; electronic spectra; TEM

1. Introduction

GABAPENTIN (Gpn; Figure 1), is sold under the brand name neurontin, and is commonly named as 2-[1-(aminomethyl)cyclohexyl]acetic acid. Gpn is a structural analogue of

the neurotransmitter gamma aminobutyric acid, which has mostly been investigated for its inhibitory effect on the central nervous system [1]. Since Gpn has both acidic groups (COOH) and a basic group (NH$_2$), it is an artificial amino acid [1,2]. It is a antiepileptic drug that is utilized as both a supplement and a stand-alone treatment for people suffering from partial seizures [2]. Gpn has also been used in the treatment of neuropathic pain. For a growing number of individuals with epilepsy, a safe and effective seizure is a major concern. Epilepsy has a significant economic impact [3]. The effectiveness, tolerability, and safety of an antiepileptic medicine are all factors to consider when choosing one. Gpn can also be regarded as an emergent solution to the "pain puzzle". Double-blind and more randomized studies comparing analgesic medications to Gpn may be useful in determining the first-line treatment for chronic and acute pain relief [4]. As a result, finding compounds to treat epilepsy is necessary [5,6]. Metal-binding or metal-recognition sites are found in a variety of drugs and potential pharmacological agents. These sites can bind or interact with metal ions, influencing their bioactivities and possibly causing damage to their target biomolecules. The literature [7–10] has numerous examples of these "metallodrugs" and "metallopharmaceuticals" and their actions. Metals and metal complexes have played an important part in the evolution of contemporary chemotherapy. Anticancer platinum drugs, for example, are used in more chemotherapy regimens than any other class of anticancer drugs, and they have played a significant role in the success of cancer treatment over the last three decades [11].
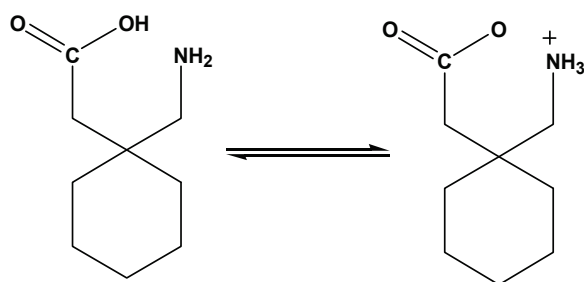

Figure 1. The zwitterion structure of the gabapentin (Gpn) drug.

After coordinating to a metal, *ligands* can play an essential role in changing the pharmacological characteristics of existing medications. Because the resulting prodrugs have varied physical and pharmacological properties, they can be delivered in a regulated manner or at a specific site [7]. This method can be used to save medications that have failed due to poor pharmacology or high toxicity. The complexation of nonsteroidal anti-inflammatory medications to copper, for example, eliminates some of the drugs' gastrointestinal adverse effects. In the hypoxic zones of solid tumors, the release of cytotoxins such as nitrogen mustards from redox-active metals such as cobalt has the potential to improve medication effectiveness and reduce toxicity [8].

Metal complexes have received less attention in medical chemistry than organic molecules [9]. Many organic chemicals employed in medicine, in reality, do not have a wholly organic mechanism of action and require the residues of metal ions for activation or biotransformation, either directly or indirectly. The status of metal ions and their complexes with biomolecules in the body affects our health, aging, physiological problems, and diseases. Metals make up about 0.03% of the weight of the human body. The concentrations of Cd, Cr, Ti, V, Cu, Se, and Zn in malignant sections of the kidney were shown to be lower than in noncancerous parts [10]. Coordination bonds can be formed by ligands with electron donor atoms such as N, O, S, and P. Chelation alters the biological properties of both ligands and metal moieties, and in many circumstances, it produces a synergistic interaction between the metal ion and the ligand [10].

Mechanosynthesis has been used to create a variety of Gpn coordination networks with Mn^{2+}, Y^{3+}, La^{3+}, Er^{3+}, Nd^{3+}, and Ce^{3+} [11,12]. In the literature survey, there appears to be a lack of study on the chelation behavior of gabapentin and its derivatives toward

metal ions [13,14]. Therefore, in this paper, the experimental plan aimed to synthesize some new Cu(II), Ni(II), Co(II), and Mn(II) complexes of gabapentin by refluxing some transition metal(II) chlorides with a basic solution of gabapentin in a 1:1 molar ratio in a methanol solvent. The structure of the obtained complexes was studied using spectral, magnetic, and morphological techniques. AutoDock Vina software was used to study the interactions between the receptors (serotonin and dopamine) and ligands [gabapentin (Gpn) and its four synthesized metal complexes ([Cu(II)–(Gpn)], [Ni(II)–(Gpn)], [Co(II)–(Gpn)], and [Mn(II)–(Gpn)]) were studied theoretically by the molecular docking method. For more clarity, the binding energy along with the aromatic, hydrogen bond, hydrophobic, SAS, ionizability, and interpolated charge surfaces at the interaction site were also generated. The molecular docking outputs were further investigated for receptor–ligand interactions through MDS (molecular dynamic simulation), which used a 100 ns run at 300 K. Structural stability, hydrogen bond interactions, SASA, compactness of structure, and residue flexibility of the complexes were studied to compare their dynamic features. The optimized geometries of ([Cu(II)–(Gpn)], [Ni(II)–(Gpn)], [Co(II)–(Gpn)], and [Mn(II)–zx(Gpn)] were obtained through the B3LYP level of theory and LanL2DZ basis set of the DFT calculations. Important parameters such as chemical, structural, and spectroscopic properties of the [Cu(II)–(Gpn)] complex were also obtained.

2. Materials and Methods

2.1. Chemicals

Metal chloride salts ($MnCl_2.4H_2O$ ($\geq$99%), $CoCl_2.6H_2O$ (98%), $CuCl_2.2H_2O$ ($\geq$99%), and $NiCl_2.6H_2O$ ($\geq$98%)) and gabapentin ($\geq$99%) were obtained from Sigma-Aldrich, USA and utilized in the preparation as received.

2.2. Instruments

The following is a list of the different types of analysis and their respective models:

Type of Analysis	Models
SEM	Quanta FEG 250 equipment
TEM	JEOL 100s microscopy
Magnetic moment	Magnetic Susceptibility Balance
Electronic spectra	UV2 Unicam UV/Vis Spectrophotometer
FTIR spectra	Bruker FTIR Spectrophotometer
Conductance	Jenway 4010 conductivity meter
Elemental analyses (C,H,N)	Perkin Elmer CHN 2400
Metal ions (Mn, Co, Cu, Ni)	An atomic absorption spectrometer model PYE-UNICAM SP 1900

2.3. Synthesis of Gpn Metal Complexes

2.3.1. Synthesis of the [Mn(Gpn)(H₂O)₃(Cl)]·4H₂O Complex

The synthesis of the manganese(II)complex was carried out by adding $MnCl_2 \cdot 4H_2O$ (1.98 g, 1.0 mmol) to the basic solution of the gabapentin ligand (Gpn) (1.72 g, 1.0 mmol) by neutralization (pH = ~7.0) using NH_3 solution. The mixture was stirred at 80 °C for 3 h. The dark brown precipitate of the manganese(II) complex was filtered and washed with distilled water three times, dried, and kept in desiccators. Yield: 77%. $C_9H_{30}ClMnNO_9$, Mwt. 386.73 g/mol (Found: C 27.87; H 7.76; N 3.59; Mn 14.08; Mwt. 386.73, calcd. C 27.95; H 7.82; N 3.62; Mn 14.21; m.p. > 234 °C).

2.3.2. Synthesis of [Co(Gpn)(H₂O)₃(Cl)]·6H₂O Complex

The synthesis of the cobalt(II) complex was carried out by adding $CoCl_2 \cdot 6H_2O$ (2.38 g, 1.0 mmol) to the basic solution of the gabapentin ligand (Gpn) (1.72 g, 1.0 mmol) by neutralization (pH = ~7.0) using the NH_3 solution. The mixture was stirred at 80 °C for 2 h. The dark blue precipitate of the cobalt(II) complex was filtered and washed with distilled water three times, dried, and kept in desiccators. Yield: 70%. $C_9H_{34}ClCoNO_{11}$,

Mwt. 426.75 g/mol (Found: C 25.23; H 7.98; N 3.24; Co13.76; Mwt. 426.75, calcd. C 25.33; H 8.03; N 3.28; Co13.81; m.p. > 237 °C).

2.3.3. Synthesis of [Cu(Gpn)(H$_2$O)$_3$(Cl)]·2H$_2$O Complex

The synthesis of copper(II) complex was carried out by adding CuCl$_2$·2H$_2$O (1.71 g, 1.0 mmol) to the basic solution of gabapentin ligand (Gpn) (1.72 g, 1.0 mmol) by neutralization (pH = ~7.0) using the NH$_3$ solution. The mixture was stirred at 80 °C for 2 h. The dark brown precipitate of the copper(II) complex was filtered and washed with distilled water three times, dried, and kept in desiccators. Yield: 72%. C$_9$H$_{26}$ClCuNO$_7$, Mwt. 359.30 g/mol (Found: C 30.03; H 7.16; N 3.87; Cu17.54; Mwt. 359.30, calcd. C 30.08; H 7.29; N 3.90; Cu17.69; m.p. > 232 °C).

2.3.4. Synthesis of [Ni(Gpn)(H$_2$O)$_3$(Cl)]·3H$_2$O Complex

The synthesis of the nickel(II) complex was carried out by adding NiCl$_2$·6H$_2$O (2.38 g, 1.0 mmol) to the basic solution of the gabapentin ligand (Gpn) (1.72 g, 1.0 mmol) by neutralization (pH = ~7.0) using the NH$_3$ solution. The mixture was stirred at 80 °C for 2 h. The green precipitate of the nickel(II) complex was filtered and washed with distilled water three times, dried, and kept in desiccators. Yield: 75%. C$_9$H$_{28}$ClNNiO$_8$, Mwt. 372.47 (Found: C 29.00; H 7.46; N 3.71; Ni 17.65; Mwt. 372.47, calcd. C 29.02; H 7.58; N 3.76; Ni 15.76; m.p. > 238 °C).

2.4. Computational Studies

2.4.1. Molecular Docking

All of the docking was conducted through an Intel(R) Core(TM) i5-4200U CPU-2.10 GHz, 64 bit processor. AutoDock Vina [15] program was used to perform the docking. The receptors serotonin and dopamine with PDB ID: 6BQH and 6CM4, respectively, were obtained through an online PDB bank [16]. Serotonin and dopamine were set up by cleaning the ligand and water molecules through Discovery Studio (DS) software (https://www.3ds.com/products-services/biovia/, accessed on 1 Febrauary 2022). DTool [17] was used to add polar hydrogen atoms and Kollman charges, while the Geistenger method was used to assign the partial charges. The ligands [gabapentin (Gpn) and its four complexes—([Mn(II)–(Gpn)], [Co(II)–(Gpn)], [Ni(II)–(Gpn)], and [Cu(II)–(Gpn)])]—in the PDBQT format were obtained using the OpenBabelIGUI program [18]. The energy of all of the ligands was minimized through PyRx-Python at 200 steps using the conjugate gradient optimization algorithm and MMFF94 force field [19]. Discovery Studio software was used to analyze the docking results.

2.4.2. Molecular Dynamics Simulation (MDS) Studies

To conduct the simulation, an "Intel(R) Xeon(R) CPU E5-2680 v4-2.40GHz, 64 bit" processor was used. MDS was performed using GROMACS version 2019.2 with a GROMOS96-43a1 force field. To initiate the MDS analysis, results obtained from molecular docking for Gpn and [Cu(II)–(Gpn)] with a high docking score were used. Topology and parameter files were created through CHARMM-GUI with the latest CGenFF [20,21]. To solve receptor–ligand structures in a triclinic box, SPC water models were used [22]. Twenty-seven Cl$^-$ and 28 Na$^+$ ions were added for neutralization at 0.15 M salt (Figure S1). A Leap-frog MD integrator for a 100 ns simulation time in the NPT/NVT equilibration run systems was exposed to the periodic boundary conditions (300 K and 1.0 bar) [23,24]. The RMSD (root mean square deviation), hydrogen bonding, SASA, and gyration radius were examined using gmx rms, gmxhbond, gmxsasa, and gmx gyrate tools, respectively [25]. PyMol/VMD and Grace Software [12,13] were used to prepare the different plots.

2.4.3. Density Functional Theory (DFT)

The Gaussian 09RevD.01 package [26] was used for the DFT/TD-DFT calculations. The molecules were optimized in their ground spin state B3LYP density functional to know

the exact position of the hydrogen atoms, as B3LYP, a hybrid method containing elements from DFT and the Hartree–Fock theory, was the first DFT exchange correlation functional to convince computational chemists that DFT could predict molecule physicochemical properties and reaction barriers with an accuracy comparable to some wave function-based methods but with much improved computational efficiency. The Los Alamos Effective Core Potentials lanL2DZ basis set was employed for the Mn, Co, Ni, and Cu atom while the split-valence 6-31G(d) basis set was applied for the other atoms [27]. A molecular electrostatic potential map (MEP) of the synthesized metal complexes were studied [28]. The IR frequencies were computed with full accuracy using animated modes of vibrations. To establish a good comparison between the experimental and theoretical wavenumbers, the scaling factor of 0.8522 was used. Moreover, structure-based molecular properties such as bond lengths, bond angles, atomic charges, total energy, electronic properties, and frontier molecular orbitals energy were calculated by this theory in the gas phase. ChemCraft 1.5 software [29] was used for visualization.

3. Results and Discussion

Herein, our paper aimed to synthesize a complexation between the gabapentin pure drug and four transition metal ions with a 1:1 molar ratio in alkaline media and check the suggested structures of the resulting complexes by spectroscopic characterizations. The difference between our synthesized complexes and others mentioned in the literature is the isolated 1:1 molar ratio complexation and the isolation at pH = 7. The articles mentioned in the literature dealing with the mixed gabapentin ligands and the isolation of the 1:2 molar ratio were different from our synthesized complexes. We looked at a lot of crystallites but could not find one that was adequate for full data capture. As a result, a complete dataset of nickel(II), cobalt(II), copper(II), and manganese(II) gabapentin complexes was not collected, and the discussion was based on the elemental analysis, melting points, molar conductivity, UV–Vis, magnetic measurements, FTIR, and surface morphology (scanning (SEM) and transmission (TEM) electron microscopes) as well as the theoretical study.

3.1. Elemental and Conductance Measurements

The gabapentin metal complexes of nickel(II), cobalt(II) copper(II), and manganese(II) are commonly soluble in DMSO (dimethyl sulfoxide) and DMF (dimethylformamide). The synthesized complexes had a stoichiometry ratio of 1:1 (metal:ligand), according to the elemental analytical data; the postulated structure of the complexes is well-supported by analytical data and other spectrum studies (Figure 2). The color, yield, and melting point data of all the compounds were introduced in experimental Section 2.3. In DMSO, the molar conductance of the solutions of all the complexes were in the range of 11–14 $\Omega^{-1}cm^2$ mole^{-1}. These experimental data indicate that complexes are non-electrolytes [30] in DMSO (10^{-3} M) at room temperature. Metal ions and Gpn ligand reactions with a 1:1 molar ratio yielded bidentate complexes. The Gpn ligand on reaction with Cu(II), Ni(II), Co(II), and Mn(II) salt yielded complexes that corresponded to the formulas $[Cu(Gpn)(H_2O)_3(Cl)]\cdot 2H_2O$, $[Ni(Gpn)(H_2O)_3(Cl)]\cdot 3H_2O$, $[Co(Gpn)(H_2O)_3(Cl)]\cdot 6H_2O$, and $[Mn(Gpn)(H_2O)_3(Cl)]\cdot 4H_2O$. The general compositions for the complexes are $[M(Gpn)(H_2O)_3(Cl)]\cdot nH_2O$ complexes (where n = 2–6). Elemental analyses of the prepared compounds indicate the formation of six coordination complexes containing one molecule of gabapentin as a bidentate ligand, one chlorine atom, and three water molecules. The absence of an absorption band at ca. 3400 cm^{-1} in the IR spectrum of the Gpn ligand shows that free amino groups were absent. A broad band was observed at ca. 1650–1680 cm^{-1}, which indicates the presence of water molecules from the complexes.
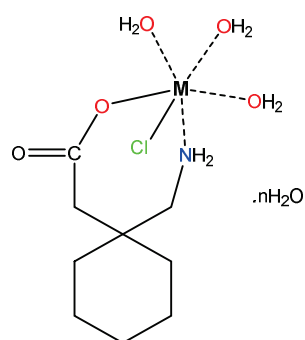
Figure 2. The structures of the synthesized Mn(II), Co(II), Ni(II), and Cu(II)–Gpn complexes, where = 2 for Cu(II), 3 for Ni(II), 4 for Mn(II), and 6 for Co(II).

The FTIR spectra of the pure gabapentin and each of the Cu(II), Ni(II), Co(II), and Mn(II)–Gpn complexes were also obtained (Figure 3 and Table 1).
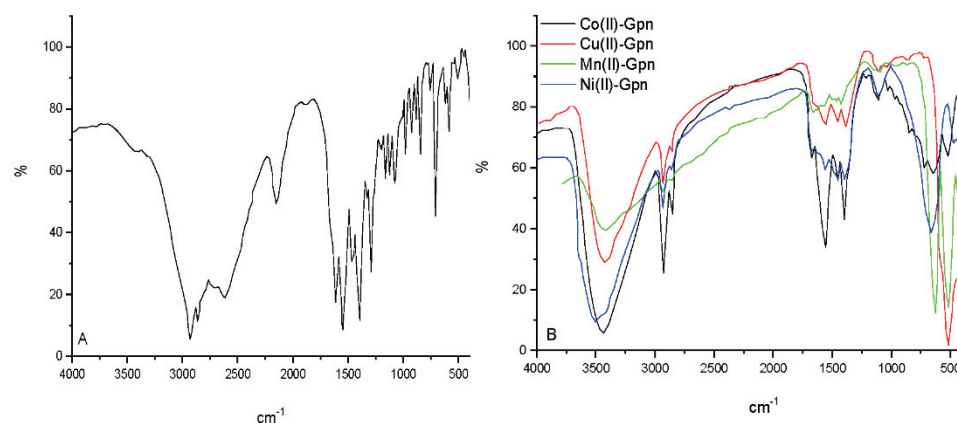

Figure 3. The infrared spectra of (**A**) Gpn free drug and (**B**) Mn(II), Co(II), Ni(II), and Cu(II)–Gpn complexes.

Table 1. Infrared spectral data (cm^{-1}) of Gpn and its complexes.

Compounds	Frequencies, cm^{-1}				
	$\nu_{as}(COO)$	$\nu_s(COO)$	$\delta(NH_2)$	$\nu(M\text{-}O)$	$\nu(M\text{-}N)$
Mn(II)	1650	1410	1568	617	502
Cu(II)	1660	1390	1558	612	516
Co(II)	1672	1398	1552	620	519
Ni(II)	1678	1395	1553	615	468

Regarding the infrared spectrum of the free gabapentin ligand, it did not show a peak of the stretching –NH within the region (3500–3300 cm^{-1}), since it is a zwitterion in the solid state [16,17]. The two main characteristic bands at 2928 and 2861 cm^{-1} were assigned to the –NH$_3^+$ stretching vibrations [31,32]. The peak at 2150 cm^{-1} was for the CN group side chain stretching vibration [32]. At 1614 and 1545 cm^{-1}, the peaks represented the stretching asymmetric vibration and vibrations of the NH$_3^+$ bending deformation of the carboxylate group, respectively [32]. In the 400–4000 cm^{-1} region, the FTIR spectra of the gabapentin complexes exhibited several bands. The $\delta(NH_2)$ bond vibration appeared at 1552–1568 cm^{-1} for the copper complex, which showed a shift to lower frequencies to free Gpn [33]. To identify the type of carboxylate binding to a transition metal ion, the value $\Delta\nu = [\nu_{as}(COO) - \nu_s(COO)]$ was employed. Generally, unidentate carboxylation is indicated by the difference in $\Delta\nu$ between the symmetric and asymmetric (COO) absorption frequencies of >200 cm^{-1}. In the nickel(II), cobalt(II), copper(II), and

manganese(II) complexes, the $\Delta\nu$ values were 283, 274, 270, and 240, cm^{-1}, indicating monodendate coordination of the carboxylate group [34]. In these synthesized complexes, it can be attributed to the Gpn ligand, which is linked to the metal ion by carboxylic acid atoms and the nitrogen of amino groups. Furthermore, the existence of ν(M–O) and ν(M–N) medium intensity bands at 612–620 cm^{-1} and 468–519, respectively, suggested the generation of Gpn complexes [35]. In the FTIR spectra, the characteristic bands of bending to water hydrated, δ(H$_2$O) at ca. 1650 cm^{-1} and broad absorption bands of (OH) with maximum at 3404–3507 cm^{-1} in synthesized metal complexes confirmed the presence of coordinated water molecules.

3.2. Electronic Spectra, and Magnetic Susceptibility Studies

3.2.1. Manganese(II) Complex

The molar conductance measurements showed that the Mn(II) complex is a non-electrolyte. Thus, it is formulated as [Mn(Gpn)(H$_2$O)$_3$(Cl)] 4H$_2$O. It showed a magnetic moment corresponding to five unpaired electrons (5.87 B.M.) at room temperature, which is close to the spin only value (5.92 B.M.). The electronic spectrum of this complex displayed weak absorption bands at 568 nm (ν1), 388 nm (ν2), 378 nm (ν3), and 369 nm (ν4), characteristic of octahedral geometry [36]. These bands may be assigned as $^6A_{1g} \rightarrow {}^4T_{1g}$, $^6A_{1g} \rightarrow {}^4E_g$, $^4A_{1g}$, $^6A_{1g} \rightarrow {}^4E_g$ and $^6A_{1g} \rightarrow {}^4T_{1g}$ transitions, respectively.

3.2.2. Cobalt(II) Complex

The molar conductance measurements showed that the complex is also a non-electrolyte. Thus, it may be formulated as [Co(Gpn)(H$_2$O)$_3$(Cl)] 6H$_2$O. At room temperature, it showed a magnetic moment of 4.90 B.M., a value in tune with a high-spin configuration showing the presence of a distorted octahedral environment around the cobalt(II) ion in the complex. The electronic spectrum of the complex displayed absorption bands at 610 and 542 nm. A distorted octahedral geometry, this complex is indicated through the investigation of this electronic spectral data [37]. The assignment of the spectral bands may be given as $^4T_1(F) \rightarrow {}^4A_2(F)$ and $^4T_1(F) \rightarrow {}^4T_1(P)$ transitions, respectively.

3.2.3. Copper(II) Complex

The molar conductance measurements showed that the complex is a non-electrolyte and that it may be formulated as [Cu(Gpn)(H$_2$O)$_3$(Cl)] 2H$_2$O. The magnetic moment of the complex was 1.96 B.M. The six-coordinate copper(II) complex had either D$_{4h}$ or C$_{4v}$ symmetry, and the E$_g$ and T$_{2g}$ levels of the 2D free ion split into B$_{1g}$, A$_{1g}$, B$_{2g}$, and E$_g$ levels, respectively. Thus, three spin-allowed transitions are expected in the visible and near-IR region, but only a few complexes are known in which such bands are resolved [38]. These bands were assigned to the following transitions, in order of increasing energy, $^2B_{1g} \rightarrow {}^2A_{1g}$, $^2B_{1g} \rightarrow {}^2B_{2g}$, and $^2B_{1g} \rightarrow {}^2E_g$. The energy level sequence will depend on the amount of tetragonal distortion due to ligand-field and Jahn–Teller effects [39]. The electronic spectrum of the complex showed a band at 722 nm and a well-defined shoulder at 620 nm, which may be assigned to the $^2B_{1g} \rightarrow {}^2A_{1g}$ and $^2B_{1g} \rightarrow {}^2E_g$ transitions, respectively.

3.2.4. Nickel(II) Complex

Nickel(II) has a (d^8) configuration with the following orgel diagram found at 780 nm, 398 nm, and 384 nm, respectively, for the nickel complex. Based on the orgel diagram, the first peak at 697 nm was assigned to $^3A_{2g} \rightarrow {}^3T_{2g}$, the second at 346 nm for $^3A_{2g} \rightarrow {}^3T_{1g}$ (F), and the third at 315 nm was due to the $^3A_{2g} \rightarrow {}^3T_{1g}$ (P) transition, respectively. This confirms the presence of an octahedral geometry for the nickel complex. The magnetic moment of the complex was 3.28 B.M. at room temperature, a value in tune with a high-spin configuration, showing the presence of a distorted octahedral environment around the nickel(II) ion in the complex. On the basis of magnetic, molar conductivity, molar ratio, UV/Vis., and the IR results, the proposed molecular structure of the synthesized complexes is octahedral (Figure 3) [37].

3.3. Scanning and Transmission Electron Microscopes

The SEM analysis was carried out to check the surface morphology of the selected complexes, and the micrographs obtained are given in Figure 4. The micrographs of the manganese(II), copper(II), cobalt(II), and nickel(II)–gabapentin complexes are given in Figure 5I–IV; it can be seen that these gave an appearance of pressed chips (a wooden board has several layers), a coral reef-like, a block of rock, and rectangular panels of different sizes, respectively.
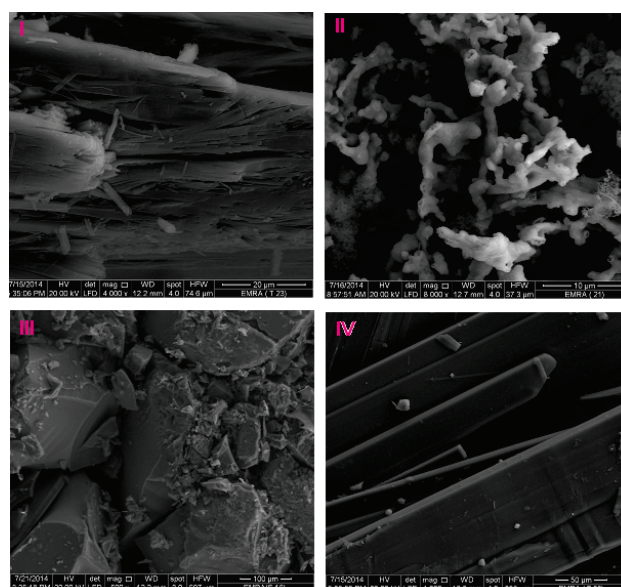

Figure 4. The SEM images of (**I**) Mn(II), (**II**) Cu(II), (**III**) Co(II), and (**IV**) Ni(II)–Gpn.
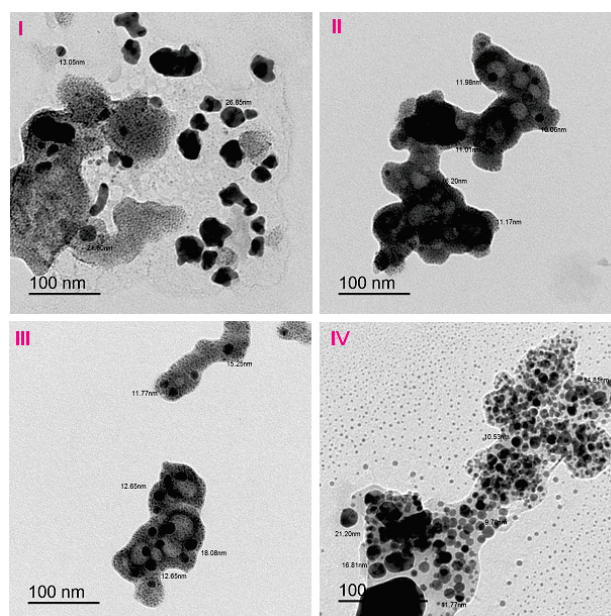

Figure 5. The TEM images of the (**I**) Mn(II), (**II**) Cu(II), (**III**) Co(II), and (**IV**) Ni(II)–Gpn complexes.

The TEM image (Figure 5I–IV) shows that the Mn(II)–Gpn, Cu(II)–Gpn, Co(II)–Gpn, and Ni(II)–Gpn complexes were aggregates with an irregular shape. The particle sizes of the [Mn(Gpn)(H$_2$O)$_3$(Cl)] 4H$_2$O, [Co(Gpn)(H$_2$O)$_3$(Cl)]·6H$_2$O, [Cu(Gpn)(H$_2$O)$_3$(Cl)] 2H$_2$O, and [Ni(Gpn)(H$_2$O)$_3$(Cl)] 3H$_2$O complexes were calculated from the TEM images with the ranges of 13–27 nm, 12–18 nm, 10–18 nm, and 10–20 nm, respectively (Figure 5).

3.4. Molecular Docking Studies

The interactions between the synthesized metal complexes—([Cu(II)–(Gpn), [Ni(II)–(Gpn)], [Co(II)–(Gpn)], and [Mn(II)–(Gpn)]]—with the prepared serotonin and dopamine receptors were studied, and the best docking poses were analyzed. For comparative purposes, the Gpn drug was used as the control. The results revealed that the potential binding energy of all of the metal complexes was higher than Gpn in both the receptors (Table 2).

Table 2. The docking score of the four metal complexes docked with two receptors [serotonin (6BQH) and dopamine (6CM4)].

S. No.	Receptor Complex	Binding Free Energy (kcal/mol)	
		PDB: 6BQH	PDB: 6CM4
1	[Mn(II)–(Gpn)]	−6.9	−6.6
2	[Co(II)–(Gpn)]	−7.0	−6.7
3	[Ni(II)–(Gpn)]	−6.9	−6.4
4	[Cu(II)–(Gpn)]	−7.2	−6.5
5	Gpn	−5.1	−4.8

Among the four metal complexes screened, [Cu(II)–(Gpn)] showed the highest docking energy. Docking of [Cu(II)–(Gpn)] with serotonin and dopamine gave the potential binding energy of −7.2 and −6.5 kcal/mol, respectively. The greater value of the binding energy in the case of [Cu(II)–(Gpn)]-serotonin (**CuGS**) suggests a stronger interaction than with dopamine. The docking data are given in Table 3, and the best docking pose (**CuGS**) is shown in Figure 6.

Table 3. The interactions of the [Cu(II)–(Gpn)] complex and Gpn with serotonin (6BQH).

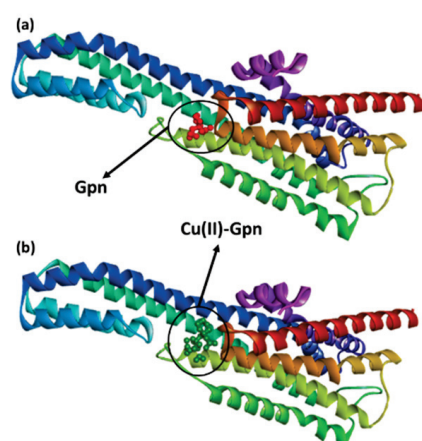| S. No.	Receptor	Binding Free Energy (kcal/mol)	Interactions	
			H-Bond	Others
1	[Cu(II)–(Gpn)]	−7.2	Arg173, Thr109, His182, and Asn187	Asp172 (Attractive charge) and Ala176, Arg173 (Alkyl)
2	Gpn	−5.1	Thr109 and Ala108	Ala321 (Alkyl)

Figure 6. The best docked pose showing a helical model of serotonin (PDB ID: 6BQH) docked with (**a**) the Gpn drug and (**b**) metal complex [Cu(II)–(Gpn)].

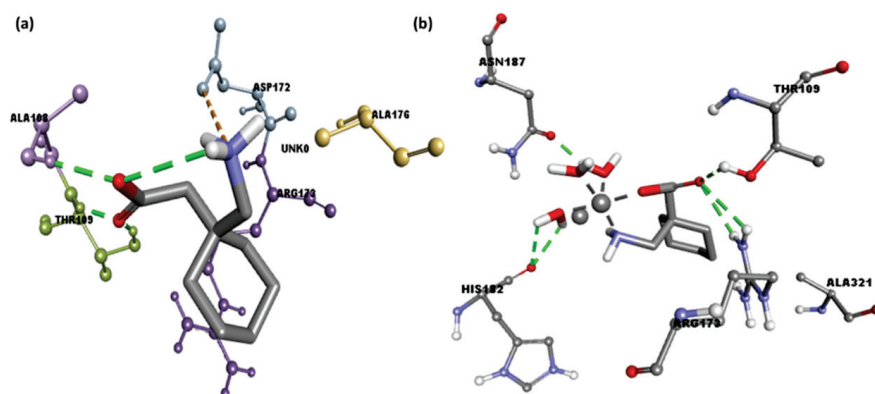An illustration of the molecular docking for the interactions of the ligands and receptor is depicted in Figure 7a,b.

Figure 7. The 3D representation of the interactions for serotonin (PDB ID: 6BQH) docked with (**a**) the Gpn drug and (**b**) metal complex [Cu(II)–(Gpn)].

As shown in Figure 8a, **CuGS** showed that the residues Arg173, Thr109, His182, and Asn187 had established hydrogen bonds. Additionally, Asp172 (Attractive charge) and Ala176 and Arg173 (Alkyl) interactions could also be seen [40,41]. Similarly, docking of the Gpn drug with serotonin and dopamine gave the potential binding energy of −5.1 and −4.8 kcal/mol, respectively. The greater value of the binding energy in the case of Gpn-serotonin (**GpnS**) suggests a stronger interaction than that with dopamine. Figure 8b shows the interaction between Gpn and serotonin, revealing that the residues Thr109 and Ala108 had established hydrogen bonds. Additionally, Ala321 showed alkyl interactions. These findings suggest that the metal [Cu(II)–(Gpn)] binds with the receptors more efficiently than the Gpn drug. The 2D representations of the interactions between the metal complex/drug and receptor are shown in Figure 8. The other binding details of the interactions are tabularized in Tables 4 and 5.
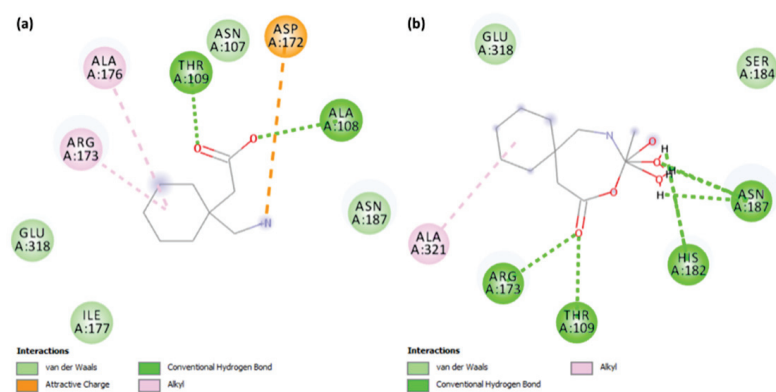

Figure 8. The 2D representation of interactions for serotonin (PDB ID: 6BQH) docked with (**a**) the Gpn drug and (**b**) metal complex [Cu(II)–(Gpn)].

**Table 4.** The [Cu(II)–(Gpn)]–serotonin interaction results by Discovery Studio.

Name	Distance	Category
THR109:HG1–[Cu(II)–Gpn]:O	2.50	Hydrogen Bond
ARG173:HH11–[Cu(II)–Gpn]:O	2.63	Hydrogen Bond
ARG173:HH12–[Cu(II)–Gpn]:O	2.78	Hydrogen Bond
ASN187:HD22–[Cu(II)–Gpn]:O	2.43	Hydrogen Bond
[Cu(II)-Gpn]:H26–HIS182:O	2.59	Hydrogen Bond
[Cu(II)-Gpn]:H26–HIS182:O	2.49	Hydrogen Bond
[Cu(II)-Gpn]:H25–ASN187:OD1	2.35	Hydrogen Bond
[Cu(II)-Gpn]:H25–ASN187:OD1	2.50	Hydrogen Bond
ALA321–[Cu(II)–Gpn]	5.31	Hydrophobic

Table 5. The Gpn–serotonin interaction results by Discovery Studio.

Name	Distance	Category
Gpn:N–ASP172:OD2	5.34	Electrostatic
ALA108:HN–Gpn:O	2.30	Hydrogen Bond
THR109:HN–Gpn:O	1.85	Hydrogen Bond
THR109:HG1–Gpn:O	1.97	Hydrogen Bond
Cu(II)-Gpn:H–Gpn:O	2.91	Hydrogen Bond
ARG173–Gpn	4.93	Hydrophobic
ALA176–Gpn	5.04	Hydrophobic

3.5. Solvent Accessible Surface, Aromatic, Ionizability, Hydrophobicity, and Hydrogen Bond Surfaces

Aromatic, hydrogen bond, hydrophobic, solvent accessible surface (SAS), ionizability, and interpolated charge surfaces at the interaction site (Figures 9 and S2) were studied through DS software [42]. The aromatic shown in Figure S2a shows the face surface as an orange color and the edge surface as a blue color. The green color in the hydrogen bond surface represents the acceptor area and the pink color is the donor area of the amino acid residues (Figure 9). The presence of hydrophilicity features of the receptor around the ligand was confirmed by the hydrophobicity surface (Figure S2b). The solvent accessibility surface (SAS) is the surface area of the receptor (Figure S2c) that is reachable to a solvent [43], the green color is the poorly accessible area, and the blue color is the highly accessible area [43]. The ionization surface reflects the acidic and basic propensity (Figure S2d, blue color = basic and red color = acidic).
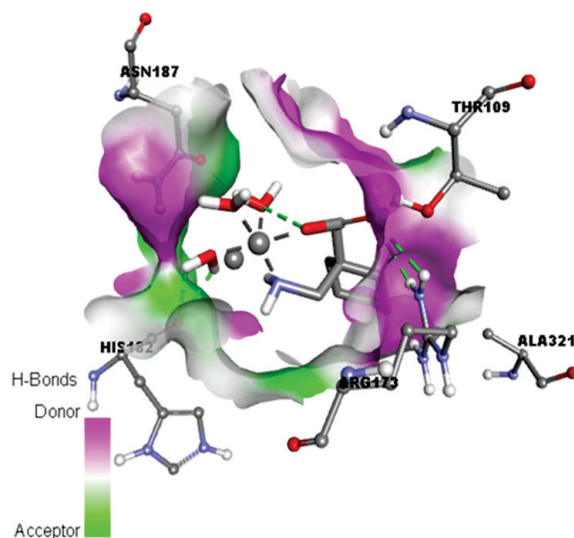
Figure 9. Representation of the hydrogen binding surface between the serotonin and metal complex [Cu(II)–(Gpn)].

3.6. MDS Analysis

The top docking results (**CuGS** and **GpnS**) were used for the MDS analysis of the 100 ns run. After studying the RMSD, it was observed that both **CuGS** and **GpnS** established a stable conformation after ~30 and ~75 ns, respectively, having appropriate values of RMSD of 2.15 and 2.75 Å, respectively (Figure 10).
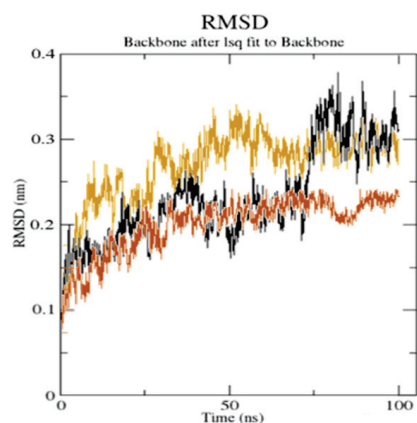
Figure 10. The root mean square deviation (RMSD) of the solvated receptor backbone and ligand complex during the 100 ns MD simulation [unbound serotonin receptor (yellow), **GpnS** complex (black), and **CuGS** complex (brown)]. According to the literature, a RMSD value under <3.0 Å is the most acceptable [44]. The drop in the RMSD value for **CuGS** showed an alteration in the secondary structure conformation of the protein due to the [Cu(II)–(Gpn)] interaction. This finding shows that **CuGS** developed a more stable combination. The results confirm that this interaction brings protein chains closer and reduces the gap between them, as shown in Figure 11 [45].
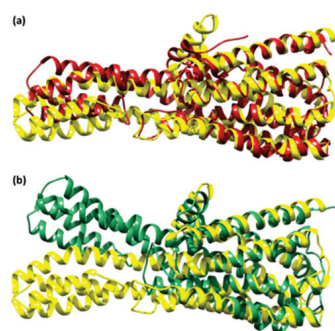

Figure 11. The superimposed structure of (**a**) the unbound serotonin receptor (yellow) and serotonin receptor after simulation (brown) for **GpnS** and (**b**) the unbound serotonin receptor (yellow) and serotonin receptor after simulation (green) for **CuGS**.

The average distance and standard deviation for all amino acid pairs between the two conformations were investigated using RR distance maps, which are two-dimensional representations of a protein's 3D structure [46]. Figure 12 represents the RR distance maps, which plot patterns of spatial interactions [47,48].
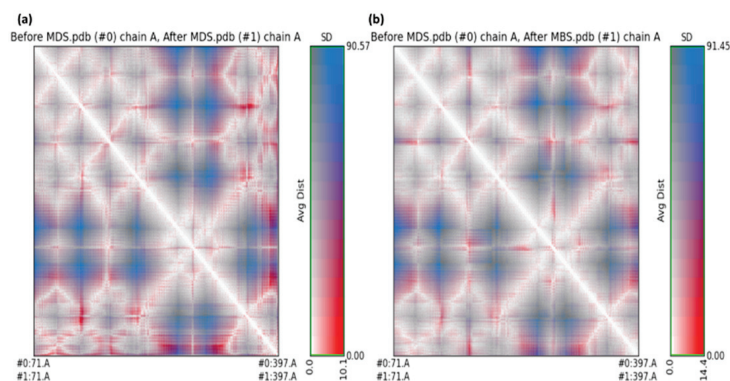

Figure 12. The RR distance map displaying patterns of spatial interactions between (**a**) the unbound serotonin receptor and the serotonin receptor after the simulation for **GpnS**; and (**b**) the unbound serotonin receptor and serotonin receptor after simulation for **CuGS**, showing the average distance and standard deviation for all amino acid pairs. (MDS = Molecular Dynamics simulation).

The zero distance between two residues is shown by the white diagonal on the map, whereas the red and blue components reflect residue pairs with the highest distance differences in the two conformations. The average radius of gyration (Rg) value of 25.75 and 26.75 Å was observed for **GpnS** and **CuGS**, respectively. It can be seen that over the simulation time, the Rg for **CuGS** decreased, indicating that the structures became more compact (Figure 13).
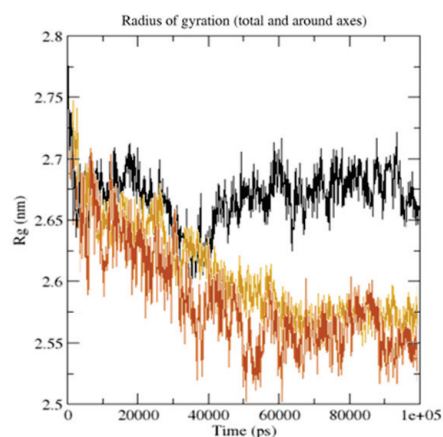

Figure 13. The radius of gyration (Rg) for the unbound serotonin receptor (yellow), **GpnS** complex (black), and **CuGS** complex (brown) during the 100 ns simulation time.

The grid search at $25 \times 11 \times 14 =$ grid and rcut = 0.35 revealed the H-bond between the receptor and ligand (**GpnS** and **CuGS**), plotted against time (Figure 14). On calculating the hydrogen bonds between the ligand (Gpn and [Cu(II)–(Gpn)]) and protein (3706 atoms), 508 donors and 987 acceptors were observed. The number of H-bonds per time frame on average were found to be 2.107 and 1.104 out of a possible 250,698 for **CuGS** and **GpnS**, respectively. Overall, it was discovered that the protein–receptor interaction increased the number of hydrogen bonds substantially, which was more in **CuGS**. Figure 15 shows that the SASA (solvent accessibility surface area) values changed due to the binding of the ligand (Gpn and [Cu(II)–(Gpn)]) to the receptor (serotonin). The decreased SASA value indicates the reduced pocket size and alteration in the protein structure conformation with increased hydrophobicity.
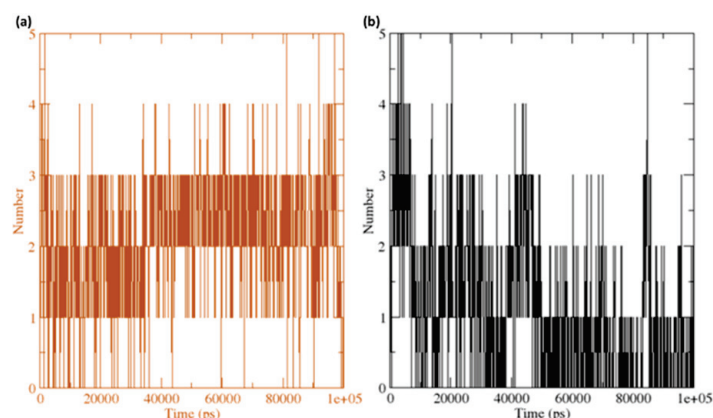

Figure 14. The number of average hydrogen bonding interactions between (**a**) the **CuGS** complex and (**b**) **GpnS** complex during the 100 ns simulation time.
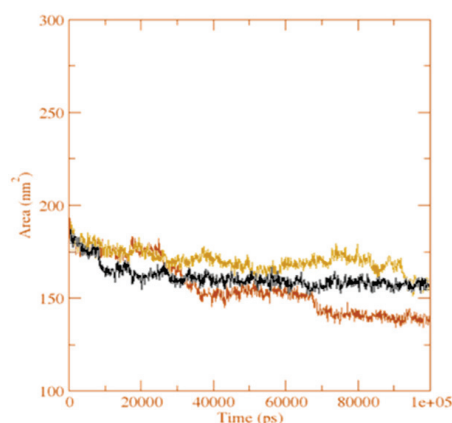
Figure 15. The solvent accessible surface area analysis for the unbound serotonin receptor (yellow), **GpnS** complex (black), and **CuGS** complex (brown) during the 100 ns simulation time.

3.7. DFT Calculations

The structures of all four synthesized metal complexes ([Mn(II)–(Gpn)], [Co(II)–(Gpn)], [Ni(II)–(Gpn)], and [Cu(II)–(Gpn)]) were optimized using the B3LYP level of theory and LanL2DZ basis set. The minimum SCF energy after 33, 22, 22, and 40 optimization steps was found to be −906.0136, −937.0486, −961.2607, and −988.0661 a.u., respectively, for ([Mn(II)–(Gpn)], [Co(II)–(Gpn)], [Ni(II)–(Gpn)], and [Cu(II)–(Gpn)], respectively. The optimized geometry of the four metal complexes is given in Figure 16.
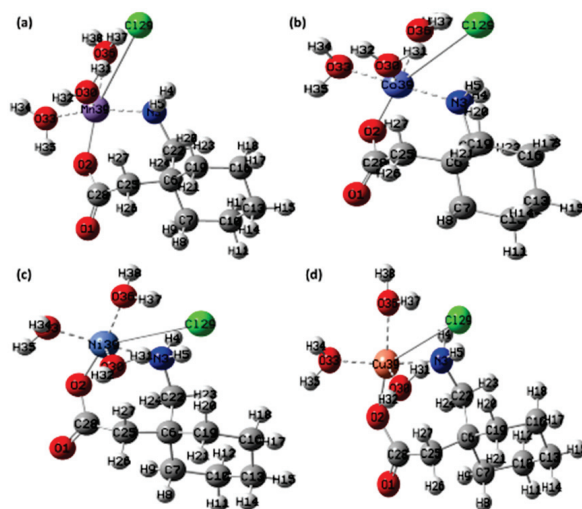

Figure 16. The optimized structure of the synthesized metal complexes (**a**) [Mn(II)–(Gpn)], (**b**) [Co(II)–(Gpn)], (**c**) [Ni(II)–(Gpn)], and (**d**) [Cu(II)–(Gpn)] with the Mulliken atom numbering scheme.

The strength of the electrostatic potentials for ([Mn(II)–(Gpn)], [Co(II)–(Gpn)], [Ni(II)–(Gpn)], and [Cu(II)–(Gpn)] was represented through the MEP map (Figure 17), in order to investigate the most electron rich and poor regions and to rationalize the noncovalent interactions. The electropositive regions are displayed in a blue color and the electronegative in a red color [49]. It was found that the area around the Cl and O atoms had strong negative electrostatic potential, and strong positive electrostatic potential could be seen around H_2O, which shows the preferential binding sites over the molecule. The MEP surface map is represented in the color scale from deep red to deep blue [50]. From the optimized structure of [Cu(II)–(Gpn)], the bond lengths and bond angles were obtained (Figure 18, Table 6). The Mulliken charges for [Cu(II)–(Gpn)] were also calculated (Table 7). The shift in the Mulliken charges were observed in atoms of the synthesized metal complexes from the reactant moieties, which suggests the formation of different complexes. The result of the MEP is in agreement with the Mulliken charges.
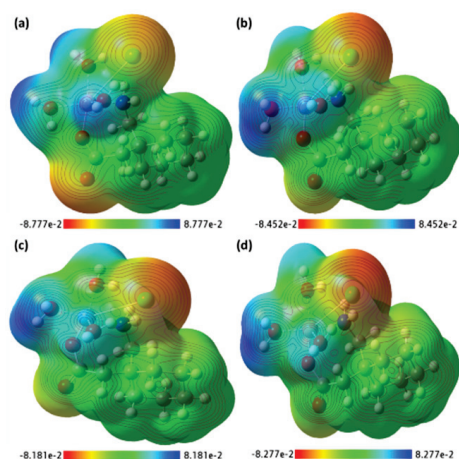
Figure 17. The MEP surface map of the synthesized metal complexes (**a**) [Mn(II)–(Gpn)], (**b**) [Co(II)–(Gpn)], (**c**) [Ni(II)–(Gpn)], and (**d**) [Cu(II)–(Gpn)] with the respective color scales.
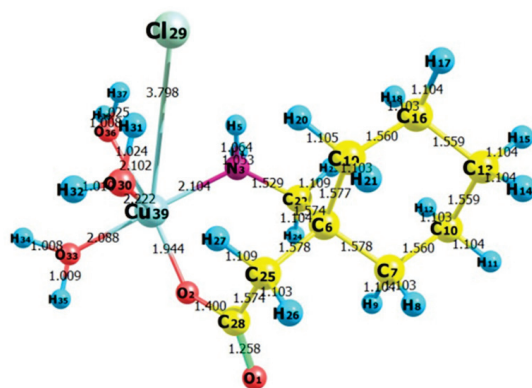

Figure 18. The optimized structure of the synthesized metal complex [Cu(II)–(Gpn)] showing bond lengths.

Table 6. The bond lengths of the metal complex [Cu(II)–(Gpn)] obtained through DFT.

S. No.	[Cu(II)–(Gpn)] (B3LYP/LanL2DZ)			
	Atom No.	Bond Length (Å)	Atom No.	Bond Length (Å)
1	R(1–28)	1.258	R(16–17)	1.104
2	R(2–28)	1.400	R(16–18)	1.103
3	R(2–39)	1.944	R(16–19)	1.56
4	R(3–4)	1.053	R(19–20)	1.105
5	R(3–5)	1.064	R(19–21)	1.103
6	R(3–22)	1.529	R(22–23)	1.109
7	R(3–39)	2.104	R(22–24)	1.104
8	R(6–7)	1.578	R(25–26)	1.103
9	R(6–19)	1.577	R(25–27)	1.109
10	R(6–22)	1.574	R(25–28)	1.574
11	R(6–25)	1.578	R(30–31)	1.024
12	R(7–8)	1.103	R(30–32)	1.01
13	R(7–9)	1.104	R(30–39)	2.222
14	R(7–10)	1.560	R(33–34)	1.008
15	R(10–11)	1.104	R(33–35)	1.009
16	R(10–12)	1.103	R(33–39)	2.088
17	R(10–13)	1.559	R(36–37)	1.025
18	R(13–14)	1.104	R(36–38)	1.008
19	R(13–15)	1.104	R(36–39)	2.102
20	R(13–16)	1.559	R(29–39)	3.798

Table 7. The Mulliken atomic charges of the metal complex [Cu(II)–(Gpn)] atoms.

S. No.	Synthesized [Cu(II)-(Gpn)] Complex			
	Mulliken Atomic Numbers	Mulliken Atomic Charges	MullikenAtomic Numbers	Mulliken Atomic Charges
1	1O	−0.19391	21H	0.06922
2	2O	−0.11703	22C	−0.06068
3	3N	−0.34646	23H	0.08103
4	4H	0.20606	24H	0.09072
5	5H	0.23817	25C	−0.16982
6	6C	0.02926	26H	0.08199
7	7C	−0.13471	27H	0.11175
8	8H	0.07097	28C	0.21118
9	9H	0.07212	29Cl	−0.7276
10	10C	−0.13351	30O	−0.28504
11	11H	0.07166	31H	0.24647
12	12H	0.06446	32H	0.20389
13	13C	−0.13247	33O	−0.25834
14	14H	0.06717	34H	0.23457
15	15H	0.06992	35H	0.23367
16	16C	−0.1326	36O	−0.28583
17	17H	0.07643	37H	0.25414
18	18H	0.06574	38H	0.21341
19	19C	−0.13937	C39u	−0.03369
20	20H	0.08705		

The IR frequencies were investigated through B3LYP/LanL2DZ (data not shown). The slight difference between the experimental and theoretical frequencies was due to the experimental values being obtained in the solid phase and theoretical values being acquired in the gas phase. The calculated vibrational frequencies varied to a smaller extent from the experimental results due to neglecting the incompleteness and anharmonicity of the basis set [51]. TD-DFT method was used to explore the nature of the electronic transitions in [Cu(II)–(Gpn)] in the gas phase. One broad electronic absorption band was obtained from TD-DFT at 569 nm. The HOMO (−4.2308 eV) to LUMO (−1.6620 eV) energy gap (ΔE) was calculated to be 2.5687 eV. The spatial arrangements of the HOMO–LUMO, associated energies, and gap are represented in Figure 19 [52–54]. Some molecular parameters in the gas phase, based on HOMO–LUMO and optimized geometry, are presented in Table 8.
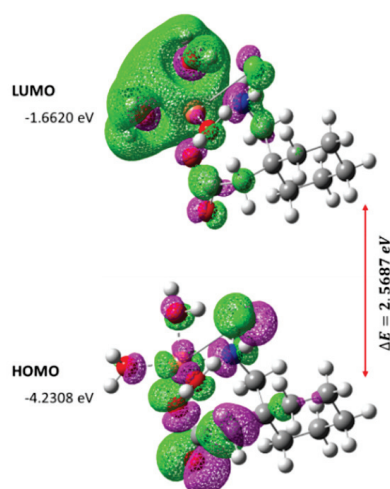

LUMO
-1.6620 eV

ΔE = 2.5687 eV

HOMO
-4.2308 eV

Figure 19. The spatial plot of HOMO and LUMO with their energy gap for the synthesized metal complex [Cu(II)–(Gpn)].

Table 8. The various other theoretical molecular parameters of the metal complex [Cu(II)–(Gpn)].

Parameters	RB3LYP/LanL2DZ
Minimum SCF energy (a.u.)	−982.219370
Polarizability (a) (a.u.)	84.074494
Dipole moment (Debye)	7.662013
Zero point vibrational energy (kcal/mol)	241.62872
Total thermal energy (kcal/mol)	253.148
Electronic spatial extent (a.u.)	5378.5506
Frontier MO energies (eV)	
LUMO	−1.6620
HOMO	−4.2308
Gap (HOMO–LUMO)	2.5687

4. Conclusions

The gabapentin drug coordinated in a 1:1 ligand to metal ratio as a monobasic bidentate (ON) donor in all of the complexes. The analytical, magnetic, molar conductance, infrared vibrational motions, and electronic spectral study suggest that the structures shown in Figure 2 have an octahedral arrangement. The TEM morphology showed that the complexes were in nanosize ranges. The molecular docking results showed that the [Cu(II)–(Gpn)] metal complex interacted with both receptors more efficiently than the gabapentin drug and among all of them, [Cu(II)–(Gpn)]–serotonin (CuGS) had the highest binding energy value. A molecular dynamic (MD) simulation with a 100 ns run revealed that the CuGS complex possesses a more stable complex with the serotonin receptor than GpnS. The theoretical data obtained by DFT calculations agreed with the experimental data.

Supplementary Materials: The following supporting information can be downloaded at: https://www.mdpi.com/article/10.3390/molecules27134311/s1, Figure S1: Receptor-ligand complex (a) CuGS and (b) GpnS in triclinic box solvated with water molecules and neutralized with 28 Na+ and 27 Cl- ions (0.15 M salt). Figure S2: Representation of (a) aromatic surface, (b) hydrophobic surface, (c) solvent accessible surface, (d) ionizability surface, and (e) Interpolated charge; between serotonin and metal complex [Cu(II)-(Gpn)].

Author Contributions: Conceptualization, formal analysis, software, and data curation. M.S.R., S.S. and A.G.; writing—original draft preparation, M.S.R. and S.S.; Validation, resources and investigation, Y.S.A., H.A. and W.F.A.; visualization, A.M.A.A., M.I.K. and K.A.A.; Funding acquisition, M.S.R. and W.F.A.; Writing—review and editing, W.F.A. and A.G. All authors have read and agreed to the published version of the manuscript.

Institutional Review Board Statement: Not applicable.

Informed Consent Statement: Not applicable.

Data Availability Statement: All of the data supporting the reported results are available in the manuscript.

Conflicts of Interest: The authors declare no conflict of interest.

References

1. Loscher, W.C. Current status and future in the pharmacology of epilepsy. *Trends Pharmacol. Sci.* **2002**, *23*, 113–118. [CrossRef]
2. Ananda, K.; Aravinda, S.; Vasudev, P.G.; Raja, K.M.P.; Sivaramakrishnan, H.; Nagarajan, K.; Shamala, N.; Balaram, P. Stereochemistry of gabapentin and several derivatives: Solid state conformations and solution equilibria. *Curr. Sci.* **2003**, *85*, 1002–1011.

3. McCabe, P.H. Role of levetiracetam in the treatment of epilepsy. *Expert Opin. Pharmacother.* **2000**, *1*, 633–674. [CrossRef]

4. Elmastas, M.; Gulcin, I.; Beydemir, S.; Kufreviogluo Aboul-Enein, H.Y. A study on the in vitro antioxidant activity of juniper seeds extracts. *Anal. Lett.* **2006**, *39*, 47–65. [CrossRef]

5. Regesta, G.; Tanganelli, P. Clinical aspects and biological bases of drug-resistant epilepsies. *Epilepsy Res.* **1999**, *34*, 109–122. [CrossRef]

6. Moretti, R.; Antonello, R.M.; Torre, P.; Cazzato, G. Headache and neck pain: Gabapentin as a possible treatment. *J. Headache Pain* **2000**, *1*, 155–161. [CrossRef]

7. Gielen, M.; Tiekink, E.R.T. (Eds.) *Metallotherapeutic Drugs and Metal-Based Diagnostic Agents, the Use of Metals in Medicine*; Wiley: Chichester, UK, 2005.

8. Weder, J.E.; Dillon, C.T.; Hambley, T.W.; Kennedy, B.J.; Lay, P.A.; Biffin, J.R.; Regtop, H.L.; Daview, N.M. Copper complexes of non-steroidal anti-inflammatory drugs: An opportunity yet to be realized. *Coord. Chem. Rev.* **2002**, *232*, 95–126. [CrossRef]

9. Nakai, M.; Sekiguchi, F.; Obata, M.; Ohtsuki, C.; Adachi, Y.; Sakurai, H.; Orvig, C.; Rehder, D.; Yano, S.J. Synthesis and insulin-mimetic activities of metal complexes with 3-hydroxypyridine-2-carboxylic acid. *Inorg. Biochem.* **2005**, *99*, 1275–1782. [CrossRef]

10. Sadler, P.J.; Guo, Z. Metal complexes in medicine: Design and mechanism of action. *Pure Appl. Chem.* **1998**, *70*, 863–871. [CrossRef]

11. Nadgi, A.; Mhlong, N.; Esoliman, M. Metal complexes in cancer therapy update from drug design perspective. *Drug Des. Dev. Ther.* **2017**, *11*, 599–618.

12. Hu, P.; Snyder, S.A. Enantiospecific Total Synthesis of the Highly Strained (−)-Presilphiperfolan-8-ol via a Pd-Catalyzed Tandem Cyclization. *J. Am. Chem. Soc.* **2017**, *14*, 5007–5017. [CrossRef] [PubMed]

13. Al-Mudhaffar, D.M.H.; Al-Mowali, A.H.; Al-Badran, U.H. Synthesis, Characterization, Biological Activities and Antioxidant Study of Gabapentin Derivatives and Their Complexes with [Cu (II), Zn (II). *Int. J. Appl.* **2018**, *8*, 105–116. [CrossRef]

14. Abd-Alrassol, K.S.; Qasim, Q.A.; AL-Salman HN, K.; Hussein, H.H. The Spectrophotometric Determination of Antiepileptic Drug in Standard and Pharmaceutical Formulations by Diazotization Coupling Reaction and Some Metals Complexes. *Syst. Rev. Pharm.* **2020**, *11*, 247–260.

15. Eberhardt, J.; Santos-Martins, D.; Tillack, A.F.; Forli, S. AutoDock Vina 1.2.0: New Docking Methods, Expanded Force Field, and Python Bindings. *J. Chem. Inf. Model.* **2021**, *61*, 3891–3898. [CrossRef] [PubMed]

16. Chu, C.-H.; Li, K.-M.; Lin, S.-W.; Chang, M.D.-T.; Jiang, T.-Y.; Sun, Y.-J. Crystal structures of starch binding domain from Rhizopus oryzae glucoamylase in complex with isomaltooligosaccharide: Insights into polysaccharide binding mechanism of CBM21 family. *Proteins Struct. Funct. Bioinform.* **2014**, *82*, 1079–1085. [CrossRef]

17. Rehman, M.T.; AlAjmi, M.F.; Hussain, A. Natural compounds as inhibitors of SARS-CoV-2 main protease (3CLpro): A molecular docking and simulation approach to combat COVID-19. *Curr. Pharm. Des.* **2021**, *27*, 3577–3589. [CrossRef]

18. O'Boyle, N.M.; Banck, M.; James, C.A.; Morley, C.; Vandermeersch, T.; Hutchison, G.R. Open Babel: An open chemical toolbox. *J. Cheminform.* **2011**, *3*, 33. [CrossRef]

19. Dallakyan, S. *PyRx-Python Prescription v. 0.8*; Scripps Research Institute: La Jolla, CA, USA, 2008; Volume 2010.

20. Bekker, H.; Berendsen, H.J.C.; Dijkstra, E.J.; Achterop, S.; Vondrumen, R.; Vanderspoel, D.; Sijbers, A.; Keegstra, H.; Renardus, M. Gromacs-a parallel computer for molecular-dynamics simulations. In *Proceedings of the 4th International Conference on Computational Physics (PC 92)*; World Scientific Publishing: Singapore, 1993; pp. 252–256.

21. Vanommeslaeghe, K.; Hatcher, E.; Acharya, C.; Kundu, S.; Zhong, S.; Shim, J.; Darian, E.; Guvench, O.; Lopes, P.; Vorobyov, I.; et al. CHARMM general force field: A force field for drug-like molecules compatible with the CHARMM all-atom additivebiological force fields. *J. Comput. Chem.* **2010**, *31*, 671–690. [CrossRef]

22. Abraham, M.J.; Murtola, T.; Schulz, R.; Páll, S.; Smith, J.C.; Hess, B.; Lindahl, E. GROMACS: High performance molecular simulations through multi-level parallelism from laptops to supercomputers. *SoftwareX* **2015**, *1*, 19–25. [CrossRef]

23. Allen, M.P.; Tildesley, D.J. *Computer Simulations of Liquids*; Clarendon Press: Oxford, UK, 1987.

24. Oostenbrink, C.; Villa, A.; Mark, A.E.; Van Gunsteren, W.F. A biomolecular force field based on the free enthalpy of hydration and solvation: The GROMOS force-field parameter sets 53A5 and 53A6. *J. Comput. Chem.* **2004**, *25*, 1656–1676. [CrossRef]

25. Steinbach, P.J.; Brooks, B.R. New Spherical-Cutoff Methods for Long-Range Forces in Macromolecular Simulation. *J. Comput. Chem.* **1994**, *15*, 667–683. [CrossRef]

26. Humphrey, W.; Dalke, A.; Schulten, K. VMD: Visual molecular dynamics. *J. Mol. Graph.* **1996**, *14*, 28–33. [CrossRef]

27. DeLano, W.L. The PyMOL Molecular Graphics System. PyMOL. DeLano Scientific. 2002. Available online: http://www.pymol.org (accessed on 15 March 2022).

28. Frisch, M.J.; Clemente, F.R. *Gaussian 09, Revision a. 01, Mjfrisch, gw Trucks, Hbschlegel, Gescuseria, ma Robb, Jrcheeseman*; Scalmani, G., Barone, V., Mennucci, B., Petersson, G.A., Nakatsuji, H., Caricato, M., Li, X., Hratchian, H.P., Izmaylov, A.F., Bloino, J., et al., Eds.; Gaussian Inc.: Wallingford, CT, USA, 2009; pp. 20–44.

29. Zhurko, G.A.; Zhurko, D.A. *Chemcraft—Graphical Program for Visualization of Quantum Chemistry Computations*; Academic Version 1.5: Ivanovo, Russia, 2004.

30. Geary, W.J. The use of conductivitymeasurements in organic solvents for the characterisation of coordination compounds. *Coord. Chem. Rev.* **1971**, *7*, 81–122. [CrossRef]

31. Hariharan, P.C.; Pople, J.A. The effect of d-functions on molecular orbital energies for hydrocarbons. *Chem. Phys. Lett.* **1972**, *16*, 217–219. [CrossRef]

32. Chimatadara, S.A.; Basavaraja, T.; Thabaja, K.A.; Sharanappa, T. Ruthenium (III) catalysed oxidation of gabapentin (neurontin) by diperiodatocuprate (III) in aqueous alkaline medium: A kinetic and mechanistic study. *J. Mol. Catal. A Chem.* **2007**, *267*, 65–71. [CrossRef]

33. Hsu, C.H.; Ke, W.T.; Lin, S.Y. Progressive steps of polymorphic transformation of gabapentin polymorphs studied by hot-stage FTIR microspectroscopy. *J. Pharm. Pharmaceut. Sci.* **2010**, *13*, 67–77. [CrossRef]

34. Kakanejadifard, A.; Esna-Ashari, F.; Hashemi, P.; Zabardasti, A. Spectrochim. *Acta A* **2013**, *106*, 80–85. [CrossRef]

35. Nakamoto, K. *Infrared Spectra of Inorganic and Coordination Compounds*, 6th ed.; Wiley: Hoboken, NJ, USA, 2009; Volume 978, p. 232.

36. Smith, H.E.; Neergaard, J.R.; Burrows, E.P.; Chen, F.M. Optically active amines. XVI. Exciton chirality method applied to the salicylidenimino chromophore. Salicylidenimino chirality rule. *J. Am. Chem. Soc.* **1974**, *96*, 2908–2916. [CrossRef]

37. Lever, A.B.P. *Inorganic Electronic Spectroscopy*; Elsevier: Amsterdam, The Netherlands, 1968; Volume 249.

38. Rana, V.B.; Singh, D.B.; Singh, P.; Teotia, M.P. Divalent nickel, cobalt and copper complexes of a tetradentate N6 macrocyclic ligand. *Transit. Met. Chem.* **1981**, *6*, 36–39. [CrossRef]

39. Procter, I.M.; Hathaway, B.J.; Nicholls, P.J. The electronic properties and stereochemistry of the copper(II) ion. Part I. Bis(ethylenediamine)copper(II) complexes. *Chem. Soc. A* **1968**, 1678–1684. [CrossRef]

40. Akram, M.; Lal, H.; Shakya, S.; Kabir-ud-Di. Multispectroscopic and Computational Analysis Insight into the Interaction of Cationic Diester-Bonded Gemini Surfactants with Serine Protease α-Chymotrypsin. *ACS Omega* **2020**, *5*, 3624–3637. [CrossRef] [PubMed]

41. Shakya, B.; Shakya, S.; Siddique, Y.H. Effect of geraniol against arecoline induced toxicity in the third instar larvae of transgenic Drosophila melanogaster (hsp70-lacZ) Bg9. *Toxicol. Mech. Methods* **2019**, *29*, 187–202. [CrossRef] [PubMed]

42. Khan, I.M.; Shakya, S.; Islam, M.; Khan, S.; Najnin, H. Synthesis and spectrophotometric studies of CT complex between 1, 2-dimethylimidazole and picric acid in different polar solvents: Exploring antimicrobial activities and molecular (DNA) docking. *Phys. Chem. Liq.* **2021**, *59*, 753–769. [CrossRef]

43. Krivák, R.; Jendele, L.; Hoksza, D. Peptide-Binding Site Prediction From Protein Structure via points on the Solvent Accessible Surface. In Proceedings of the 2018 ACM International Conference on Bioinformatics, Computational Biology, and Health Informatics, Washington, DC, USA, 29 August–1 September 2018.

44. Ranjbar, A.; Jamshidi, M.; Torabi, S. Molecular modelling of the antiviral action of Resveratrol derivatives against the activity of two novel SARS-CoV-2 and 2019-nCoV receptors. *Eur. Rev. Med. Pharmacol. Sci.* **2020**, *24*, 7834–7844. [PubMed]

45. Kufareva, I.; Abagyan, R. Methods of protein structure comparison. *Methods Mol. Biol.* **2012**, *857*, 231–257. [PubMed]

46. Khan, M.D.; Shakya, S.; Vu HH, T.; Habte, L.; Ahn, J.W. Low concentrated phosphorus sorption in aqueous medium on aragonite synthesized by carbonation of seashells: Optimization, kinetics, and mechanism study. *J. Environ. Manag.* **2021**, *280*, 111652. [CrossRef]

47. Dahham, S.S.; Ali, M.N.; Tabassum, H.; Khan, M. Studies on antibacterial and antifungal activity of pomegranate (*Punica granatum* L.). *Am. Eurasian J. Agric. Environ. Sci.* **2010**, *9*, 273–281.

48. Sohn, H.-Y.; Kwon, C.-S.; Son, K.-H. Fungicidal effect of prenylated flavonol, papyriflavonol A, isolated from *Broussonetiapapyrifera* (L.) vent. against Candida albicans. *J. Microbiol. Biotechnol.* **2010**, *20*, 1397–1402. [CrossRef]

49. Edziri, H.; Mastouri, M.; Mahjoub, M.A.; Mighri, Z.; Mahjoub, A.; Verschaeve, L. Antibacterial, Antifungal and Cytotoxic Activities of Two Flavonoids from Retama raetam Flowers. *Molecules* **2012**, *17*, 7284–7293. [CrossRef]

50. Shakya, S.; Khan, I.M.; Ahmad, M. Charge transfer complex based real-time colorimetric chemosensor for rapid recognition of dinitrobenzene and discriminative detection of Fe^{2+} ions in aqueous media and human hemoglobin. *J. Photochem. Photobiol. A Chem.* **2020**, *392*, 112402. [CrossRef]

51. Foresman, J.B. *Exploring Chemistry with Electronic Structure Methods: A Guide to Using Gaussian*; Frisch, E., Ed.; Gaussian, Incorporated: Pittsburg, PA, USA, 1996.

52. Islam, M.R.; Shakya, S.; Selim, A.; Alam, M.S.; Ali, M. Solvatochromic Absorbance and Fluorescence Probe Behavior within Ionic Liquid+ γ-Butyrolactone Mixture. *J. Chem. Eng. Data* **2019**, *64*, 4169–4180. [CrossRef]

53. Murugavel, S.; Ravikumar, C.; Jaabil, G.; Alagusundaram, P. Synthesis, crystal structure analysis, spectral investigations (NMR, FT-IR, UV), DFT calculations, ADMET studies, molecular docking and anticancer activity of 2-(1-benzyl-5-methyl-1H-1, 2, 3-triazol-4-yl)-4-(2-chlorophenyl)-6-methoxypyridine–a novel potent human topoisomerase IIα inhibitor. *J. Mol. Struct.* **2019**, *1176*, 729–742.

54. Khan, I.M.; Shakya, S. Exploring Colorimetric Real-Time Sensing Behavior of a Newly Designed CT Complex toward Nitrobenzene and Co^{2+}: Spectrophotometric, DFT/TD-DFT, and Mechanistic Insights. *ACS Omega* **2019**, *4*, 9983–9995. [CrossRef] [PubMed]